UNIVERSITÀ DEGLI STUDI DI MILANO
FACOLTÀ DI SCIENZE E TECNOLOGIE

GOETHE UNIVERSITÄT
FRANKFURT AM MAIN

Doctorate in

Chemistry, XXXV Cycle

Boraheterohelicenes: synthetic methodologies and properties of a novel class of boron π-conjugated systems

Luigi Menduti

Tutor

Prof. Emanuela Licandro

Prof. Dr. Matthias Wagner

Co-tutor

Dr. Clara Baldoli

Table of contents

List of abbreviations

α_D	Specific rotation
°C	Celsius degrees
Å	Ångström
BHHs	BoraHeteroHelicenes
$\Delta G_{rac}^{\ddagger}$	Racemization Gibbs Free Energy
$\Delta G_{enant}^{\ddagger}$	Enantiomerization Gibbs Free Energy
ΔE	Enantiomerization barrier measured by DFT
ε	Molar absorptivity
λ_{em}	Emission wavelength
λ_{abs}	Absorption wavelength
Φ_{PL}	Photoluminescence Quantum Yield
7TH	Tetrathia[7]helicene
ACQ	Aggregation Caused Quenching
AIE	Aggregation Induced Emission
APT	Attached Proton Test
Ar	Aryl
BDT	Benzo[1,2-b:4,3-b']dithiophene
Bu	Butyl
CD	Circular Dichroism
***c*-hexane**	Cyclohexane
COD	Cyclooctadiene
CPL	Circular Polarized Luminescence
CSP	Chiral Stationary Phase
CV	Cyclic Voltammetry
DFT	Density Functional Theory
DMF	*N,N*-dimethylformamide
ETL	Electron Transport Layer
dppf	1,1'-(diphenylphosphino)ferrocene
ee	Enantiomeric Excess
EI	Electron Ionisation
E_g	Energy gap, HOMO-LUMO gap
E_g^{opt}	Optical Energy gap
E_g^{CV}	Electrochemical Energy gap
E_{pa}	Electrochemical Oxidation Potential
E_{pc}	Electrochemical Reduction Potential
eV	Electron Volt
Fc	Ferrocene
FcH/FcH$^+$	Ferrocene/Ferrocenium couple
g_{abs}	Absorption dissymmetry factor
g_{lum}	Luminescence dissymmetry factor
HOMO	Highest Occupied Molecular Orbital
^{HH}COSY	H,H Correlation Spectroscopy
HMBC	Heteronuclear Multiple Bond Correlation
HPLC	High Performance Liquid Chromatography
HSQC	Heteronuclear Single Quantum Coherence Spectroscopy

HRMS High Resolution Mass Spectrometry

HTL Hole Transport Layer

hυ Light Irradiation

Hz Hertz

k Kinetic rate constant

k_{rac} Racemization kinetic rate constant

k_{enant} Enantiomerization kinetic rate constant

IR InfraRed spectroscopy

K Kelvin

LED Light-Emitting Diode

LUMO Lowest Unoccupied Molecular Orbital

m/z Mass to charge ratio

MALDI Matrix-Assisted Laser Desorption/Ionization

Me Methyl

Mes Mesityl

^{F}Mes 1,3,5-tris(trifluoromethyl)benzene

***n*-Bu** Normal butyl

[*n*Bu$_4$N]I Tetrabutylammonium iodide

NBS *N*-bromosuccinimide

NMR Nuclear Magnetic Resonance

OFET Organic Field-Effect Transistor

OLED Organic Light Emitting Diode

OPVC Organic Photo-Voltaic Cell

ORD Optical Rotatory Dispersion

ORTEP Oak Ridge Thermal Ellipsoid Plot Program

OTFT Organic Thin-Film Transistor

OMe Methoxy

Ph Phenyl

PAH Polycyclic Aromatic Hydrocarbon

R_f Retention Factor

R_t HPLC Retention Time

r.t. Room temperature

TBAPF$_6$ Tetrabutylammonium Hexafluorophosphate

TD-DFT Time-Dependent Density Functional Theory

***t*-Bu** *Tert*-butyl

THF Tetrahydrofuran

TLC Thin Layer Chromatography

TMSn Trimethylstannyl

TS Transition State

UV/vis Ultra-Violet/visible

V Volt

Zusammenfassung

Die Einführung eines trigonalen Boratoms in den Kern eines polyaromatischen Kohlenwasserstoffs (PAH) ist ein äußerst leistungsfähiges Werkzeug, um organische Gerüste mit optoelektronischen Eigenschaften und optimaler Verdichtung im festen Zustand zu versehen.[1] Bor-dotierte PAHs (B-PAHs) lassen sich jedoch aufgrund ihrer schlechten Löslichkeit oft schlecht verarbeiten. Die Verzerrung des Molekülgerüsts ist eine geeignete Strategie, um die Löslichkeitseigenschaften von B-PAHs zu verbessern und gleichzeitig gute Stapelungseigenschaften und eine ausreichende elektronische Konjugation zu erhalten. Eine extreme Verzerrung der Molekülstruktur kann bei schraubenförmigen PAHs erreicht werden, nämlich bei Helicenen[2] , bei denen es sich um schraubenförmige, inhärent chirale Polyzyklen handelt, die aus ortho-fusionierten aromatischen oder heteroaromatischen Ringen bestehen. Es wird erwartet, dass das Vorhandensein einer Helixstruktur in B-PAHs ihre physikalisch-chemischen Eigenschaften stark beeinflusst und zu Verbindungen führt, die sich durch besondere Merkmale auszeichnen, die für Anwendungen in funktionellen Materialien der nächsten Generation vielversprechend sind. Trotz des großen Potenzials dieser Verbindungsklasse sind in der Literatur nur wenige Beispiele für Borahelicene bekannt, die hauptsächlich aus Strukturen auf der Basis von Carbohelicenen bestehen.[3–5] Die beträchtliche strukturelle Vielfalt, die durch die Einführung verschiedener Bora-Heterocyclen (Oxaborin, Borol, Borepin) und anderer heteroaromatischer Ringe (Thiophen, Furan, Pyrrol) in dasselbe helikale Gerüst erreicht werden kann, deutet jedoch darauf hin, dass eine große Vielfalt von Verbindungen mit faszinierenden Eigenschaften über derzeit unerforschte synthetische Wege zugänglich sein könnte. Der Entwurf, die Synthese und die Untersuchung der Eigenschaften neuer Boraheterohelicene (**BHHs**) ist daher ein wichtiges Forschungsthema und Gegenstand dieses PhD-Projekts, das darauf abzielt, mehrere **BHHs** mit struktureller Vielfalt zu erhalten, sowie ihre Reaktivität, elektrochemischen und photophysikalischen Eigenschaften zu untersuchen, um ihr Potenzial als Bausteine für die Materialwissenschaft besser zu verstehen.

Die Arbeit wurde zum Teil an der Universität Mailand in den Labors von Prof. Emanuela Licandro und zum Teil an der Goethe-Universität Frankfurt am Main unter der Leitung von Prof. Dr. Matthias Wagner im Rahmen eines Co-Tutelle-Programms durchgeführt. Aufgrund der langjährigen Erfahrung der Gruppe von Prof. Licandro in der Synthese von Tetrathia[7]helicenen (**7TH**, Abbildung 1) und der Gruppe von Prof. Dr. Wagner in der Synthese von Bor-dotierten PAHs (z.B. Bor[4]helicen **4BH**; Abbildung 1) habe ich dieses Promotionsprojekt konzipiert, um eine Reihe von Thiahelicenen zu entwickeln, die eine oder mehrere B-O-Bindungen im Helixgerüst enthalten.

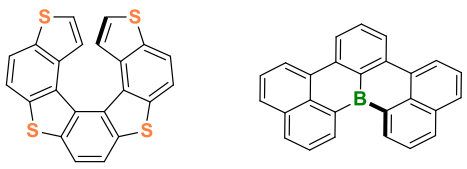

7TH 4BH

Abbildung 1. Tetrathia[7]helicen (**7TH**) und Bor[4]helicen (**4BH**).

Tetrathia[7]helicene, die aus abwechselnd fusionierten Thiophen- und Benzolringen bestehen, sind konfigurationsstabile Heterohelicene, die als Enantiomerenpaar vorliegen.[6] Diese Molekülklasse ist besonders interessant, da sie die Eigenschaften von Oligothiophenen mit denen von Helicenen vereint, was zu Systemen mit besonderen elektronischen und chiroptischen Eigenschaften führt, die sie zu attraktiven Bausteinen für Anwendungen in zahlreichen Wissenschaftsbereichen machen, darunter Optoelektronik,[7] Katalyse,[8] und Biologie.[9] Die Einführung eines trigonalen Boratoms in ein Thiahelicen-Gerüst führt zu einer neuen Klasse von unerforschten Bor-π-konjugierten Molekülen mit potenziell interessanten Eigenschaften.

Die vorliegende Doktorarbeit sollte daher einen bedeutenden Beitrag zur Entwicklung innovativer und vielseitiger Synthesen von BO-dotierten Tetrathia[7]helicenen sowie zur Untersuchung ihrer stereochemischen und optoelektronischen Eigenschaften leisten, um mögliche Anwendungen dieser Systeme in der Materialwissenschaft zu ermitteln.

Die ersten ausgewählten Strukturen mit einem oder zwei Oxaborinringen im Helixgerüst sind in Abbildung 2 dargestellt. Die Anwesenheit der sperrigen Mesitylgruppe am Boratom ist notwendig, um die Stabilität des Moleküls zu gewährleisten. Es ist bemerkenswert, dass Verbindung **2** das Skelettisomer von **1** ist, da die Richtung der B-O-Bindung in den beiden Molekülen entgegengesetzt ist. Im Verlauf der Forschungsarbeit wurde nach der Bewertung der photophysikalischen Eigenschaften von **1** das Helicen **2** entwickelt, um Informationen über die Struktur-Eigenschafts-Beziehung zu erhalten und zu bewerten, wie die Position der BO-Bindung im Helixgerüst die elektronischen Eigenschaften von BO-dotierten Thiahelicenen beeinflussen kann.

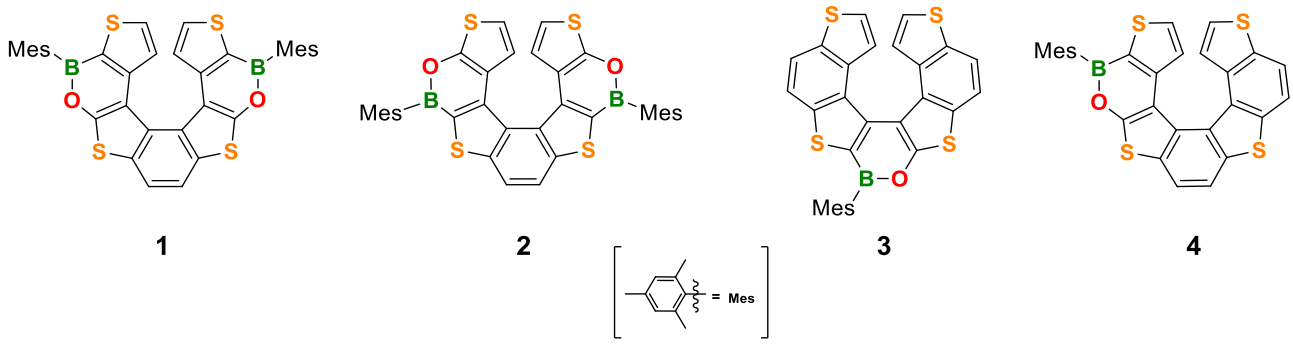

Abbildung 2. Erste ausgewählte Borathia[7]helicen-Strukturen.

Im Einzelnen hat sich die Arbeit auf die folgenden Hauptziele konzentriert:

1) Untersuchung der Synthese und der Eigenschaften des doppelt BO-dotierten Tetrathia[7]helicen **1** und seines "BO-Isomers" **2**;
2) Vorstudie zur Synthese von einfach BO-dotierten Tetrathia[7]helicenen **3** und **4**.

Untersuchung der Synthese und der Eigenschaften von BO-dotiertem Tetrathia[7]helicen 1

In der Literatur sind keine Beispiele für borhaltige Tetrathiahelicene bekannt. Im Rahmen dieses Forschungsprojekts haben wir mehrere geeignete Strategien für die Synthese der Zielmoleküle und ihrer Vorstufen entwickelt. In einem allgemeinen Syntheseschema wurde die Dithienooxaborin-**5**-Einheit als potenzieller gemeinsamer Baustein für die in Schema 1 dargestellten ausgewählten Strukturen **1**, **3** und **4** identifiziert.

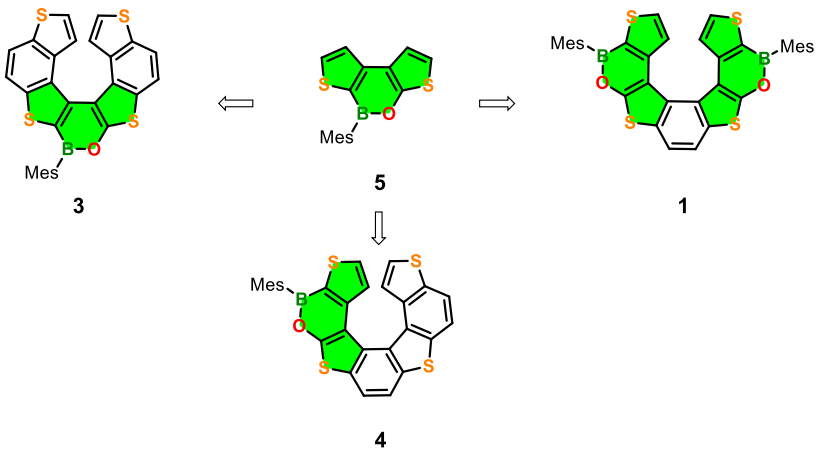

Schema 1. Allgemeines Syntheseschema für BO-dotierte Thiahelicene **1**, **3**, **4**.

Die Synthese des in der Literatur unbekannten Dithienooxaborins **5** (Schema 2) war das erste Ziel der Arbeit und wurde wie in Schema 2 gezeigt durch Behandlung des bekannten Methoxybithiophens **S1**[6] mit BCl_3 in Gegenwart von Et_3 N und [nBu_4 N]I realisiert, um das Zwischenprodukt **5-Cl** zu erhalten, das nach Behandlung mit MesMgBr das gewünschte Dithienyloxaborin **5** in 77 % Ausbeute ergab.

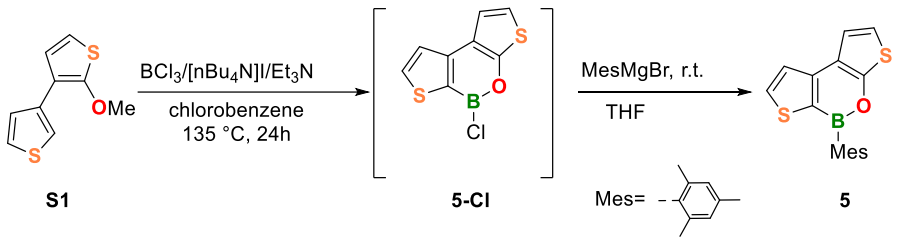

Schema 2. Synthese von **5**.

Ausgehend von Oxaborin **5** haben wir zunächst verschiedene Ansätze zur Herstellung von Helicen **1** in Betracht gezogen (Schema 3), entschieden uns aber unter Einbeziehung einiger vorläufiger Experimente für den in Schema 3 dargestellten Weg der Retrosynthese, bei dem das Ziel-Helicen **1** durch Photocyclisierung des BO-haltigen Alkenvorläufers **6** aus Dithieno-Oxaborin **5** erhalten wird**.**

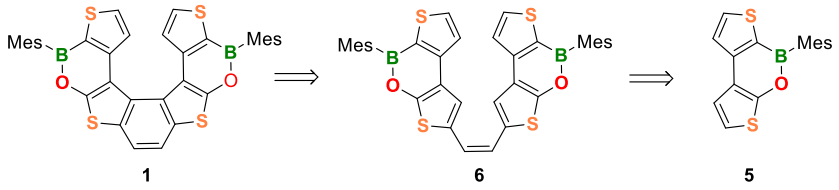

Schema 3. Vorgeschlagene retrosynthetische Analyse für **1**.

Die Synthese von **1** wird in Schema 4 näher erläutert.

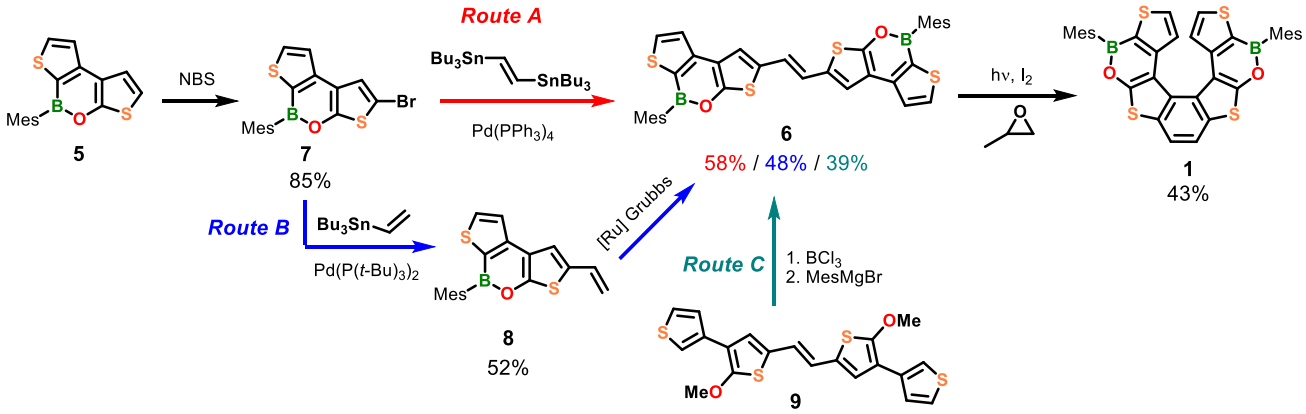

Schema 4. Syntheseweg zu Dioxabora-tetrathia[7]helicen **1.**

Ausgehend von Oxaborin **5** wurde die Synthese des Schlüsselintermediats Alken **6** eingehend untersucht und über drei verschiedene Routen (*Route A*, *B*, *C*) durchgeführt.

In den *Routen A* und *B* wurde das Oxaborin **5** mit N-Bromsuccinimid (NBS) bromiert, um α-Bromoxaborin **7** zu erhalten, das in der *Route A* mit 1,2-Bis(tributylstannyl)ethen durch eine Stille-Kupplung unter Verwendung von Pd(PPh)$_{34}$ als Katalysator umgesetzt wurde und Alken ***trans*-6** mit 58 % Ausbeute lieferte. Bei der *Route B* wurde **7** zunächst einer Stille-Kupplung mit Vinyltributylzinn unter Verwendung von Pd[P(*t-Bu*)]$_{32}$ als Katalysator unterzogen, was **8** in 52 % Ausbeute ergab, gefolgt von einer Dimerisierung durch eine Grubbs-Metathese, die zu **6** in 48 % Ausbeute führte. Die alternative *Route C* ermöglichte es, das Alken **6** in 39 % Ausbeute durch eine andere Strategie zu erhalten, die eine späte Bildung der beiden Oxaborinringe ausgehend von dem geeigneten bis-methoxyfunktionalisierten Alken **9** beinhaltet.[10] Trotz der geringeren Ausbeute ist es bemerkenswert, dass dieser Weg potenziell geeignet ist, um auf einfache Weise oxaborinsubstituierte Alkene mit verschiedenen heteroaromatischen Ringen zu erhalten.

Der letzte Schritt, die Photocyclisierung von Alken **6**, wurde in Benzol unter Verwendung einer 405-nm-LED-Lampe in Gegenwart von I_2 und Propylenoxid (um das in der Photocyclisierung gebildete HI einzufangen) durchgeführt und ergab erfolgreich das neue doppelt BO-dotierte Thiahelicen **1** in 43 % Ausbeute. Alle in Schema 4 gezeigten Verbindungen sind neu und wurden durch ^{1}H, ^{13}C und ^{11}B NMR, HRMS, CV und UV/Vis-Analyse vollständig charakterisiert und ihre Molekularstrukturen durch Röntgenkristallographie aufgeklärt. Die molekulare Röntgenstruktur des Targets Dioxabora-Thiahelicen **1** ist in Abbildung 3 dargestellt.

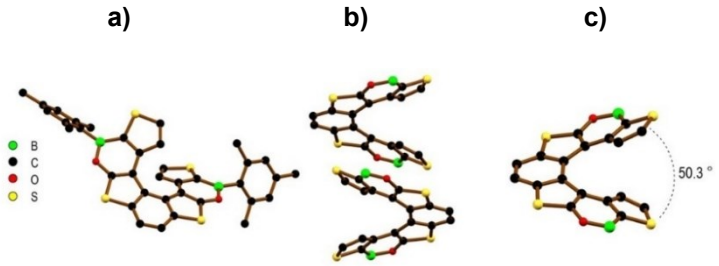

Abbildung 3. a) Röntgenmolekülstruktur des **1**-(*M*)-Enantiomers. b) Packung des (*P*)/(*M*)-Paares der Enantiomere c) Seitenansicht, Interplanarwinkel zwischen den beiden endständigen Thiophenringen; in b) und c) sind die Mesitylgruppen aus Gründen der Übersichtlichkeit weggelassen.

Wie bereits erwähnt, ist Borahelicen **1** ein chirales Molekül. Chiroptische und kinetische Studien zu **1** wurden in Zusammenarbeit mit der Gruppe von Prof. Claudio Villani (Universität Rom "La Sapienza") und Prof. Giovanna Longhi (Universität Brescia) durchgeführt. Die beiden Enantiomere (*P*)-/(*M*)-**1** wurden durch chirale HPLC aufgetrennt (Abbildung 4a, blaue Spur) und erwiesen sich bei Raumtemperatur als konfigurationsstabil mit optischen Rotationswerten von +97.7° bzw. –97.5°. An den Enantiomeren von **1** wurden optische Stabilitätsstudien durchgeführt, die es ermöglichten, die freie Energie der Racemisierung $\Delta G_{rac}^{\ddagger} = 26.9 \pm 0.1$ kcal mol^{-1} zu bestimmen, die deutlich niedriger ist als die der Thiahelicene,[11] was darauf hindeutet, dass die BO-Dotierung die mechanische Festigkeit des Helixgerüsts stark beeinflusst. Zirkulardichroismus (CD)-Spektren der beiden Enantiomere zeigten ein perfektes spiegelbildliches Verhältnis (Abbildung 4b, schwarze und rote Spur). Zur Bestimmung der absoluten Konfigurationen der beiden Enantiomere wurde das CD-Spektrum von (*M*)-**1** mit TD-DFT berechnet (Abbildung 4b, orange gestrichelte Spur). Die gute Übereinstimmung zwischen den berechneten und den experimentellen Daten ermöglichte es, die (*M*)-Konfiguration dem zweiten eluierten Enantiomer zuzuordnen ($\alpha_D = -97.5°$).

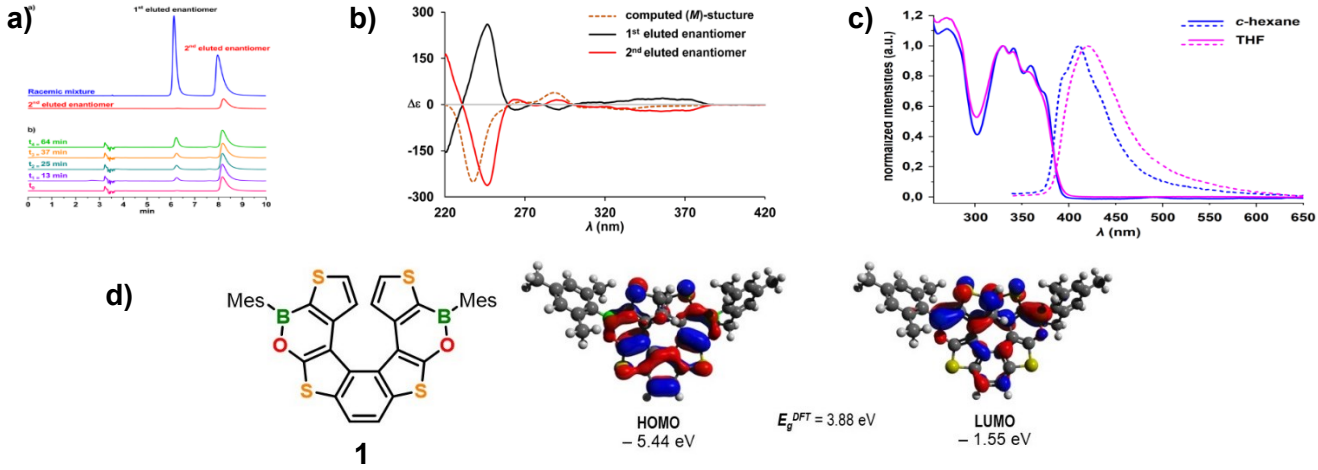

Abbildung 4. a) oben: Analytische HPLC-Auflösung von **1** in n-Hexan/CH_2Cl_2 (95:5), schwarze und rote Spur; berechnetes CD-Spektrum von (*M*)-**1** auf dem e M06/6-311g G(d,p)-Niveau, orange gestrichelte Spur. c) Absorptions-/Emissionsspektren von **1** in *c*-Hexan und THF. d) HOMO/LUMO-Verteilungen von **1** berechnet auf dem B3LYP/6-31G*-Niveau.

Um das Potenzial von BO-dotiertem Helicen **1** für materialwissenschaftliche Anwendungen zu bewerten (z. B. als Baustein für Emissions-/Elektronentransportmaterialien für OLED-Geräte), wurden seine Eigenschaften auch mittels zyklischer Voltammetrie, UV/Fluoreszenzspektroskopie sowie DFT/TD-DFT-Berechnungen untersucht. Die zyklische Voltammetrie zeigte zwei irreversible Redoxereignisse mit Spitzenpotentialen von E_{pc} = –2.83 und -3,01 V im kathodischen Scan. DFT-Berechnungen ergaben, dass die LUMO-Orbitale (E_{LUMO}^{DFT} = -1.55 eV) hauptsächlich an den terminalen, formal B(sp^2)-substituierten Thiophenringen lokalisiert sind, während die HOMO-Orbitale (E_{HOMO}^{DFT} = –5.44 eV) über das gesamte helikale Fragment verteilt sind (Abbildung 4d). Die UV-/Fluoreszenzspektroskopie ergab, dass **1** ein blauer Emitter ist und seine Emissionsbande eine teilweise aufgelöste Schwingungsfeinstruktur in *c*-Hexan zeigt (Abbildung 4c, blaue Spur) mit einer Photolumineszenz-Quanteneffizienz von Φ_{PL} = 6 % (*c*-Hexan*;* vgl. Vorläufer **7TH**: $\lambda_{em} \approx$ 405 nm, Φ_{PL} = 5%). [12] Die Ergebnisse der optoelektronischen Studien zeigen, dass **1** nicht für Anwendungen in funktionellen Materialien geeignet ist, aber dass die vielseitigen synthetischen Ansätze zu seiner Herstellung (siehe Schema 4) vielfältige strukturelle Modifikationen (Umkehrung der BO-Vektoren, BN-Dotierung) ermöglichen, die als Werkzeug zur Gewinnung neuer Derivate mit verbesserten optoelektronischen Leistungen dienen könnten. Helicen **1** ist das erste BO-dotierte Thiahelicen in der Literatur und die Ergebnisse dieser Studie wurden als Forschungsartikel in Angewandte Chemie Int. Ed. veröffentlicht.[13]

Untersuchung der Synthese und der Eigenschaften von BO-dotiertem Tetrathia[7]helicen 2

Auf der Grundlage der photophysikalischen Eigenschaften von **1** und mit dem Ziel, seine optoelektronischen Eigenschaften zu verbessern (z. B. rotverschobene Absorption-Emission/ höheres Φ_{PL}), haben wir das Helicen **2** (Abbildung 5) entwickelt, ein Skelettisomer von **1**, das durch die formale Umkehrung der beiden BO-Bindungen im Ausgangsmaterial **1** entstanden ist.

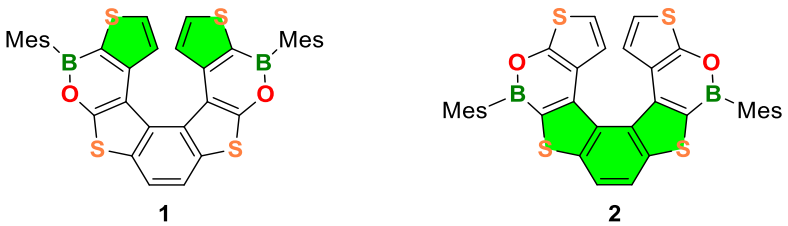

Abbildung 5. Struktur und LUMO-Verteilung (grün) von **1** und, erwartete LUMO-Verteilung des 2-Isomers mit BO-invertierten Bindungen.

Es wird erwartet, dass **2** LUMO-Orbitale aufweist, die sich über das gesamte zentrale Thiophen-Benzol-Thiophen-Fragment (BDT) erstrecken und nicht über die endständigen Thiophenringe wie in **1** (Abbildung 5). Die Erweiterung der LUMO-Orbitale sollte zu einer verringerten Energielücke, rotverschobenen

Absorptions-/Emissionsbanden, erhöhtem Reduktionsvermögen und somit zu verbesserten optoelektronischen Leistungen führen. Diese Hypothese wurde auch durch vorläufige DFT-Berechnungen bestätigt (Abbildung 6b).

Das Bora-Helicen-Isomer **2** wurde nach der späteren Borylierungsstrategie synthetisiert (siehe *Route C* für **1** in Schema 4). Zu diesem Zweck wurde das Alken **10,** das in guter Ausbeute aus 3-Brom-2-thiophencarbaldehyd hergestellt wurde (Schema 5), zunächst boryliert, um **11** zu erhalten und dann mit einer LED-Lampe bei 395 nm photocyclisiert, wodurch das Ziel-Helicen **2** entstand.

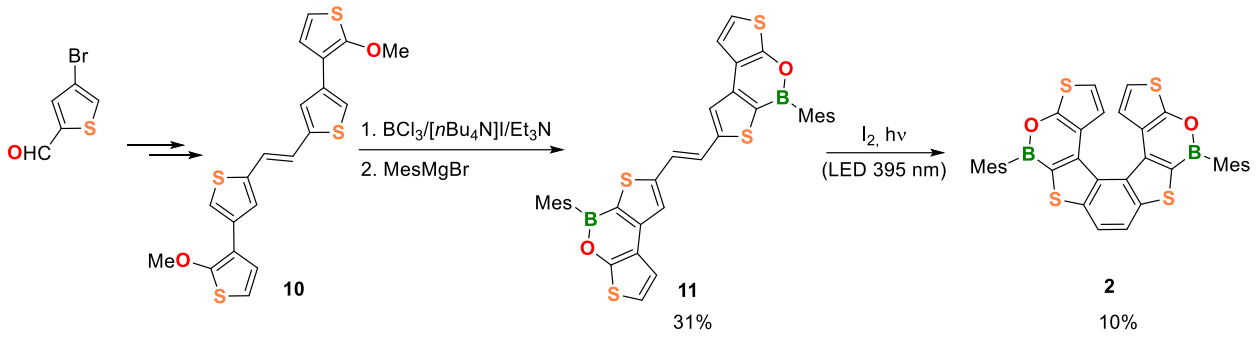

Schema 5. Syntheseweg zum BO-dotierten Tetrathia[7]helicen-Isomer **2**.

Obwohl das Syntheseprotokoll noch optimiert werden muss, konnte mit dem Verfahren Bora-Helicen **2** als zweites Beispiel für ein doppelt mit Bor dotiertes Thiahelicen in ausreichender Menge für die analytische und photophysikalische Charakterisierung gewonnen werden (Abbildung 6).

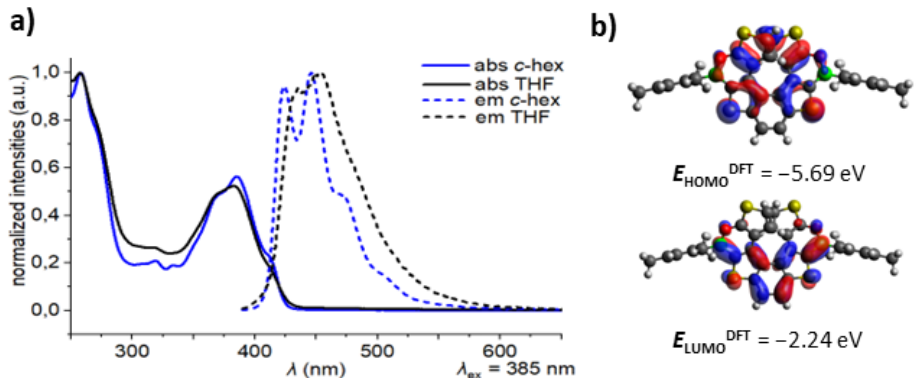

Abbildung 6. a) UV/Fluoreszenzspektren von **2** in *c*-Hexan (blaue Spur) und THF (schwarze Spur). b) HOMO/LUMO-Verteilung von **2**, berechnet auf dem B3LYP/6-31G*-Niveau.

In *c*-Hexan weist **2** eine strukturierte UV/Vis-Absorptionsbande auf, wobei die am stärksten bathochrome Schulter bei 413 nm erscheint (Abbildung 6a, blaue Linie). Zum Vergleich: Die entsprechende Schulter im Spektrum von **1** befindet sich bei 374 nm. **2** ist ein blauer Emitter, und seine Emissionsbande zeigt eine teilweise aufgelöste Schwingungsfeinstruktur mit der hypsochromen Schulter bei 472 nm und einer Photolumineszenz-Quanteneffizienz von Φ_{PL} = 7% (*c*-Hexan; vgl. **1**: $\lambda_{em} \approx$ 411 nm, Φ_{PL} = 6%). Die Absorptions- und Emissionsbanden von **2** sind gegenüber denen von **1** deutlich rotverschoben. DFT-

Berechnungen ergaben, dass das LUMO von **2** über das gesamte zentrale Thiophen-Benzol-Thiophen-Fragment verteilt ist und sich somit weiter erstreckt als das von **1**.

Zusammengenommen haben diese Ergebnisse gezeigt, dass die Inversion der BO-Vektoren ein geeignetes Mittel zur Abstimmung des LUMO von BO-dotierten Thiahelicenen darstellt. Obwohl sie im speziellen Fall von **2** keine nennenswerten Auswirkungen auf die optoelektronischen Leistungen hatte (immer noch niedriges Φ_{PL} und nur geringfügige Senkung der LUMO-Energie), bilden sie die Grundlage für die strukturelle Entwicklung neuer Derivate mit abgestimmten elektronischen Eigenschaften. Die Razemisierungskinetik und die chiroptischen Eigenschaften von **2** werden in Zukunft untersucht werden. In der Zwischenzeit war die Arbeit auf die Synthese der Oxabora-Thiahelicene **3** und **4** ausgerichtet, die einen Oxaborinring in verschiedenen Positionen des Helixgerüsts enthalten (siehe Abbildung 2).

Vorläufige Studie über die Synthese von einfach BO-dotierten Tetrathia[7]helicenen 3 und 4

Für die Synthese von mono-BO-dotiertem Thiahelicen **3** haben wir erneut die Borylierung von Bis-Alken **12** in Betracht gezogen, um das Oxaborin-Derivat **13** vor dem Schritt der Photocyclisierung zu erhalten. Dieser letzte Schritt zur Gewinnung von **3** wird derzeit untersucht, obwohl erste photochemische Versuche es ermöglichten, ein fast äquimolares Gemisch von cis/trans-Isomeren des mono ringgeschlossenen Produkts **14** zu isolieren (Schema 6). Die beiden Strukturen wurden durch ^{1}H NMR und ^{HH}COSY-Spektren identifiziert. Darüber hinaus wurden Kristalle von ***trans*-14** gewonnen, deren Struktur durch HRMS und Röntgenanalyse bestätigt wurde (Abbildung 7).

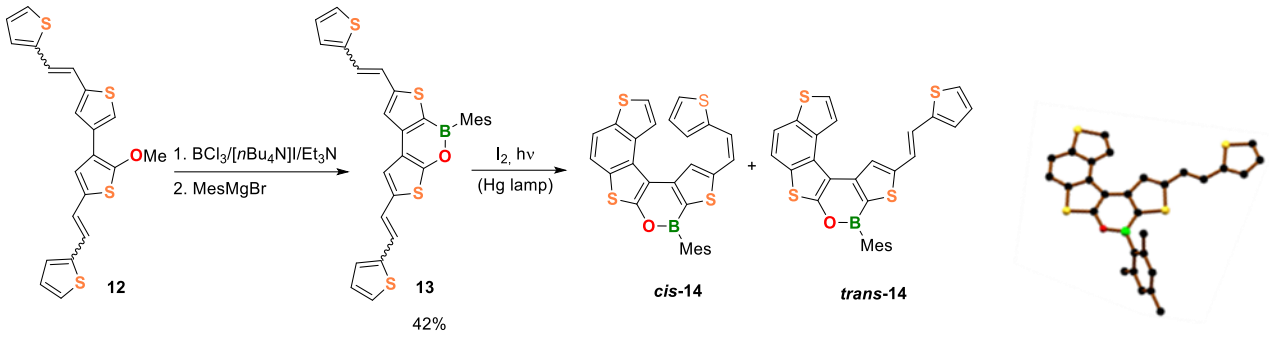

Schema 6. Synthese und Photocyclisierung von **13**.

Abbildung 7. Röntgenstruktur von ***trans*-14**.

Derselbe Syntheseansatz wurde auch verwendet, um mono-BO-dotiertes Helicen **4** (Schema **7**) zu erhalten, ausgehend von dem benzodithiofenfunktionalisiertem Alken **15**, das in guter Ausbeute zum Alken **16** boryliert wurde und dessen optoelektronische und elektrochemische Eigenschaften untersucht wurden. Die anschließende Photocyclisierung von **16** zu Helicen **4** wird derzeit untersucht, da der photochemische Schritt bisher den Engpass beider Synthesesequenzen darstellt.

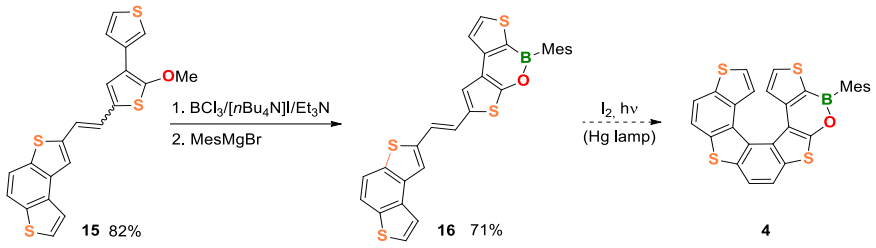

Schema 7. Synthetischer Weg zu **4**.

Schlussfolgerungen

Ziel dieser Doktorarbeit war die Untersuchung einer neuen Klasse von chiralen Thiaheterohelicenen, die mit einer oder zwei BO-Bindungen dotiert sind. Trotz der besonders anspruchsvollen Herausforderung aus synthetischer Sicht konnten die neuartigen Borahelicene **1** und **2** erfolgreich hergestellt und im Fall von **1** die vollständige optoelektronische, elektrochemische und stereochemische Untersuchung abgeschlossen und in Angewandte Chemie Int. Ausgabe publiziert werden.[13] Darüber hinaus wurde die synthetische Untersuchung von zwei weiteren Borahelicenen, nämlich **3** und **4,** fortgesetzt und wird derzeit noch weiter untersucht.

Referenzen

[1] E. von Grotthuss, A. John, T. Kaese, M. Wagner, *Asian J. Org. Chem.* 2018, *7*, 37-53.

[2] Y. Shen, C.-F. Chen, *Chem. Rev.* 2012, *112*, 1463-1535.

[3] T. Hatakeyama, S. Hashimoto, T. Oba, M. Nakamura, *J. Am. Chem. Soc*. 2012, *134*, 19600-19603.

[4] H- Hirai, K. Nakajima, K. Shiren, J. Ni, S. Nomura, T. Ikuta, T. Hatakeyama, *Angew. Chem. Int. Ed.* 2015, *54*, 13581-13585.

[5] T. Katayama, S. Nakatsuka, H. Hirai, N. Yasuda, J. Kumar, T. Kawai, T. Hatakeyama, *J. Am. Chem. Soc.* 2016, *138*, 5210-5213.

[6] S. Cauteruccio, D. Dova und E. Licandro, *Adv. Heterocycl. Chem.,* 2016, *118*, 1.

[7] A. Bossi, E. Licandro, S. Maiorana, C. Rigamonti, S. Righetto, G. R. Stephenson, M. Spassova, E. Botek und B. Champagne, *J. Phys. Chem. C,* 2008, *112*, 7900.

[8] S. Cauteruccio, A. Loos, A. Bossi, D. Dova, F. Rominger, S. Prager, M. C. Blanco Jaimes, A. Dreuw, E. Licandro, A. S. K. Hashmi und A. K. Stephen, *Inorg. Chem.,* 2013, *52*, 7995; S. Cauteruccio, D. Dova, A. Genoni, M. Orlandi, M. Benaglia und E. Licandro, *Eur. J. Org. Chem,* 2014, 2694.

[9] S. Cauteruccio, C. Bartoli, C. Carrara, D. Dova, C. Errico, G. Ciampi, D. Dinucci, F. Chiellini, E. Licandro, *ChemPlusChem,* 2015, *80*, 490.

[10] El Jaouhari, Y. Wang, B. Zhang, X. Liu, J. Zhu *Mat. Science & Engineer. C* 2020, *114*, 111067.

[11] K. Yamada, H. Nakagawa, H. Kawazura, Bull. Chem. Soc. Jpn.1986, *59*, 2429-243.

[12] T. Caronna, M. Catellani, S. Luzzati, L. Malpezzi, S. V . Meille, A. Mele, C. Richter, R. Sinisi, *Chem. Mater.* 2001, *13*, 3906-391.

[13] L. Menduti, C. Baldoli, S. Manetto, M. Bolte, H.-W. Lerner, G. Longhi, C. Villani, E. Licandro, M. Wagner *Angew. Chem. Int. Ed.* 2022, e202215468.

1. Abstract

The introduction of a trigonal boron atom into a polyaromatic hydrocarbon (PAH) core is an extremely powerful tool to provide organic scaffolds with optoelectronic properties as well as optimal packing in the solid state.[1] However, boron-doped PAHs (B-PAHs) often display low processability due to their poor solubility. The distortion of the molecular scaffold provides a suitable strategy to enhance the solubility properties of B-PAHs while maintaining good stacking properties and sufficient electronic conjugation. Extreme distortion of the molecular structure can be achieved in helical-shaped PAHs, namely helicenes[2] which are screw-shaped inherently chiral polycycles, formed by ortho-fused aromatic or heteroaromatic rings. The presence of a helical structure in B-PAHs is expected to strongly influence their physico-chemical properties leading to compounds characterized by peculiar features promising for applications in next generation functional materials. Despite the great potential of this class of compounds, only few examples of borahelicenes have been reported in the literature and those mainly consist of carbohelicene-based structures.[3–5] However, the considerable structural diversity achievable by introducing different bora-heterocycles (oxaborine, borole, borepin) and other heteroaromatic rings (thiophene, furan, pyrrole) into the same helical scaffold, suggests that a large variety of compounds with intriguing features could be accessible via currently unexplored synthetic routes. The design, synthesis, and properties investigation of new boraheterohelicenes (**BHHs**) is therefore a relevant research topic and is the object of this PhD project, aimed to obtain several **BHHs** with structural diversity, as well as to study their reactivity, electrochemical and photophysical features for better understanding their potential as building blocks for material science.

The thesis work was carried out in part at the University of Milan in the laboratories of Prof. Emanuela Licandro and in part at the Goethe Universität Frankfurt am Main under the supervision of Prof. Dr. Matthias Wagner, within a co-tutelle programme.

Owing to the long-standing expertise of Prof. Licandro group in the synthesis of tetrathia[7]helicenes (**7TH** Figure 1) and that of Prof. Dr. Wagner group in the synthesis of boron-doped PAHs (e.g. boron[4]helicene **4BH**; Figure 1), I conceived this PhD project designing a series of thiahelicenes containing one or more B-O bond into the helical scaffold.

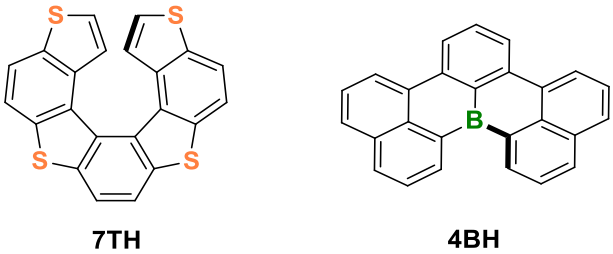

7TH **4BH**

Figure 1. Tetrathia[7]helicene (**7TH**) and boron[4]helicene (**4BH**).

Tetrathia[7]helicenes, consisting of thiophene and benzene rings fused in an alternating fashion, are configurationally stable heterohelicenes which exist as pair of enantiomers.[6] This class of molecules is

particularly interesting since it merges the properties of oligothiophenes with those of helicenes, giving rise to systems with peculiar electronic and chiroptical properties which make them appealing building blocks for applications in manifold fields of science, including optoelectronics,[7] catalysis,[8] and biology.[9] The introduction of trigonal boron atom into a thiahelicene scaffold gives rise to a novel class of unexplored boron π-conjugated molecules with potentially interesting features.

The present Ph.D. thesis was therefore intended to provide a meaningful contribution in the development of innovative and versatile syntheses of BO-doped tetrathia[7]helicenes as well as the study of their stereochemical and optoelectronic properties to identify potential applications of these systems in material science.

The first selected structures containing one or two oxaborine rings in the helical scaffold are shown in figure 2. The presence of the bulky mesityl group at the boron atom is necessary to ensure stability to the molecule. It is noteworthy that compound **2** is the skeletal isomer of **1**, as the direction of the B-O bond is opposite in the two molecules. In the course of the research work, after the evaluation of the photophysical properties of **1,** helicene **2** was designed to get information on the structure-property relationship and evaluate how the position of the BO-bond into the helical scaffold can influence the electronic properties of BO-doped thiahelicenes.

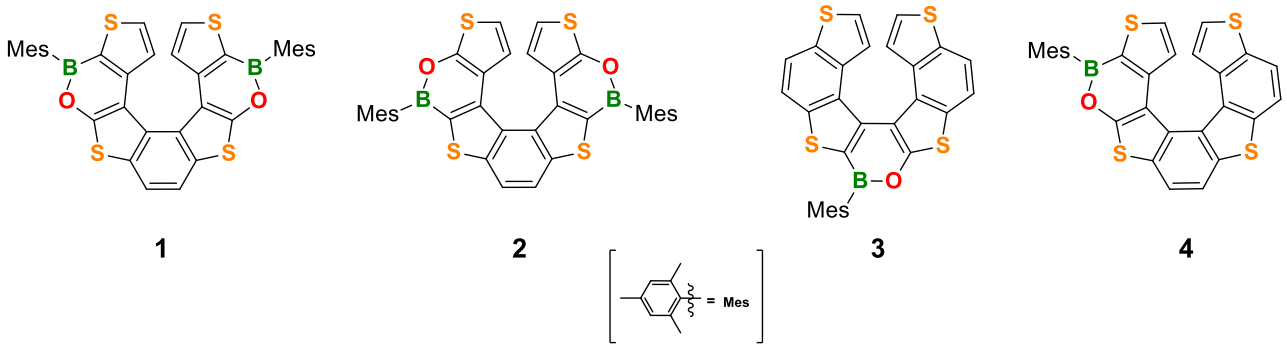

Figure 2. First selected borathia[7]helicene structures.

In detail the thesis work has been focused on the following main goals:

1) study of the synthesis and properties of the doubly BO-doped tetrathia[7]helicene **1**; and its "BO- isomer" **2**;

2) preliminary study of the synthesis of singly BO-doped tetrathia[7]helicenes **3** and **4**.

Study of the synthesis and properties of the BO-doped tetrathia[7]helicene 1

No examples of boron containing tetrathiahelicenes have been reported in the literature and within this research project we have designed several suitable strategies for the synthesis of the target molecules and their precursors. In a general synthetic scheme, dithienooxaborine **5** unit was identified as a potential common building block for the selected structures **1**, **3** and **4** reported in Scheme 1.

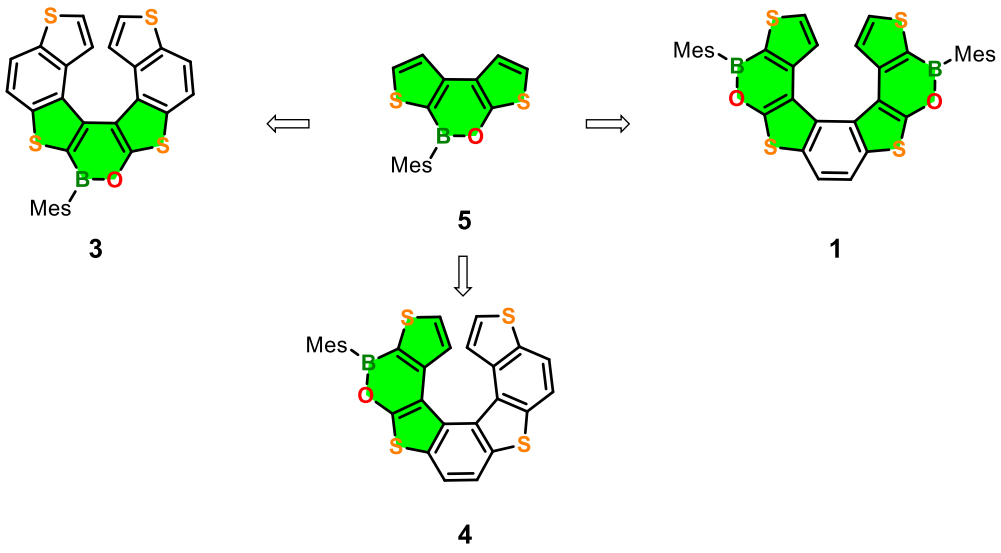

Scheme 1. General synthetic scheme for BO-doped thiahelicenes **1**, **3**, **4**.

The synthesis of dithienooxaborine **5** (Scheme 2), unknown in the literature was the first target of the work and was realized as shown in Scheme 2 by treatment of the known methoxy bithiophene **S1**[6] with BCl_3 in the presence of Et_3N and [nBu$_4$N]I to give the intermediate **5-Cl** which, upon treatment with MesMgBr afforded the target dithienyloxaborine **5** in 77% yield.

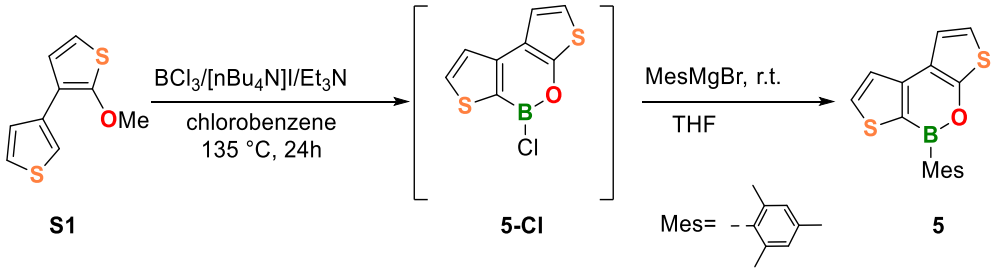

Scheme 2. Synthesis of **5**.

Starting from oxaborine **5** we considered different approaches to helicene **1** (Scheme 3) but, also in the light of some preliminary experiments, we selected the route showed as retrosynthesis in Scheme 3, in which the target helicene **1** is obtained by photocyclization of the BO-containing alkene precursor **6** prepared from dithieno oxaborine **5**.

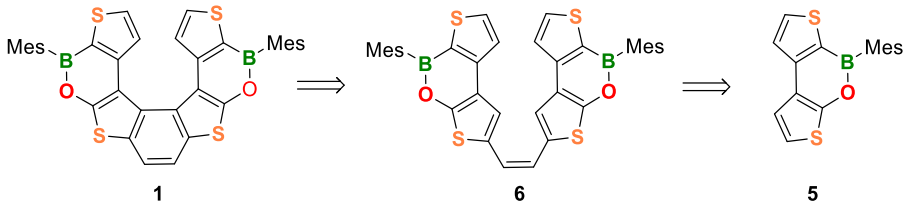

Scheme 3. Proposed retrosynthetic analysis for **1**.

The synthesis of **1** is further detailed in Scheme 4.

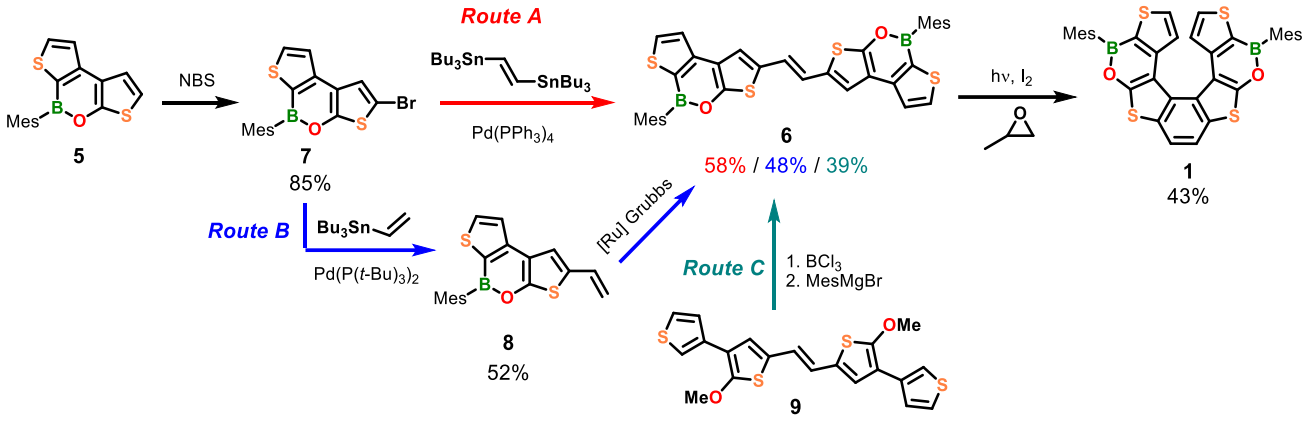

Scheme 4. Synthetic route to dioxabora-tetrathia[7]helicene **1**.

Starting from oxaborine **5** the synthesis of key intermediate alkene **6,** was deeply investigated and carried out *via* three different routes (*Route A*, *B*, *C*).

In the *Route A* and *B*, the oxaborine **5** was brominated with *N*-bromosuccinimide (NBS) to give α-bromo oxaborine **7** which in the *Route A,* was reacted with 1,2-bis(tributylstannyl)ethene, through a Stille coupling, using $Pd(PPh_3)_4$ as catalyst affording alkene *trans*-**6** in 58% yield. In the *route B*, **7** was, firstly, submitted to a Stille coupling with vinyl tributyltin using $Pd[P(t\text{-}Bu)_3]_2$ as catalyst, giving **8** in 52% yield, followed by dimerization *via* Grubbs metathesis, leading to **6** in 48% yield. Alternative *Route C* allowed to get the alkene **6** in 39% through a different strategy that involves a late-stage formation of the two oxaborine rings starting from the suitable bis-methoxy functionalized alkene **9**.[10] Although the lower yield, it is noteworthy that this route is potentially suitable to get in an easy way oxaborine substituted alkenes containing different heteroaromatic rings.

As last step, the photocyclization of alkene **6**, was performed in benzene by using a 405 nm LED lamp in the presence of I_2 and propylene oxide (to trap HI formed in the photocyclization step) and successfully gave the new doubly BO-doped thiahelicene **1** in 43% yield. All the compounds shown in Scheme 4 are new and were completely characterized by ^{1}H, ^{13}C, and ^{11}B NMR, HRMS, CV and UV/Vis analysis and their molecular structures elucidated by X-ray crystallography. The molecular X-ray structure of the target dioxabora-thiahelicene **1** is shown in Figure 3.

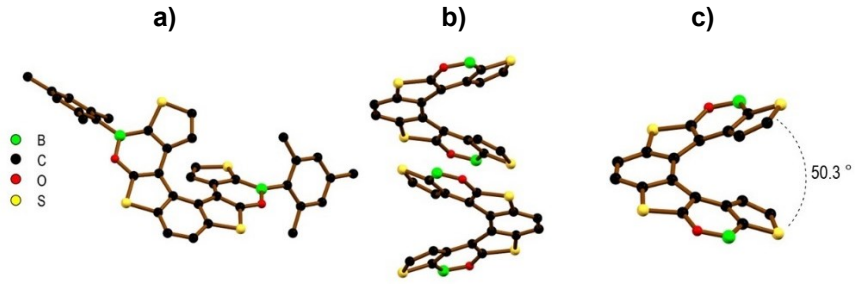

Figure 3. a) X-ray molecular structure of **1**-(*M*)-enantiomer. b) packing of the (*P*)/(*M*)-pair of enantiomers c) side view, interplanar angle between the two terminal thiophene rings; in b) and c) mesityl groups are omitted for clarity.

As previously mentioned, borahelicene **1** is a chiral molecule and chiroptical and kinetic studies on **1** were conducted in collaboration with the group of Prof. Claudio Villani (University of Rome "La Sapienza") and Prof. Giovanna Longhi (University of Brescia).

The two enantiomers (*P*)-/(*M*)-**1** were resolved by chiral-HPLC (Figure 4a, blue trace) and revealed to be configurationally stable at room temperature with optical rotation values of +97.7° and –97.5°, respectively. Optical stability studies were conducted on the **1** enantiomers allowing to determine the free energy of racemization $\Delta G_{rac}^{\ddagger}$ = 26.9 ± 0.1 kcal mol^{-1}, which is significantly lower than that of thiahelicenes,[11] thus indicating that BO-doping strongly influences the mechanical rigidity of the helical framework. Circular dichroism (CD) spectra of the two enantiomers showed a perfect mirror-image relationship (Figure 4b, black and red trace). To determine the absolute configurations of the two enantiomers, the CD spectrum of (*M*)-**1** was calculated by TD-DFT (Figure 4b, orange dashed trace) and the good correspondence between computed and experimental data allowed to assign the (*M*)-configuration to the second eluted enantiomer (α_D= –97.5°).

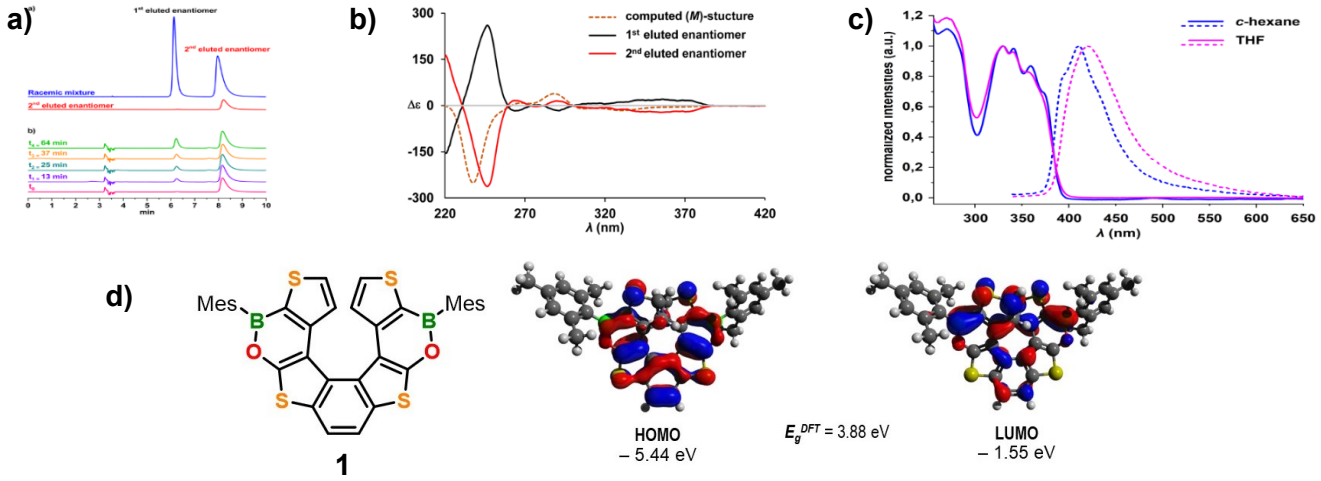

Figure 4. a) top: Analytical HPLC resolution of **1** in *n*-hexane/CH_2Cl_2 (95:5), black and red trace; computed CD spectrum of (*M*)-**1** at the e M06/6-311g G(d,p) level, orange dashed trace. c) absorption/emission spectra of **1** in *c*-hexane and THF. d) HOMO/LUMO distributions of **1** calculated at the B3LYP/6-31G* level.

To evaluate the potential of BO-doped helicene **1** for applications in material science (*e.g.,* building block for emissive/electron transport materials for OLED devices), its properties were also investigated by means of cyclic voltammetry, UV/Fluorescence spectroscopy, as well as DFT/TD-DFT calculations. Cyclic voltammetry showed two irreversible redox events with peak potentials of E_{pc} = –2.83 and –3.01 V in the cathodic scan. DFT calculations revealed as LUMO orbitals (E_{LUMO}^{DFT} = –1.55 eV) are mainly localized on the terminal, formally B(sp^2)-substituted thiophene rings, while HOMO orbitals (E_{HOMO}^{DFT} = –5.44 eV) spread over the whole helical fragment (Figure 4d). UV/Fluorescence spectroscopy proved that **1** is a blue emitter and its emission band shows a partially resolved vibrational fine structure in *c*-hexane (Figure 4c, blue trace) with a photoluminescence quantum efficiency is Φ_{PL} = 6% (*c*-hexane; *cf.* parent **7TH**: $\lambda_{em} \approx 405$ nm, Φ_{PL} = 5%).[12] Results of optoelectronic studies revealed as **1** is not suitable for applications in functional materials but the versatile synthetic approaches set-up for its preparation (see Scheme 4) open up to manifold structural modifications (inversion of BO vectors, BN doping) which could serve as tool to obtain new derivatives with enhanced optoelectronic performances. Out to date, helicene **1** represents the first BO-doped thiahelicene in the literature, and the results of this study has been published as a research article in Agewandte Chemie Int. Ed..[13]

Study of the synthesis and properties of the BO-doped tetrathia[7]helicene 2

On the basis of the photophysical properties of **1**, with the aim of improving its optoelectronic properties (*e.g.,* red-shifted absorption-emission/ higher Φ_{PL}), we designed the helicene **2** (Figure 5), skeletal isomer of **1**, which is derived by the formal inversion of the two BO bonds in the parent **1** that we presumed could be a tool to affect the electronic properties, by influencing the distribution and the extension of the LUMO orbitals within the helical framework.

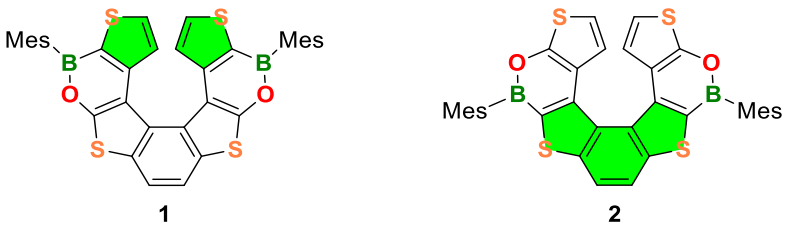

Figure 5. Structure and LUMO distribution (green) of **1** and, expected LUMO distribution of the **2** isomer with BO-inverted bonds.

In fact, **2** is expected to display LUMO orbitals extended over the whole thiophene-benzene-thiophene (BDT) central fragment rather than terminal thiophene rings as in **1** (Figure 5). The LUMO extension should provide a narrowed energy-gap, redshifted absorption/emission bands, increased reducing abilities and thus enhanced optoelectronic performances. This hypothesis was also supported by preliminary DFT calculation (Figure 6b).

Borahelicene isomer **2** was synthesised following the late stage borylation strategy (see *Route C* for **1** in Scheme 4). To this aim the alkene **10,** prepared in good yield from 3-bromo-2-thiophencarbaldehyde (Scheme 5), was first borylated to give **11**, then submitted to photocyclization using a 395 nm LED lamp affording the target helicene **2.**

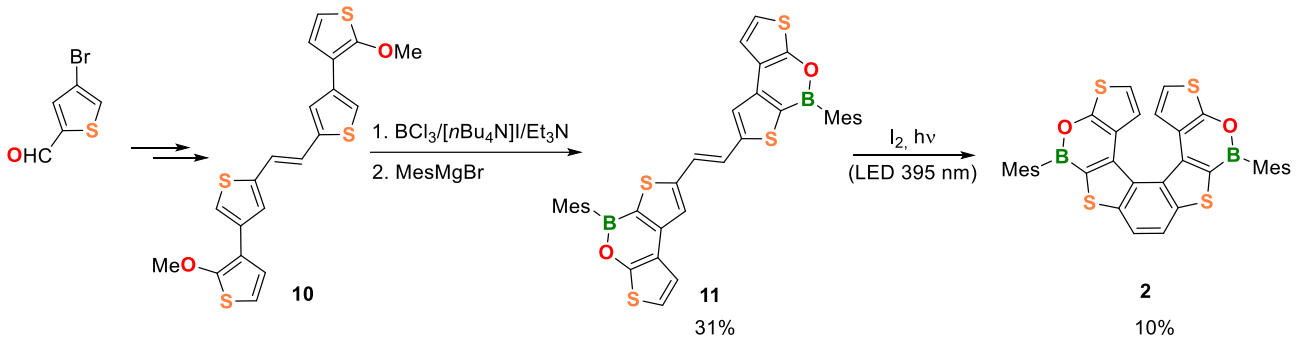

Scheme 5. Synthetic route to BO-doped tetrathia[7]helicene isomer **2**.

Although the synthetic protocol needs to be optimized, the procedure allowed to obtain bora-helicene **2** as a second example of doubly boron-doped thiahelicene, and in enough amount for the analytical and photophysical characterization (Figure 6).

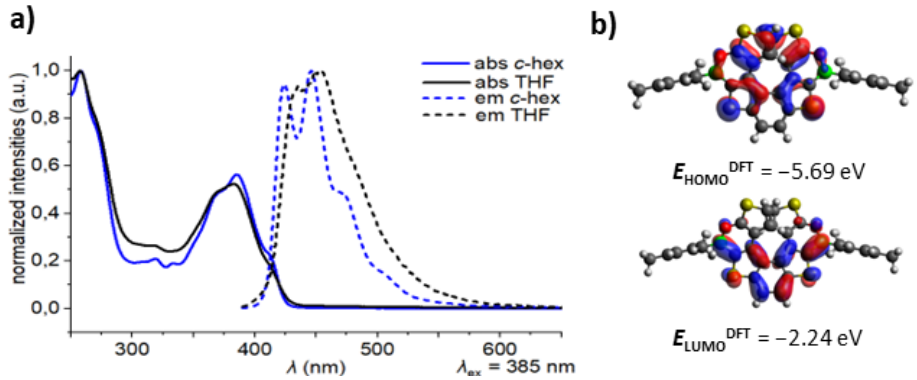

Figure 6. a) UV/Fluorescence spectra of **2** in *c*-hexane (blue trace) and THF (black trace). b) HOMO/LUMO distribution of **2** calculated at the B3LYP/6-31G* level.

In *c*-hexane, **2** exhibits a structured UV/vis absorption band with the most bathochromic shoulder appearing at 413 nm (Figure 6a, blue line). For comparison, the corresponding shoulder in the spectrum of **1** is found at 374 nm. **2** is a blue emitter, and its emission band shows a partly resolved vibrational fine structure with the most hypsochromic shoulder at 472 nm and a photoluminescence quantum efficiency is Φ_{PL} = 7% (*c*-hexane; *cf.* **1**: $\lambda_{em} \approx$ 411 nm, Φ_{PL} = 6%). Absorption and emission bands of **2** are substantially red-shifted with respect to those of **1**. DFT calculations showed as the LUMO of **2** is distributed over the whole thiophene-benzene-thiophene central fragment and thus is more extended than that of **1**.

Taken together, these results revealed as the inversion of BO vectors represents a suitable tool to tune the LUMO of BO-doped thiahelicenes and, although in the specific case of **2** it did not have appreciable effect

on the optoelectronic performances (still low Φ_{PL} and only slight lowering of the LUMO energy), they set the basis for the structural design of new derivatives with tuned electronic properties. Racemization kinetics and chiroptical properties of **2** will be carried out in the future, meanwhile the thesis work was addressed to the synthesis of oxabora thiahelicenes **3** and **4** containing one oxaborine ring in different position of the helical scaffold (see Figure 2).

Preliminary study of the synthesis of singly BO-doped tetrathia[7]helicenes 3 and 4

For the synthesis of mono-BO-doped thiahelicene **3**, again we considered the borylation of bis-alkene **12** to give oxaborine derivative **13,** before the photocyclization step. This latter to achieve **3** is currently under investigation although first photochemical trials allowed to isolate an almost equimolar mixture of *cis*/*trans* isomers of the mono ring-closed product **14** (Scheme 6). The two structures were identified by ^{1}H NMR, ^{HH}COSY spectra. In addition, crystals of *trans*-**14** were obtained, and its structure was confirmed by HRMS and X-ray analysis (Figure 7).

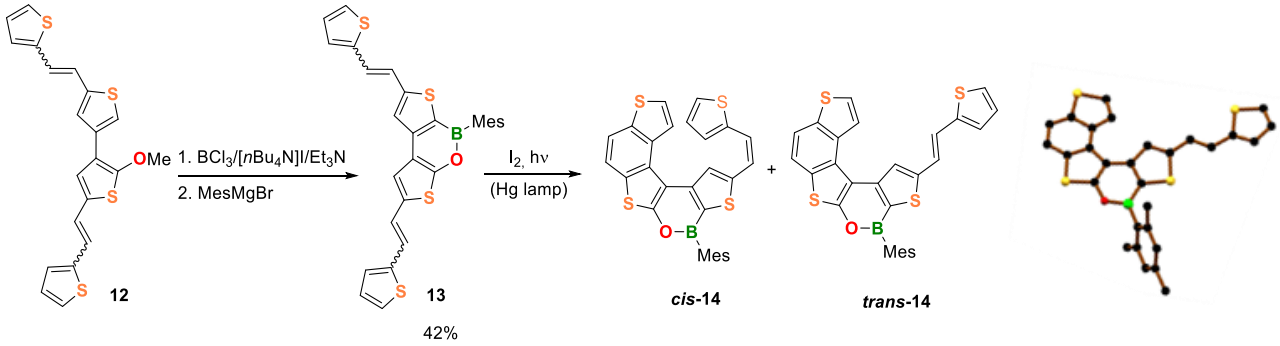

Scheme 6. Synthesis and photocyclization of **13**.

Figure 7. X-ray structure of *trans*-**14**.

The same synthetic approach was also used to obtain mono-BO-doped helicene **4** (Scheme **7**), starting from the benzodithiofene functionalized alkene **15** that was borylated in good yield to give alkene **16**, whose optoelectronic and electrochemical properties were investigated. The subsequent photocyclization of **16** to helicene **4** is currently under investigation as the photochemical step, up to now, represents the bottleneck of both synthetic sequences.

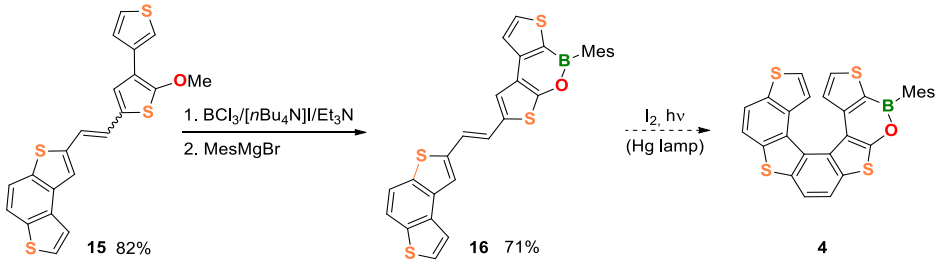

Scheme 7. Synthetic route to **4**.

Conclusions

This PhD thesis aimed at investigating a new class of chiral thiaheterohelicenes doped with one or two BO-bonds. This challenge has been particularly demanding from a synthetic point of view, but novel borahelicenes **1** and **2** have successfully been prepared and, in the case of **1**, its complete optoelectronic, electrochemical and stereochemical study was completed and published on Angewandte Chemie Int. Ed.[13] Moreover, the synthetic study of two additional borahelicenes, namely **3** and **4** has been carried on and is currently still ongoing.

References

[1] E. von Grotthuss, A. John, T. Kaese, M. Wagner, *Asian J. Org. Chem.* **2018**, *7*, 37–53.

[2] Y. Shen, C.-F. Chen, *Chem. Rev.* **2012**, *112*, 1463–1535.

[3] T. Hatakeyama, S. Hashimoto, T. Oba, M. Nakamura, *J. Am. Chem. Soc*. **2012**, *134*, 19600–19603.

[4] H- Hirai, K. Nakajima, K. Shiren, J. Ni, S. Nomura, T. Ikuta, T. Hatakeyama, *Angew. Chem. Int. Ed.* **2015**, *54*, 13581–13585.

[5] T. Katayama, S. Nakatsuka, H. Hirai, N. Yasuda, J. Kumar, T. Kawai, T. Hatakeyama, *J. Am. Chem. Soc.* **2016**, *138*, 5210–5213.

[6] S. Cauteruccio, D. Dova and E. Licandro, *Adv. Heterocycl. Chem.,* **2016**, *118*, 1.

[7] A. Bossi, E. Licandro, S. Maiorana, C. Rigamonti, S. Righetto, G. R. Stephenson, M. Spassova, E. Botek and B. Champagne, *J. Phys. Chem. C,* **2008**, *112*, 7900.

[8] S. Cauteruccio, A. Loos, A. Bossi, D. Dova, F. Rominger, S. Prager, M. C. Blanco Jaimes, A. Dreuw, E. Licandro, A. S. K. Hashmi and A. K. Stephen, *Inorg. Chem.,* **2013**, *52*, 7995; S. Cauteruccio, D. Dova, A. Genoni, M. Orlandi, M. Benaglia and E. Licandro, *Eur. J. Org. Chem.,* **2014**, 2694.

[9] S. Cauteruccio, C. Bartoli, C. Carrara, D. Dova, C. Errico, G. Ciampi, D. Dinucci, F. Chiellini, E. Licandro, *ChemPlusChem,* **2015**, *80*, 490.

[10] El Jaouhari, Y. Wang, B. Zhang, X. Liu, J. Zhu *Mat. Science & Engineer. C* **2020**, *114*, 111067.

[11] K. Yamada, H. Nakagawa, H. Kawazura, Bull. Chem. Soc. Jpn.**1986**, *59*, 2429–243.

[12] T. Caronna, M. Catellani, S. Luzzati, L. Malpezzi, S. V. Meille, A. Mele, C. Richter, R. Sinisi, *Chem. Mater.* **2001**, *13*, 3906–391.

[13] L. Menduti, C. Baldoli, S. Manetto, M. Bolte, H.-W. Lerner, G. Longhi, C. Villani, E. Licandro, M. Wagner *Angew. Chem. Int. Ed.* **2022**, e202215468.

2. Introduction

2.1 Conjugated materials

In recent years conjugated organic materials have attracted much attention for applications in organic electronics, because these molecular systems offer many advantages as potential replacement for conventional inorganic materials (*i.e.*, silicon and metals) in terms of cheap fabrication and environmental friendly devices.[1] In contrast to silicon-based technologies, organic materials[2] can be used for a variety of applications due to their processing advantages (e.g. low temperatures and cost) and their unique physical, optical and electronic properties. Organic components can be produced using processes such as gas phase deposition, spin coating or printing processes that do not require highly equipped clean room laboratories and enables particularly rapid coverage of large substrates. In particular, the fabrication of multi-layer components, *e.g.,* by sequential application of individual layers, is proving to be extremely effective.[3] The combination of transparent substrates with transparent electrodes also makes it possible to produce fully transparent devices that would not be possible using inorganic semiconductors. In addition, processing at low temperatures and the mechanical flexibility of organic materials make flexible or foldable displays (or solar cells) accessible, thus opening up completely new areas of technology and application.[4]

The most established sectors of organic electronics are those regarding *light-emitting* devices and lighting elements namely: organic light-emitting diode (OLED),[5] organic thin-film transistors (OTFT),[6] organic field-effect transistor (OFET)[7] and organic photo-voltaic cell (OPVC).[8] Among these, OLEDs are among the most studied electronic devices whose structure and basic operating principle are illustrated by a schematic diagram in Figure 1.

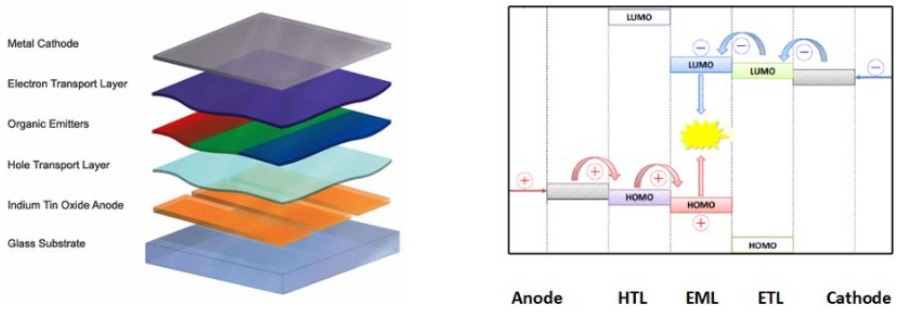

Figure 1. OLED structure and working principle.

OLEDs consist of several thin layers of organic semiconductor materials that are sandwiched between two contacts (anode and cathode). In general, light production is induced by electric charges, exploiting the electroluminescence of the semiconducting material. Electrons or holes are respectively injected into the LUMO (lower unoccupied molecular orbital) or HOMO (highest occupied molecular orbital) of the emitting organic layer (EML) and move in an externally applied field to the so-called recombination region. As soon as the distance between the charge carriers becomes smaller than the Coulomb capture radius, Frenkel excitons (electron-hole pairs) are formed. By recombining the charge carriers, the electrons fall into the lower energy level and release this energy in the form of photons, thus the excited molecules relax into their electronic ground state. The wavelength or colour of the emitted light depends on the size of the band gap between the HOMO and LUMO levels of the emitter materials.[7] If the emitted light is to be within the visible light spectrum, this distance shall be between 1.6 and 3.3 eV.[9]

Modern multi-layer OLEDs have also additional layers to simplify carrier injection at the electrode interfaces and to divide the large potential barriers between the individual layers into smaller potential differences.[10] For this purpose, hole transport layers (HTL) and electron transport layers (ETL) with different properties are used. Organic p-type semiconductors such as diphenyl amine or carbazole derivatives, characterized by a high HOMO level, are typically used as HTL materials. On the other hand, for ETL materials organic n-type semiconductors such as phenanthroline, which enable particular high electron mobility, are used.

Especially in the development of efficient ETL materials there is still a great need for research, since the general electron mobility in organic materials is very low compared to inorganic materials and therefore the selection of organic n-type semiconductors is reduced to a very small number of electron-poor compounds.[9]

For a few years now, organoboranes have come to the fore as candidates for ETL materials. These compounds not only have excellent redox properties, but often exhibit strong luminescence with high quantum yields.

As one of the first examples, compound **I** (Figure 2),[11] which consists of two boron-doped acceptor units and a thiophene (n = 1) or 2,2'-bithiophene (n = 2) donor bridge, was successfully integrated into OLEDs as ETL material. Compound **I** showed a comparable performance as the tris(8-hydroxyquinoline)aluminium **II** complex (Figure 2), which has been predominantly used in OLEDs so far.[12]

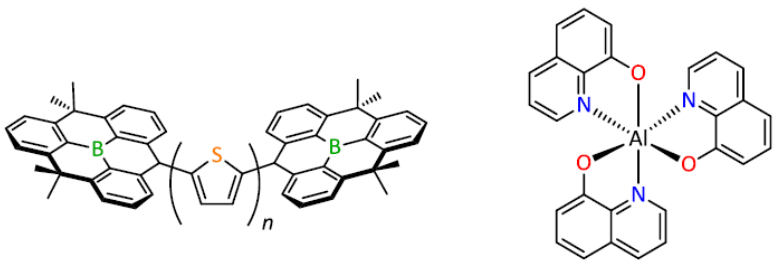

I **II**

Figure 2. Boron and aluminium organo-complexes usued in OLED.

2.1.1. Photophysical principles of light or current absorption

Interactions of organic molecules with light or electric current strongly depend on the electronic structure and the energetic states of each compound. If the energy of an incident photon corresponds to the energy difference of the two energetic states of the molecule, the photon is absorbed (e.g., S_0->S_1). According to the Franck-Condon principle, higher vibronic states of excited levels are occupied. Relaxation processes following the absorption ones lead to both radiant and radiation-free transitions, which return the molecule to its ground state.[13] Main relaxation process can be divided into different groups: fluorescence (FL), internal conversion (IC), intersystem crossing (ISC) and phosphorescence (P), shown in Figure 3 as Jablonski diagram.

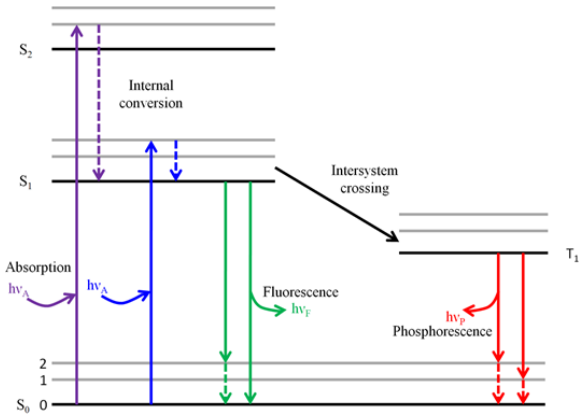

Figure 3. *Jablonski* diagram.

In fluorescence (F), a large part of the absorbed energy is spontaneously re-emitted as electromagnetic radiation. According to Kasha's rule, this is usually done from the lowest vibronic state v_0 of S_1 and is therefore independent of the excitation wavelength, however also weak $S_2 \rightarrow S_0$ transitions take place. The wavelength of the electromagnetic radiation is redshifted in relation to the wavelength of the incoming photon, since a part of the originally absorbed energy is released non radiatively by oscillation relaxation. The difference between the excitation wavelength and the emission wavelength is called Stokes shift.

The most important parameter to evaluate fluorophores is the quantum yield Φ_{PL}. It corresponds to the ratio of the absorbed photons and the photon emitted by fluorescence.

Many chromophores show intensive fluorescence in diluted solution after excitation. As the concentration increases, the fluorescence intensity is attenuated. This phenomenon, called *self-quenching,* is often observed in aromatic compounds and plays an important role especially in molecules with small Stokes shifts, since absorption and emission spectra partially overlap.[14] In extreme cases, strong intermolecular π-π interactions (π-stacking) in condensed phase lead to radiation-free deactivation processes of the aggregated molecules, e.g. via external vibrational relaxation. The phenomenon is called *aggregation-caused quenching* (ACQ).[13]

A opposite photophysical phenomenon is *aggregation-induced-emission* (AIE). In AIE, weakly luminescent chromophores become efficient emitters due to the formation of aggregates.[15]

Suitable fluorophores for semiconductor materials must have a sufficiently small band gap in addition to the delocalized π system.[16] A suitable strategy to adjust the band gap of a π conjugated system is the introduction of suitable π-electron donor and π-electron acceptor substituents into the carbon skeleton. Electron donor and electron-acceptor groups influence HOMO and LUMO energy levels and thus the optoelectronic properties of the molecules. As an alternative adjusting tool, the exchange of a carbon atom with a heteroatom is a suitable option. Basically, two cases can be distinguished:

i) the doping with an electron donor atom, such as nitrogen, sulphur, phosphorus or oxygen;
ii) the incorporation of an electron acceptor atom, such as boron.

In the literature, various examples of polycyclic (hetero)aromatic hydrocarbons doped with boron, nitrogen, phosphorus, oxygen, and sulphur atoms can be found.[17] Among these, organic boron chromophores in which a trigonal-planar boron atom is present in π conjugated aromatic systems are, nowadays, really important in the field of organic electronics. These include an abundance of organoboron compounds, which are now mainly established in the field of OLED, OPVC, and OTFT materials.[18,17a]

2.2 Polycyclic aromatic hydrocarbons (PAHs) and helicenes

2.2.1 General concepts

Polycyclic aromatic hydrocarbons (PAHs)[19] are composed of several fused aromatic rings, which are characterized by more or less pronounced delocalized π–electron systems. Within the scaffolds, all carbon atoms are sp^2-hybridized, while the non-hybridized p_z orbitals are perpendicular to the molecular plane therefore allowing overlap over the entire system.

Proper design of PAH molecular structures allows to obtain systems often showing narrowed band gaps, predictable supramolecular arrangements, and enhanced charge-carrier properties,[20] thus providing materials for organic light-emitting diodes (OLEDs), organic field-effect transistors (OFETs), organic photovoltaic cells (OPVs), and for lithium batteries.

As an example of PAHs widely used in optoelectronic devices,[21] anthracene, tetracene and pentacene structures are reported in Figure 4.

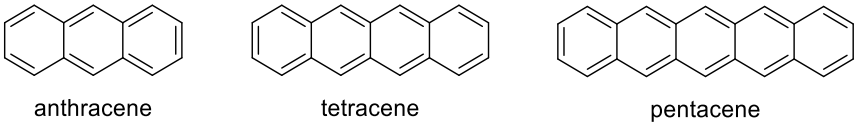

Figure 4. Anthracene, tetracene and pentacene structures.

The increasing number of *ortho*-fused benzene rings strongly contributes to the extension of the π-conjugated system of acenes, leading to redshift absorption and emission bands and narrower band gaps. However, despite their excellent photophysical and electrochemical properties,[22] flat polyaromatics often display scarce solubility in common organic solvents thus reducing processability and characterizability in the liquid phase.

To overcome these drawbacks, a suitable option is to introduce solubilizing groups such as alkyl chains or bulky aryl groups. However, the introduction of side groups often interferes with the stacking properties of the related molecules, leading to reduced charge carrier mobilities and therefore reduced optoelectronic performances.

As an alternative to the introduction of solubilizing group, the distortion of the molecular scaffold can enhance the solubility of PAHs, leading to better processability in solution without dramatically altering their stacking abilities. Furthermore, distortion of the carbon skeleton leaves orbital interactions within the π-system sufficiently large to produce similar properties as in comparable planar compounds.

Abolition of planarity can be achieved by linking of neighbouring rings in different ways leading to diverse structural features of PAHs peripheral regions, which can generally be divided into three subcategories: bay, cove and fjord regions (Figure 5).[23]

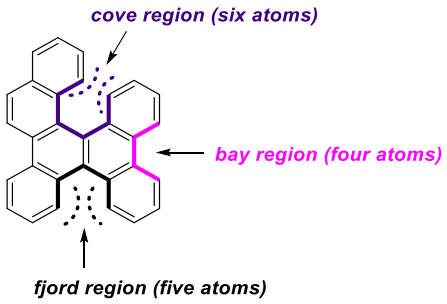

Figure 5. Schematic representation of the different peripheral regions in PAHs.

In contrast to bay regions, the occurrence of fjord or cove regions leads to a distortion of the three-dimensional structure of PAHs. Responsible for this is the steric repulsion of the hydrogen atoms that protrude into the corresponding regions. The extreme case of a particularly strong twist can be observed in the structural class of helicenes. The first helicene was synthesized in the early '900,[24] but the term "helicene" was first introduced almost 60 years later.[25]

Helicenes are characterized by non-planar screw-shaped skeletons formed by ortho-fused benzene or other aromatic rings, which adopt a helical configuration, due to geometrical constraints and overlapping of the terminal rings (Figure 6).[26]

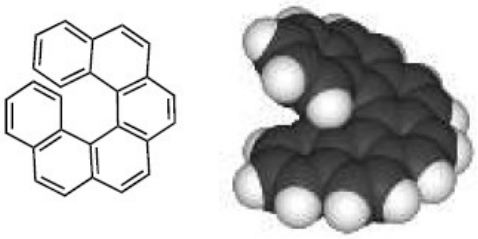

Figure 6. Carbo[6]helicene 2D and 3D structure.

Because of the steric hindrance of the terminal rings, helicenes can wind in opposite directions; they are chiral molecules even in absence of stereogenic centres, and possess a C2-symmetric axis, which is perpendicular to the helical axis (Figure 7).

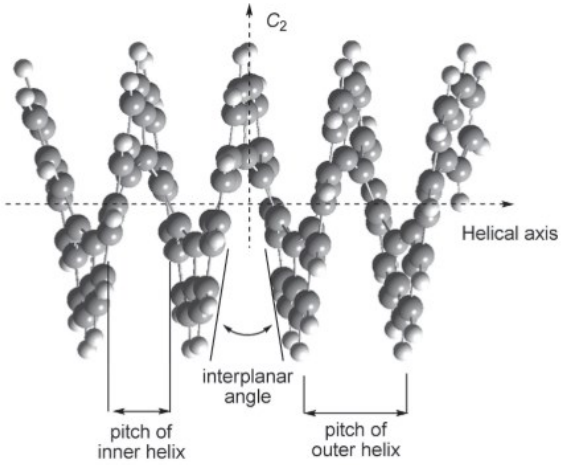

Figure 7. Helicene C2-symmetric axis.

The interconversion barrier between carbohelicene enantiomers, composed by six or more *ortho*-fused benzene rings, is sufficiently high to allow the existence of two optical antipodes, and on the basis of the helicity rule proposed by Cahn, Ingold and Prelog in 1966, a left-handed helix is designated "minus" and denoted by *M*, whereas a right-handed one is designated "plus" and denoted by *P* (Figure 8a).[27] Moreover, according to the results of ORD and CD spectroscopy, as a general trend in a homochiral series, the *P* series of helicenes has a (+) dextrorotatory specific rotation and the *M* series has a (−) levorotatory specific rotation.[28] The helical topology of helicenes provides a high optical rotation and high circular dichroism values.

As the number of fused rings increases, the helicene spirals up along the helical axis to form a cylindrical structure with a constant pitch (in both the inner and the outer helixes). For helicenes composed of six membered aromatic rings, it takes nearly six rings to cover a complete 360 °C rotation of a screw while, in structures containing five-member heterocycles, more rings are required: this is due to the smaller in-plane turn (θ) that five-membered rings contribute to the helical structure (Figure 8b).

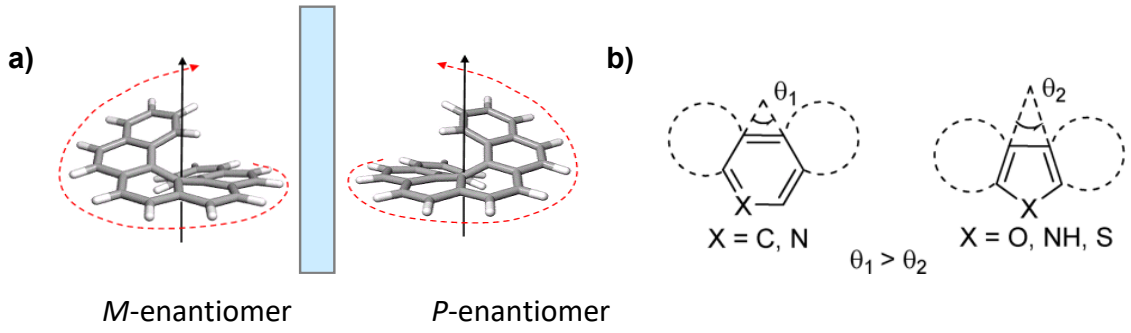

Figure 8. a) Carbo[6]helicene *P*- and *M*- enantiomers; b) in-plane turn (θ) of six- and five-membered rings.

About the nomenclature, according to IUPAC rules, helicene are named as follows: 1) number of fused aromatic rings in helical framework, indicated by the number *n* in brackets "[*n*]", followed by 2) the term "helicene". A helicene composed by six aromatic rings will be therefore named [6]helicene.

Helicenes which are exclusively composed by fused benzene rings are classified as carbohelicenes (the prefix *carbo*- is added before the name), while helicenes incorporating heteroaromatic rings into the helical scaffold are named as heterohelicenes (the prefix *hetero*- is added before the name).

Most of the reported heterohelicenes incorporate p-block elements-based heteroaromatic rings: pyrroles (N, *aza*-), thiophenes (S, *thia*-), furans (O, *oxa*-), phopholanes (P, *phospha*-), siloles (Si, *sila*-). Following the nomenclature those will be therefore named as aza[n]helicenes, thia[n]helicenes, oxa[n]helicenes, phospha[n]helicenes, and sila[n]helicenes, respectively (Figure 9).[29] The number of heteroaromatic rings is indicated using the prefix: "di" for 2, "tri" for 3, "tetra" for 4, and so on.

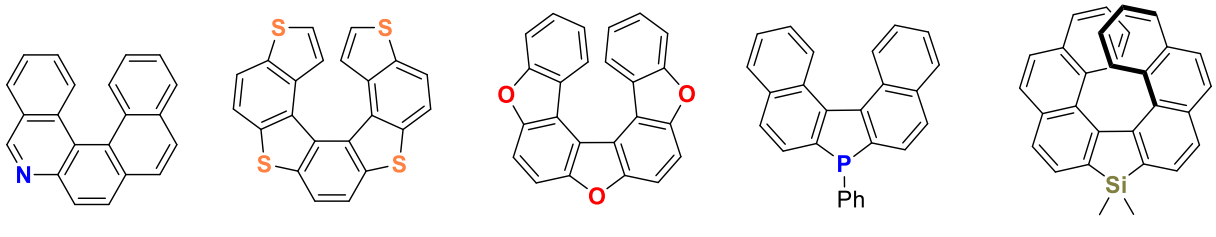

Figure 9. Examples of heterohelicenes.

2.2.2 Properties and applications of helicenes

Helicenes combine the key attributes of both PAHs and chiral molecules and show interesting electronic and optical properties.

Furthermore configurationally stable helicenes show unique solid-state packing (due to chiral recognition), unusual molecular dynamics (as 'molecular springs'), and remarkable optoelectronic properties (due to their chiral electronically excited states) and thus they are particularly interesting in the field of materials science *e.g.*, to develop antiglare displays consisting of OLEDs in which the electroluminescence is directly circularly polarized (CP-OLED).[30]

The π-interactions within the polyaromatic system of helicenes give rise to structured absorption and emission bands and, despite the non-planarity, in helicenes HOMO-LUMO overlap is still sufficient to get peculiar intermolecular electronic interactions.[31] Generally, the increase of the number of ortho fused rings results in helicenes with a reduced HOMO-LUMO gap (E_g), as effect of the π-π overlap across the helix.[32] Helicenes often display fluorescence but the associated quantum yields (Φ_{PL}) are low due to non-emissive quenching processes (intersystem crossing).

The functionalization of the helix with suitable accepting or donor groups represents a suitable tool to get compounds with tuned optoelectronic properties. However, this strategy is scarcely appealing since it could have a strong influence on the intermolecular interactions (π-stacking) and therefore be detrimental for charge carrier properties. In the last decades, the incorporation of p-block atoms into the helix has come to the fore as a tool to obtain systems with enhanced optoelectronic properties, without heavily influencing the π-stacking properties.

2.2.3 Synthesis of helicenes

From a synthetic point of view, the most relevant strategy to prepare helicenes is the Mallory photocyclization of suitable stilbene derivatives [33] The oxidative photocyclization of stilbene derivatives was first used in 1967 by Martin [34] (Scheme 1a) for the synthesis of carbo[7]helicenes starting from a *cis*/*trans*-mixture of the corresponding stilbene precursor.

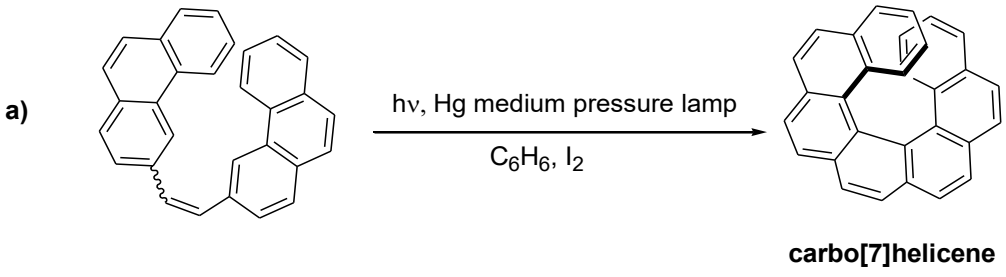

Scheme 1a. First example of photochemical synthesis of [7]helicene.

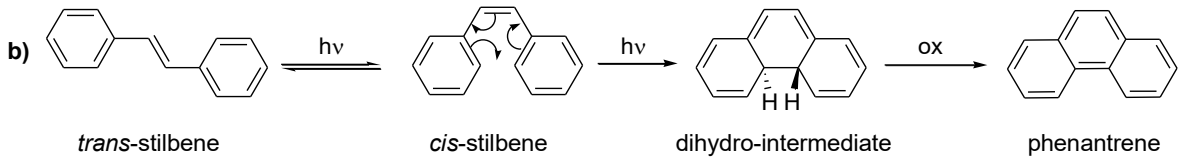

Scheme 1b. Mechanism of the Mallory photocyclization.

The Mallory photocyclization (illustrated for the simple stilbene in Scheme 1b) occurs on *cis*-isomer, but in general, it is not necessary to prepare selectively the *cis*-isomer of the starting alkene because even using *trans*-stilbene or a *trans*/*cis* mixture, the first step of the reaction is the light-promoted *trans*-to-*cis* isomerization. The subsequent cyclization gives the dihydro intermediate that is oxidized to helicene in the presence of air or iodine.

The Mallory photocyclization for obtaining helicenes was widely investigated and later optimized in terms of yield and selectivity[35] Although widely used, this synthetic way still presents some drawbacks, mainly related to the high-dilution conditions, which are required to avoid intermolecular dimerization, and the specific photochemical equipment needed (photochemical reactors/lamp).

In the last decades, alternative strategies for helicene synthesis have been reported[36] and these include the use of different reactions among which Diels-Alder[37] cycloadditions (Scheme 2a), Stille coupling[38] (Scheme 2b), metal-catalyzed [2+2+2] cycloisomerization (Scheme 2c,d),[39, 40] ring-closing metathesis[41] (Scheme 2e).

No enantioselective version of photocyclization reactions have been currently reported while several methods involving the use of Diels-Alder,[42] metal-catalysed cyclizations,[43] and metathesis[44] have been described in the literature for the synthesis of enantiopure helicenes.

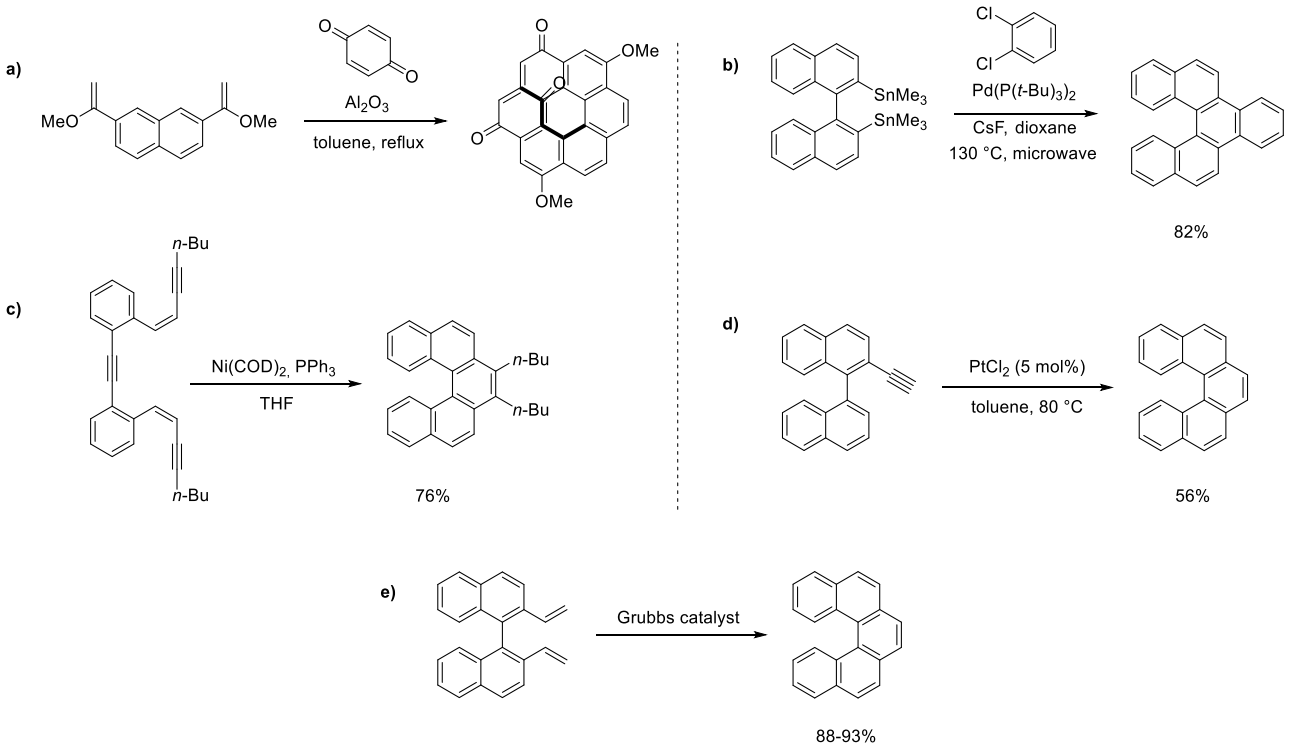

Scheme 2. Alternative methods for helicene synthesis: a) two-fold Diels-Alder; b) two-fold Stille coupling; c) Ni(0)-catalysed intramolecular [2+2+2] cycloaddition; d) π-acid catalysed cycloisomerization using a Pt(II)-catalyst; e) ring-closing metathesis.

Despite the huge development of alternative methods and the known drawbacks, the Mallory photocyclization of stilbene derivatives still represents one of the most efficient and popular methods to prepare helicenes and heterohelicenes, due to its versatility and owing to the easy preparation of stilbene precursors.

Photocyclization reactions have been largely applied as key step in the synthesis of heterohelicenes, and especially of tetrathia[7]helicenes (**7THs**).[45] which are an interesting class of heterohelicene combining the properties of oligo-thiophenes with those of helicenes (Scheme 3). The presence of sulphur atoms along the outer ridge of the helix provides the opportunity to modify the electronic and optical properties thanks, *inter alia*, to S-S interactions in the solid state.[46]

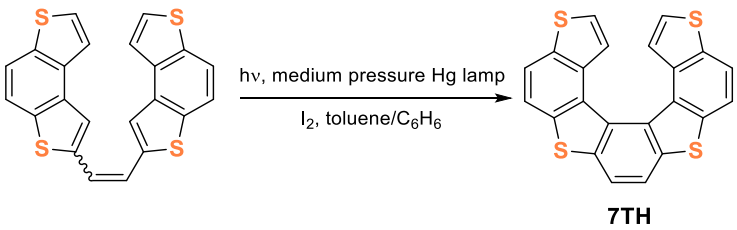

Scheme 3. Synthesis of tetrathia[7]helicene (**7TH**) *via* oxidative photocyclization.

Our research group has a long-standing expertise in the synthesis of thiahelicene systems and, in the last years, contributed to the development of this field with the setup of innovative strategies to prepare different functionalized tetrathia[7]helicenes **7THs** *e.g., via* a stereospecific Suzuki-type reaction using (Z)-boronic esters or *via* a metal catalysed annulation of suitable precursors.[47] Hence, steric and electronic properties of thiahelicenes can be modulated by introducing substituents of different nature and size on the helical scaffold and this is facilitated by the presence of the thiophene rings. In fact, exploiting the thiophene reactivity, thiahelicene or its precursors can be easily and regioselectively functionalized by direct electrophilic substitution or through generation of α-anions followed by reaction with electrophiles.

Tetrathia[7]helicenes also represent an example of how the presence of a heteroatom in the helical skeleton could be a tool to obtain systems with enhanced optoelectronic properties, without heavily influencing the π-stacking properties (Figure 10).

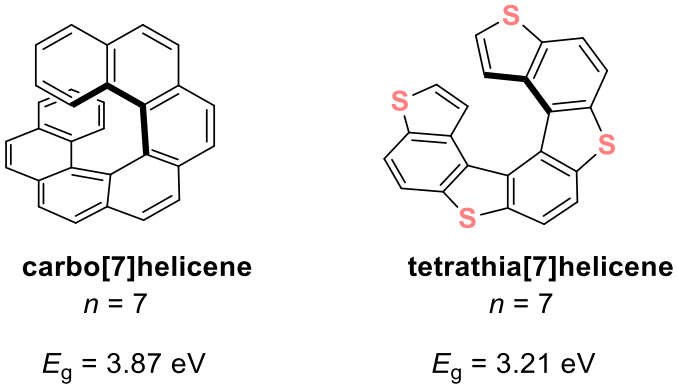

Figure 10. E_g values of selected helicene and heterohelicene systems.

In fact ranging from carbo[7]helicene to [7]helicene (7TH) a ≈0.7 eV E_g reduction can be obtained (Figure 10).[48] This last example shows as the doping of helicene scaffolds with p-block elements, is nowadays the most effective strategy to get helical systems with fine-tuned electronic properties and thus is a promising tool for the development of new building blocks for functional materials.

In this context, the introduction of trigonal boron atom into a thiahelicene scaffold could give rise to a novel class of unexplored boron π-conjugated molecules with potentially intriguing properties.

2.3 Boron containing π-systems: general concepts

Tri-coordinate boron π-systems, characterized by uncharged boron atoms, are isostructural and isoelectronic to carbenium ions with a trigonal-planar geometry. The boron vacant p_z orbital extends the π-conjugation pathway and exerts a strong π-acceptor effect (Figure 11).

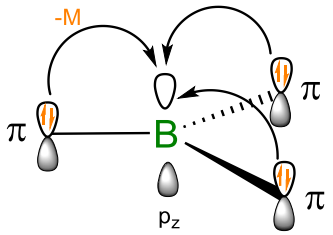

Figure 11. Electronic structure of a tri-coordinate boron π–system.

Generally, the insertion of trigonal boron centres contributes to stabilizing the LUMO of the molecule and, to less extent, the HOMO. The resulting decrease in the LUMO energy affects the energy gap and in turn optoelectronic characteristics of the compound as well as its electron accepting abilities.[49]

Furthermore, boron functionalized π–systems often display high luminescence performances making them suitable building blocks for emissive materials as well as for n-type semiconductors.

As a drawback, the empty p_z orbital of the boron atom behaves as a Lewis acid and generally makes tri-coordinate boron compounds extremely reactive towards Lewis bases, including water.

When a Lewis base is coordinated to the boron atom, the geometry of the boron in the corresponding Lewis acid-base adduct changes from trigonal-planar to tetrahedral, thus interrupting the π–conjugation (Scheme 4).

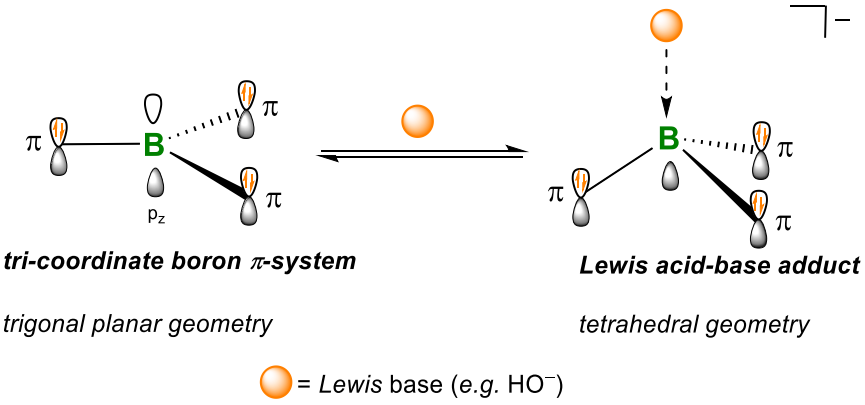

Scheme 4. Lewis acid-base adduct formation.

To discourage adduct formation, a rational structural design of the molecule is always required: three different stabilization strategies have been regarded as suitable tools to stabilize the trigonal geometry in boranes (Figure 12).

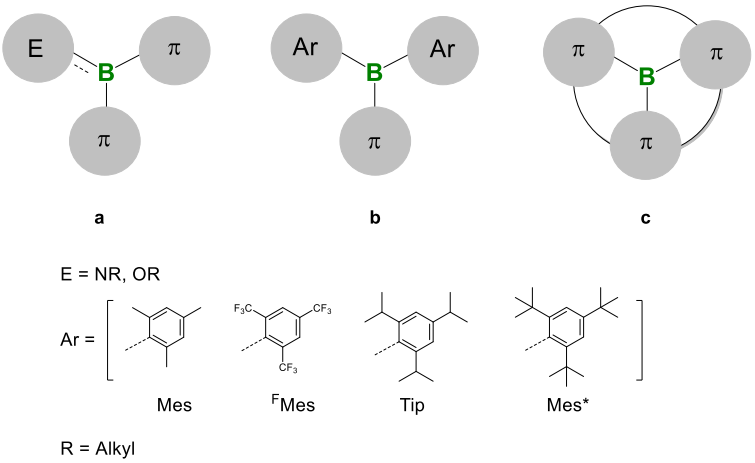

Figure 12. Boranes stabilization strategies.

a) Introduction of a π-donor substituent "**E**", such as an amino or alkoxy group, to reduce the electron deficiency at the boron atom through partial double-bond formation.[17a]

b) Introduction of one or two bulky "Ar" groups, such as mesityl (Mes), fluoromesityl (^{F}Mes) etc., onto the boron site: the "propeller arrangement" of such *o*-substituted benzenes generally shields the p_z orbital from Lewis bases attack.[50]

c) Incorporation of the boron atom at the central position of the π-system (*e.g.* in the core of a carbon skeleton) to provide full structural constraint of the boron atom within the rigid carbon skeleton.[51] Although these compounds do not have any steric protection of the boron site in the vertical direction, the Lewis acid-base adduct formation is less feasible since the reaction of the planar carbon structure with a Lewis base would lead to a thermodynamically unfavoured adduct with tetrahedral geometry, in which the rigid carbon skeleton is highly distorted.

Despite the attack from nucleophiles is hampered, air-stable boranes can still exert Lewis acidic character and are reactive towards small anions such as fluoride and cyanide (Scheme 5) and in this case the adduct formation can be exploited in chemo-sensors.[52]

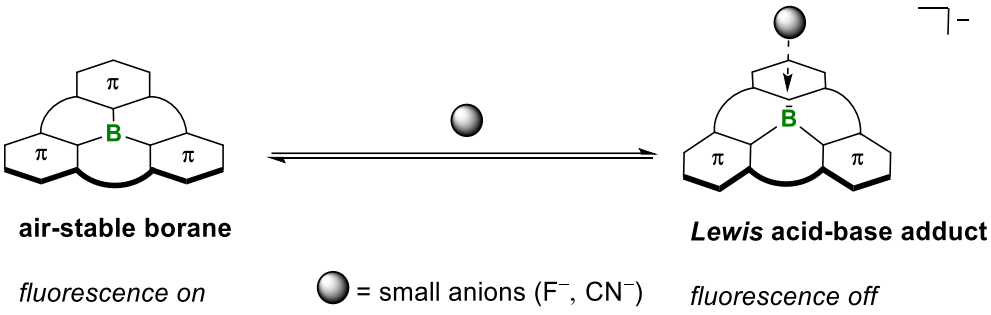

Scheme 5. Reaction of an air-stable borane with small anions.

In fact, in the adduct the interruption of the conjugation brings to quenching of the fluorescence, thus allowing the detection of the anions. This phenomenon can be reversibly switched on or off in many cases.

Due to the above-mentioned features, organoboranes are extremely attractive building blocks in various fields of applications ranging from material science to biology, and several conjugated molecules doped with one or more trigonal boron atoms have been reported over the past decades. [17,18]

In particular, the formal insertion of boron atom(s) into polycyclic aromatic hydrocarbons[19] is of great interest as it enables the formation of a powerful class of molecules, namely boron-doped PAHs.[17a]

Recently, these boron-embedded polycycles have polarised the research interest as they combine excellent luminescence and charge transport properties with predictable supramolecular arrangements, making them promising building blocks for next generation functional materials.

For the classification of B-PAH structures is helpful to define the nomenclature of bora-heterocycles[53] which are formally derived from the 1) insertion of borylene unit(s) into cyclobutadiene, fulvene and benzene, which generates the antiaromatic borole **A**, 1,4-dibora-2,5-cyclohexadiene **B**, borine **C** and the aromatic borepin **D**, or 2) replacement of a benzene C=C bond with a B=E (E = O, N) bond, which generates the aromatic 1,2-oxa/aza- borine ring **F** (Figure 13).

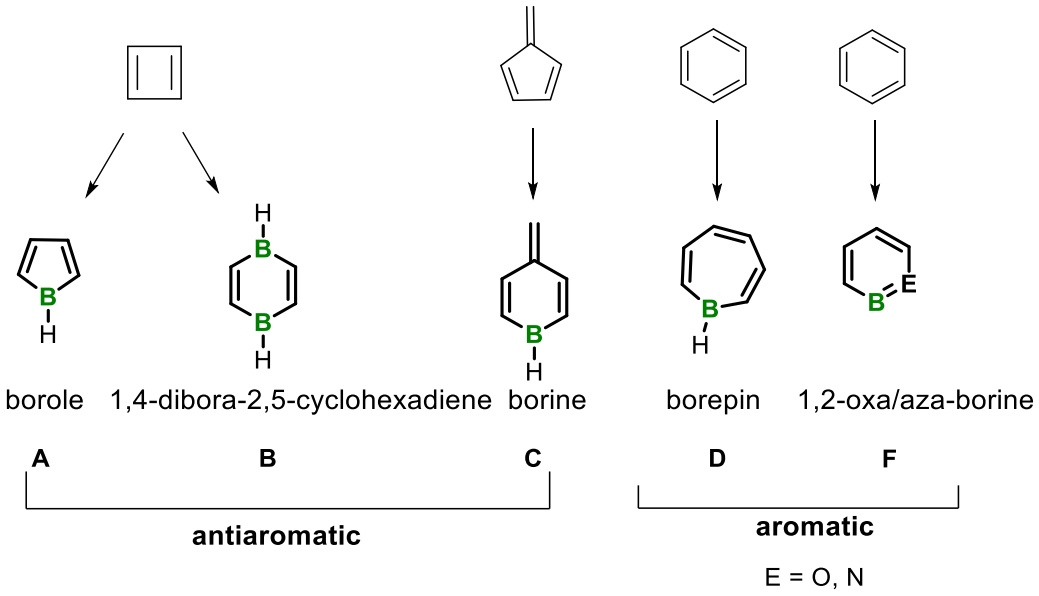

Figure 13. Nomenclature of bora-heterocycles.

More extended π-structures incorporating bora heterocycles **A**, **B**, **D**, **F** can be further defined as borafluorene, diboraanthracene, dibenzo borepine and oxa/azabora phenanthrene and have been synthesized over the past decades (Figure 14).[54]

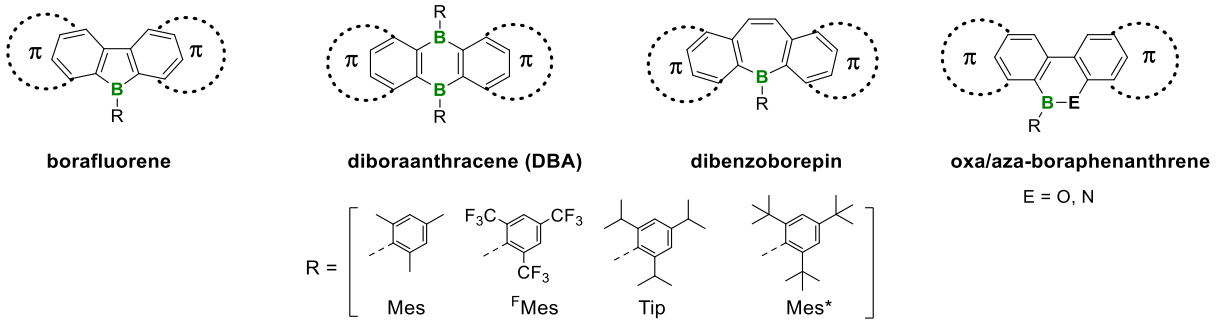

Figure 14. General borafluorene, diboraanthracene and dibenzoborepin structures.

2.3.1 Properties and applications of distorted B-PAHs and B-doped helicenes

Boron containing polycyclic aromatic compounds (B-PAHs) usually show peculiar spectroscopic and electrochemical properties such as red-shifted emission and absorption bands, high photoluminescence quantum yields (Φ_{PL}) and low reduction potentials (E_{red}) suitable for applications in optoelectronics.

In addition to planar compounds, recently, configurationally stable distorted boron-doped PAHs have also been reported and showed good solubility properties, unaltered stacking abilities and appreciable orbital interactions to produce similar performance as comparable planar systems.[55]

Most frequently, sp^2 hybridized boron atoms [B(sp^2)] are linked to an electron donor heteroatom (N, O) and resulting B–N/B–O linkages are beneficial for the stability of the boron centre, due to its partial double bond formation.

Despite their great potential, B(sp^2)-doped helicenes are rare and the large part of the reported boron-doped helicenes includes B(sp^3)-doped compounds.[56] Very recently, some helical-shaped B(sp^2)-PAHs have been reported and, in addition to interesting photophysical and redox properties, they showed unprecedented charge carrier mobilities.

As representative examples, borahelicenes **1**-**7** are shown in Figure 15.

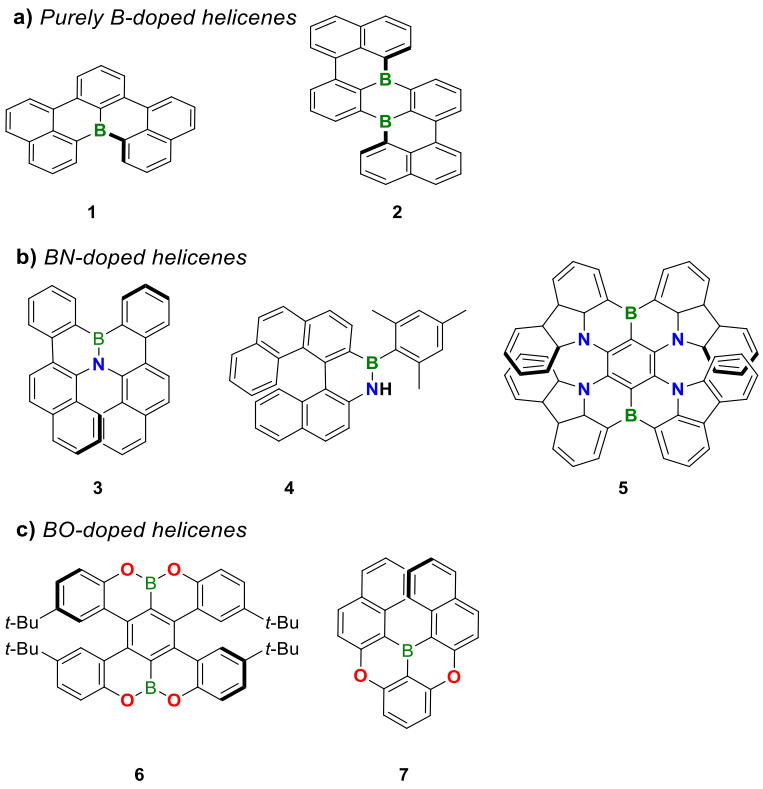

Figure 15. Structure of borahelicenes **1-7**.

Two examples of purely B-doped helicenes (**1** and **2**) have been reported (across 2015 and 2019) by Wagner.[57,58] In particular, the B-doped [4]helicene **1** that showed E_g = 2.60 eV, Φ_{PL} = 81% and suitable redox features, was successfully integrated as emissive component in an OLED device.

Regarding BN-doped helicene, the helicene **3** showed unprecedented and interesting spin carrier inversion[55] between racemate and single enantiomers, which display p- and n-type semiconducting character respectively. Recently Wang reported a double helicene **5** incorporating 1,4-azaborine rings which showed E_g = 1.81 eV and Φ_{PL} = 100%.[59]

Oxaborine-containing helicenes **6** and **7** also showed peculiar properties. Remarkably **6** showed Φ_{PL} = 65% and an excellent ambipolar semiconductor activity; moreover **6** resulted to be CPL-active with a g_{lum} = 1.7×10^{-3} for both enantiomers.[60,61]

In general, all the B-doped helical structures containing aza- and oxa-borine rings (**1-7**) displayed excellent solubility, spectroscopic, electrochemical, and stacking properties.

Moreover, in addition to their optical and redox properties, borahelicenes, due to their inherent chirality and configurational stability, are also attractive in the field of asymmetric synthesis therefore expanding the range of their potential applications.

2.3.2 Synthesis of B-doped helicenes

Synthetic methods reported for the preparation of borahelicenes have as a crucial step the introduction of boron atoms into the molecular scaffold, to form a boron-containing ring. This step is performed *via* intramolecular Friedel-Craft-type electrophilic aromatic substitution [62] and, for the synthesis of heterocycles containing the BN/BO bond, a N- or O- *ortho*-directing group is needed.[63] Generally these reactions require forcing experimental conditions (heating at elevated temperatures) and, the use of a non-nucleophilic base (acting as proton scavenger) is crucial. In some cases, the addition of a Lewis acid can be used as tool to enhance the electrophilicity of the borylating species.

In general, the synthetic strategies reported for the synthesis of borahelicenes are be divided in two main categories:

a) *synthetic strategies involving the introduction of boron at the late-stage* through an intramolecular electrophilic borylation (Scheme 6a) - when boron is positioned at the outer edge of the helix, the electrophilic borylation is followed by a nucleophilic substitution to introduce bulky substituents on the boron centre (using organometallic reagents, *e.g.,* aryl Grignard);

b) *construction of the helical scaffold starting from a B-doped building block* (Scheme 6b).

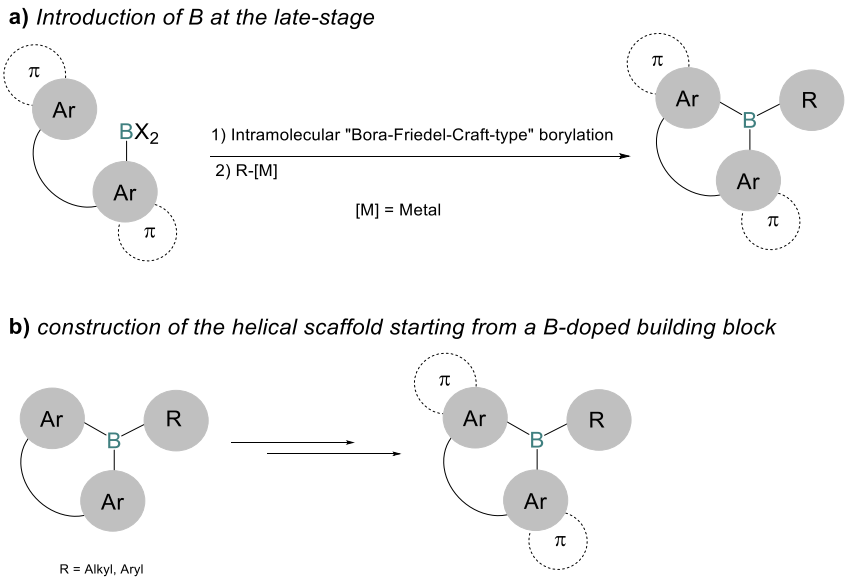

Scheme 6. Main synthetic strategies reported for the synthesis of borahelicenes.

Boron-doped aromatics are often very reactive towards nucleophiles, including water and sometimes not benchtop-stable. Furthermore, organoboranes are incompatible with some of the commonly used organic

transformations. Due to these drawbacks, for both B(sp^2) and B(sp^3)-doped helicenes, most of the reported syntheses exploit the first strategy, while the second one is rare (Scheme 7a, 7b).

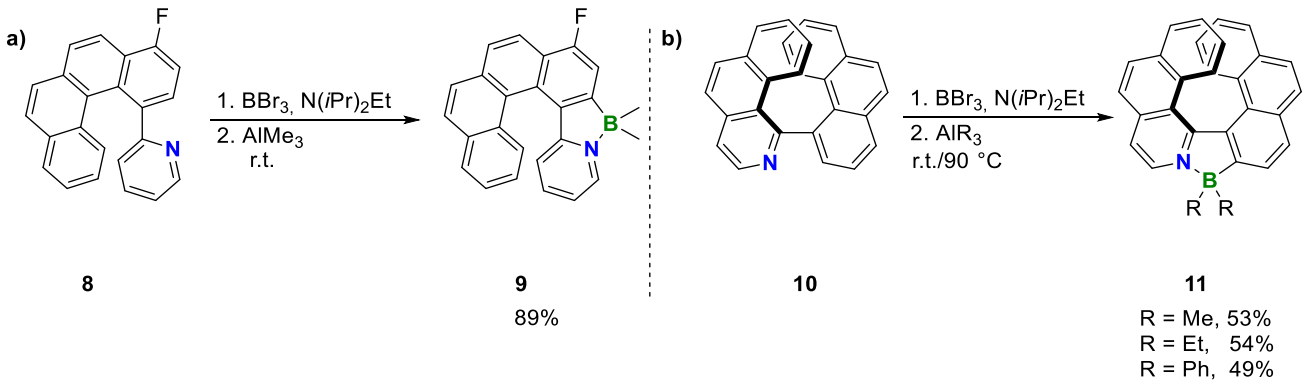

Scheme 7. Selected examples of B(sp^3)-doped helicenes synthesized by introduction of the boron at the late stage.

Regarding B(sp^3)-doped helicenes, in 2017 Crassous *et al*. reported a series of B(sp^3)-N doped helicenes obtained by N-directed borylation performed by treatment of aryl substituted 2-pyridines **8** with BBr_3 in presence of N(*i*Pr)$_2$Et, followed by the addition of $AlMe_3$ to introduce methyl groups onto the boron atom(s). As an example, the synthesis of **9** is reported in Scheme 7a.[56] This protocol allows to get access to a wide series of helicenes in mild conditions. Later in 2021 Nowak-Krol, using the same synthetic approach, reported new examples of B(sp^3)-N helicenes, showing as by increasing the temperature at the nucleophilic substitution stage, is it possible to introduce also aryl groups on the boron atom (Scheme 7b, reaction of **10** to **11**).[64]

More recently, the same group reported the first example of enantiospecific synthesis of BN-doped helicenes starting from axially chiral biaryls (Scheme 8).[65]

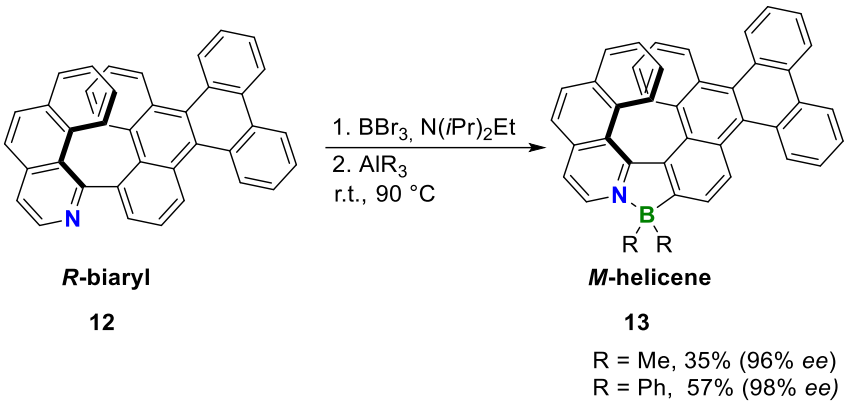

Scheme 8. First reported example of enantioselective synthesis of B(sp^3)N-helicenes. For simplicity only the synthesis of the *M*-helicene is reported.

The synthesis, performed starting from both enantiomers of biaryl **12** (pure enantiomers were obtained *via* chiral-HPLC separation exploits the axial-to-helical chirality transfer and allowed to get *P* and *M* helicenes **13** in high *ee%* (only the reaction of the *R*-enantiomer has been shown in Scheme 8).

Regarding trigonal B(sp^2)-helicenes, the late-stage borylation reactions can be divided in two sub-classes:

- *heteroatom-directed borylations*, for the synthesis of BO/BN bonds containing helicenes, involving an Ar-E-BX_2 (X = Cl, Br) intermediate (Scheme 9a);

- *direct carbon electrophilic borylations*, involving an Ar-BX_2 (X = Cl, Br) intermediate, for the synthesis of purely B(sp^2)-doped helicenes – (Scheme 9b) or helicenes in which the boron atom is not directly linked to a heteroatom (*e.g.,* 1,4-oxaborine-containing helicenes, *Scheme* 9c).
Representative examples for both cases were reported by Hatakeyama (Scheme 9).[55,66,61]

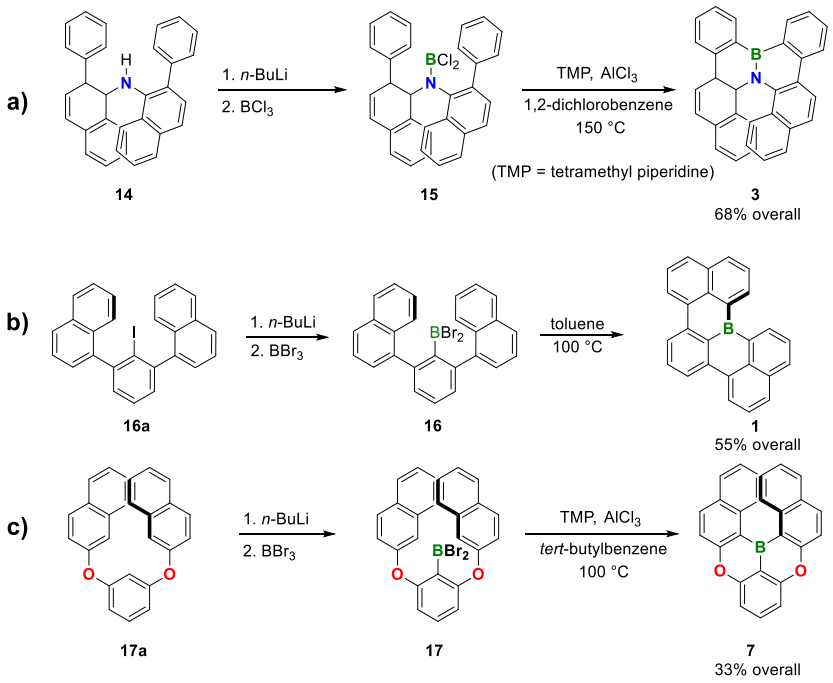

Scheme 9. Selected examples of B(sp^2)-doped helicenes synthesized by introduction of the boron at the late stage.

In detail, for the synthesis of BN-doped helicenes, the treatment of the suitable diaryl amine **14** with *n*-BuLi followed by the addition of BCl_3 gives access to the Ar_2N-BCl_2 intermediate **15** which**,** heated in the presence of tetrametylpyridine (TMP) and $AlCl_3$ gives the helicene **3** *via* two-fold intramolecular electrophilic borylation (Scheme 9a).[55] In the case of the purely B-doped **1** and 1,4-oxaborine containing **7,** the procedure is similar but the two-fold intramolecular borylation proceeds *via* an Ar-BX_2 intermediate (**16**/**17**) (Scheme 9b,c).[66,61]

One of the main disadvantages of introducing B(sp^2) atoms at the late-stage, is that this strategy dictates the helicene topology by imposing π-extended architectures and thus limiting the number of regular helical structures achievable (*e.g.* **3** in Scheme 9a or **5** in Figure 15).[55,59]

Especially for the synthesis of B(sp^2)-doped helicenes, a second drawback of the late-stage procedure is the formation of the B(sp^2)-C(sp^2) bond that, very often in the case of long (extended)helices, must occur against the steric strain of the helix making the ring-closure unfavourable. Therefore, in those cases, the borylation requires forcing conditions, which could lead to unwanted side-reactions like Lewis-acid-mediated Scholl reactions[67] (**18** to **19** Scheme 10a).

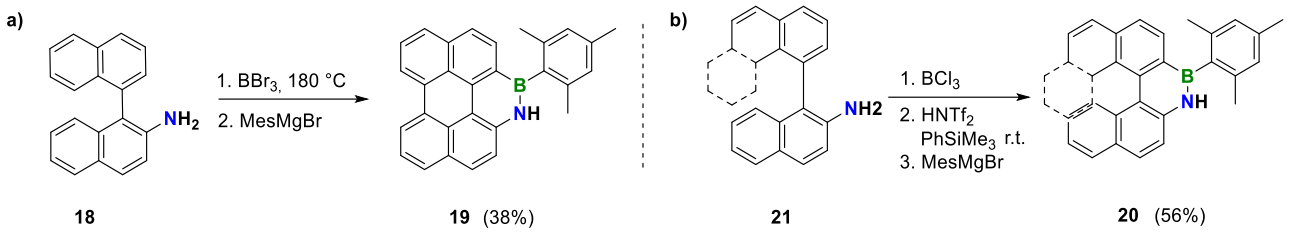

Scheme 10.

To overcome these issues, recently, Ingleson, Nowak-Krol and co-workers reported an enhanced procedure which allows the synthesis of BN-doped [6]helicenes in mild conditions (Scheme 10b).[68] In this case the use of $HNTf_2$ and $PhSiMe_3$ resulted to be crucial and allowed to achieve helicenes **20** in good yield using mild conditions starting from the corresponding binaphtyl amine **21**. Despite these encouraging results, steric strain remains as one of the main issues in the use of the late-stage strategy, especially in the case of long-sized helicenes.

Regarding the second strategy, that is the construction of the π-conjugated system starting from a B-doped building blocks, only few examples have been reported in the literature.

As one of the rare examples, recently Wagner reported the synthesis of mono- and doubly-B(sp^2)-doped helicenes **1**[57] and **2**[58] through two-fold intramolecular Yamamoto coupling starting from suitably functionalized triarylborane/diboraanthracene building blocks **22**/**23**. (Scheme 11).

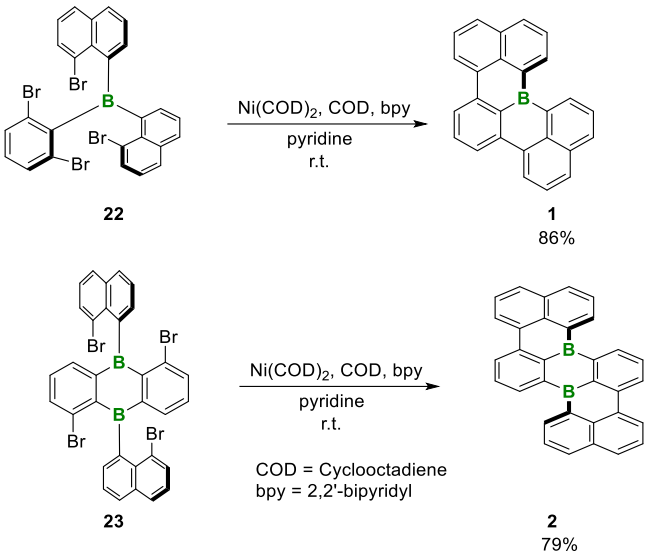

Scheme 11.

As a second example, recently Dou and Wang reported the synthesis of B-doped nanoribbons incorporating one or two B-[4]helicene moieties using a photocyclization reaction in the last step (Scheme 12), and this is one of the rare case of photocyclization involving boron containing aromatics.[69]

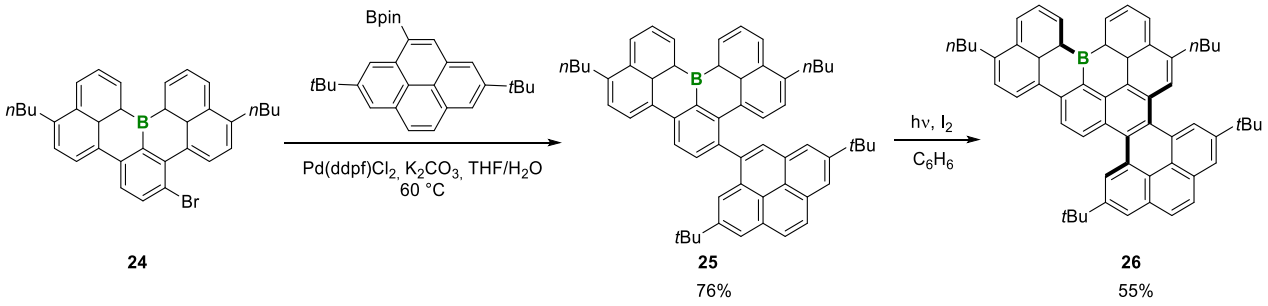

Scheme 12. Example of photocyclization involving boron containing aromatics

In detail the synthesis starts from the brominated B-doped building block **24** which is then functionalized *via* Suzuki coupling to give **25** and finally photocyclized *via* irradiation in benzene in presence of I_2 to give the double-helicene **26** (Scheme 12). This is one of the few examples of the use of a photocyclization involving boron containing aromatics, since photochemical conditions are often incompatible with most boron componds and constitute a good premise to the design of synthetic strategy to B-doped helical molecules involving photo-induced ring closures.

Considering the state of the art of the research on borahelicenes and the promising features of this class of compounds, the design and the setup of new synthetic routes to get new borahelicenes, as well as the investigation of their physico-chemical properties, is therefore a relevant research topic and is the object of the present Ph.D. thesis.

3. Aim of the project

This Ph.D. project was aimed to study and develop innovative and versatile syntheses of new boraheterohelicenes as well as the study of their stereochemical and optoelectronic properties to identify potential applications of these systems in material science.

The thesis work was carried out in part at the University of Milan in the laboratories of Prof. Emanuela Licandro and in part at the Goethe Universität Frankfurt am Main under the supervision of Prof. Dr. Matthias Wagner, within a co-tutelle programme. Owing to the long-standing expertise of Prof. Licandro group in the synthesis of tetrathia[7]helicenes (**7TH**) and that of Prof. Dr. Wagner group in the synthesis of boron-doped PAHs, I conceived this PhD project designing a series of tetrathia[7]helicenes incorporating one or two oxaborine rings into the helical scaffold and bearing mesityl group(s) on the boron atom(s) (Figure).

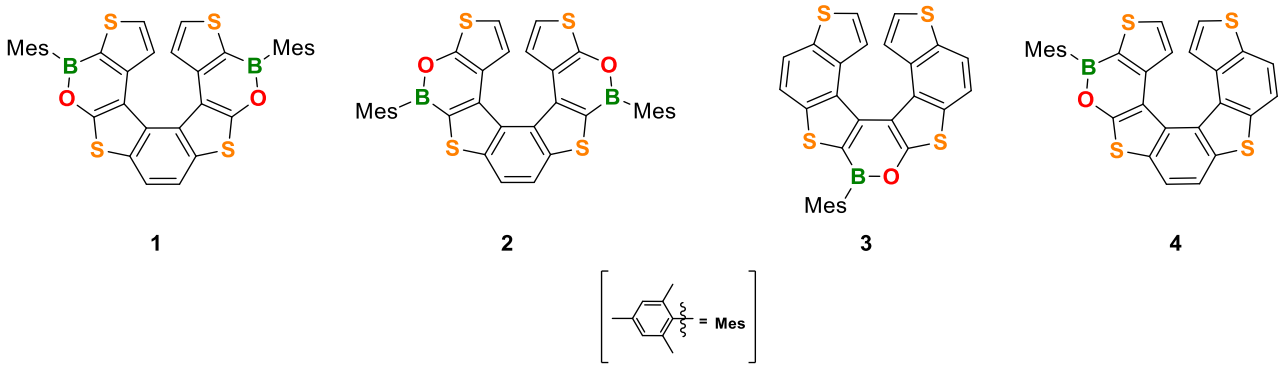

Figure: Designed BO-doped tetrathia[7]helicenes.

In detail, **1** and **2** structures incorporate two 1,2-oxaborine rings into the lateral region of the helical scaffold, while **3** and **4** contain one 1,2-oxaborine ring into the central or lateral part of the helix respectively.

The main goals of the present thesis can be divided as follows:

i. *the study of methodologies for the synthesis of the designed BO-doped tetrathia[7]helicenes;*

ii. *the study of the electrochemical, photophysical properties of all of the new BO-doped helicenes and intermediates by a combined experimental and theoretical effort (analysis/investigation) ;*

iii. *the study of the stereochemical and chiroptical properties of the BO-doped tetrathia[7]helicene target structures.*

For the sake of simplicity, results obtained concerning the topics covered in this PhD thesis have been organized in three chapters.

- *Chapter 1*: *Study of the synthesis and properties of the doubly BO-doped tetrathia[7]helicene **1***.

  This chapter deals with the study of synthetic methodologies to achieve **1** as well as the study of the electrochemical, photophysical and theoretical properties of **1** and all its BO-doped intermediates. Results of the stereochemical studies conducted on **1** are also discussed.

- *Chapter 2*: *Study of the synthesis and properties of the doubly BO-doped tetrathia[7]helicene* **2**.

  This chapter deals with the study of synthetic methodologies to achieve **2** as well as the study of the electrochemical, photophysical and theoretical properties of **2** and all its BO-doped intermediates.

  *Chapter 3: Preliminary study of the synthesis of the singly BO-doped tetrathia[7]helicene **3** and **4**.* This chapter deals with the study of synthetic methodologies to obtain BO-doped and precursors of **3** and **4,** as well as the study of electrochemical, photophysical and theoretical properties of the most relevant intermediates.

References

[1] J. K. Borchardt, *Materials Today* **2004**, *7*, 42–46.

[2] M.S. Alsalhi, J. Alam, L. A. Dass, M. Raja, *Int. J. Mol. Sci.* **2011**, *12*, 2036-2054.

[3] J. Sun, B. Zhang, H. E. Katz, *Adv. Funct. Mat.* **2011**, *21*, 29-45.

[4] Z.B. Wang, M.G. Helander, J. Qiu, D. P. Puzzo, M. T. Greiner, Z. M. Hudson, S. Wang, Z. W. Liu, Z. H. Lu, *Nature Photonics* **2011**, *5*, 753-757.

[5] a) S. Chen, L. Deng, J. Xie, L. Peng, L. Xie, Q. Fan, W. Huang, *Adv. Mater.* **2010**, *22*, 5227–5239;

b) A. P. Kulkarni, C. J. Tonzola, A. Babel, S. Jenekhe, *A. Chem. Mater.* **2004**, *16*, 4556–4573.

[6] H. Klauk, *Chem. Soc. Rev.* **2010**, *39*, 2643-2666.

[7] J. Bridle rope, H. Sirringhaus, *Chem. Rev.* **2007**, *107*, 1296-1323.

[8] M. C. Scharber, N. S. Sariciftci, *Prog Polym Sci* **2013**, *38*, 1929-1940.

[9] A. C. Grimsdale, K. L. Chan, R. E. Martin, P. G. Jokisz, A. B. Holmes, *Chem. Rev.* **2009**, *109*, 897-1091.

[10] T.-F. Guo, F.-S. Yang, Z.-J. Tsai, T.-C. Wen, S.-N. Hsieh, Y.-S- Fu, *Appl. Phys. Lett.* **2005**, *87*, 013504.

[11] A. Shuto, T. Kushida, T. Fukushima, H. Kaji, S. Yamaguchi, *Org. Lett.* **2013**, *15*, 6234.

[12] M. Cölle, J. Gmeiner, W. Milius, H. Hillebrecht, W. Brütting, *Adv. Funct. Mat.* **2003**, *13*, 108-112.

[13] J. R. Lakowicz, J. R. *Principles of Fluorescence Spectroscopy*; Springer: New York, **2006**.

[14] N. J. Turro, *Modern Molecular Photochemistry*; Univ. Science Books: Sausalitos, **1991**.

[15] Y. Hong, J. W. Y. Lam, B. Z. Tang *Chem. Soc. Rev.*, **2011**, *40*, 5361-5388.

[16] A. C. Grimsdale, K. Müllen, *Angew. Chem. Int. Ed.* **2005**, *44*, 5592-5629.

[17] a) E. von Grotthuss, A. John, T. Kaese, M. Wagner, *Asian J. Org. Chem.* **2018**, *7* (1), 37–53;

b) M. Stępien, E. Gońka, M. Żyła, N. Sprutta, *Chem. Rev.* **2017**, *117*, 3479−3716;

c) M. Hirai, N. Tanaka, M. Sakai, S. Yamaguchi, Chem. Rev., **2019**, *119* (14), 8291-8331.

[18] L. Ji, S. Griesbeck, T. B. Marder, *Chem. Sci.* **2017**, *8*, 846.

[19] R. G. Harvey, *Polycyclic Aromatic Hydrocarbons*; Wiley, **1997**.

[20] J. Wu, W. Pisula, K. Müllen, *Chem. Rev.* **2007**, *107*, 718.

[21] J. E. Anthony, *Angew. Chemie - Int. Ed.* **2008**, *47* (3), 452–483.

[22] R. Rieger, K. Müllen, *J. Phys. Org. Chem.* **2010**, *23* (4), 315–325.

[23] C. L. Hilton, J. M. Crowfoot, P. Rempala, B. T. King, **2008**, *8*, 13392–13399.

[24] J. Meisenheimer, K. Witte, *Berichte der Dtsch. Chem. Gesellschaft*, 1903, **36**, 4153–4164.

[25] M. S. Newman, D. Lednicer, *J. Am. Chem. Soc.*, 1956, **78**, 4765–4770.

[26] R. H. Martin, M. J. Marchant, *Tetrahedron Lett.*, 1972, **13**, 3707–3708.

[27] R. S. Cahn, C. Ingold, V. Prelog, *Angew. Chemie Int. Ed.*, **1966**, *5* (4), 385–415.

[28] H. Wynberg, *J. Am. Chem. Soc.* **1971**, No. 3, 2968–2974.

[29] a) Y. Ren, F. Jäkle, *Dalt. Trans.* **2016**, *45* (36), 13996–14007;

b)L. Ji, S. Griesbeck, T.B. Marder,. *Chem. Sci.* **2017**, *8* (2), 846–863.

[30] Turkoglu, G.; Cinar, M. E.; Ozturk, T. Triarylborane-Based Materials for OLED Applications. *Molecules* **2017**, *22* (9).

[31] J.M. Schulman, R. L. Disch, *J. Phys. Chem. A*, 1999, **103**, 6669–6672.

[32] Y. H. Tian, G. Park, M. Kertesz, *Chem. Mater.*, 2008, **20**, 3266–3277.

[33] a) F. B. Mallory,C. W. MalloryinOrganicReactions, Vol. 30 (Ed.:W. G. Dauben),Wiley,NewYork,1984,pp. 1–456;

b) K. B. Jørgensen, *Molecules* 2010, **15**, 4334–4358.

[34] M. Flammang-Barbieux, J. Nasielski, R. H. Martin, *Tetrahedron Lett.*, 1967, **8**, 743–744.

[35] a) L. Liu, B. Yang, T. J. Katz, M. K. Poindexter, *J. Org. Chem.*, 1991, **56**, 3769–3775;

b) N. Hoffmann, *J. Photochem. Photobiol. C:* Photochemistry Reviews **2014**, *19*, 1-19.

c) K. B. Jørgensen, *Molecules* **2010**, *15*, 4334– 4358.

[36] A. V. Gulevskaya, I. D. Tonkoglazova, *Adv. Synth. Catal.*, **2022**, *364*(15), 2502-2539.

[37] L. Liu, T. J. Katz, *Tetrahedron Lett.*, **1990**, *31*, 3983–3986.

[38] K. Kamikawa, I. Takemoto, S. Takemoto, H. Matsuzaka, *J. Org. Chem.*, **2007**, *72*, 7406–7408.

[39] F. Teplý, I. G. Stará, I. Starý, A. Kollárovič, D. Šaman, L. Rulíšek, P. Fiedler, *J. Am. Chem. Soc.*, **2002**, *124*, 9175–9180.

[40] V. Mamane, P. Hannen, A. Fürstner, *Chem. - A Eur. J.*, **2004**, *10*, 4556–4575.

[41] S. K. Collins, A. Grandbois, M. P. Vachon, J. Côté, *Angew. Chem. Int. Ed.*, **2006**, *45*, 2923–2926.

[42] M. C. Carreno, R. Hernandez-Sanchez, J. Mahugo, A. Urbano, *J. Org. Chem.*, **1999**, *64*, 1387–1390.

[43] I. G. Sánchez, M. Šámal, J. Nejedlý, M. Karras, J. Klívar, J. Rybáček, M. Buděšínský, L. Bednárová, B. Seidlerová, I. G. Stará, I. Starý, *Chem. Commun.*, **2017**, *53*, 4370–4373

[44] S. K. Collins, A. Grandbois, M. P. Vachon, J. Côté, *Angew. Chem. Int. Ed.*, **2006**, *45*, 2923–2926.

[45] S. Cauteruccio, D. Dova, E. Licandro, Thiahelicenes: From Basic Knowledge to Applications. *Adv. Heterocycl. Chem.* **2016**, *118*, 1–46.

[46] 1998CC1141, 2002CC932.

[47] V. Pelliccioli, D. Dova C. Baldoli, C. Graiff, E. Licandro, S. Cauteruccio, *Eur. J. Org. Chem.* **2021**, 383–395.

[48] A. Bossi, L. Falciola, C. Graiff, S. Maiorana, C. Rigamonti, A. Tiripicchio, E. Licandro, P. R. Mussini, *Electrochimica Acta*, **2009**, *54*, 5083–5097.

[49] G. Turkoglu, M. E. Cinar, T. Ozturk, *Molecules* **2017**, *22* (9).

[50] a) H. C. Brown, V. H. Dodson, *J. Am. Chem. Soc.* **1957**, *79* (9), 2302–2306; Doty, J. C.; Babb, B.;

b) J. P. Grisdale, M. Glogowski, J. L. R. Williams, J. L. R. *J. Organomet. Chem.* **1972**, *38*, 229–236.

[51] Z. Zhou, A. Wakamiya, T. Kushida, S. Yamaguchi, *J. Am. Chem. Soc.* **2012**, *134* (10), 4529–4532.

[52] F. Jakle, *Chem. Rev.* **2010**, No. 2, 3985–4022.

[53] B. Su, R. Kinjo, *Synth.* **2017**, *49* (14), 2985–3034.

[54] a) A. Wakamiya, K. Mishima, K. Ekawa, S. Yamaguchi, *Chem. Commun.* **2002**, *8* (5), 579–581;

b) A. John, S. Kirschner, M. K. Fengel, M. Bolte, H.-W. Lerner, M. Wagner, *Dalt. Trans.* **2019**, *48* (5), 1871–1877;

c) L. G. Mercier, W. E. Piers, M. Parvez, *Angew. Chemie - Int. Ed.* **2009**, *48* (33), 6108–6111.

[55] T. Hatakeyama, S. Hashimoto, T. Oba, M. Nakamura, *J. Am. Chem. Soc.* **2012**, *134*, 19600– 19603;

[56] a) C. Shen, M. Srebro-Hooper, M. Jean, N. Vanthuyne, L. Toupet, J. A. G. Williams, A. R. Torres, A. J. Riives, G. Muller, J. Autschbach, J. Crassous, *Chem. Eur. J.* **2017**, *23*, 407– 418;

b) Z. Domínguez, R. López-Rodríguez, E. Álvarez, S. Abbate, G. Longhi, U. Pischel, A. Ros, *Chem. Eur. J.* **2018**, *24*, 12660– 12668;

c) J. Full, S. P. Panchal, J. Götz, A. M. Krause, A. Nowak-Król, *Angew. Chem. Int. Ed.* **2021**, *60*, 4350– 4357.

[57] K. Schickedanz, T. Trageser, M. Bolte, H. W. Lerner, M. Wagner, *Chem. Commun.* **2015**, *51*, 15808– 15810.

[58] J. Radtke, K. Schickedanz, M. Bamberg, L. Menduti, D. Schollmeyer, M. Bolte, H. W. Lerner, M. Wagner, *Chem. Sci.*, **2019**, *10*, 9017– 9027.

[59] J.-K. Li, X.-Y. Chen, Y.-L. Guo, X.-C. Wang, A. C.-H. Sue, X.-Y. Cao, X.-Y. Wang, *J. Am. Chem. Soc.* **2021**, *143*, 17958−17963.

[60] T. Katayama, S. Nakatsuka, H. Hirai, N. Yasuda, J. Kumar, T. Kawai, T. Hatakeyama, *J. Am. Chem. Soc.* **2016**, *138* (16), 5210–5213;

[61] H. Hirai, K. Nakajima, S. Nakatsuka, K. Shiren, J. Ni, S. Nomura, T. Ikuta, T. Hatakeyama, *Angew. Chemie - Int. Ed.* **2015**, *54* (46), 13581–13585.

[62] a) M.J.Ingleson, *Synlett*, **2012**, 1411–1415;

b) F.G.Fontaine, E´.Rochette, *Acc. Chem. Res.*, **2018**, *51*, 454–464;

c) T.S. DeVries, A. Prokofjevsand, E. Vedejs, *Chem. Rev.*, **2012**, *112*, 4246–4282.

[63] S. A. Iqbal, J. Pahl, K. Yuan, M. J. Ingleson *Chem. Soc. Rev.*, **2020**, *49*,4564.

[64] J. Full, S. P. Panchal, J. Götz, A. M. Krause, A. Nowak-Król, *Angew. Chem. Int. Ed*. **2021**, *60*, 4350– 4357.

[65] F. Full, M. J. Wildervanck, D. Volland, A. Nowak-Król, *Synlett* **2022**, *33*.

[66] F. Miyamoto, S. Nakatsuka, K. Yamada, K.-i- Nakayama, T. Hatakeyama, *Org. Lett.* **2015**, *17*, 6158−6161.

[67] Z. Jiang, S. Zhou, W. Jin, C. Zhao, Z. Liu, X. Yu *Org. Lett.* **2022**, *24*(4) 1017–1021.

[68] K. Yuan, D. Volland, S. Kirschner, M. Uzelac, G. S. Nichol, A. Nowak-Król, M. J. Ingleson, *Chem. Sci.* **2022**, *13*, 1136– 1145.

[69] a) V. M. Hertz, J. G. Massoth, M. Bolte, H. W. Lerner, M. Wagner, *Chem. Eur. J.* **2016**, *22*, 13181–13188;

b) W. Sun, J. Guo, Z. Fan, L. Yuan, K. Ye, C. Dou, Y. Wang, *Angew. Chem. Int. Ed.* **2022**, *61*, e202209271; c) A. John, S. Kirschner, M. K. Fengel, M. Bolte, H.-W. Lerner, M. Wagner *Dalton Trans*., **2019**, *48*, 1871-1877.

4. Results and Discussion

4.1 Study of the synthesis and properties of the BO-doped tetrathia[7]helicene 1

4.1.1 Synthesis, NMR and crystallographic characterization of 1

In the first part of my PhD I faced the synthesis of the doubly BO-doped tetrathia[7]helicene **1**, which incorporates four thiophene rings and two oxaborine rings into the helical scaffold and bears mesityl groups on the boron atoms. Looking at a possible retrosynthetic analysis of **1** (Scheme 1), the mesityl dithienooxaborine **5**, was identified as potential building block.

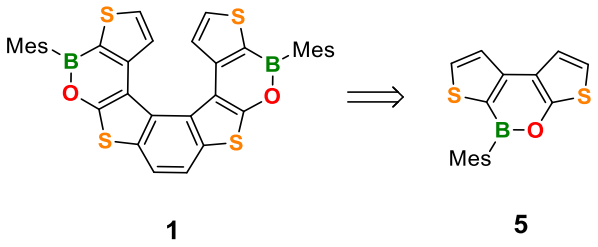

1 **5**

Scheme 1. Dithienooxaborine **5** as potential building block for **1**.

Although some dithieno oxaborines are known in the literature,[1] the mesityl oxaborine **5** has not been reported and therefore its synthesis was setup starting from the known methoxy bithiophene **S1** (prepared according to the literature;[1] see Section 2.1 of the Experimental Part) *via* intramolecular demethylative borylation followed by the addition of an organometallic reagent to introduce the mesityl group (Scheme 2).

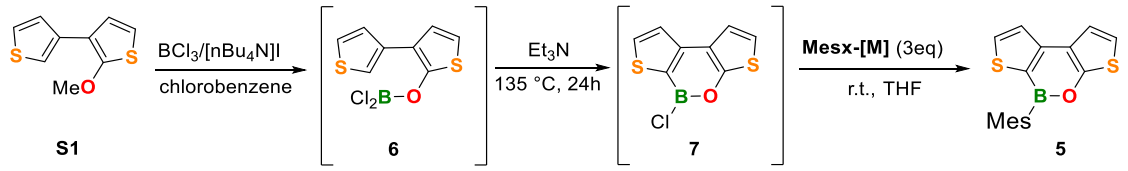

Mes_x-[M]	
MesMgBr	62 - 77%
MesCu	26%
MesLi	4%
Mes_2Zn	0%

Scheme 2. Synthesis of the mesityl diethienooxaborine **5**.

In detail **S1** was treated with BCl_3 and [*n*Bu_4N]I at room temperature, giving the demethylated Ar-O-BCl_2 species **6** (the use of [*n*Bu_4N]I is needed to promote the demethylation). The heating of **6** at 135 °C in the presence of Et_3N (acting as proton scavenger) furnished the intermediate **7** through intramolecular borylation.[2] Finally the treatment of **7** with the suitable organometallic reagent, allowed to introduce the mesityl ring *via* nucleophilic substitution at the boron atom.

It is worth to mention that the study of this one-pot procedure required a careful setup of the experimental protocol, including: the choice of proper glassware (Schlenk apparatus, J-Young flask), the preparation of the organometallic reagents (*e.g.,* mesityl Grignard) and the purification of solvents and additives (chlorobenzene, Et_3N were distilled over CaH_2).

Several organometallic reagents were tested, among them MesMgBr (3 eq is the optimal stoichiometry) gave the best results affording **5** in yields up to 77% on a 500 mg-scale. The structure of **5**, that proved to be a benchtop-stable compound, was elucidated by accurate NMR analyses, and confirmed by X-ray (Figure 1 and Figure S87). Diagnostic proton and carbon shifts mentioned in the following discussion are recaped in Figure 4.

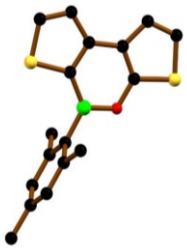

Figure 1. X-ray crystal structure of **5**. Crystal system: monoclinic, space group: P 21/n. B: green, C: black, O: red, S: yellow spheres; picture generated with the crystallographic software *Mercury*.

In the ^{1}H NMR spectrum, of high diagnostic value are the signals of protons in the α positions of the two thiophene rings of **5**: due to π-conjugation with the electron-withdrawing B or the electron-donating O atom, the CH nuclei of the electron-poor borylated thiophene are significantly deshielded ($\delta(^1H)$ = 7.98, $\delta(^{13}C)$ = 138.2) compared to those of the electron-rich oxygenated thiophene ($\delta(^1H)$ = 6.96, $\delta(^{13}C)$ = 114.8).

Once optimized the synthesis of **5**, its stability and reactivity have been investigated as a premise to the design of a suitable synthetic way to helicene **1**. Reactions carried out on **5** are depicted in Scheme 3.

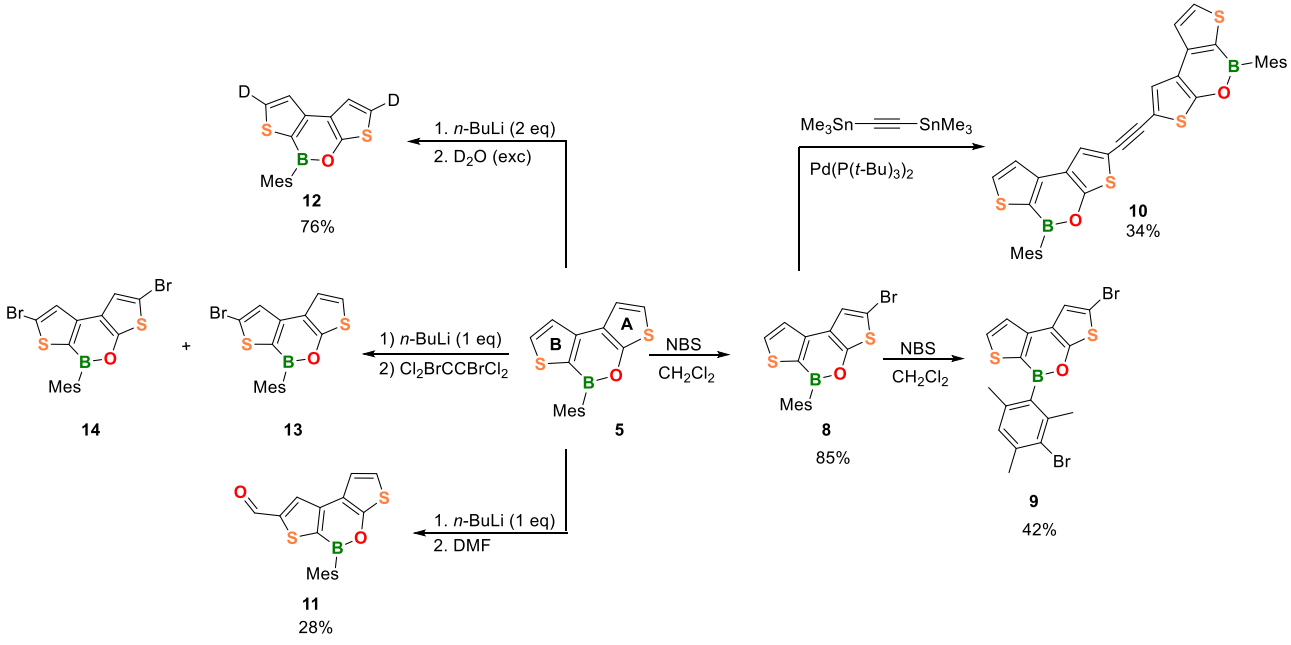

Scheme 3. Investigation of the mesityl diethienooxaborine **5** reactivity.

Given the presence of the B-O bond, we hypothesized different reactivity of the two thiophene rings A and B: "oxygenated thiophene A" was supposed to be the most electron rich, and thus more reactive towards electrophiles, while "borylated thiophene B" was expected to be less electron rich and having the more acidic α-proton. To test the possibility of a selective functionalization of the two thiophene rings we performed a series of experiments (Scheme 3 and Section 13 of the Experimental Part).

Bromination with *N*-bromosuccinimide (NBS) revealed that **5** is reactive towards electrophiles and can be selectively brominated on the α position of the oxygenated thiophene ring using a slight excess (1.2 eq) of NBS that gave the brominated **8** in 85% yield (Scheme 3, right).

Bromo-dithienooxaborine **8** was completely characterized and the NMR analysis confirmed that the Br atom was selectively introduced next to the S atom into the oxygenated thiophene ring A, as evidenced of the disappearance of the proton resonance at 6.96 ppm and by a further upfield shift of the corresponding ^{13}C resonance (from 114.8 to 103.1 ppm) as a result of the magnetic anisotropy effect of the attached Br substituent (see Figure 4). The structure of **8** was further confirmed by X-ray analysis (Figure 2 and Figure S88).

Figure 2. X-ray crystal structure of **8**. Crystal system: monoclinic, space group: C 2/c. B: green, C: black, O: red, S: yellow, Br: brown spheres; picture generated with the crystallographic software *Mercury*.

To evaluate the possibility to achieve double bromination, **8** was in turn treated with 1.5 eq of NBS but the reaction led to the bromination on the mesityl ring, and **9** was the only isolated compound. Furthermore, the reaction of **8** with 1,2-bis(trimethyl)stannylacetylene in the presence of $Pd(P(t\text{-}Bu)_3)_2$ as catalyst gave **10** in 34% yield, showing as α-brominated oxaborine **8** is a potentially useful building block for the construction of more extended systems (Scheme 3, right).

Next, we tested the reactivity of **5** towards strong bases (*e.g., n*-BuLi; Scheme 3, left). The treatment of **5** with 1 eq of *n*-BuLi followed by the addition of an excess of DMF gave **11** in 28% yield, showing that it is possible to selectively functionalize the "borylated thiophene" α-position under these conditions. Although the possibility to get the di-anion on the two thiophene α-positions was confirmed by deuteration test (**12** obtained in 76% yield), attempts of two-fold formylation, using 2 eq of *n*-BuLi resulted in decomposition products.

We then tried to achieve selective bromination of the "borylated thiophene B" and thus **5** was treated with *n*-BuLi and then reacted with $Cl_2BrCCBrCl_2$ giving the expected brominated product **13** in modest yield besides the doubly brominated **14** and starting oxaborine **5**.

These preliminary tests showed how the dithienooxaborine **5** can be a useful building block with peculiar reactivity at the two thiophene α positions and could allow the preparation of a wide range of derivatives.

As the bromoderivative **8** can be obtained in mild conditions and in good yield, we selected a synthetic route to helicene **1** starting from **8** (Scheme 4) used as precursor of alkene **15**, (for simplicity, in the scheme, only the *cis*-isomer **15** is indicated) from which **1** can be obtained *via* Mallory photocyclization.

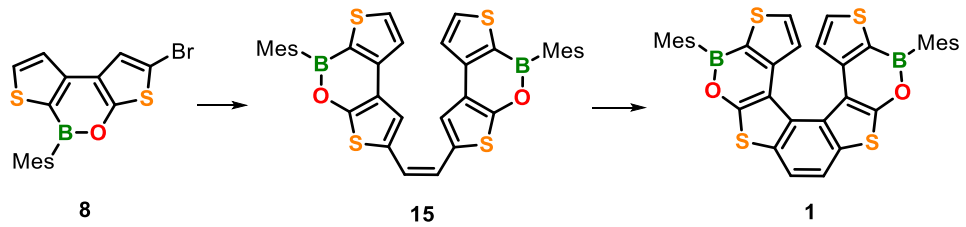

Scheme 4. Synthetic route designed for **1**.

The synthesis of alkene **15** was deeply investigated and carried out using three synthetic routes (*Route A*, *Route B*, *Route C*) as shown in Scheme 6.

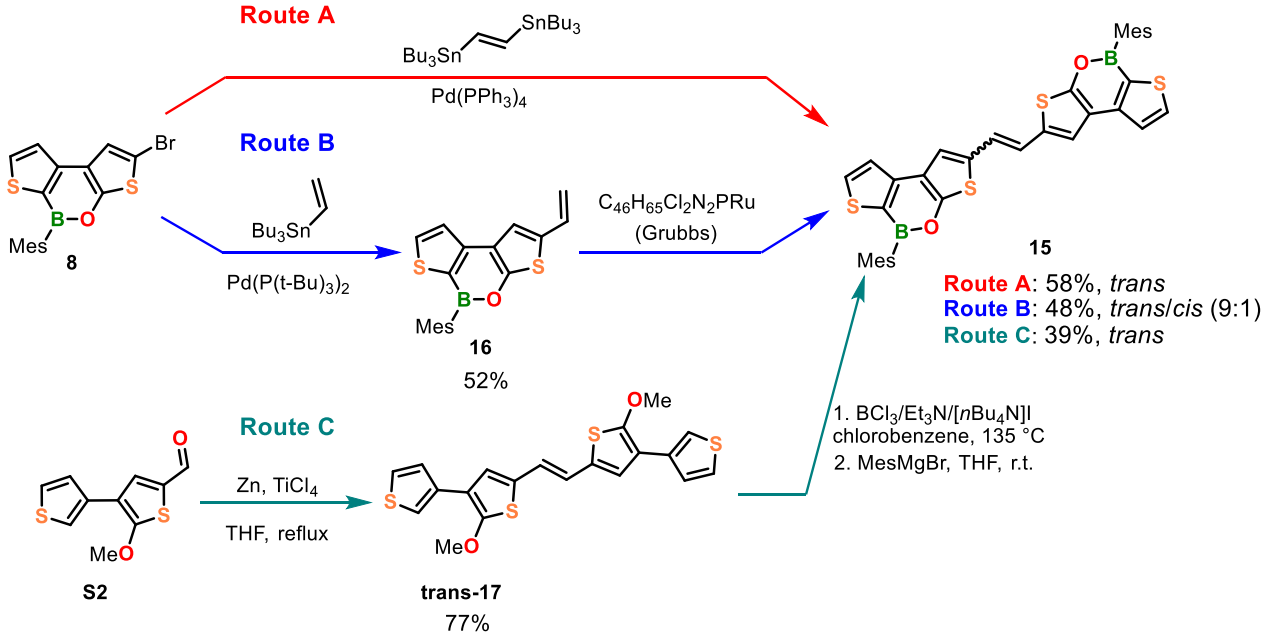

Scheme 6. Synthetic routes to the stilbene derivative **15**.

In both *Route A* and *Route B* brominated oxaborine **8** was used as starting material.

Following *Route A*, **8** was subjected to a Stille coupling with the commercially available *trans*-1,2-bis(tributylstannyl)ethylene in the presence of $Pd(PPh_3)_4$ as catalyst and gave the target stilbene derivative **15**

in 58% yield as *trans*-isomer. The *trans*-**15** NMR spectra (Figure 4), showed for protons of the terminal thiophene rings signals at δ = 7.99 and δ = 7.60 and the corresponding carbon nuclei at C(α) = 138.4 ppm and C(β) = 123.0 ppm. Moreover, the ethylene bridge protons give rise to new resonances at $\delta(^1H)$ = 7.02 and $\delta(^{13}C)$ = 121.6. The *trans*-configuration was confirmed by X-ray crystallography (Figure 3 and Figure S89).

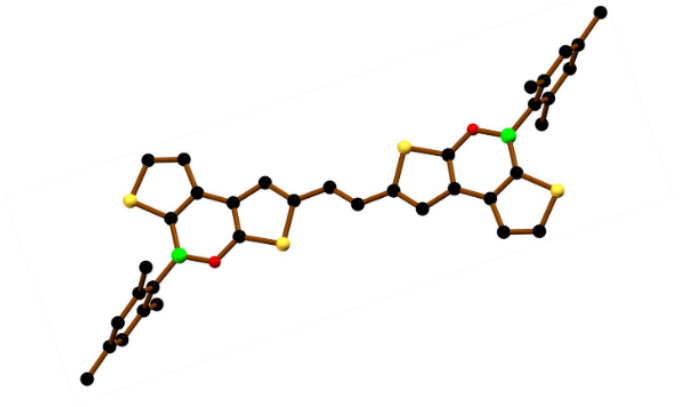

Figure 3. X-ray crystal structure of *trans*-**15**. Crystal system: monoclinic, space group: P 21/c. B: green, C: black, O: red, S: yellow spheres picture generated with the crystallographic software *Mercury*.

In the *Route B* (Scheme 6), **5** was first submitted to a Stille coupling with the commercial tributylvinyltin and Pd(P(*t*-Bu)$_3$)$_2$ and gave the vinyl derivative **16** (y = 52%) which was then dimerized *via* metathesis reaction, to give the alkene **15** in 48% yield as *trans*/*cis* (9:1) mixture (NMR resonance of the olefinic proton of the *trans*-isomer at $\delta(^1H)$ = 7.02 while that of the *cis*-isomer at $\delta(^1H)$ = 6.67; Figure 4).

Although this second route has a modest yield, it is worth to note that the metathesis reaction of **16** represents the first example of such a reaction carried out on a BO-doped aromatic.

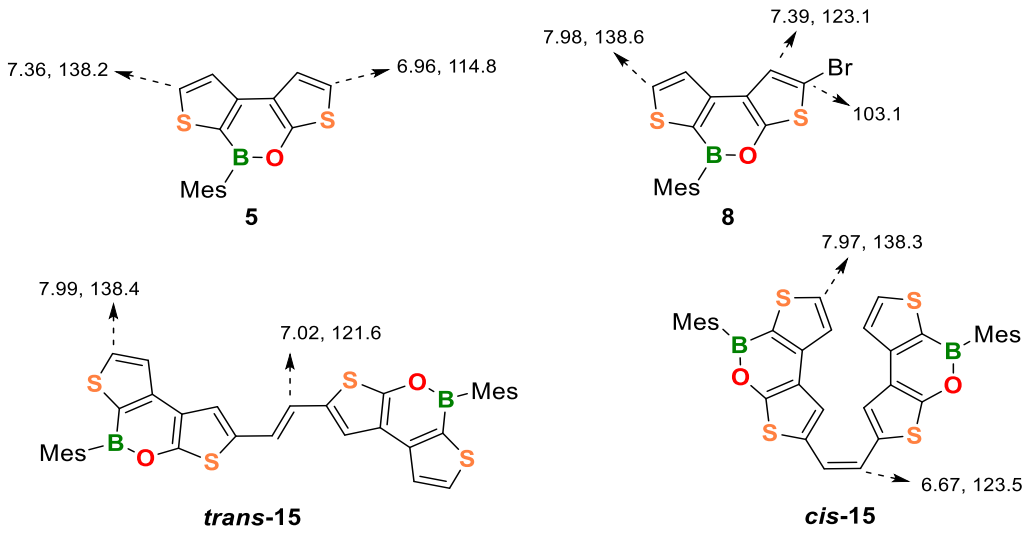

Figure 4. Diagnostic proton and carbon shifts of **5**, **8**, *trans*-**15** and *cis*-**15**.

In Route *C* (Scheme 6), a different approach to **15** was considered, in which the oxaborine rings are constructed, as late stage, on a suitable alkene derivative, in this case *trans*-**17**, that was prepared in 77% yield by a McMurry coupling of methoxy bithienyl aldehyde **S2**.[3] The subsequent borylation of *trans*-**17**, gave **15** in 39% yield as *trans*-isomer.

Although this last synthesis showed a modest yield, it represents a more versatile method as by varying nature of the starting methoxy aldehyde, it could be possible to have access to stilbene derivatives incorporating different heteroaromatic rings.

The final step to obtain **1** is a Mallory photocyclization that required an accurate setup. As previously explained (see Introduction) the first step of this reaction is the photoinduced *trans*/*cis* isomerisation. As in our case *trans*-**15** was always obtained as major isomer, before starting investigating the photocyclization step, the photochemical interconversion of *trans*-**15** to *cis*-**15** was tested by NMR experiments in C_6D_6 with different light sources. (Figure S1 and S2). A 405 nm LED performed the task most efficiently (*trans*/*cis* (1:4) after 30 min; C_6D_6, r.t.) and was therefore used for the subsequent synthesis of the helicene **1** (Scheme 7).

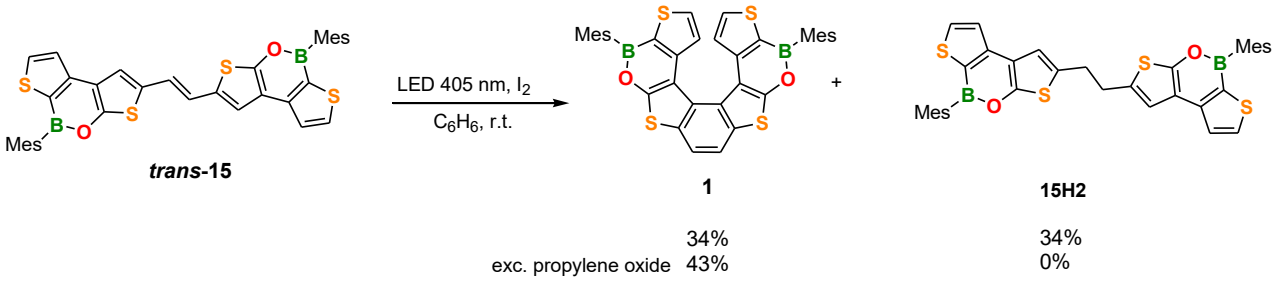

Scheme 7. Synthesis of tetrathia[7]helicene **1**.

The photocyclization was therefore carried out using a 405 nm LED lamp in benzene as solvent and using I_2 as oxidant (Figure S3). The target helicene **1** was obtained in 34% besides an almost equimolar amount of the hydrogenated alkene side-product **15H2** (structure confirmed by NMR and X-ray analysis; Figure S93), generated by the reduction of the double bond by HI produced during the photochemical process.[4]

To suppress the formation of **15H2**, the photocyclization was performed in the same conditions but using an excess of propylene oxide (as HI scavenger) and **1** was isolated in 43% yield as sole product; **1** represents the first example of BO-doped tetrathia[7]helicenes and its structure **1** was confirmed by accurate NMR experiments and X-ray analysis (Figure 5, Figure 6; full details are provided in the Experimental Part).

In the NMR spectrum of **1**, (Figure 5) the former ethylene bridge CH groups, now in the benzene ring resonate at $\delta(^1H)$ = 7.81 and $\delta(^{13}C)$ = 119.0. Moreover, the signal for the H atoms in the β-positions of the thiophene adjacent to the former double bond has disappeared, and the resonance of the appended (now quaternary) C atoms is detectable at 117.3 ppm (see Figure 4). The protons on the α and β position in the terminal thiophene rings resonate at $\delta(^1H)$ = 7.37 and δ (^1H) = 7.19 while in the precursor *trans*-**15** those are significantly deshielded and resonate at $\delta(^1H)$ = 7.99 and $\delta(^1H)$ = 7.60 (*cf.* in **7TH** $\delta(^1H)$ = 6.83 and 6.67).

This shielding effect could be attributed to the helical 3D-strucutre, in which each terminal thiophene ring falls in the shielding region of the corresponding ring in the opposite helicene wing.

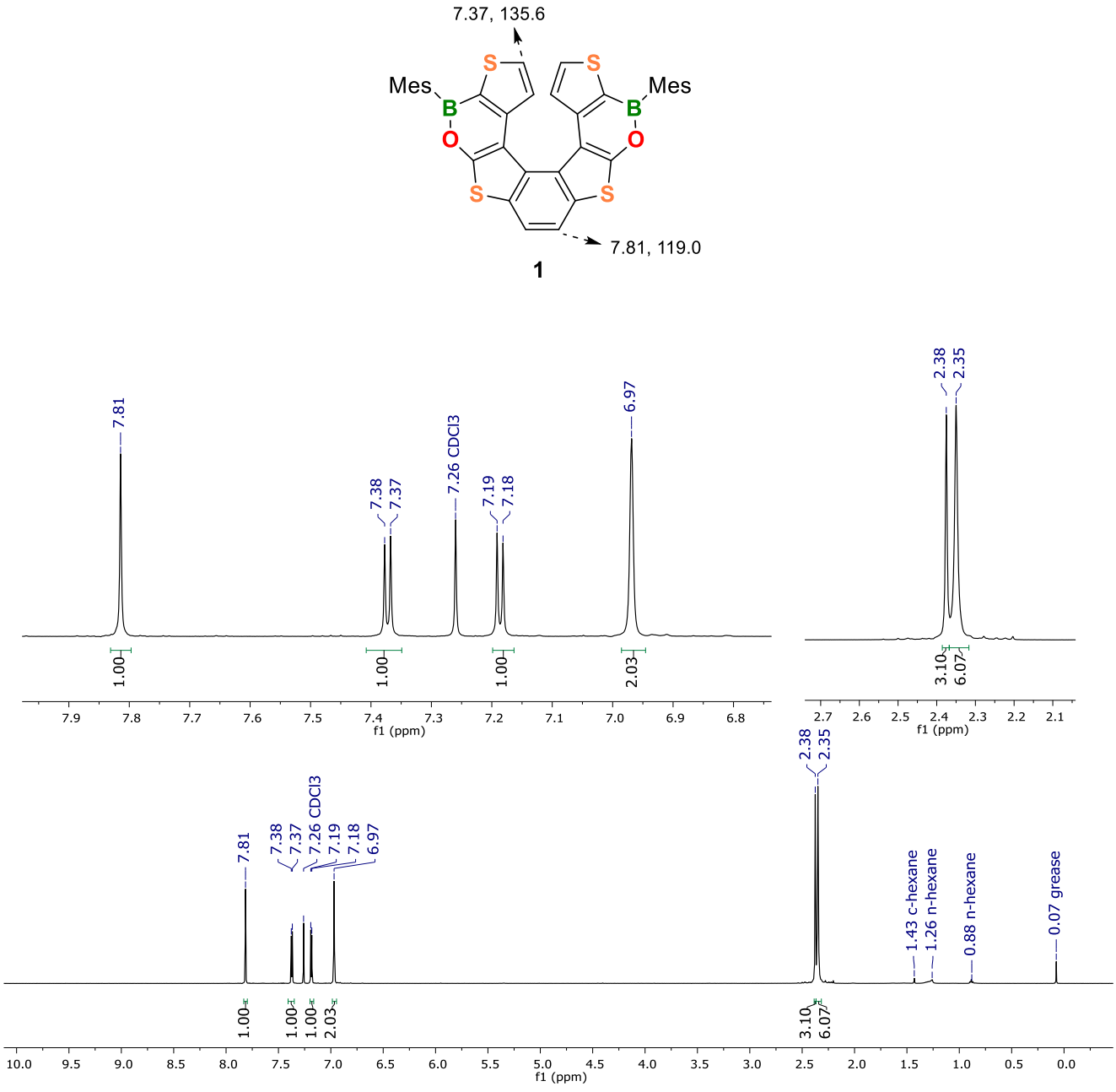

Figure 5. Top: diagnostic proton and carbon shifts of **1**; bottom: ^{1}H NMR spectrum of **1**.

Helicene **1** crystallizes as racemic mixture of the (*P*)- and (*M*)-enantiomers in the low-symmetric triclinic crystal system (Figure 6a,c). A dihedral angle of 50.26(9)° between the two terminal thiophene rings is

associated with intramolecular centroid···centroid distances of 4.153(6) Å (Figure 6b). The central benzene ring is significantly twisted, as indicated by a torsion angle of 9.7° between the (H)C–C(H) vector and the opposite C–C bond. Unlike most mesityl-protected B-doped polycyclic aromatic hydrocarbons (PAHs),[6] the mesityl substituents in **1** are not orthogonally positioned to the attached B-containing heterocycles.

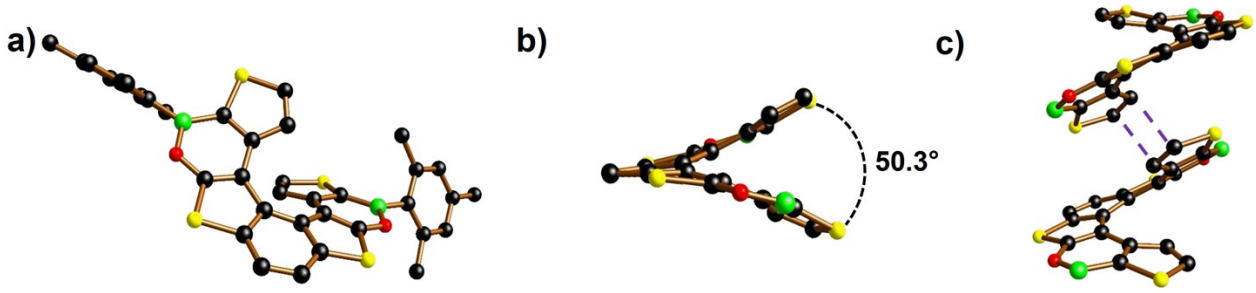

Figure 6. a) Front view of (*M*)-**1** with H atoms omitted for clarity.[5] b) Dihedral angle between the terminal thiophene rings of (*M*)-**1**; H atoms and Mes rings are omitted for clarity. c) π-Stacking interaction between a (*P*)/(*M*)-pair of **1** with H atoms and mesityl rings omitted for clarity. Grey lines indicate the shortest intermolecular C···C contacts; crystal system: triclinic, space gorup: P -1. B: green, C: black, O: red, S: yellow spheres; X-ray picture generated with the crystallographic software *Diamond*.

The reason apparently lies in the neighboring O/S atoms and the annulated five-membered thiophene ring, which impose a lower steric strain compared to CH fragments and annulated six-membered aryl units. The B–O bond lengths of 1.402(4) and 1.401(5) Å are slightly larger than that in the reference compound 9-mesityl-10,9-oxaboraphenanthrene (av. B–O = 1.378 Å; av. Mes//O–B–C = 104.1(3) and 84.8(3)° for two crystallographically independent molecules in the asymmetric unit.[7] In the crystal, the two enantiomers show heterochiral assembly; alternating molecules of (*P*)- and (*M*)-**1** form infinite rods by means of π-stacking interactions between thiophene rings with shortest intermolecular C···C contacts of 3.427(5) and 3.457(4) Å (grey lines in Figure 6c; in this respect, the packing of (*P*)-/(*M*)-**1** and **7TH** are the same[7a]). Remarkably, the shortest intermolecular S···S distances are smaller than the intramolecular ones (3.9911(14) and 5.8156(2) Å, respectively).

4.1.2 Stereochemical studies of 1

Once setup the synthesis of **1**, the work continued with the investigation of its chiroptical, kinetic and theoretical studies. Chiroptical and kinetic studies on **1** were conducted in collaboration with the group of Prof. Giovanna Longhi (University of Brescia) and Prof. Claudio Villani (University of Rome "La Sapienza").

Preliminary racemization tests showed that the enantiomers of **1** are stereochemically stable at room temperature. Thus, the analytical HPLC resolution was scaled up to the semipreparative level using the same

eluent (*n*-hexane/CH_2Cl_2 (95:5); Chiralpak IA). Racemization studies were conducted on the second eluted enantiomer, which was isolated in slightly higher enantiomeric excess (*e.e.*=97.4 %, R_t≈8 min; Figure 7a, red trace). The collected fractions containing only the second eluted enantiomer were combined and evaporated at room temperature. The solid residue was dissolved in decalin and subjected to thermal racemization at 80 °C. The changes in the enantiomeric excess of the sample were monitored by chiral-HPLC (Figure 7b). The racemization progress was monitored by the decrease in the enantiomeric excess of the sample. The interconversion of the two enantiomers proceeded smoothly: after only 13 min, the *e.e.* dropped from 97.4 % to 80.6 % and the elution peak of the first enantiomer (R_t ≈ 6 min) began to emerge (Figure 7b, purple trace). The *e.e.* data were collected over 64 min and used to determine the enantiomerization constant k_{enant}=8.15×10^{-5} s^{-1} (see Section 10 of the Experimental Part) and the associated free energy of activation $\Delta G_{enant}^{\neq}$=27.4±0.1 kcal mol^{-1} (at 353 K).[8] The $\Delta G_{enant}^{\neq}$ value of the $(BO)_2$-doped tetrathia[7]helicene **1** is considerably lower than the corresponding values determined for the enantiomerization of the parent **7TH** ($\Delta G_{enant}^{\neq}$=39.4 kcal mol^{-1})[9] and even carbo[6]helicene ($\Delta G_{enant}^{\neq}$=36.4 kcal mol^{-1}).[10] Thus, the formal replacement of two C=C bonds by B=O bonds within the helical framework apparently increases the flexibility of the molecular scaffold, consistent with the lower double-bond character of the latter.

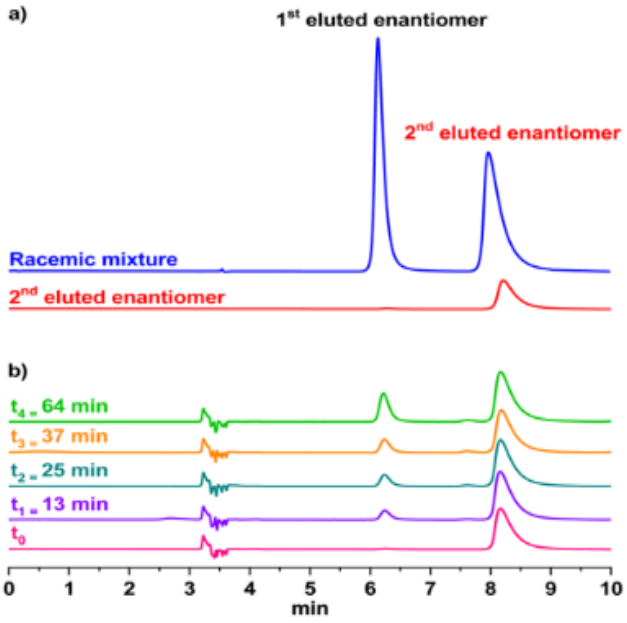

Figure 7. a) top: Analytical HPLC resolution of **1** (Chiralpak IA, *n*-hexane/CH_2Cl_2 (95:5)); bottom: thermal racemization studies of **1** second eluted enantiomer (R_t ≈ 8 min) in decalin at 80 °C; solvent peak: R_t ≈ 3 min.

Circular dichroism (CD) spectra of the two enantiomers showed a perfect mirror-image relationship between the first and second eluted enantiomer of **1** (Figure 8, black and red trace); the optical rotation values are +97.7° and −97.5°, respectively.

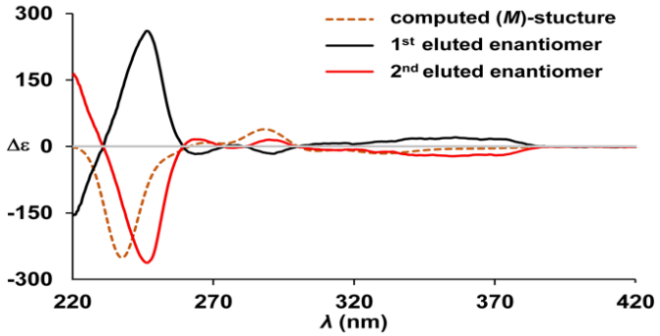

Figure 8. Circular dichroism (CD) spectra of the first (black trace) and the second (red trace) eluted enantiomer of **1**, recorded in *n*-hexane/CH_2Cl_2 (95 : 5) at 20 °C. Computed CD spectrum for the optimized (*M*)-structure (orange dashed trace; multiplied by a factor of 1.5).

To determine the absolute configurations of the two eluted enantiomers, the (*M*)-structure of **1** was optimized at the M06/6-311g G(d,p) level of theory. Only one energy minimum was obtained, and no other stable conformer was found, even about a possible different orientation of the mesityl groups. The optimized gas-phase structure (C_2 symmetry) compares well with the crystallographically determined molecular geometry; the experimentally observed marked deviation of the dihedral angle Mes//O−B−C from 90° is qualitatively reproduced (calcd. 65.5°; av. exptl. 58.8°). The CD spectrum of (*M*)-**1** was calculated by TD-DFT at the same level of theory (Figure 8, orange dashed trace). The agreement between the computed and one of the experimental CD spectra allows us to assign the (*M*)-configuration with certainty to the second eluted enantiomer (R_t≈8 min): good correspondence is observed for the broad negative feature centred at 350 nm, which can be attributed to the first three transitions with weak negative rotational strength (Figures 8 and S107). The two weak positive peaks experimentally observed at 293 and 265 nm are also well reproduced, as is the intense negative feature at 247 nm (calcd. 240 nm). The relatively small rotational strength computed for the first transition (HOMO→LUMO) is due to the fact that the electric and magnetic transition dipole moments are nearly perpendicular to each other. The CD spectrum of (*M*)-**1** is different from those of typical helicenes[11] and thiahelicenes,[12] in that it shows only weak features in the 370–260 nm range (Figure S107), but with a more intense absorption feature for the first electronic transition (Figures S107, S108, and Tables S18, S19). This is another example for the well-known fact that the lowest-energy transitions of helicenes are substituent-sensitive,[13] while the overall shape of the spectrum is determined by the helicene backbone.

The energy barrier for enantiomerization of **1** was computed by optimizing the ground state of (*M*)-**1** and the transition state to (*P*)-**1** at the PBE1-PBE/TZVP level with empirical dispersion corrections.[14] The obtained enantiomerization barrier of 35 kcal mol^{-1} is about 8 kcal mol^{-1} higher than the experimentally found value of $\Delta G_{enant}^{\neq}$=27.4±0.1 kcal mol^{-1} (at 353 K);[15] the same barrier was obtained for the model compound **1*** carrying H atoms in place of the Mes groups. We also compared the enantiomerization barrier of the model compound **1*** with those of carbo[6]helicene and tetrathia[7]helicene **7TH** by performing a relaxed interconversion scan considering also diffuse functions at the PBE1-PBE/6-311++G(d,p) level with empirical dispersion corrections (Figures S109 and S110). Despite the seven-ring backbone of **1***, its barrier

is the lowest of the three compounds (**1***: 35 kcal mol^{-1}, carbo[6]helicene: 38 kcal mol^{-1}, and **7TH**: 40 kcal mol^{-1}). A comparison of the minimum and transition-state structures of **1*** and **7TH** indicates that the smaller double-bond character of the B=O pairs indeed allows for greater flexibility of the six-membered heterocycle compared to a carbonaceous benzene ring (Figure 9 and Figure S58).

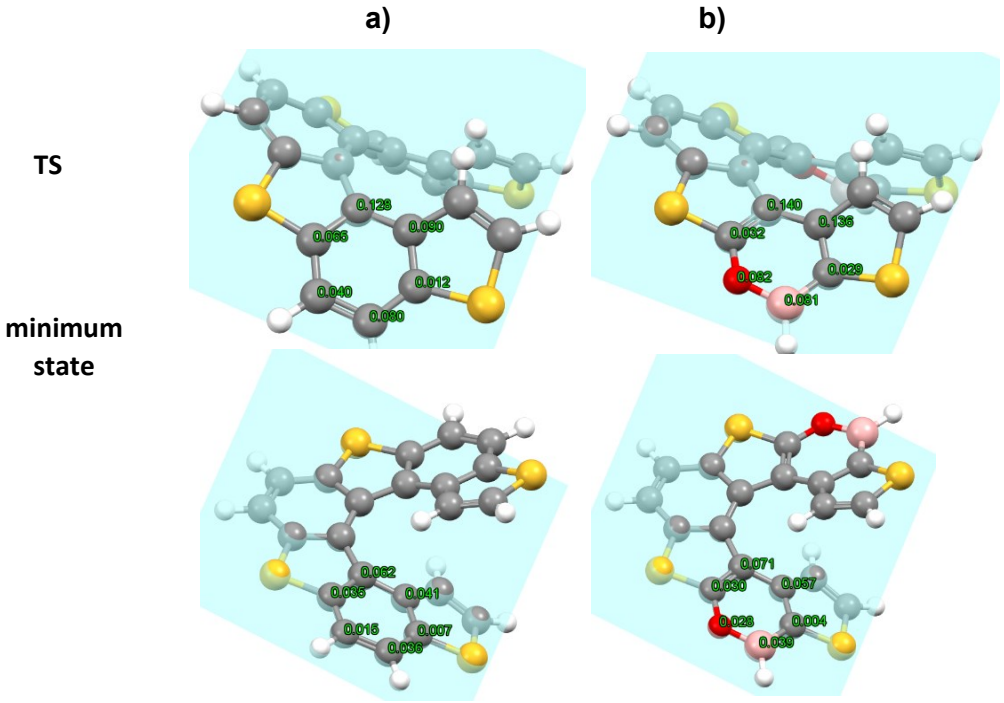

7TH	1*
Minimum	
0.062	0.071
0.041	0.057
0.007	0.004
0.036	0.039
0.015	0.028
0.035	0.030
TS	
0.128	0.140
0.090	0.136
0.012	0.029
0.080	0.081
0.040	0.082
0.065	0.032

Figure 9. Level of calculation PBE1-PBE/6-311++G(d,p). Distances atom-ring plane (Å) for tetrathia[7]helicene **7TH** (a) and the six-membered ring containing oxygen and boron atoms of model compound **1*** (b) in the calculated transition state structure (top) and the minimum state structure (bottom). The above-mentioned atom-ring plane distances are listed in the right top corner.

4.1.3 Electrochemical and spectroscopic characterization and DFT calculation of 1 and its BO-doped intermediates

Cyclic voltammograms were recorded in THF with [*n*Bu$_4$N][PF$_6$] as supporting electrolyte and are referenced against the ferrocene/ferricinium couple (FcH/FcH$^+$). In the cathodic scan, borahelicene **1** shows two irreversible redox events with peak potentials of E_{pc} = −2.83 and −3.01 V (Table 1 and Figure S61, S62). For comparison, the starting oxaborine **5** is somewhat harder to reduce with an E_{pc} value of −2.96 V (Figure S59). When two redox-active **5**-type sites are connected via a 1,2-ethenediyl bridge (as in the case of *trans*-**15**), the first reduction event at $E_{1/2}$ = −2.54 V becomes quasi-reversible while the second remains largely irreversible (E_{pc} = −2.90 V). We attribute the easier reduction of *trans*-**15** relative to **5** to the more extended π-conjugation pathway in the former (*trans*-**15** adopts a fully planar structure in the solid state; Figure 3 and Figure S89). This interpretation is supported by the fact that the redox potential of saturated **15H2** is again

cathodically shifted to E_{pc} = −2.90 V (Figure S68). In summary, the degree of electronic communication between the two **5**-type sites in the helically twisted compound **1** appears to be lower than in its planar precursor *trans*-**15**.

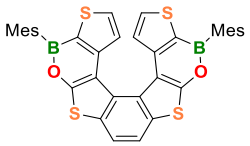

1

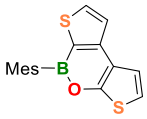

5

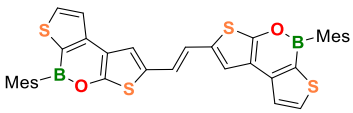

***trans*-15**

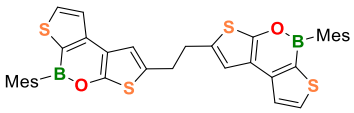

15H2

Table 1. Photophysical and electrochemical data of the compounds **1**, *trans*-**15**, **15H2**, and **5**. Optical measurements were performed in *c*-hexane, and electrochemical measurements were performed in THF (r.t., supporting electrolyte: [nBu$_4$N][PF$_6$] (0.1 M), scan rate 200 mV s^{-1}).

	λ_{max} [nm]	λ_{em}[a] [nm]	Φ_{PL}[b] [%]	E_{pc} [V]	E_g^{opt}[c] [eV]	E_{LUMO}[d] [eV]
1	269 330 341 359 374 [e] (*363*) [f]	392 411	6 4[f]	–2.83 –3.01	3.16	—
trans-**15**	278 344 [e] 364 383 403 (*395*) [f]	419 443	11 13[g]	–2.54[h] –2.90	2.93	–2.26
15H2	318 [e] 326 342 [e]	374 388	7 7[g]	–2.90	3.51	—
5	313 [e] 320 335 [e] (*301*) [f]	366 380	6 9[g]	–2.96	3.57	—

[a] Resolved vibrational fine structure. [b] Quantum yields were determined by using a calibrated integrating sphere. [c] Optical band gap E_g^{opt} = 1240/ λ_{onset}. [d] E_{LUMO} = −4.8 eV − $E_{1/2}^{Red1}$ (FcH/FcH$^+$ = –4.8 eV vs vacuum level). [e] Shoulder. [f] Computed value (TD-DFT). [g] Quantum yields measured in THF. [h] $E_{1/2}$ value of the quasi-reversible process.

UV/vis absorption was recorded in cyclohexane and THF; in *c*-hexane, **1** exhibits a structured band with the most bathochromic shoulder appearing at 374 nm (Figure 7a, blue trace; Table 1). For comparison, the corresponding shoulder in the spectrum of tetrathia[7]helicene **7TH** is found at 392 nm.[16] **1** is a blue emitter and its emission band shows a partly resolved vibrational fine structure with the most hypsochromic shoulder at 411 nm; the photoluminescence quantum efficiency is Φ_{PL} = 6% (*c*-hexane; cf. tetrathia[7]helicene: $\lambda_{em} \approx$ 405 nm, Φ_{PL} = 5%).[17] The reference systems **5**, **15H2**, and *trans*-**15** absorb/emit at 335/366 nm, 342/374 nm, and 403/419 nm, respectively (Table 1, Figure 10a-c).

According to time-dependent density functional theory (TD-DFT) calculations, the first transitions of **1**, *trans*-**15**, and **5** are HOMO→LUMO transitions (Table 1, see also Tables S18–S20, Figure S108, and section 10.3 of the Experimental Part). Despite the smaller dihedral angles Mes//O–B–C (59.0(5)°, 58.6(6)°), the contributions of the mesityl substituents to the HOMO/LUMO frontier orbitals of **1** is negligible (Figure 10d). Moreover, it is worth to note that HOMO-LUMO calculations showed as while HOMO is spread over the entire helical scaffold, LUMO localizes on the two terminal thiophene rings, close to the boron atoms (Figure 10d). Taken together, these results confirm that **1** has a much more delocalized π-electron system than **5** and **15H2**, but the effective conjugation length is smaller than for *trans*-**15**. We therefore conclude that BO-doping does not have a major influence on the electronic spectra of $\mathbf{7}^{\mathbf{TH}}$.

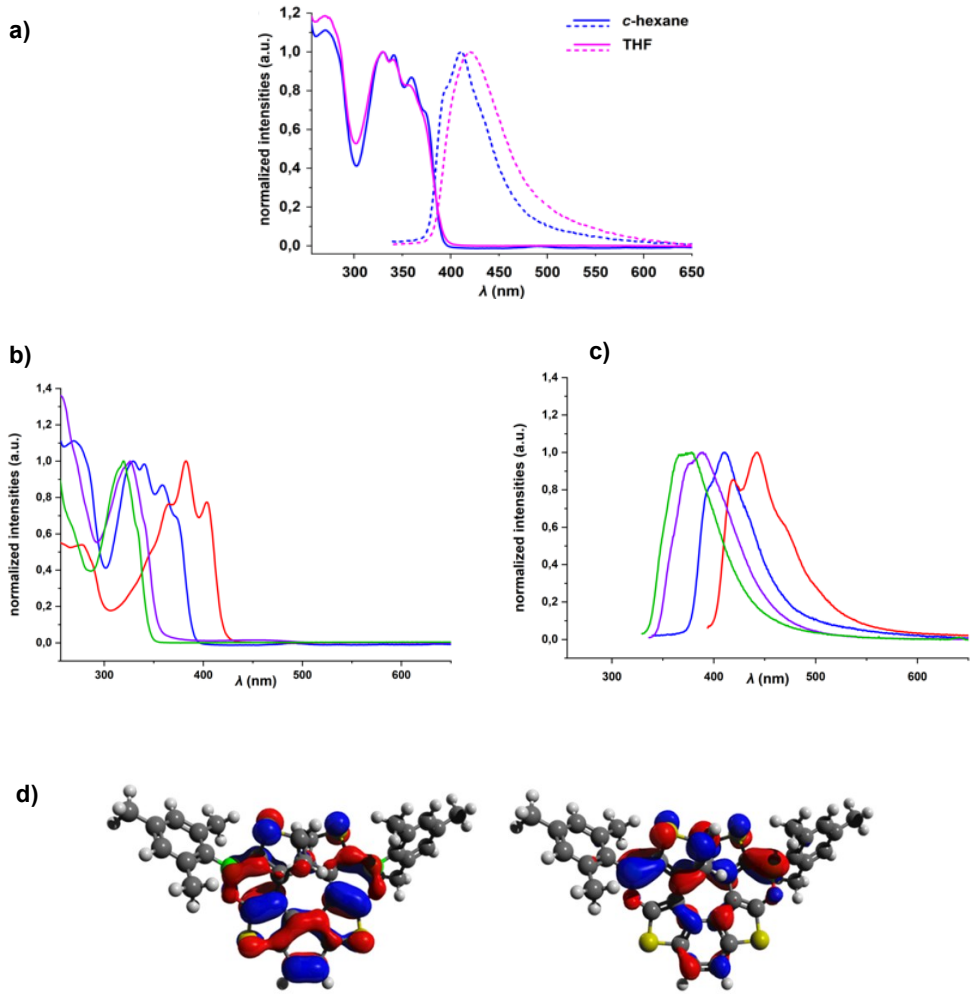

Figure 10. a) Absorption and emission spectra of **1** in *c*-hexane (blue) and THF (purpple). b) Absorption spectra of **5** (green), *trans*-**15** (red), **15H2** (purple), **1** (blue) in *c*-hexane. c) Emission spectra of **5** (green), *trans*-**15** (red), **15H2** (purple), **1** (blue) in *c*-hexane. d) HOMO (left) and LUMO (right) of **1**, calculated at the B3LYP/6-31G* level.

Conclusions

The $(BO)_2$-doped tetrathia[7]helicene **1** was obtained via an efficient four-step synthesis, including a Mallory photocyclization step, which has rarely been used for the synthesis of B-containing polycyclic aromatic hydrocarbons. Despite its configurational stability at room temperature, the racemization and enantiomerization barriers of **1** are significantly lower than that of its non-doped congener, the tetrathia[7]helicene **(7TH)**. This is presumably due to the weaker π-donor bond within the BO pair, which renders the oxaborine heterocycles more conformationally flexible than benzene rings. To date, boron-heteroatom doping has been performed mainly on planar polycyclic aromatic hydrocarbons, where conformational flexibility is not an issue, and is therefore considered primarily as a tool for manipulating the electronic structures of π-electron systems. Our results now indicate that the incorporation of BO pairs can also be a means of influencing the mechanical rigidity of polyaromatic entities. Even though **1** has a rather low photoluminescence quantum efficiency of Φ_{PL} = 6%, its synthesis protocol should allow manifold optimizations in the future, such as BN doping, inversion of the BO/BN vectors, or facile late-stage derivatization at the terminal thiophene rings.

4.2 Study of the synthesis and properties of the BO-doped tetrathia[7]helicene 2

On the basis of the photophysical properties of borahelicene **1** and with the aim of obtaining structures with better optoelectronic properties than **1**, I designed helicene **2**, isomer of **1** which is derived by the formal inversion of the two BO bonds in the parent **1** (Figure 11). I assumed that this structural modification could be a tool to affect the electronic properties, by influencing the distribution and the extension of the LUMO orbitals within the helical framework.

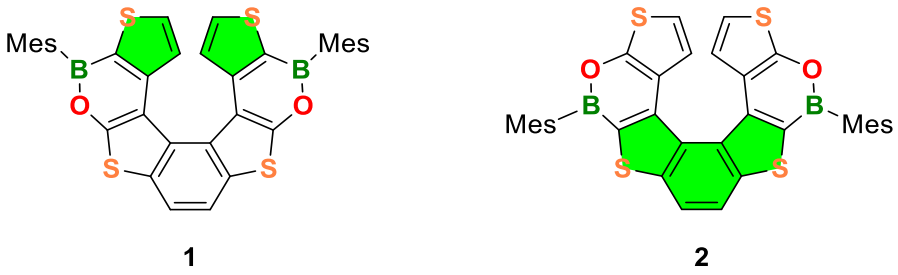

Figure 11. Structure and LUMO distribution (green) of **1** and, expected LUMO distribution of the **2** isomer with BO-inverted bonds.

In fact, **2** is expected to display LUMO orbitals extended over the whole *thiophene-benzene-thiophene* (BDT) central fragment rather than over the terminal thiophene rings (Figure 11). Extension of the LUMO contributes to provide narrowed energy-gap, redshifted absorption/emission bands, increased reducing abilities and thus enhancing optoelectronic performances. This hypothesis was also supported by preliminary DFT calculation.

4.2.1 Synthesis and NMR characterization of 2

The designed synthesis of **2** (as in *Route C* for **1)** involves, in the last step, the photocyclization of the alkene **18** (isomer of **15**), which in turn can be synthesized by late-stage borylation of the bis-methoxy functionalized alkene **19** (Scheme 8).

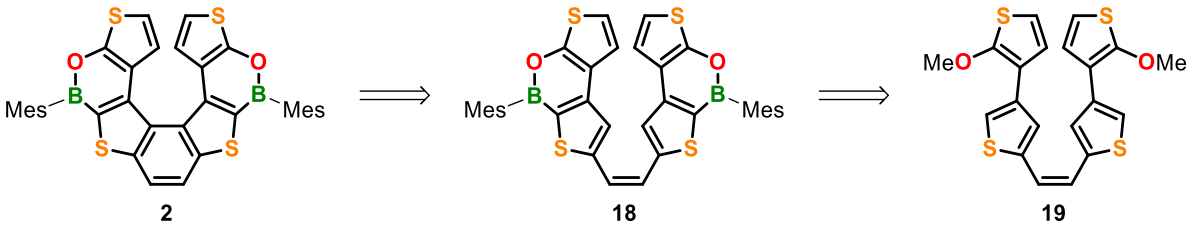

Scheme 8. Designed retrosynthetic analysis for **2**.

The whole synthetic scheme to obtain **2**, starting from 4-bromo-2-thiophenecarbaldehyde, is depicted in scheme 9.

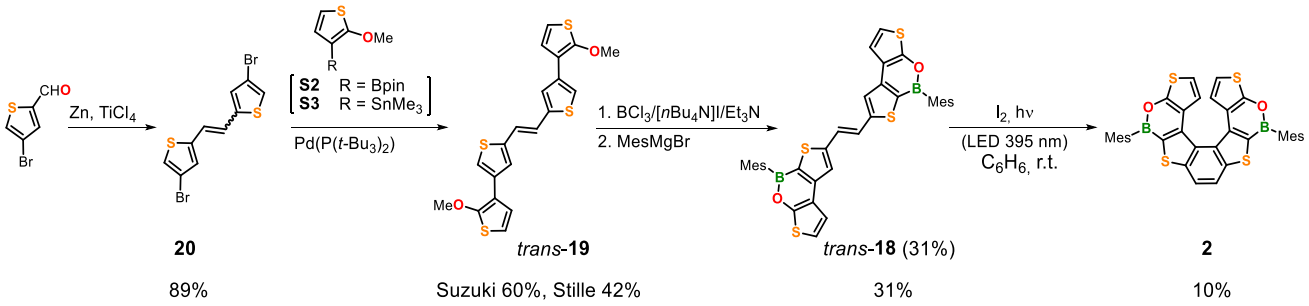

Scheme 9. Synthetic route to **2**.

In detail, 4-bromo-2-thiophenecarbaldehyde was converted into dibromo alkene *trans*-**20** *via* McMurry coupling in 89% yield; the *trans* configuration was confirmed by X-ray crystallography (Figure 12a and Figure S94). Suzuki or Stille coupling with the corresponding coupling partners (boronic ester **S2** or stannane **S3**) gave dimethoxy alkene **19** in 60% and 42% yield respectively. Although the Suzuki coupling gave a better yield, the preferred route for **19** relies on the Stille coupling, due to the difficult synthesis of the boronic ester **S2**. The *trans* configuration of **19** was again confirmed by X-ray crystallography (Figure 12b and Figure S95). The following borylation of **19** was performed by using the standard borylation procedure with BCl_3/[nBu$_4$N]I/Et$_3$N in chlorobenzene at 135 °C and subsequent addition of an excess of MesMgBr. *Trans*-**18** was obtained in 31% yield after purification; also in this case the *trans*-configuration was confirmed by X-ray crystallography (Figure 12c and Figure S96).

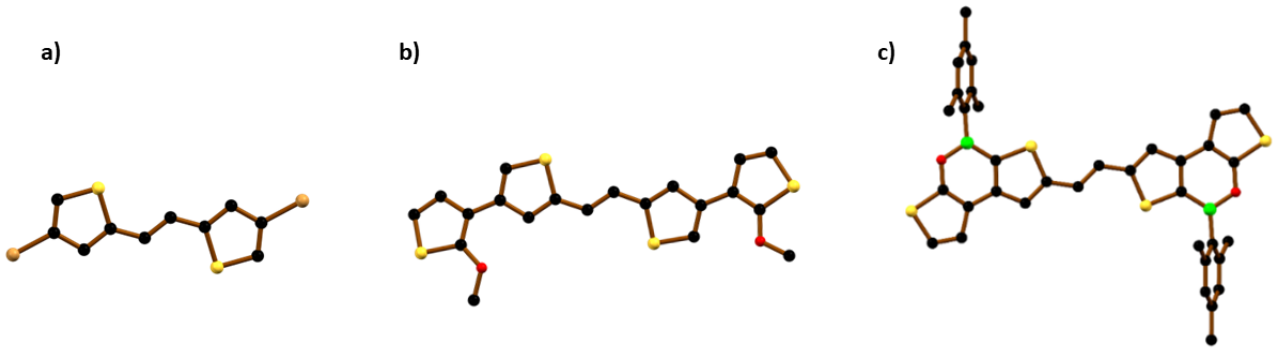

Figure 12. X-ray crystal structure of: a) *trans*-**20**, crystal system: orthorombic, space group: Pbca b) *trans*-**19**, crystal system: orthorhombic, space group: F d d 2 and c) *trans*-**18**, crystal system: monoclinic, space group: P21/c. B: green, C: black, O: red, S: yellow, Br: brown spheres; picture generated with the crystallographic software *Mercury*.

NMR spectrum of *trans*-**18** showed that the inversion of BO-bonds (with respect to *trans*-**15**) causes a substantial upfield shift of both proton and carbon resonances (see Figure 13). As an example, in *trans*-**18** protons on the α and β position in the terminal thiophene rings, substituted with the electron donor O atom, resonate at $\delta(^1H)$ = 7.32 and $\delta(^1H)$ = 6.96 respectively while in the corresponding isomer *trans*-**15** are significantly deshielded and resonate at $\delta(^1H)$ = 7.99 and $\delta(^1H)$ = 7.60 due to the electron withdrawing effect of the B atom. The same effect can be observed in ^{13}C shifts: *trans*-**18** C(α) and C(β) resonate at 120.3 ppm and 114.9 ppm, while are significantly deshielded in *trans*-**15**, C(α) = 138.4 ppm and C(β) = 123.0 ppm (see Figure 13).

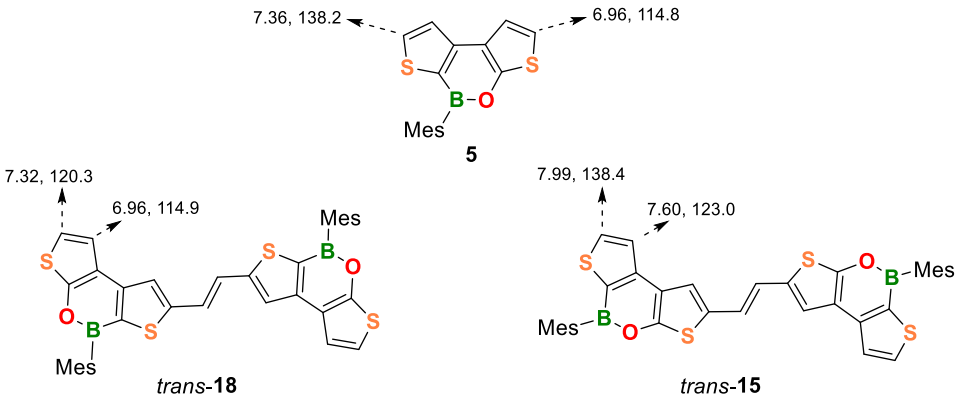

Figure 13. Diagnostic proton and carbon shifts of **5**, *trans*-**15**, *trans*-**18**.

The photocyclization of *trans*-**18** was performed using a 395 nm LED lamp in the presence of I_2 as oxidant and furnished the desired helicene **2** in 10% yield; **2** was fully characterized from analytical, computational, and optoelectronic point of view. Comparison of the NMR spectra of **2** and its isomer **1**, reflect the switch of the electronic properties caused by the BO-bonds inversion (Figure 13a).

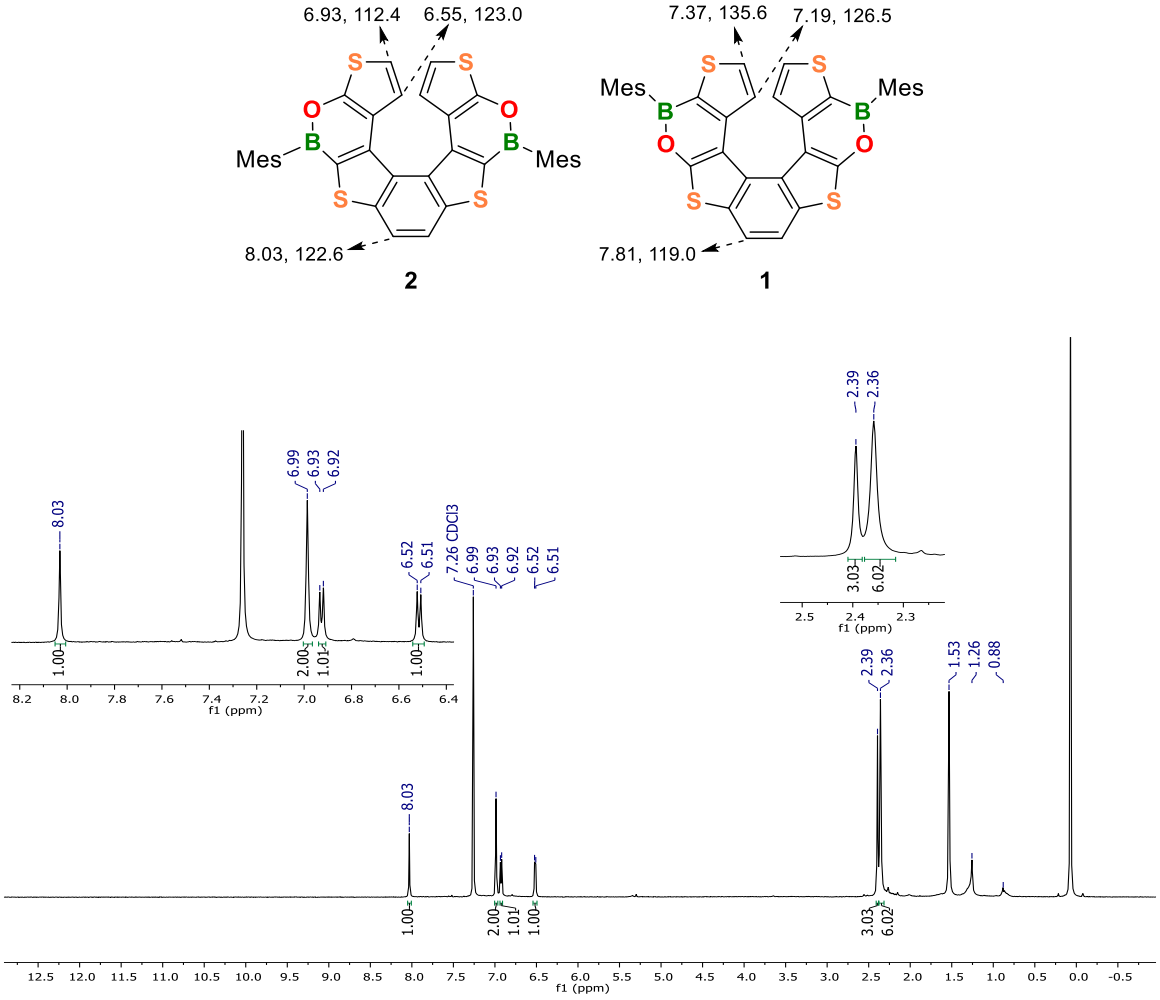

Figure 13a. Top: diagnostic proton and carbon shifts of **1** and **2**; bottom: ^{1}H NMR spectrum of **2**.

In detail, in helicene **2** protons on the α and β position in the terminal "oxygenated thiophene rings", resonate at $\delta(^1H)$ = 6.93 and δ (^1H) = 6.52 respectively, while in helicene **1** the same protons resonate at $\delta(^1H)$ = 7.37 and $\delta(^1H)$ = 7.19 (*cf.* in **7TH** $\delta(^1H)$ = 6.83 and 6.67). Interestingly α and β protons of the terminal thiophene rings of **2** are upfielded in the olefinic region and revealed to be even more shielded of the corresponding protons in the dithienyloxaborine **5** ($\delta(^1H)$ = 6.96 and $\delta(^1H)$ = 7.36 respectively). The same trend can be observed in ^{13}C shifts: **2** C(α) and C(β) resonate at 112.4 and 123.0 ppm respectively, while are significantly deshielded in **1,** C(α) = 135.6 ppm and C(β) = 126.5 ppm (Figure 13).

This behaviour, as for **1**, could be attributed to the effect of the helical 3D-structure, in which each terminal thiophene ring falls in the shielded region of the corresponding ring in the opposite helicene wing.

Similarly to what observed for thiophene rings, due to proximity of the trigonal boron atoms, protons of the central benzene ring in **2** are significantly downshielded and resonate at $\delta(^1H)$ = 8.03, while those of **1** resonate at $\delta(^1H)$ = 7.81 ppm. The same trend can be observed in the ^{13}C NMR ($\delta(^{13}C)$ = 122.6 and $\delta(^{13}C)$ = 119.0 respectively; see Figure 13).

The study was then completed investigating the optoelectronic properties of borahelicene **2** and its borylated alkene precursor **18** and comparing them with those of isomers **1** and **15** previously synthesized.

4.2.3 Electrochemical, spectroscopic, and theoretical characterization of 2 and *trans*-18

Comparison of BO-doped tetrathia[7]helicenes 2 and 1

HOMO/LUMO distributions of **2** were calculated at the B3LYP/6-31G* level of theory (figure 14). Calculations revealed that the inversion of BO-bonds in helicene **2** produces peculiar and different electronic properties than those of the parent **1**. By looking at the HOMO orbitals, these stay pretty unchanged in both terms of energy and distribution over the helical scaffold. Interestingly, contrary to **1**, in **2** the central benzene ring outer C=C bond does not give any contribution to HOMO.

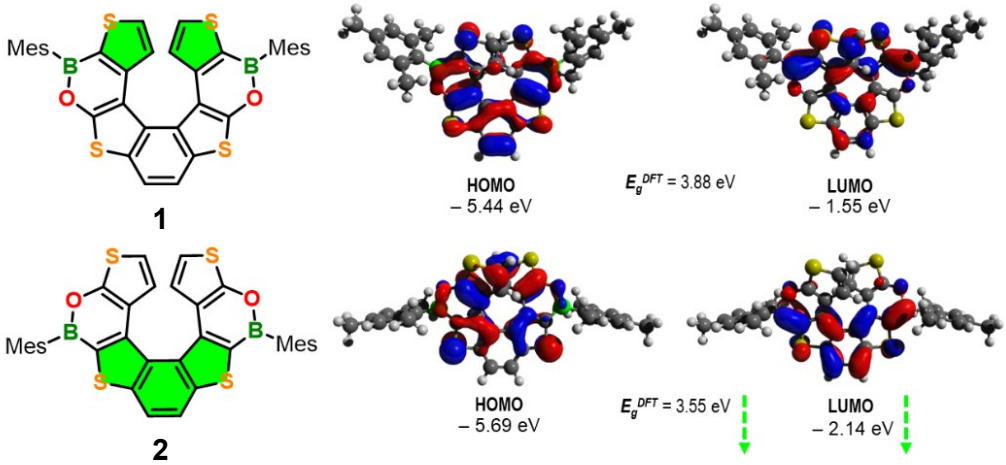

Figure 14. HOMO/LUMO distributions of **2** and **1** calculated at the B3LYP/6-31G* level.

Regarding LUMO orbitals, comparing **2** and **1**, calculations show how the LUMO of **2** is significantly lower than that of **1** (–2.14 eV *vs.* –1.55 eV) and, as expected, it is localized over the thiophene-benzene-thiophene central fragment of the molecule.

Cyclic voltammetry measurements of **2** (recorded in THF with [nBu$_4$N][PF$_6$] as supporting electrolyte and referenced against (FcH/FcH$^+$ couple) showed one irreversible reduction process E_{pc} = −2.68 V in the cathodic scan and an irreversible oxidation peak in the anodic scan E_{pa} = 0.82 V (Table 2 and Figure S72, S73).

Helicene **2** is easier to be reduced than its isomer **1** (E_{pc} = –2.83 V), thus indicating that the BO-bond inversion affects the LUMO orbitals. In fact, experimental LUMO of **2** E_{LUMO} = –2.12 eV, is slightly lower than that of **1** E_{LUMO} = –1.97 eV.

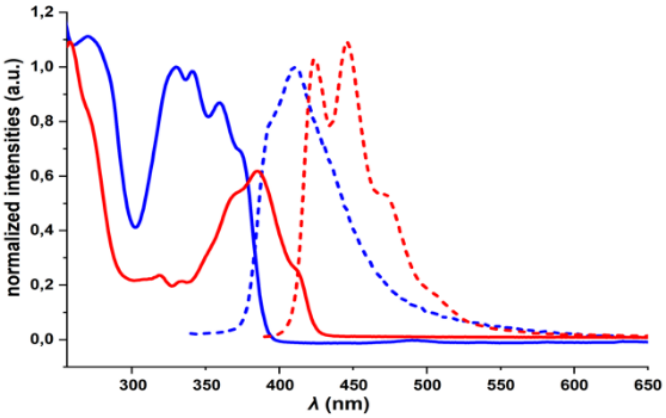

Figure 15. Absorption (solid lines) and emission (dashed lines) spectra of **2** (red) and **1** (blue) in *c*-hexane.

In *c*-hexane, **2** exhibits a structured UV/vis absorption band with the most bathochromic shoulder appearing at 413 nm (Figure 15, blue line; Table 2). For comparison, the corresponding shoulder in the spectrum of **2** is found at 374 nm. **2** is a blue emitter and its emission band shows a partly resolved vibrational fine structure with the most hypsochromic band at 472 nm (Figure 15, red dashed line; Table 2); the photoluminescence quantum efficiency is Φ_{PL} = 7% (*c*-hexane; *cf.* **1**: $\lambda_{em} \approx$ 411 nm, Φ_{PL} = 6%). Optical measurements revealed as the BO-bonds inversion produces a substantial redshift in both absorption and emission bands accompanied by a reduction of the energy gap ($E_g^{opt}{}_{\mathbf{2}}$ = 2.90 eV *vs.* $E_g^{opt}{}_{\mathbf{1}}$ =3.16 eV), while photoluminescence efficiency remained unaffected.

Comparison between alkenes trans-18 and trans-15

Cyclic voltammograms of *trans*-**18**, similar to what observed for *trans*-**15**, showed a quasi-reversible reduction process $E^{I}_{pc} = -1.97$ V, accompanied by a largely irreversible reduction peak $E^{II}_{pc} = -2.26$ V in the cathodic scan (Figure S70; Table 2). The effect of the BO-inversion is evidenced, when comparing the potential values of the two stilbenes *trans*-**18**/*trans*-**15**, $E^{I}_{pc\mathbf{18}} = -1.97$, $E^{II}_{pc\mathbf{18}} = -2.26$ V / $E^{I}_{pc\mathbf{15}} = -2.54$, $E^{II}_{pc\mathbf{15}} = -2.90$ V: *trans*-**18** shows significantly lower reduction potentials, compatible with its structure, supposed to be more electron-poor than that of the parent *trans*-**15**. For *trans*-**18** no oxidation peaks were observed in the anodic scan, as in the case of *trans*-**15**.

Experimental LUMO values measured for *trans*-**18** ($E_{LUMO} = -2.83$ eV) is lower than that of its isomer *trans*-**15** ($E_{LUMO} = -2.26$ eV) and DFT calculations revealed as, for both isomers, HOMO and LUMO are mainly localized in the central thiophene-ethylene-thiophene fragment (Figure 16a).

Regarding the optical properties, in the absorption spectrum (Figure 16b) *trans*-**18** shows main bands at 370, 393 nm, slightly blueshifted with respect to *trans*-**15** (383, 403 nm) and a shoulder at 414 nm with an associated energy gap of $E_g^{opt} = -2.85$ eV close to that of *trans*-**15** ($E_g^{opt} = -2.93$ eV).

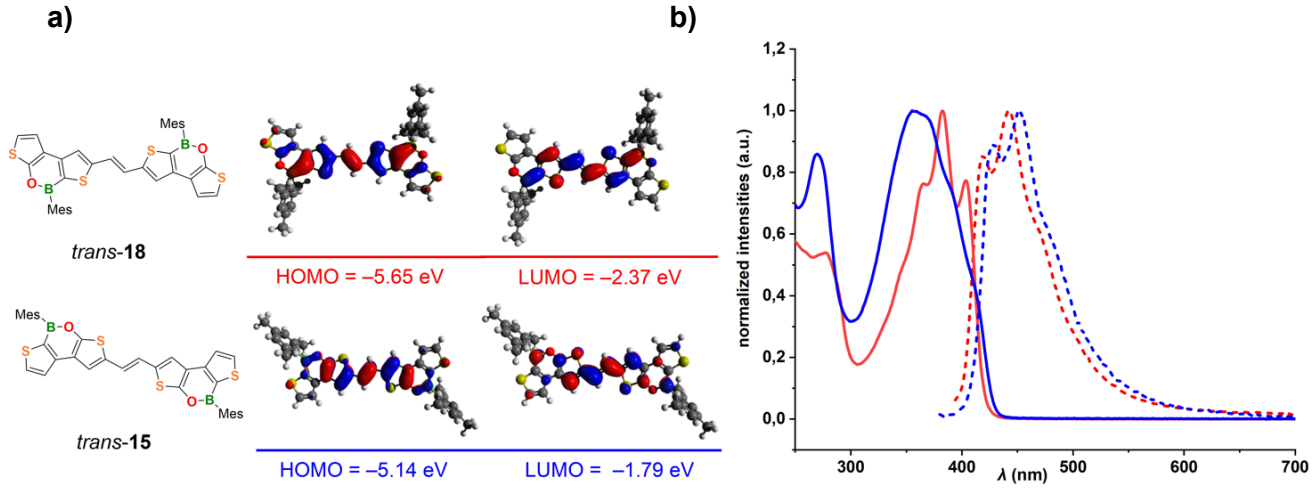

Figure 16. a) HOMO/LUMO distributions of *trans*-**18** and *trans*-**15** calculated at the B3LYP/6-31G* level. b) Absorption (solid lines) and emission (dashed lines) spectra of *trans*-**18** (blue) and *trans*-**15** (red) in *c*-hexane.

Conversely, in the *trans*-**18** emission spectra two structurally fine resolved bands can be found at 429 and 452 nm, and these are slightly redshifted with respect to these of *trans*-**15** (419, 443 nm). *Trans*-**18** showed $\Phi_{PL} = 6\%$ in *c*-hexane, considerably lower than that of *trans*-**15** (the same trend was observed in THF, see Table 2).

Table 2: Photophysical and electrochemical data of the boron-doped compounds. Optical measurements were performed in *c*-hexane, and electrochemical measurements were performed in THF (room temperature, supporting electrolyte: [nBu$_4$N][PF$_6$] (0.1 M), scan rate 100 or 200 mV s^{-1}).

	λ_{abs} [nm] [a]	λ_{em} [nm]	Φ_{PL} [%] [b]	E_g^{opt} [eV] [c]	E_{LUMO} [eV] [d]	$E_{1/2}$ [V]	E_{pc} [V]
trans-**15**	278 344 (sh) 364 383 403	419 443	11 13[f]	2.93	–2.26[d]	–2.54[g]	–2.54 –2.90
1	269 330 341 359 374 (sh)	392 411	6 4[f]	3.16	—1.97[i]	-[h]	–2.83 –3.01
trans-**18**	270 355 370 393 414 (sh)	429 452 489 (sh)	6 5[f]	2.85	–2.83[d]	–1.97[g]	–2.68 –1.97
2	258 320 (sh) 322 (sh) 368 385 413	424 446 472 506 (sh)	7 5[f]	2.90	–2.12[i]	-[h]	–2.68

[a] Resolved vibrational fine structure. [b] Quantum yields were determined by using a calibrated integrating sphere. [c] Optical band gap E_g^{opt} = 1240/ λ_{onset}. [d] E_{LUMO} = −4.8 eV − $E_{1/2}^{Red1}$ (FcH/FcH$^+$ = –4.8 eV vs vacuum level). [e] Shoulder. [f] Quantum yields measured in THF. [g] $E_{1/2}$ value of the quasi-reversible process. [h] Compound shows no reversible reduction. [i] E_{HOMO}/E_{LUMO} calculated with the *maxima criterion*: E_{HOMO} = −1e×((E^{I}_{pa}/V([FcH]$^+$ | FcH)+4.8 V([FcH]$^+$ | FcH vs. zero)); E_{LUMO} = −1e×((E^{I}_{pc}/V([FcH]$^+$ | FcH)+4.8 V([FcH]$^+$ | FcH vs. zero)).

Conclusions

Taken together, these results revealed as the inversion of BO vectors in the thiahelicene scaffold did not have appreciable effect on the optoelectronic performances in the specific case of **1** and **2** (Φ_{PL1} = 6%/ Φ_{PL2} = 7%) but anyway it represents a valuable strategy to modulate the properties of this class of compounds. In fact, the position of boron in the helical scaffold resulted to be a suitable tool to influence the extension of LUMO and get red-shifted absorption and emission bands, thus setting the basis for the structural design of new derivatives.

Future studies will also include the investigation of racemization kinetics and chiroptical properties of **2**.

References

[1] Shigemori, K.; Watanabe, M.; Kong, J.; Mitsudo, K.; Wakamiya, A.; Mandai, H.; Suga *Org. Lett.* **2019**, *21* (7), 2171–2175.

[2] S. A. Iqbal, J. Pahl, K. Yuan, M. J. Ingleson *Chem. Soc. Rev*., **2020**, *49*,4564.

[3] A. El Jaouhari, Y. Wang, B. Zhang, X. Liu, J. Zhu, *Materials Science & Engineering, C: Materials for Biological Applications*, **2020**, *114*, 111067.

[4] Liu, B. Yang, T. J. Katz, M. K. Poindexter, *J. Org. Chem.* **1991**, *56*, 3769–3775.

[5] Deposition numbers 2211410 (for **1**), CCDC 2211405 (for **5**), CCDC 2211406 (for **8**), CCDC 2211409 (for *trans*-**15**), CCDC 2211407 (for **16**), CCDC 2211408 (for **17**) and CCDC 2211411 (for **15H2**) contain the supplementary crystallographic data for this paper. These data are provided free of charge by the joint Cambridge Crystallographic Data Centre and Fachinformationszentrum Karlsruhe Access Structures service.

[6] For representative examples, see: C. Hoffend, M. Diefenbach, E. Januszewski, M. Bolte, H. W. Lerner, M. C. Holthausen, M. Wagner, *Dalton Trans.* **2013**, *42*, 13826–13837.

[7] A. Budanow, E. v. Grotthuss, M. Bolte, M. Wagner, H. Lerner, *Tetrahedron* **2016**, *72*, 1477–1484.

[7a] H. Nakagawa, A. Obata, K.-i. Yamada, H. Kawazura, *J. Chem. Soc. Perkin Trans. II*, **1985**, 1899-1903.

[8] D. C. Patel, R. M. Woods, Z. S. Breitbach, A. Berthod, D. W. Armstrong, *Tetrahedron: Asymmetry* **2017**, *28*, 1557–1561.

[9] K. Yamada, H. Nakagawa, H. Kawazura, *Bull. Chem. Soc. Jpn.* **1986**, *59*, 2429–2432.

[10] H. Janke, G. Haufe, E. U. Würthwein, J. H. Borkent, *J. Am. Chem. Soc.* **1996**, *118*, 6031–6035.

[11] a) Y. Nakai, T. Mori, K. Sato, Y. Inoue, *J. Phys. Chem. A* **2012**, *116*, 7372–7385;
b) S. Abbate, G. Longhi, F. Lebon, E. Castiglioni, S. Superchi, L. Pisani, F. Fontana, F. Torricelli, T. Caronna, C. Villani, R. Sabia, M. Tommasini, A. Lucotti, D. Mendola, A. Mele, D. A. Lightner, *J. Phys. Chem. C* **2014**, *118*, 1682–1695.

[12] a) V. Pelliccioli, F. Cardano, G. Renno, F. Vasile, C. Graiff, G. Mazzeo, A. Fin, G. Longhi, S. Abbate, A. Rosetti, G. Viscardi, E. Licandro, S. Cauteruccio, *Catalysts* **2022**, *12*, 366;
b) S. Abbate, G. Longhi, T. Mori, in Helicenes *Synth. Prop. Appl.* (Eds.: J. Crassous, I. Stará, I. Starý), Wiley-VCH, Weinheim, **2022**, pp. 373–394.

[13] a) Y. Nakai, T. Mori, K. Sato, Y. Inoue, *J. Phys. Chem. A* **2012**, *116*, 7372–7385;
b) S. Abbate, G. Longhi, F. Lebon, E. Castiglioni, S. Superchi, L. Pisani, F. Fontana, F. Torricelli, T. Caronna, C. Villani, R. Sabia, M. Tommasini, A. Lucotti, D. Mendola, A. Mele, D. A. Lightner, *J. Phys. Chem. C* **2014**, *118*, 1682–1695.

[14] a) J. Barroso, J. L. Cabellos, S. Pan, F. Murillo, X. Zarate, M. A. Fernandez-Herrera, G. Merino, *Chem. Commun.* **2018**, *54*, 188–191;
b) S. Grimme, J. Antony, S. Ehrlich, H. Krieg, *J. Chem. Phys.* **2010**, *132*, 154104.

[15] Enantiomerization is the reversible conversion of a single enantiomer into the other one. The corresponding rate constant is k_{enant}. Racemization is the irreversible conversion of a sample of single enantiomers or of a non-racemic mixture of enantiomers into the racemate. The corresponding rate constant is k_{rac}. Comparison of calculated and experimental energy barriers was done using the enantiomerization barrier obtained from k_{enant}, which is calculated from the experimentally determined k_{rac} according to: $k_{enant} = 0.5k_{rac}$=8.15×10−5 s−1. The

free energy for the enantiomerization process ($\Delta G_{enant}^{\neq}$) was obtained by using the Eyring equation and setting a transmission coefficient equal to 1.

[16] M. B. Groen, H. Wynberg, *J. Am. Chem. Soc.* **1971**, *93*, 2968–2974.

[17] T. Caronna, M. Catellani, S. Luzzati, L. Malpezzi, S. V. Meille, A. Mele, C. Richter, R. Sinisi, *Chem. Mater.* **2001**, *13*, 3906–3914.

4.3 BO-doped tetrathia[7]helicenes 3 and 4

Once completed the synthesis of the doubly BO-doped helicenes **1** and **2**, in the last part of my Ph.D. I focused on the study of the synthesis of singly BO-doped helicenes **3** and **4** (Figure 17).

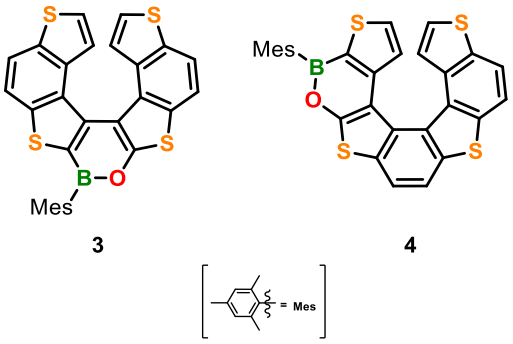

Figure 17. Structure of singly BO-doped tetrathia[7]helicenes **3** and **4**.

In detail **3** incorporates one oxaborine ring into the central region of the helical scaffold, while in **4** the oxaborine ring is positioned in the side of the helix.

4.3.1 Preliminary study of the synthesis of tetrathia[7]helicene 3

For the synthesis of **3**, the methoxy functionalized bis-benzodithiophene (bis-BDT) **21** was selected as possible direct precursor (Scheme 10), on which to run the oxaborine ring closure.

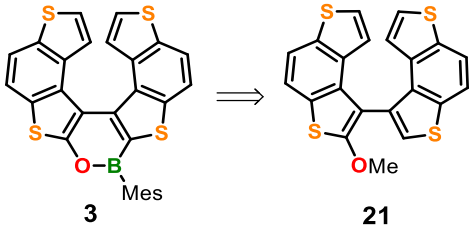

Scheme 10. Possible retrosynthetic analysis of **3**.

The synthesis of **21** (Scheme 11) was carried out starting from 3-bromo-4-methoxythiophene-2-carbaldehyde **S3**, which was in turn prepared following a known procedure[1] (Section 2.1 in the Experimental Part).

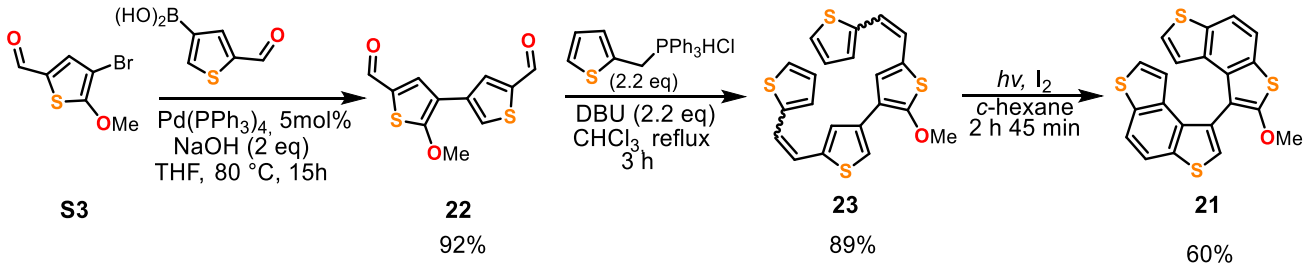

Scheme 11. Synthesis of the bis-BDT **21**.

Aldehyde **S3** was then subjected to a Suzuki coupling with the commercially available thiophene-2-carbaldehyde-4-boronic acid using $Pd(PPh_3)_4$ as catalyst and gave the dialdehyde **22** in 92% yield. The structure of **22** was also confirmed by X-ray analysis (Figure 18 and Figure S97).

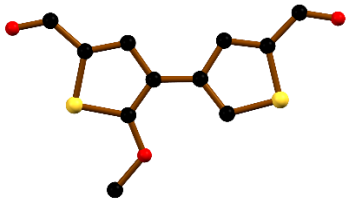

Figure 18. X-ray crystal structure of **22**. Crystal system: monoclinic, space group: P 21/n. C: black, O: red, S: yellow spheres. Picture generated with the crystallographic software *Mercury*.

Subsequent double-Wittig reaction of **22** with thiophene triphenylphosphonium bromide gave the corresponding bis-alkene derivative **23** in 89% yield as a mixture of four isomers (*cis*,*cis*; *cis*,*trans*; *trans,trans*; *trans*,*cis*). **23** was treated with Et_2O and filtered. The residue thus obtained was dissolved in *n*-pentane/CH_2Cl_2 and let evaporate slowly. *Trans*,*trans*-**X3** isomer crystallized out of the mixture (Figure 19 and S98) and its structure confirmed by X-ray analysis. (Figure 19)

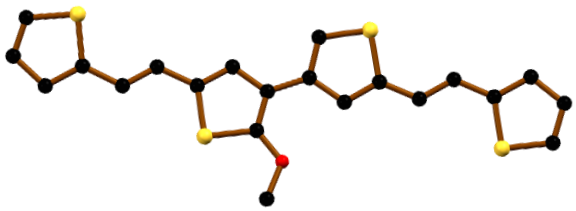

Figure 19. X-ray crystal structure of *trans,trans*-**23**. Crystal system: orthorombic, space group: F d d 2. C: black, O: red, S: yellow spheres. Picture generated with the crystallographic software *Mercury*.

Finally, photocyclization of **23** isomers using a medium pressure mercury lamp and I_2 as oxidant, afforded the desired methoxy bis-BDT **21** in 60% yield after chromatographic purification. Next, the borylation step was investigated (Scheme 12).

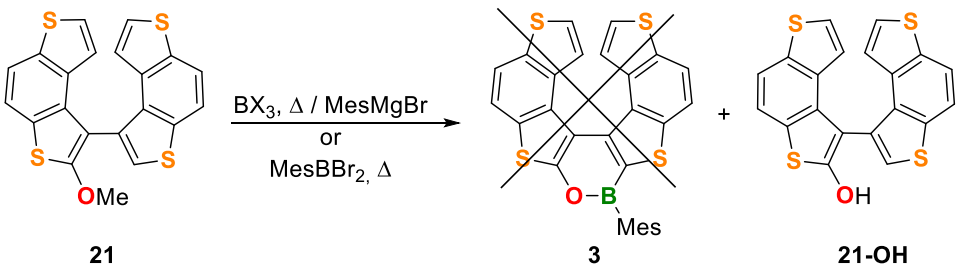

Scheme 12. Demethylative borylation of **21**.

Borylation was attempted by using various boron sources (BCl_3, BBr_3, $MesBBr_2$) at different temperatures (Table 3) but all the trials failed to provide the desired helicene **3**, and only the hydroxy derivative **21-OH** was isolated beside unidentified degradation products.

Table 3. Borylation attempts. Entry 1, 2: preparative experiments; entry 3: NMR experiment performed using a flame-sealed NMR tube in a thermostated oven.

Entry	Borane	Base	additive	solvent	temperature
1	BCl_3 (1.0 M in THF)	Et_3N (1.0 eq.)	*n*[Bu_4N]I (1.2 eq.)	chlorobenzene	135 °C
2	BBr_3 (0.5 M in *n*-hexane)	Et_3N (1.0 eq.)	//	chlorobenzene	135 °C
3	$MesBBr_2$	Et_3N (1.0 eq.)	//	C_6D_6	135 to 180 °C

21-OH was characterized by NMR analysis: in both ^1H and ^{13}C NMR spectra the OMe signal ($\delta(^1H)$ = 3.91) disappeared, a new proton signal was present at $\delta(^1H)$= 6.31 which was assigned to the -OH group as also confirmed through a deuteration experiment (see Figure S46A); full assignment of **21**/**21-OH** protons and carbon resonances is given in the Experimental Part.

The isolation of **21-OH** suggests as the first demethylation step of **21** works and gives the intermediate **24**, which then fails to undergo intramolecular electrophilic borylation and is then hydrolyzed during the purification step to give **21-OH** (Scheme 13).

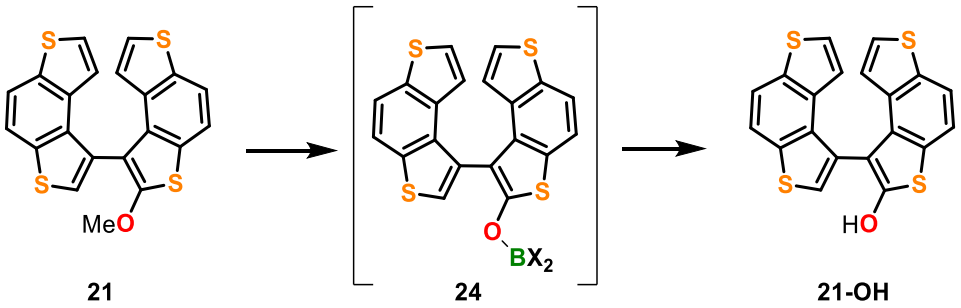

Scheme 13. Formation of the **21-OH** by-product.

A possible rationale for this result can be found in the intrinsic nature of the intermediate **24** (Figure 20) since: 1) the α position of the BDT, which should undergo the borylation, is scarcely activated to SEAr and 2) the rotation around the C-C bond connecting the BDT fragments placed in a twisted conformation, is probably hindered.

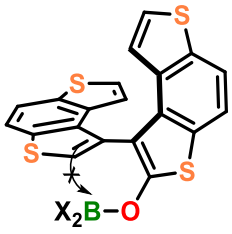

24
X = Cl, Br

Figure 20. Intermediate **24**.

Attempts to get single crystals of **24** or **21-OH** suitable for X-ray analysis unfortunately failed, but it was possible to obtain crystals of the starting bis-BDT **21** (Figure 10). X-ray diffraction of **21** revealed the presence of four conformers which are characterized by the different reciprocal orientation of the -OMe group and the unfunctionalized BDT fragment (Figure 21 and Figure S99).

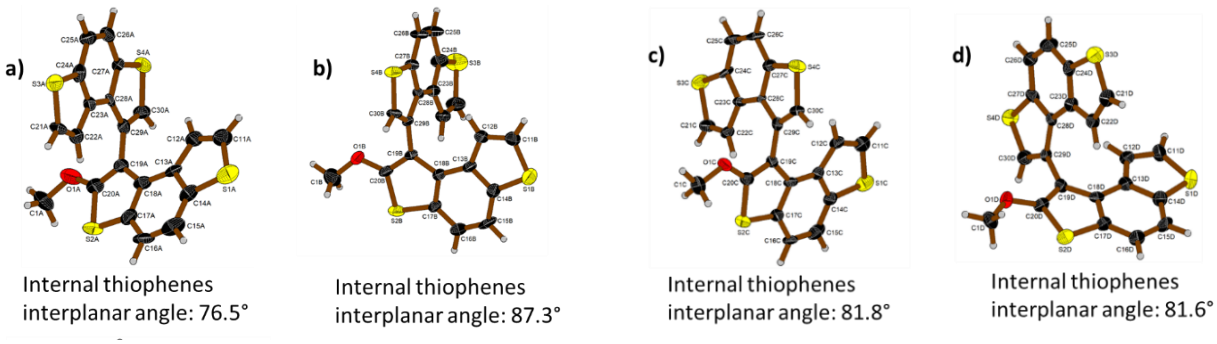

Figure 21. X-ray crystal structure of the four **21** conformers. Crystal system: triclinic, space group: P $^{-}$1. C: black, O: red, S: yellow spheres. ORTEPs generated with the IUCr Web service (http://publcif.iucr.org/services/tools/).

However, in the four conformations the two internal thiophene rings are twisted by an angle ranging from 76.5 to 87.3 ° (Figure 21) as result of the hindered rotation around the C-C bond connecting the two BDT fragments. These structural data support the previous hypothesis that the B(sp^2)-C(sp^2) bond must build against steric factors making ring-closure unfavourable.

In light of these considerations, we thought to modify the synthetic strategy and we runned the borylation before the formation the BDT rings on the less sterically constrained bisalkene precursor **23** (Scheme 14). The borylation, using "our standard conditions" gave the bis-olefinated oxaborine **25,** in moderate yield (42%) after column chromatography, as a mixture of *cis/trans* isomers.

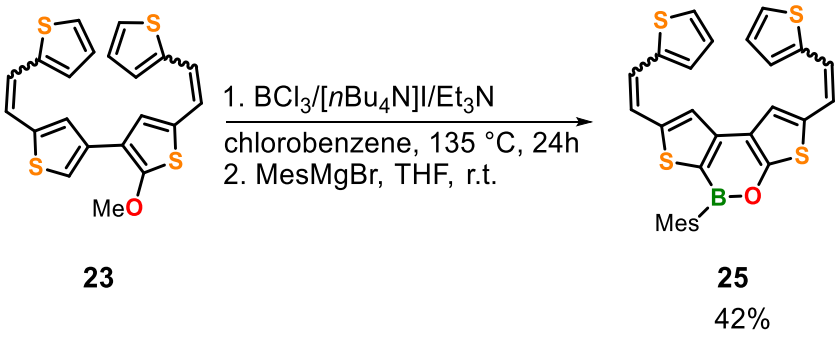

23 **25**
42%

Scheme 14. Synthesis of the bis-olefinated oxaborine **25**.

The subsequent treatment with *n*-pentane allowed to isolate the pure *trans*,*trans*-isomer of **25**, whose structure was confirmed by NMR and X-ray analysis (Figure 22 and Figure S100).

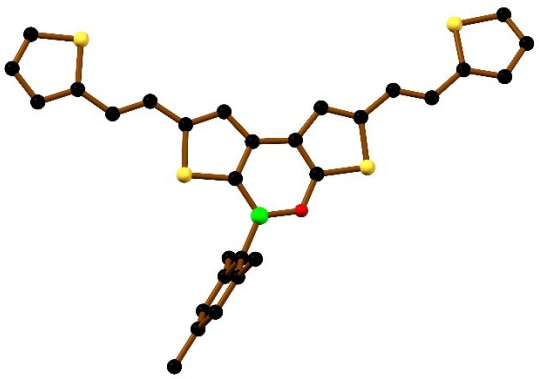

Figure 22. X-ray crystal structure of **25**. Crystal system: orthorombic, space group: P 21 21 21. B: green, C: black, O: red, S: yellow spheres. Picture generated with the crystallographic software *Mercury*.

All proton and carbon resonances of **25** were assigned. It is worth to note that proton resonances of **25** well reflect the different electronic features of the two formally B- and O-substituted fragments of the molecule. As an example, protons on the α and β position of the terminal thiophene on the "B-substituted side" of the molecule resonate at $\delta(^1H)$ = 7.27 and $\delta(^1H)$ = 7.21, while the corresponding protons "on the O-substituted side" are significantly shielded upfield and resonate in the 7.01-7.03 ppm region; the same trend is observed for olefinic protons (see Figure 23). The ^{11}B shift for **25** is $\delta(^{11}B)$ = 41.70 (Figure 23).

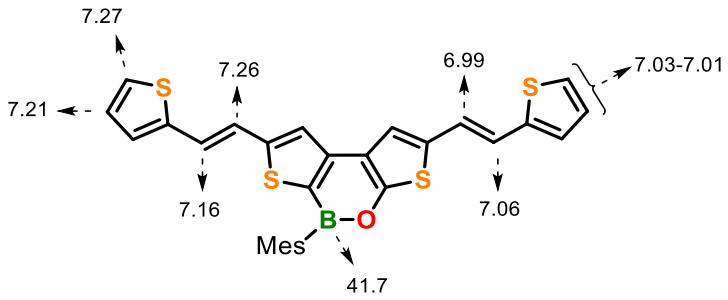

Figure 23. Diagnostic proton and boron shifts of *trans,trans*-**25**.

Cyclovoltammetry of *trans,trans*-**25** was run in THF solution (Figure S74, S75) and showed an irreversible reduction peak in the cathodic scan, E_{pc} = –2.21 V. *trans,trans*-**25** is thus easier to reduce than the oxaborine substructure **5** (E_{pc} = –2.96 V), according to its more extended conjugation pathway. Interestingly, in the anodic scan, **25** showed a first quasi-reversible oxidation event E_{pa} = 0.61 V, accompanied by a largely irreversible process E_{pa} = 0.99 V which could be attributed to oxidation processes involving the α-positions of the two terminal thiophene rings.

Absorption and emission spectra of *trans,trans*-**25** were performed in *c*-hexane THF and $CHCl_3$ (Figure 24). Absorption spectrum of *trans,trans*-**25** showed three main bands at 283, 365 and 382 nm; the calculated energy gap is Eg^{opt} = 2.69 eV, which is the lowest of all the whole BO-doped series of compounds presented in this thesis. Compound **25** is a blue emitter and its fluorescence spectrum (*c*-hexane) and showed (Figure 24) resolved vibrational fine structure with maxima at 445, 472 and 500 nm, accompanied by a shoulder at 535 nm. The associated quantum yield of **25** in *c*-hexane is Φ_{PL} = 12% while the quantum yields in polar

solvents are significantly lower (Φ_{PL}^{THF} = 3%, $\Phi_{PL}^{CHCl_3}$ = 5%). Interestingly, *trans,trans*-**25** is characterized by a considerable solvatochromic effect and emits in the green in polar solvents (THF, λ_{em} = 535 nm; $CHCl_3$, λ_{em} = 553 nm), thus revealing a polar excited state.

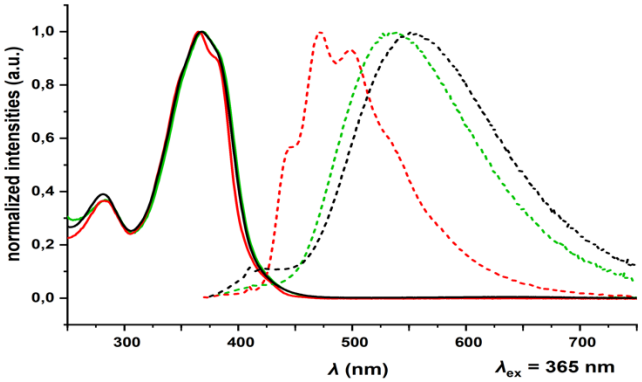

Figure 24. Absorption (solid line) and emission (dashed line) spectra of **25** in *c*-hexane (red), THF (black) and $CHCl_3$ (green).

DFT calculations revealed as the HOMO and LUMO are located on the O- and B- fragment respectively (Figure 25), similarly to what observed for the BO-doped compounds previously showed (see Chapter 1, 2).

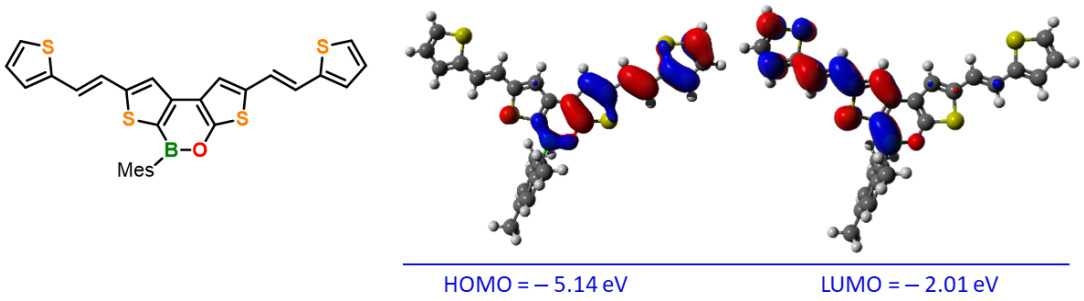

Figure 25. HOMO (left) and LUMO (right) distributions of **25** calculated at the B3LYP/6-31G* level.

The photocyclization of **25** was then investigated, the reaction was performed in benzene solution irradiating for 3.5 h with a 385 nm LED lamp at room temperature in the presence of 2 equiv of I_2 and an excess of propylene oxide (Scheme 15). Only the mono-ring closure product **26** was obtained, after chromatographic purification, as an inseparable mixture of *trans*- and *cis*- isomers in ≈60:40 ratio. The increasing of the irradiation time to 12 h allowed to obtain a mixture enriched in the *cis*-isomer (≈40:60, see Figure S50, S51).

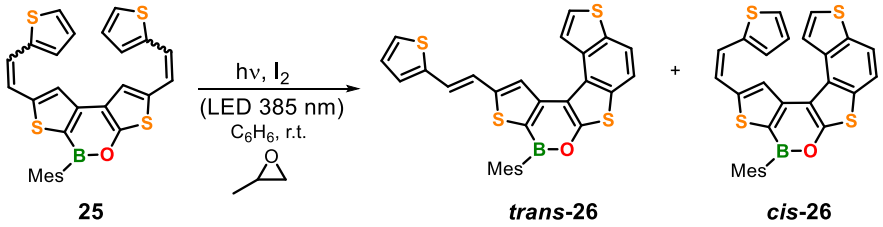

Scheme 15. Photocyclization of **25**.

^{1}H NMR analysis (aided by ^{HH}COSY experiments) performed on the isomeric mixtures of **26** allowed to assign most of the proton resonances of both structures (see Experimental Part). Moreover, the structure was confirmed by HRMS and, single crystals of *trans*-**26** suitable for X-ray analysis, were obtained by slow evaporation of a saturated solution of *trans*/*cis*-**26** (≈60:40) (Figure 26 and Figure S100).

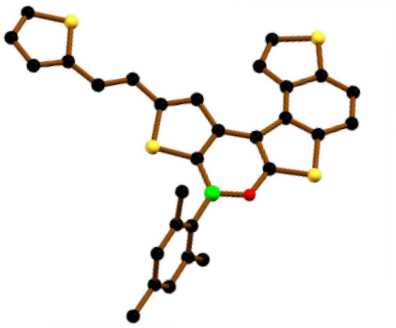

Figure 26. X-ray crystal structure of *trans*-**26** by-product. B: green, C: black, O: red, S: yellow spheres. Picture generated with the crystallographic software *Mercury*.

These preliminary results about the photocyclization of **25** are rather promising for the obtainment of helicene **3** and deserve a further investigation, that is currently ongoing. Although the target borahelicene **3** has still not been isolated, DFT calculations were run to get insights about its HOMO-LUMO distribution (Figure 27). Similarly to the case of its bisalkene precursor *trans,trans*-**25**, HOMO is mainly located in the oxygenated helicene wing, while LUMO is mainly spread on the opposite borylated wing. Taken together, these results confirm that, as in the case of borahelicenes **1** and **2**, the HOMO and LUMO distributions strongly depends on the position of the B-O bond(s) into the helical scaffold.

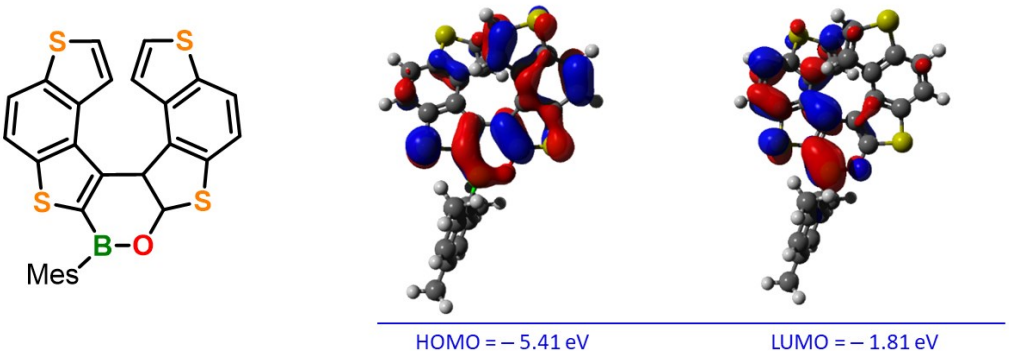

Figure 27. HOMO (left) and LUMO (right) distributions of **3** calculated at the B3LYP/6-31G* level.

4.3.2 Preliminary study of the synthesis of tetrathia[7]helicene 4

Finally, I started investigating the synthesis of borahelicene **4** which contains one 1,2-oxaborine ring in the side position of the helical scaffold. The synthesis of **4** again exploits the photocyclization of the "oxaborine containing" alkene **27**, which in turn can be synthesized by late-stage borylation of the methoxy functionalized alkene **28** (Scheme 16).

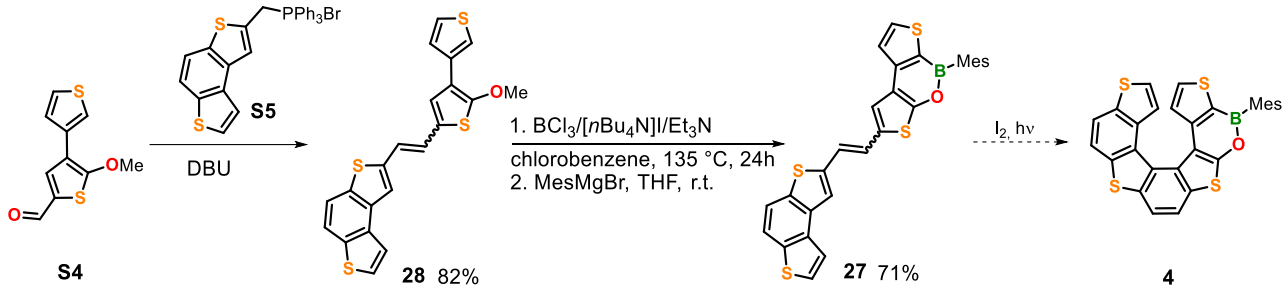

Scheme 16. Designed synthetic route to **4**.

The starting material of this sequence is the methoxy bithiophene aldehyde **S4** which was prepared according to literature procedures and completely characterized, since just few data were reported in the original article[2] (see Section 2.1). The following Wittig olefination with the BDT phosphonium salt **S5**, using DBU as base, gave **28** in 82% average yield, in a ≈3:2 *trans*/*cis* ratio.

The isomers of alkene **28** were separated by column chromatography. *Trans*-**28** NMR characterization was quite difficult, due to its scarce solubility (slightly soluble only in DMSO, THF, chlorobenzene). However, it was possible to assign most of the proton and carbon resonances and assign the *trans*/*cis*-configuration of the two isomers of 28 on the basis of their olefinic protons coupling constants, $^{3}J(\mathrm{H,H})_{trans}$ = 15.9 Hz and $^{3}J(\mathrm{H,H})_{cis}$ = 12.4 Hz.

Alkene **28** was therefore subjected to borylation reaction following our standard procedure and gave the key precursor **27** that was obtained in good yield (71%), predominantly as *trans* isomer. In the NMR spectrum of *trans*-**27** olefinic protons at $\delta(^{1}\mathrm{H})$ = 7.15 and $\delta(^{1}\mathrm{H})$ = 7.20, showed a reciprocal coupling constant of ^{3}J = 15.7 Hz, again the borylated thiophene α proton was significantly deshielded and resonates at $\delta(^{1}\mathrm{H})$ = 8.00, similarly to that of *trans*-**15** $\delta(^{1}\mathrm{H})$ = 7.99, which incorporates the same substructure (see Figure 28). The ^{11}B NMR shift measured for **27** is $\delta(^{11}\mathrm{B})$ = 42.12.

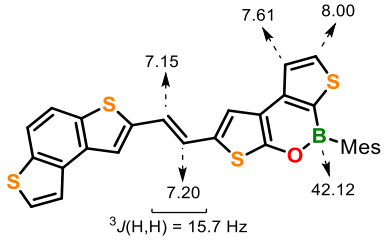

Figure 28. Diagnostic proton and boron shifts of *trans*-**27**.

Cyclic voltammetry measurements of *trans*-**27** were performed in THF. In the cathodic scan, *trans*-**27** showed an irreversible reduction process, with peak potential at E_{pc} = – 2.37 V. Similarly to what observed for the bisalkene **25**, two irreversible oxidation processes resulted from the anodic scan (E^{I}_{pa} = 0.63 V, E^{II}_{pa} = 0.76 V) and again these can be attributed to oxidation processes involving the terminal thiophene ring α positions. Alkene *trans*-**27** is harder to be reduced than the singly BO-doped bisalkene *trans*,*trans*-**25** (– 2.37 V *vs*. – 2.21 V; – 2.43 eV *vs*. – 2.59 eV) and the experimental HOMO and LUMO values are –5.43 eV and – 2.43 eV respectively.

DFT calculations revealed that both HOMO and LUMO are spread over the central thiophene-ethylene-thiophene fragment of the molecule 27 (Figure 29a), (as in the case of the alkenes *trans*-**15** and *trans*-**18** (See Chapter 1 and 2)). Absorption and emission spectra were measured in *c*-hexane and THF but the solvatochromic effect was negligible. Absorption spectrum of *trans*-**27** in *c*-hexane showed main absorption bands at 388 and 410 nm and an associated E_g^{opt} = 2.89 eV (Figure 29b).

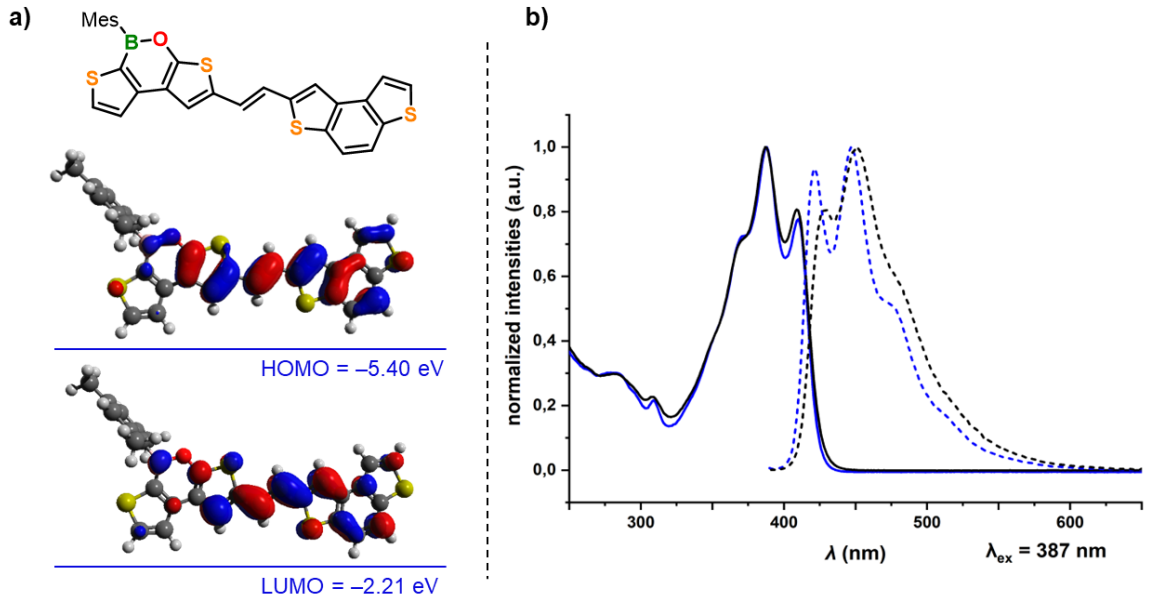

Figure 29. a) HOMO (top) and LUMO (bottom) distributions of *trans*-**27** calculated at the B3LYP/6-31G* level. b) Absorption (solid lines) and emission (dashed lines) spectra of *trans*-**27** in in *c*-hexane (blue) and THF (black).

In the emission spectra *trans*-**27** shows two bands with resolved vibrational fine structure at 421 and 488 nm accompanied by a shoulder at 517. *Trans*-**27** is a blue emitter; the associated quantum yield in *c*-hexane is Φ_{PL} = 23%, while is slightly lower in THF, Φ_{PL} = 17%. Thus, *trans*-**27** is the most efficient emitter in the whole series of BO-doped compounds presented in this thesis. The photocyclization of **27** to **4** will be investigated soon and once completed the synthesis, its analytical, spectroscopic, electrochemical, theoretical, stereochemical characterization will be performed.

References

[1] PCT Int. Appl., 2010040839; CAS 77133-21-2.

[2] El Jaouhari, Y. Wang, B. Zhang, X. Liu, J. Zhu *Mat. Science & Engineer. C* **2020**, *114*, 111067.

5. Conclusions

This PhD thesis was aimed at investigating a new class of chiral thiaheterohelicenes doped with one or two boron atoms. Few borahelicenes examples have been reported in the literature and the synthetic strategies and routes to access this class of compounds are still underdeveloped. This target has been particularly challenging and demanding from a synthetic point of view, and it required a meticulous setup of the experimental procedures, especially for the borylation steps.

Novel chiral borahelicenes **1** and **2** were successfully obtained following unprecedented synthetic routes which combine the chemistry of helicenes and that of boron-doped PAHs, and the investigation of the synthesis of two additional borahelicenes, namely **3** and **4** has already been started and is presently still ongoing.

In particular the doubly (BO)-doped tetrathia[7]helicene **1** was obtained via an efficient four-step synthesis, including a Mallory photocyclization step, which has rarely been used for the synthesis of B-containing polycyclic aromatic hydrocarbons. The chiroptical properties of **1** were investigated, its (*P*)-/(*M*)-enantiomers were resolved by chiral HPLC and their absolute configuration was established combining computed and experimental CD spectra. The results of this complete study were published as research article on *Angewandte Chemie Int. Ed.* (L. Menduti, C. Baldoli, S. Manetto, M. Bolte, H.-W. Lerner, G. Longhi, C. Villani, E. Licandro, M. Wagner *Angew. Chem. Int. Ed.* **2023**, *62*, *5*, e202215468).

In general, the extensive experimental work was supported by a deep NMR and crystallographic characterization of all synthesized compounds which allowed their correct identification and characterization. The electrooptical features of new molecules were investigated by cyclic voltammetry, UV/Vis and fluorescence spectroscopy while DFT calculations were run to analyse the energetic landscape of these systems.

The synthetic routes developed in this thesis should allow for manifold optimizations in the future (such as BN-doping, introduction of different heteroaromatic rings) and thus open up for the synthesis of new and more complex borahelicene structures.

Taken together, the results presented in this thesis represent a meaningful contribution to the development of the field of borahelicenes and, in the specific case of BO-doped thiahelicenes, thus setting solid basis for the development in the design and the synthesis of new helicene derivatives with enhanced properties.

UNIVERSITÀ DEGLI STUDI DI MILANO
FACOLTÀ DI SCIENZE E TECNOLOGIE

GOETHE UNIVERSITÄT
FRANKFURT AM MAIN

Doctorate in

Chemistry, XXXV Cycle

Boraheterohelicenes: synthetic methodologies and properties of a novel class of boron π-conjugated systems

Experimental Part

Luigi Menduti

Tutor

Prof. Emanuela Licandro

Prof. Dr. Matthias Wagner

Co-tutor

Dr. Clara Baldoli

Table of contents

1. General experimental remarks

If not stated otherwise, all reactions and manipulations were carried out under dry nitrogen atmosphere using Schlenk techniques. THF was distilled from Na/benzophenone and degassed by purging with dry argon or nitrogen for at least 30 min (coupling reactions). Chlorobenzene, dimethylformamide (DMF) and Et_3N were distilled from CaH_2 and stored over molecular sieves (3 Å). C_6D_6 and $CDCl_3$ were stored over molecular sieves (3 Å). MesMgBr and *n*-BuLi were titrated according to literature prior to use.[S1] Reaction mixtures in flasks were heated by using an oil bath.

If not stated otherwise, commercially available compounds were used as received.

In photochemical experiments, a medium-pressure Hg lamp (Helios Italquartz; 150 W) or 385, 395 and 405 nm LED lamps (*Sahlmann Photochemical Solutions*) were used.

Column chromatography was performed using silica gel 60 (*Macherey–Nagel*, *Simga Aldrich*; 70–230 mesh). Melting points were measured with Melting points were recorded with a Büchi Melting Point B-540 apparatus. NMR spectra were recorded at 298 K using the following spectrometers: Bruker Avance-300, Avance-400, Avance Neo-400, Avance-500, or DRX-600. Chemical shift values are referenced to (residual) solvent signals ($^1H/^{13}C\{^1H\}$; C_6D_6: δ = 7.16/128.06; $CDCl_3$: δ = 7.26/77.16) or external BF_3•Et_2O (^{11}B: δ = 0.00). Abbreviations: s = singlet, d = doublet, dd = doublet of doublets, br. = broad, n.o. = not observed, eq. = equivalent, Mp = melting point. Resonances of carbon atoms attached to boron atoms were typically broadened and sometimes not observed due to the quadrupolar relaxation of boron. Resonance assignments were aided by ^{13}C APT, ^{H,H}COSY, ^{H,C}HSQC, and ^{H,C}HMBC spectra.

High-resolution mass spectra were measured using: electron ionization (EI) spectrometer (FISONS-Vg Autospec-M246), *Thermo Fisher Scientific* MALDI LTQ Orbitrap XL spectrometer (2,5-dihydroxybenzoic acid or α-cyano-4-hydroxycinnamic acid as the matrix), MALDI-TOF/TOF Autoflex III-Bruker Daltonics.

UV–vis absorption spectra were obtained on a *Shimadzu* UV–vis–NIR 3600 spectrophotometer or a *Varian* Cary 50 Scan or a *Varian* Cary 60 Scan UV/Vis spectrophotometer in a 1 cm path length quartz cell.

Photoluminescence quantum yields (Φ_{PL}) were measured with a *Jasco* FP-8300 spectrofluorometer equipped with a calibrated *Jasco* ILF-835 100 mm-diameter integrating sphere and analyzed using the *Jasco* FWQE-880 software or a C11347 *Quantaurus* - Absolute Photoluminescence Quantum Yield Spectrometer (Hamamatsu Photonics U.K), equipped with a 150 W Xenon lamp, an integrating sphere and a multi-channel detector.

Steady state emission and excitation spectra and photoluminescence lifetimes were obtained with a FLS 980 spectrofluorimeter (Edinburg Instrument Ltd.). Continuous excitation for the steady state measurements was provided by a 450 W Xenon arc lamp. Emission spectra were corrected for the detector sensitivity. Photoluminescence lifetime measurements, determined by TCSPC (time-correlated single-photon counting) method, were performed using an Edinburgh Picosecond Pulsed Diode Laser EPL-445 (Edinburg Instrument Ltd.), in nitrogen degassed solutions (10^{-5}-10^{-7} mol L^{-1}).

Cyclic voltammetry (CV) measurements of **5**, **15**, **16**, **1**, and **15H2** were performed in a glovebox at room temperature in a one-chamber, three-electrode cell using an *EG&G* Princeton Applied Research 263A potentiostat. A platinum-disk electrode (2.00 mm diameter) was used as the working electrode with a platinum-wire counter electrode and a silver-wire reference electrode, which was coated with AgCl by immersion into HCl/HNO_3 (3:1). Prior to measurements, THF was dried with Na/benzophenone, and degassed by three freeze-pump-thaw cycles. [nBu$_4$N][PF_6] (used as received; *Sigma Aldrich*) was employed as the supporting electrolyte (0.1 mol L^{-1}). All potential values were referenced against the FcH/FcH^+ redox couple (FcH = ferrocene; $E_{1/2}$ = 0 V). Scan rates were varied between 100 and 400 mV s^{-1}.

Cyclic voltammetry (CV) measurements of **18**, **2**, **25**, and **27** were performed using an AutoLab PGStat potentiostat and a classical three electrode glass minicell (working volume about 3 mL), including as working electrode a glassy carbon GC disk (Metrohm, S=0.033 cm2) polished by diamond powder (1 μm Aldrich) on a wet cloth (Struers DP-NAP), as counter electrode a platinum disk, and as reference electrode a saturated aqueous calomel one (SCE) inserted in a compartment with the working medium ending in a porous frit, to avoid contamination of the working solution by water and KCl traces. Experiments were run at scan rates ranging 0.1–2 V/s on 0.00075 M solutions in THF+0.1 M tetrabutylammonium hexafluorophosphate $TBAPF_6$ as the supporting electrolyte, previously deaerated by nitrogen bubbling. Positive and negative half cycles have been separately recorded to avoid reciprocal contamination by electron transfer products. The reported potentials have been normalized vs. the formal potential of the intersolvental ferricinium/ferrocene (FcH+|FcH) reference redox couple, recorded in the same conditions. HPLC-resolution and semipreparative separation of the enantiomers were carried using a *Dionex* Ultimate 300 RS HPLC system equipped with a column (250×4.6 mm I.D. 5, 10 μm) containing the Chiralpak IA chiral stationary phase; eluant was delivered at flow rate of 1.0 mL/min. Optical rotation and CD spectra were recorded on a *Jasco J 715* CD spectrometer.

2. Starting materials preparation

2.1 Thiophene starting materials

2.1.1 Synthesis of S7[S2]

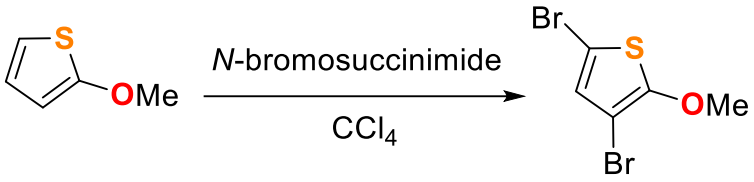

S7

A 250 ml two-necked flask equipped with a thermometer was charged with 2-methoxythiophene (5.00 g, 43.80 mmol) and CCl_4 (88 mL). The resulting yellowish solution was cooled to 5 °C and *N*-bromosuccinimide (15.65 g, 87.93 mmol, 2.00 equiv) was added in six portions during 1 h. The reaction mixture (yellow) was therefore allowed to warm up to room temperature and stirred for 24 hours (the reaction progress was checked by ^{1}H NMR). The reaction mixture was cooled with ice and then filtered to remove insoluble residues. The solution thus obtained was washed with water (150 mL). The organic phases were dried over Na_2SO_4, filtered and the solvent removed under reduced pressure. The crude product thus obtained was distilled under vacuo (bp. 94-95 °C, 2.5 mmHg) yielding 10.90 g of **S7** as a yellow oil (40.1 mmol, 92%).

^{1}H NMR (250 MHz, $CDCl_3$): δ = 6.75 (s, 1H), 3.93 (s, 3H).

2.1.2 Synthesis of S8[S2]

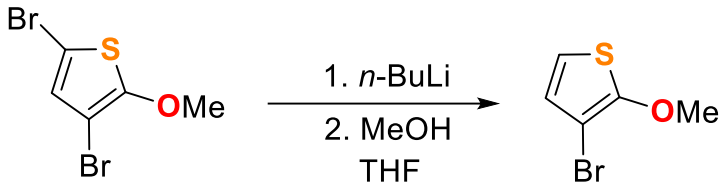

S7 **S8**

A 100 ml flame dried two-necked flask (equipped with a dropping funnel) was charged with **S7** (3.71 g, 14.32 mmol, 1 equiv) and THF (34 mL). The resulting dark red solution was cooled to –78 °C and *n*-BuLi (1.35 M in hexanes; 10.6 mL, 14.32 mmol, 1.05 eq) was diluted with dry THF (9 mL) and added dropwise (20 min). The resulting brown mixture was therefore stirred at the same temperature for 10 min, quenched with MeOH (5 mL, added slowly) and allowed to warm up to room temperature.

The solvent was removed and the residue was taken up with CH_2Cl_2 (50 ml). Water (70 mL) was added, the organic phase was separated and the aqueous phase was extracted with CH_2Cl_2 (4×30 mL). The combined organic layers were dried over Na_2SO_4 and filtered. The solvent was removed and the crude product was distilled under vacuo (56-58 °C, 1.5 mmHg) yielding 2.15 g of **S8** as a yellowish oil (11.15 mmol, 82%). The ^{1}H NMR chemical shifts correspond to the reference values.

^{1}H NMR (600 MHz, $CDCl_3$): δ = 6.75 (d, ^3J(H,H) = 6.0 Hz, 1H), 6.65 (d, ^3J(H,H) = 6.0 Hz, 1H), 3.97 (s, 3H).

2.1.3 Synthesis of S1[S3]

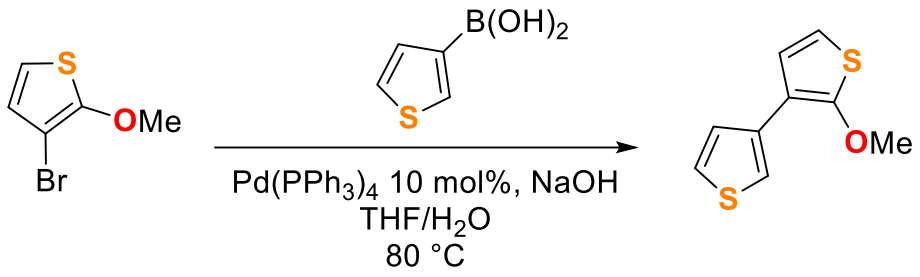

S8 **S1**

A flame-dried 100 mL J-Young flask was charged with **S8** (524 mg, 2.71 mmol), 3-thienylboronic acid (417 mg, 3.26 mmol, 1.20 equiv), $Pd(PPh_3)_4$ (157 mg, 0.135 mmol, 0.05 equiv) and THF (12 mL). NaOH 3M (1.8 mL, 5.43 mmol, 2.0 equiv) was added and the resulting dark reaction mixture warmed up to 80 °C and stirred for 2.5 d.

After cooling to room temperature, the THF was removed and the reaction mixture was taken up with CH_2Cl_2 (20 mL), water (10 mL) was added, and the two phases separated. The aqueous phase was extracted with CH_2Cl_2 (3 × 15 mL). The collected organic phases were dried over Na_2SO_4, filtered and the solvent was evaporated. The crude product was purified via column chromatography (*c*-hexane/CH_2Cl_2 (10:1)) affording **S1** as a yellowish oil (478 mg, 2.43 mmol, 90%).

^{1}H NMR (250 MHz, $CDCl_3$): δ = 7.53 (dd, *J*(H,H) = 3.0 Hz, *J*(H,H) = 1.3 Hz, 1H), 7.44 (dd, *J*(H,H) = 5.0 Hz, *J*(H,H) = 1.3 Hz, 1H), 7.32 (dd, *J*(H,H) = 5.0 Hz, *J*(H,H) = 3.0 Hz, 1H), 7.07 (d, *J*(H,H) = 5.9 Hz, 1H), 6.62 (d, *J*(H,H) = 5.9 Hz, 1H,), 4.00 (s, 3H).

2.1.4 Synthesis of S9[S4]

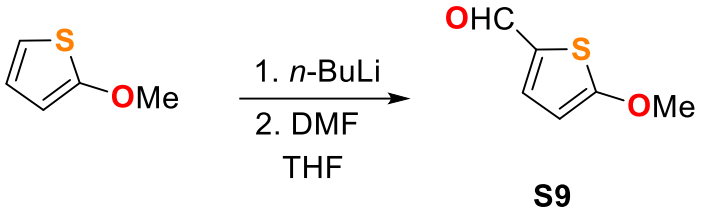

S9

A flame-dried two-necked flask equipped with a dropping funnel was charged with 2-methoxythiophene (2.5 g, 21.19 mmol) and THF (30 mL). The resulting yellowish mixture was cooled to –78 °C. *n*-BuLi (1.40 M in hexanes; 16.12 mL, 22.68 mol, 1.04 eq.) was added dropwise during 10 min and the resulting yellow clear solution was stirred at –78 °C for 1 hour.

DMF (4.72 g, 64.6 mmol, 2.95 eq.) was added dropwise yielding a deep yellow solution which was stirred at –78 °C for 45 min. NH_4Cl sat. aqueous solution (5 mL) was added, and the reaction mixture was allowed to warm up to room temperature. THF was removed and the residue was taken up with AcOEt (30 mL). Water (50 mL) was added, and the two layers were separated. The aqueous phase was extracted with AcOEt (3×20 mL) and the combined organic phases were dried over Na_2SO_4 and filtered. **S9** was obtained as a red-orange oil (3.10 g, 21.8 mmol, y = quantitative) and it was proved to be the desired product by ^{1}H NMR analysis.

^{1}H NMR (300 MHz, $CDCl_3$): δ = 9.66 (s, 1H), 7.50 (d, *J*(H,H) = 4.3 Hz, 1H), 6.34 (d, *J*(H,H) = 4.3 Hz, 1H), 3.98 (s, 3H).

2.1.5 Synthesis of S4[S5]

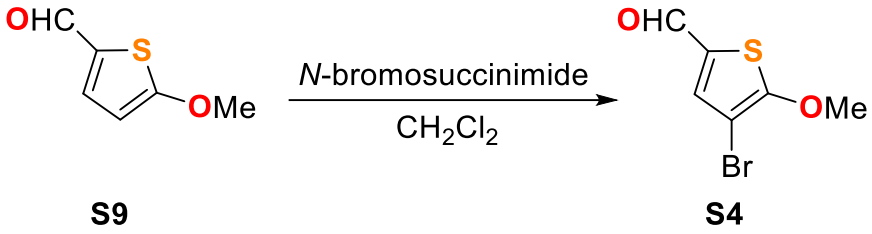

S9 **S4**

S9 (2.02 g, 14.18 mmol) was dissolved in CH_2Cl_2 (30 mL) and the resulting mixture was treated with *N*-bromo succinimide (2.63 g, 14.75 mmol, 1.04 eq.), added in portions during 30 min. The reaction progress was checked by TLC. After 5 h, TLC showed complete conversion of the starting material.

The reaction mixture was thus poured into water (50 mL) and, after separation of the two layers, the organic phase was washed with water (3×30 mL), while the aqueous phase was extracted with CH_2Cl_2 (30 mL). The combined organic phases were dried over Na_2SO_4, filtered and the solvent was removed. The crude product thus obtained was washed with Et_2O yielding **S4** as a pale-yellow solid (2.27 g, 10.30 mmol, 73%). Et_2O mother liquors were evaporated and the residue thus obtained was purified *via* column chromatography (*n*-hexane/CH_2Cl_2 (1:3)), yielding additional 630 mg of **S4** (2.85 mmol, 20%). Total yield: 93%.

The ^{1}H NMR chemical shifts correspond to the reference values.

^{1}H NMR (300 MHz, $CDCl_3$): δ = 9.66 (s, 1H), 7.55 (s, 1H), 4.09 (s, 3H).
Mp: 113-114 °C.

2.1.6 Synthesis of S5[S6]

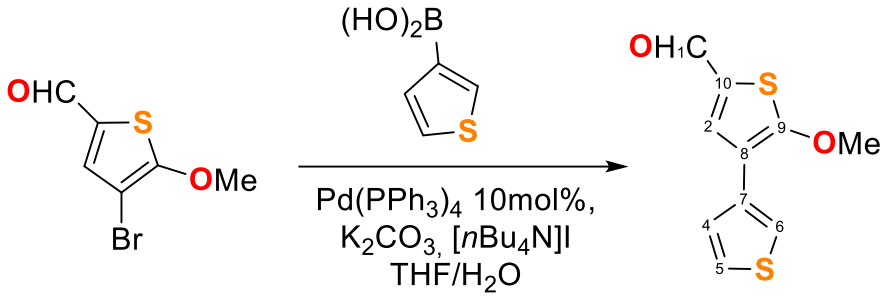

S4 **S5**

A flame-dried J-Young flask was charged with **S4** (502 mg, 2.26 mmol), 3-thienylboronic acid (296 mg, 2.26 mmol, 1 eq.), [*n*Bu$_4$N]Br (83 mg, 0.23 mmol, 0.1 eq.), K_2CO_3 (629 mg, 4.53 mmol, 2 eq.) and a THF/H_2O (5:1) solvent mixture (12 mL). $Pd(PPh_3)_4$ (213 mg, 0.18 mmol, 0.08 eq.) was added and the resulting yellow mixture was heated to 80 °C and stirred for 12 h. The reaction progress was checked by TLC (*n*-hexane/CH_2Cl_2 (1:3)). TLC after 12 h showed complete conversion of the starting material.

The reaction mixture was thus allowed to cool to room temperature and the solvent was evaporated. The residue was taken up with CH_2Cl_2 (30 mL) and water (20 mL) was added. After separation of the two layers, the aqueous phase was extracted with CH_2Cl_2 (3×15 mL). The collected organic phases were dried over Na_2SO_4 and filtered. The solvent was removed, and the crude product was purified *via* column chromatography (*n*-hexane/CH_2Cl_2 (1:3)). **S5** was thereby obtained as an orange solid (404 mg, 1.80 mmol, 80%).

S5 *^{1}H and ^{13}C resonances assignment:*

^{1}H NMR (300 MHz, $CDCl_3$): δ = 9.72 (s, 1H; H-1), 7.82 (s, 1H; H-2), 7.59 (dd, ^3J (H,H) = 2.9, ^4J (H,H) = 1.3 Hz, 1H; H-6), 7.40 (dd, ^3J (H,H) =5.0 Hz, ^5J (H,H)=1.3 Hz, 1H; H-4), 7.38 (dd, ^3J(H,H) =5 Hz, dd, ^4J (H,H) =2.9 Hz, 1H; H-5), 4.14 (s, 3H; OMe).

^{13}C{^{1}H}NMR (75 MHz, $CDCl_3$): δ = 182.2 (C-1), 170.1 (C-10), 137.1 (C-2), δ=133.4 (C-9), 128.2 (C-8), 126.55 (C-4), 125.7 (C-5), δ=121.5 (C-6), 118.7 (C-7), 61.9 (OMe).

IR: $\nu_{C=O}$: 1631 cm^{-1}.

Mp: 87.7 – 88.2 °C.

2.1.1 Synthesis of S2[S8]

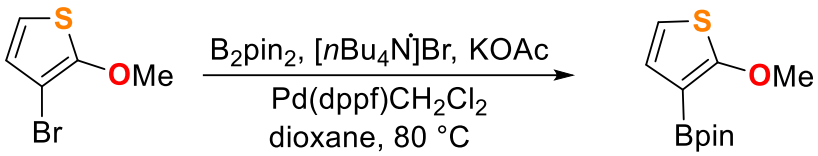

S8 **S2**

A flame-dried J-Young flask was charged with **S8** (1.50 g, 7.77 mmol, 1.00 eq.), bis-pinacolato diboron (2.24 g, 9.32 mmol, 1.20 eq.), KOAc (1.53 g, 15.5 mmol, 2.00 eq.), TBAB (56 mg, 170 µmol, 0.025 eq.), Pd(dppf)·CH_2Cl_2 (140 mg, 155 µmol, 0.02 eq.) and evacuated for 1 h. Dioxane (8 mL) was added and the resulting mixture was heated to 80 °C for 18 h. The solvent was evaporated, and the residue was purified via column chromatography (*c*-hex/CH_2Cl_2 (1:1)). **S2** was obtained as a yellow solid, in mixture with 7% B_2pin_2 (255 mg, 1.06 mmol, 14%).

^{1}H NMR (250 MHz, $CDCl_3$): δ = 7.01 (d, ^3J(H,H) = 5.7 Hz, 1H), 6.53 (d, ^3J(H,H) = 5.7 Hz, 1H), 3.98 (s, 3H), 1.32 (s, 12H).

2.1.2 Synthesis of S3[S7]

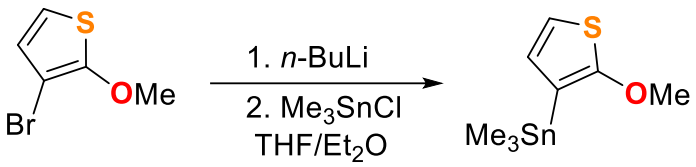

S8 **S3**

A flame-dried two-necked flask equipped with a dropping funnel was charged with **S8** (3.22 g, 16.68 mmol) and Et_2O (16 mL). The orange solution thus obtained was cooled to –78 °C and *n*-BuLi (1.40 M in hexanes; 13 mL, 18.20 mmol , 1.05 eq.) was added dropwise during 15 min. The dropping funnel was washed with THF (16 mL).

The orange suspension thus obtained was stirred at –78 °C for additional 45 min and then treated with a THF solution (16 mL) of Me_3SnCl (3.08 g, 19.05 mmol, 1.1 eq.), added during 3-5 min. The resulting orange solution was stirred at –78 °C for 2 h. The reaction mixture was therefore allowed to warm up to room temperature and water (30 mL) was added. The two layers were separated, and the aqueous phase was extracted with Et_2O. The combined organic phases were dried over Na_2SO_4, filtered and the solvent evaporated. The crude product was purified *via* distillation under vacuum (55-58 °C, 0.7 mmHg). **S3** was thereby obtained as yellowish oil (4.06 g, 14.65 mmol, 88%).

^{1}H NMR (300 MHz, $CDCl_3$): δ = 6.73 (d, *J*(H,H) = 5.5 Hz, 1H), 6.71 (d, *J*(H,H) = 5.5 Hz, H), 3.89 (s, 3H), 0.28 (s, 9H).

2.2 Benzodithiophene (BDT) starting materials

Benzodithiophene (BDT) was prepared according to literature procedures.[S9]

2.2.1 Synthesis of S10[S10]

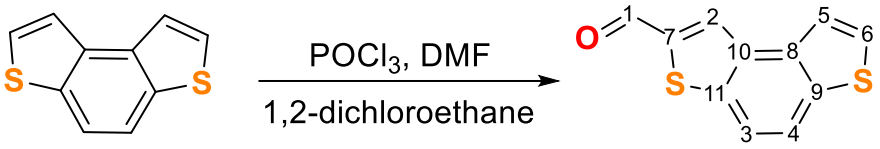

BDT **S10**

Preparation of the Vilsmeier salt:

A 100 mL two-necked flask was charged with DMF (12 ml, 159 mmol, 30 eq.) and 1,2-dichloroethane (5 mL). The reaction mixture was cooled to 0 °C and $POCl_3$ (15 mL, 159 mmol, 30 eq.) was added. The resulting yellow solution was therefore allowed to warm up to room temperature and then heated to 50 °C and stirred for 1 h.

*Preparation of **10**:*

A 100 mL two-necked flask equipped with a reflux condenser was charged with **BDT** (1.0 g, 5.30 mmol, 1 eq.) and 1,2-dichloroethane (22 mL). The Vilsmeier salt (30 eq.) was added dropwise at room temperature (using a Pasteur pipette) during 30 min. The resulting orange reaction mixture was heated to 85 °C and stirred for 24 h. The reaction progress was checked by TLC.

Note: reaction mixture samples were washed with water prior to deposition onto the TLC plate.

After cooling to room temperature, the solvent was evaporated. The residue was taken up with AcOEt (100 mL), poured into ice-cold water (150 mL) and the resulting biphasic mixture was stirred for 15 min. After separation of the two layers, the aqueous phase was extracted with CH_2Cl_2 and the collected organic phases were dried over Na_2SO_4 and filtered. The solvent was removed, and the crude product was purified *via* column chromatography (*n*-hexane/CH_2Cl_2 (6:4)). **S10** was obtained as a yellow solid (838 mg, 3.84 mmol, 72%).

^{1}H NMR (400 MHz, $CDCl_3$): δ = 10.16 (s, 1H; H-1), 8.38 (s,1H; H-2), 7.98 (d, ^3J(H,H) = 8.7 Hz, 1H; H-3), 7.82 (d, ^3J(H,H) =8.7 Hz, 1H; H-4), 7.77 (d, ^3J(H,H) = 5.4 Hz, 1H; H-5), 7.68 (d, ^3J(H,H) = 5.4 Hz, 1H; H-6).
^{13}C{^{1}H}NMR (75 MHz, $CDCl_3$): δ = 184.38 (C-1), 143.26 (C-7), 140.73 (C-10), 137.31 (C-8), 136.15 (C-11), 133.98 (C-9), 131.79 (C-2), 128.51 (C-6), 123.07 (C-3), 121.28 (C-5), 119.17 (C-4).
M.p.: 101.8-102.6 °C.

2.2.2 Synthesis of S11[S11]

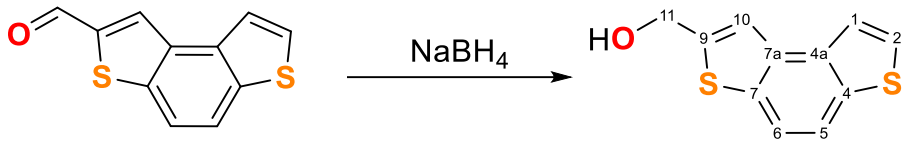

S10 **S11**

A 50 mL two-necked flask was charged with **S10** (838 mg, 3.84 mmol), THF (8 mL) and EtOH (10 mL). The resulting solution was cooled to 0 °C and $NaBH_4$ (146 mg, 3.84 mmol, 1eq.) was added. The reaction mixture was therefore allowed to warm up to room temperature and stirred for 5 h. The reaction progress was checked by TLC (CH_2Cl_2).

The solvent was evaporated, and the residue was taken up with CH_2Cl_2 and washed with water. The organic phases were dried over Na_2SO_4, filtered and the solvent was removed under reduced pressure. **S11** was thereby obtained as a white solid (806 mg, 3.66 mmol, 95%).

^{1}H NMR (400 MHz, $CDCl_3$): δ = 7.83 (d, 2H, H-5), 7.73 (d, 2H, H-6), 7.66 (d, ^2J(H-H)=5.4 Hz, 1H, H-1), 7.61 (s,1H, H-10), δ=7.56 (d, ^2J (H,H) =5.4 Hz, 1H; H-2), δ=5.04 (d, ^2J(H,H) =6 Hz, 1H, H-11), δ=1.93 (t, ^2J(H,H) =6 Hz, 1H, OH)

^{13}C{^{1}H}NMR (75 MHz, $CDCl_3$): δ = 145.22 (C-9), 136.73 (C-4a/ C-7a), 136.68 (C-4a/ C-7a), 134.73 (C-4/ C-7), 134.64 (C-4/ C-7), 126.74 (C-2), 121.90 (C-1), 119.88 (C-10), 119.01 (C-5/ C-6), 118.86 (C-5/ C-6), 61.1 (C-11).

2.2.3 Synthesis of S6

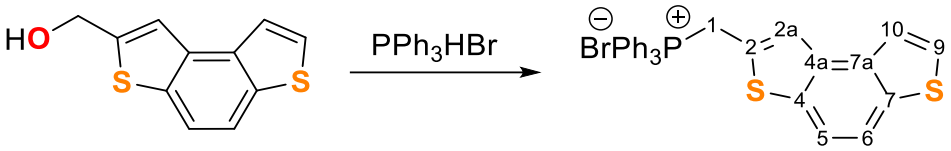

S11 **S6**

A 50 mL two-necked flask equipped with a reflux condenser was charged with **S11** (2.06 g, 9.35 mmol), $CHCl_3$ (52 mL) and PPh_3HBr (5.45 g, 15.9 mmol, 1.7 eq.). The resulting yellow mixture was heated to reflux for 5 h. The reaction progress was checked by TLC (CH_2Cl_2).

The solvent was removed, and the residue was washed with Et_2O (to remove triphenylphosphine by-product; $^{31}P\{^1H\}$ (122 MHz, DMSO): δ = –5.0) and $CHCl_3$ (to remove the chloroform phosphonium salt side-product; $^{31}P\{^1H\}$ (122 MHz, DMSO): δ = 29.3).

S6 was thereby obtained as a white solid (5.0 g, 9.17 mmol, y = 98%).

^{1}H NMR (300 MHz, DMSO): δ = 7.14-6.69 (m, 7 H), 6.99-6.82 (m, 11H), 6.83 (d, *J*(H,H) = 5.3 Hz, 1H), 6.69 (d, *J*(H,H) = 3.2 Hz, 1H), 4.89 (d, ^{2}*J*(H,P) = 15.1 Hz, 2H; H-1).

^{13}C{^{1}H}NMR (75 MHz, $CDCl_3$): δ = 136.4 (d, *J*(C,P) = 9.9 Hz), 135.36 (*p*-CH phenyl group), 133.96 (d, *J*(C,P) = 10.0 Hz; *o*/*m*-CH phenyl group), 133.32 (d, *J*(C,P) = 2.5 Hz), 130.28 (d, *J*(C,P) = 12.5 Hz; *o*/*m*-CH phenyl group), 128.43, 125.58 (d, *J*(C,P) = 8.6 Hz), 121.88, 119.74, 118.53, 118.23, 117.10, 25.09 (d, *J*(C,P) = 50.7 Hz; C-1).

^{31}P{^{1}H}NMR (121.5 MHz, $CDCl_3$): δ = 21.6.

3. Synthesis of tetrathia[7]helicene 1

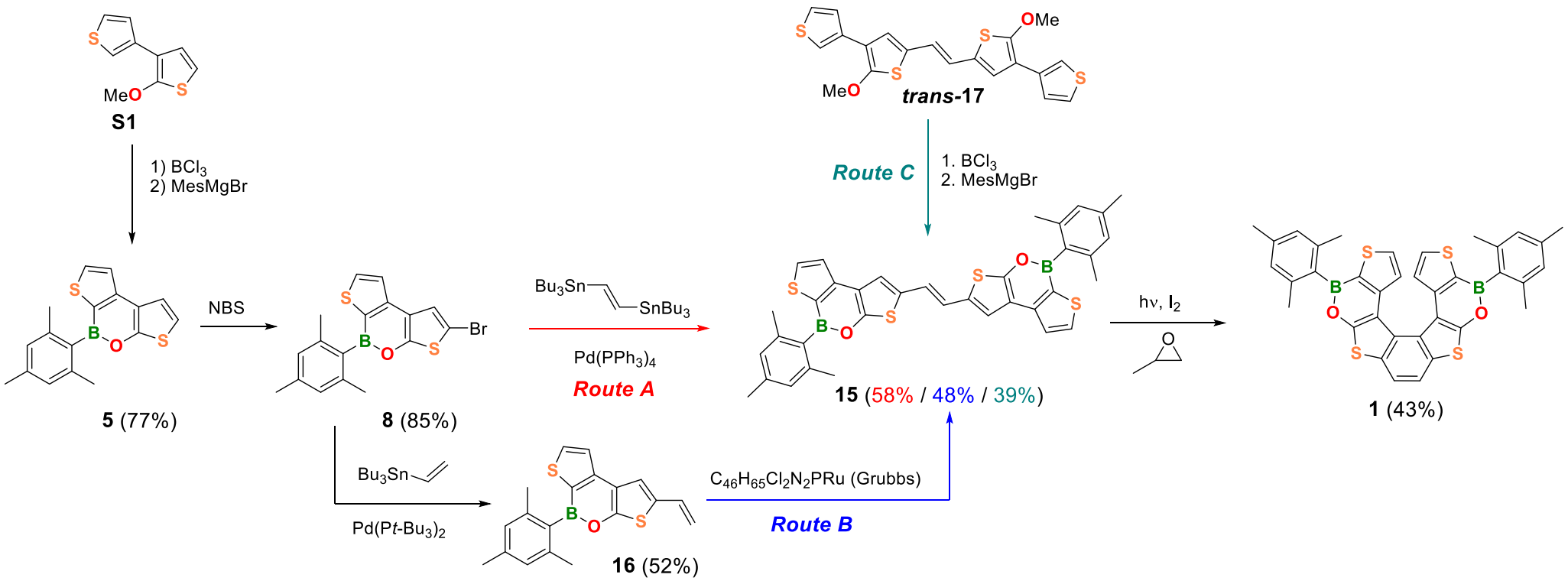

Scheme S1: Synthetic route to tetrathia[7]helicene **1**. Full details about the synthesis of **S1** are provided in section *2.1 Thiophene starting materials*.

3.1 Synthesis of 5

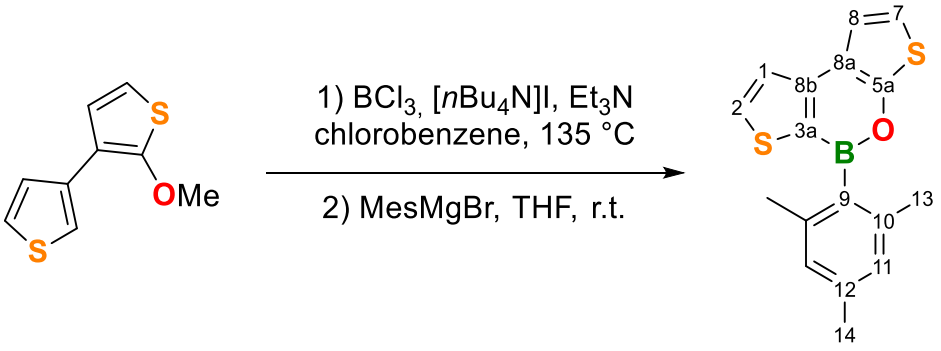

S1 **5**

A flame-dried 100 mL J-Young tube was charged with **S1** (510 mg, 2.60 mmol), [*n*Bu$_4$N]I (1.15 g, 3.12 mmol, 1.20 eq.), and chlorobenzene (18 mL). The yellowish mixture was treated with BCl_3 (1.0 M in hexanes; 3.90 mL, 3.90 mmol, 1.50 eq.) and stirred at room temperature for 2 min. Et_3N (362 µL, 2.60 mmol, 1.00 eq.) was added and the orange mixture thus obtained was heated to 135 °C and stirred for 24 h. After cooling to room temperature, the solvent was evaporated to dryness and THF (18 mL) was added. MesMgBr (1.0 M in THF; 7.79 mL, 7.79 mmol, 3.00 eq.) was added dropwise at room temperature to give a clear, orange-colored solution, which was stirred for 1 h. The solvent was removed under reduced pressure and the residue was purified by column chromatography (15 cm silica gel, d = 3.5 cm, *c*-hexane, R_f = 0.20). **5** was obtained as an off-white solid (620 mg, 2.00 mmol, 77%). Single crystals suitable for X-ray crystallography were grown by slow evaporation of a saturated solution of **5** in *n*-hexane/CH_2Cl_2 (1:1).

^{1}H NMR (500 MHz, $CDCl_3$): δ = 7.98 (d, ^3J(H,H) = 4.8 Hz, 1H; H-2), 7.64 (d, ^3J(H,H) = 4.8 Hz, 1H; H-1), 7.36 (d, ^3J(H,H) = 5.9 Hz, 1H; H-8), 6.96 (d, ^3J(H,H) = 5.9 Hz, 1H; H-7), 6.92 (s, 2H; H-11), 2.35 (s, 3H; H-14), 2.25 (s, 6H; H-13).

^{13}C{^{1}H} NMR (126 MHz, $CDCl_3$): δ = 158.4 (C-5a), 147.5 (C-8b), 140.6 (C-10), 138.9 (C-12), 138.2 (C-2), 133.7* (C-9), 131.8* (C-3a), 127.6 (C-11), 123.0 (C-1), 120.38 (C-8), 120.35 (C-8a), 114.8 (C-7), 22.8 (C-13), 21.5 (C-14). *) unequivocally detected only in the ^{H,C}HMBC spectrum.

^{11}B NMR (96 MHz, $CDCl_3$): δ = 41.7 ($h_{1/2} \approx$ 180 Hz).

HRMS (MALDI): Calculated *m/z* for $[C_{17}H_{15}BOS_2]^+$: 310.0652; found: 310.0655.

UV/Vis (*c*-hexane): λ_{max} (ε / mol^{-1}dm^{3}cm^{-1}) = 313 (sh), 320 (24300), 335 (sh).

Fluorescence (*c*-hexane, λ_{ex} = 320 nm): λ_{max} = 366, 380 nm (resolved vibrational fine structure); Φ_{PL} = 6%.

Cyclic voltammetry (THF, 0.1 M [*n*Bu$_4$N][PF$_6$], 200 mV s^{-1}, vs. FcH/FcH$^+$): Cathodic scan: E_{pc} = −2.96 V, E_{pa} = −2.81 V.

Mp: 102.5-104.5 °C.

3.2 Synthesis of 8

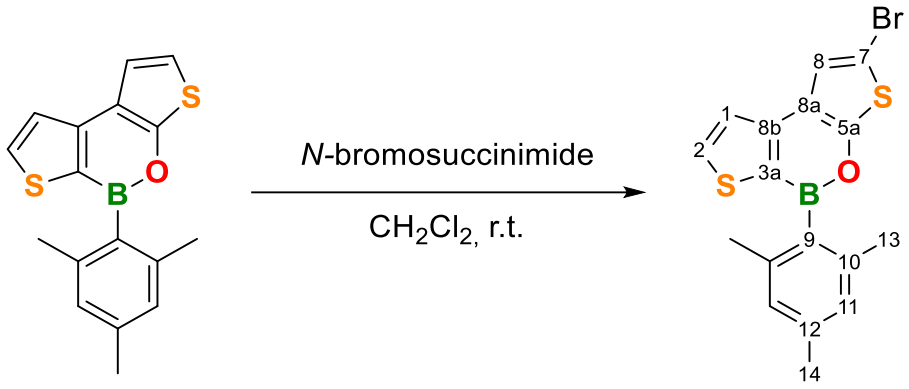

5 **8**

A 50 mL flask was charged with **5** (500 mg, 1.61 mmol) and CH_2Cl_2 (18 mL). Neat *N*-bromosuccinimide (344 mg, 1.93 mmol, 1.20 eq.) was added in one portion at room temperature and the resulting clear, orange-colored solution was stirred overnight (the completion of the reaction was confirmed by TLC). The solvent was removed under reduced pressure, and the solid residue was purified by column chromatography (15 cm silica gel, d = 3.5 cm, *c*-hexane, R_f = 0.30). **8** was obtained as a white solid (530 mg, 1.36 mmol, 85%). Single crystals suitable for X-ray crystallography were grown by slow evaporation of a saturated solution of **8** in *n*-hexane/CH_2Cl_2 (2:1).

^{1}H NMR (500 MHz, $CDCl_3$): δ = 7.98 (d, ^3J(H,H) = 4.8 Hz, 1H; H-2), 7.56 (d, ^3J(H,H) = 4.8 Hz, 1H; H-1), 7.39 (s, 1H; H-8), 6.92 (s, 2H; H-11), 2.35 (s, 3H; H-14), 2.23 (s, 6H; H-13).

^{13}C{^{1}H} NMR (126 MHz, $CDCl_3$): δ = 157.5 (C-5a), 146.3 (C-8b), 140.6 (C-10), 139.1 (C-12), 138.6 (C-2), 133.3* (C-9), 132.2* (C-3a), 127.6 (C-11), 123.1 (C-8), 122.9 (C-1), 120.8 (C-8a), 103.1 (C-7), 22.7 (C-13), 21.5 (C-14). *) unequivocally detected only in the ^{H,C}HMBC spectrum.

^{11}B NMR (96 MHz, $CDCl_3$): δ = 41.5 ($h_{1/2}$ ≈ 210 Hz).

HRMS (MALDI): Calculated *m/z* for $[C_{17}H_{14}BBrOS_2]^+$: 387.9757; found: 387.9755.

Mp: 134-136 °C.

3.3 Synthesis of 15 (*via* Stille-type coupling)

Note: *trans*-1,2-bis(*n*Bu$_3$Sn)ethylene was purchased from *Alfa Aesar* and used as received; the same chemical purchased from different suppliers may be contaminated with *trans*-1,2-bis(*n*Bu$_3$Sn)acetylene.

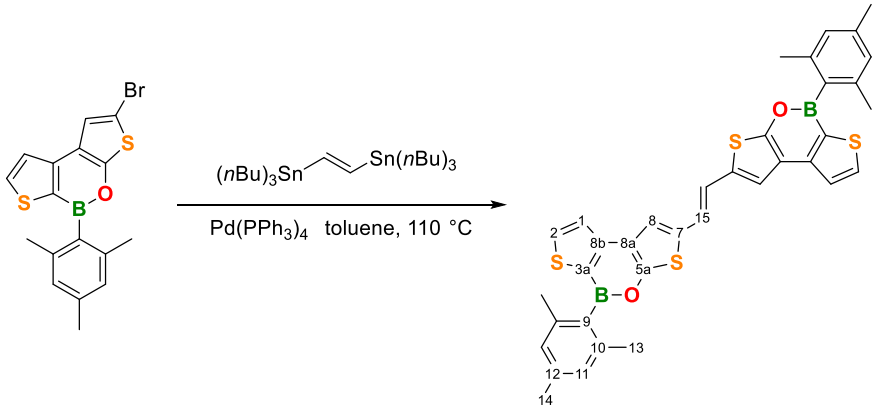

8 ***trans*-15**

A flame-dried 250 mL J-Young round-bottom flask was charged with **16** (304 mg, 0.78 mmol) and evacuated for 30 min. Toluene (40 mL), *trans*-1,2-bis(*n*Bu$_3$Sn)ethylene (216 µL, 0.39 mmol, 0.50 eq.), and Pd(PPh$_3$)$_4$ (108 mg, 0.094 mmol, 0.12 eq.) were added, the Young-tap was closed, and the red mixture was heated with stirring to 110 °C for 24 h. After cooling to room temperature, the solvent was removed under reduced pressure, and the residue was purified by column chromatography (13 cm silica gel, d = 3.0 cm, *c*-hexane/CH_2Cl_2 (5:1), R_f = 0.28). The fractions containing *trans*-**15** (with only traces of *cis*-**15**) were combined and evaporated to dryness. The dark yellow residue was treated with *n*-hexane (to remove soluble *n*Bu$_3$SnBr and *cis*-**15**), and the resulting suspension was filtered. *trans*-**15** was thereby isolated as a yellow solid (146 mg, 0.23 mmol, 58%). Single crystals suitable for X-ray crystallography were grown by slow evaporation of a saturated solution of *trans*-**15** in $CDCl_3$.

^{1}H NMR (500 MHz, $CDCl_3$): δ = 7.99 (d, ^3J(H,H) = 4.7 Hz, 2H; H-2), 7.60 (d, ^3J(H,H) = 4.8 Hz, 2H; H-1), 7.29 (s, 2H; H-8), 7.02 (s, 2H; H-15), 6.93 (s, 4H; H-11), 2.36 (s, 6H; H-14), 2.27 (s, 12H; H-13).

^{13}C{^{1}H} NMR (126 MHz, $CDCl_3$): δ = 157.3 (C-5a), 147.0 (C-8b), 140.7 (C-10), 139.1 (C-12), 138.4 (C-2), 133.5 (br.; C-9), 132.1 (br.; C-3a), 131.9 (C-7), 127.6 (C-11), 123.0 (C-1), 121.6 (C-15), 121.1 (C-8a), 119.4 (C-8), 22.8 (C-13), 21.5 (C-14).

^{11}B NMR (96 MHz, $CDCl_3$): δ = 41.4 ($h_{1/2} \approx$ 490 Hz).

HRMS (MALDI): Calculated *m/z* for $[C_{36}H_{30}B_2O_2S_4]^+$: 644.1309; found: 644.1322.

UV/Vis (*c*-hexane): λ_{max} (ε / mol^{-1}dm^{3}cm^{-1}) = 278 (26300), 344 (sh), 364 (44100), 383 (58700), 403 (45100).

Fluorescence (*c*-hexane, λ_{ex} = 385 nm): λ_{max} = 419, 443 nm (resolved vibrational fine structure); Φ_{PL} = 11%.

Cyclic voltammetry (THF, [*n*Bu$_4$N][PF$_6$] 0.1 M, 200 mV s^{-1}, vs. FcH/FcH$^+$): Cathodic scan: $E^{I}_{1/2}$ = – 2.54 V, E^{II}_{pc} = –2.90 V, E^{II}_{pa} = – 2.79 V.

Mp: >300 °C (decomposition).

3.4 Synthesis of 16

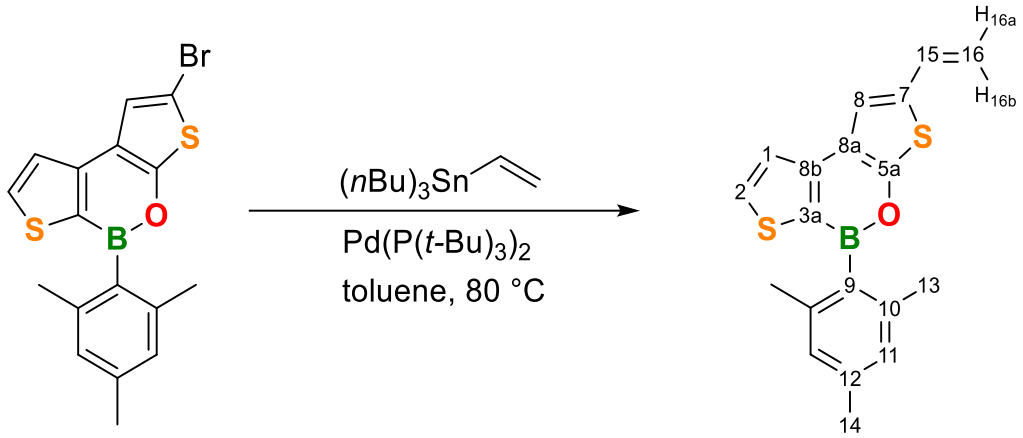

8 **16**

A flame-dried 250 mL J-Young round-bottom flask was charged with **8** (449 mg, 1.15 mmol) and evacuated for 30 min. Toluene (60 mL), nBu$_3$(vinyl)Sn (369 µL, 1.27 mmol, 1.1 eq.), and Pd(P(t-Bu)$_3$)$_2$ (29.5 mg, 0.058 mmol, 0.05 eq.) were added, the Young-tap was closed, and the red mixture was heated with stirring to 80 °C for 24 h. After cooling to room temperature, the solvent was removed under reduced pressure and the solid residue was purified by column chromatography (13 cm silica gel, d = 3.0 cm, c-hexane/CH_2Cl_2 (5:1), R_f = 0.42). The fractions containing **16** were combined and evaporated to dryness. The yellow residue was treated with n-pentane and the resulting suspension was filtered to remove nBu$_3$SnBr. **8** was isolated as a pale-yellow solid (200 mg, 0.59 mmol, 52%). Single crystals suitable for X-ray crystallography were grown by slow evaporation of a saturated solution of **16** in n-hexane/CH_2Cl_2 (2:1).

^{1}H NMR (500 MHz, $CDCl_3$): δ = 7.97 (d, ^3J(H,H) = 4.8 Hz, 1H; H-2), 7.58 (d, ^3J(H,H) = 4.8 Hz, 1H; H-1), 7.21 (s, 1H; H-8), 6.92 (s, 2H; H-11), 6.83 (dd, ^3J(H,H) = 17.2, 10.8 Hz, 1H; H-15), 5.53 (d, ^3J(H,H) = 17.2 Hz, 1H; H-16b), 5.17 (d, ^3J(H,H) = 10.8 Hz, 1H; H-16a), 2.34 (s, 3H; H-14), 2.24 (s, 6H; H-13).

^{13}C{^{1}H} NMR (126 MHz, $CDCl_3$): δ = 157.3 (C-5a), 147.2 (C-8b), 140.6 (C-10), 139.0 (C-12), 138.3 (C-2), 132.7 (C-7), 132.6* (C-9), 132.0* (C-3a) 130.6 (C-15), 127.6 (C-11), 122.9 (C-1), 120.7 (C-8a), 119.1 (C-8), 113.0 (C-16), 22.7 (C-13), 21.5 (C-14). *) unequivocally detected only in the ^{H,C}HMBC spectrum.

^{11}B NMR (96 MHz, $CDCl_3$): δ = 41.4 ($h_{1/2} \approx$ 250 Hz).

HRMS (MALDI): Calculated m/z for $[C_{19}H_{17}BOS_2]^+$: 336.08084; found: 336.08085.

UV/Vis (c-hexane): λ_{max} (ε / mol^{-1}dm^{3}cm^{-1}) = 265 (27700), 275 (sh), 328 (26400).

Fluorescence (c-hexane, λ_{ex} = 328 nm): λ_{max} = 388, 402 nm (resolved vibrational fine structure); Φ_{PL} = 15%.

Cyclic voltammetry (THF, [nBu$_4$N][PF$_6$] 0.1 M, 200 mV s^{-1}, vs. FcH/FcH$^+$): Cathodic scan: E_{pc} = −2.93 V.

Mp: 108.7-110.8 °C.

3.5 Synthesis of 15 (*via* Grubbs metathesis)

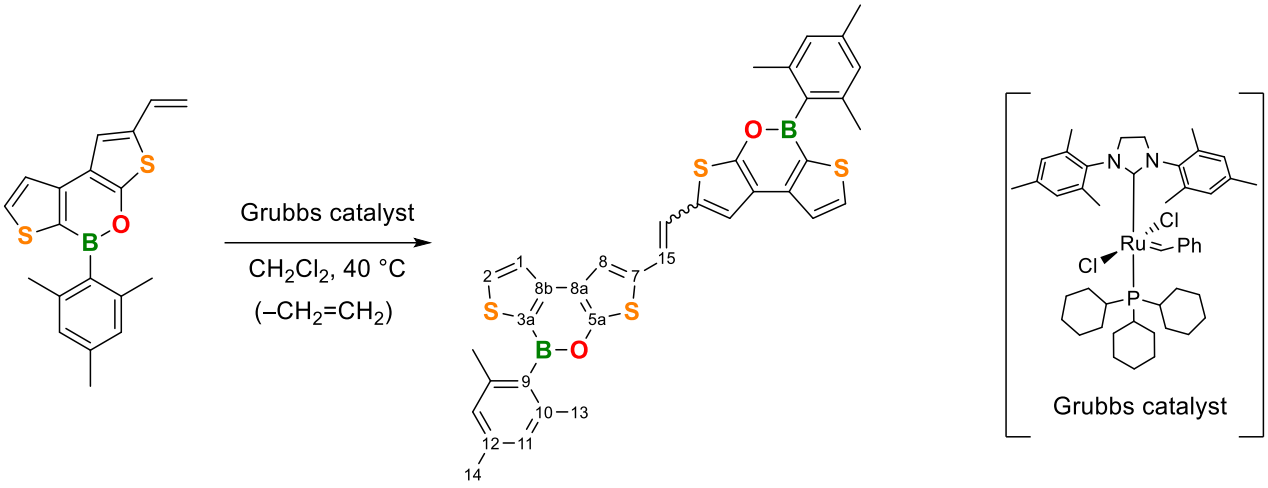

16 **15**

A flame-dried 40 mL Schlenk flask was charged with **16** (85 mg, 0.25 mmol), Grubbs catalyst (8.6 mg, 0.01 mmol, 0.04 eq.), and CH_2Cl_2 (1 mL). The dark-red solution thus obtained was stirred at 40 °C for 2 d (the reaction progress was monitored by TLC). **Note:** The reaction mixture was briefly exposed to vacuum after 1 d to remove the ethylene byproduct. After cooling to room temperature, the solvent was removed under reduced pressure and the dark red residue was purified by column chromatography (12 cm silica gel, d = 2.0 cm, *c*-hexane/CH_2Cl_2 (5:1), R_f = 0.28). **15** was obtained as a yellow solid (39 mg, 0.06 mmol, 48%); *trans/cis* ratio ≈ 9:1 (determined by ^{1}H NMR spectroscopy).

trans-15

^{1}H NMR (500 MHz, $CDCl_3$): δ = 7.99 (d, ^3J(H,H) = 4.7 Hz, 2H; H-2), 7.60 (d, ^3J(H,H) = 4.8 Hz, 2H; H-1), 7.29 (s, 2H; H-8), 7.02 (s, 2H; H-15), 6.93 (s, 4H; H-11), 2.36 (s, 6H: H-14), 2.27 (s, 12H; H-13).

^{13}C{^{1}H} NMR (126 MHz, $CDCl_3$): δ = 157.3 (C-5a), 147.0 (C-8b), 140.7 (C-10), 139.1 (C-12), 138.4 (C-2), 133.5 (br.; C-9), 132.1 (br.; C-3a), 131.9 (C-7), 127.6 (C-11), 123.0 (C-1), 121.6 (C-15), 121.1 (C-8a), 119.4 (C-8), 22.8 (C-13), 21.49 (C-14).

cis-15

^{1}H NMR (500 MHz, $CDCl_3$): δ = 7.97 (d, ^3J(H,H) = 4.8 Hz, 2H; H-2), 7.59 (d, 2H; partially overlapped with ***trans*-15**-H-1; H-1), 7.46 (s, 2H; H-8), 6.89 (s, 4H; H-11), 6.67 (s, 2H; H-15), 2.33 (s, 6H: H-14), 2.23 (s, 12H; H-13).

^{13}C{^{1}H} NMR (126 MHz, $CDCl_3$): δ = 158.9 (C-5a), 140.6 (C-10), 138.9 (C-12), 138.3 (C-2), 133.5* (br. C-9, overlapped with ***trans*-15**-C-9), 132.1* (br.; C-3a, overlapped with ***trans*-15**-C-3a), 128.2 (C-7), 127.6 (C-11), 123.5 (C-15), 123.0 (C-1, overlapped with ***trans*-15**-C-1), 122.0 (C-8), 120.2 (C-8a), 22.8 (C-13, overlapped with ***trans*-15**-C-13), 21.47 (C-14, partially overlapped with ***trans*-15**-C-14), n.o. (C-8b).

*) unequivocally detected only in the ^{H,C}HMBC spectrum.

^{11}B NMR (96 MHz, $CDCl_3$): δ = 41.4 ($h_{1/2}$ ≈ 520 Hz).

3.6 Synthesis of 17

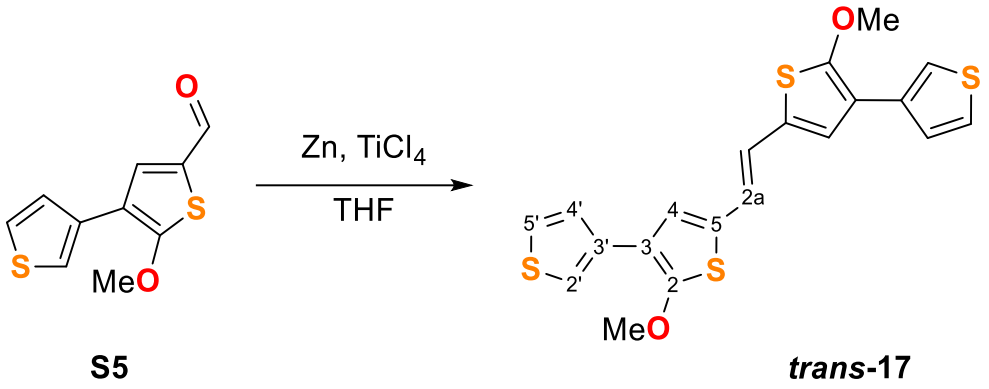

S5 ***trans*-17**

A flame-dried three-necked 100 mL flask (equipped with a thermometer and a reflux condenser) was charged with zinc powder (365 mg, 5.58 mmol, 2.5 eq.) and THF (17 mL). The mixture was cooled to –20 °C, and $TiCl_4$ (294 µL, 2.68 mmol, 1.2 eq.) was added. **S5** (500 mg, 2.23 mmol) was added dropwise as a THF solution (8 mL). After warming to room temperature, the reaction mixture was stirred for 1 h at 40 °C (the reaction progress was monitored by TLC). After cooling to room temperature, the reaction mixture was quenched by addition of ice-cold water (10 mL) and HCl (1.0 M; 15 mL). THF was removed using a rotary evaporator and CH_2Cl_2 (20 mL) was added. The (biphasic) mixture was thereafter filtered on a Celite® bed (washing with CH_2Cl_2). Water (20 mL) was added to the filtrate, and the two layers were separated. The aqueous phase was extracted with CH_2Cl_2 (4 × 15 mL). The combined organic phases were dried over Na_2SO_4, filtered, and the solvent was removed from the filtrate under reduced pressure. The dark brown crude product was purified by column chromatography (25 cm silica gel, d = 4.0 cm, *n*-hexane/CH_2Cl_2 (1:1), R_f = 0.48). The fractions containing *trans*-**17** (with only traces of *cis*-**17**) were combined and evaporated to dryness. The dark yellow residue was treated with *n*-pentane and the resulting suspension was filtered. *trans*-**17** was thereby isolated as a yellow solid (359 mg, 0.86 mmol, 77%). Single crystals suitable for X-ray crystallography were grown by slow evaporation of a solution of *trans*-**17** in *n*-pentane/CH_2Cl_2 (2:1).

^{1}H NMR (500 MHz, $CDCl_3$): δ = 7.51* (dd, ^4J(H,H) = 3.0 Hz, ^4J(H,H) = 1.3 Hz, 2H; H-2'), 7.41 (dd, ^3J(H,H) = 5.0 Hz, ^4J(H,H) = 1.3 Hz, 2H; H-4'), 7.33* (dd, ^3J(H,H) = 5.0 Hz, ^4J(H,H) = 3.0 Hz, 2H; H-5'), 6.96 (s, 2H; H-4), 6.72 (s, 2H; H-2a), 4.02 (s, 6H; CH_3). *) Proton shifts and J(H,H) coupling constants were assigned according to a related compound from the literature.[S12]

^{13}C{^{1}H} NMR (126 MHz, $CDCl_3$): δ = 158.9 (C-2), 134.7 (C-3'), 128.4 (C-5), 126.9 (C-4'), 125.2 (C-5'), 124.5 (C-4), 120.4 (C-2'), 119.6 (C-2a), 117.2 (C-3), 61.8 (CH_3).

HRMS (MALDI): Calculated *m/z* for $[C_{20}H_{16}O_2S_4]^+$: 416.0028; found: 416.0026.

Mp: 182.5-185.0 °C.

3.7 Synthesis of 15 (*via* late stage borylation)

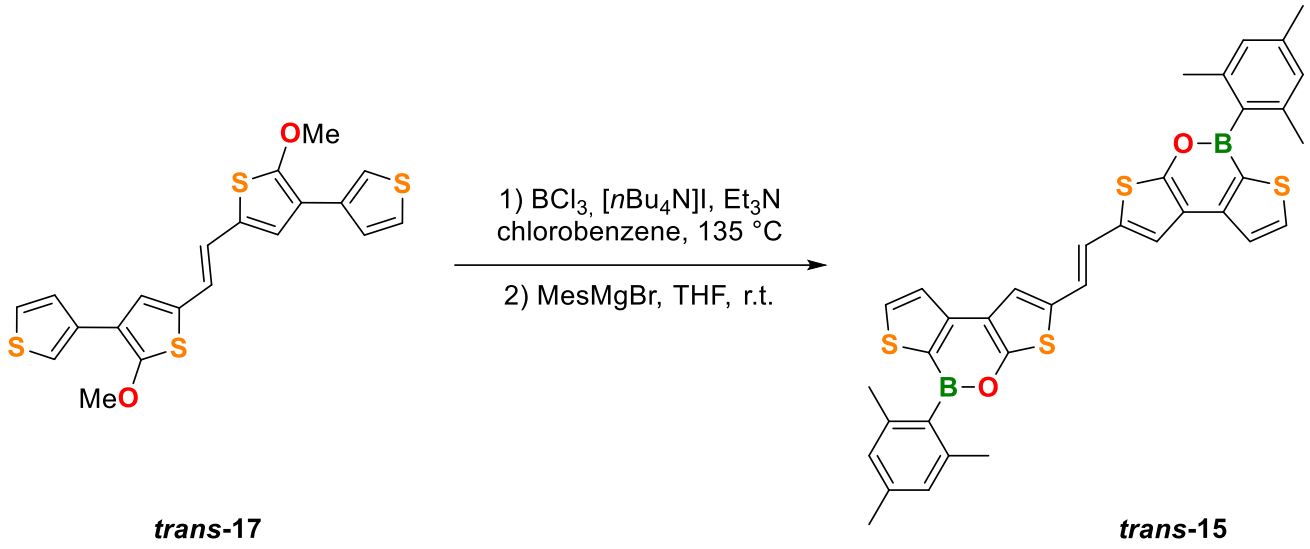

***trans*-17** ***trans*-15**

A flame-dried 100 mL J-Young flask was charged with *trans*-**17** (200 mg, 0.48 mmol) and [nBu$_4$N]I (426 mg, 1.15 mmol, 2.40 eq.) and then evacuated for 30 min. Chlorobenzene (3.5 mL) was added and the mixture was cooled to –10 °C. BCl_3 (1.0 M in hexanes; 1.06 mL, 1.06 mmol, 2.20 eq.) and Et_3N (134 µL, 0.96 mmol, 2.00 eq.) were added, the Young-tap was closed, and the reaction mixture was allowed to warm to room temperature. The red mixture thus obtained was stirred for 24 h at 135 °C. After cooling to room temperature, the mixture was evaporated to dryness and THF (3.5 mL) was added. MesMgBr (1.0 M in THF; 2.88 mL, 2.88 mmol, 6.00 eq.) was added dropwise at room temperature to give a clear, orange-colored solution, which was stirred for 1 h. The solvent was removed under reduced pressure and the residue was purified by column chromatography (17 cm silica gel, d = 2.0 cm, c-hexane/CH_2Cl_2 (5:1), R_f = 0.28). The fractions containing *trans*-**15** (with only traces of *cis*-**15**) were combined and evaporated to dryness. The residue was treated with n-hexane (to remove soluble *cis*-**15** and an unknown minor impurity), and the resulting suspension was filtered. *trans*-**15** was thereby obtained as a yellow solid (121 mg, 0.19 mmol, 39%).

3.8 Isomerization tests of trans-15: An NMR tube was charged with *trans*-**15** (7 mg, 0.01 mmol) and C_6D_6 (1 mL) and placed close (approx. 5 cm) to the irradiation source (Hg lamp or LED lamps). The isomerization progress was monitored by ^{1}H NMR spectroscopy after 30 min of irradiation, taking the decrease of the proton signal of *trans*-**15** (6.73 ppm) and the increase of the corresponding peak of the *cis*-isomer (6.38 ppm) as diagnostic tools.

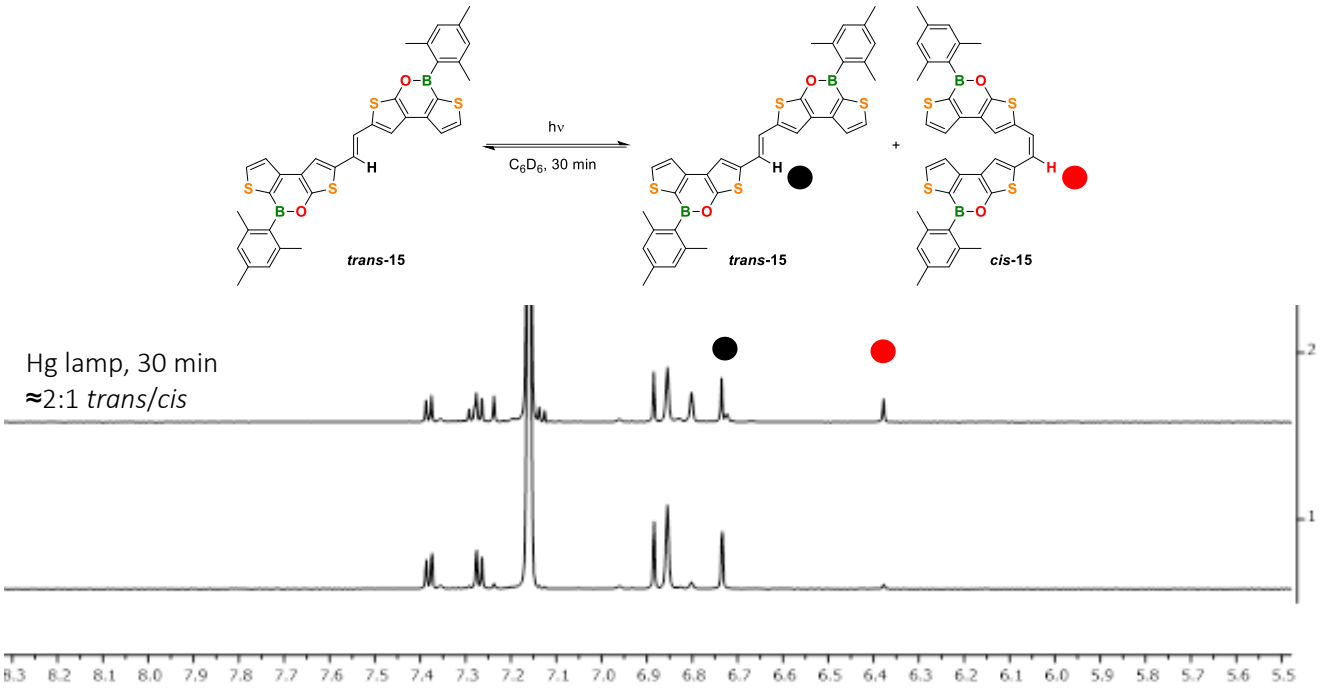

Figure S1: Irradiation of *trans*-**15** using a medium-pressure Hg lamp - ^{1}H NMR (400 MHz, C_6D_6) starting spectrum (bottom) and spectrum after 30 min of irradiation (top).

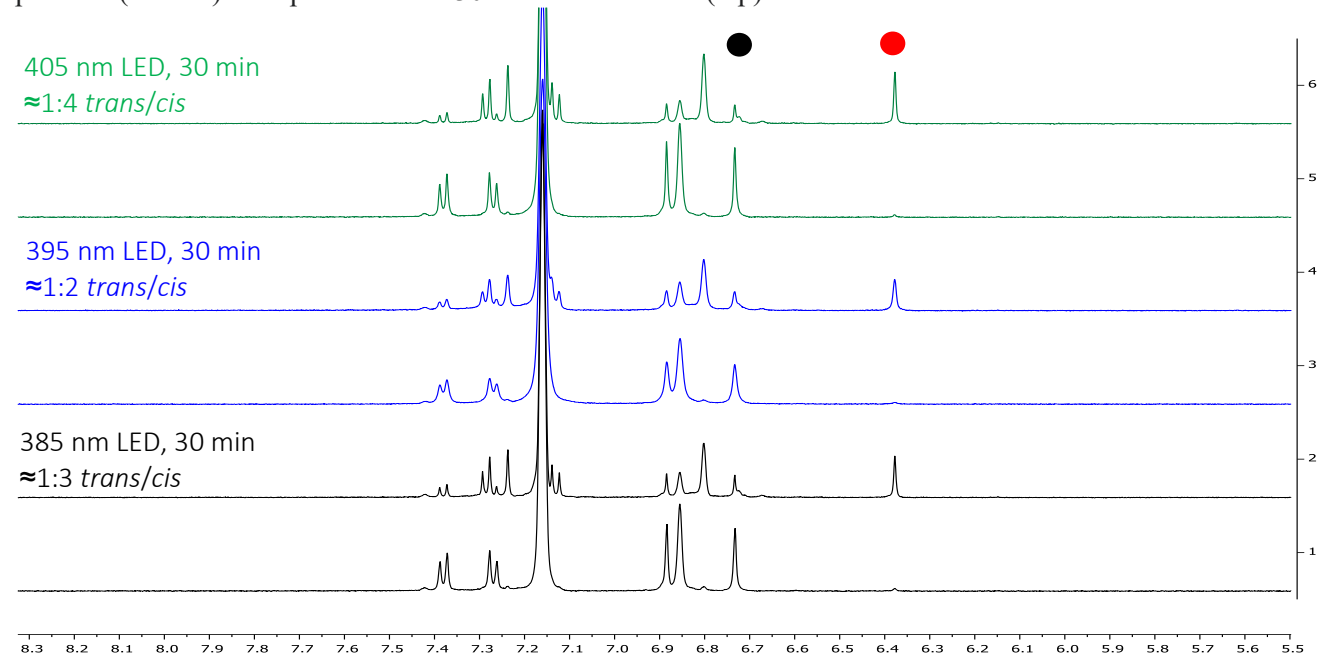

Figure S2: Irradiation of *trans*-**15** using a 385 (black spectra), 395 (blue spectra) and 405 nm (green spectra) LED - The ^{1}H NMR (300 MHz, C_6D_6) starting spectrum (bottom) and the spectrum after 30 min (top) is reported for each experiment. The outcome of the screening test of the three different LED lamps led us to use the 405-nm LED for subsequent photocyclization experiments that require *cis*-**15** as the immediate precursor.

3.9 Synthesis of 1 via photocyclization without HI scavenger

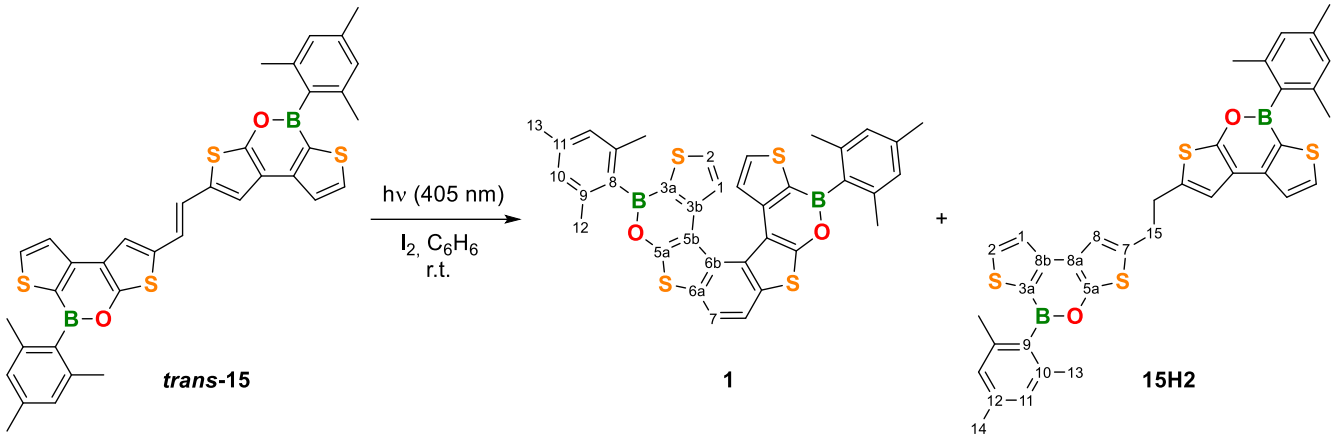

A flame-dried 250 mL J-Young tube was charged with *trans*-**15** (70 mg, 0.11 mmol) and evacuated for 30 min. C_6H_6 (150 mL) was added and the resulting yellow solution was treated with I_2 (28 mg, 0.11 mmol, 1 eq.). The red solution thus obtained was irradiated for 1.5 h with an LED lamp (405 nm - placed close to the reaction vessel, approx. 5 cm, Figure **S3**; the Duran® glass used is transparent to 405 nm light).[S13] The reaction progress was monitored by TLC. The solvent was evaporated, and the residue was purified by column chromatography (13 cm silica gel, d = 2.0 cm, *c*-hexane/CH_2Cl_2 (3:1)) to furnish **1** as a white solid (24 mg, 0.037 mmol, 34%, R_f = 0.50) and **15H2** as a yellowish solid (24 mg, 0.037 mmol, 34%, R_f = 0.25).

Single crystals of **1** suitable for X-ray crystallography were grown by slow evaporation of a solution of **1** in *n*-hexane/CH_2Cl_2 (2:1) in a glovebox.

Single crystals of **15H2** suitable for X-ray crystallography were grown by slow evaporation of a solution of **15H2** in *n*-hexane/CH_2Cl_2 (3:1).

Note: H_2 transfer during photocyclization reactions using I_2, but no HI scavenger (such as propylene oxide), has been reported for stilbene derivatives.[S14]

*Characterization data of **1***:

^{1}H NMR (500 MHz, $CDCl_3$): δ = 7.81 (s, 2H; H-7), 7.37 (d, ^3J(H,H) = 4.9 Hz, 2H; H-2), 7.19 (d, ^3J(H,H) = 4.9 Hz, 2H; H-1), 6.97 (s, 4H; H-10), 2.38 (s, 6H; H-13), 2.35 (s, 12H; H-12).

^{13}C{^{1}H} NMR (126 MHz, $CDCl_3$): δ = 159.8 (C-5a), 148.3 (C-3b), 140.8 (C-9), 139.3 (C-11), 135.6 (C-2), 133.2 (br.; C-8), 131.3 (br.; C-3a), 130.9 (C-5b), 128.2 (C-6a), 127.8 (C-10), 126.5 (C-1), 119.0 (C-7), 117.3 (C-6b), 22.9 (C-12), 21.5 (C-13).

^{11}B NMR (96 MHz, $CDCl_3$): δ = 41.9 ($h_{1/2}$ = 600 Hz).

HRMS (MALDI): Calculated *m/z* for $[C_{36}H_{28}B_2O_2S_4]^+$: 642.1153; found: 642.1171.

UV/Vis (*c*-hexane): λ_{max} (ε / $mol^{-1}dm^3cm^{-1}$) = 269 (32400), 330 (29100), 341 (28600), 359 (25300), 374 (sh).

Fluorescence (*c*-hexane, λ_{ex} = 330 nm): λ_{max} = 392, 411 nm (resolved vibrational fine structure); Φ_{PL} = 6%.

Cyclic voltammetry (THF, [*n*Bu$_4$N][PF$_6$] 0.1 M, 200 mV s^{-1}, vs. FcH/FcH$^+$): Cathodic scan: E^{I}_{pc} = − 2.83 V, E^{II}_{pc} = − 3.01; anodic scan: E_{pa} = − 0.09 V.

Mp: 260 °C (decomposition).

*Characterization data of **15H2***:

^{1}H NMR (500 MHz, $CDCl_3$): δ = 7.95 (d, ^{3}J(H,H) = 4.8 Hz, 2H; H-2), 7.56 (d, ^{3}J(H,H) = 4.8 Hz, 2H; H-1), 7.12 (s, 2H; H-8), 6.91 (s, 4H; H-11), 3.29 (s, 4H; H-15), 2.34 (s, 6H; H-14), 2.24 (s, 12H; H-13).

^{13}C{^{1}H} NMR (126 MHz, $CDCl_3$): δ = 156.7 (C-5a), 147.4 (C-8b), 140.6 (C-10), 138.9 (C-12), 138.1 (C-2), 133.6* (C-9), 132.7 (C-7), 131.7* (C-3a), 127.6 (C-11), 123.0 (C-1), 120.0 (C-8a), 117.8 (C-8), 32.9 (C-15), 22.8 (C-13), 21.5 (C-14). *) unequivocally detected only in the ^{H,C}HMBC spectrum.

^{11}B NMR (96 MHz, $CDCl_3$): δ = 41.1 ($h_{1/2} \approx$ 450 Hz).

HRMS (MALDI): Calculated *m/z* for $[C_{36}H_{32}B_2O_2S_4]^+$: 646.1466; found: 646.1417.

UV/Vis (*c*-hexane): λ_{max} (ε / $mol^{-1}dm^3cm^{-1}$) = 318 (sh), 326 (21900), 342 (sh).

Fluorescence (*c*-hexane, λ_{ex} = 326 nm): λ_{max} = 374, 388 nm (resolved vibrational fine structure); Φ_{PL} = 7%.

Cyclic voltammetry (THF, [*n*Bu$_4$N][PF$_6$] 0.1 M, 200 mV s^{-1}, vs. FcH/FcH$^+$): Cathodic scan: E_{pc} = − 2.90 V, E_{pa} = −2.79 V.

Mp: 258-260 °C (decomposition).

3.9.1 Synthesis of 1 *via* photocyclization using propylene oxide as HI scavenger

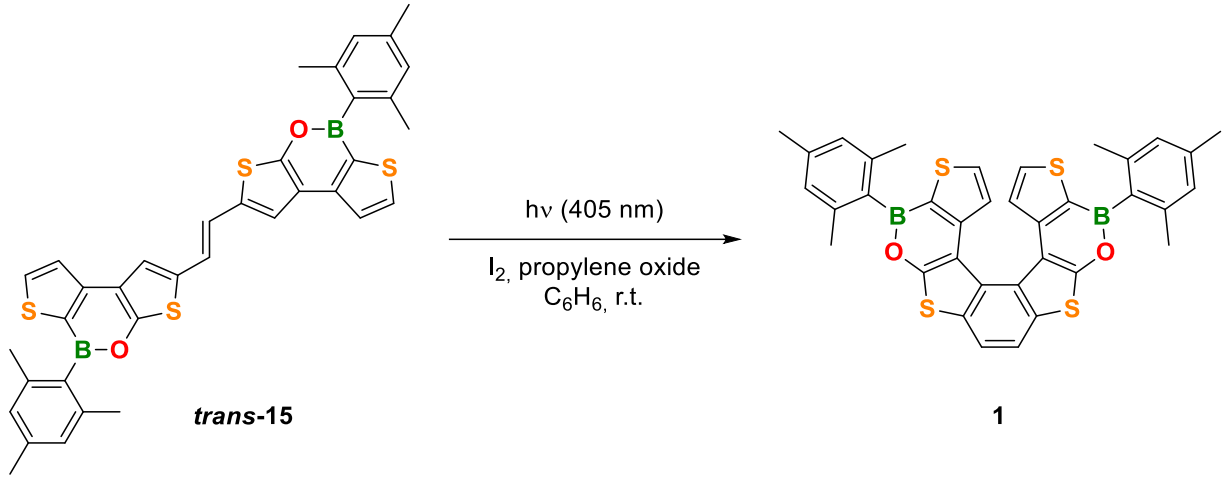

***trans*-15** **1**

A flame-dried 250 mL J-Young tube was charged with *trans*-**15** (70 mg, 0.11 mmol) and evacuated for 30 min. C_6H_6 (150 mL) was added and the resulting yellow solution was treated with I_2 (28 mg, 0.11 mmol, 1 eq.) and propylene oxide (760 µL, 10.86 mmol, 100 eq.). The red solution thus obtained was irradiated for 2.5 h with an LED lamp (405 nm - placed close to the reaction vessel, approx. 5 cm, Figure **S3**; the Duran® glass used is transparent to 405 nm light).[S13] The reaction progress was monitored by TLC and **1** was detected as sole product. The solvent was evaporated to dryness and the solid residue was purified by column chromatography (13 cm silica gel, d = 2.0 cm, *c*-hexane/CH_2Cl_2 (3:1), R_f = 0.50) to give **1** (30 mg, 0.047 mmol, 43%).

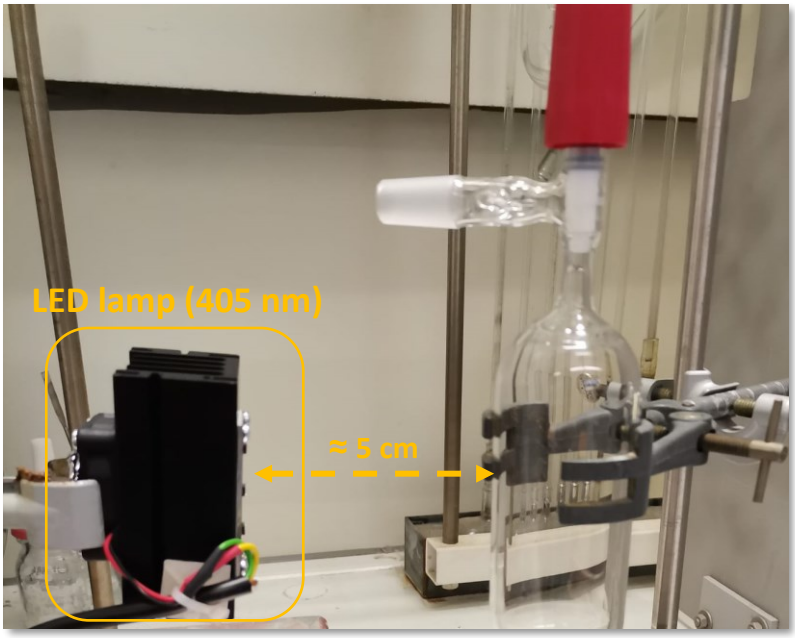

Figure S3: 1 photochemical experiments set-up.

4. Synthesis of tetrathia[7]helicene 2

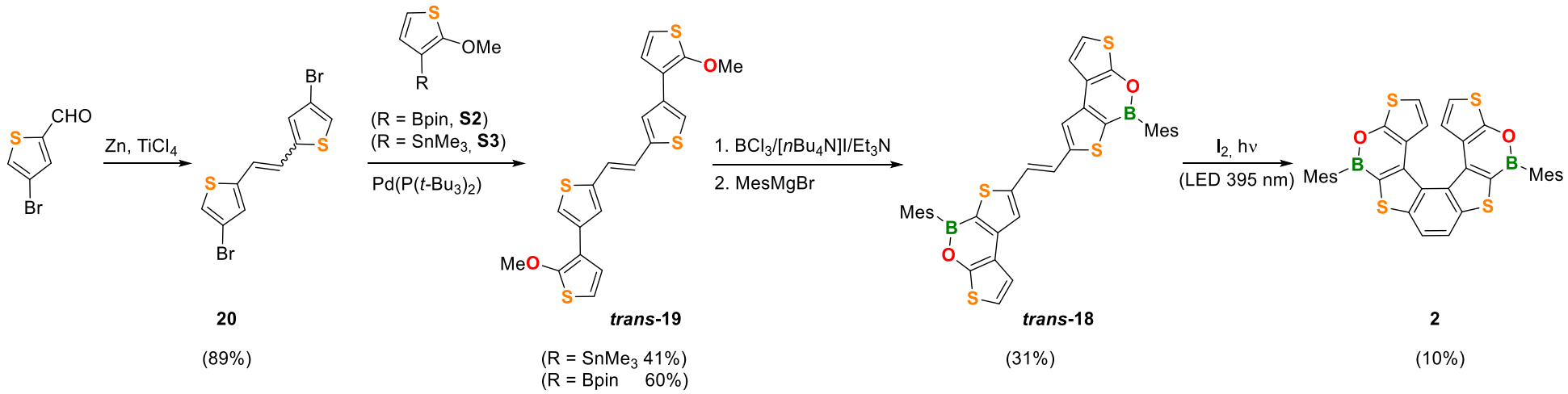

Scheme S2: Synthetic route to tetrathia[7]helicene **2**.

Synthesis of S3[S7] and S2[S8] starting materials

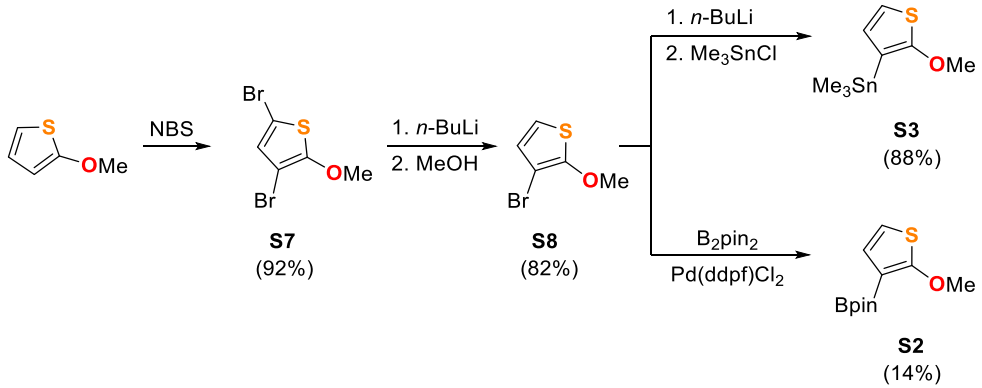

Scheme S3: Preparation of tetrathia[7]helicene **2** intermediates. Full details about the synthesis of **S7**, **S8**, **S2** and **S3** are provided in section *2.1 Thiophene starting materials*.

4.1 Synthesis of 20

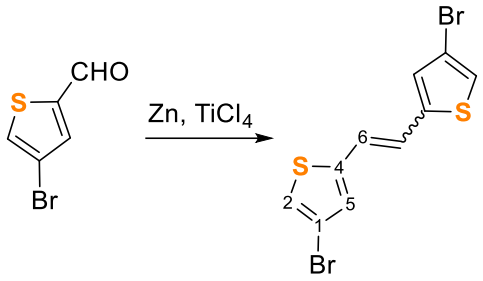

20
(89%)

A three-necked flame-dried 250 mL flask equipped with a thermometer and a reflux condenser was charged with THF (50 mL) and zinc powder (3.45 g, 52.67 mmol, 2.57 eq.). The resulting suspension was cooled to 0 °C and $TiCl_4$ (2.70 mL, 25.13 mmol, 1.2 eq.) was added dropwise during 10 min.

Note: the temperature increased due to the progressive addition of $TiCl_4$ (to ≈10-15 °C). The dark-green mixture thus obtained was heated to reflux for 1 h. In the meantime, a dropping funnel (equipped with a stirring bar) was flame-dried under vacuum and then charged with 4-bromo-2-thiophencarbaldehyde (3.91 g, 20.49 mmol) and THF (20 mL). The aldehyde solution was added dropwise during 10 min and the reaction mixture thus obtained was refluxed for 2 h. The reaction progress was checked by TLC.

After cooling to room temperature the THF was removed under reduced pressure, the residue was taken up with CH_2Cl_2 and filtered over a celite plug (washing with CH_2Cl_2). The CH_2Cl_2 black solution was treated with water (200 mL) and after separation of the two layers, the aqueous phase was extracted with CH_2Cl_2.

Note: for each extraction step, after separation of the two phases, the organic layer was filtered over a celite plug prior to combine with the collected organic phases.

The collected organic phases were dried over Na_2SO_4, filtered and the solvent was removed under reduced pressure. The crude product was washed with Et_2O yielding 2.93 g (8.37 mmol, 82%) of an orange solid which was proved to be *trans*-**20** *via* ^{1}H NMR analysis.

Et_2O mother liquors were evaporated to dryness yielding a dark brown wet solid which was purified *via* column chromatography (*n*-hexane/CH_2Cl_2 (2:1)) yielding 263 mg (0.75 mmol, 7%) of a yellow solid which was proved to be a *cis/trans* mixture (3:1) of **20** as inferred from ^{1}H NMR analysis. Total yield = 89%.

Trans-**20** single crystals suitable for X-ray crystallography were obtained by slow evaporation of a *trans*-**20** CH_2Cl_2 saturated hot solution.

Characterization data of *trans*-**20**:

^{1}H NMR (300 MHz, $CDCl_3$): δ = 7.10 (d, ^4J(H,H) = 1.3 Hz, 2H; H-2), 6.97 (d, ^4J(H,H) = 1.3 Hz, 2H; H-5), 6.94 (s, 2H; H-6).

^{13}C{^{1}H} NMR (75 MHz, $CDCl_3$): δ = 142.6 (C-4), 128.6 (C-5), 122.0 (C-2), 121.4 (C-6), 110.6 (C-1).

HRMS (EI+): Calculated *m/z* for $[C_{10}H_6Br_2S_2]^+$: 347.8278; found: 347.8288.

Characterization data of a **20** cis/trans (3:1) mixture:

^{1}H NMR (300 MHz, $CDCl_3$): δ = 7.17 (d, ^{3}J(H,H) = 1.4 Hz, 2H), 7.10 (d, ^{3}J(H,H) = 1.3 Hz; *trans*-**20-**H-2), 7.00 (d, ^{3}J(H,H) = 1.3 Hz, 2H), 6.97 (d, ^{3}J(H,H) = 1.3 Hz; *trans*-**20-**H-5), 6.94 (s; *trans*-**20-**H-6), 6.55 (s, 2H).

^{13}C{^{1}H} NMR (75 MHz, $CDCl_3$): δ = 142.6 (*trans*-**20-**C-4), 139.7 (C-4), 130.9 (C-5), 128.6 (*trans*-**20-**C-5), 124.0 (C-2), 123.2 (C-6), 122.0 (*trans*-**20-**C-2), 121.4 (*trans*-**20-**C-6), 110.6 (*trans*-**20-**C-1), 109.9 (C-1).

4.2 Synthesis of 19 *via* Suzuki coupling

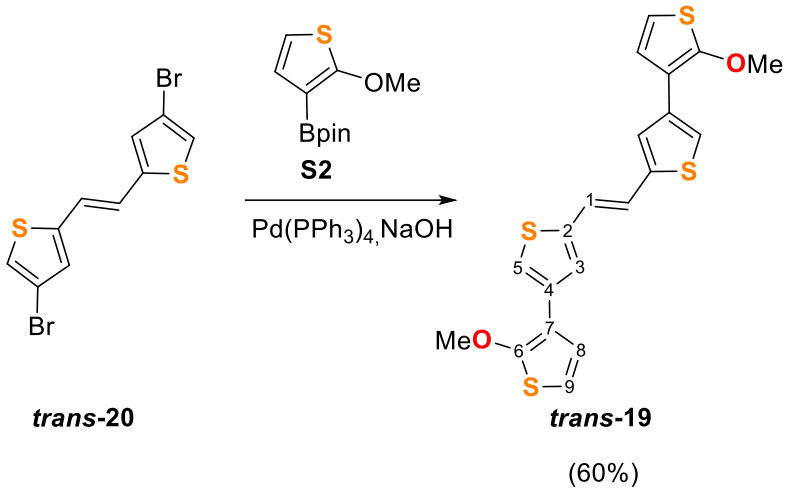

***trans*-20** ***trans*-19**

(60%)

A flame-dried J-young flask was charged with *trans*-**20** (153 mg, 0.44 mmol) and **S2** (252 mg, 1.05 mmol, 2.40 eq.) and then evacuated for 30 min. THF (9 mL), $NaOH_{(aq)}$ (3M; 0.58 mL, 1.75 mmol, 4.0 eq.) and $Pd(PPh_3)_4$ (51 mg, 0.044 mmol, 0.10 eq.) were added. The dark brown mixture thus obtained was heated to 80 °C for 15 h. After cooling to room temperature, the solvent was removed under reduced pressure and the crude product was purified *via* column chromatography (*n*-hexane/CH_2Cl_2 (1:1), R_f = 0.60). The fraction containing *trans*-**19** were evaporated to dryness and the yellow residue thus obtained was washed with *n*-pentane (to remove unknown minor impurities). *Trans*-**19** was obtained as a pale-yellow solid (110 mg, 0.26 mmol, 60%). Single crystals of *trans*-**19** were obtained by slow evaporation of a saturated solution of *trans*-**19** in CH_2Cl_2/*n*-hexane (2:1).

^{1}H NMR (500 MHz, $CDCl_3$): δ = 7.39 (d, ^4J(H, H) = 1.4 Hz, 2H, H-3), 7.36 (d, ^4J(H, H) = 1.4 Hz, 2H, H-5), 7.08 (s, 2H, H-1), 7.04 (d, ^3J(H, H) = 5.9 Hz, 2H, H-9), 6.62 (d, ^3J(H, H) = 5.9 Hz, 2H, H-8), 4.01 (s, 6H, OMe).

^{13}C{^{1}H} NMR (126 MHz, $CDCl_3$): δ = 160.7 (C-6), 141.9 (C-2), 135.6 (C-4), 125.8 (C-3), 125.7 (C-9), 121.7 (C-1), 119.2 (C-5), 116.3 (C-7), 111.1 (C-8), 61.9 (OMe).

HRMS (MALDI): *Calc*. *m/z* for $[C_{20}H_{16}O_2S_4]^+$: 416.0028, found 416.0026.

4.3 Synthesis of 19 *via* Stille coupling

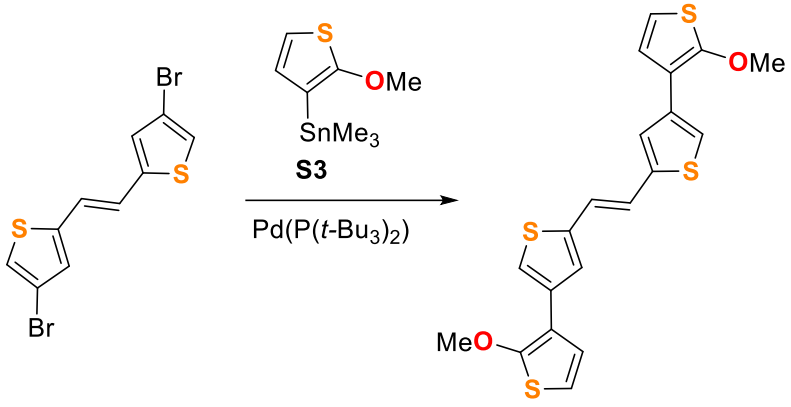

***trans*-20** ***trans*-19**

(42%)

A flame-dried 250 mL J-Young tube was charged with *trans*-**20** (430 mg, 1.23 mmol) and evacuated for 30 min. Toluene (60 mL) was added and the orange solution thus obtained was treated with **S3** (714 mg, 2.58 mmol, 2.10 eq.) and Pd(P(*t*-Bu_3)$_2$) (61 mg, 0.12 mmol, 0.10 eq.) and the resulting deep orange solution was heated to 80 °C and stirred for 17 h.

Note: after roughly 10 min heating the reaction mixture turns to dark brown.

After cooling to room temperature, toluene was removed under reduced pressure and the grey residue thus obtained was purified *via* column chromatography (*n*-hexane/CH_2Cl_2 (2:1)). The fractions containing *trans*-**19** were combined and evaporated to dryness. The yellow residue thus obtained was washed with *n*-pentane (to remove the stannane homocoupling byproduct and unknown minor impurities). *Trans*-**19** was thereby obtained as a pale-yellow solid (215 mg, 0.52 mmol, 42%).

4.4 Synthesis of 18

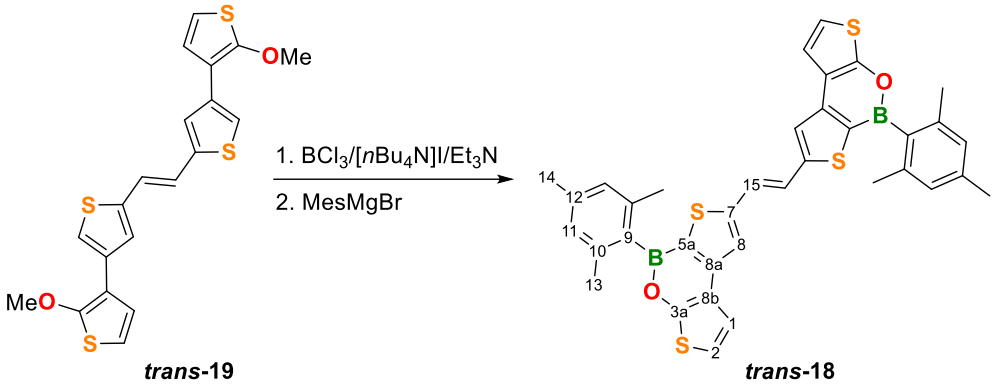

A flame-dried 100 mL J-Young tube was charged with *trans*-**19** (150 mg, 0.36 mmol), [nBu$_4$N]I (319 mg, 0.86 mmol, 2.40 eq.) and then evacuated for 30 min. Chlorobenzene (15 mL) was added and the mixture was cooled to –10 °C. BCl_3 (1.0 M in hexanes; 0.79 mL, 0.79 mmol, 2.20 eq.) and Et_3N (1.0 M in chlorobenzene; 0.72 mL, 0.72 mmol, 2.00 eq.) were added, the Young-tap was closed, and the reaction mixture was allowed to warm to room temperature. The mixture thus obtained was stirred for 24 h at 135 °C. After cooling to room temperature, the yellow-brown mixture was evaporated to dryness and THF (15 mL) was added. MesMgBr (0.95 M in THF; 2.27 mL, 2.16 mmol, 6.00 eq.) was added dropwise at room temperature to give a red mixture, which was stirred for 1 h. The solvent was removed under reduced pressure and the residue was purified by column chromatography (d = 2.0 cm, n-hexane/CH_2Cl_2 (2:1)). The fractions containing *trans*-**18** were combined and evaporated to dryness. The yellow residue thus obtained was treated with n-pentane (to remove unknown minor impurities). *Trans*-**18** was thereby obtained as a yellow solid (72 mg, 0.11 mmol, 31%).
Single crystals of *trans*-**18** suitable for X-ray analysis were obtained by slow evaporation of a saturated solution of *trans*-**18** in n-hexane/CH_2Cl_2 (2:1).

^{1}H NMR (400 MHz, $CDCl_3$): δ = 7.56 (s, 2H; H-8), 7.37 (s, 2H; H-15), 7.32 (d, ^3J(H,H) = 6.0 Hz, 2H; H-2), 6.96 (d, ^3J(H,H) = 6.0 Hz, 2H; H-1), 6.93 (s, 4H; H-11), 2.36 (s, 6H; H-14), 2.27 (s, 12H; H-13).
^{13}C{^{1}H} NMR (101 MHz, $CDCl_3$): δ = 158.9 (C-3a), 153.2 (C-8a), 147.9 (C-7), 140.6 (C-10), 139.0 (C-12), 133.6 (C-9), 131.6 (C-5a), 127.6 (C-5a), 124.8 (C-11), 122.5 (C-15), 120.3 (C-8), 120.3 (C-2), 120.0 (C-8b), 114.9 (C-1), 22.8 (C-13), 21.5 (C-14).
^{11}B NMR (128 MHz, $CDCl_3$): not detected.
Note: the presence of boron is evidenced by the typical broadened resonances of B(sp^2)-bound quaternary carbons (C-9, C-5a) and by the ^3J(C,H) coupling between C-9 (133.6 ppm) and H-11 (6.93 ppm) observed in the ^{H,C}HMBC spectrum.
HRMS (MALDI): Calculated m/z for $[C_{36}H_{30}B_2O_2S_4]^+$: 644.1315; found: 644.1326.
UV/Vis (*c*-hexane): λ_{max} (ε / mol^{-1}dm^{3}cm^{-1}) = 270 (26500), 355 (30700), 370 (30000), 393 (21500), 414 (sh).
Fluorescence (*c*-hexane, λ_{ex} = 375 nm): λ_{max} = 429, 452 nm (resolved vibrational fine structure), 489 nm (sh); Φ_{PL} = 6%.

Cyclic voltammetry (THF, 0.1 M [*n*Bu$_4$N][PF$_6$], 200 mV s^{-1}, vs. FcH/FcH$^+$): Cathodic scan: $E^{I}_{1/2}$ = −1.97 V, E^{II}_{pc} = −2.26 V, E^{II}_{pa} = −2.14 V.

4.5 Synthesis of 2

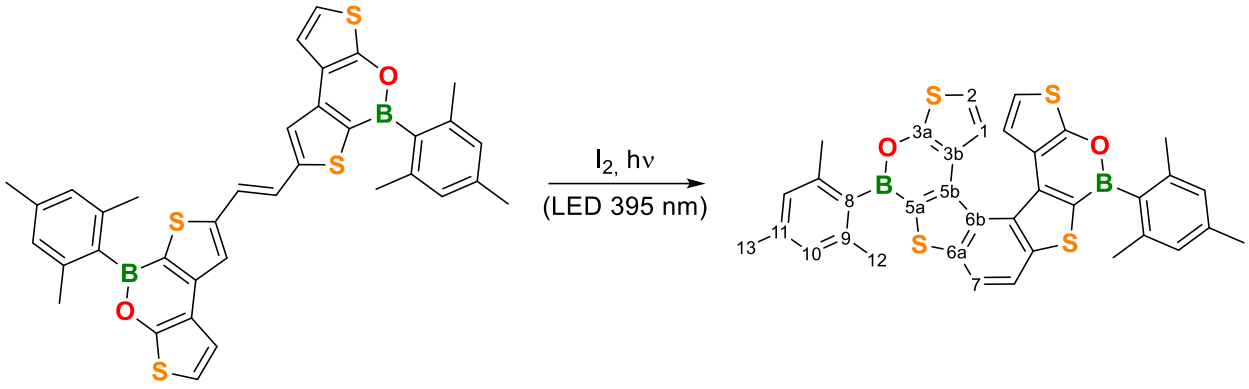

trans-**18** **2** (10%)

Seven different glass tester tubes were charged with *trans*-**18** (10 mg, 0.015mmol) and C_6H_6 (23 mL) and the resulting yellow solution was treated with I_2 (0.023 M in C_6H_6; 200 µL, 0.0045 mmol, 0.30 eq.). The orange-red solutions thus obtained were irradiated for 1.5 h with an LED lamp equipped with a glass water cooling jacket (395 nm; approx 1 cm; Figure S4; both cooling jacket glass and tester tubes glass are transparent to 395 nm light[S13]). The reaction progress was monitored by TLC. Reaction mixture of the seven tester tubes were combined, the solvent was evaporated, and the brown crude product thus obtained was purified by preparative TLC (*n*-hexane/CH_2Cl_2 (3:1)). The yellow residue thus obtained was washed with CH_2Cl_2 giving **2** as an off-white solid (7 mg, 0.01 mmol, 10%).

^{1}H NMR (400 MHz, $CDCl_3$): δ = 8.03 (s, 2H; H-7), 6.99 (s, 4H; H-10), 6.93 (d, ^3J(H,H) = 6.0 Hz, 2H; H-2), 6.52 (d, ^3J(H,H) = 6.1 Hz, 2H; H-1), 2.39 (s, 3H; H-13), 2.36 (s, 6H; H-12).

^{13}C{^{1}H} NMR (100.6 MHz, $CDCl_3$): δ = 158.8* (C-3a), 145.5 (C-6a), 140.8 (C-11), 139.3 (C-9), 133.3* (C-8), 131.0 (C-6b), 127.8 (C-10), 123.0 (C-2), 122.6 (C-7) 121.3 (C-3b), 112.4 (C-1), 22.9 (C-12), 21.5 (C-13). *) unequivocally detected only in the ^{H,C}HMBC spectrum. C-5a, C-6a n.o.

^{11}B NMR (128.4 MHz, $CDCl_3$): not detected.

Note: the presence of boron is evidenced by the ^3J(C,H) coupling between C-8 (133.3 ppm) and H-10 (6.99 ppm) observed in the ^{H,C}HMBC spectrum.

HRMS (EI+): Calculated *m/z* for $[C_{36}H_{28}B_2O_2S_4]^+$: 642.1158; found: 642.1128.

UV/Vis (*c*-hexane): λ_{max} (ε / $mol^{-1}dm^3cm^{-1}$) = 258 (20800), 320 (sh), 322 (sh) 368 (9800), 385 (11600), 413 (4700).

Fluorescence (*c*-hexane, λ_{ex} = 385 nm): λ_{max} = 424, 446, 472 nm (resolved vibrational fine structure); 506 nm (sh); Φ_{PL} = 7%.

Cyclic voltammetry (THF, 0.1 M [*n*Bu$_4$N][PF$_6$], 200 mV s^{-1}, vs. FcH/FcH$^+$): Cathodic scan: E_{pc} = −2.68 V, E_{pa} = 0.82 V.

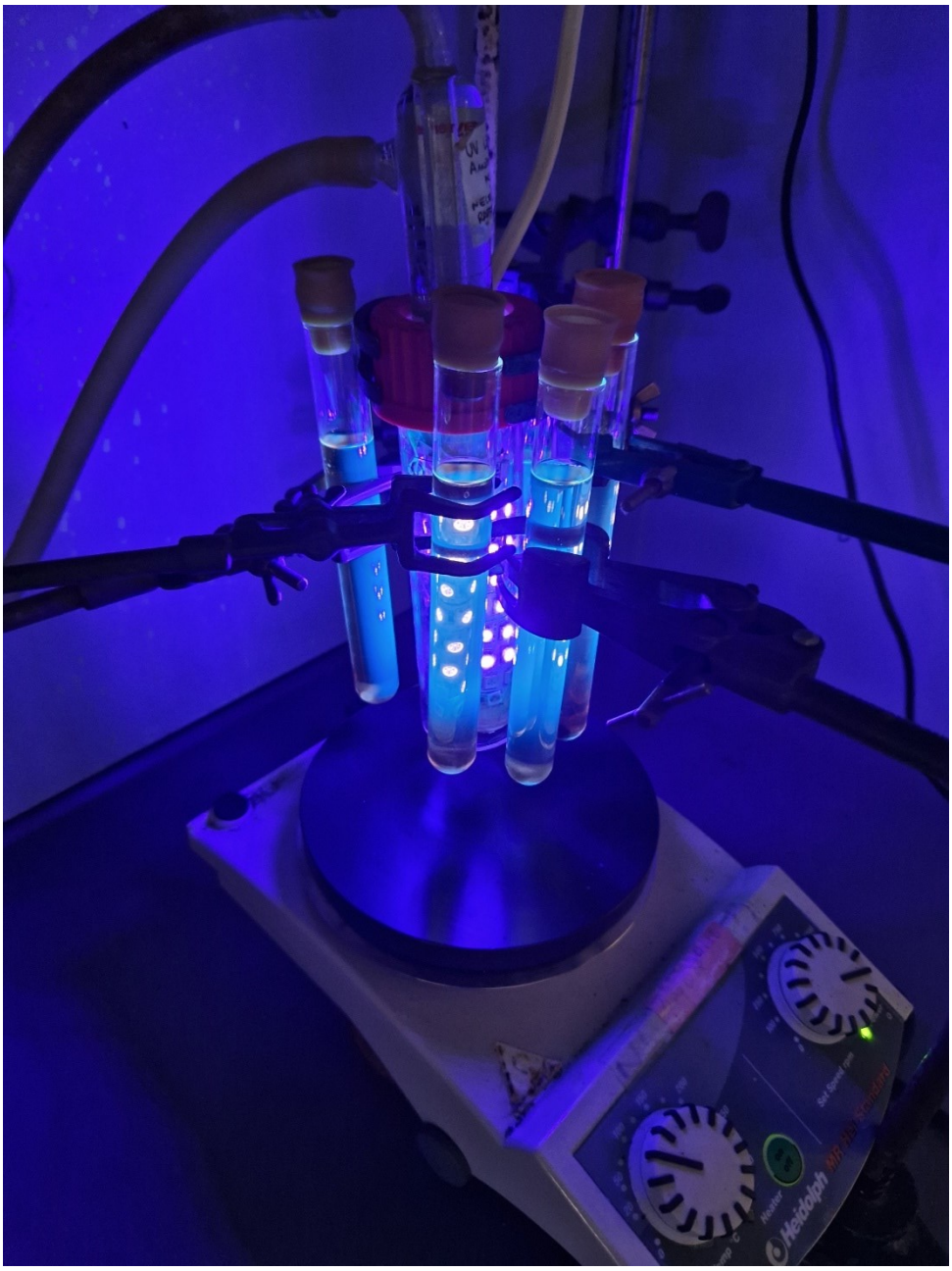

Figure S4: 2 photochemical experiments set-up.

5. Synthesis of tetrathia[7]helicene 3

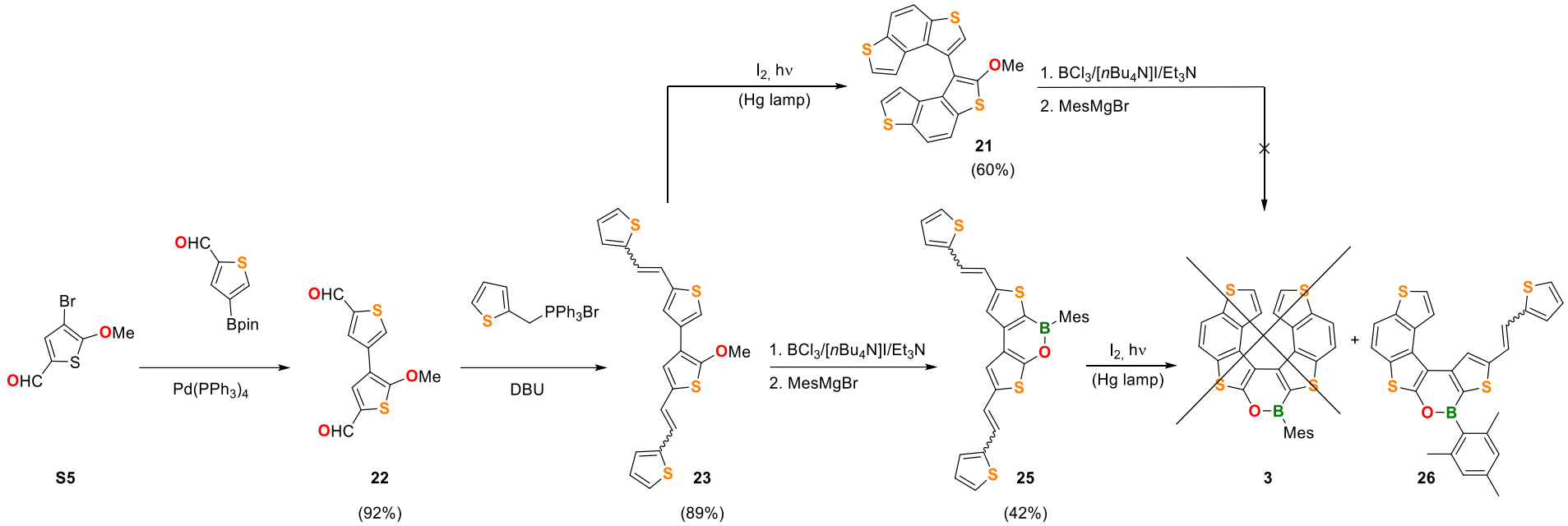

Scheme S4: Synthetic route to tetrathia[7]helicene **3**.

Synthesis of S5[S6]

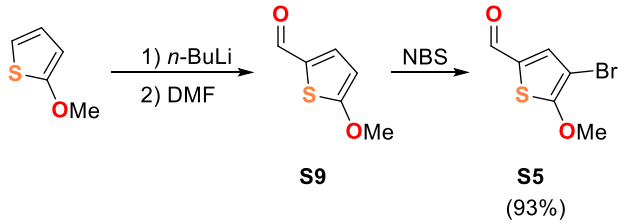

Scheme S5: Preparation of tetrathia[7]helicene **3** intermediates. Full details about the synthesis of **S9** and **S5** are provided in section *2.1 Thiophene starting materials*.

5.1 Synthesis of 22

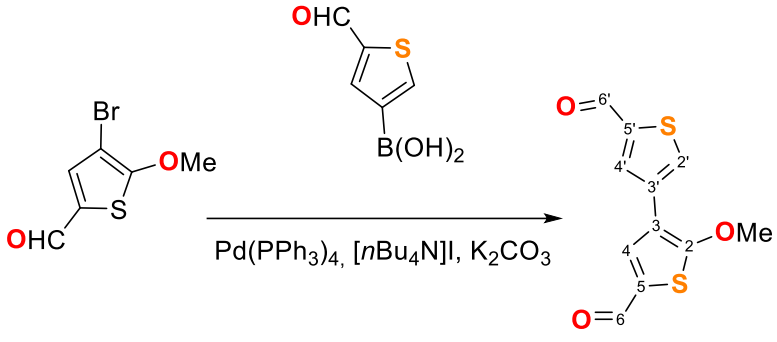

S4 **22**

(92%)

A flame-dried 100 mL J-Young tube was charged with 2-thiophenecarbaldehyde-3-boronic acid (332 mg, 1.50 mmol), **S4** (357 mg, 1.50 mmol, 1.0 eq.), [nBu$_4$N]I (48 mg, 0.15 mmol, 0.1 eq) and then evacuated for 20 min. THF/H_2O (5:1; 11 mL) was added and the resulting suspension was treated with $Pd(PPh_3)_4$ (87 mg, 0.075 mmol, 0.05 eq) and K_2CO_3 (415 mg, 3.0 mmol, 2 eq). The Young-tap was closed, and the black mixture thus obtained was heated with stirring to 80 °C for 14 h. After cooling to room temperature, the solvent was removed under reduced pressure, and the residue was purified by column chromatography (CH_2Cl_2, then CH_2Cl_2/AcOEt (20:1), R_f = 0.30). **22** was obrained as a yellow solid (350 mg, 1.39 mmol, 92%). Single crystals of **S4** suitable for X-ray crystallography were grown by slow evaporation of a saturated solution of **22** in n-pentane/CH_2Cl_2 (1:1).

^{1}H NMR (500 MHz, $CDCl_3$): δ = 9.97 (d, ^4J(H,H) = 1.3 Hz, 1H; H-6'), 9.74 (s, 1H; H-6), 8.07 (d, ^3J(H,H) = 1.3 Hz, 1H; H-2'), 7.97 (t, ^3J(H,H) = 1.3 Hz, 1H; H-4'), 7.83 (s, 1H; H-4), 4.18 (s, 3H; CH_3).
Note: H-4' couples with H-6' and H-2' (as evidenced by the ^{HH}COSY spectrum) with almost identical coupling constant (1.2, 1.4, 1.3 Hz respectively, which have been all rounded to 1.3 Hz) giving rise to a triplet (originated by a collapsed doublet of doublets).

^{13}C{^{1}H} NMR (126 MHz, $CDCl_3$): δ = 183.00 (C-6'), 182.11 (C-6), 170.62 (C-2), 143.90 (C-3'), 136.14 (C-4), 134.87 (C-2'), 130.44 (C-4'), 128.69 (C-5), 117.05 (C-3), 62.13 (CH_3), n.o. (C-5).
HRMS (MALDI): Calculated m/z for $[C_{11}H_9O_3S_2]^+$: 252.9988; found: 252.9988.

5.2 Synthesis of 23

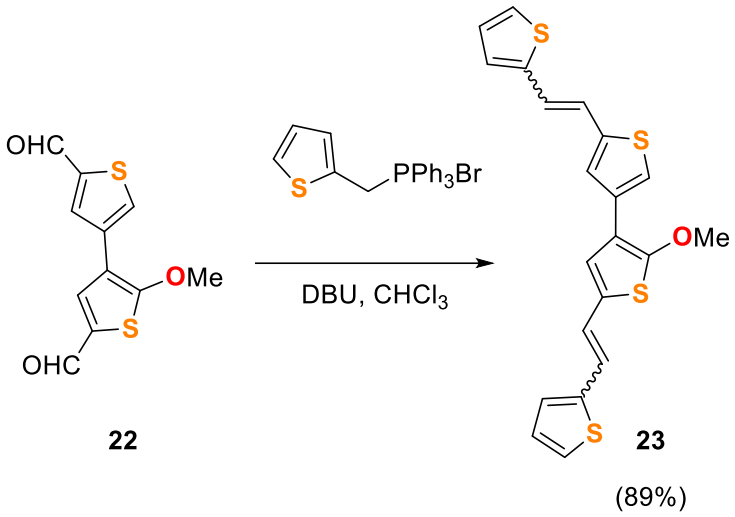

22 **23**

(89%)

A three-necked flask (equipped with a reflux condenser and a thermometer) was charged with triphenyl(2-thienylmethyl)phosphonium bromide (1.20 g, 2.73 mmol, 2.2 eq) and $CHCl_3$ (30 mL). DBU (416 mg, 2.73 mmol, 2.2 eq) was added and the rsulting orange solution was heated to 40 °C. **22** (313 mg, 1.24 mmol) was added in portions (during 5 min) as $CHCl_3$ suspension (12 mL). The reaction mixture was heated to 60 °C and stirred for 4 h. TLC after 4 h showed complete conversion of the starting aldehyde **22** and the presence of the desired compound **23** (R_f = 0.95) besides the mono-olefinated compound (R_f = 0.50). Additional 0.2 eq of DBU were added and the reaction mixture was stirred at 60 °C for additional 3 h. After cooling to room temperature the reaction mixture was poured into water (20 mL) and HCl 0.5 M (10 mL) was added. After separation of the two layers, the aqueous phase was extracted with CH_2Cl_2 (3 × 25 mL). The combined organic phases were dried over Na_2SO_4, filtered and the solvent removed. The brown residue thus obtained was purified by column chromatography (30 cm silica gel, d = 2.5 cm, CH_2Cl_2, R_f = 0.95). **22** was obtained as a yellow-brown solid (456 mg, 1.10 mmol, 89%). ^{1}H NMR (Figure S40) revealed the presence of the four isomers (*trans,trans; trans,cis; cis,trans; cis,cis*): those are easily detectable since the -OMe group shows four well-distinguished resonances in the ^{1}H NMR spectrum. Single crystals of *trans*,*trans*-**23** suitable for X-ray crystallography were grown by slow evaporation of a saturated solution of **22** in *n*-pentane/CH_2Cl_2 (1:1).

To reduce the complexity of the isomers mixture and facilitate NMR characterization, **22** was treated with Et_2O and *n*-pentane and decanted and the solid thus obtained was used for NMR characterization (^{1}H and ^{13}C spectra in Figure S40 and S41). Assignment of **22** proton and carbon resonances was attempted but, due to the high complexity of both 1D and 2D spectra, it was only possible to identify few resonances (aromatic CH, double bonds and OMe protons). For simplicity, ^{1}H NMR integrals have not been listed and are shown in Figure S40 and S41. Quaternary carbons (Cq), CH (CH) and CH_3 (OMe) resonances were identified *via* ^{13}C APT.

Note: following photocyclization and borylation experiments were carried out using **22** as obtained after column chromatography purification (mixture of the four isomers, ^{1}H in Figure S40).

^{1}H NMR (500 MHz, $CDCl_3$): δ 7.46 (s, 13H), 7.42 (d, J = 1.3 Hz, 11H), 7.35 (d, J = 1.3 Hz, 12H), 7.34 (s, 13H), 7.33 – 7.32 (m, 13H), 7.29 (dd, J = 5.1, 1.1 Hz, 5H), 7.27 (s, 3H), 7.19 (t, J = 4.4 Hz, 18H), 7.17 – 7.13 (m, 60H), 7.11 (s, 4H), 7.06 (s, 23H), 7.06 – 6.97 (m, 123H), 6.96 (s, 9H), 6.92 (dd, J = 15.8, 6.7 Hz, 23H), 6.84 (dd, J (H,H) = 15.8; two overlapped isomers double bond resonances), 6.64 (d, J(H,H) = 12.0 Hz; double bond), 6.60 (d, J(H,H) = 12.0 Hz; double bond), 6.49 (d, J(H,H) = 12.0 Hz; double bond), 6.48 (d; double bond), 4.01 (s; OMe), 3.96 (s; OMe), 3.93 (s; OMe).

^{13}C NMR (126 MHz, $CDCl_3$): δ = 160.93 (Cq), 159.33 (Cq), 159.21 (Cq), 142.62 (Cq), 142.61 (Cq), 142.40 (Cq), 141.83 (Cq), 141.76 (Cq), 139.09 (Cq), 138.64 (Cq), 135.06 (Cq), 134.99 (Cq), 134.27 (Cq), 128.45 (Cq), 128.16 (Cq), 127.94 (Cq), 127.92 (Cq), 127.83 (CH), 127.68 (CH), 127.65 (CH), 127.48 (CH), 126.97 (CH), 126.83 (CH), 126.26 (CH), 126.05 (CH), 125.66 (CH), 125.59 (CH), 125.35 (CH), 125.32 (CH), 125.01 (CH), 124.92 (CH), 124.34 (CH), 124.31 (CH), 123.83 (CH), 123.80 (CH), 123.03 (CH), 122.70 (CH), 122.09 (CH), 122.05 (CH), 121.58 (CH), 121.55 (CH), 121.52 (CH), 121.45 (CH), 121.19 (CH), 120.16 (CH), 119.30 (CH), 118.89 (CH), 118.82 (CH), 116.86 (Cq), 116.72 (Cq), 115.74 (Cq), 61.71 (OMe), 61.69 (OMe), 61.55 (OMe).

HRMS (MALDI): Calculated *m/z* for $[C_{21}H_{16}OS_4]^+$: 412.0078; found: 412.0077.

5.3 Synthesis of 21

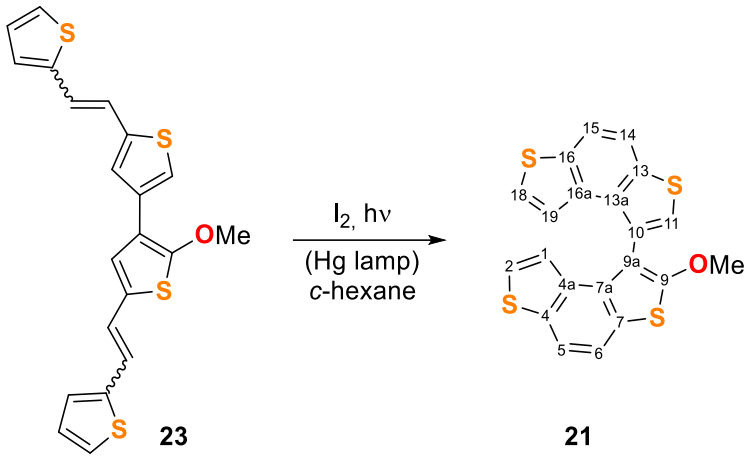

23 **21**

(60%)

A solution of **23** (0.48 mmol) and iodine (18 mg, 0.14 mmol, 0.3 eq) in *c*-hexane (750 mL) was stirred at room temperature and irradiated with a 125 W medium-pressure Hg lamp for 2 h and 45 min. The reaction progress was checked by TLC. After the complete conversion of the starting material, the reaction mixture was filtered to remove insolubles. The purple clear solution thus obtained was washed with a saturated aqueous solution of $Na_2S_2O_3$ yielding a yellow solution. The collected organic phases were dried over Na_2SO_4, filtered and the solvent was removed under reduced pressure. The brown oily residue thus obtained was purified by column chromatography (15 cm silica gel, d = 2.0 cm, n-hexane/CH_2Cl_2 (3:1), R_f = 0.32). **21** was obtained as an off white solid (119 mg, 0.29 mmol, 60%).

^{1}H NMR (300 MHz, $CDCl_3$): δ = 7.92 (d, ^3J(H,H) = 8.6 Hz, 1H; H-15), 7.88 (d, ^3J(H,H) = 8.7 Hz, 1H; H-14), 7.78 (d, ^3J(H,H) = 8.6 Hz, 1H; H-6), 7.72 (d, ^3J(H,H) = 8.6 Hz, 1H; H-5), 7.56 (s, 1H; H-11), 7.17 (d, ^3J(H,H) = 5.5 Hz, 1H; H-19), 7.04 (d, ^3J(H,H) = 5.5 Hz, 1H; H-1), 6.82 (d, ^3J(H,H) = 5.5 Hz, 1H; H-18), 6.41 (d, J = 5.5 Hz, 1H; H-2), 3.91 (s, 3H).

^{13}C NMR (75 MHz, $CDCl_3$): δ = 162.36 (C-9), 138.20 (C-4), 137.66 (C-16), 137.12 (C-10), 134.85 (C-16a), 134.10 (C-9a), 133.83 (C-4a), 133.33 (C-7), 130.07 (C-13), 126.57 (C-11), 126.33 (C-7a), 126.25 (C-19), 125.58 (C-1), 121.69 (C-18), 121.48 (C-2), 119.49 (C-14), 119.23 (C-15), 118.72 (C-5), 117.75 (C-6), 112.21 (C-13a), 62.00 (CH_3).

HRMS (EI+): Calculated *m/z* for $[C_{21}H_{12}OS_4]^+$: 407.9737; found: 407.9771.

5.4 21 borylation attempts

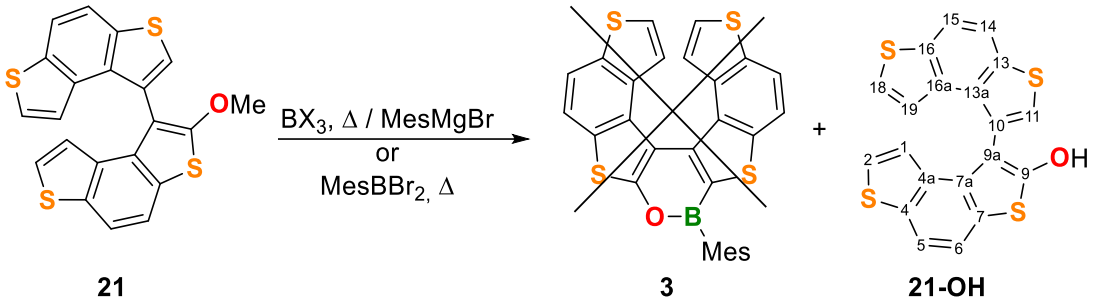

21 borylation attempts. Entry 1, 2 preparative experiments; entry 2, 3 NMR experiments performed using a flame-sealed NMR tube in a thermostated oven.

Entry	Borane	Base	additive	solvent	temperature
1	BCl_3 (1.0 M in THF)	Et_3N (1.0 eq.)	*n*[Bu_4N]I (1.2 eq.)	chlorobenzene	135 °C
2	BBr_3 (0.5 M in *n*-hexane)	Et_3N (1.0 eq.)		chlorobenzene	135 °C
3	$MesBBr_2$	Et_3N (1.0 eq.)	//	C_6D_6	135 to 180 °C

Note: **21-OH** was purified *via* column chromatography or preparative TLC (*n*-hexane/CH_2Cl_2 (7:3).

*Characterization data of **21-OH**:*

^{1}H NMR (400 MHz, $CDCl_3$): δ = 8.16 (d, ^3J(H,H) = 5.5 Hz, 1H; H-19), 7.97 – 7.91 (m, 2H; H-6, H-15), 7.83 (d, ^3J(H,H) = 8.6 Hz, 1H; H-14), 7.67 (d, ^3J(H,H)= 5.6 Hz, 1H; H-18), 7.46 (d, ^3J(H,H) = 8.4 Hz, 1H; H-5), 7.34 (d, ^3J(H,H) = 5.5 Hz, 1H; H-1), 6.85 (s, 1H; H-11), 6.62 (d, ^3J(H,H) = 5.5 Hz, 1H; H-2), 6.31 (s, 1H; OH). Note: the assignment of the -OH resonance (6.31 ppm) was confirmed by deuteration test, see Figure S45A.

^{13}C{^{1}H} NMR (101 MHz, $CDCl_3$) δ = 139.01 (C-4), 138.47 (C-16), 138.21 (C-13), 136.43 (C-4a), 134.15 (C-16a), 132.76 (C-13/13a), 131.87 (C-13/13a), 131.03 (C-9a), 129.99 (C-7/C-7a) , 129.94 (C-7/C-7a), 129.34 (C-1), 126.69 (C-18), 125.35 (C-11), 123.67 (C-5), 122.04 (C-19), 121.77 (C-2), 119.75 (C-15), 119.42 (C-14), 118.96 (C-5). C-9 n.o.

HRMS (MALDI): Calculated *m/z* for $[C_{20}H_{10}OS_4]^+$: 392.9536; found: 392.9536.

5.5 Synthesis of 25

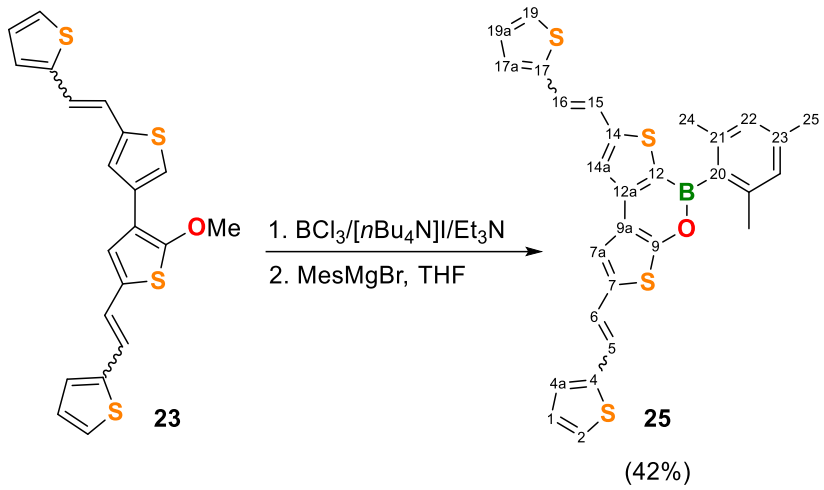

A flame-dried 100 mL J-Young tube was charged with **23** (150 mg, 0.36 mmol), [nBu$_4$N]I (161 mg, 0.44 mmol, 1.20 eq.), and evacuated for 30 min. Chlorobenzene (10 mL) was added and the resulting solution was cooled to –10 °C. BCl_3 (1.0 M in hexanes; 400 µL, 0.40 mmol, 1.1 eq.) and Et_3N (0.5 M in chlorobenzene; 730 µL, 0.36 mmol, 1.00 eq.) were added, the Young-tap was closed and the yellow-green reaction mixture was allowed to warm up to room temperature. The reaction mixture thus obtained was heated to 135 °C and stirred for 24 h. After cooling to room temperature a brown mixture was obtained. The solvent was evaporated to dryness and THF (10 mL) was added. MesMgBr (1.0 M in THF; 1.08 mL, 1.08 mmol, 3.00 eq.) was added dropwise at room temperature to give a red mixture, which was stirred for 1 h. The solvent was removed under reduced pressure and the residue was purified by column chromatography (17 cm silica gel, d = 2.0 cm, n-hexane/CH_2Cl_2 (5:1), R_f = 0.30). The fractions containing **25** were evaporated giving a yellow solid (80 mg, 0.15 mmol, 42%) containing the *trans,trans*-isomer as major component. **25** was washed with n-pentane and *trans,trans*-**25** (70 mg, 0.13 mmol, 37%) was thereby obtained as a bright-yellow solid. Single crystals of *trans,trans*-**25** suitable for X-ray crystallography were obtained by slow evaporation of a *trans,trans*-**25** saturated solution in n-heptane/CH_2Cl_2 (1:1).

^{1}H NMR (500 MHz, $CDCl_3$): δ = 7.46 (s, 1H; H-14a), 7.28/7.25 (d, ^3J(H,H) = 15.8 Hz, 1H; H-15), 7.27/7.26 (d, ^3J(H,H) = 5.2 Hz, 1H; H-19), 7.22 (s, 1H; H-7a), 7.21/7.20 (d, ^3J(H,H) = 5.2 Hz, 1H; H-19a), 7.18/7.15 (d, ^3J(H,H) = 15.8 Hz, 1H; H-16), 7.11(d, ^3J(H,H) = 3.4 Hz, 1H; H-17a), 7.08+7.05 (d, ^3J(H,H) = 15.8 Hz, 1H; H-6), 7.07 (d, ^3J(H,H) = 3.5 Hz, 1H; H-4a), 7.03-7.01 (dd, ^3J(H,H) = 4.8 Hz, ^4J(H,H) = 3.5 Hz, 2H; H-2, H-1), 7.01/6.98 (d, ^3J(H,H) = 15.8 Hz, 1H; H-5), 6.92 (s, 2H; H-22), 2.35 (s, 3H; H-25), 2.28 (s, 6H; H-24).
Note: Note: most of the proton resonances are overlapped and, ^{1}H assignment was aided by the analyisis of coupling constants and correlations found in ^{HH}COSY and HMBC spectra. When a single proton is indicated by two resonances separated by "/", each resonance is referred to a single peak of the corresponding doublet; for simplicity, in the section *Results and Discussion* the average has been given (es. for H-5 (δ(^{1}H) = 7.08/7.05) the given value is δ(^{1}H) = 7.06).

$^{13}C\{^1H\}$ NMR (126 MHz, $CDCl_3$): δ = 157.6 (C-9), 154.5 (C-14), 147.4 (C-12a), 142.3 (C-4), 141.8 (C-17), 140.6 (C-21), 139.0 (C-23), 133.5 (br.; C-20), 132.0 (C-7), 130.7 (br.; C-12), 128.0 (C-1/C-2), 128.0 (C-1/C-2), 127.8 (C-17a), 127.6 (C-22) , 126.3 (C-4a), 125.9 (C-19), 125.6 (C-15), 124.6 (C-19a), 122.0 (C-5), 121.2 (C-14a), 121.1 (C-6), 120.9 (C-16), 120.7 (C-9a), 119.1 (C-7a), 22.8 (C-25), 21.5 (C-24).

^{11}B NMR (96 MHz, $CDCl_3$): δ = 41.70 ($h_{1/2} \approx$ 375 Hz).

HRMS (MALDI): Calculated *m/z* for $[C_{29}H_{23}BOS_4]^+$: 526.0719; found: 526.0717.

UV/Vis (*c*-hexane): λ_{max} (ε / $mol^{-1}dm^3cm^{-1}$) = 283 (15400), 365 (41000), 382 (36500).

Fluorescence (*c*-hexane, λ_{ex} = 365 nm): λ_{max} = 445, 472, 500 nm (resolved vibrational fine structure), 535 (sh); Φ_{PL} = 12%.

Cyclic voltammetry (THF, 0.1 M [nBu$_4$N][PF$_6$], 200 mV s^{-1}, vs. FcH/FcH$^+$): Cathodic scan: E_{pc} = −2.21 V, E^{I}_{pa} = 0.61V, E^{II}_{pa} = 0.99 V.

5.6 Attempts of 25 photocyclization

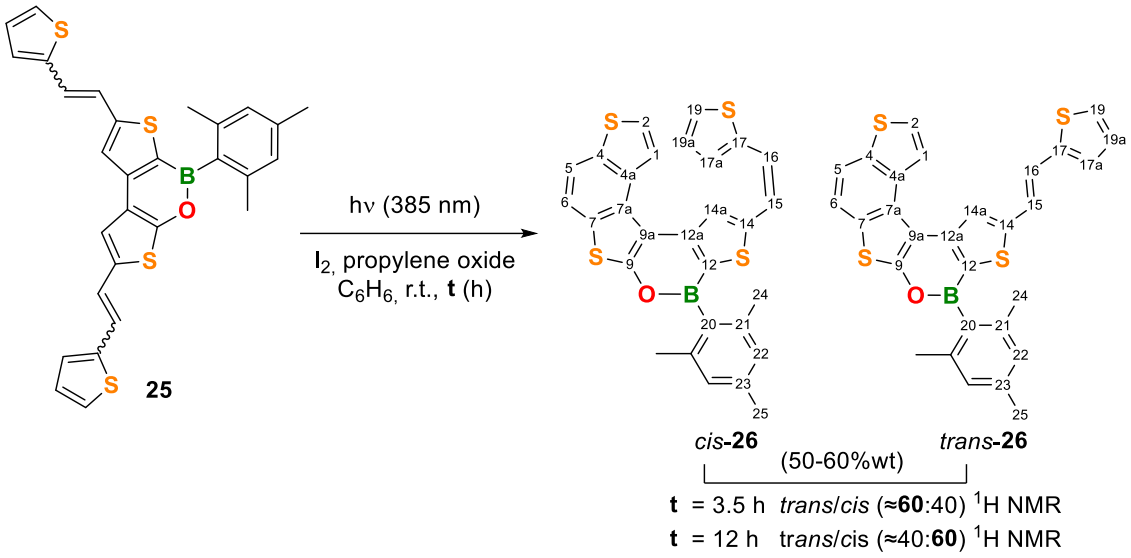

*General procedure for **25** photocyclization:*

A flame-dried 250 mL J-Young tube was charged with **25** (70 mg, 0.13 mmol) and evacuated for 30 min. C_6H_6 (150 mL) was added and the resulting green solution was treated with I_2 (70 mg, 0.27 mmol, 2.1 eq.) and propylene oxide (1.86 mL, 26.5 mmol, 200 eq.). The red solution thus obtained was irradiated with an LED lamp (385 nm - placed close to the reaction vessel, approx. 5 cm, Figure **S3**; the Duran® glass used is transparent to 385 nm light).[S6] The reaction progress was monitored by TLC (*c*-hexane/CH_2Cl_2 (5:1)).

Note: Even though *Rf* of **25** and **26** is almost identical, it is possibile to differentiate the two products on TLC: **25** shows a yellow spot under 254, 366 nm light (the spot turns to green after exposure to air); **26** shows blue spot at 254 nm and light-blue spot at 366 nm.

The solvent was evaporated, and the residue was purified by column chromatography (15 cm silica gel, *d* = 2.0 cm, *n*-hexane/CH_2Cl_2 (5:1)). A green-yellow solid (50-60%wt) was obtained and it was proved to be a mixture of *trans*-**26**/*cis*-**26** by ^{1}H, ^{HH}COSY NMR analysis.

Experiment 1, irradiation time **t** = 3.5 h: *trans*-**26**/*cis*-**26** (≈60:40) mixture obtained after purification;
Experiment 2, irradiation time **t** = 12 h: *trans*-**26**/*cis*-**26** (≈40:60) mixture obtained after purification.

Single crystals of *trans*-**26** suitable for X-ray crystallography were grown by slow evaporation of a saturated solution of the *trans*-**26**/*cis*-**26** (≈60:40) mixture in *n*-pentane/CH_2Cl_2 (2:1) in a glovebox.

Characterization data of *cis*-**26** (see Figure S50):

^{1}H NMR (400MHz, CD_2Cl_2): δ = 8.24 (s, 1H; H-14a, 8.08 (d, ^3J(H,H) = 5.6 Hz, 1H; H-1), 7.98-7.93 (m, 1H; H-5, overlapped with *trans*-**26**), 7.80-7.75 (m, 2H; H-5/H-6, overlapped with *trans*-**26**), 7.57 (d, ^3J(H,H) = 5.6 Hz, 1H; H-2), 7.33 (d, J(H,H) = 3.7 Hz, 1H; H-17a/H-19/H-19a, overlapped with *trans*-**26**), 7.22 (d, ^3J = 3.7 Hz, 1H; H-17a/H-19/H-19a), 7.01 (t (originated by two collapsed doublets), ^3J = 3.7 Hz, 1H; H-17a/H-19/H-

19a), 6.93 (s, 2H; H-22), 6.89 (d, ^3J = 11.9 Hz, 1H; H-15), 6.77 (d, ^3J = 11.9 Hz, 1H; H-16), 2.34 (s, 3H; H-25), 2.28 (s, 6H; H-24). Assignment was aided by ^{HH}COSY spectrum.

Note: of high diagnostic value are the resonances of protons H-15 (6.89 ppm) and H-16 (6.77 ppm) showing a typical *cis*-coupling constant $^3J(H,H)_{cis}$ = 11.9 Hz.

Characterization data of *trans*-**26** (see Figure S51):

^{1}H NMR (400MHz, CD_2Cl_2): δ = 8.28 (d, ^3J(H,H) = 5.6 Hz, 1H; H-1/H-2), 8.16 (s, 1H; H-14a), 7.98-7.96 (m, 1H; H-15/16, overlapped with H-5/H-6 and *cis*-26 resonances), 7.97 (dd, ^3J(H,H) = 8.5 Hz, 1H; H-5/H-6, partly overlapped with *cis*-26 resonances), 7.80-7.75 (m, 1H; H-15/16, overlapped with H-5/H-6 and *cis*-26 resonances) 7.79(7.80/7.78) (d, ^3J(H,H) = 8.5 Hz, 1H; H-5/H-6, overlapped with *cis*-26 resonances), 7.76 (d, ^3J(H,H) = 5.6 Hz, 1H; H-1/H-2, overlapped with H-5/H-6 and *cis*-26 resonances), 7.34 (d, 1H; ^3J(H,H) = 4.1 Hz, 1H; H-17a/H-19/H-19a overlapped with *cis*-26), 7.16 (d, ^3J(H,H) = 3.5 Hz, 1H; H-17a/H-19/H-19a), 7.05 (dd, J = ^3J(H,H) = 5.1, ^3J(H,H) = 3.5 Hz, 1H; H-17a/H-19/H-19a), 6.95 (s, 2H), 2.36 (s, 3H), 2.30 (s, 6H).

^{11}B NMR (128 MHz, CD_2Cl_2): δ = 40.9 ($h_{1/2} \approx$ 220 Hz).

HRMS (MALDI): Calculated *m/z* for $[C_{29}H_{21}BOS_4]^+$: 524.0563; found: 524.0567.

6. Synthetic route to tetrathia[7]helicene 4

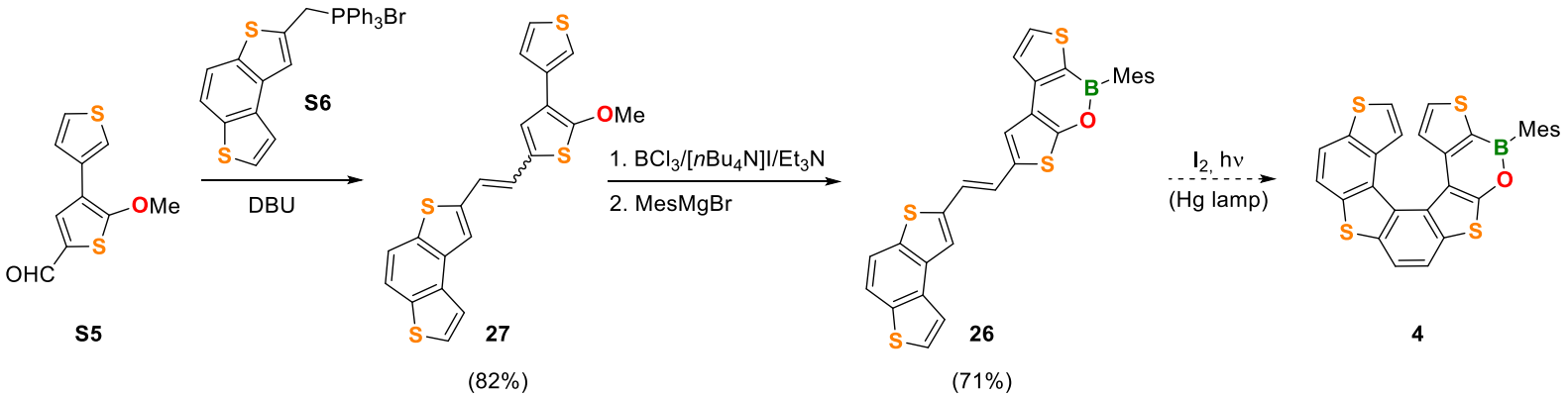

Scheme S3: Synthetic route to tetrathia[7]helicene **4**.

Synthesis of S5[S6] and S6 starting materials

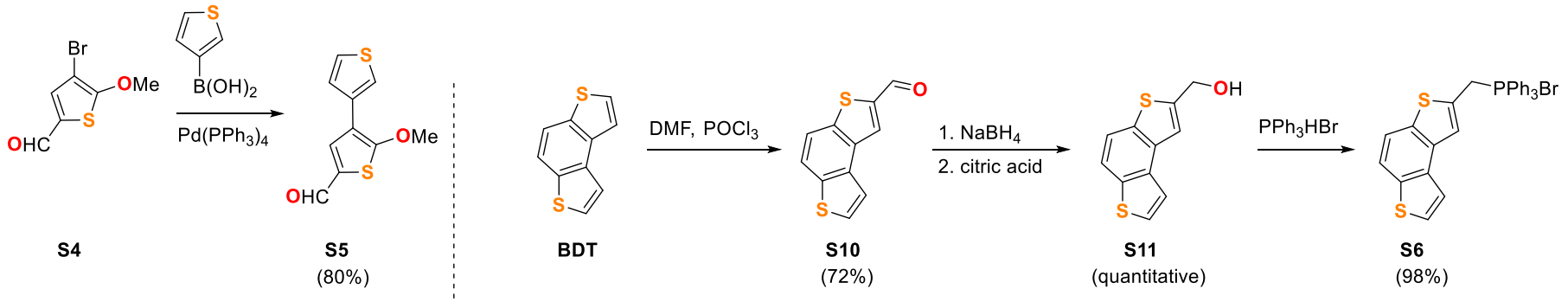

Scheme S4: Preparation of tetrathia[7]helicene **Y1** intermediate. Full details about the synthesis of **S4**/**S5** and **S10**/**S11**/**S6** are provided in section *2.1 Thiophene starting materials* and section *2.2. BDT starting materials*.

6.1 Synthesis of 28

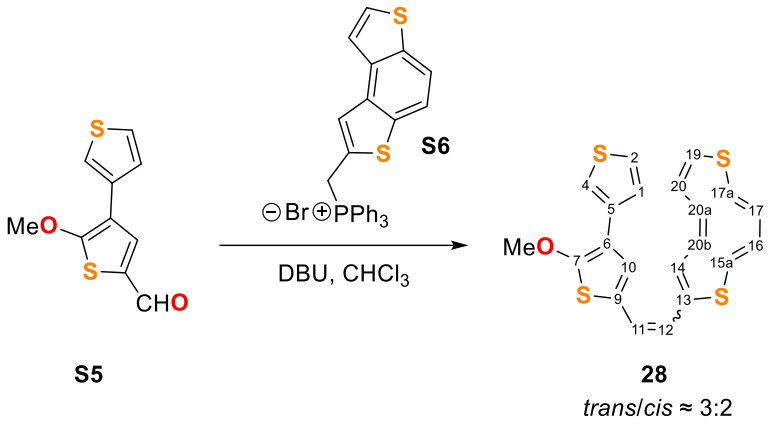

A flame-dried100 mL three-necked flask equipped with a reflux condenser was charged with **S5** (814 mg, 1.53 mmol, 1.2 eq.) and evacuated for 30 min. $CHCl_3$ (31 mL), 1,8-diazabiciclo[5.4.0]undec-7-ene (DBU) (291 mg, 1.91 mmol, 0.37 mL, 1.5 eq.) were added and the resulting yellow-orange mixture was heated to 40 °C and stirred for 30 min. **S5** (286 mg, 1.27 mmol, 1 eq.) was added and the reaction mixture was heated to reflux and stirred for 17 h. The reaction progress was checked by TLC.

After cooling to room temperature, water (150 mL) was added. After separation of the two layers, the aqueous phase was extracted with CH_2Cl_2 (3×100 mL) and the collected organic phases were dried over Na_2SO_4, filtered and the solvent was removed under reduced pressure.

Note: *trans*-**28** is scarcely soluble in common organic solvents and thus it is crucial to wash the filter with a large amount of CH_2Cl_2 to avoid loss of product.

The crude product was purified *via* column chromatography (*n*-hexane/AcOEt (90:10)). Purification yielded three main fractions:

a) **Me-BDT** side product, white solid (41 mg, 0.2 mmol, 11%);

b) fraction enriched in *cis*-**28**, yellow-orange solid (163 mg, 0.40 mmol, 31%);

c) fraction enriched in *trans*-**28**, bright yellow solid (266 mg, 0.65 mmol, 51%). Total yield: 82%.

The two fractions enriched in *trans*-**28** and *cis*-**28** respectively, were combined and used in the following borylation step.

Characterization data of the fraction enriched in trans-**28**

^{1}H NMR (400 MHz, DMSO): δ = 7.96 – 7.90 (m, 4H; H-16/17+H-19/20), 7.93 (s, 1H; H-14) 7.88 (dd, J(H,H) = 8.9, J(H,H) = 5.0 Hz, 1H), 7.71 (dd, J(H,H) = 2.9, J(H,H) = 1.2 Hz, 1H; H-4), 7.59 (dd, J(H,H) = 5.0, J(H,H) = 3.0 Hz, 1H; H-1), 7.50 (d, J(H,H)= 1.2 Hz, 1H; H-2), 7.49 (s, 1H; H-10), 7.17 (d, J (H,H) = 15.9 Hz, 1H; H-12), 7.10 (d, J (H,H) = 15.9 Hz, 1H; H-11), 3.88 (s; *cis*-**28**), 4.06 (s, 3H; OMe).

^{13}C{^{1}H}NMR (1001 MHz, $CDCl_3$): δ = 142.6, 134.9, 127.9, 127.0 (C-10), 126.8, 126.6 (C-2), 126.0 (C-1), *124.2 (C-12), 122.3, 121.1, 120.6 (C-4), 119.3, 118.7, 118.6 (C-11), 62.10 (OMe). *) unequivocally detected only in the HMBC spectrum.

Note: the scarce solubility of *trans*-**28** made its ^{13}C NMR characterization difficult; although a long measurement time was employed, seven carbon resonances are missing.

*Characterization data of the fraction enriched in **cis**-**28**.*

^{1}H NMR (400 MHz, DMSO) δ = 8.06 (s, 1H; H-14), 7.96 – 7.93 (m, 2H; H-16/17+H-19/20, overlapped with the same protons of *trans*-**28**), 7.91 – 7.86 (m, 2H; H-16/17+H-19/20, overlapped with the same protons of *trans*-**28**), 7.71 (dd; *trans*-**28**, 7.68 (dd, *J*(H,H) = 3.0 Hz, *J*(H,H) = 1.3 Hz, 1H; H-4), 7.59 (dd, *J*(H,H) = 5.0 Hz, *J*(H,H) = 3.0 Hz), 7.56 (dd, *J*(H,H) = 5.0 Hz, *J*(H,H) = 3.0 Hz, 1H; H-1), 7.48 ((s, 1H; H-10)+ 7.47(d, *J*(H,H) = 1.3 Hz, 1H; H-2)), 7.17 (d, *J*(H,H) = 15.9 Hz; *trans*-**28**-H-11), 7.10 (d, *J*(H,H) = 15.9 Hz; *trans*-**28**-H-12), 6.76 (d, *J*(H,H) = 12.3 Hz, 1H; H-11), 6.71 (d, *J*(H,H) = 12.5 Hz, 1H; H-12), 4.06 (s; *trans*-**28**), 3.88 (s, 3H; OMe).

Note: for simplicity integrals of the residual *trans*-**28** have been omitted and are shown in Figure S54.

^{13}C{^{1}H}NMR (101 MHz, DMSO): δ = 160.4 (C-7), 142.5 (Cq), 139.3 (C-13), 136.2 (Cq), 136.1 (Cq), 134.2 (Cq), 134.0 (Cq), 129.1 (C-2), 127.9 (C-16/17+19/20), 127.0 (*trans*-**28**), 126.7 (C-10), 126.0 (*trans*-**28**), 125.9 (C-1), 125.0 (C-12), 124.2 (*trans*-**28**), 123.8 (C-14), 123.4 (C-9), 122.4 (C-16/17+19/20), 122.2 (*trans*-**28**), 121.1 (*trans*-**28**), 120.6 (*trans*-**28**), 120.5 (C-4), 119.9 (C-11), 119.4 (C-16/17+19/20), 119.3 (*trans*-**28**), 118.6 (*trans*-**28**), 118.6 (C-16/17+19/20), 115.6 (Cq), 62.1 (OMe; *trans*-**28**), 61.8 (OMe).

HRMS (MALDI): Calculated *m/z* for $[C_{21}H_{14}OS_4]^+$: 409.9927; found: 409.9925.

Mp: 235.5-238.4 °C.

6.2 Synthesis of 27

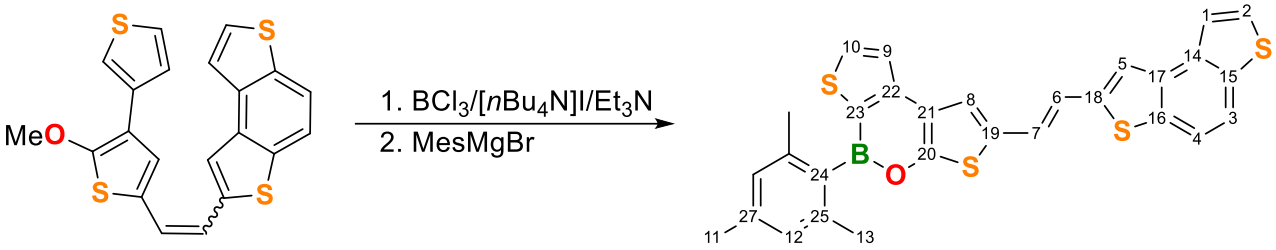

28 ***trans*-27**

A flame-dried 100 mL J-Young flask was charged with **28** (306 mg, 0.57 mmol), [*n*BuN]I (326 mg, 0.69 mmol, 1.2 eq.) and chlorobenzene (46 mL). The rtesulting mixture was cooled to –10 °C and BCl_3 (1.0 M in hexanes; 0.8 mL, 0.8 mmol, 1.4 eq.) was added, yielding a brownish mixture. Et_3N (0.5 M in chlorobenzene; 1.1 mL, 0.57 mmol, 1 eq.) was added and the resulting orange solution was heated to 135 °C and stirred for 24 h. After cooling to room temperature, the mixture was evaporated to dryness and THF (60 mL) was added. MesMgBr (0.9 M in THF; 2.0 mL, 1.8 mmol, 3.16 eq.) was added dropwise at room temperature and the reaction mixture was stirred for 1 h. The solvent was removed under reduced pressure and the residue was purified by column chromatography (*n*-hexane/AcOEt (95:5)). *trans*-**27** was thereby obtained as yellow solid (139 mg, 0.26 mmol, 46%).

A second fraction containing *trans*-**27** (72 mg, 0.14 mmol, 26%; determined by ^{1}H NMR) in mixture with unreacted **28** was also recovered. Total yield: 71%.

^{1}H NMR (400 MHz, $CDCl_3$): δ = 8.00 (d, ^3J(H,H) = 4.8 Hz, 1H; H-10), 7.80 (d, ^3J(H,H) = 8.6 Hz, 1H; H-3/H-4), 7.72 (d, ^3J(H,H) = 8.6 Hz, 1H; H-3/H-4), 7.67 (d, ^3J(H,H) = 5.4 Hz, 1H; H-1/H-2), 7.62 (s, 1H; H-5 – overlapped with H-9), 7.61 (d, ^3J(H,H)= 4.8 Hz, 1H; H-9 – overlapped with H-5), 7.57 (d, ^3J(H,H) = 5.4 Hz, 1H; H-1/H-2), 7.35 (s, 1H; H-8), δ= 7.20 (d, ^3J(H,H) = 15.7 Hz, 1H; H-6), 7.15 (d, ^3J(H,H)= 15.7 Hz, 1H; H-7), 6.93 (s, 2H; H-12), 6.85 (s; *cis*-**27**), 2.36 (s, 3H; H-11), 2.30 (s; *cis*-**27**), 2.27 (s, 6H; H-13), 2.14 (s; *cis*-**27**).

^{13}C{^{1}H} NMR (100.6 MHz, $CDCl_3$): δ = 157.78 (C-20), 146.88 (C-22), 142.70 (C-18), 140.66 (C-25), 139.08 (C-27), 138.47 (C-8), 137.09 (C-15), 135.69 (C-16), 135.41 (C-17), 134.47 (C-14), 133.63* (C-24), 132.29* (C-23), 131.75 (C-19), 127.66 (C-12), 126.94 (C-2), 124.28 (C-6/C-7), 122.98 (C-9), 121.99 (C-1), 121.50 (C-6/C-7), 121.39 (C-5), 121.25 (C-21), 120.07 (C-8), 119.42 (C-4), 118.60 (C-3), 22.80 (C-13), 21.49 (C-11).

*) unequivocally detected only in the ^{H,C}HMBC spectrum.

^{11}B NMR (128.4 MHz, $CDCl_3$) δ = 42.12 ($h_{1/2}$≈ 320 Hz).

HRMS (MALDI): Calculated *m/z* for $[C_{29}H_{21}BOS_4]^+$: 523.0605; found: 523.0603.

UV/Vis (*c*-hexane): λ_{max} (ε / mol^{-1}dm^{3}cm^{-1}) = 282 (sh), 309 (12500), 370 (sh), 388 (60600), 410 (47000).

Fluorescence (*c*-hexane, λ_{ex} = 375 nm): λ_{max} = 421, 488 nm (resolved vibrational fine structure), 477, 517 nm (sh); Φ_{PL} = 23%.

Cyclic voltammetry (THF, 0.1 M [*n*Bu$_4$N][PF$_6$], 100 mV s^{-1}, vs. FcH/FcH$^+$): Cathodic scan: $E^{I}_{1/2}$ = −2.37 V, E^{I}_{pa} = 0.63 V, E^{II}_{pa} = 0.76 V.

Mp: 127.3 – 129.7 °C.

7. Plots of ^{1}H, ^{11}B and $^{13}C\{^{1}H\}$ NMR spectra of all new compounds

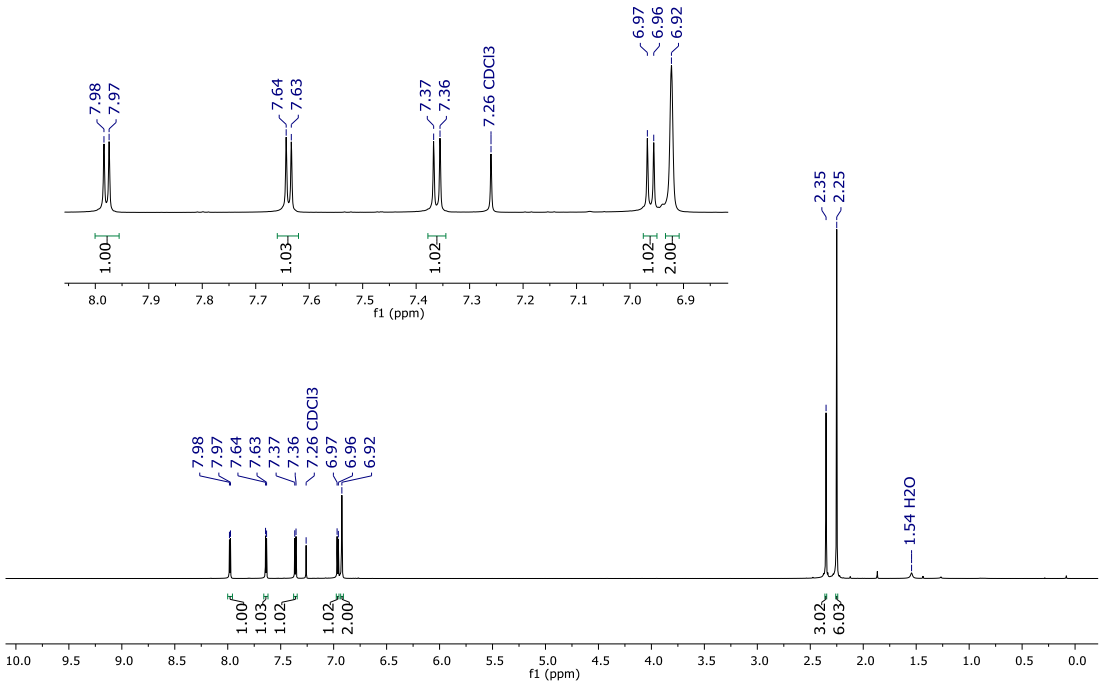

Figure S5: ^{1}H NMR spectrum of **5** ($CDCl_3$, 500 MHz).

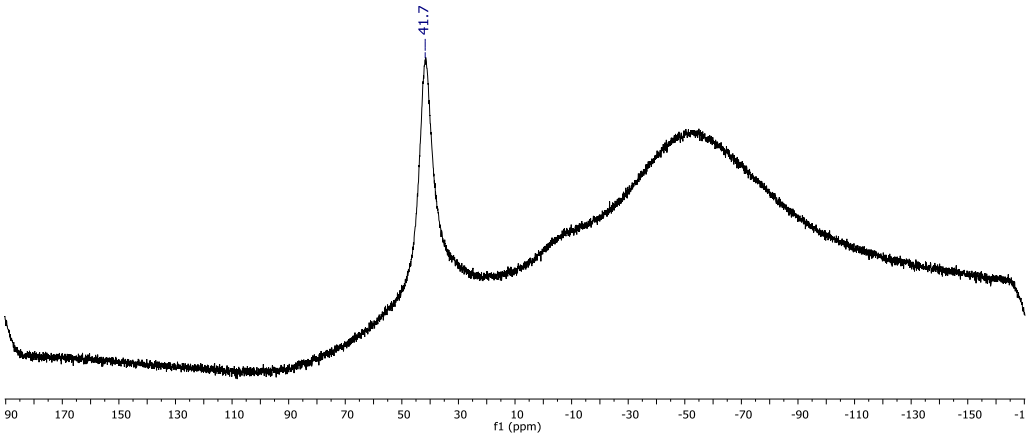

Figure S6: ^{11}B NMR spectrum of **5** ($CDCl_3$, 96 MHz).

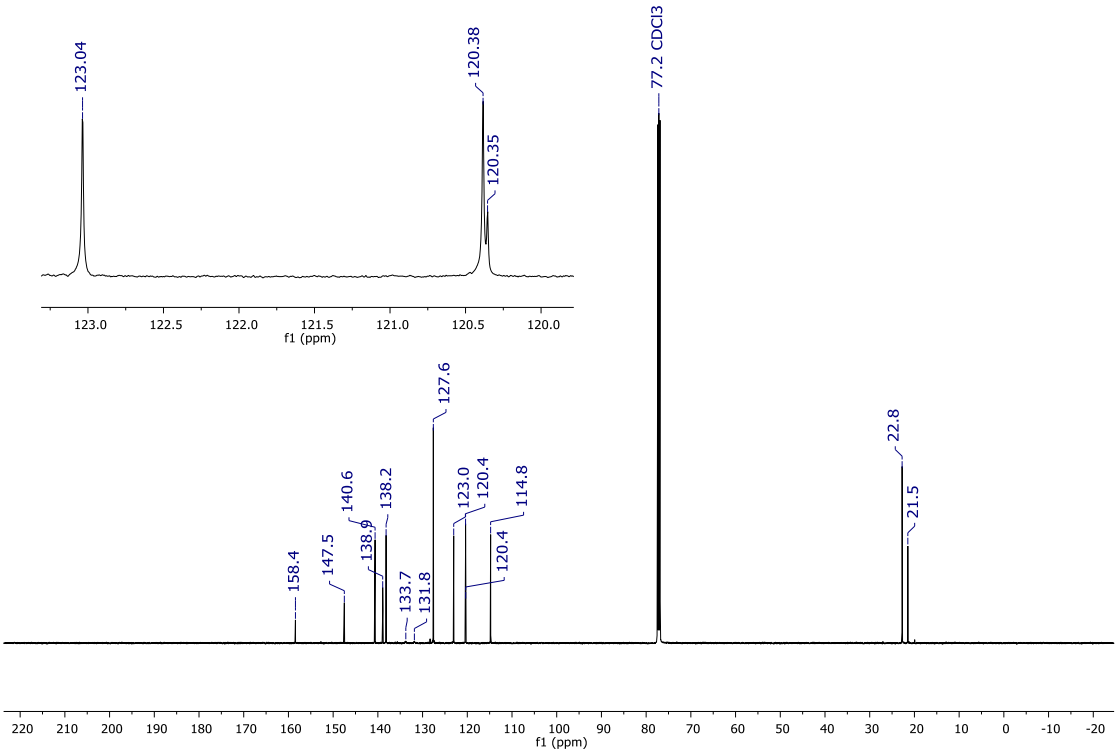

Figure S7: $^{13}C\{^{1}H\}$ NMR spectrum of **5** ($CDCl_3$, 126 MHz).

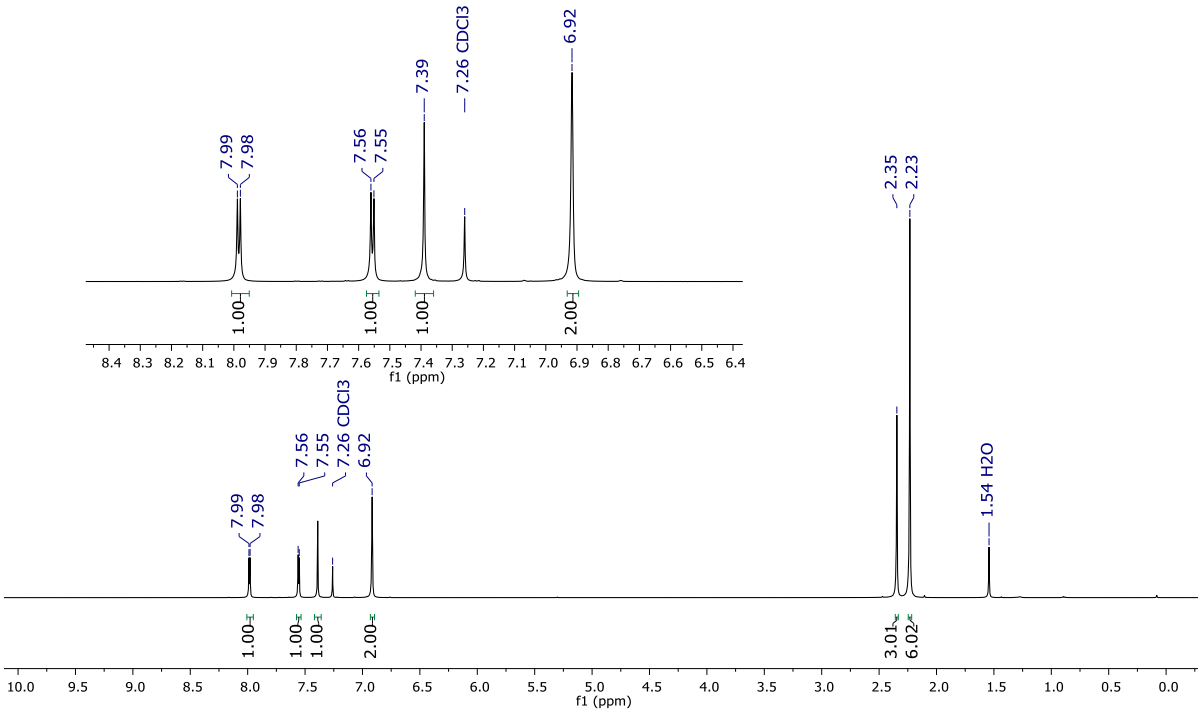

Figure S8: ^{1}H NMR spectrum of **8** ($CDCl_3$, 500 MHz).

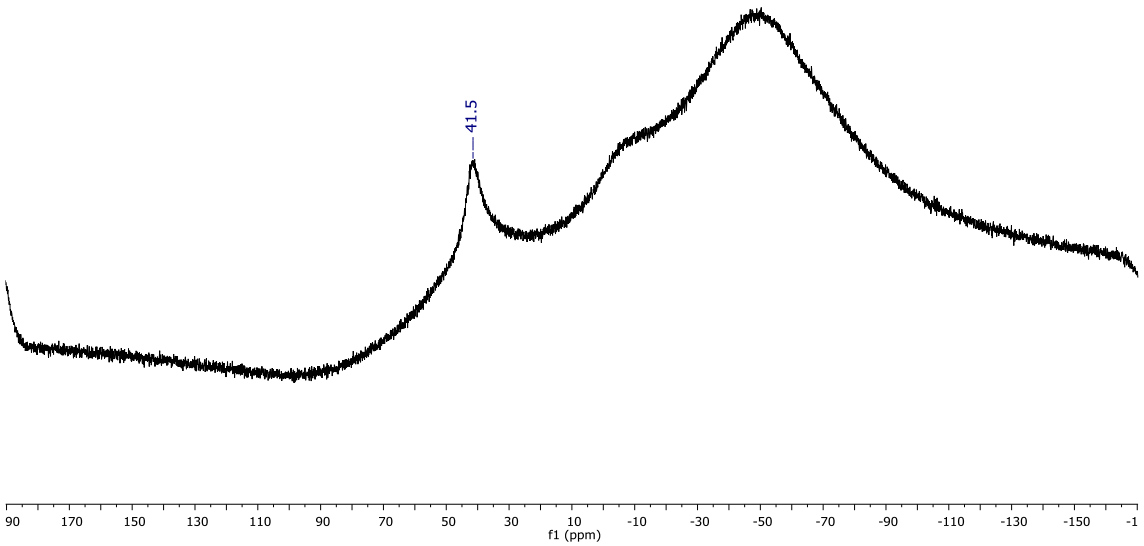

Figure S9: ^{11}B NMR spectrum of **8** ($CDCl_3$, 96 MHz).

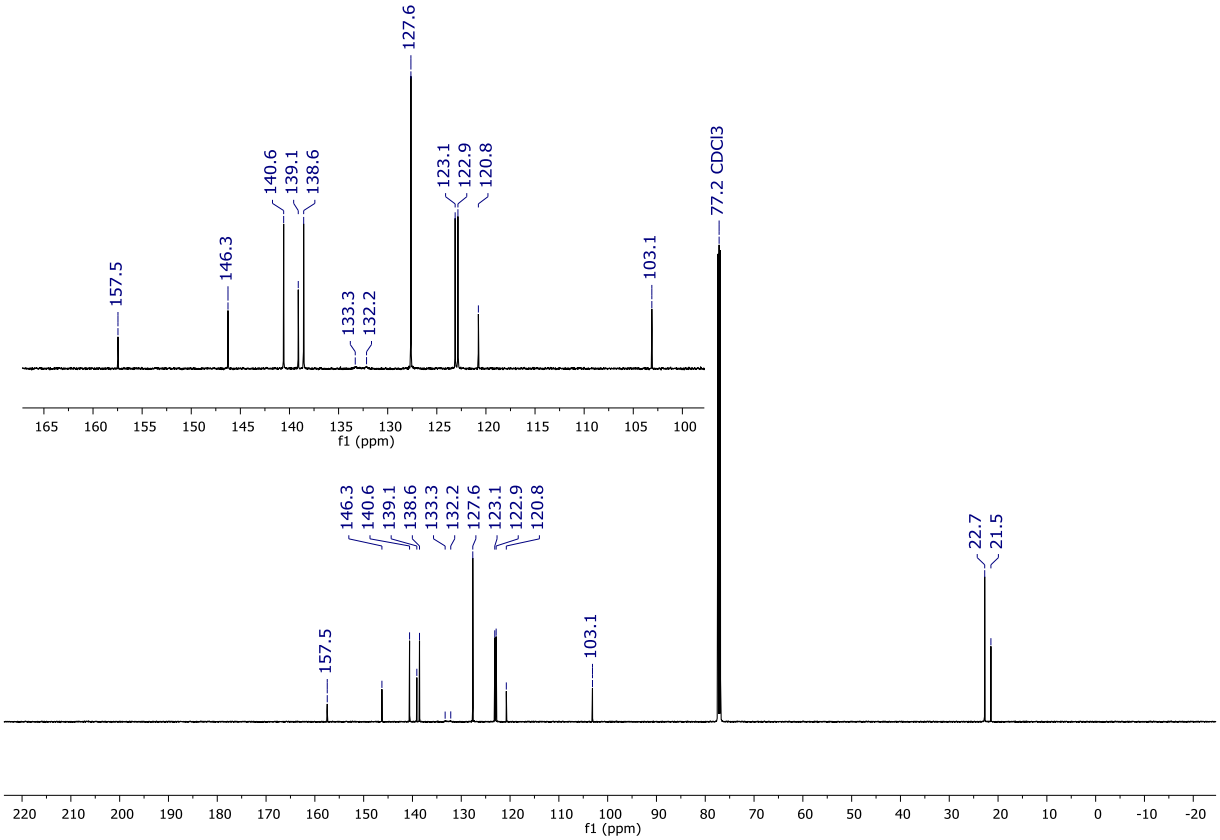

Figure S10: $^{13}C\{^{1}H\}$ NMR spectrum of **8** ($CDCl_3$, 126 MHz).

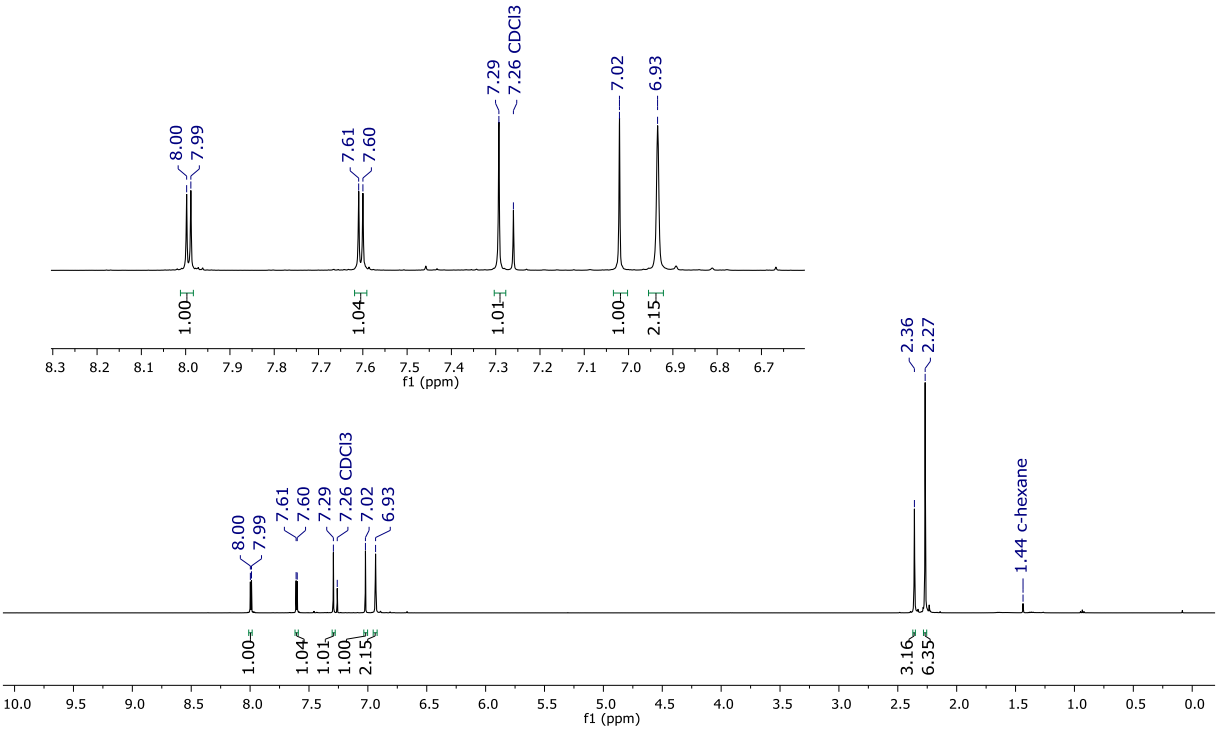

Figure S11: ^{1}H NMR spectrum of *trans*-**15** ($CDCl_3$, 500 MHz).

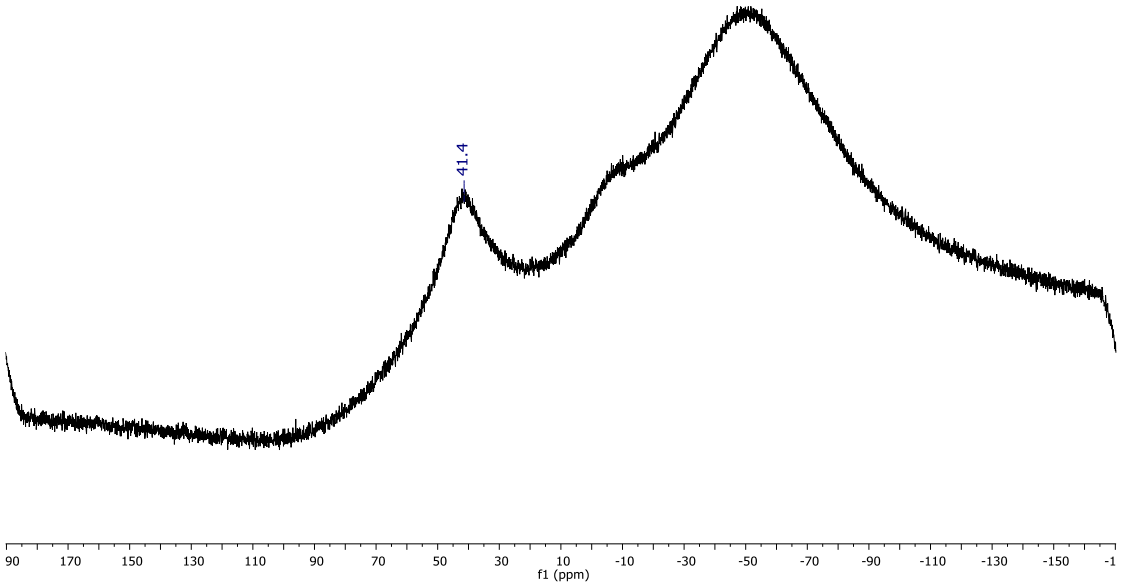

Figure S12: ^{11}B NMR spectrum of *trans*-**15** ($CDCl_3$, 96 MHz).

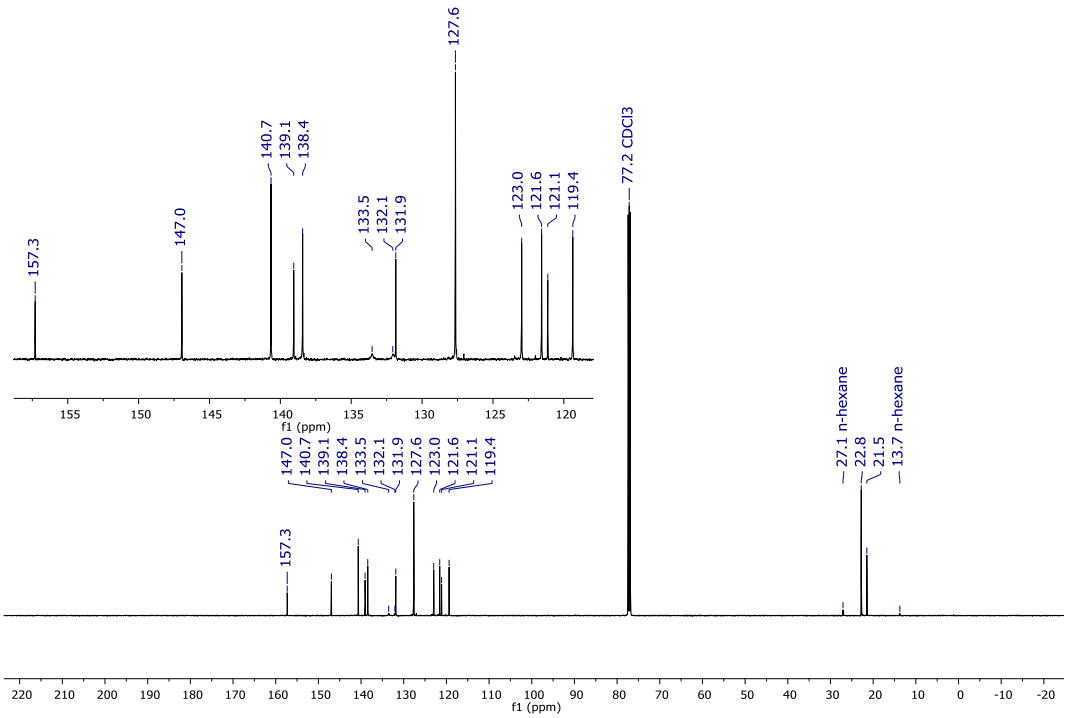

Figure S13: $^{13}C\{^{1}H\}$NMR spectrum of *trans*-**15** ($CDCl_3$, 126 MHz).

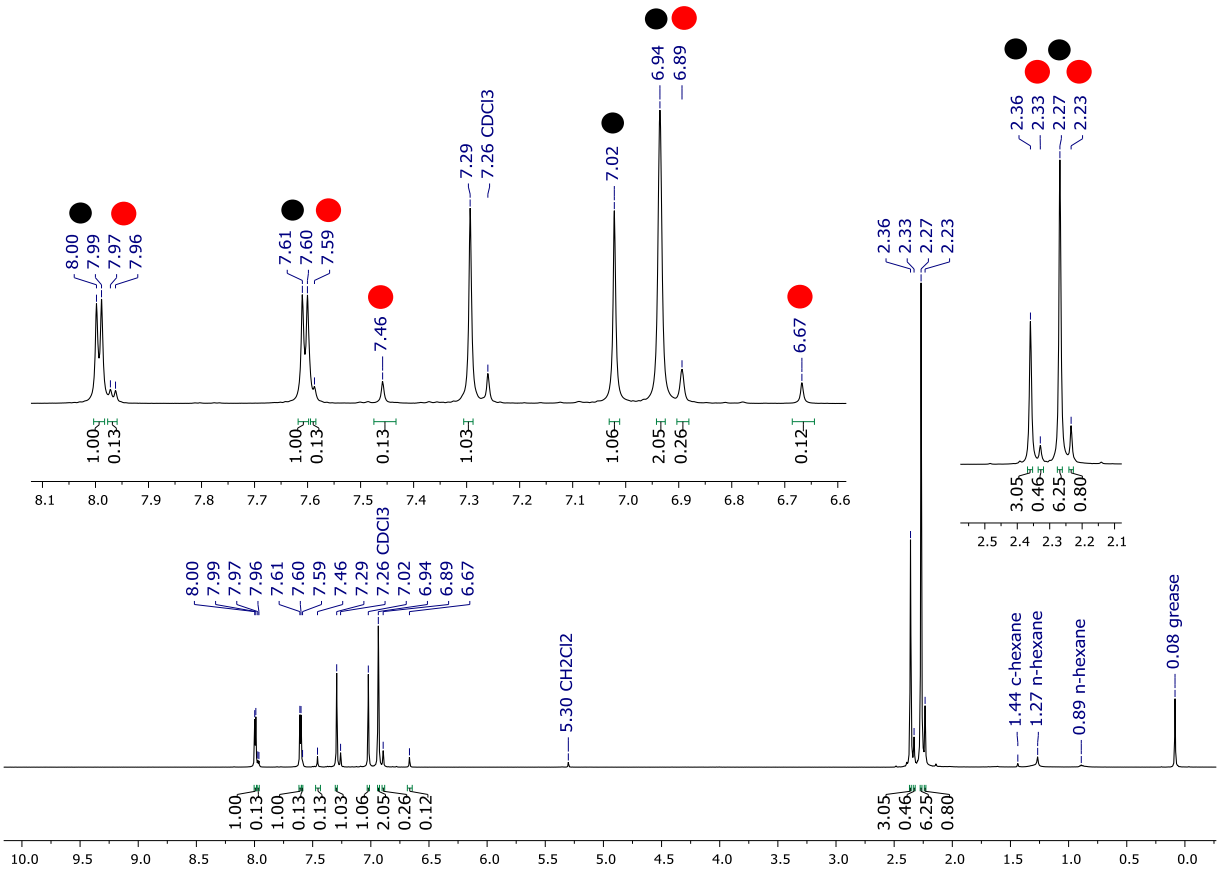

Figure S14: ^{1}H NMR spectrum of a *trans/cis* (≈ 9:1) mixture of **15** ($CDCl_3$, 500.2 MHz; ● *trans*-isomer, ● *cis*-isomer).

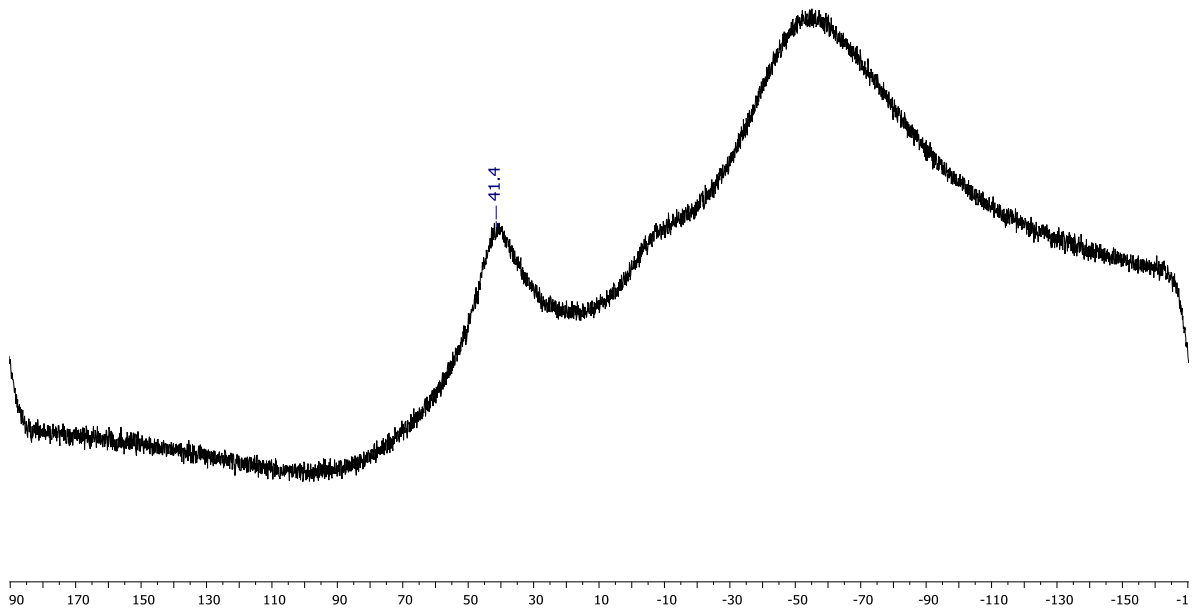

Figure S15: ^{11}B NMR spectrum of a *trans/cis* (≈ 9:1) mixture of **15** ($CDCl_3$, 96 MHz).

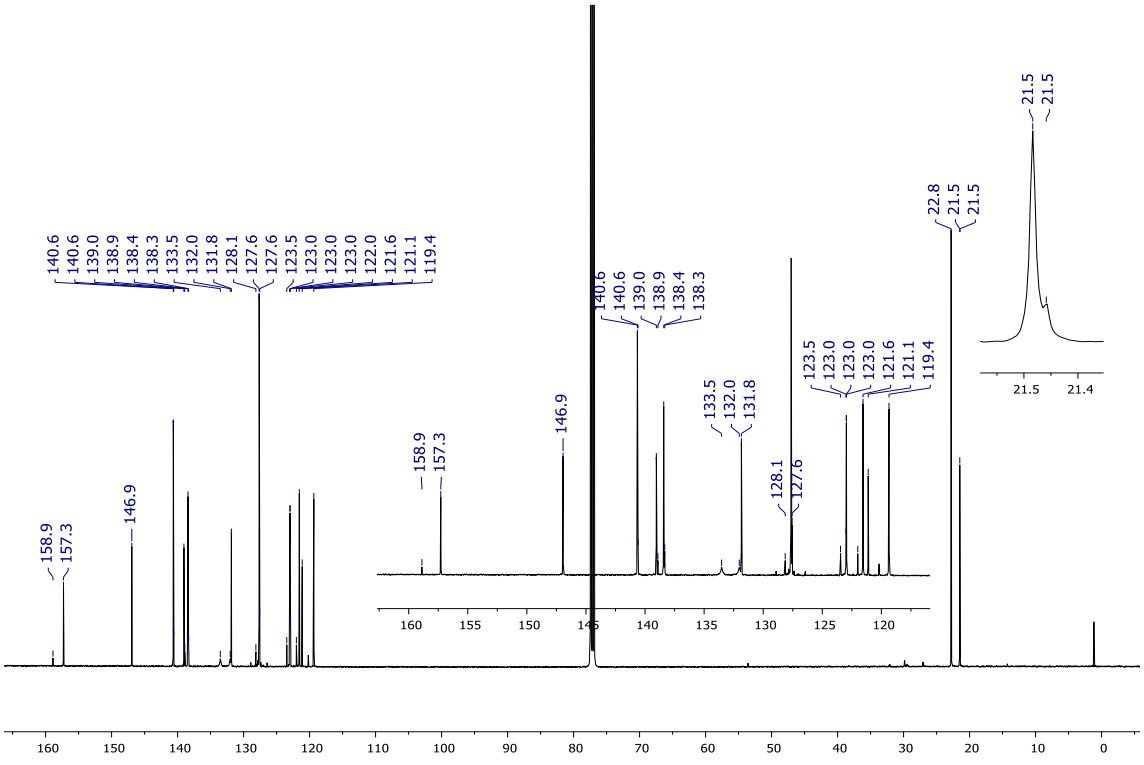

Figure S16: ^{13}C{^{1}H}NMR spectrum of a *trans/cis* (≈ 9:1) mixture of **15** ($CDCl_3$, 126 MHz).

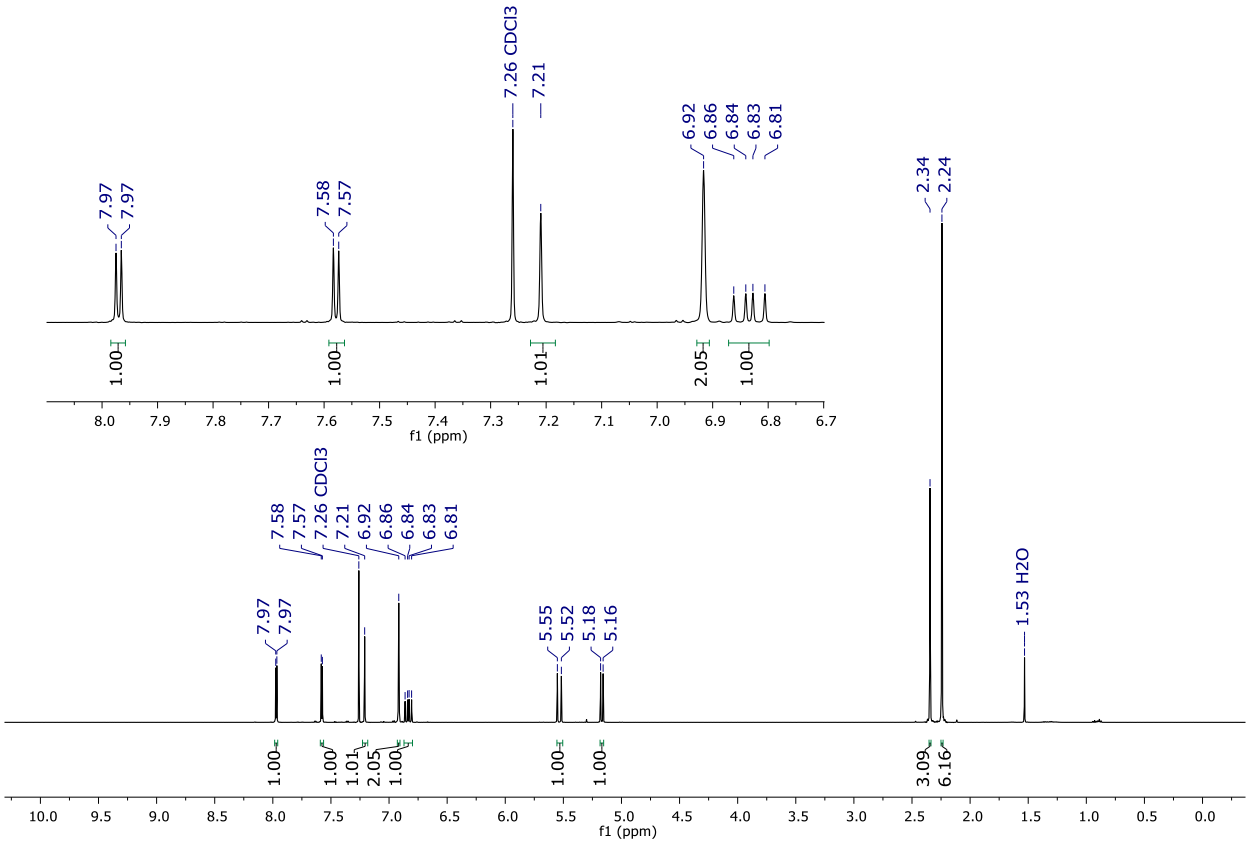

Figure S17: ^{1}H NMR spectrum of **16** ($CDCl_3$, 500 MHz).

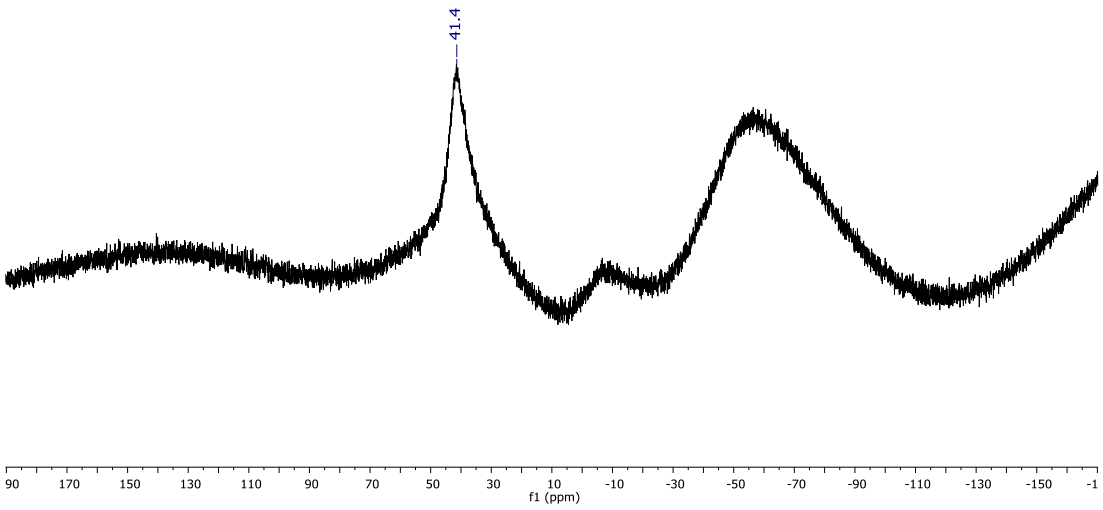

Figure S18: ^{11}B NMR spectrum of **16** ($CDCl_3$, 96 MHz).

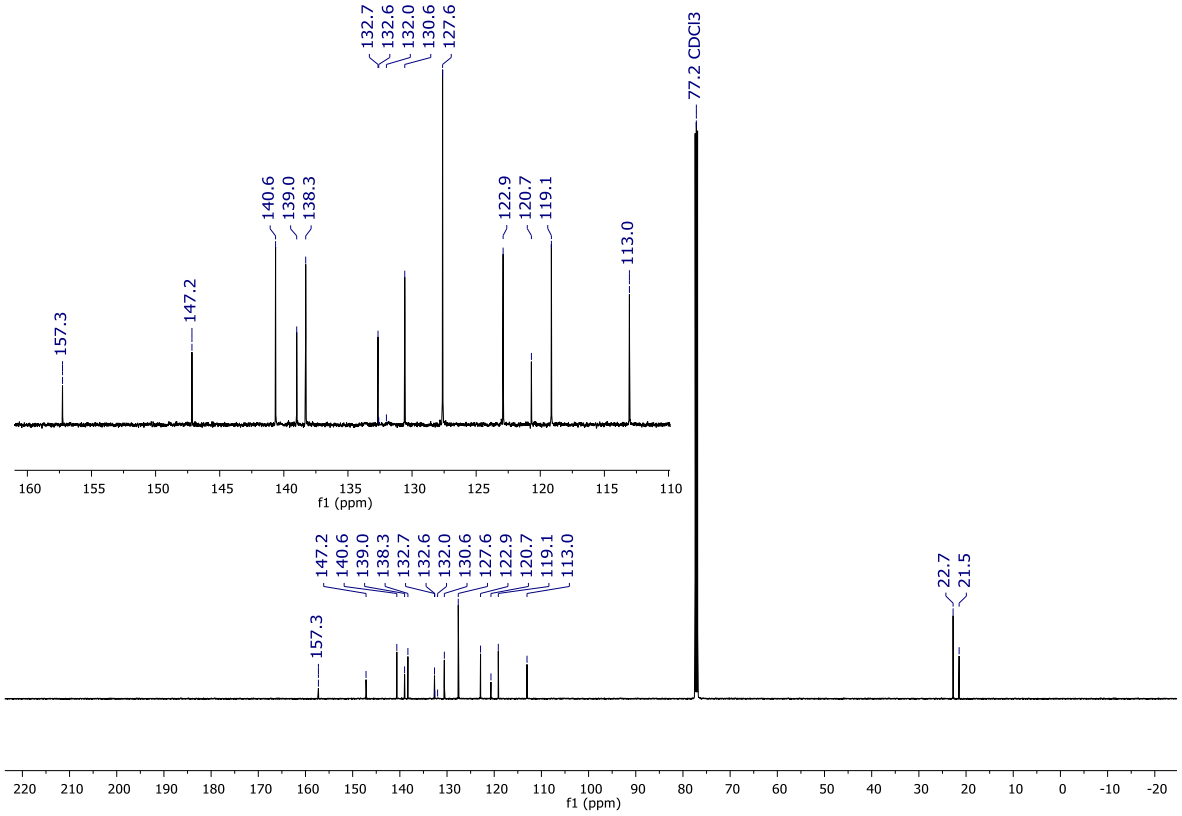

Figure S19: $^{13}C\{^{1}H\}$ NMR spectrum of **16** ($CDCl_3$, 126 MHz).

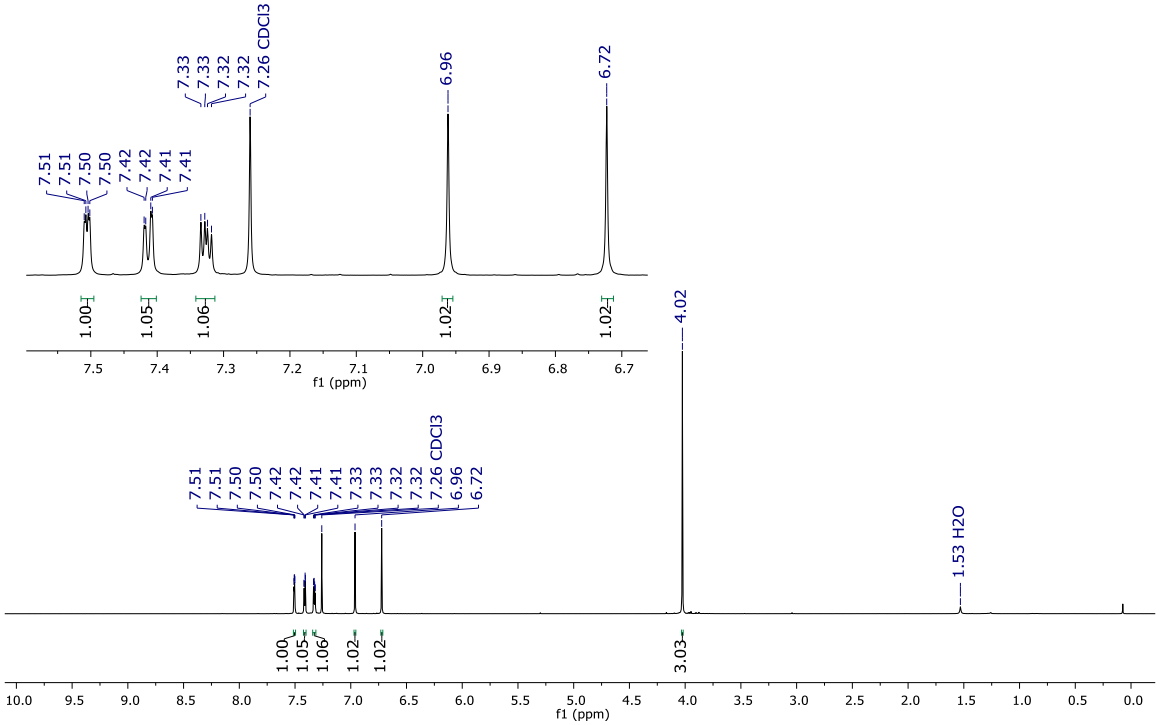

Figure S20: ^{1}H NMR spectrum of *trans*-**17** ($CDCl_3$, 500 MHz).

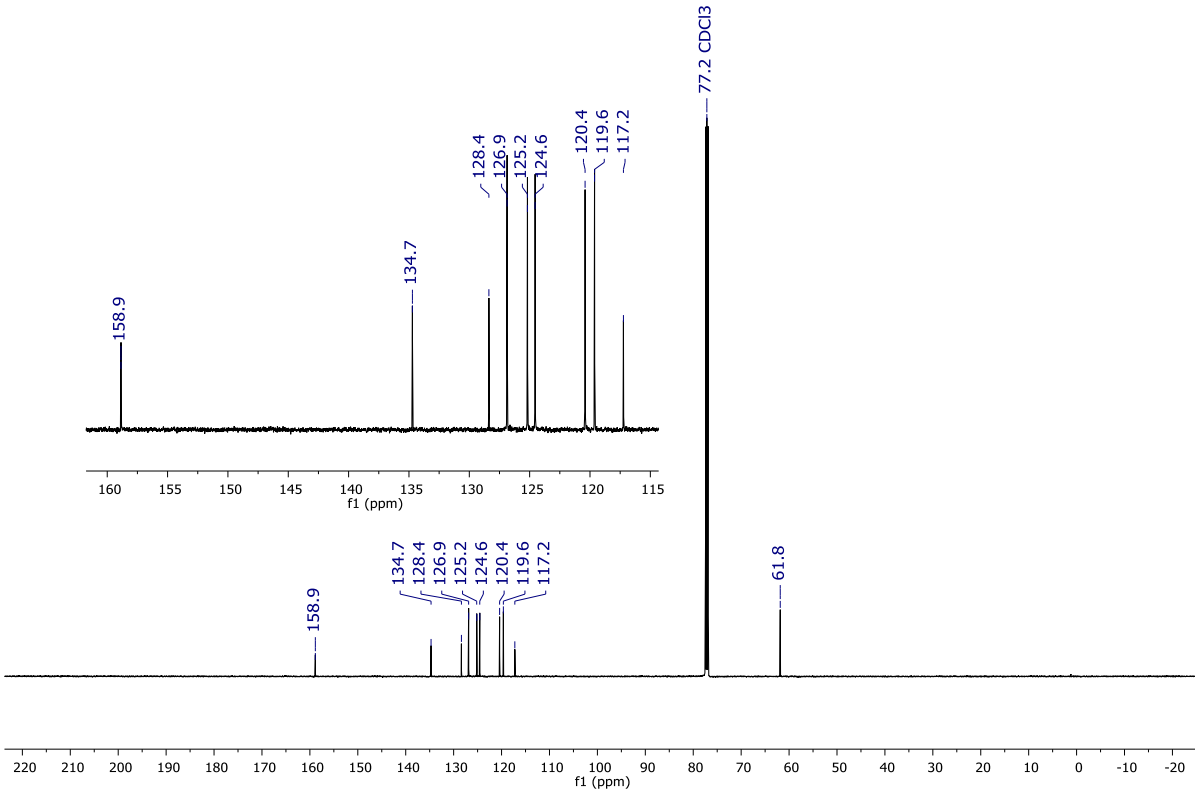

Figure S21: ^{13}C{^{1}H}NMR spectrum of *trans*-**17** ($CDCl_3$, 126 MHz).

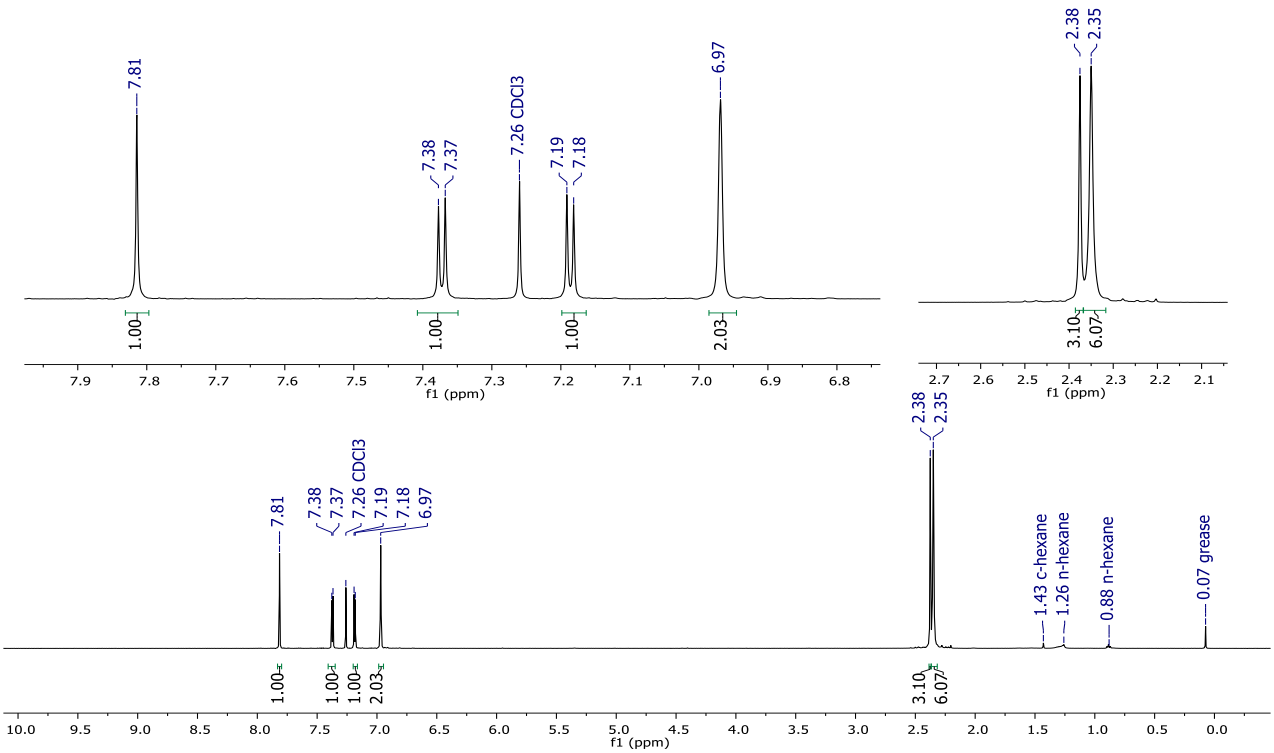

Figure S22: ^{1}H NMR spectrum of **1** ($CDCl_3$, 500 MHz).

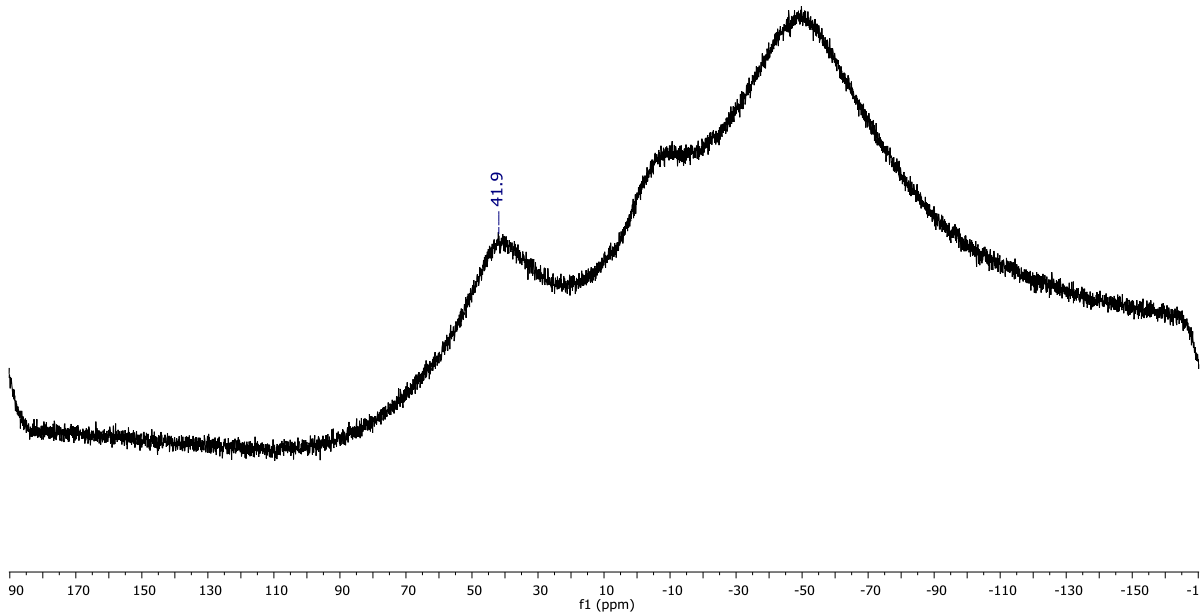

Figure S23: ^{11}B NMR spectrum of **1** ($CDCl_3$, 96 MHz).

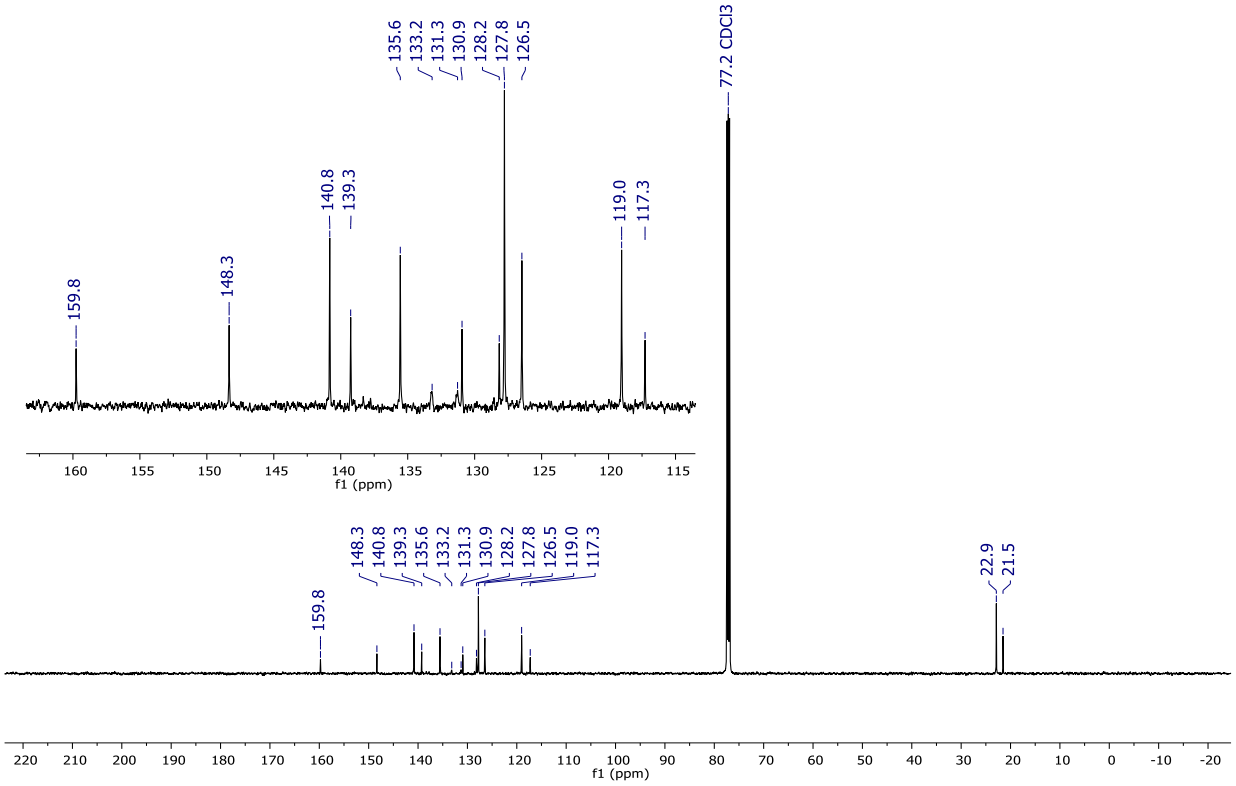

Figure S24: $^{13}C\{^{1}H\}$NMR spectrum of **1** ($CDCl_3$, 126 MHz).

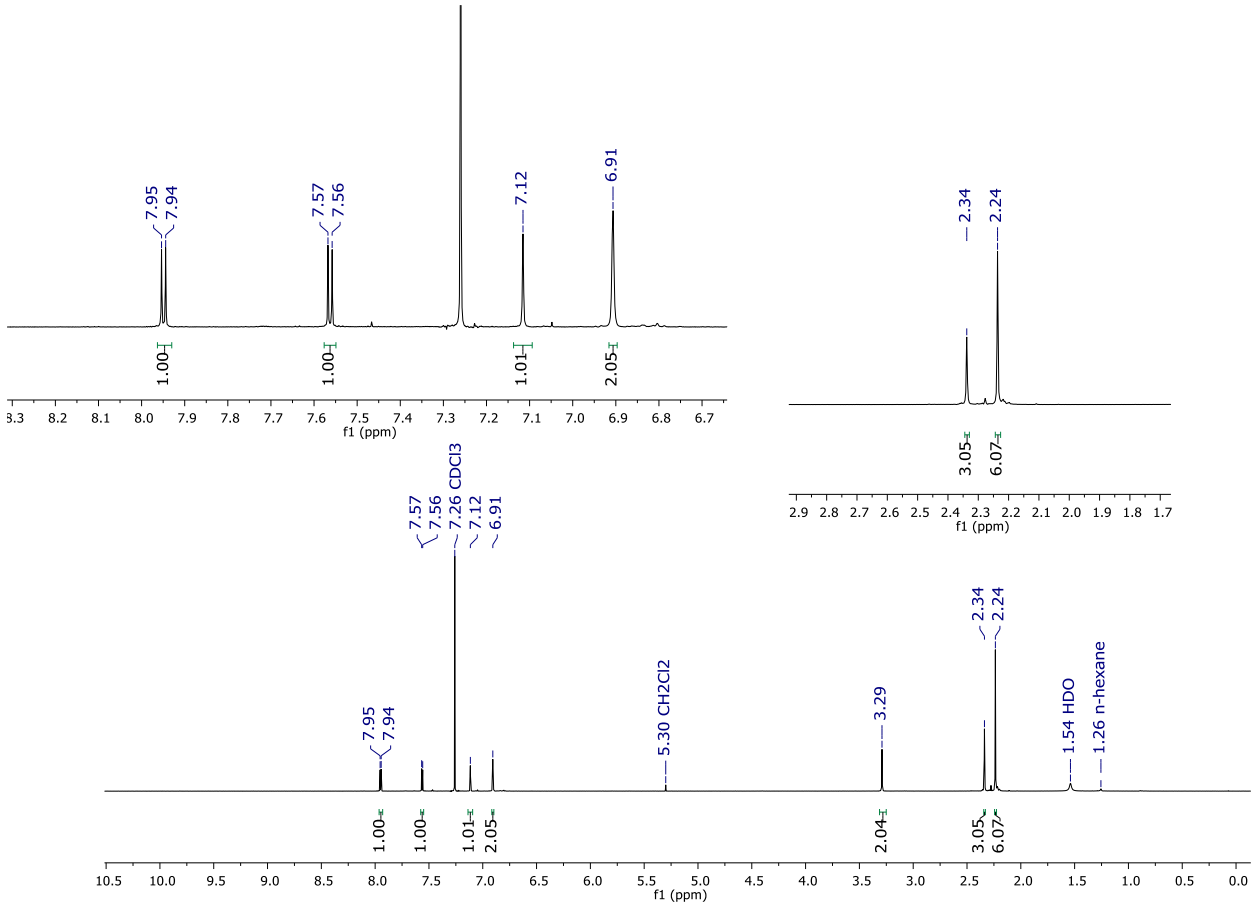

Figure S25: ^{1}H NMR spectrum of **15H2** ($CDCl_3$, 500 MHz).

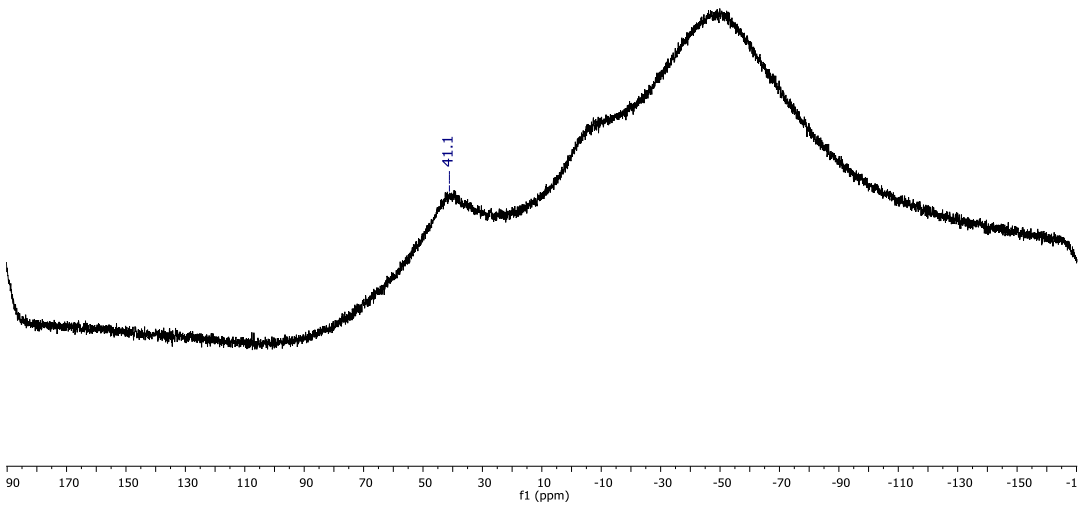

Figure S26: ^{11}B NMR spectrum of **15H2** ($CDCl_3$, 96 MHz).

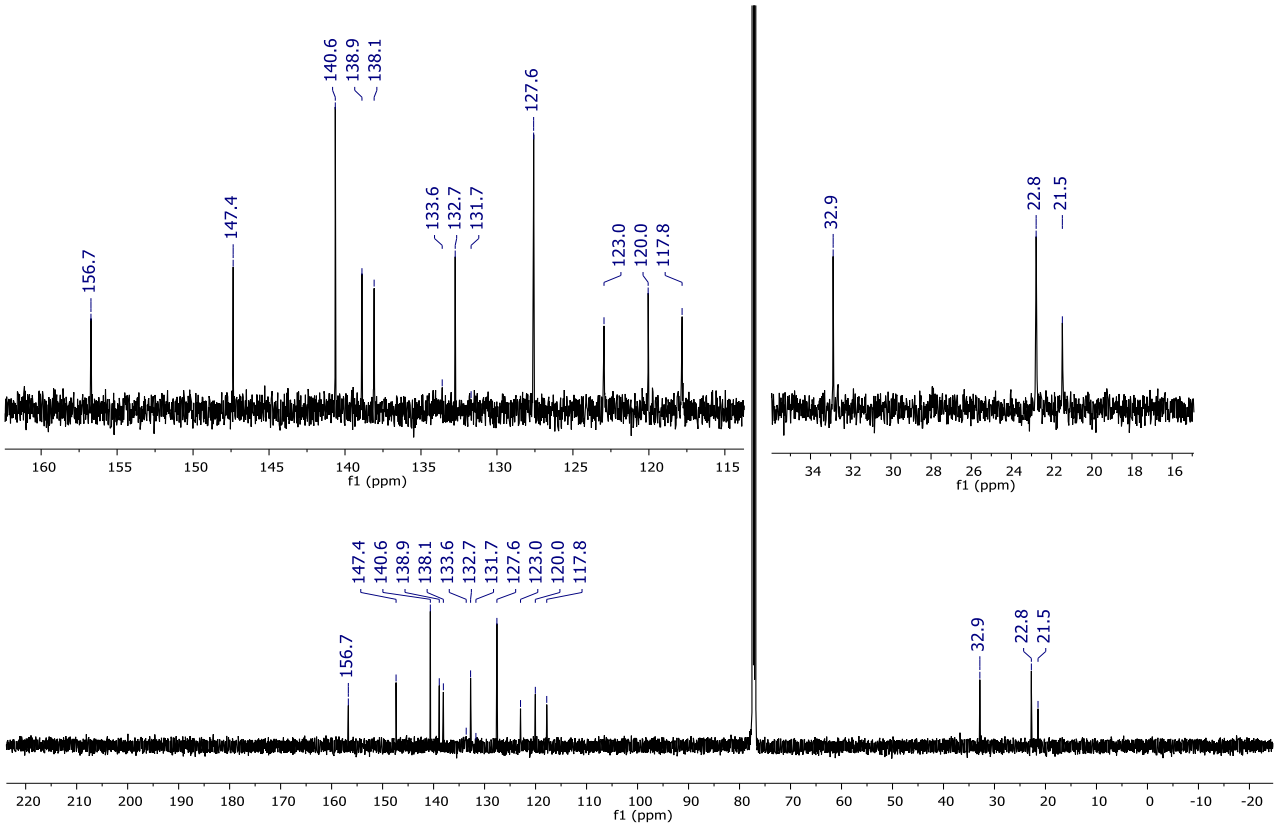

Figure S27: $^{13}C\{^{1}H\}$ NMR spectrum of **15H2** ($CDCl_3$, 126 MHz).

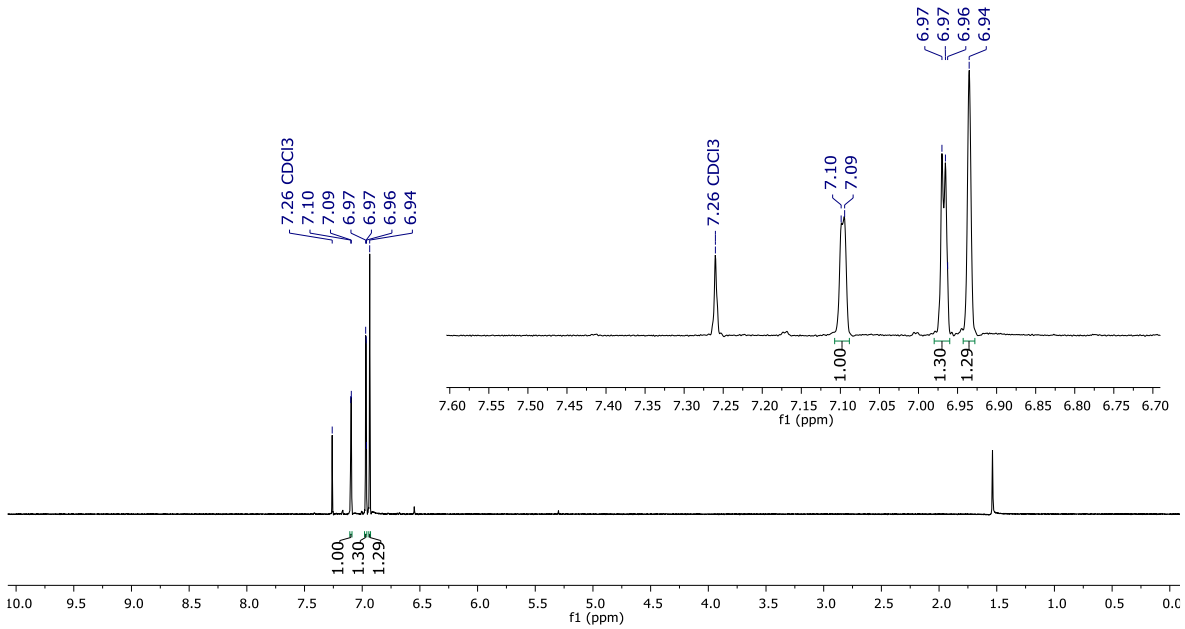

Figure S28: $^{13}C\{^{1}H\}$ NMR spectrum of *trans*-**20** ($CDCl_3$, 300 MHz).

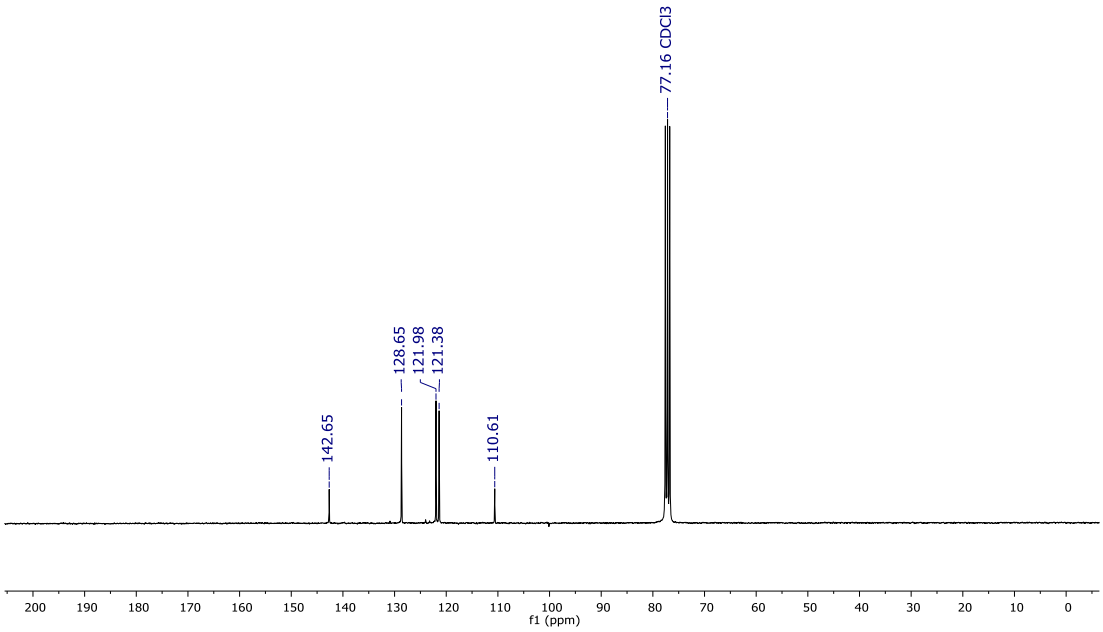

Figure S29: $^{13}C\{^{1}H\}$ NMR spectrum of *trans*-**20** ($CDCl_3$, 75 MHz).

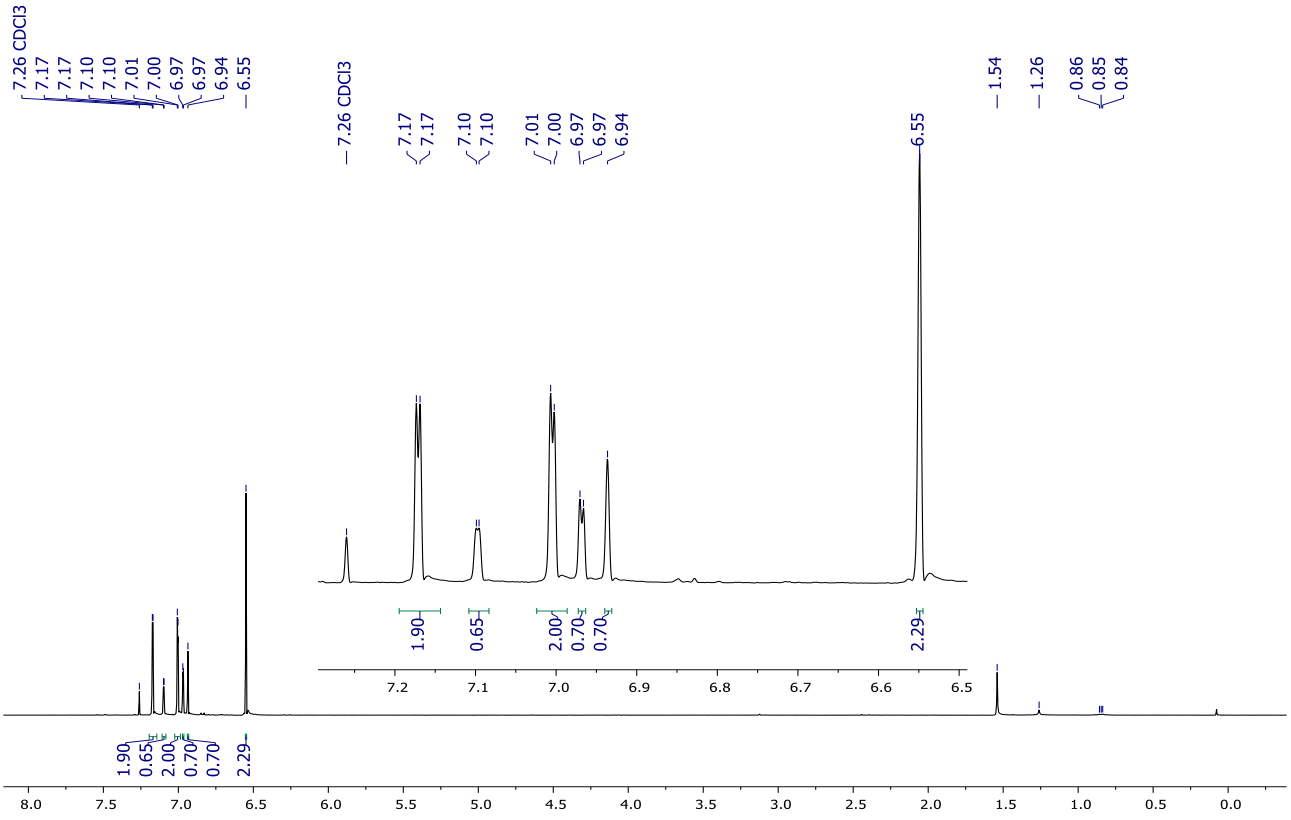

Figure S30: ^{1}H NMR spectrum of a cis/*trans*-**20** (≈3:1) mixture ($CDCl_3$, 300 MHz).

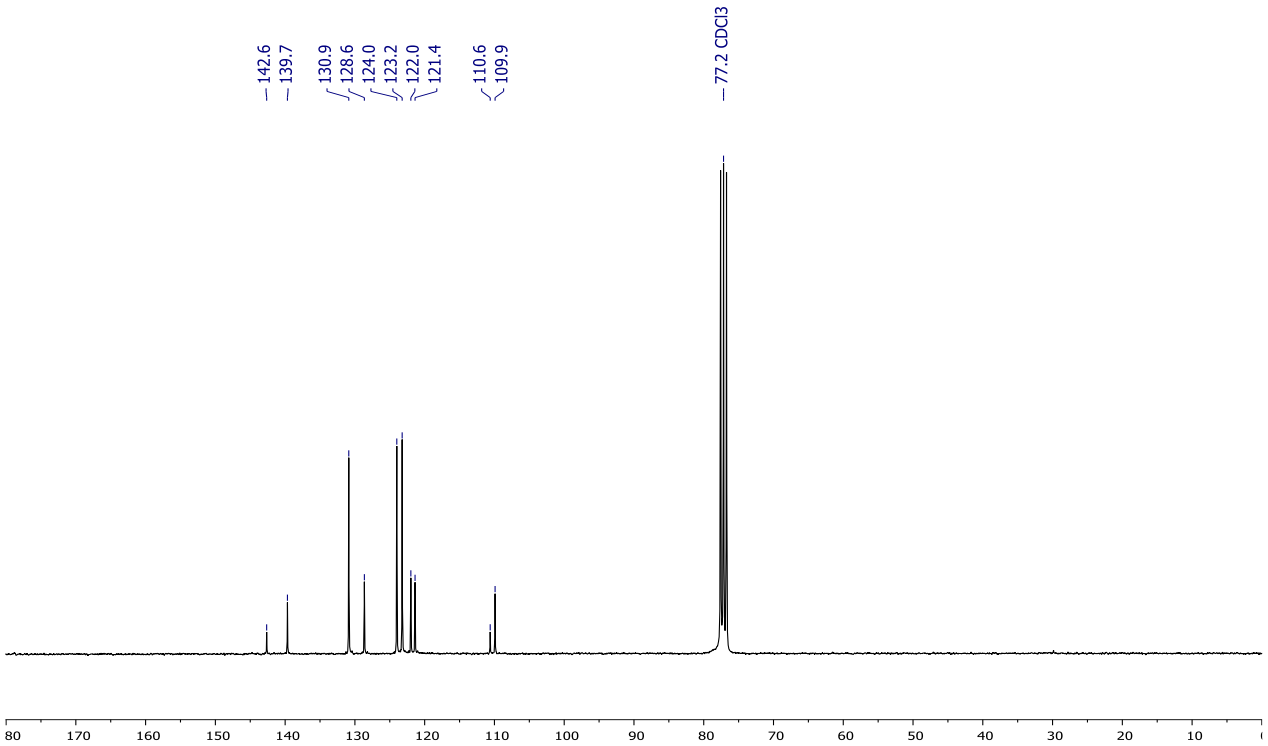

Figure S31: ^{13}C{^{1}H} NMR spectrum of a cis/*trans*-**20** (≈3:1) mixture ($CDCl_3$, 75 MHz).

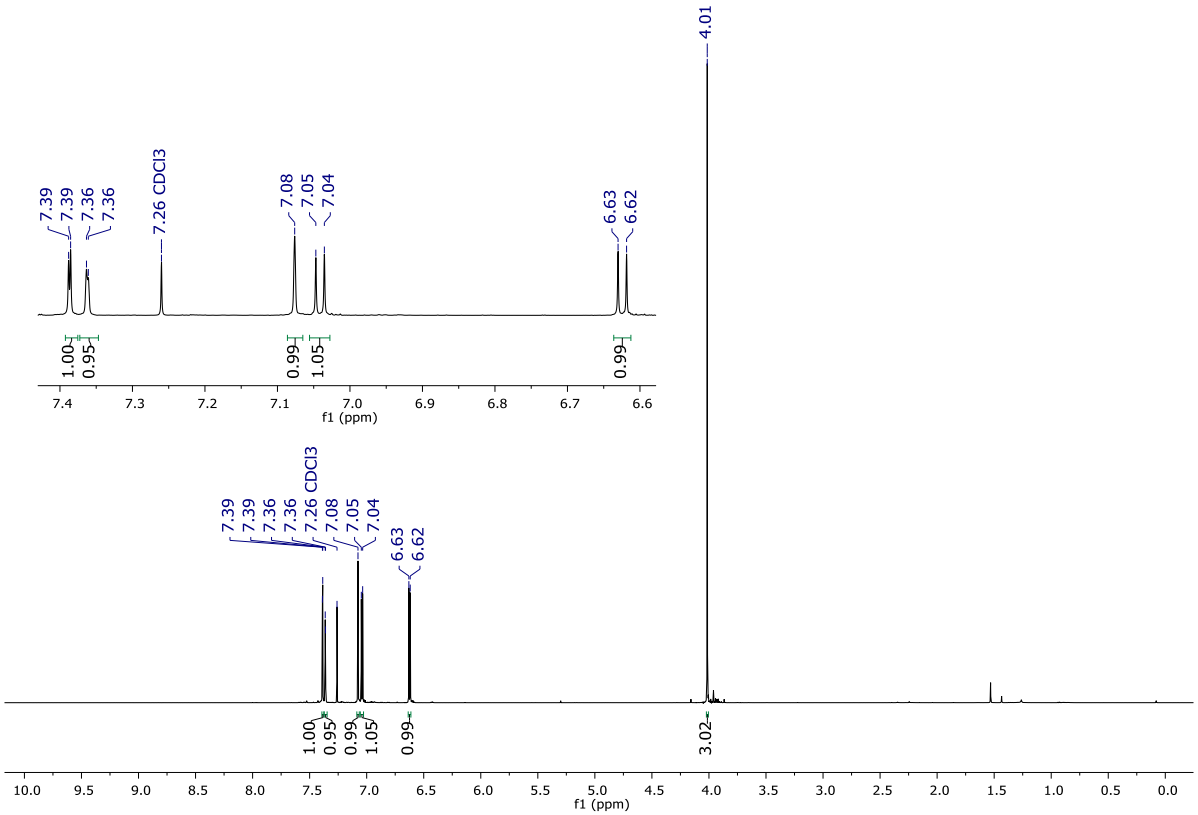

Figure S32: ^{1}H NMR spectrum of *trans*-**19** ($CDCl_3$, 500 MHz).

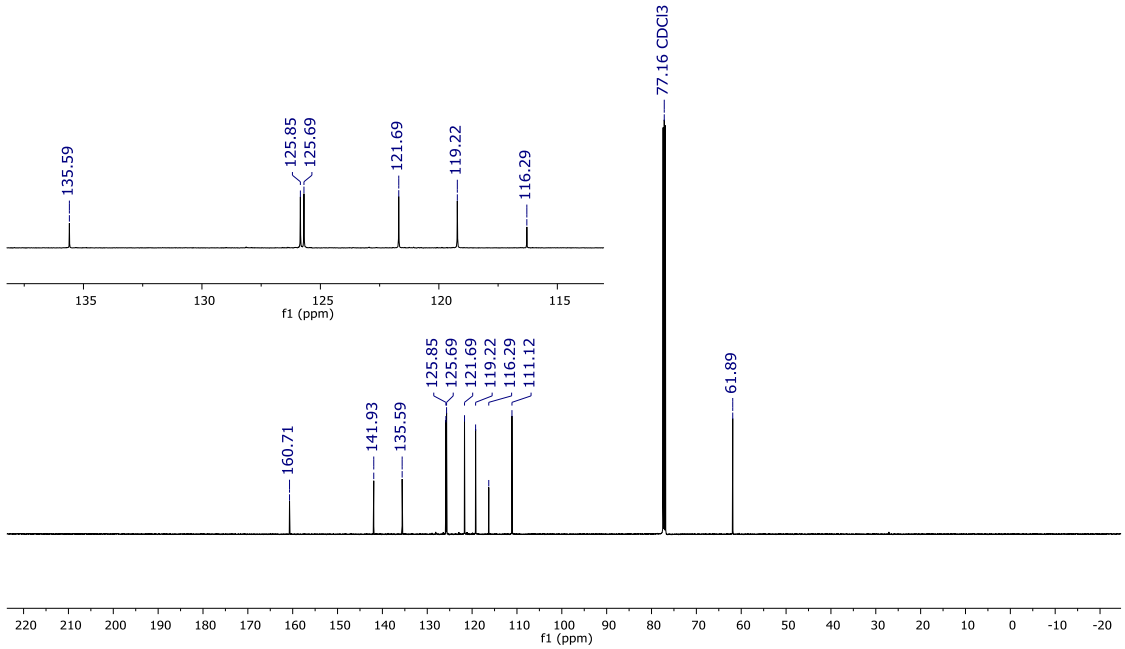

Figure S33: ^{13}C{^{1}H} NMR spectrum of *trans*-**19** ($CDCl_3$, 126 MHz).

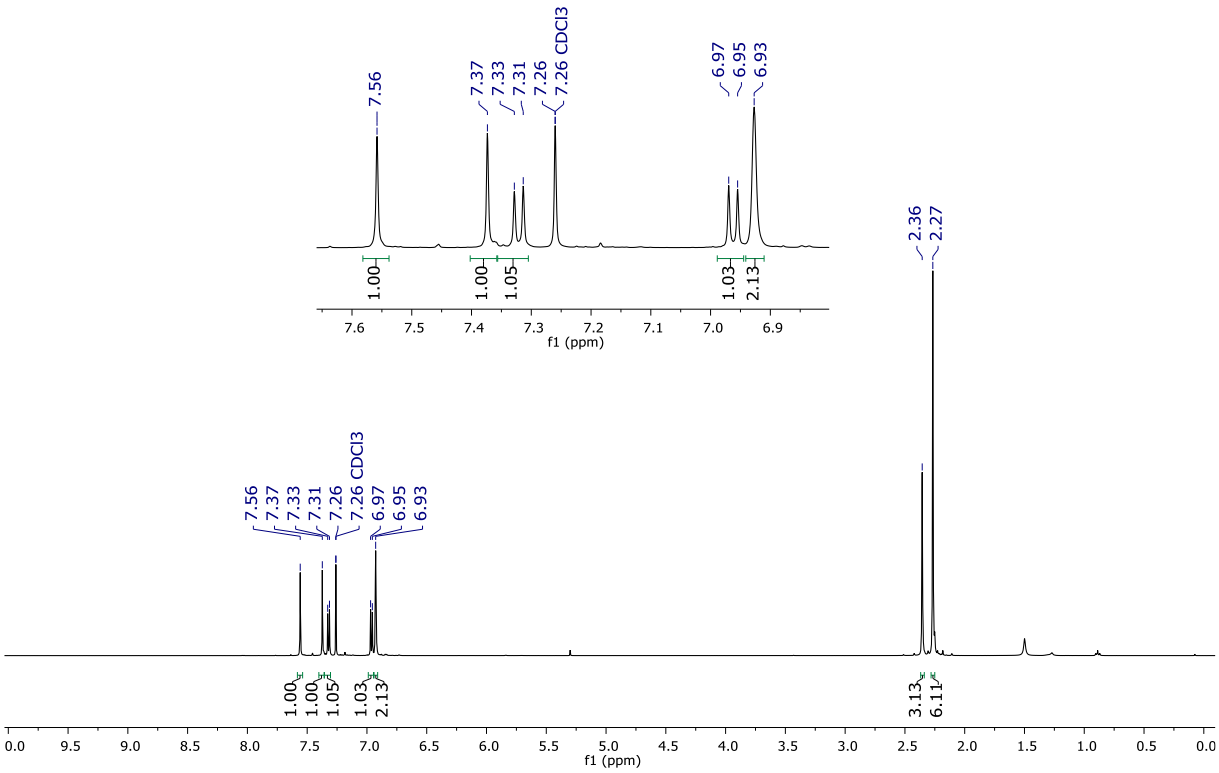

Figure S34: ^{1}H NMR spectrum of *trans*-**18** ($CDCl_3$, 400 MHz).

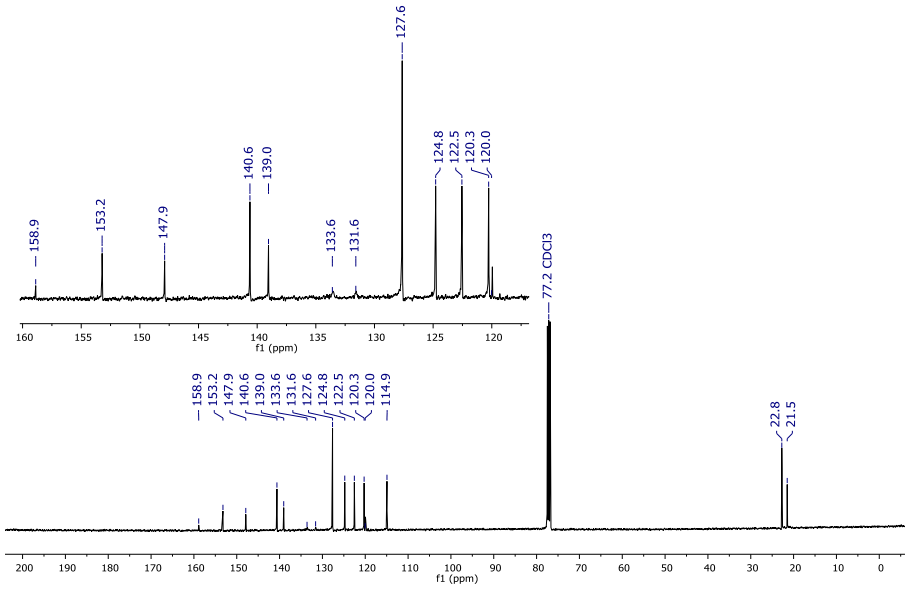

Figure S35: $^{13}C\{^{1}H\}$ NMR spectrum of *trans*-**18** ($CDCl_3$, 101 MHz).

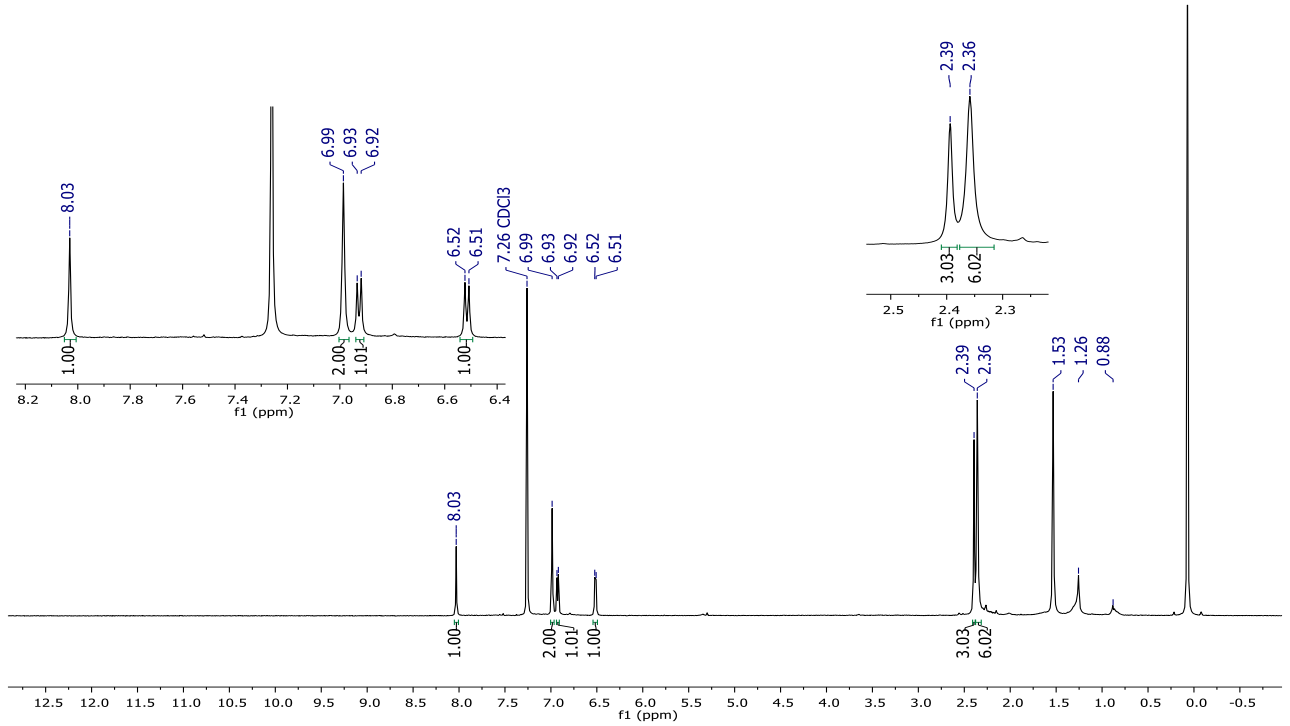

Figure S36: ^{1}H NMR spectrum of **2** ($CDCl_3$, 400 MHz).

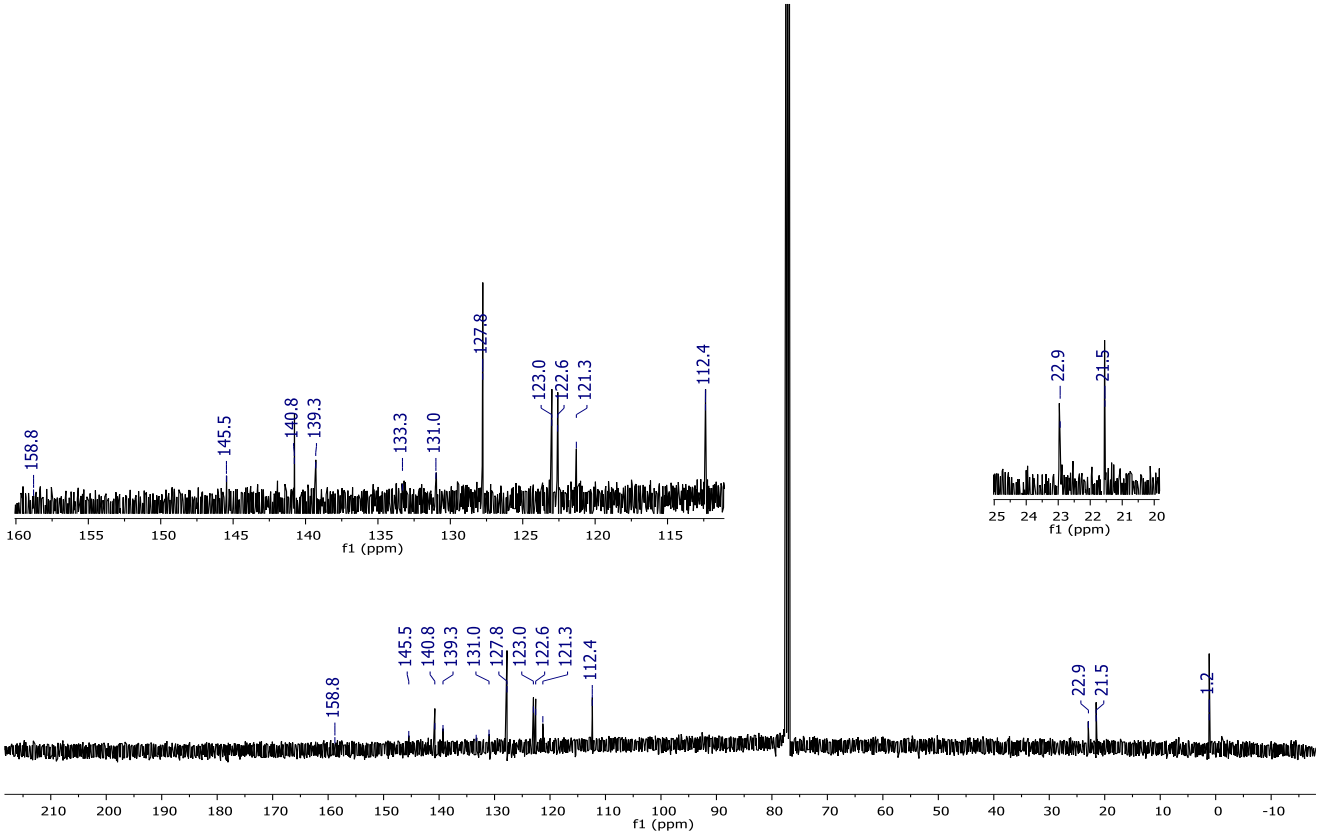

Figure S37: $^{13}C\{^{1}H\}$ NMR spectrum of **2** ($CDCl_3$, 101 MHz).

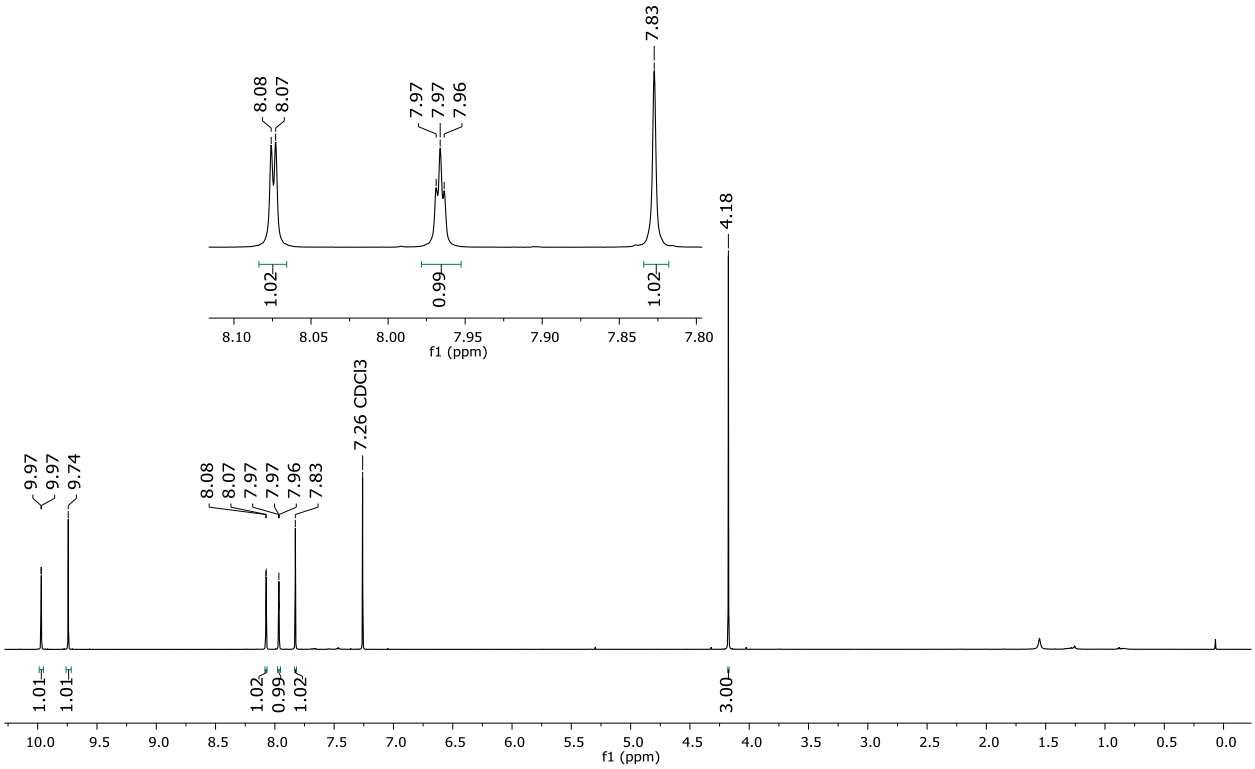

Figure S38: ^{1}H NMR spectrum of **22** ($CDCl_3$, 500 MHz).

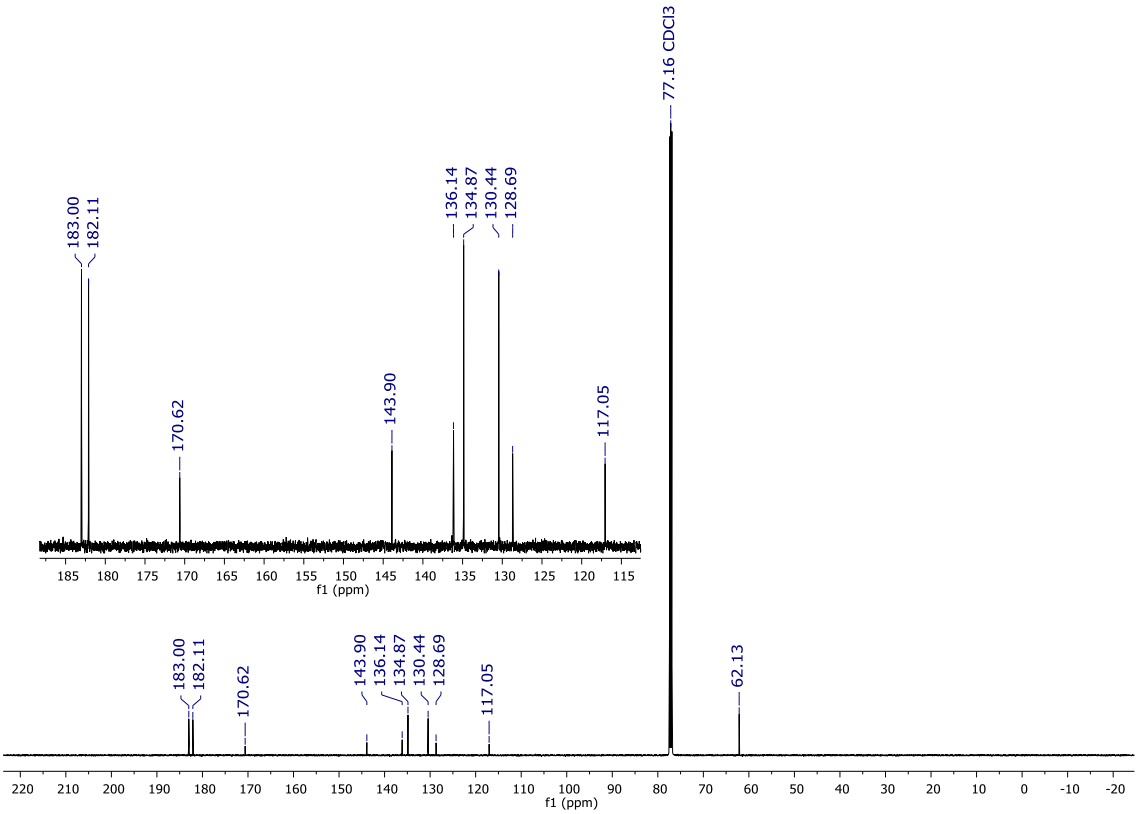

Figure S39: ^{13}C{^{1}H} NMR spectrum of **22** ($CDCl_3$, 126 MHz).

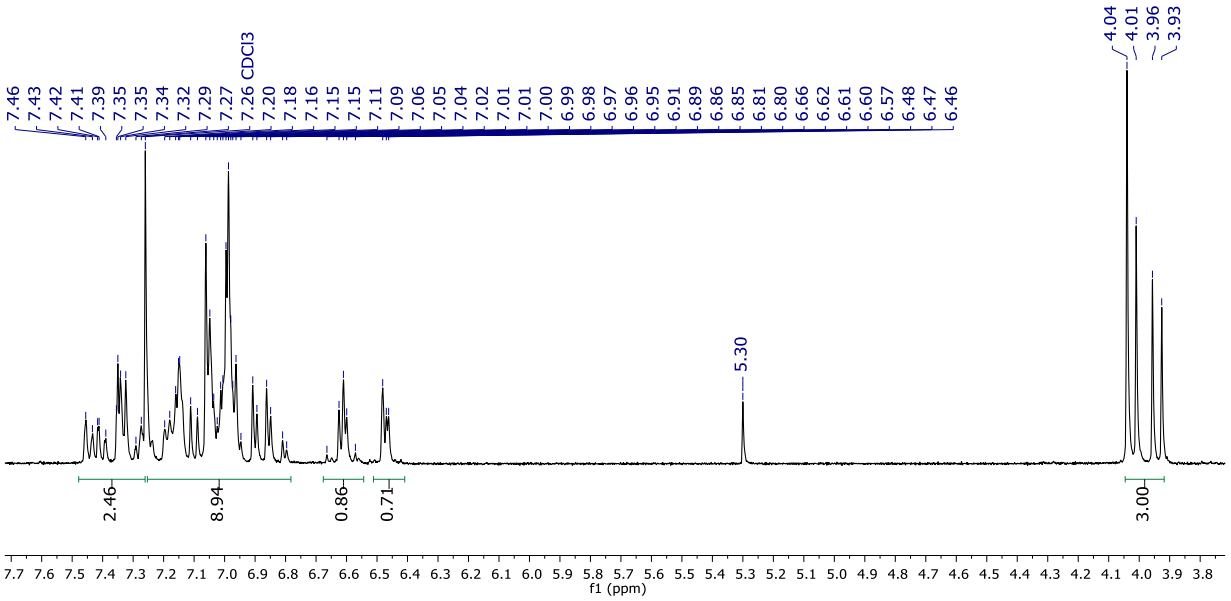

Figure S40: ^{1}H NMR spectrum of **23** mixture of isomers afer column chromatography ($CDCl_3$, 300 MHz).

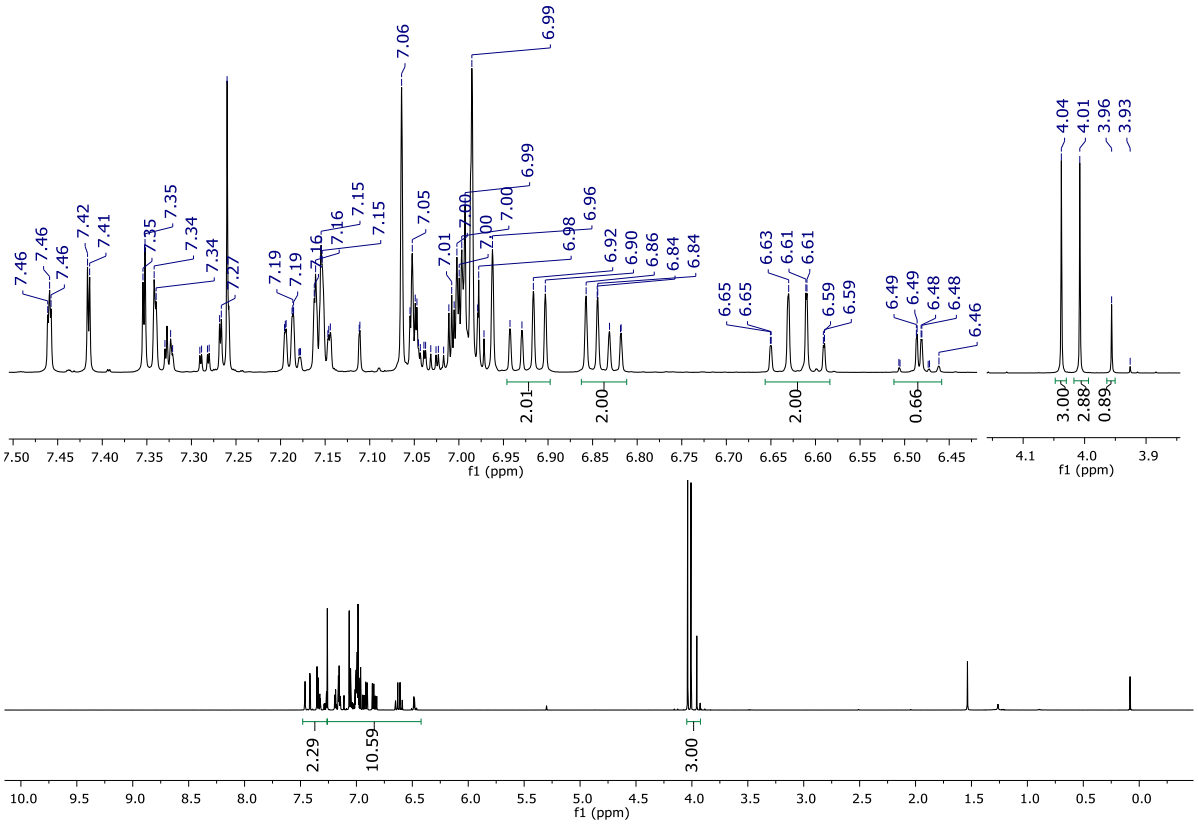

Figure S41: ^{1}H NMR spectrum of **23** after Et_2O and *n*-pentane washings ($CDCl_3$, 500 MHz).

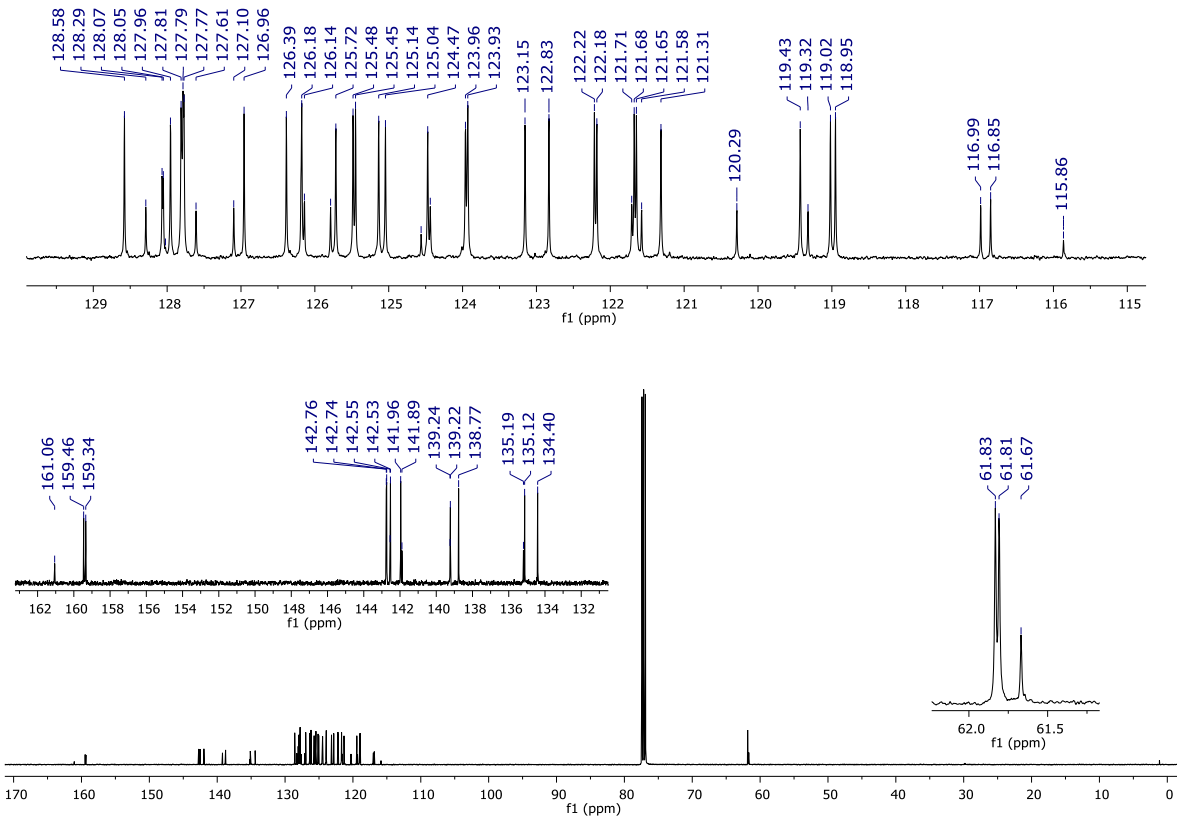

Figure S42: $^{13}C\{^{1}H\}$ NMR spectrum of **23** after Et_2O and *n*-pentane washings ($CDCl_3$, 126 MHz).

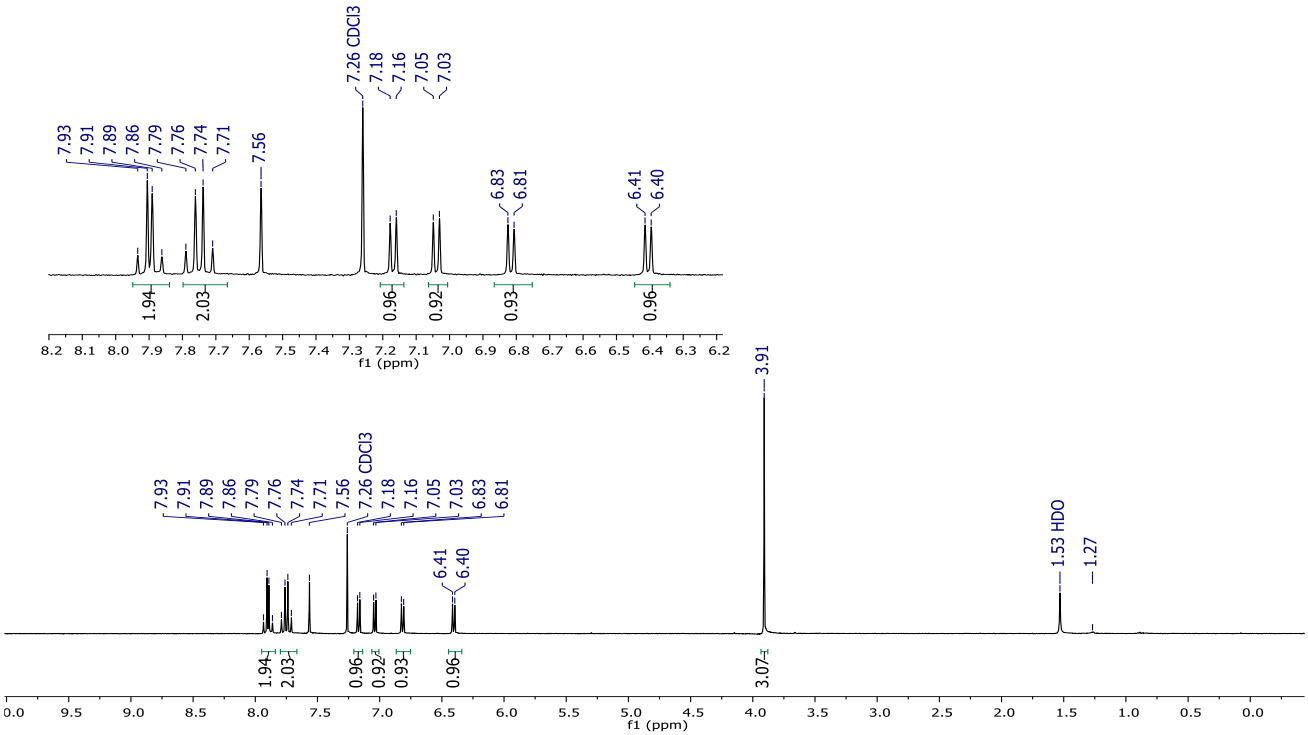

Figure S43: ^{1}H NMR spectrum of **21** ($CDCl_3$, 300 MHz).

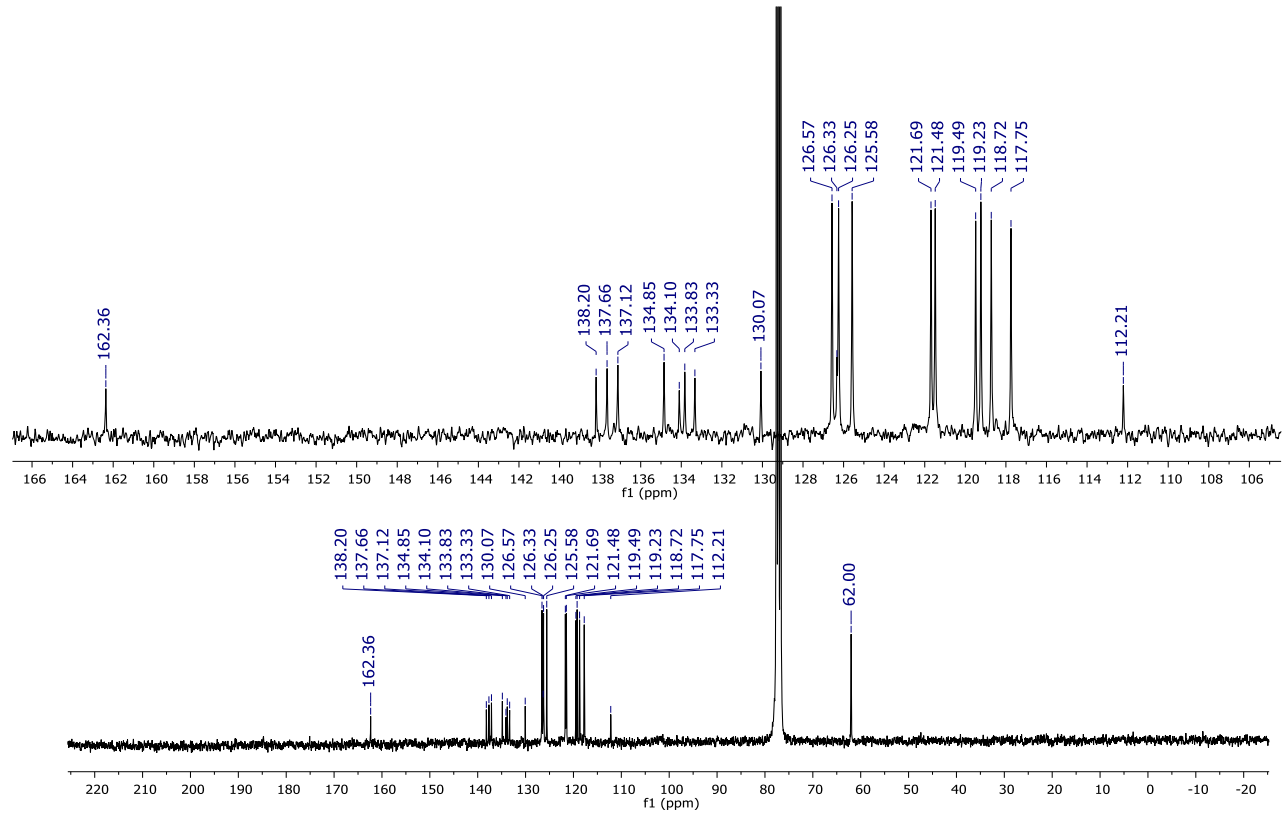

Figure S44: $^{13}C\{^{1}H\}$ NMR spectrum of **21** ($CDCl_3$, 75 MHz).

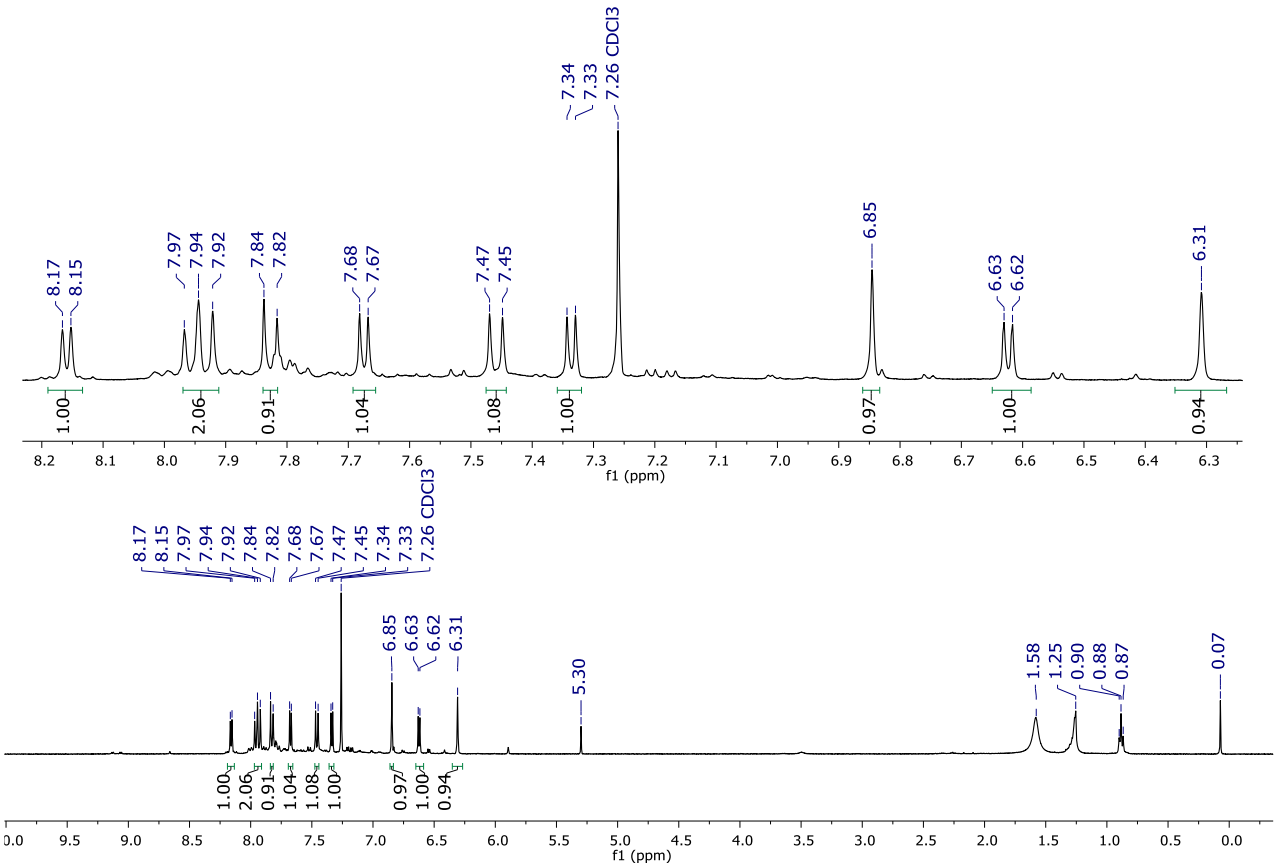

Figure S45: ^{1}H NMR spectrum of **21** ($CDCl_3$, 400 MHz).

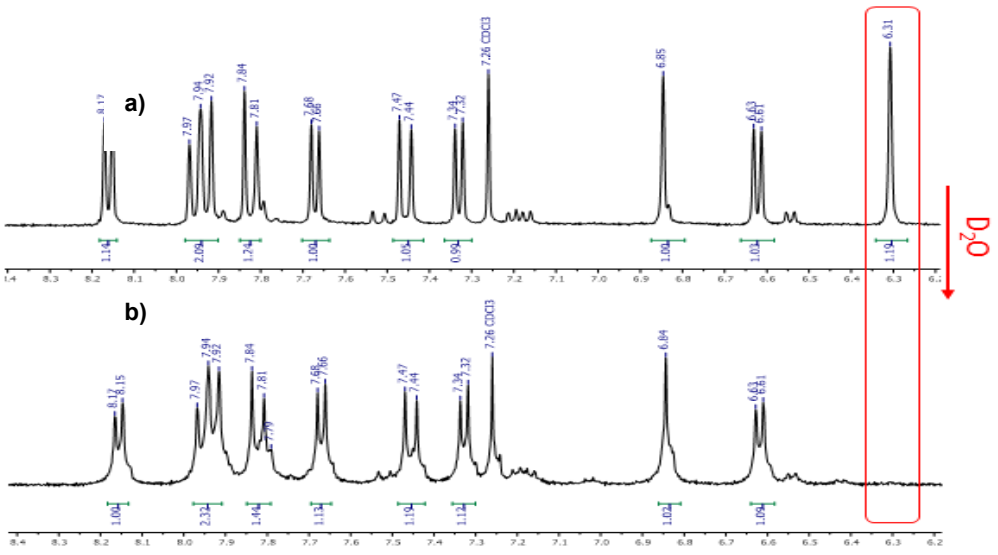

Figure S45A: Deuteration test of **21-OH**, ^{1}H NMR spectrum ($CDCl_3$, 400 MHz). a) ^{1}H NMR of the **21-OH** sample; b) ^{1}H NMR of **21-OH** after the addition of D_2O.

The proton at 6.31 ppm (assigned to the -OH group) disappears after the addition of D_2O, red box.

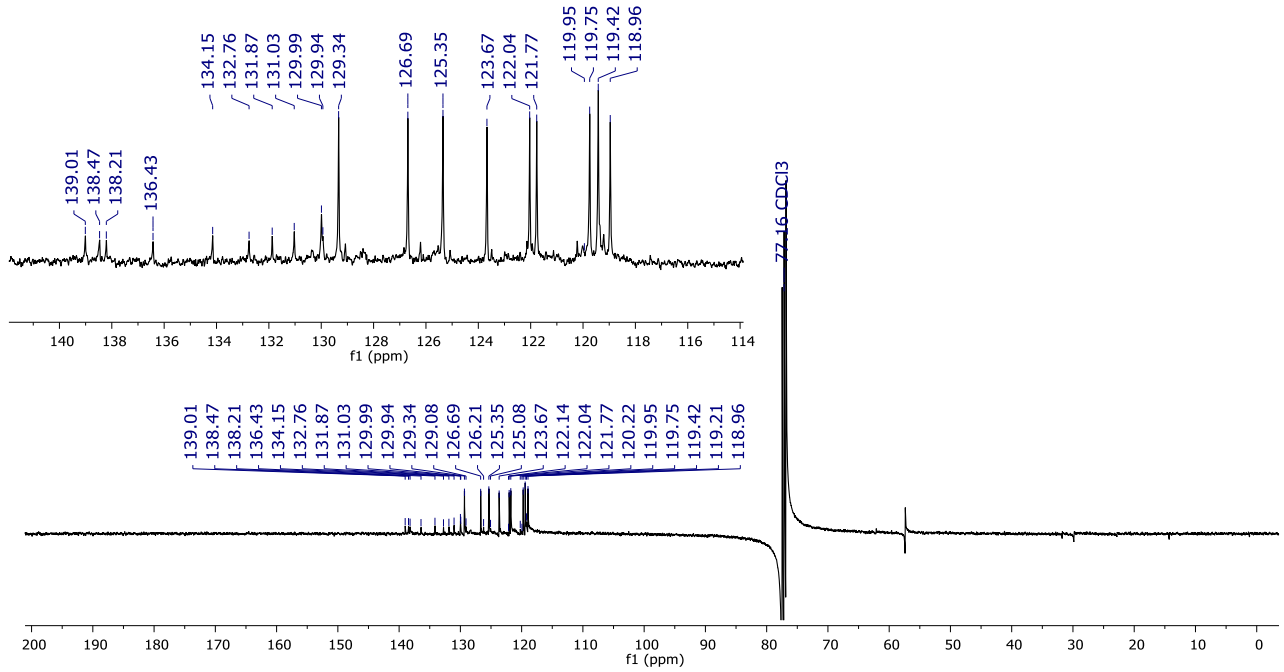

Figure S46: $^{13}C\{^{1}H\}$ NMR spectrum of **21-OH** ($CDCl_3$, 101 MHz).

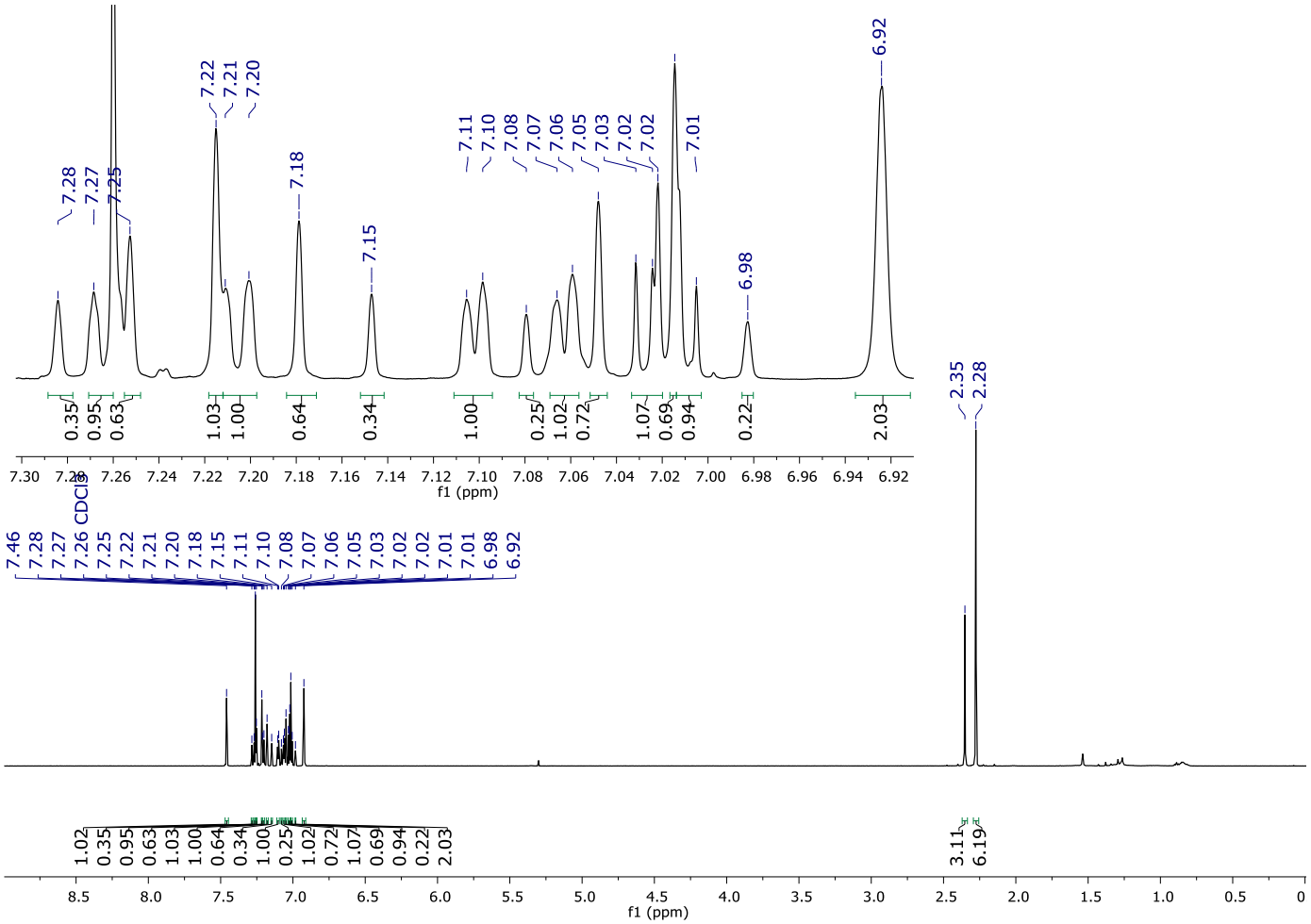

Figure S47: ^{1}H NMR spectrum of *trans,trans*-**25** ($CDCl_3$, 500 MHz).

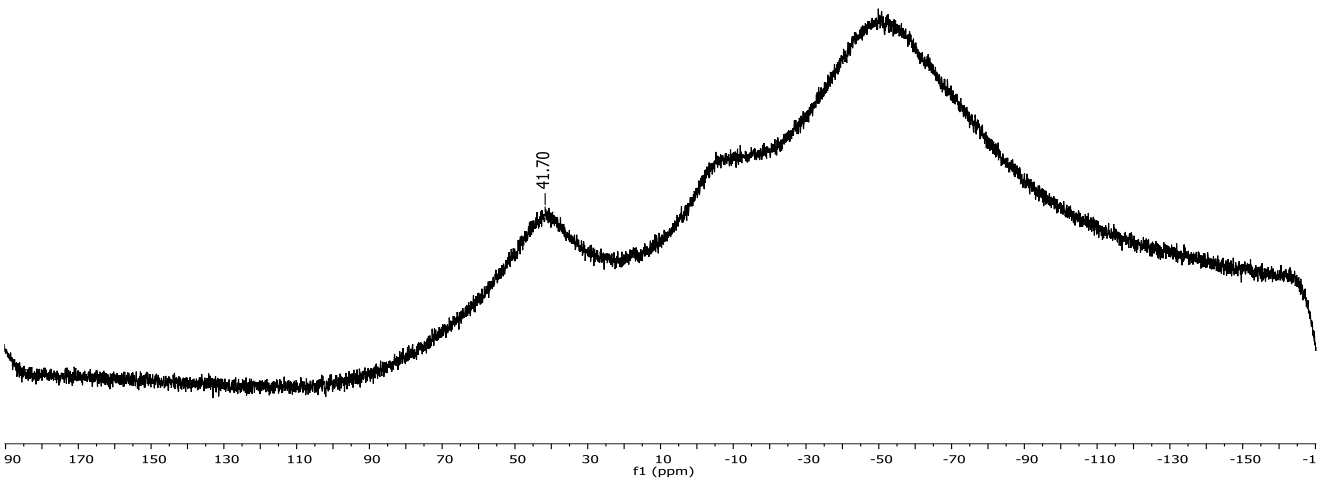

Figure S48: ^{11}B NMR spectrum of **25** ($CDCl_3$, 96 MHz).

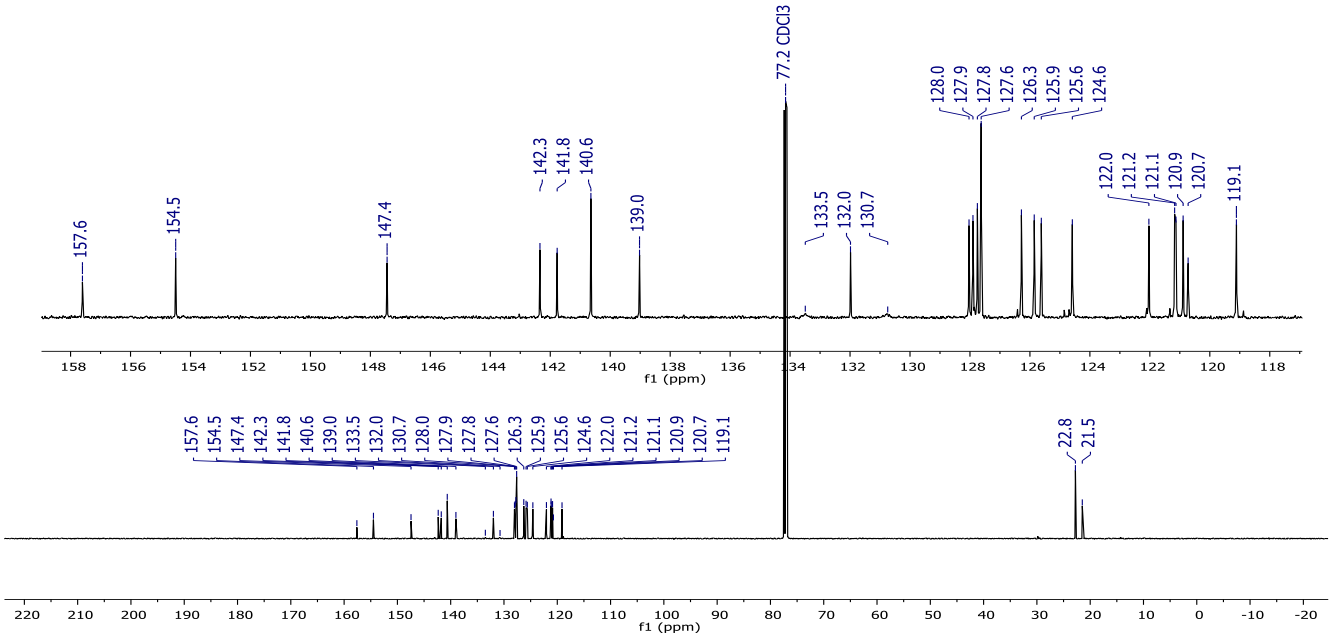

Figure S49: $^{13}C\{^{1}H\}$ NMR spectrum of **25** ($CDCl_3$, 500 MHz).

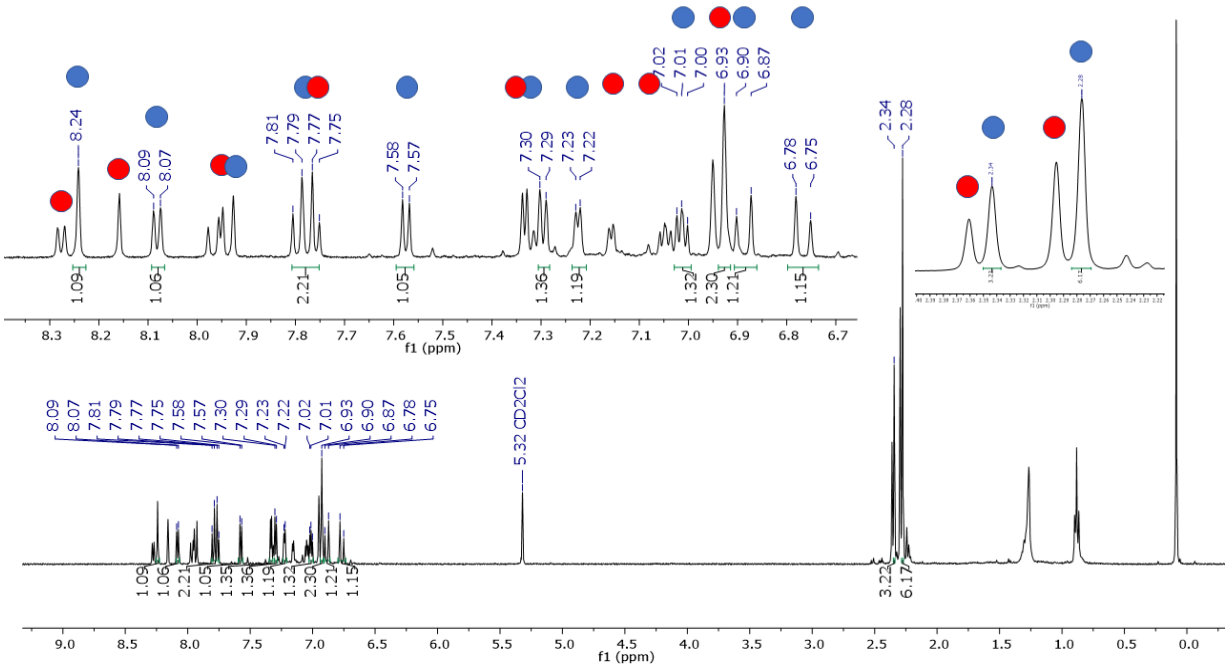

Figure S50: ^{1}H NMR spectrum of a *trans*/cis-**26** (≈40:60) mixture (CD_2Cl_2, 400 MHz). Blue circles indicates *cis*-isomer proton resonances; red circles indicates *trans*-isomer resonances.

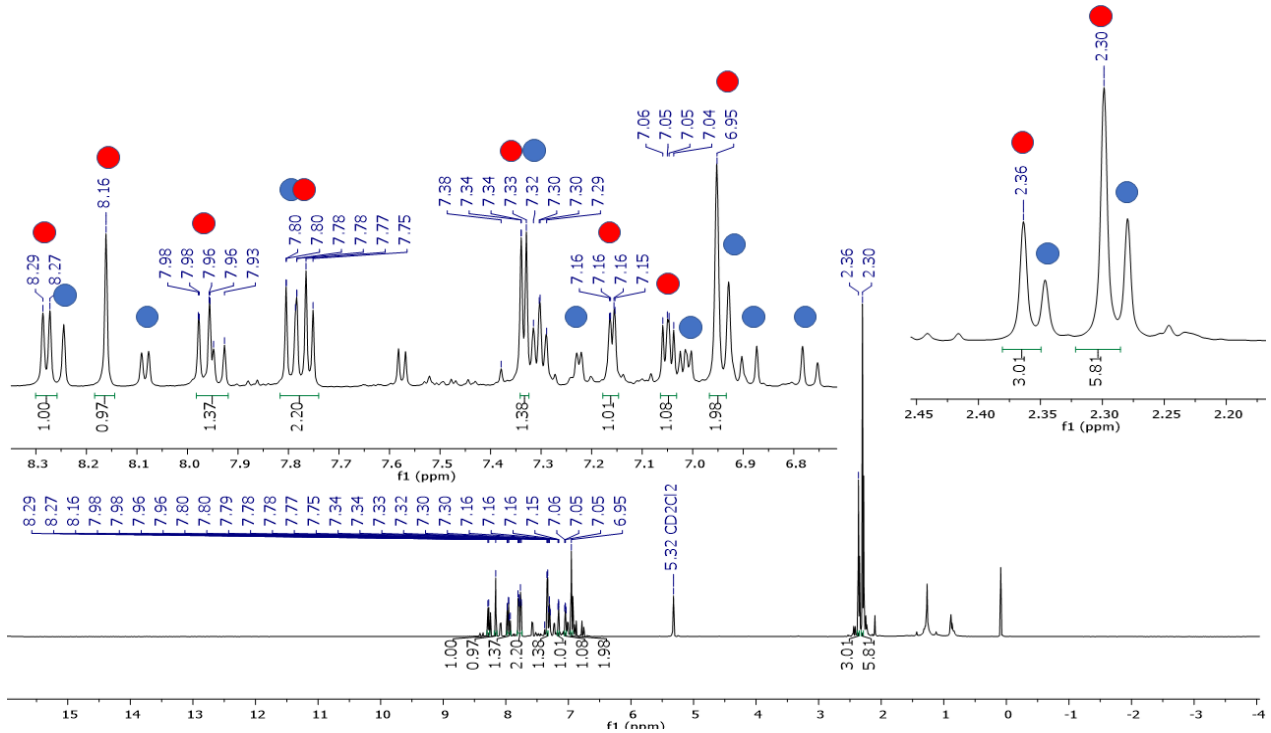

Figure S51: ^{1}H NMR spectrum of a *trans*/cis-**26** (≈60:40) mixture (CD_2Cl_2, 400 MHz). Blue circles indicates *cis*-isomer proton resonances; red circles indicates *trans*-isomer resonances.

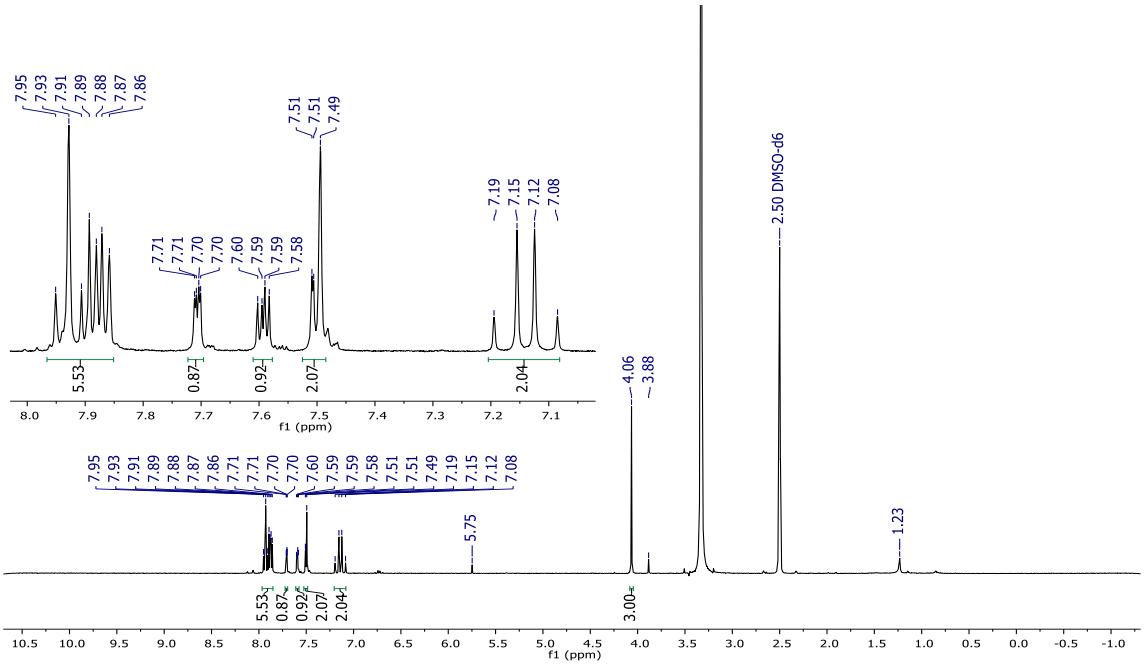

Figure S52: ^{1}H NMR spectrum of ***trans*-28** (DMSO, 400 MHz).

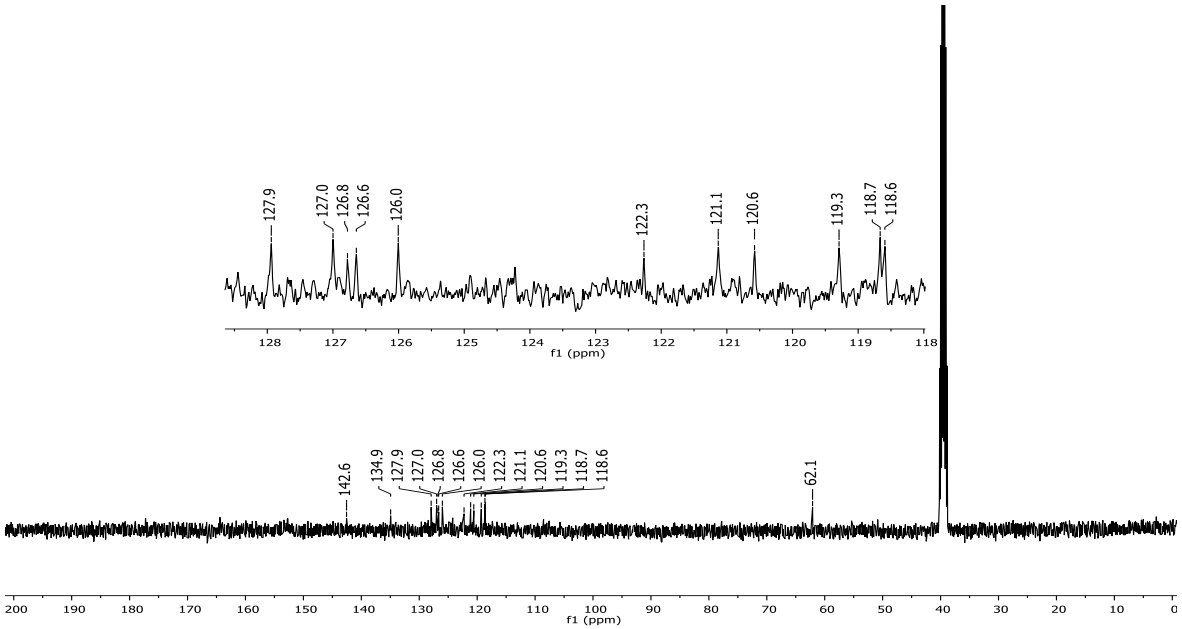

Figure S53: ^{13}C{^{1}H} NMR spectrum of ***trans*-28** (DMSO, 101 MHz).

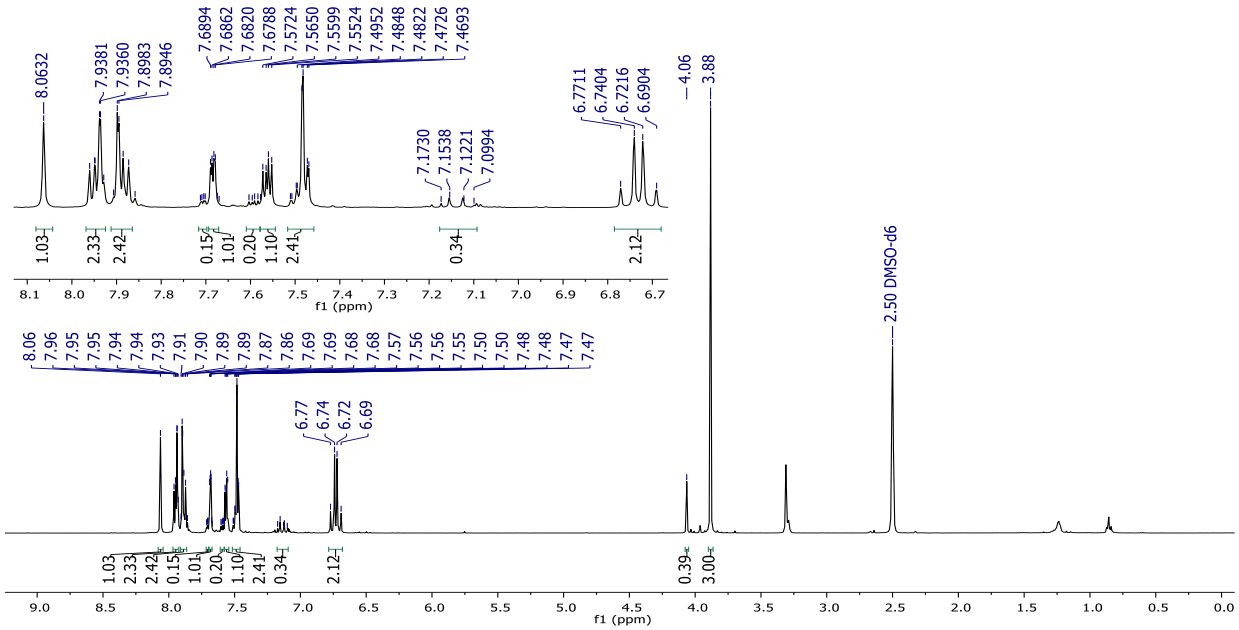

Figure S54: ^{1}H NMR spectrum of ***cis*-28** (DMSO, 400 MHz).

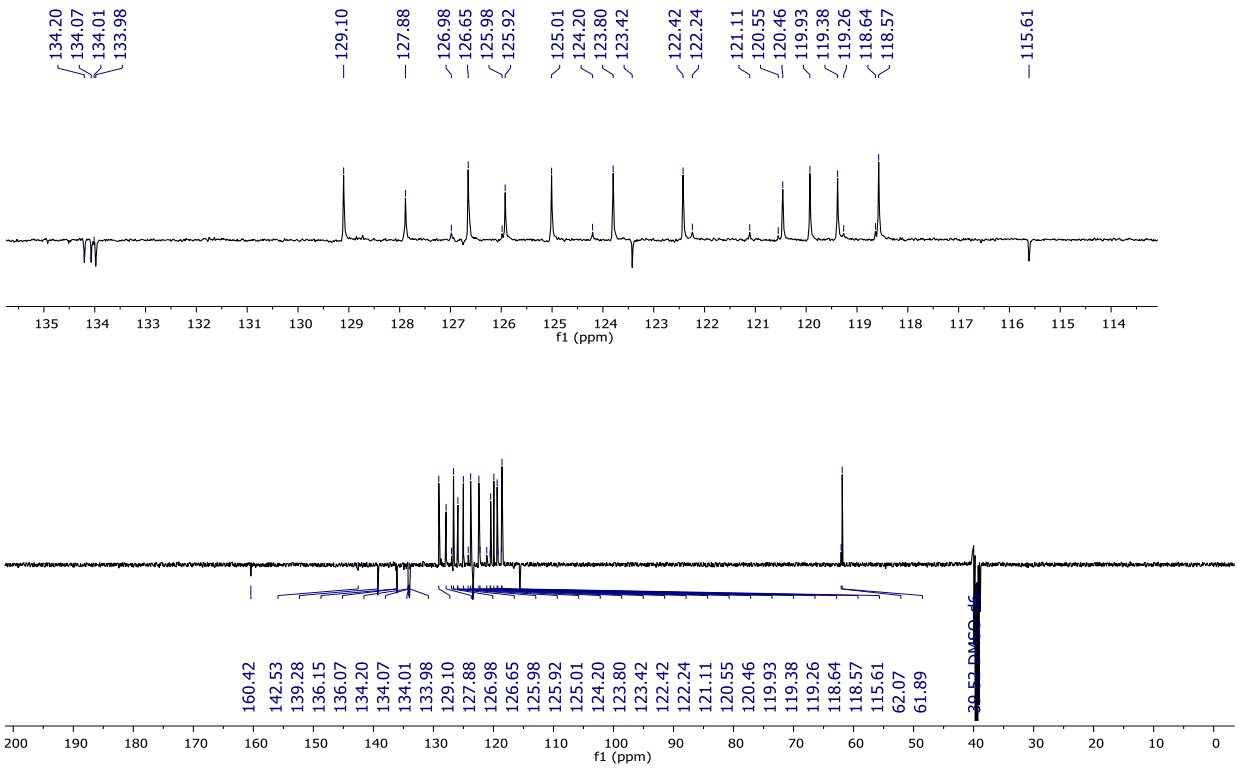

Figure S55: ^{13}C APT NMR spectrum of ***cis*-28** (DMSO, 101 MHz).

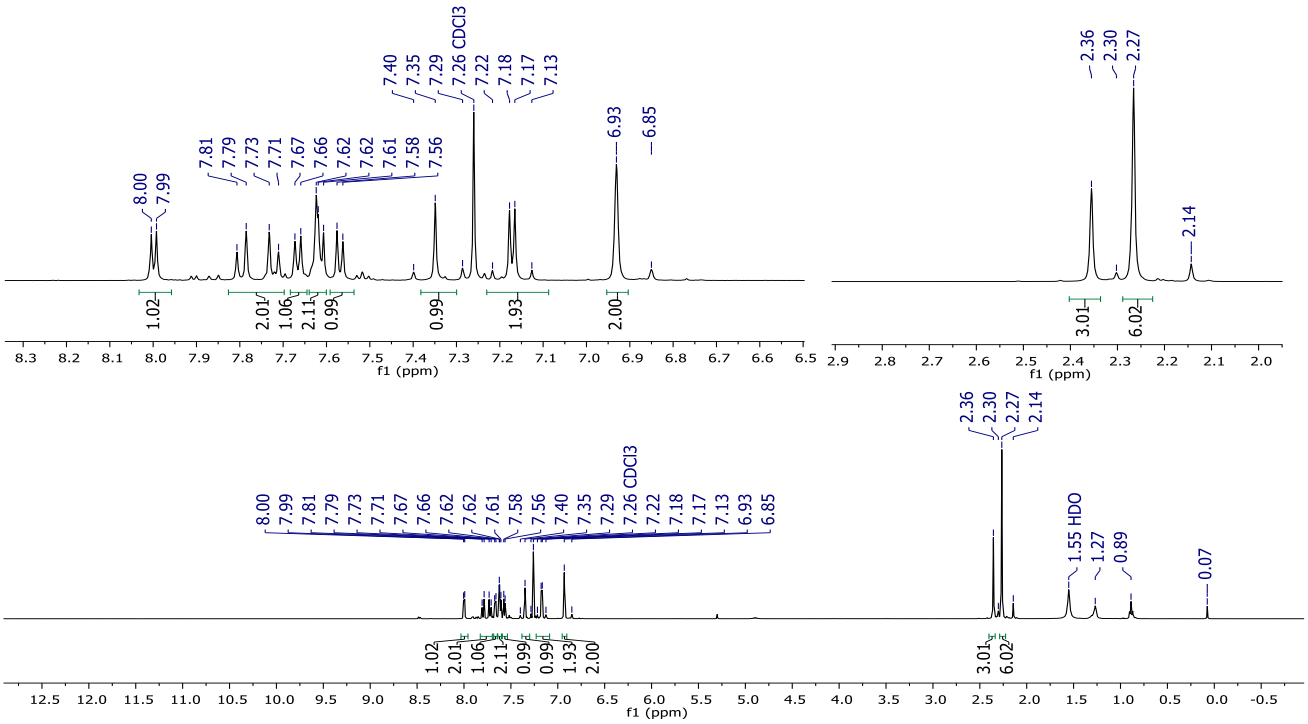

Figure S56: ^{1}H NMR spectrum of *trans*-**27** ($CDCl_3$, 400 MHz).

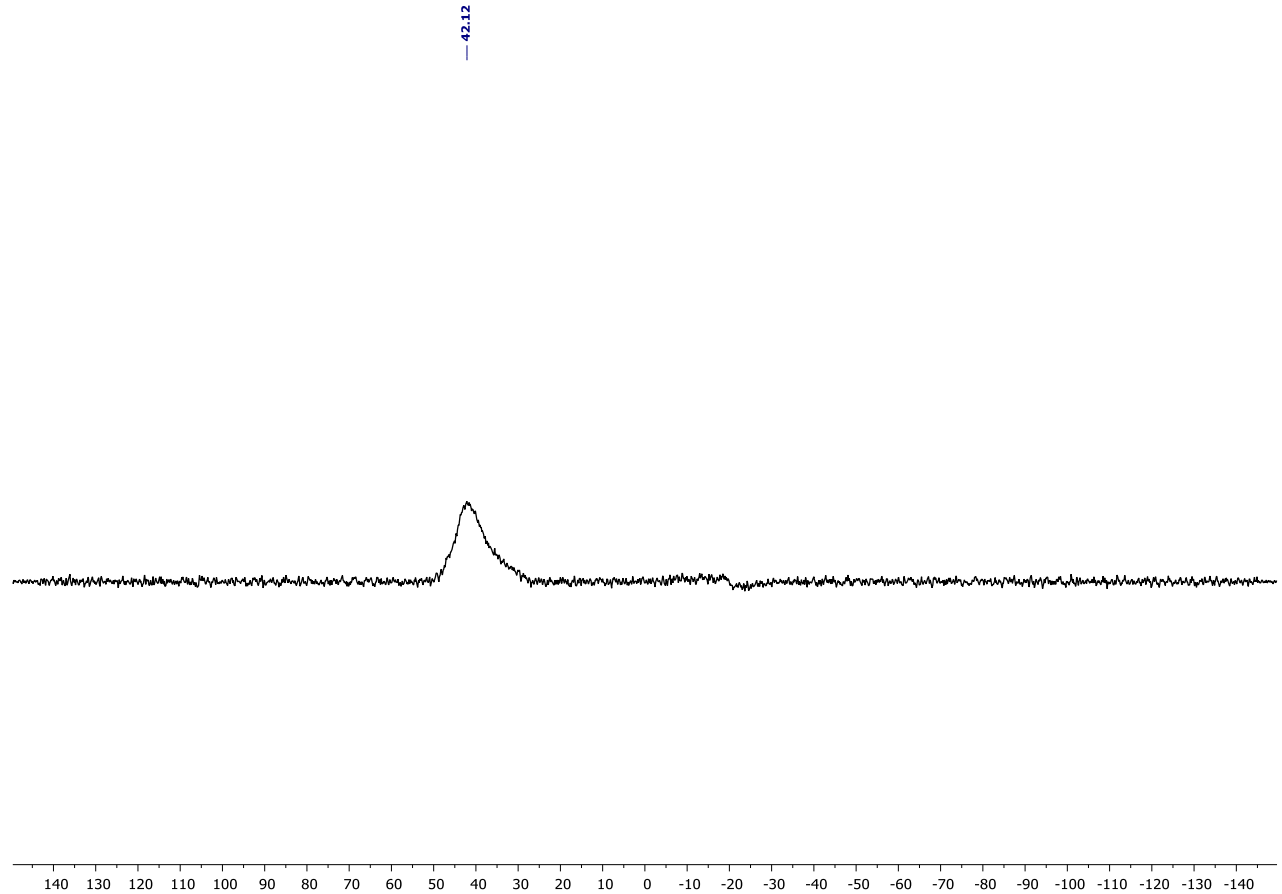

Figure S57: ^{11}B NMR spectrum of *trans*-**27** ($CDCl_3$, 128 MHz).

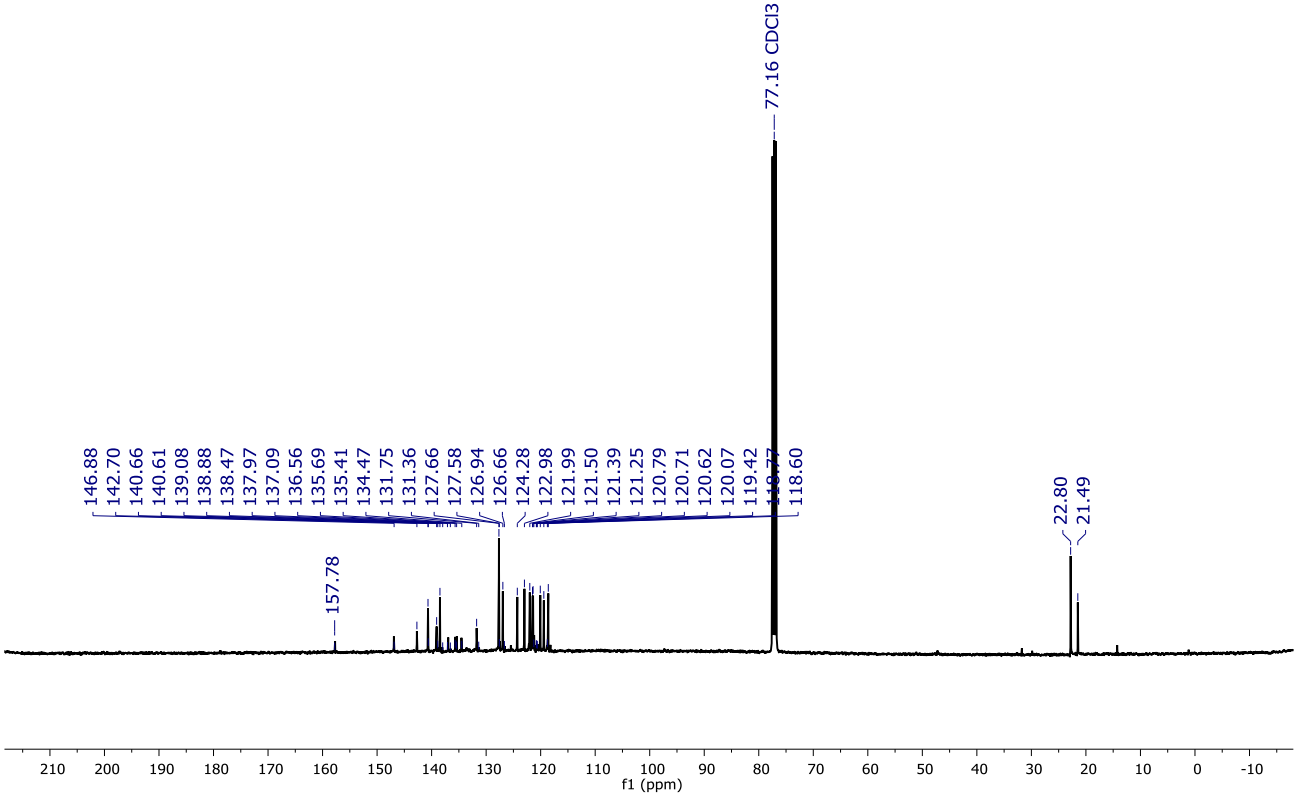

Figure S58: $^{13}C\{^{1}H\}$ NMR spectrum of *trans*-**27** ($CDCl_3$, 101 MHz).

8. Electrochemical and photophysical properties of the BO-doped compounds

8.1 Plots of cyclic voltammograms

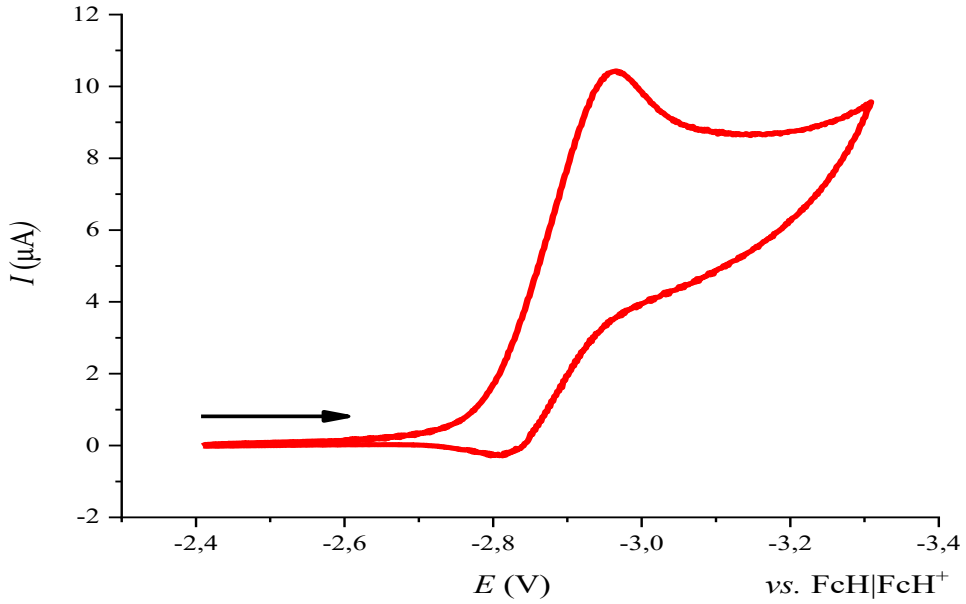

Figure S59: Cyclic voltammogram of **5** in THF (cathodic scan; room temperature, supporting electrolyte: [*n*Bu$_4$N][PF$_6$] (0.1 M), scan rate 200 mV s^{-1}).

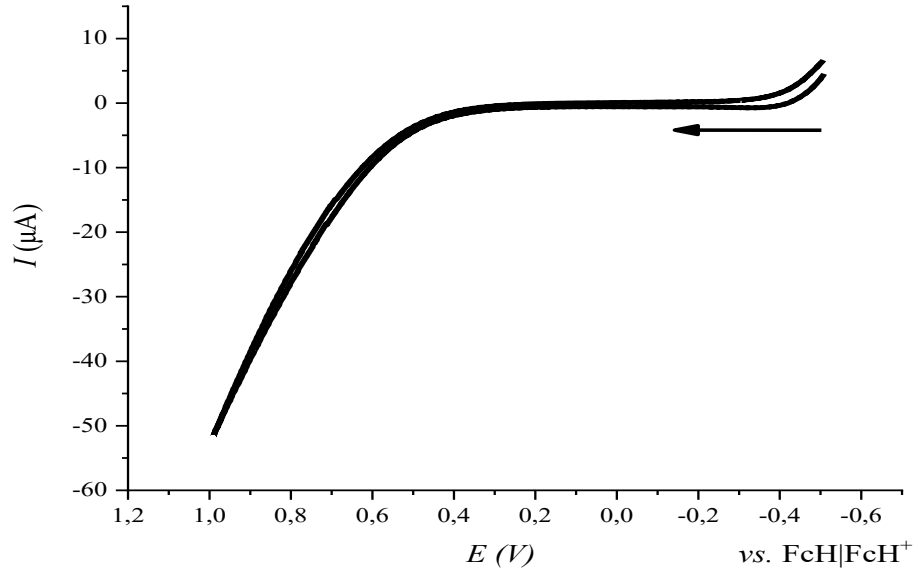

Figure S60: Cyclic voltammogram of **5** in THF (anodic scan; room temperature, supporting electrolyte: [*n*Bu$_4$N][PF$_6$] (0.1 M), scan rate 200 mV s^{-1}).

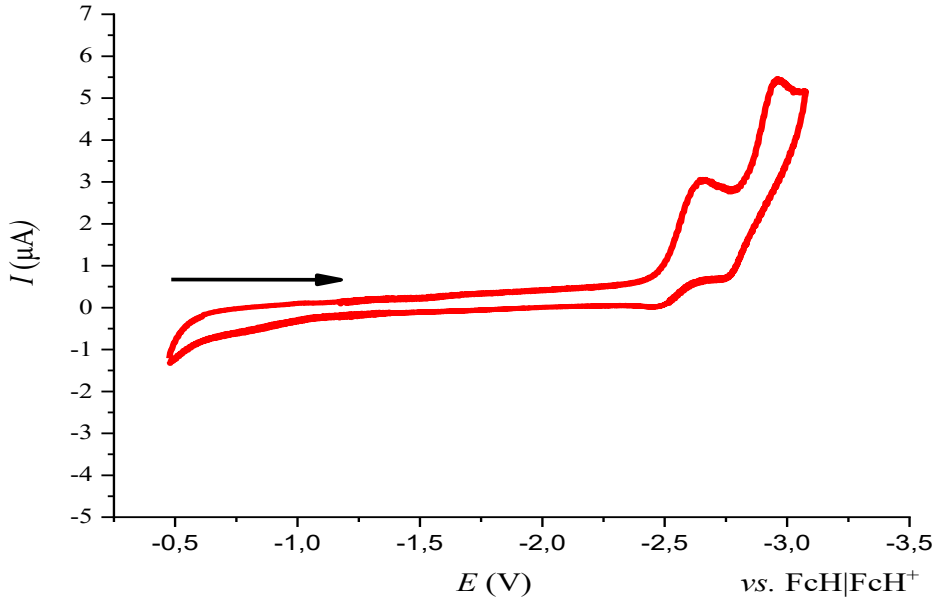

Figure S61: Cyclic voltammogram of *trans*-**15** in THF (cathodic scan; room temperature, supporting electrolyte: [nBu$_4$N][PF$_6$] (0.1 M), scan rate 200 mV s^{-1}).

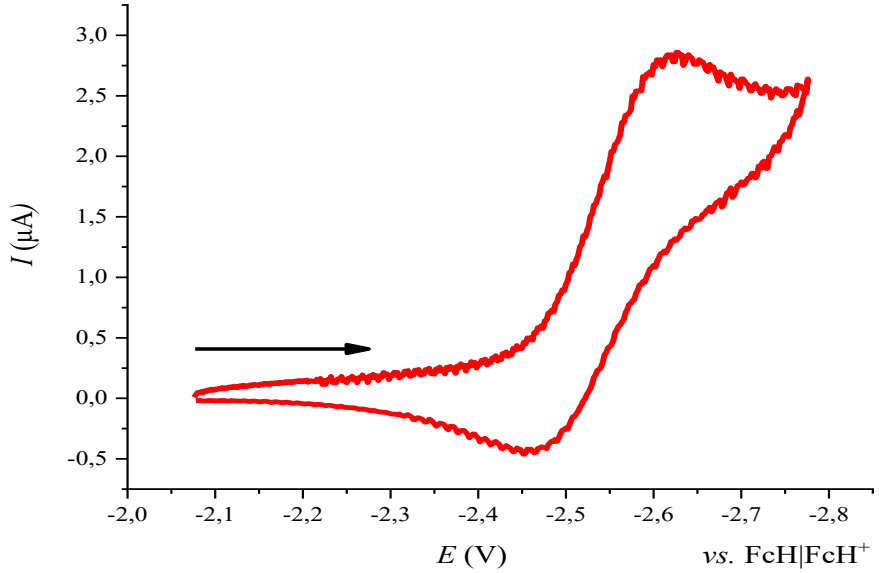

Figure S62: Cyclic voltammogram of the first reduction event of *trans*-**15** in THF (cathodic scan; room temperature, supporting electrolyte: [nBu$_4$N][PF$_6$] (0.1 M), scan rate 200 mV s^{-1}).

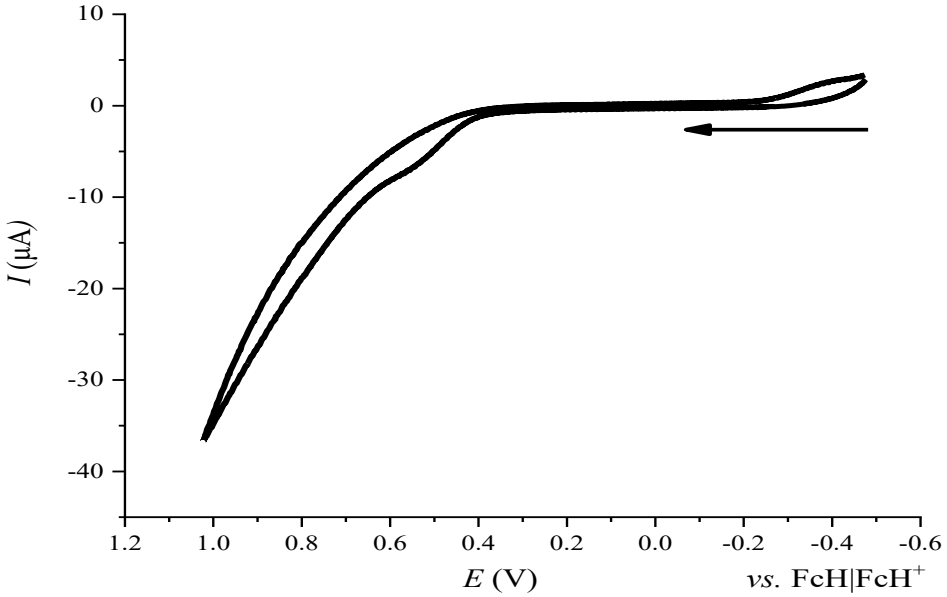

Figure S63: Cyclic voltammogram of *trans*-**15** in THF (anodic scan; room temperature, supporting electrolyte: [nBu$_4$N][PF$_6$] (0.1 M), scan rate 200 mV s^{-1}).

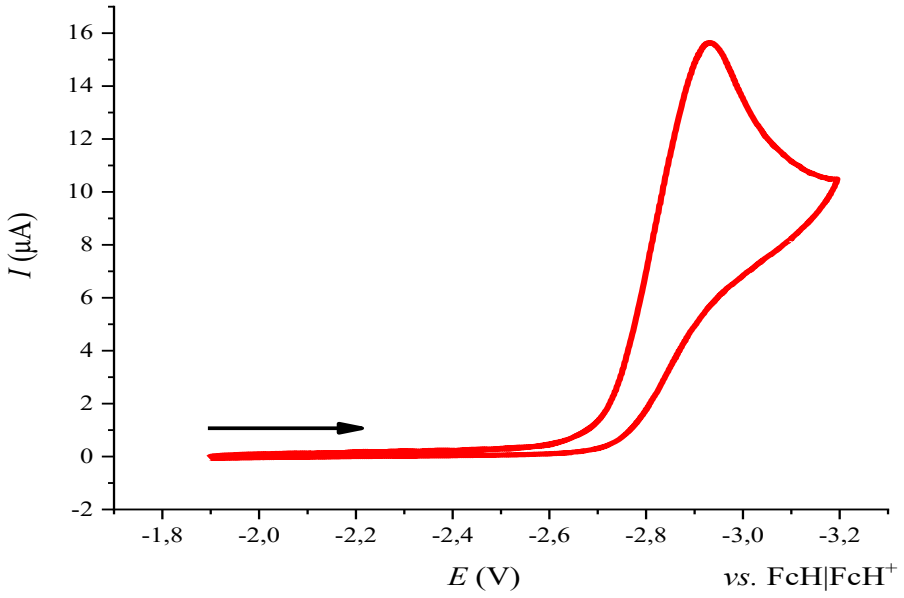

Figure S64: Cyclic voltammogram of **16** in THF (cathodic scan; room temperature, supporting electrolyte: [nBu$_4$N][PF$_6$] (0.1 M), scan rate 200 mV s^{-1}).

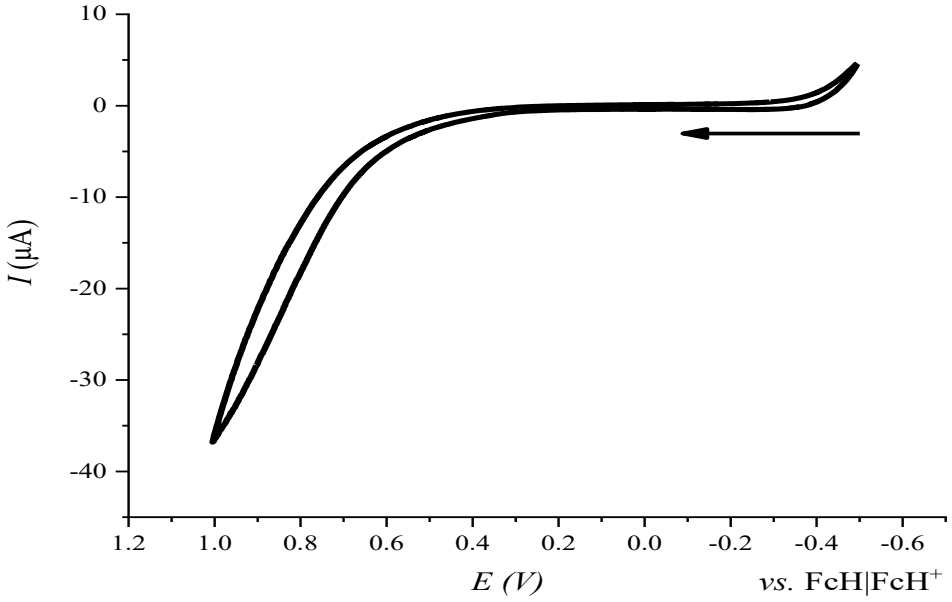

Figure S65: Cyclic voltammogram of **16** in THF (anodic scan; room temperature, supporting electrolyte: [*n*Bu$_4$N][PF$_6$] (0.1 M), scan rate 200 mV s^{-1}).

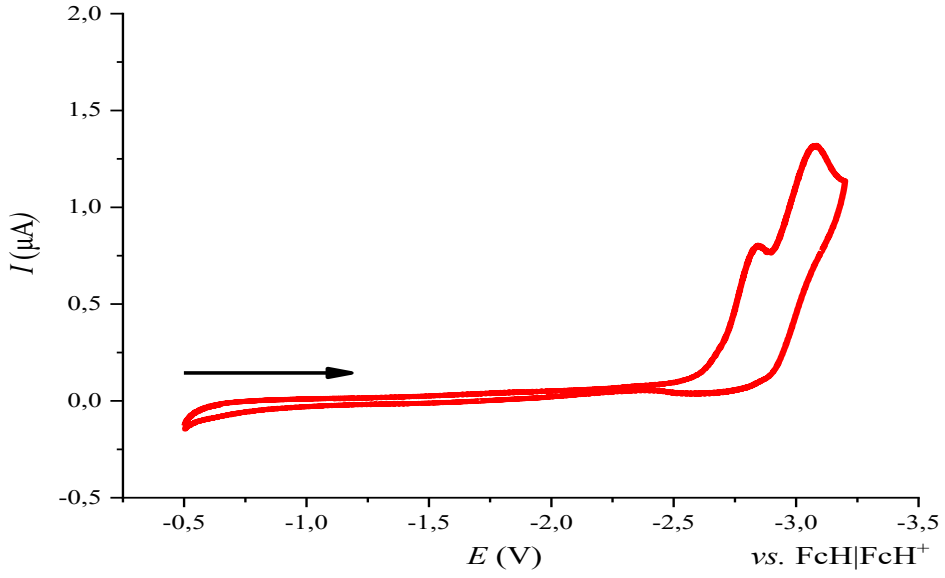

Figure S66: Cyclic voltammogram of **1** in THF (cathodic scan; room temperature, supporting electrolyte: [*n*Bu$_4$N][PF$_6$] (0.1 M), scan rate 200 mV s^{-1}).

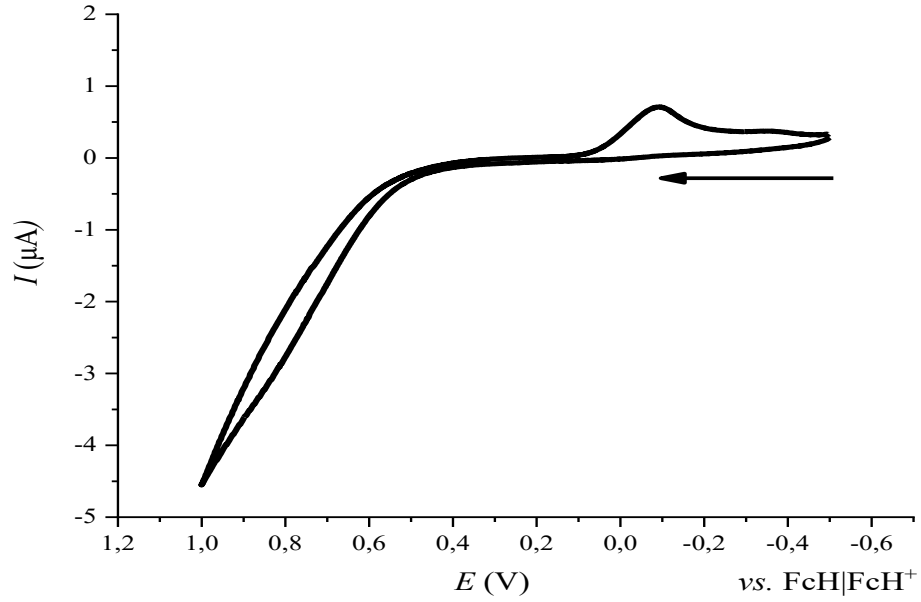

Figure S67: Cyclic voltammogram of **1** in THF (anodic scan; room temperature, supporting electrolyte: [*n*Bu$_4$N][PF$_6$] (0.1 M), scan rate 200 mV s^{-1}).

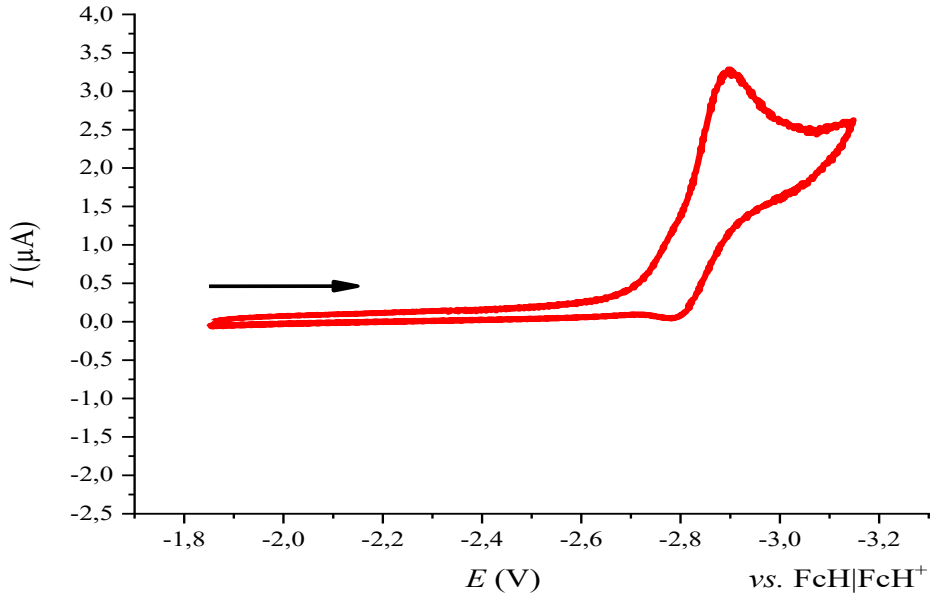

Figure S68: Cyclic voltammogram of **15H2** in THF (cathodic scan; room temperature, supporting electrolyte:[*n*Bu$_4$N][PF$_6$] (0.1 M), scan rate 200 mV s^{-1}).

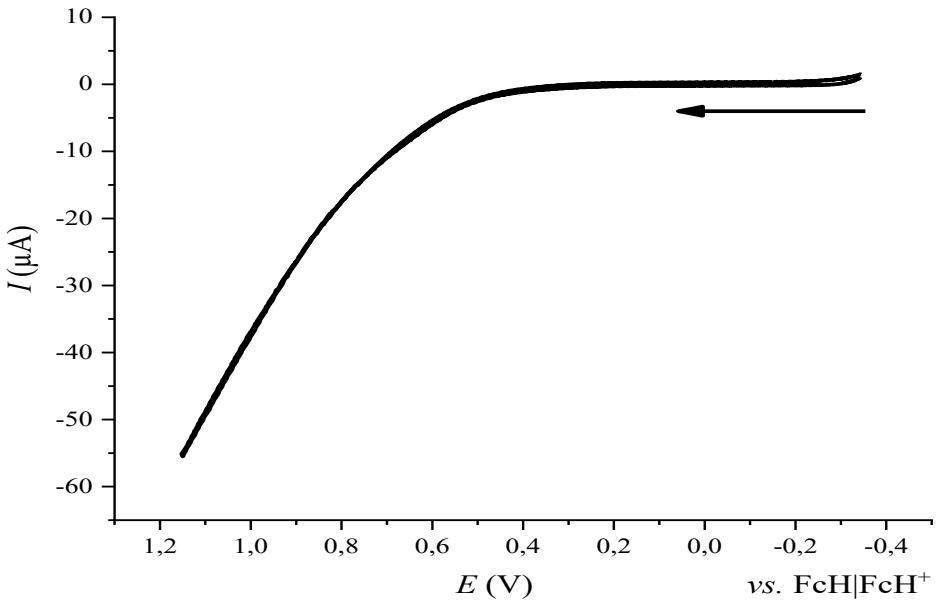

Figure S69: Cyclic voltammogram of **15H2** in THF (anodic scan; room temperature, supporting electrolyte: [nBu$_4$N][PF$_6$] (0.1 M), scan rate 200 mV s^{-1}).

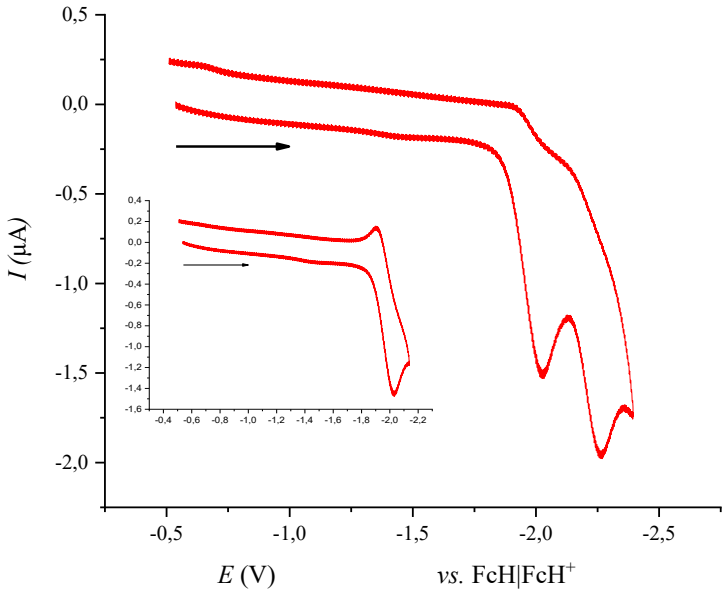

Figure S70: Cyclic voltammogram of *trans*-**18** in THF (cathodic scan; room temperature, supporting electrolyte:
[nBu$_4$N][PF$_6$] (0.1 M), scan rate 200 mV s^{-1}). The small box refers to the cyclic voltammogram of *trans*-**18** first reduction process.

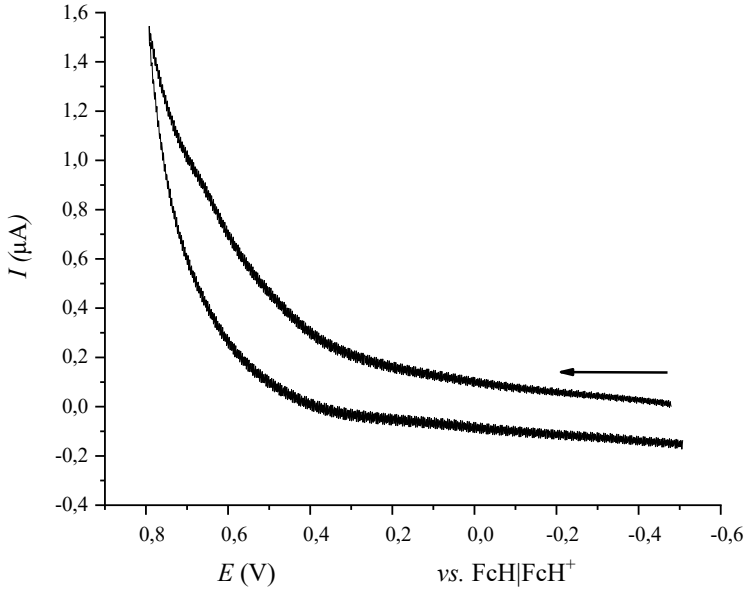

Figure S71: Cyclic voltammogram of *trans*-**18** in THF (anodic scan; room temperature, supporting electrolyte:
[*n*Bu$_4$N][PF$_6$] (0.1 M), scan rate 200 mV s^{-1}).

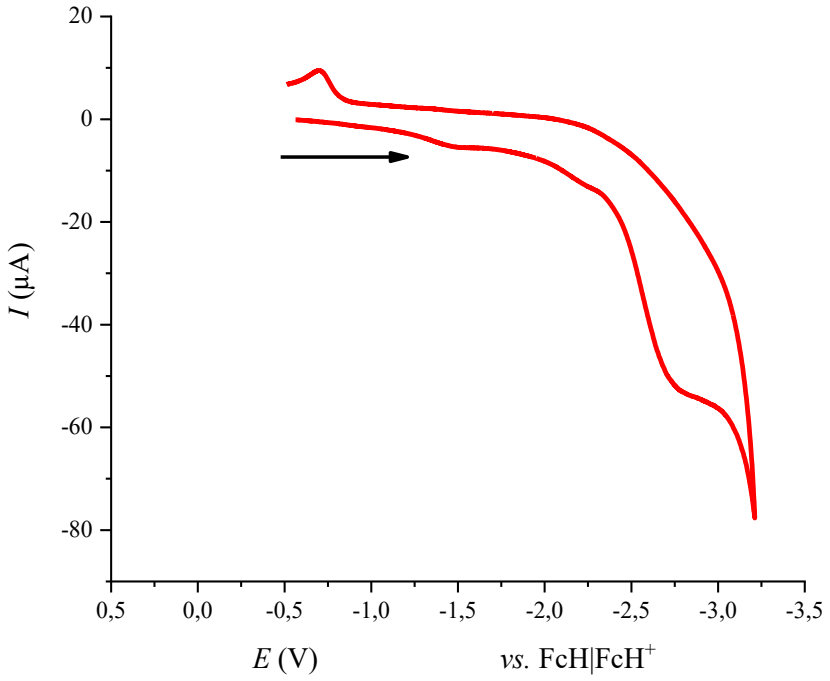

Figure S72: Cyclic voltammogram of **2** in THF (cathodic scan; room temperature, supporting electrolyte: [*n*Bu$_4$N][PF$_6$] (0.1 M), scan rate 200 mV s^{-1}).

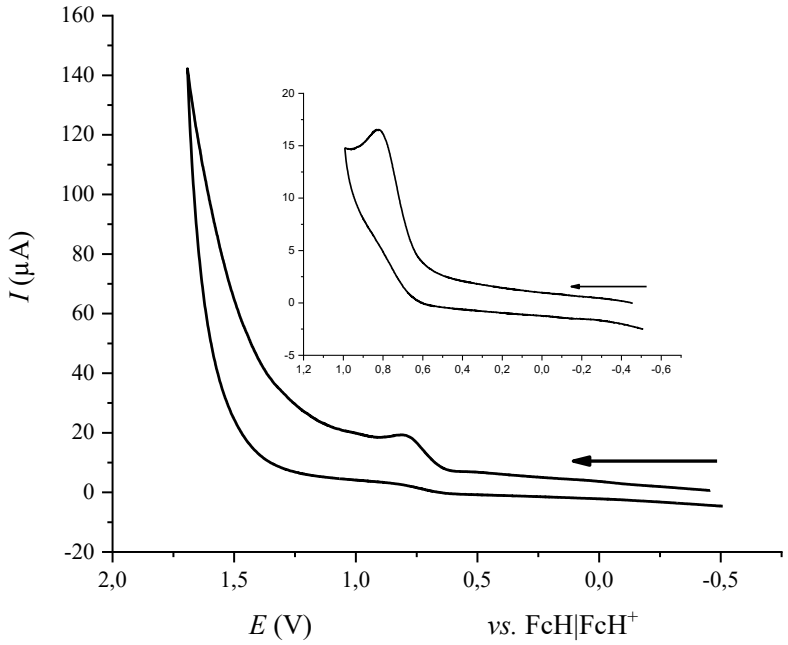

Figure S73: Cyclic voltammogram of **2** in THF (anodic scan; room temperature, supporting electrolyte: [*n*Bu$_4$N][PF$_6$] (0.1 M), scan rate 200 mV s^{-1}). The small box refers to the cyclic voltammogram of **2** first oxidation process.

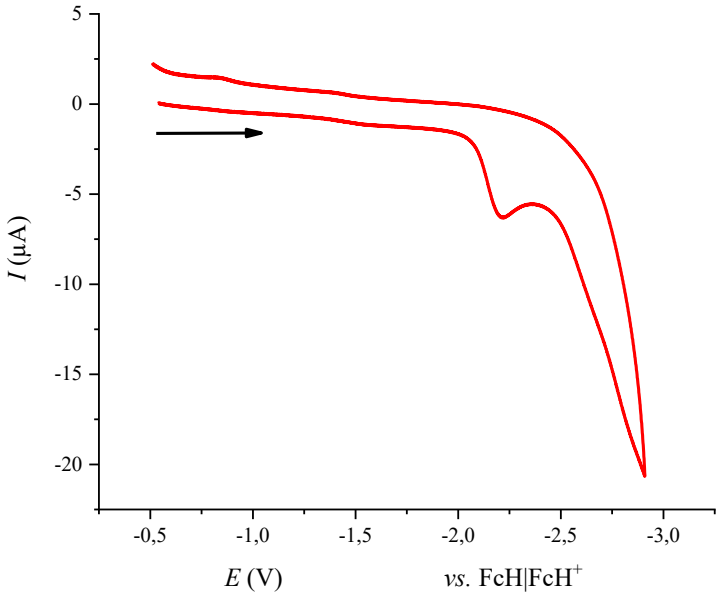

Figure S74: Cyclic voltammogram of *trans,trans*-**25** in THF (cathodic scan; room temperature, supporting electrolyte:
[*n*Bu$_4$N][PF$_6$] (0.1 M), scan rate 200 mV s^{-1}).

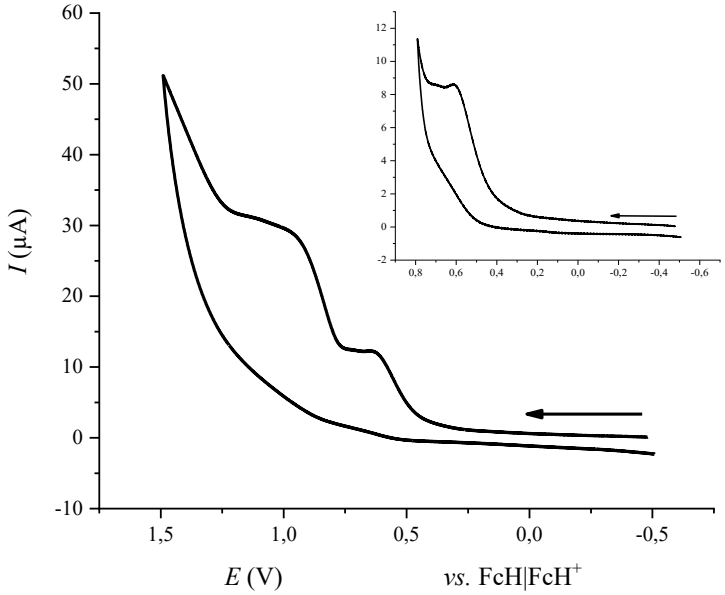

Figure S75: Cyclic voltammogram of *trans,trans*-**25** in THF (anodic scan; room temperature, supporting electrolyte:[nBu$_4$N][PF$_6$] (0.1 M), scan rate 200 mV s^{-1}). The small box refers to the cyclic voltammogram of **25** first oxidation process (100 mV s^{-1}).

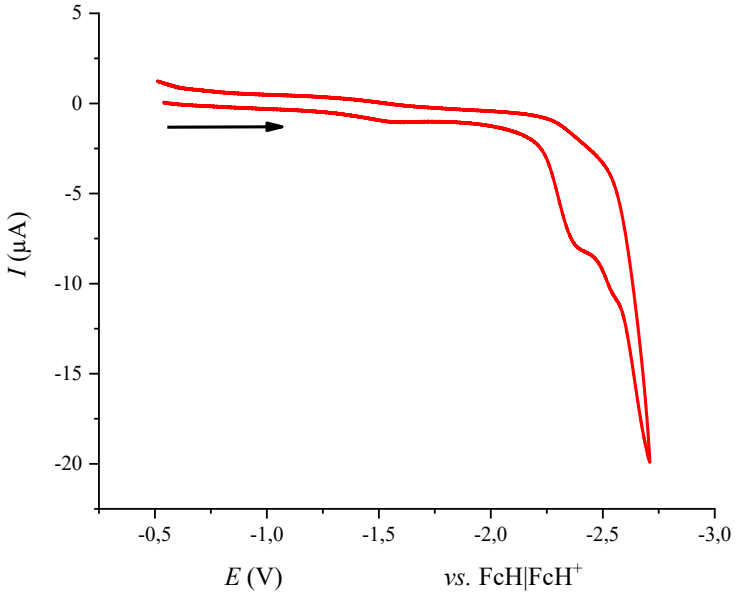

Figure S76: Cyclic voltammogram of *trans*-**27** in THF (cathodic scan; room temperature, supporting electrolyte:[nBu$_4$N][PF$_6$] (0.1 M), scan rate 100 mV s^{-1}).

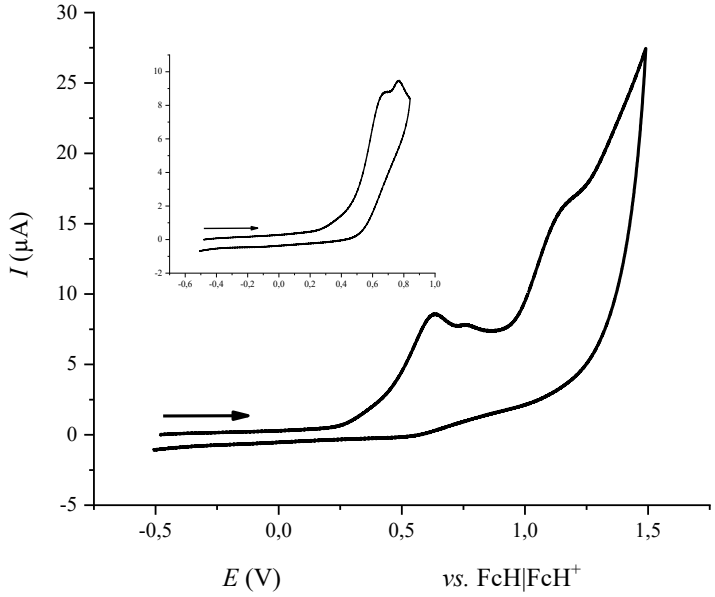

Figure S77: Cyclic voltammogram of *trans*-**27** in THF (anodic scan; room temperature, supporting electrolyte:[nBu$_4$N][PF$_6$] (0.1 M), scan rate 200 mV s^{-1}). The small box refers to the cyclic voltammogram of **Y2** first oxidation process (100 mV s^{-1}).

8.2 UV/Vis absorption and emission spectra

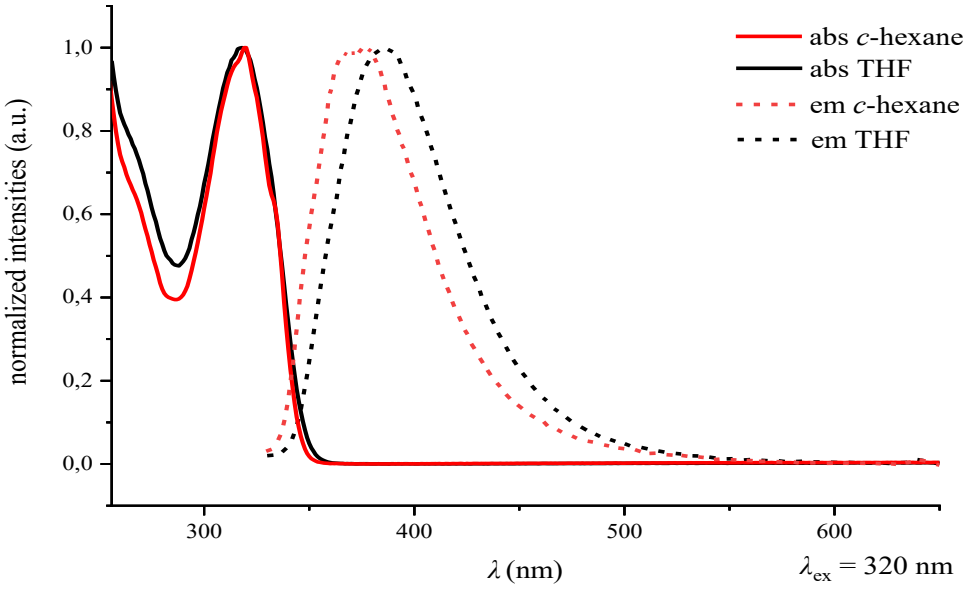

Figure S78: Normalized UV/Vis absorption and emission spectra of **5** in *c*-hexane and THF.

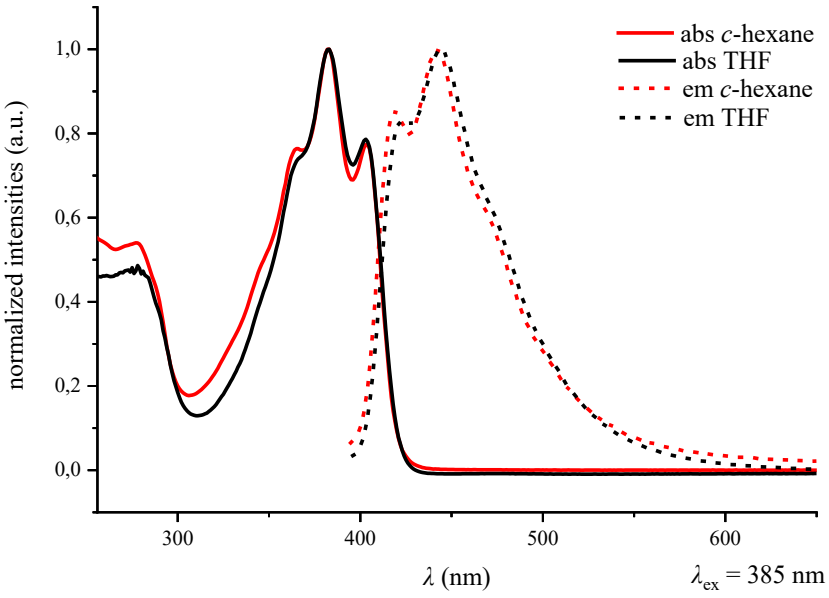

Figure S79: Normalized UV/Vis absorption and emission spectra of *trans*-**15** in *c*-hexane and THF.

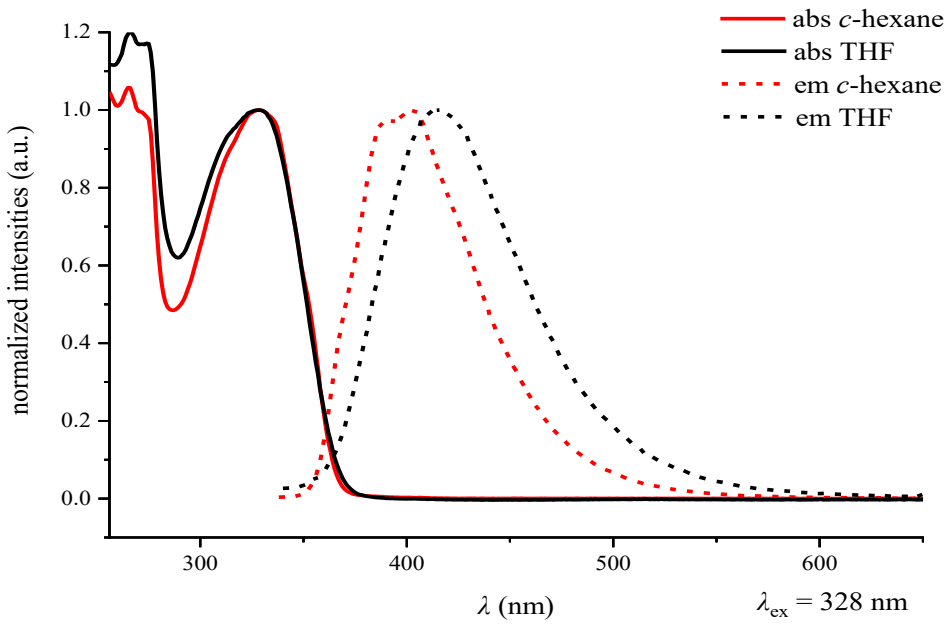

Figure S80: Normalized UV/Vis absorption and emission spectra of **16** in *c*-hexane and THF.

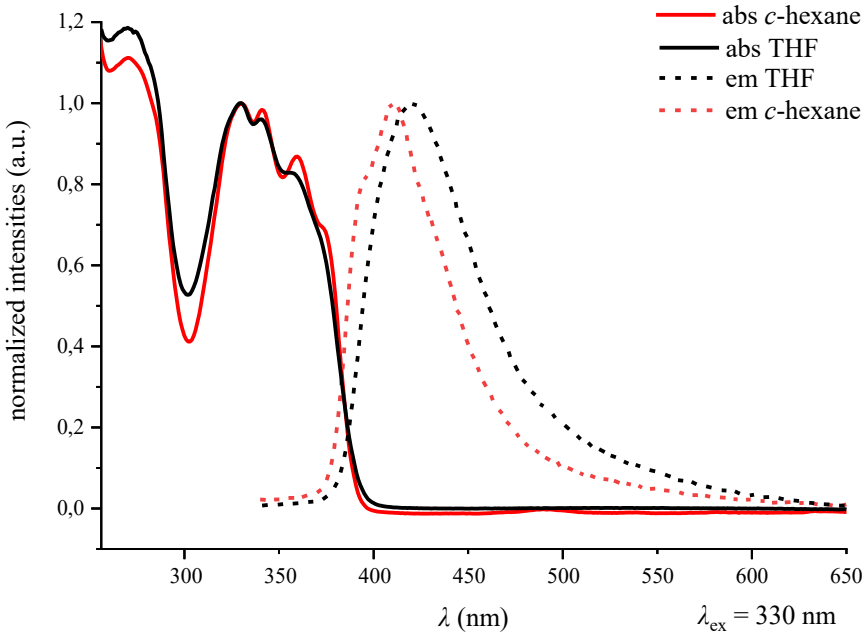

Figure S81: Normalized UV/Vis absorption and emission spectra of **1** in *c*-hexane and THF.

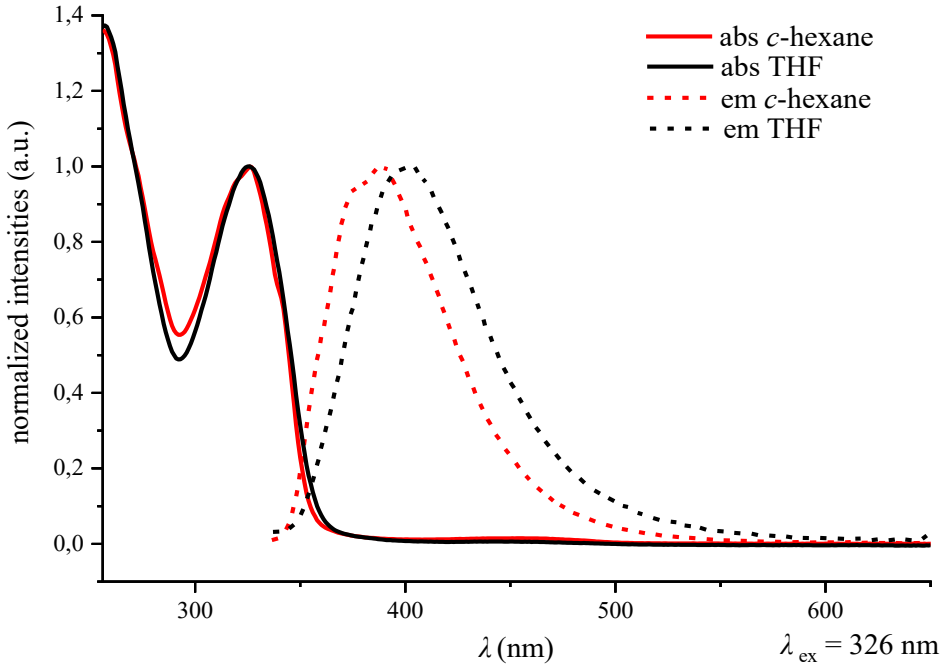

Figure S82: Normalized UV/Vis absorption and emission spectra of **15H2** in *c*-hexane and THF.

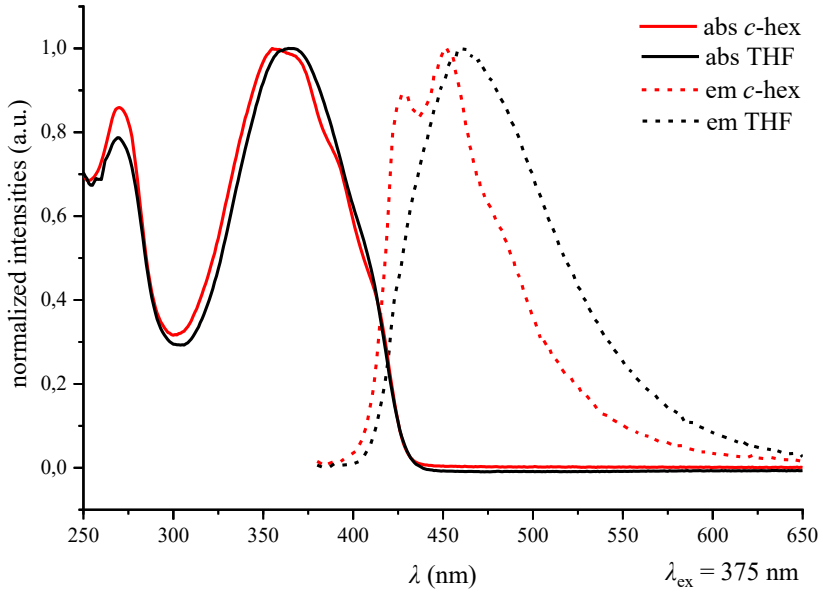

Figure S83: Normalized UV/Vis absorption and emission spectra of *trans*-**18** in *c*-hexane and THF.

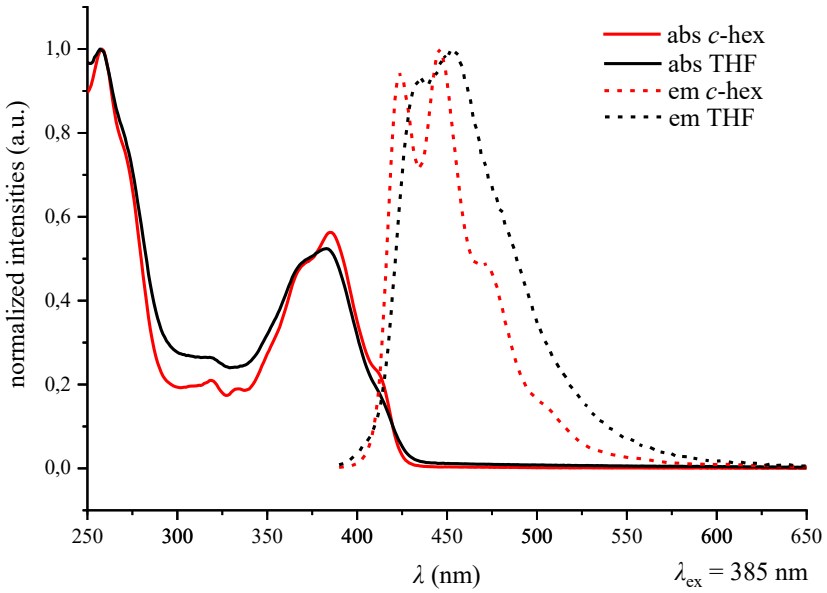

Figure S84: Normalized UV/Vis absorption and emission spectra of **2** in *c*-hexane and THF.

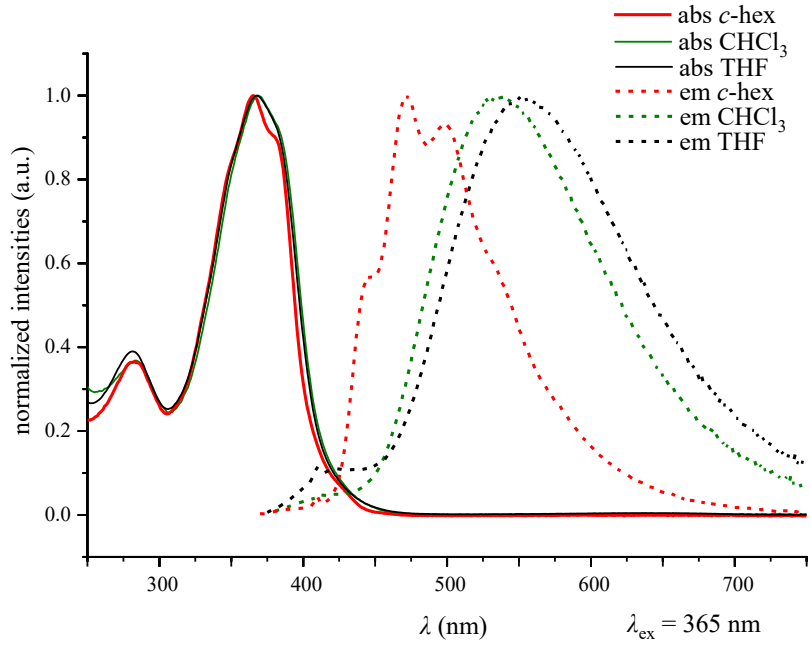

Figure S85: Normalized UV/Vis absorption and emission spectra of *trans*,*trans*-**25** in *c*-hexane, THF and $CHCl_3$.

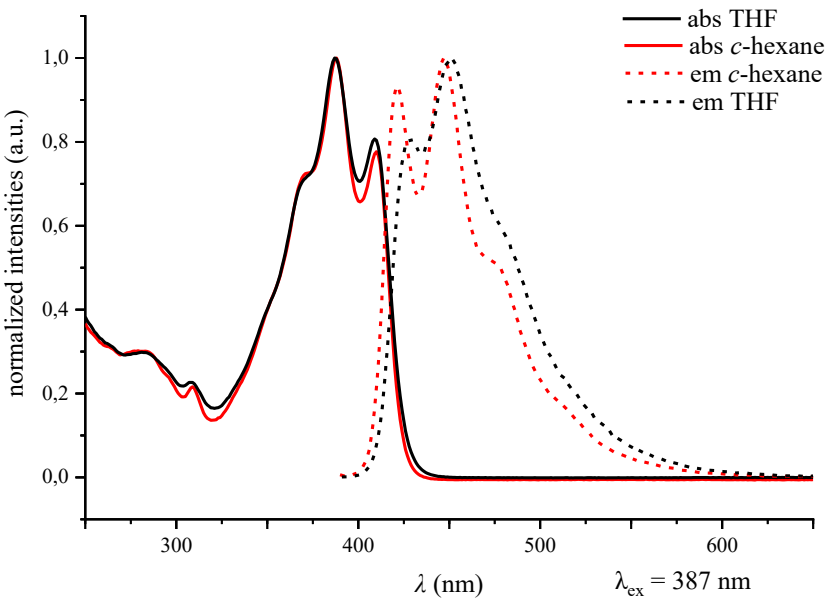

Figure S86: Normalized UV/Vis absorption and emission spectra of *trans*-**27** in *c*-hexane and THF.

8.3 Photophysical and electrochemical data

Table S1: Photophysical and electrochemical data of the boron-doped compounds. Optical measurements were performed in *c*-hexane, and electrochemical measurements were performed in THF (room temperature, supporting electrolyte: [nBu$_4$N][PF$_6$] (0.1 M), scan rate 100 or 200 mV s^{-1}).

	λ_{abs} [nm] (ε [mol^{-1}dm^{3}cm^{-1}])	λ_{onset} [nm][a]	λ_{ex} [nm]	λ_{em} [nm] [b]	Φ_{PL} [%][c]	E_{HOMO}/E_{LUMO} [eV][d]	$E_{1/2}$ [V]	E_g^{opt} [eV][e]
5	313 (sh) 320 (24300) 335 (sh)	347	320	366 380	6 9[f]	-[h] / –1.84[i]	- [k]	3.57
trans-**15**	278 (26300) 344 (sh) 364 (44100) 383 (58700) 403 (45100)	423	385	419 443	11 13[f]	–5.19 / –2.26	–2.54	2.93
16	265 (27700) 275 (sh) 328 (26400)	366	328	388 402	15 10[f]	-[h] / –1.87[i]	-[k]	3.39
1	269 (32400) 330 (29100) 341 (28600) 359 (25300) 374 (sh)	393	330	392 411	6 4[f]	–4.89 / –1.97[i]	-[k]	3.16
15H2	318 (sh) 326 (21900) 342 (sh)	353	326	374 388	7 7[f]	-[h] / –1.90[i]	-[k]	3.51
trans-**18**	270 (26500) 355 (30700) 370 (30000) 393 (21500) 414 (sh)	435	375	429 452 489 (sh)	6 5[g]	–5.68 / –2.83[d] –5.63/ –2.78[i]	–1.97	2.85
2	258 (20800) 320 (sh) 322 (sh) 368 (9800) 385 (11600) 413 (4700)	428	385	424 446 472 506 (sh)	7 5[g]	–5.62 / –2.12[i]	-[k]	2.90
trans, trans-**25**	283 (15400) 365 (41000) 382 (36500)	460	365	445 472 500 535 (sh)	12 3[f] 5[g]	–5.41/–2.59[i]	-[k]	2.69
trans-**27**	282 (sh) 309 (12500) 370 (sh) 388 (60600) 410 (47000)	429	387	421 488 477 517 (sh)	23 17[f]	–5.43/–2.43[h]	-[k]	2.89

[a] Each onset wavelength (λ_{onset}) was determined by constructing a tangent on the point of inflection of the bathochromic slope of the most red-shifted absorption maximum. [b] Resolved vibrational fine structure. [c] Quantum yields were determined by using a calibrated integrating sphere. [d] $E_{HOMO} = E_{LUMO} - E_g^{opt}$, $E_{LUMO} = -4.8$ eV$-E_{1/2}^{Red1}$ (FcH/FcH$^+$ = – 4.8 eV vs vacuum level). [e] Optical band gap $E_g^{opt} = 1240/\lambda_{onset}$. [f] Quantum yields measured in THF. [g] Quantum yields measured in $CHCl_3$. [h] Compound shows no oxidation. [i] E_{HOMO}/E_{LUMO} calculated with the *maxima criterion*: $E_{HOMO} = -1e\times((E^I_{pa}/V([FcH]^+|FcH)+4.8$ V$([FcH]^+|FcH$ vs. zero)); $E_{LUMO} = -1e\times((E^I_{pc}/V([FcH]^+|FcH)+4.8$ V$([FcH]^+|FcH$ vs. zero)). [k] Compound shows no reversible reduction. sh = shoulder.

9. X-ray crystal structure analyses

Data for all structures were collected on a STOE IPDS II two-circle diffractometer with a Genix Microfocus tube with mirror optics using MoK_α radiation (λ = 0.71073 Å). The data were scaled using the frame scaling procedure in the *X-AREA* program system (Stoe & Cie, 2002).[S15] The structures were solved by direct methods using the program *SHELXS* (Sheldrick, 2008) and refined against F^2 with full-matrix least-squares techniques using the program *SHELXL* (Sheldrick, 2008).[S16]

Compounds **5**, **8**, and **16** (CCDC 2211405, CCDC 2211406, CCDC 2211407), require no special comments.

trans-**15** (CCDC 2211409) is located on a center of inversion. There is one $CDCl_3$ molecule in the asymmetric unit forming a C-H…π hydrogen bond to the center (cog) of the mesityl ring (H1L…cog = 2.42Å, C1L-H1L…cog = 160.9°; see Figure S89).

The molecule of ***trans*-17** (CCDC 2211408) is located on a center of inversion. The terminal thienyl rings are disordered over two positions with a site occupation factor of 0.515(4) for the major occupied orientation. The disordered S and C atoms sharing the same site were refined with the same coordinates and the same displacement parameters.

1 (CCDC 2211410) crystallizes as a racemic mixture of the *P* and *M* enantiomers.

In **15H2** (CCDC 2211411), one methyl group is disordered over two positions with a site occupation factor of 0.52(6) for the major occupied site.

CCDC files **5**, **8**, **16**, **17**, **15**, **1** and **15H2** (CCDC 2211405, CCDC 2211406, CCDC 2211407, CCDC 2211408, CCDC 2211409, CCDC 2211410, CCDC 2211411) contain the supplementary crystallographic data for this paper and can be obtained free of charge from he Cambridge Crystallographic Data Centre via www.ccdc.cam.ac.uk/data_request/cif.

Note: bond lengths (A), bond angles (°), and torsion angles (°) for crystal structures with R indices>20 have been not explicited.

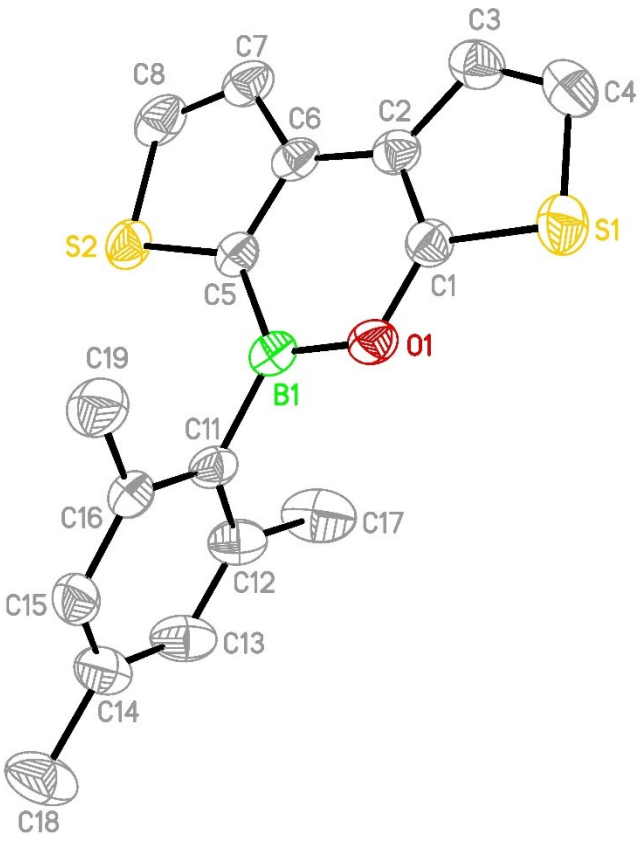

Figure S87 (CCDC 2211405): Molecular structure of **5** in the solid state. Displacement ellipsoids are drawn at the 50% probability level. Selected bond lengths (A), bond angles (°), and torsion angles (°): O(1)-B(1) = 1.395(2), B(1)-C(5) = 1.519(2), B(1)-C(11) = 1.563(3); O(1)-B(1)-C(5) = 115.66(16), O(1)-B(1)-C(11) = 117.40(15), C(5)-B(1)-C(11) = 126.94(17), O(1)-C(1)-S(1) = 120.26(13), B(1)-C(5)-S(2) = 127.45(14); C(1)-O(1)-B(1)-C(5) = –1.1(2), C(3)-C(2)-C(6)-C(7) = –0.4(3), B(1)-O(1)-C(1)-S(1) = –179.23(13), O(1)-B(1)-C(5)-S(2) = –179.70(13).

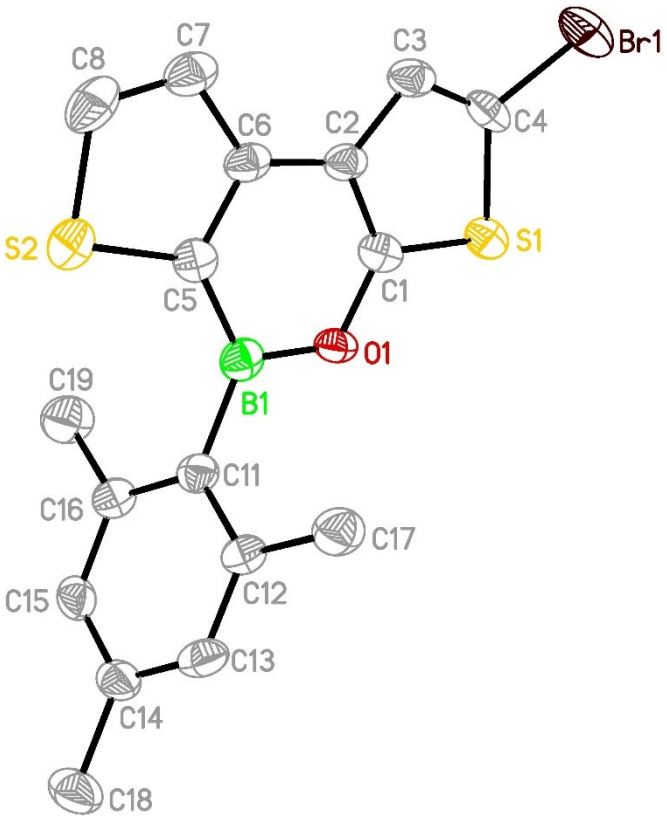

Figure S88 (CCDC 2211406): Molecular structure of **8** in the solid state. Displacement ellipsoids are drawn at the 50% probability level. Selected bond lengths (A), bond angles (°), and torsion angles (°): O(1)-B(1) = 1.400(6), B(1)-C(5) = 1.516(6), B(1)-C(11) = 1.565(6); O(1)-B(1)-C(5) = 115.0(4), O(1)-B(1)-C(11) = 116.2(3), C(5)-B(1)-C(11) = 128.7(4), O(1)-C(1)-S(1) = 120.4(3), B(1)-C(5)-S(2) = 128.0(3), S(1)-C(4)-Br(1) = 119.6(3); C(1)-O(1)-B(1)-C(5) = –0.2(5), C(3)-C(2)-C(6)-C(7) = -2.4(7), B(1)-O(1)-C(1)-S(1) = –177.2(3), O(1)-B(1)-C(5)-S(2) = 179.4(3).

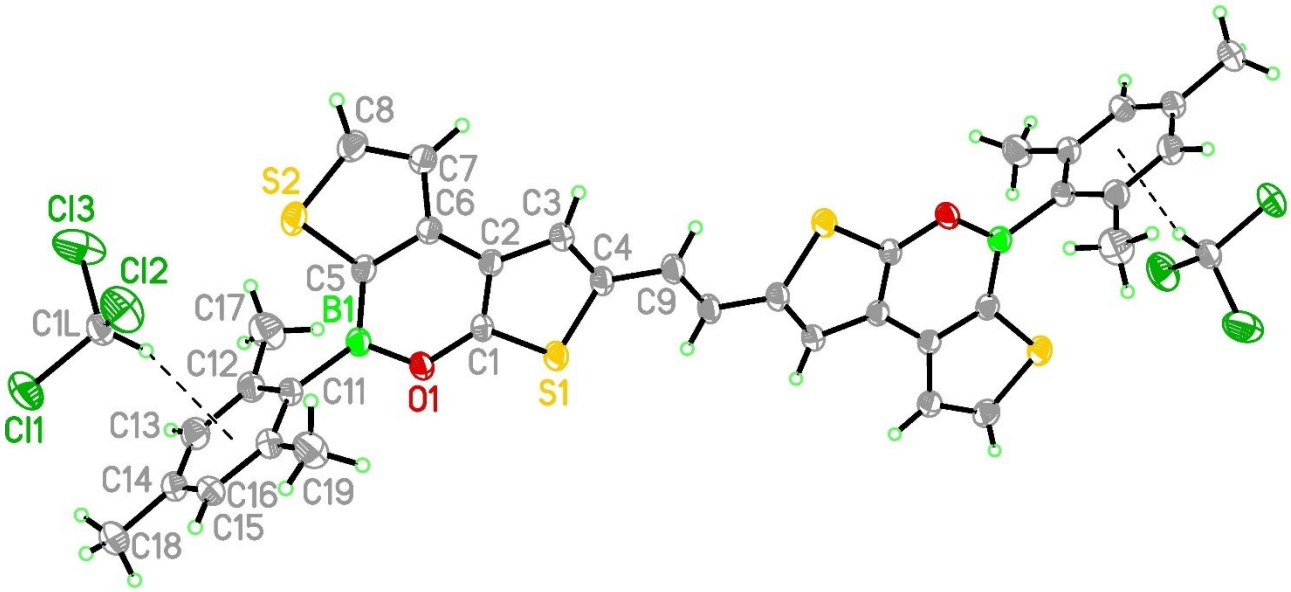

Figure S89 (CCDC 2211409): Molecular structure of *trans*-**15** in the solid state. Displacement ellipsoids are drawn at the 50% probability level. Selected bond lengths (A), bond angles (°), and torsion angles (°): B(1)-O(1) = 1.399(2), B(1)-C(5) = 1.517(3), B(1)-C(11) = 1.575(2), C(9)-C(9A) = 1.332(4); O(1)-B(1)-C(5) = 115.33(15), O(1)-B(1)-C(11) = 115.98(16), C(5)-B(1)-C(11) = 128.68(16), C(3)-C(4)-C(9) = 126.46(17), C(9A)-C(9)-C(4) = 126.7(2); C(3)-C(2)-C(6)-C(7) = –1.0(3), C(5)-B(1)-O(1)-C(1) = –0.8(2), O(1)-B(1)-C(5)-S(2) = –177.07(13), B(1)-O(1)-C(1)-S(1) = 177.91(13). Symmetry operator for generating equivalent atoms (A): -x+2, -y+2, -z+1.

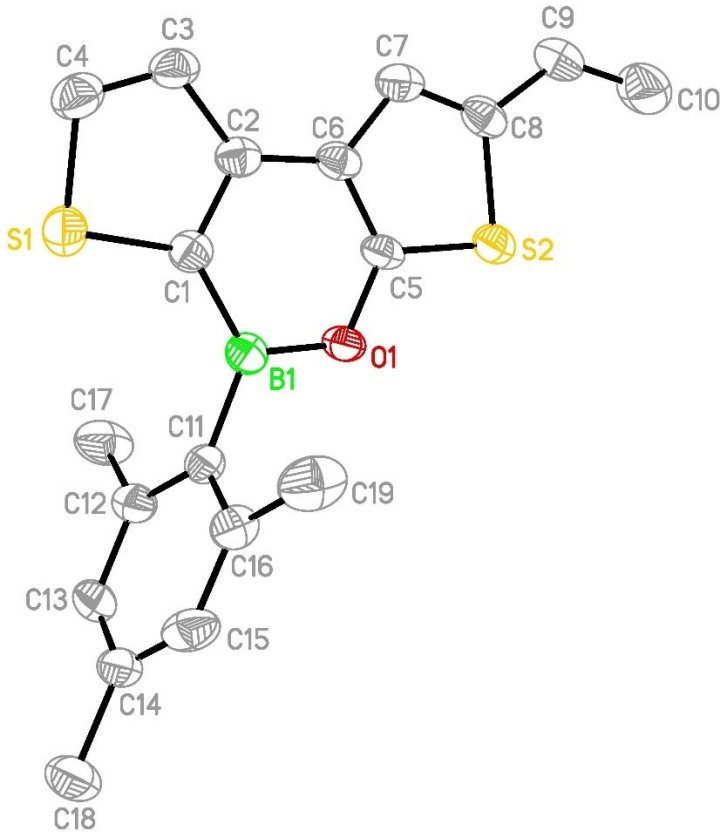

Figure S90 (CCDC 2211407): Molecular structure of **16** in the solid state. Displacement ellipsoids are drawn at the 50% probability level. Selected bond lengths (A), bond angles (°), and torsion angles (°): O(1)-B(1) = 1.399(5), B(1)-C(1) = 1.528(6), B(1)-C(11) = 1.553(6), C(9)-C(10) = 1.298(7); O(1)-B(1)-C(1) = 114.8(4), O(1)-B(1)-C(11) = 117.8(4), C(1)-B(1)-C(11) = 127.4(4), O(1)-C(5)-S(2) = 120.0(3), B(1)-C(1)-S(1) = 127.5(3); C(1)-B(1)-O(1)-C(5) = –0.1(5), C(3)-C(2)-C(6)-C(7) = –3.0(7), O(1)-B(1)-C(1)-S(1) = –178.4(3), B(1)-O(1)-C(5)-S(2) = –178.0(3).

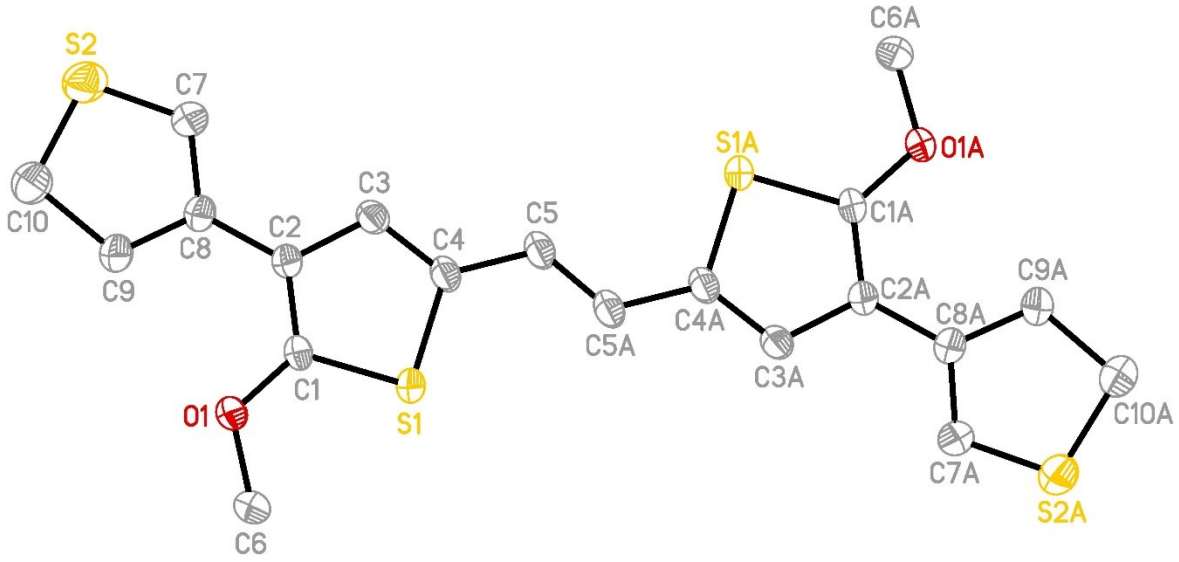

Figure S91 (CCDC 2211408): Molecular structure of *trans*-**17** in the solid state. Displacement ellipsoids are drawn at the 50% probability level. Selected bond lengths (A), bond angles (°), and torsion angles (°): O(1)-C(1) = 1.348(2), O(1)-C(6) = 1.433(3), C(2)-C(8) = 1.469(3), C(5)-C(5A) = 1.344(4); C(4)-S(1)-C(1) = 91.06(10), C(7)-S(2)-C(10) = 99.92(11), C(1)-O(1)-C(6) = 117.06(16), O(1)-C(1)-S(1) = 121.75(15), C(5A)-C(5)-C(4) = 125.7(3); C(3)-C(4)-C(5)-C(5A) = –178.2(3), S(1)-C(4)-C(5)-C(5A) = 3.1(4), C(3)-C(2)-C(8)-C(9) = 175.0(2). Symmetry operator for generating equivalent atoms (A): -x, -y+1, -z+1.

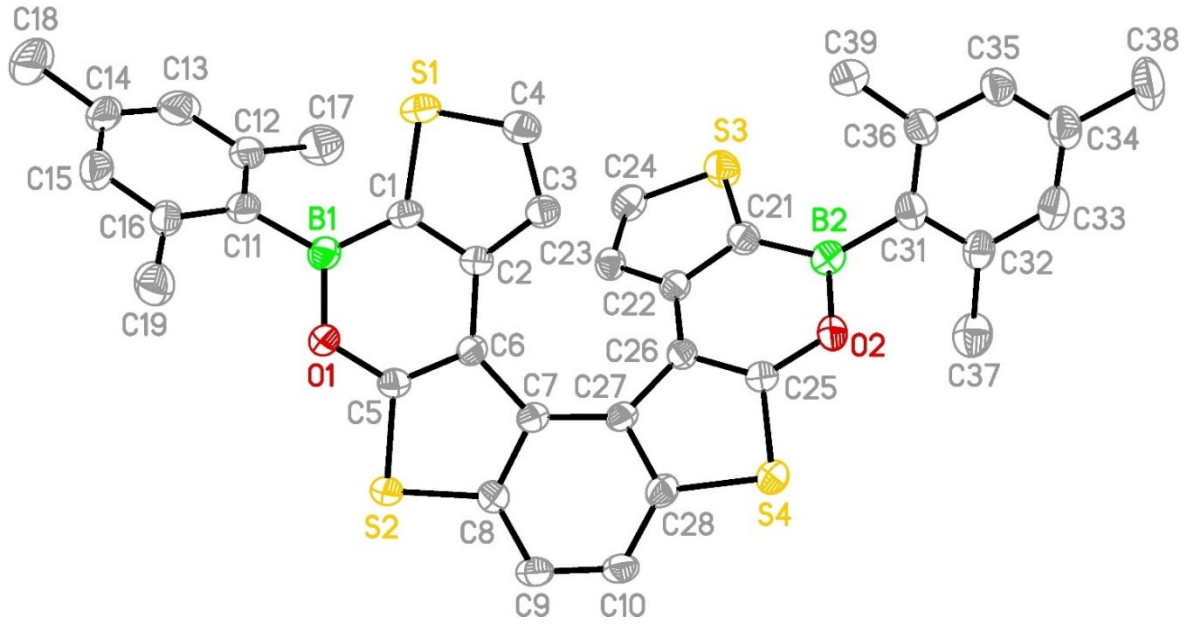

Figure S92 (CCDC 2211410): Molecular structure of **1** in the solid state. Displacement ellipsoids are drawn at the 50% probability level. Selected bond lengths (A), bond angles (°), and torsion angles (°): O(1)-B(1) = 1.402(4), O(2)-B(2) = 1.401(5), B(1)-C(1) = 1.516(5), B(1)-C(11) = B(2)-C(31) = 1.563(5), B(2)-C(21) = 1.524(5); O(1)-B(1)-C(1) = 114.2(3), O(1)-B(1)-C(11) = 118.6(3), C(1)-B(1)-C(11) = 127.1(3), O(2)-B(2)-C(21) = 114.0(3), O(2)-B(2)-C(31) = 115.5(3), C(21)-B(2)-C(31) = 130.5(3); C(5)-O(1)-B(1)-C(1) = –5.7(5), C(25)-O(2)-B(2)-C(21) = –7.2(5), C(3)-C(2)-C(6)-C(7) = –4.3(6), C(23)-C(22)-C(26)-C(27) = –5.4(6), C(6)-C(7)-C(27)-C(26) = –18.7(6), O(2)-B(2)-C(21)-S(3) = –165.9(3), O(1)-B(1)-C(1)-S(1) = –165.5(3), B(2)-O(2)-C(25)-S(4) = 175.9(3), B(1)-O(1)-C(5)-S(2) = 172.2(3). Dihedral angle between the two terminal thiophene rings: 50.26(9).

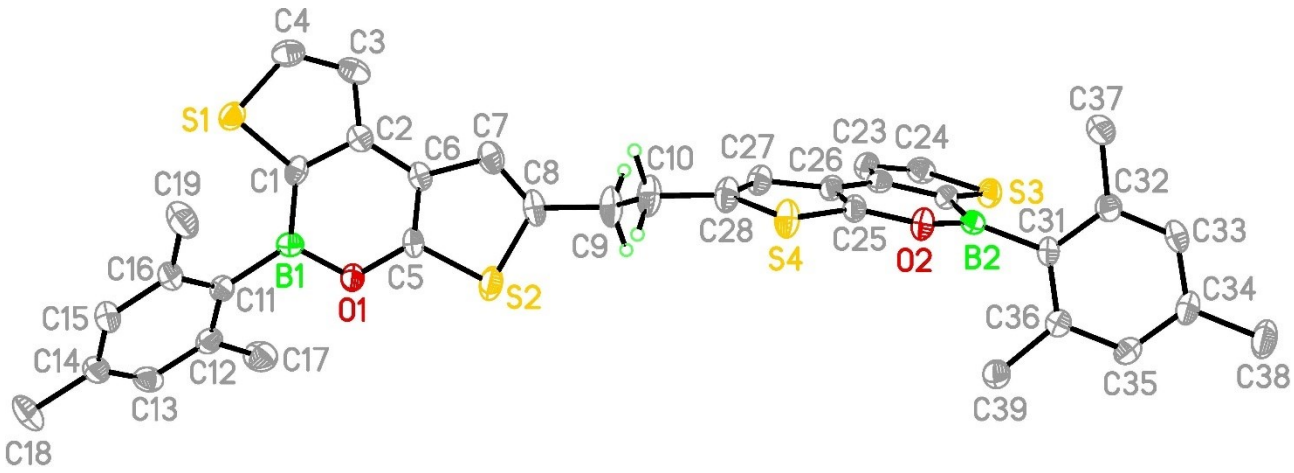

Figure S93 (CCDC 2211411): Molecular structure of **15H2** in the solid state. Displacement ellipsoids are drawn at the 50% probability level. Selected bond lengths (A), bond angles (°), and torsion angles (°): O(1)-B(1) = 1.399(5), O(2)-B(2) = 1.406(5), B(1)-C(1) = 1.512(6), B(2)-C(21) = 1.521(6), B(1)-C(11) = 1.560(6), B(2)-C(31) = 1.565(6), C(9)-C(10) = 1.492(6); O(1)-B(1)-C(1) = 115.3(4), O(1)-B(1)-C(11) = 117.0(4), O(2)-B(2)-C(31) = 117.6(4), C(1)-B(1)-C(11) = 127.7(4), C(21)-B(2)-C(31) = 127.0(4), C(7)-C(8)-C(9) = 128.1(5), C(27)-C(28)-C(10) = 128.6(4), C(10)-C(9)-C(8) = 115.8(4), C(9)-C(10)-C(28) = 111.6(4); C(5)-O(1)-B(1)-C(1) = –0.7(5), C(3)-C(2)-C(6)-C(7) = 1.2(8), C(25)-O(2)-B(2)-C(21) = 5.0(6), C(23)-C(22)-C(26)-C(27) = 0.5(7), B(1)-O(1)-C(5)-S(2) = –179.1(3), O(1)-B(1)-C(1)-S(1) = 179.3(3), B(2)-O(2)-C(25)-S(4) = 173.3(3), O(2)-B(2)-C(21)-S(3) = –176.9(3).

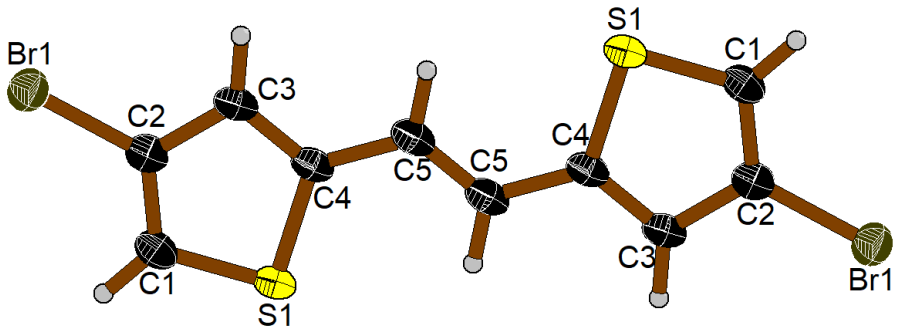

Figure S94: Molecular structure of *trans*-**20** in the solid state. Displacement ellipsoids are drawn at the 50% probability level. Displacement ellipsoids are drawn at the 50% probability level. Selected bond lengths (A), bond angles (°), and torsion angles (°): Br1-C2 = 1.883 (2), S1-C1 = 1.713 (2), S1-C4 = 1.734 (2), C1-C2 = 1.356 (3), C2-C3 = 1.421 (3), C3-C4 = 1.369 (3), C4-C5 = 1.453 (3), C5-C5^{i} = 1.336 (5); C1-S1-C4 = 92.16 (11), C2-C1-S1 = 110.98 (16), C1-C2-C3 = 114.0 (2), C1-C2-Br1 = 123.68 (17), C3-C2-Br1 = 122.34 (16), C4-C3-C2 = 111.89 (19), C3-C4-C5 = 125.99 (19), C3-C4-S1 = 110.98 (17), C5-C4-S1 = 123.02 (18), C5^{i}-C5-C4 = 125.9 (3); C4-S1-C1-C2 = –0.59 (16), S1-C1-C2-C3 = 1.0 (2), S1-C1-C2-Br1 = 179.81 (11), C1-C2-C3-C4 = –1.1 (3), Br1-C2-C3-C4 = –179.85 (14), C2-C3-C4-C5 = –179.89 (19), C2-C3-C4-S1 = 0.6 (2), C1-S1-C4-C3 = 0.00 (17), C1-S1-C4-C5 = –179.56 (18), C3-C4-C5-C5^{i} = 178.0 (3), S1-C4-C5-C5^{i} = –2.6 (4). Symmetry code(s): (i) -*x*+1, -*y*+1, -*z*+1.

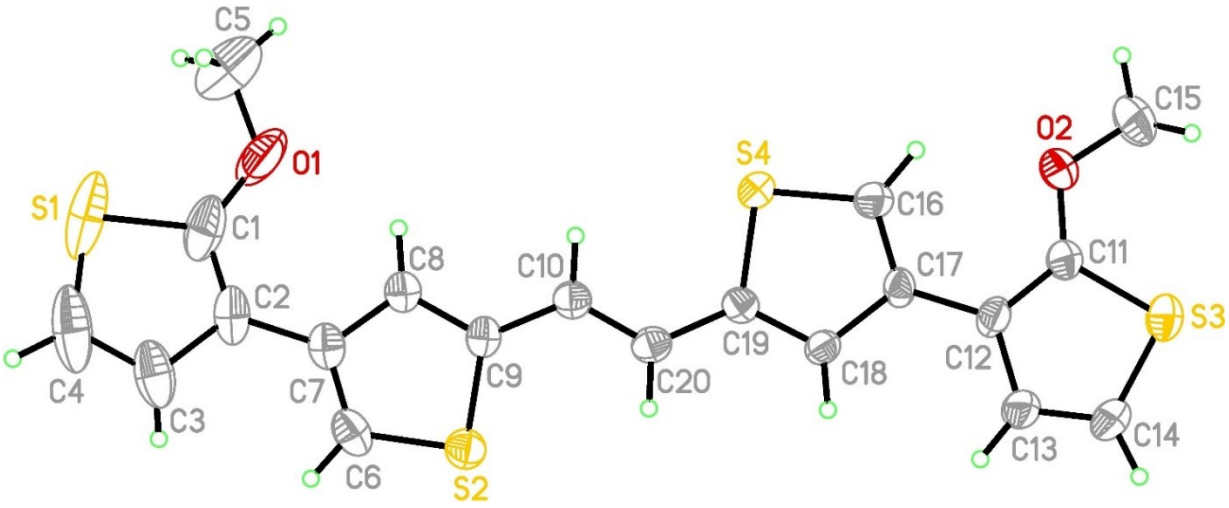

Figure S95: Molecular structure of *trans*-**19** in the solid state. Displacement ellipsoids are drawn at the 50% probability level. Selected bond lengths (A), bond angles (°), and torsion angles (°): O(1)-C(1) = 1.355(13), O(2)-C(15) = 1.411(13), C(2)-C(7) = 1.473(9), C(12)-C(17) = 1.475(8), C(10)-C(20) = 1.348(9); C(4)-S(1)-C(1) = 90.5(5), C(14)-S(3)-C(11) = 90.8(4), C(1)-O(1)-C(5) = 120.2(8), O(1)-C(1)-S(1) = 121.7(7), C(20)-C(10)-C(9) = 127.7(6); C(8)-C(9)-C(10)-C(20) = –174.9(6), S(2)-C(9)-C(10)-C(20) = – 4.8(9), C(3)-C(2)-C(7)-C(8) = –160.0(7), C(9)-C(10)-C(20)-C(19) = –178.9(6).

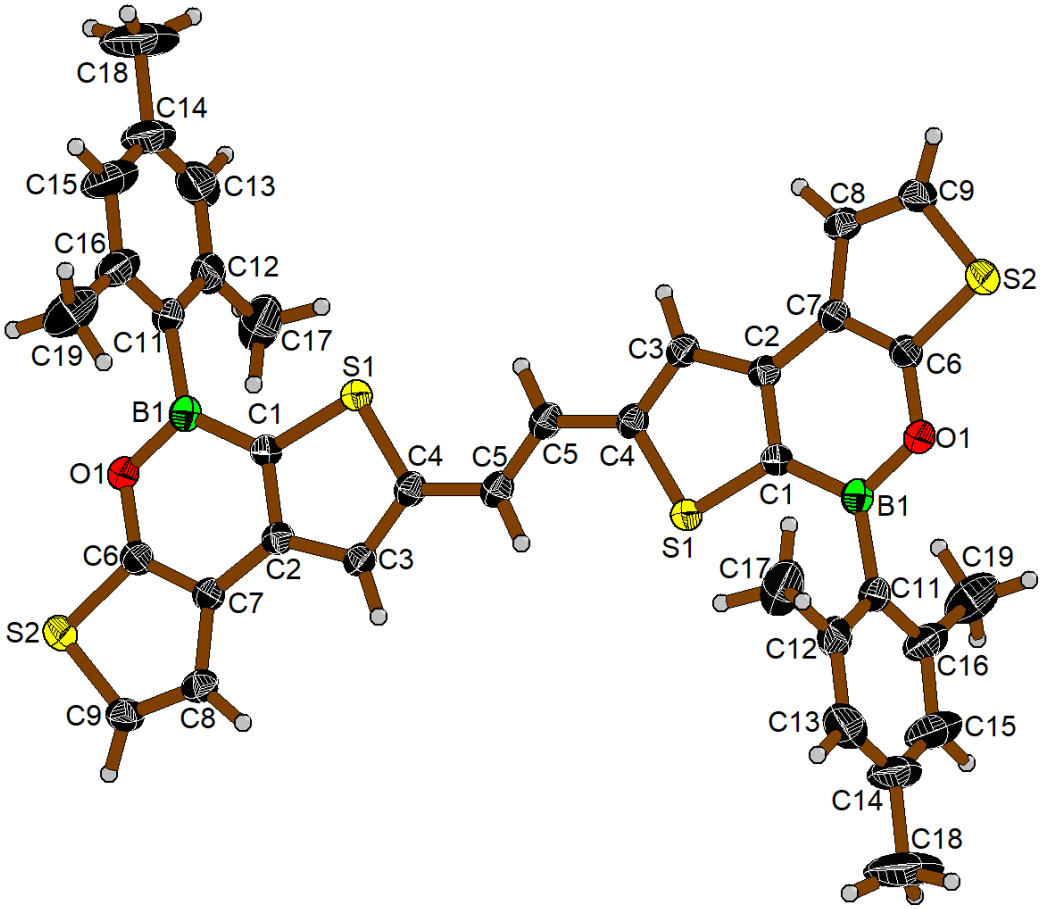

Figure S96: Molecular structure of *trans*-**18** in the solid state. Displacement ellipsoids are drawn at the 50% probability level. Displacement ellipsoids are drawn at the 50% probability level. Selected bond lengths (A), bond angles (°), and torsion angles (°): B1-O1 = 1.400 (3), B1-C1 = 1.518 (3), B1-C11 = 1.568 (3), S1-C1 = 1.727 (2), C5-C5^{i} = 1.337 (4), S2-C6 = 1.725 (2), C4-C5 = 1.447 (3); O1-B1-C1 = 115.26 (19), O1-B1-C11 = 119.24 (18), C1-B1-C11 = 125.5 (2), C5^{i}-C5-C4 = 125.7 (2); C1-B1-O1-C6 = 0.7 (3), C11-B1-O1-C6 = –179.8 (2), O1-B1-C1-C2 = 1.5 (3), C11-B1-C1-C2 = –178.0 (2), O1-B1-C1-S1 = 177.10 (16), C3-C4-C5-C5^{i} = 177.9 (3), S1-C4-C5-C5^{i} = –2.0 (4). Symmetry code(s): (i) -*x*+2, -*y*+2, -*z*+1.

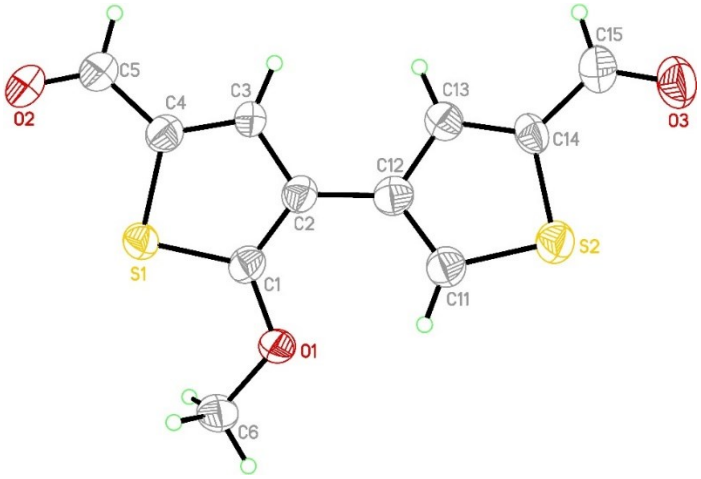

Figure S97: Molecular structure of **22** in the solid state. Displacement ellipsoids are drawn at the 50% probability level.

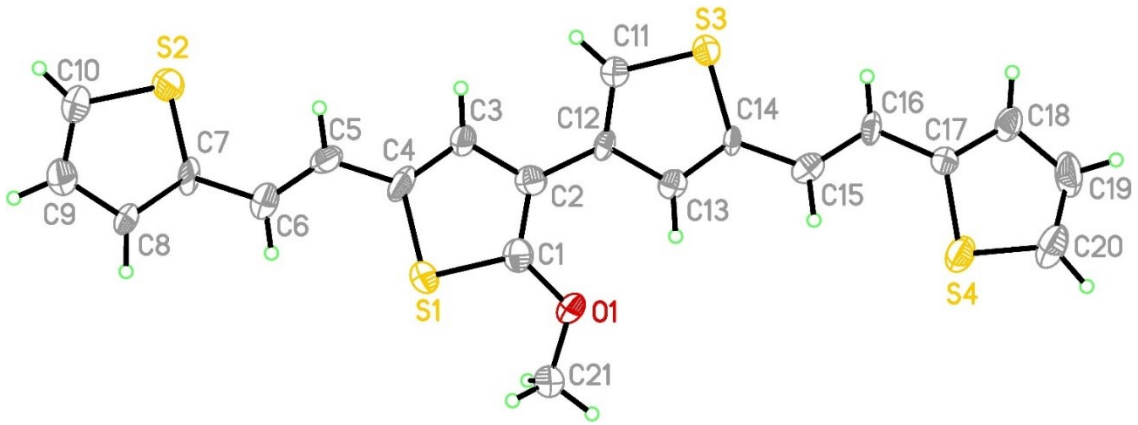

Figure S98: Molecular structure of *trans,trans*-**23** in the solid state. Displacement ellipsoids are drawn at the 50% probability level.

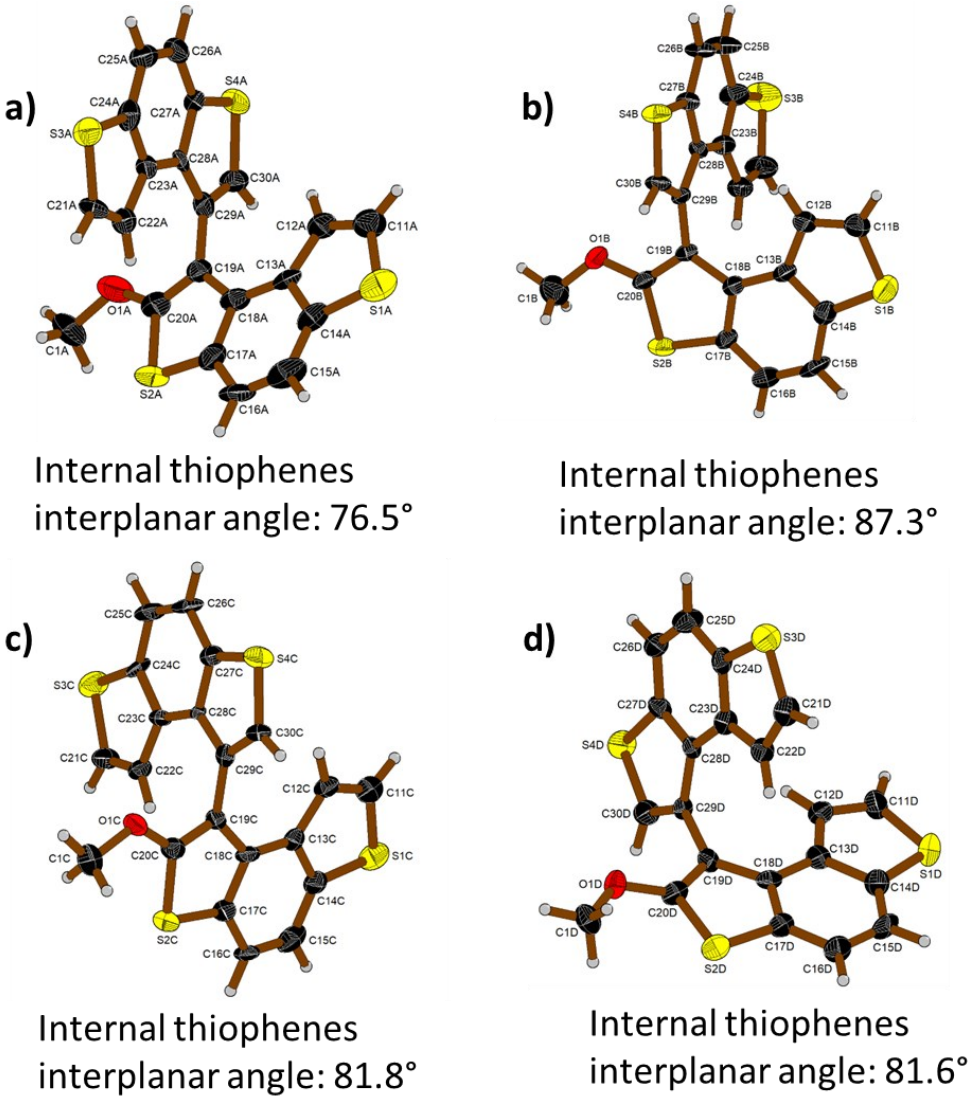

Figure S99: Molecular structure of **21** in the solid state. **21** showed four conformations a, b, c, and d. Displacement ellipsoids are drawn at the 50% probability level. Displacement ellipsoids are drawn at the 50% probability level. Bond lengths (A), bond angles (°), and torsion angles (°) are shown in Table S14A and S14B.

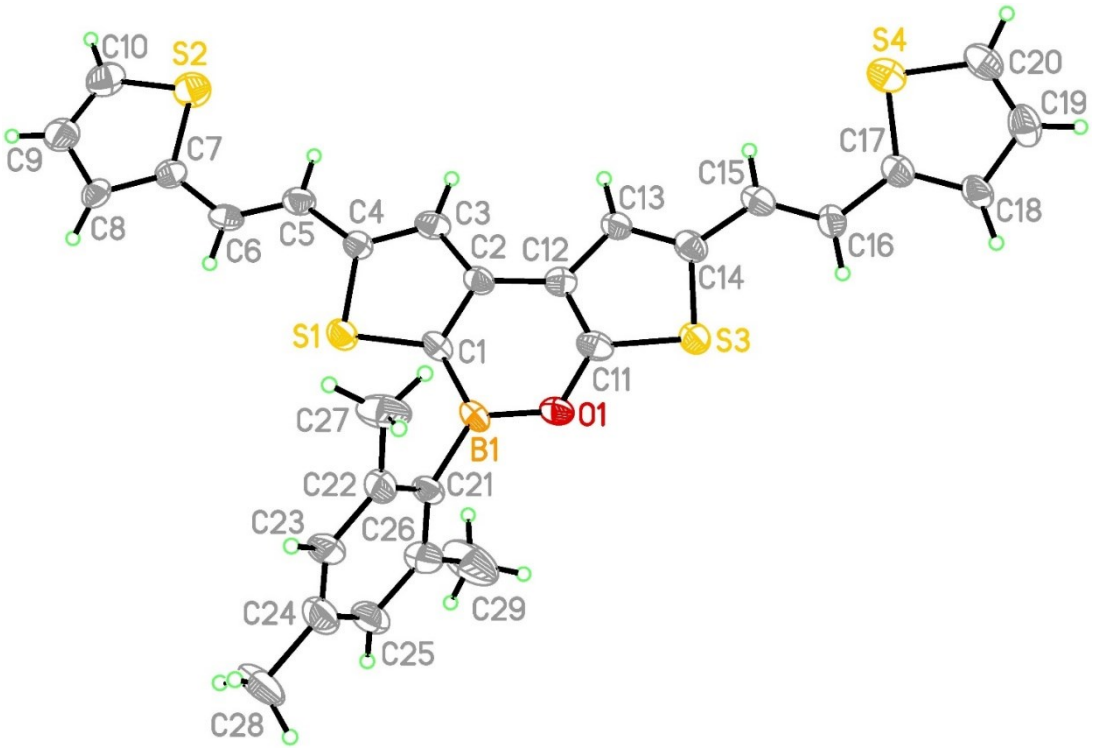

Figure S100: Molecular structure of *trans,trans*-**25** in the solid state. Displacement ellipsoids are drawn at the 50% probability level. Selected bond lengths (A), bond angles (°), and torsion angles (°): O(1)-B(1) = 1.418(13), B(1)-C(1) = 1.516(14), B(1)-C(21) = 1.563(12), C(5)-C(6) = 1.342(14), C(15)-C(16) = 1.334(14); O(1)-B(1)-C(1) = 115.6(8), O(1)-B(1)-C(21) = 120.4(9), C(1)-B(1)-C(21) = 123.9(9), C(6)-C(5)-C(4) = 127.9(9), C(5)-C(6)-C(7) = 126.5(8), C(16)-C(15)-C(14) = 127.4(9), C(15)-C(16)-C(17) = 124.9(9); C(4)-C(5)-C(6)-C(7) = –178.8(9), C(11)-O(1)-B(1)-C(1) = 1.3(12), O(1)-B(1)-C(1)-S(1) = 179.9(7), B(1)-O(1)-C(11)-S(3) = 179.6(7), C(14)-C(15)-C(16)-C(17) = –175.6(9).

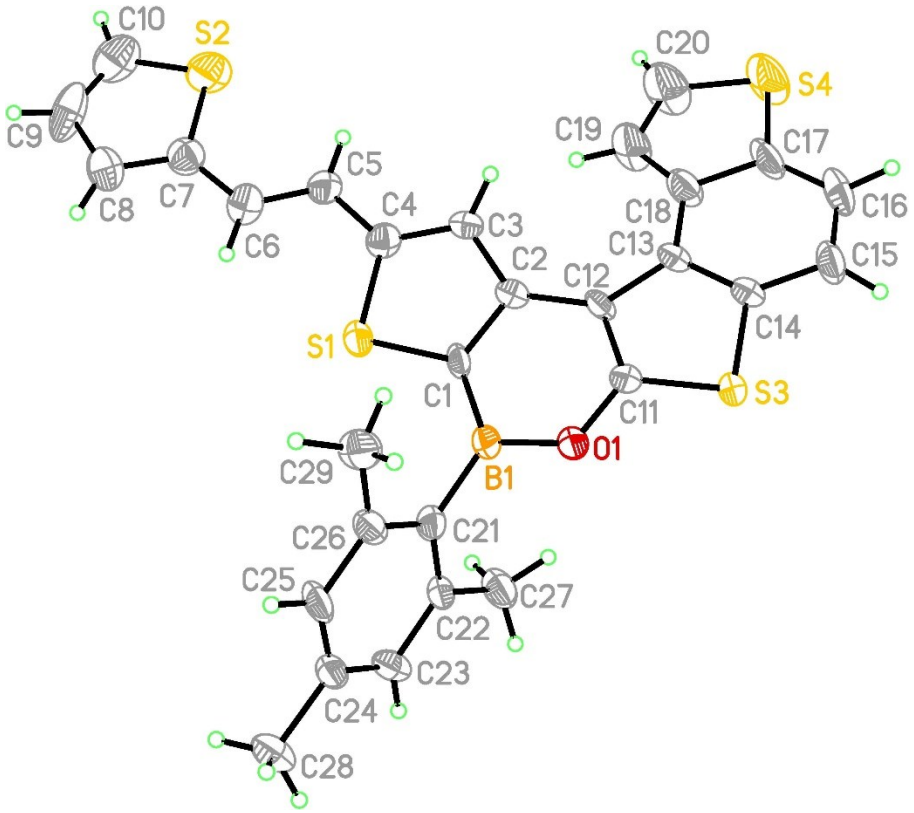

Figure S101: Molecular structure of *trans*-**26** in the solid state. Displacement ellipsoids are drawn at the 50% probability level.

Table S2: Selected crystallographic data for **5**.

Identification code	CCDC 2211405	
Empirical formula	C_{17} H_{15} B O S_2	
Formula weight	310.22	
Temperature	173(2) K	
Wavelength	0.71073 Å	
Crystal system	Monoclinic	
Space group	P 21/n	
Unit cell dimensions	a = 10.9168(6) Å	α = 90°.
	b = 9.8870(4) Å	β = 108.748(5)°.
	c = 15.7757(10) Å	γ = 90°.
Volume	1612.40(16) $Å^3$	
Z	4	
Density (calculated)	1.278 Mg/m^3	
Absorption coefficient	0.324 mm^{-1}	
F(000)	648	
Crystal size	0.190 x 0.160 x 0.040 mm^3	
Theta range for data collection	3.418 to 25.628°.	
Index ranges	-13<=h<=13, -11<=k<=12, -19<=l<=19	
Reflections collected	22255	
Independent reflections	3026 [R(int) = 0.0272]	
Completeness to theta = 25.000°	99.7 %	
Absorption correction	Semi-empirical from equivalents	
Max. and min. transmission	1.000 and 0.329	
Refinement method	Full-matrix least-squares on F^2	
Data / restraints / parameters	3026 / 0 / 193	
Goodness-of-fit on F^2	1.113	
Final R indices [I>2sigma(I)]	R1 = 0.0375, wR2 = 0.0991	
R indices (all data)	R1 = 0.0423, wR2 = 0.1018	
Extinction coefficient	n/a	
Largest diff. peak and hole	0.234 and -0.259 $e.Å^{-3}$	

Table S3: Selected crystallographic data for **8**.

Identification code	CCDC 2211406	
Empirical formula	C_{17} H_{14} B Br O S_2	
Formula weight	389.12	
Temperature	173(2) K	
Wavelength	0.71073 Å	
Crystal system	Monoclinic	
Space group	C 2/c	
Unit cell dimensions	a = 28.461(3) Å	α = 90°.
	b = 8.0254(9) Å	β = 97.265(7)°.
	c = 14.5732(14) Å	γ = 90°.
Volume	3302.0(6) $Å^3$	
Z	8	
Density (calculated)	1.566 Mg/m^3	
Absorption coefficient	2.740 mm^{-1}	
F(000)	1568	
Crystal size	0.180 x 0.170 x 0.140 mm^3	
Theta range for data collection	3.514 to 25.614°.	
Index ranges	-34<=h<=23, -9<=k<=9, -17<=l<=17	
Reflections collected	6330	
Independent reflections	3063 [R(int) = 0.0448]	
Completeness to theta = 25.000°	98.9 %	
Absorption correction	Semi-empirical from equivalents	
Max. and min. transmission	1.000 and 0.874	
Refinement method	Full-matrix least-squares on F^2	
Data / restraints / parameters	3063 / 0 / 202	
Goodness-of-fit on F^2	0.951	
Final R indices [I>2sigma(I)]	R1 = 0.0454, wR2 = 0.0816	
R indices (all data)	R1 = 0.0813, wR2 = 0.0908	
Extinction coefficient	n/a	
Largest diff. peak and hole	0.467 and -0.370 $e.Å^{-3}$	

Table S4: Selected crystallographic data for *trans*-**15**.

Identification code	CCDC 2211409	
Empirical formula	C_{38} H_{32} B_2 Cl_6 O_2 S_4	
Formula weight	883.19	
Temperature	173(2) K	
Wavelength	0.71073 Å	
Crystal system	Monoclinic	
Space group	P 21/c	
Unit cell dimensions	a = 14.5712(5) Å	α = 90°.
	b = 8.6646(3) Å	β = 92.111(3)°.
	c = 16.0522(6) Å	γ = 90°.
Volume	2025.27(12) $Å^3$	
Z	2	
Density (calculated)	1.448 Mg/m^3	
Absorption coefficient	0.665 mm^{-1}	
F(000)	904	
Crystal size	0.230 x 0.220 x 0.140 mm^3	
Theta range for data collection	3.461 to 27.566°.	
Index ranges	-18<=h<=18, -11<=k<=11, -20<=l<=20	
Reflections collected	35354	
Independent reflections	4661 [R(int) = 0.0304]	
Completeness to theta = 25.000°	99.7 %	
Absorption correction	Semi-empirical from equivalents	
Max. and min. transmission	1.000 and 0.651	
Refinement method	Full-matrix least-squares on F^2	
Data / restraints / parameters	4661 / 0 / 238	
Goodness-of-fit on F^2	1.113	
Final R indices [I>2sigma(I)]	R1 = 0.0404, wR2 = 0.0952	
R indices (all data)	R1 = 0.0463, wR2 = 0.0980	
Extinction coefficient	n/a	
Largest diff. peak and hole	0.536 and -0.498 e.$Å^{-3}$	

Table S5: Selected crystallographic data for **16**.

Identification code	CCDC 2211407	
Empirical formula	C_{19} H_{17} B O S_2	
Formula weight	336.25	
Temperature	173(2) K	
Wavelength	0.71073 Å	
Crystal system	Monoclinic	
Space group	C 2/c	
Unit cell dimensions	a = 32.004(3) Å	α = 90°.
	b = 7.9964(4) Å	β = 113.798(6)°.
	c = 14.8098(12) Å	γ = 90°.
Volume	3467.8(5) $Å^3$	
Z	8	
Density (calculated)	1.288 Mg/m^3	
Absorption coefficient	0.307 mm^{-1}	
F(000)	1408	
Crystal colour, shape	colourless plate	
Crystal size	0.140 x 0.090 x 0.030 mm^3	
Theta range for data collection	3.175 to 25.702°.	
Index ranges	-38<=h<=35, -9<=k<=9, -18<=l<=17	
Reflections collected	12695	
Independent reflections	3251 [R(int) = 0.0627]	
Completeness to theta = 25.000°	99.7 %	
Absorption correction	Semi-empirical from equivalents	
Max. and min. transmission	1.000 and 0.497	
Refinement method	Full-matrix least-squares on F^2	
Data / restraints / parameters	3251 / 0 / 211	
Goodness-of-fit on F^2	1.207	
Final R indices [I>2sigma(I)]	R1 = 0.0702, wR2 = 0.1237	
R indices (all data)	R1 = 0.1137, wR2 = 0.1469	
Extinction coefficient	n/a	
Largest diff. peak and hole	0.361 and -0.330 $e.Å^{-3}$	

Table S6: Selected crystallographic data for *trans*-**17**.

Identification code	CCDC 2211408	
Empirical formula	$C_{20}\ H_{16}\ O_2\ S_4$	
Formula weight	416.57	
Temperature	173(2) K	
Wavelength	0.71073 Å	
Crystal system	Monoclinic	
Space group	C 2/c	
Unit cell dimensions	a = 24.2514(14) Å	α = 90°.
	b = 5.4536(2) Å	β = 129.150(4)°.
	c = 18.9753(11) Å	γ = 90°.
Volume	1946.20(19) $Å^3$	
Z	4	
Density (calculated)	1.422 Mg/m^3	
Absorption coefficient	0.500 mm^{-1}	
F(000)	864	
Crystal size	0.230 x 0.150 x 0.140 mm^3	
Theta range for data collection	3.360 to 27.630°.	
Index ranges	-31<=h<=31, -7<=k<=6, -24<=l<=24	
Reflections collected	14476	
Independent reflections	2251 [R(int) = 0.0377]	
Completeness to theta = 25.000°	99.7 %	
Absorption correction	Semi-empirical from equivalents	
Max. and min. transmission	1.000 and 0.331	
Refinement method	Full-matrix least-squares on F^2	
Data / restraints / parameters	2251 / 0 / 120	
Goodness-of-fit on F^2	1.151	
Final R indices [I>2sigma(I)]	R1 = 0.0442, wR2 = 0.1043	
R indices (all data)	R1 = 0.0524, wR2 = 0.1110	
Extinction coefficient	n/a	
Largest diff. peak and hole	0.621 and -0.373 $e.Å^{-3}$	

Table S7: Selected crystallographic data for **1**.

Identification code	CCDC 2211410	
Empirical formula	$C_{36}\ H_{28}\ B_2\ O_2\ S_4$	
Formula weight	642.44	
Temperature	173(2) K	
Wavelength	0.71073 Å	
Crystal system	Triclinic	
Space group	P -1	
Unit cell dimensions	a = 11.5402(7) Å	α = 83.728(5)°.
	b = 11.8194(7) Å	β = 69.057(4)°.
	c = 13.9246(8) Å	γ = 65.913(4)°.
Volume	1617.87(18) $Å^3$	
Z	2	
Density (calculated)	1.319 Mg/m^3	
Absorption coefficient	0.326 mm^{-1}	
F(000)	668	
Crystal size	0.170 x 0.150 x 0.110 mm^3	
Theta range for data collection	3.513 to 25.696°.	
Index ranges	-14<=h<=12, -14<=k<=14, -16<=l<=16	
Reflections collected	17846	
Independent reflections	6047 [R(int) = 0.0336]	
Completeness to theta = 25.000°	99.6 %	
Absorption correction	Semi-empirical from equivalents	
Max. and min. transmission	1.000 and 0.684	
Refinement method	Full-matrix least-squares on F^2	
Data / restraints / parameters	6047 / 0 / 403	
Goodness-of-fit on F^2	1.318	
Final R indices [I>2sigma(I)]	R1 = 0.0676, wR2 = 0.1252	
R indices (all data)	R1 = 0.0833, wR2 = 0.1315	
Extinction coefficient	n/a	
Largest diff. peak and hole	0.272 and -0.265 e.$Å^{-3}$	

Table S8: Selected crystallographic data for **15H2**.

Identification code	CCDC 2211411	
Empirical formula	$C_{36}\ H_{32}\ B_2\ O_2\ S_4$	
Formula weight	646.47	
Temperature	173(2) K	
Wavelength	0.71073 Å	
Crystal system	Monoclinic	
Space group	P 21/n	
Unit cell dimensions	a = 13.5466(6) Å	α= 90°.
	b = 7.9085(2) Å	β= 101.858(3)°.
	c = 30.8935(12) Å	γ = 90°.
Volume	3239.1(2) $Å^3$	
Z	4	
Density (calculated)	1.326 Mg/m^3	
Absorption coefficient	0.326 mm^{-1}	
F(000)	1352	
Crystal size	0.160 x 0.030 x 0.020 mm^3	
Theta range for data collection	2.273 to 25.312°.	
Index ranges	-16<=h<=16, -9<=k<=8, -37<=l<=37	
Reflections collected	23526	
Independent reflections	5811 [R(int) = 0.0648]	
Completeness to theta = 25.000°	99.9 %	
Absorption correction	Semi-empirical from equivalents	
Max. and min. transmission	1.000 and 0.457	
Refinement method	Full-matrix least-squares on F^2	
Data / restraints / parameters	5811 / 0 / 405	
Goodness-of-fit on F^2	1.231	
Final R indices [I>2sigma(I)]	R1 = 0.0705, wR2 = 0.1392	
R indices (all data)	R1 = 0.1008, wR2 = 0.1579	
Extinction coefficient	0.0017(3)	
Largest diff. peak and hole	0.382 and -0.384 $e.Å^{-3}$	

Table S9: Selected crystallographic data for *trans*-**20**.

Identification code	**wa3339**
Crystal data	
Chemical formula	$C_{10}H_6Br_2S_2$
M_r	350.09
Crystal system, space group	Orthorhombic, *Pbca*
Temperature (K)	173
***a*, *b*, *c* (Å)**	10.3682 (4), 7.5629 (3), 14.4299 (6)
***V* (Å^3)**	1131.49 (7)
Z	4
***F*(000)**	672
D_x **(Mg m^{-3})**	2.055
Radiation type	Mo *K*a
m (mm^{-1})	7.49
Crystal shape	Plate
Colour	Brown
Crystal size (mm)	0.26 × 0.25 × 0.06
Data collection	
Diffractometer	STOE *IPDS* II two-circle-diffractometer
Absorption correction	Multi-scan
T_{min}, T_{max}	0.171, 1.000
No. of measured, independent and observed [$I > 2s(I)$] reflections	21643, 1516, 1344
R_{int}	0.061
q values (°)	q_{max} = 29.1, q_{min} = 4.4
Range of *h*, *k*, *l*	*h* = -14®14, *k* = -10®10, *l* = -19®18
Refinement	
$R[F^2 > 2s(F^2)]$, $wR(F^2)$, *S*	0.026, 0.061, 1.11
No. of reflections	1516
No. of parameters	65
Dρ$_{max}$, Dρ$_{min}$ (e Å^{-3})	0.33, -0.50
Extinction coefficient	0.0022 (4)

Table S10: Selected crystallographic data for *trans*-**19**.

Identification code	wa3210	
Empirical formula	C20 H16 O2 S4	
Formula weight	416.57	
Temperature	173(2) K	
Wavelength	0.71073 Å	
Crystal system	Orthorhombic	
Space group	F d d 2	
Unit cell dimensions	a = 35.371(2) Å	a= 90°.
	b = 38.7786(17) Å	b= 90°.
	c = 5.5772(3) Å	g = 90°.
Volume	7650.0(7) $Å^3$	
Z	16	
Density (calculated)	1.447 Mg/m^3	
Absorption coefficient	0.509 mm^{-1}	
F(000)	3456	
Crystal colour, shape	colourless needle	
Crystal size	0.220 x 0.040 x 0.040 mm^3	
Theta range for data collection	3.356 to 25.687°.	
Index ranges	-42<=h<=42, -45<=k<=46, -6<=l<=6	
Reflections collected	13908	
Independent reflections	3586 [R(int) = 0.0553]	
Completeness to theta = 25.000°	99.7 %	
Absorption correction	Semi-empirical from equivalents	
Max. and min. transmission	1.000 and 0.335	
Refinement method	Full-matrix least-squares on F^2	
Data / restraints / parameters	3586 / 1 / 235	
Goodness-of-fit on F^2	1.163	
Final R indices [I>2sigma(I)]	R1 = 0.0584, wR2 = 0.1238	
R indices (all data)	R1 = 0.0800, wR2 = 0.1379	
Absolute structure parameter	0.01(18)	
Extinction coefficient	n/a	
Largest diff. peak and hole	0.239 and -0.270 e.$Å^{-3}$	

Table S11: Selected crystallographic data for *trans*-**18**.

Identification code	**wa3333**
Crystal data	
Chemical formula	$C_{36}H_{30}B_2O_2S_4$
M_r	644.46
Crystal system, space group	Monoclinic, $P2_1/c$
Temperature (K)	173
***a*, *b*, *c* (Å)**	12.7041 (5), 6.2990 (3), 20.8628 (11)
b (°)	99.828 (4)
***V* (Å^3)**	1645.01 (13)
Z	2
***F*(000)**	672
D_x **(Mg m^{-3})**	1.301
Radiation type	Mo *K*a
m (mm^{-1})	0.32
Crystal shape	Plank
Colour	Brown
Crystal size (mm)	0.55 × 0.30 × 0.03
Data collection	
Diffractometer	STOE *IPDS* II two-circle-diffractometer
Absorption correction	Multi-scan
T_{min}, T_{max}	0.081, 1.000
No. of measured, independent and observed [$I > 2s(I)$] reflections	11399, 3352, 2506
R_{int}	0.059
q values (°)	q_{max} = 26.4, q_{min} = 3.8
Range of *h*, *k*, *l*	*h* = -14®15, *k* = -7®7, *l* = -26®25
Refinement	
$R[F^2 > 2s(F^2)]$, $wR(F^2)$, *S*	0.043, 0.115, 1.04
No. of reflections	3352
No. of parameters	202
Dρ$_{max}$, Dρ$_{min}$ (e Å^{-3})	0.44, -0.22

Table S12: Selected crystallographic data for **22**.

Identification code	wa3190	
Empirical formula	C11 H8 O3 S2	
Formula weight	252.29	
Temperature	173(2) K	
Wavelength	0.71073 Å	
Crystal system	Monoclinic	
Space group	P 21/n	
Unit cell dimensions	a = 3.8784(4) Å	a= 90°.
	b = 8.6819(5) Å	b= 91.605(7)°.
	c = 32.214(3) Å	g = 90°.
Volume	1084.28(16) $Å^3$	
Z	4	
Density (calculated)	1.546 Mg/m^3	
Absorption coefficient	0.477 mm^{-1}	
F(000)	520	
Crystal size	0.090 x 0.020 x 0.010 mm^3	
Theta range for data collection	2.430 to 25.168°.	
Index ranges	-4<=h<=4, -10<=k<=10, -37<=l<=38	
Reflections collected	1964	
Independent reflections	1964 [R(int) = ?]	
Completeness to theta = 25.000°	99.9 %	
Absorption correction	Semi-empirical from equivalents	
Max. and min. transmission	1.000 and 0.435	
Refinement method	Full-matrix least-squares on F^2	
Data / restraints / parameters	1964 / 0 / 148	
Goodness-of-fit on F^2	1.149	
Final R indices [I>2sigma(I)]	R1 = 0.0935, wR2 = 0.2324	
R indices (all data)	R1 = 0.1510, wR2 = 0.2858	
Extinction coefficient	n/a	
Largest diff. peak and hole	0.507 and -0.481 $e.Å^{-3}$	

Table S13: Selected crystallographic data for *trans,trans*-**23.**

Identification code	wa3200	
Empirical formula	C21 H16 O S4	
Formula weight	412.58	
Temperature	173(2) K	
Wavelength	0.71073 Å	
Crystal system	Monoclinic	
Space group	P 21/n	
Unit cell dimensions	a = 27.958(2) Å	a= 90°.
	b = 5.6274(5) Å	b= 93.926(6)°.
	c = 28.917(3) Å	g = 90°.
Volume	4538.9(7) $Å^3$	
Z	8	
Density (calculated)	1.208 Mg/m^3	
Absorption coefficient	0.425 mm^{-1}	
F(000)	1712	
Crystal colour, shape	colourless needle	
Crystal size	0.120 x 0.030 x 0.020 mm^3	
Theta range for data collection	3.150 to 25.750°.	
Index ranges	-33<=h<=34, -6<=k<=6, -35<=l<=35	
Reflections collected	20423	
Independent reflections	8480 [R(int) = 0.1811]	
Completeness to theta = 25.000°	99.6 %	
Absorption correction	Semi-empirical from equivalents	
Max. and min. transmission	1.000 and 0.588	
Refinement method	Full-matrix least-squares on F^2	
Data / restraints / parameters	8480 / 6 / 469	
Goodness-of-fit on F^2	1.136	
Final R indices [I>2sigma(I)]	R1 = 0.1444, wR2 = 0.2541	
R indices (all data)	R1 = 0.2740, wR2 = 0.3173	
Extinction coefficient	n/a	
Largest diff. peak and hole	0.610 and -0.567 $e.Å^{-3}$	

Table S14: Selected crystallographic data for **21**.

Identification code	**wa3335**
Crystal data	
Chemical formula	$C_{21}H_{12}OS_4$
M_r	408.55
Crystal system, space group	Triclinic, $P\bar{1}$
Temperature (K)	173
***a*, *b*, *c* (Å)**	15.1300 (11), 15.3597 (9), 17.5595 (16)
a, b, g (°)	102.360 (7), 108.006 (8), 102.859 (6)
***V* (Å^3)**	3603.2 (5)
Z	8
***F*(000)**	1680
***D*$_x$ (Mg m^{-3})**	1.506
Radiation type	Mo *K*a
m (mm^{-1})	0.54
Crystal shape	Plate
Colour	Light yellowish-brown
Crystal size (mm)	0.42 × 0.41 × 0.05
Data collection	
Diffractometer	STOE *IPDS* II two-circle-diffractometer
Absorption correction	Multi-scan
T_{min}, T_{max}	0.791, 1.000
No. of measured, independent and observed [$I > 2s(I)$] reflections	16557, 16557, 6590
R_{int}	0.141
q values (°)	q_{max} = 26.4, q_{min} = 3.7
Range of *h*, *k*, *l*	*h* = -18®18, *k* = -19®19, *l* = -21®21
Refinement	
$R[F^2 > 2s(F^2)]$, $wR(F^2)$, S	0.053, 0.093, 0.74
No. of reflections	16557
No. of parameters	942
Dρ$_{max}$, Dρ$_{min}$ (e Å^{-3})	0.31, -0.36

Table S14A: Selected geometric parameters (Å, º) for **21**.

S1A—C11A	1.728 (6)	S1C—C11C	1.729 (5)
S1A—C14A	1.745 (6)	S1C—C14C	1.738 (6)
S2A—C17A	1.741 (7)	S2C—C17C	1.744 (6)
S2A—C20A	1.775 (6)	S2C—C20C	1.755 (5)
S3A—C24A	1.732 (6)	S3C—C21C	1.740 (6)
S3A—C21A	1.733 (5)	S3C—C24C	1.742 (6)
S4A—C27A	1.726 (6)	S4C—C27C	1.720 (6)
S4A—C30A	1.756 (5)	S4C—C30C	1.731 (5)
O1A—C20A	1.339 (7)	O1C—C20C	1.355 (6)
O1A—C1A	1.427 (6)	O1C—C1C	1.424 (6)
C11A—C12A	1.317 (8)	C11C—C12C	1.336 (7)
C12A—C13A	1.433 (7)	C12C—C13C	1.430 (7)
C13A—C14A	1.386 (8)	C13C—C18C	1.399 (7)
C13A—C18A	1.425 (8)	C13C—C14C	1.422 (7)
C14A—C15A	1.413 (8)	C14C—C15C	1.399 (8)
C15A—C16A	1.367 (8)	C15C—C16C	1.351 (8)
C16A—C17A	1.406 (8)	C16C—C17C	1.418 (7)
C17A—C18A	1.400 (7)	C17C—C18C	1.400 (7)
C18A—C19A	1.431 (8)	C18C—C19C	1.438 (7)
C19A—C20A	1.321 (8)	C19C—C20C	1.331 (7)
C19A—C29A	1.499 (7)	C19C—C29C	1.506 (7)
C21A—C22A	1.329 (7)	C21C—C22C	1.350 (7)
C22A—C23A	1.452 (7)	C22C—C23C	1.447 (7)
C23A—C24A	1.385 (7)	C23C—C24C	1.390 (7)
C23A—C28A	1.427 (7)	C23C—C28C	1.414 (7)
C24A—C25A	1.419 (7)	C24C—C25C	1.391 (7)
C25A—C26A	1.360 (7)	C25C—C26C	1.363 (7)
C26A—C27A	1.391 (7)	C26C—C27C	1.415 (7)
C27A—C28A	1.415 (7)	C27C—C28C	1.408 (7)
C28A—C29A	1.421 (7)	C28C—C29C	1.424 (7)
C29A—C30A	1.361 (7)	C29C—C30C	1.358 (7)
S1B—C14B	1.728 (6)	S1D—C14D	1.726 (6)
S1B—C11B	1.735 (6)	S1D—C11D	1.729 (5)
S2B—C17B	1.740 (6)	S2D—C20D	1.749 (5)
S2B—C20B	1.755 (5)	S2D—C17D	1.753 (6)
S3B—C24B	1.724 (6)	S3D—C21D	1.711 (6)
S3B—C21B	1.730 (6)	S3D—C24D	1.748 (6)
S4B—C27B	1.721 (5)	S4D—C30D	1.720 (5)
S4B—C30B	1.741 (5)	S4D—C27D	1.741 (5)
O1B—C20B	1.332 (7)	O1D—C20D	1.355 (6)
O1B—C1B	1.413 (6)	O1D—C1D	1.433 (6)

C11B—C12B	1.351 (8)	C11D—C12D	1.342 (7)
C12B—C13B	1.440 (7)	C12D—C13D	1.441 (7)
C13B—C14B	1.403 (8)	C13D—C18D	1.428 (8)
C13B—C18B	1.413 (8)	C13D—C14D	1.443 (7)
C14B—C15B	1.440 (7)	C14D—C15D	1.368 (7)
C15B—C16B	1.353 (8)	C15D—C16D	1.377 (7)
C16B—C17B	1.365 (7)	C16D—C17D	1.375 (7)
C17B—C18B	1.418 (7)	C17D—C18D	1.397 (7)
C18B—C19B	1.424 (7)	C18D—C19D	1.425 (7)
C19B—C20B	1.374 (7)	C19D—C20D	1.371 (7)
C19B—C29B	1.477 (6)	C19D—C29D	1.479 (7)
C21B—C22B	1.349 (7)	C21D—C22D	1.334 (7)
C22B—C23B	1.463 (7)	C22D—C23D	1.439 (7)
C23B—C24B	1.371 (7)	C23D—C24D	1.382 (7)
C23B—C28B	1.421 (7)	C23D—C28D	1.418 (7)
C24B—C25B	1.445 (7)	C24D—C25D	1.418 (7)
C25B—C26B	1.391 (7)	C25D—C26D	1.382 (7)
C26B—C27B	1.393 (7)	C26D—C27D	1.406 (7)
C27B—C28B	1.388 (6)	C27D—C28D	1.390 (7)
C28B—C29B	1.431 (7)	C28D—C29D	1.421 (7)
C29B—C30B	1.344 (6)	C29D—C30D	1.369 (7)

C11A—S1A—C14A	90.3 (3)	C11C—S1C—C14C	91.1 (3)
C17A—S2A—C20A	89.8 (3)	C17C—S2C—C20C	89.5 (3)
C24A—S3A—C21A	90.0 (3)	C21C—S3C—C24C	92.0 (3)
C27A—S4A—C30A	91.6 (3)	C27C—S4C—C30C	91.5 (3)
C20A—O1A—C1A	120.9 (5)	C20C—O1C—C1C	118.7 (4)
C12A—C11A—S1A	114.5 (5)	C12C—C11C—S1C	113.2 (5)
C11A—C12A—C13A	111.9 (6)	C11C—C12C—C13C	113.9 (5)
C14A—C13A—C18A	118.0 (6)	C18C—C13C—C14C	118.1 (5)
C14A—C13A—C12A	112.8 (6)	C18C—C13C—C12C	131.2 (5)
C18A—C13A—C12A	129.0 (6)	C14C—C13C—C12C	110.7 (5)
C13A—C14A—C15A	123.2 (7)	C15C—C14C—C13C	122.4 (6)
C13A—C14A—S1A	110.4 (5)	C15C—C14C—S1C	126.5 (5)
C15A—C14A—S1A	126.3 (6)	C13C—C14C—S1C	111.1 (5)
C16A—C15A—C14A	118.6 (7)	C16C—C15C—C14C	119.4 (5)
C15A—C16A—C17A	119.2 (6)	C15C—C16C—C17C	119.5 (6)
C18A—C17A—C16A	122.8 (6)	C18C—C17C—C16C	122.3 (6)
C18A—C17A—S2A	111.9 (5)	C18C—C17C—S2C	112.3 (4)
C16A—C17A—S2A	125.3 (6)	C16C—C17C—S2C	125.5 (5)
C17A—C18A—C13A	117.9 (6)	C13C—C18C—C17C	118.4 (5)
C17A—C18A—C19A	111.4 (6)	C13C—C18C—C19C	130.1 (5)
C13A—C18A—C19A	130.6 (5)	C17C—C18C—C19C	111.4 (5)

C20A—C19A—C18A	113.9 (6)	C20C—C19C—C18C	112.7 (5)
C20A—C19A—C29A	123.0 (6)	C20C—C19C—C29C	122.9 (5)
C18A—C19A—C29A	122.1 (6)	C18C—C19C—C29C	124.1 (5)
C19A—C20A—O1A	126.3 (6)	C19C—C20C—O1C	124.0 (5)
C19A—C20A—S2A	112.8 (5)	C19C—C20C—S2C	114.1 (4)
O1A—C20A—S2A	120.8 (5)	O1C—C20C—S2C	121.9 (4)
C22A—C21A—S3A	114.4 (5)	C22C—C21C—S3C	111.3 (4)
C21A—C22A—C23A	111.9 (5)	C21C—C22C—C23C	114.1 (5)
C24A—C23A—C28A	118.9 (5)	C24C—C23C—C28C	118.4 (5)
C24A—C23A—C22A	111.2 (5)	C24C—C23C—C22C	111.4 (5)
C28A—C23A—C22A	129.9 (5)	C28C—C23C—C22C	130.1 (5)
C23A—C24A—C25A	122.8 (5)	C23C—C24C—C25C	123.0 (6)
C23A—C24A—S3A	112.4 (5)	C23C—C24C—S3C	111.1 (4)
C25A—C24A—S3A	124.8 (4)	C25C—C24C—S3C	125.9 (5)
C26A—C25A—C24A	118.5 (5)	C26C—C25C—C24C	119.3 (6)
C25A—C26A—C27A	120.1 (5)	C25C—C26C—C27C	119.6 (5)
C26A—C27A—C28A	123.0 (5)	C28C—C27C—C26C	121.4 (5)
C26A—C27A—S4A	126.2 (4)	C28C—C27C—S4C	111.6 (4)
C28A—C27A—S4A	110.9 (4)	C26C—C27C—S4C	126.9 (5)
C27A—C28A—C29A	112.5 (5)	C27C—C28C—C23C	118.2 (5)
C27A—C28A—C23A	116.8 (5)	C27C—C28C—C29C	111.3 (5)
C29A—C28A—C23A	130.6 (5)	C23C—C28C—C29C	130.5 (5)
C30A—C29A—C28A	113.0 (5)	C30C—C29C—C28C	113.2 (5)
C30A—C29A—C19A	124.0 (5)	C30C—C29C—C19C	123.6 (5)
C28A—C29A—C19A	122.8 (5)	C28C—C29C—C19C	123.1 (5)
C29A—C30A—S4A	112.0 (4)	C29C—C30C—S4C	112.3 (4)
C14B—S1B—C11B	90.6 (3)	C14D—S1D—C11D	92.4 (3)
C17B—S2B—C20B	91.0 (3)	C20D—S2D—C17D	90.6 (3)
C24B—S3B—C21B	90.8 (3)	C21D—S3D—C24D	90.6 (3)
C27B—S4B—C30B	90.8 (3)	C30D—S4D—C27D	90.7 (3)
C20B—O1B—C1B	119.5 (5)	C20D—O1D—C1D	116.8 (4)
C12B—C11B—S1B	113.5 (5)	C12D—C11D—S1D	113.1 (5)
C11B—C12B—C13B	112.5 (6)	C11D—C12D—C13D	113.3 (5)
C14B—C13B—C18B	118.6 (5)	C18D—C13D—C12D	130.9 (5)
C14B—C13B—C12B	111.0 (6)	C18D—C13D—C14D	118.0 (6)
C18B—C13B—C12B	130.4 (6)	C12D—C13D—C14D	111.1 (6)
C13B—C14B—C15B	121.6 (6)	C15D—C14D—C13D	120.8 (6)
C13B—C14B—S1B	112.4 (5)	C15D—C14D—S1D	129.0 (5)
C15B—C14B—S1B	126.1 (5)	C13D—C14D—S1D	110.2 (5)
C16B—C15B—C14B	118.1 (6)	C14D—C15D—C16D	121.5 (5)
C15B—C16B—C17B	121.4 (6)	C17D—C16D—C15D	118.2 (6)
C16B—C17B—C18B	122.5 (6)	C16D—C17D—C18D	124.4 (6)
C16B—C17B—S2B	126.6 (5)	C16D—C17D—S2D	125.4 (5)

C18B—C17B—S2B	110.9 (5)	C18D—C17D—S2D	110.2 (4)
C13B—C18B—C17B	117.8 (5)	C17D—C18D—C19D	114.8 (6)
C13B—C18B—C19B	129.0 (5)	C17D—C18D—C13D	117.0 (5)
C17B—C18B—C19B	113.2 (5)	C19D—C18D—C13D	128.1 (6)
C20B—C19B—C18B	111.8 (5)	C20D—C19D—C18D	110.4 (5)
C20B—C19B—C29B	122.0 (5)	C20D—C19D—C29D	121.3 (5)
C18B—C19B—C29B	126.1 (5)	C18D—C19D—C29D	127.9 (5)
O1B—C20B—C19B	123.8 (5)	O1D—C20D—C19D	123.9 (5)
O1B—C20B—S2B	123.1 (5)	O1D—C20D—S2D	122.1 (5)
C19B—C20B—S2B	113.0 (4)	C19D—C20D—S2D	113.9 (4)
C22B—C21B—S3B	112.6 (4)	C22D—C21D—S3D	114.1 (5)
C21B—C22B—C23B	113.0 (5)	C21D—C22D—C23D	112.3 (5)
C24B—C23B—C28B	119.5 (5)	C24D—C23D—C28D	118.2 (5)
C24B—C23B—C22B	110.0 (5)	C24D—C23D—C22D	111.8 (5)
C28B—C23B—C22B	130.5 (5)	C28D—C23D—C22D	130.0 (5)
C23B—C24B—C25B	122.1 (5)	C23D—C24D—C25D	124.6 (5)
C23B—C24B—S3B	113.6 (4)	C23D—C24D—S3D	111.1 (4)
C25B—C24B—S3B	124.3 (5)	C25D—C24D—S3D	124.2 (5)
C26B—C25B—C24B	117.7 (5)	C26D—C25D—C24D	117.6 (5)
C25B—C26B—C27B	119.3 (5)	C25D—C26D—C27D	117.4 (5)
C28B—C27B—C26B	123.5 (5)	C28D—C27D—C26D	126.0 (5)
C28B—C27B—S4B	111.6 (4)	C28D—C27D—S4D	111.3 (4)
C26B—C27B—S4B	124.9 (4)	C26D—C27D—S4D	122.7 (4)
C27B—C28B—C23B	117.9 (5)	C27D—C28D—C23D	116.2 (5)
C27B—C28B—C29B	112.4 (5)	C27D—C28D—C29D	112.7 (5)
C23B—C28B—C29B	129.7 (5)	C23D—C28D—C29D	131.1 (5)
C30B—C29B—C28B	112.1 (5)	C30D—C29D—C28D	111.6 (5)
C30B—C29B—C19B	121.9 (5)	C30D—C29D—C19D	123.8 (5)
C28B—C29B—C19B	126.0 (5)	C28D—C29D—C19D	124.5 (5)
C29B—C30B—S4B	113.0 (4)	C29D—C30D—S4D	113.5 (4)

C14A—S1A—C11A—C12A	-0.3 (6)	C14C—S1C—C11C—C12C	0.4 (5)
S1A—C11A—C12A—C13A	1.7 (8)	S1C—C11C—C12C—C13C	-0.3 (7)
C11A—C12A—C13A—C14A	-2.7 (8)	C11C—C12C—C13C—C18C	178.3 (6)
C11A—C12A—C13A—C18A	-176.1 (6)	C11C—C12C—C13C—C14C	0.0 (7)
C18A—C13A—C14A—C15A	-5.5 (9)	C18C—C13C—C14C—C15C	0.8 (9)
C12A—C13A—C14A—C15A	-179.7 (5)	C12C—C13C—C14C—C15C	179.3 (5)
C18A—C13A—C14A—S1A	176.6 (4)	C18C—C13C—C14C—S1C	-178.3 (4)
C12A—C13A—C14A—S1A	2.5 (7)	C12C—C13C—C14C—S1C	0.2 (6)
C11A—S1A—C14A—C13A	-1.3 (5)	C11C—S1C—C14C—C15C	-179.3 (6)
C11A—S1A—C14A—C15A	-179.1 (6)	C11C—S1C—C14C—C13C	-0.3 (4)
C13A—C14A—C15A—C16A	6.2 (10)	C13C—C14C—C15C—C16C	-0.9 (9)
S1A—C14A—C15A—C16A	-176.3 (5)	S1C—C14C—C15C—C16C	178.0 (5)

C14A—C15A—C16A—C17A	-2.3 (10)	C14C—C15C—C16C—C17C	1.3 (10)
C15A—C16A—C17A—C18A	-1.9 (10)	C15C—C16C—C17C—C18C	-1.7 (10)
C15A—C16A—C17A—S2A	177.3 (5)	C15C—C16C—C17C—S2C	178.3 (5)
C20A—S2A—C17A—C18A	-2.7 (5)	C20C—S2C—C17C—C18C	1.7 (5)
C20A—S2A—C17A—C16A	178.0 (6)	C20C—S2C—C17C—C16C	-178.3 (5)
C16A—C17A—C18A—C13A	2.5 (9)	C14C—C13C—C18C—C17C	-1.1 (9)
S2A—C17A—C18A—C13A	-176.8 (4)	C12C—C13C—C18C—C17C	-179.2 (6)
C16A—C17A—C18A—C19A	-176.0 (6)	C14C—C13C—C18C—C19C	-176.4 (5)
S2A—C17A—C18A—C19A	4.7 (7)	C12C—C13C—C18C—C19C	5.4 (11)
C14A—C13A—C18A—C17A	1.1 (9)	C16C—C17C—C18C—C13C	1.5 (9)
C12A—C13A—C18A—C17A	174.2 (6)	S2C—C17C—C18C—C13C	-178.5 (4)
C14A—C13A—C18A—C19A	179.3 (6)	C16C—C17C—C18C—C19C	177.7 (5)
C12A—C13A—C18A—C19A	-7.6 (11)	S2C—C17C—C18C—C19C	-2.3 (6)
C17A—C18A—C19A—C20A	-4.9 (8)	C13C—C18C—C19C—C20C	177.4 (6)
C13A—C18A—C19A—C20A	176.9 (6)	C17C—C18C—C19C—C20C	1.8 (7)
C17A—C18A—C19A—C29A	163.9 (5)	C13C—C18C—C19C—C29C	3.7 (10)
C13A—C18A—C19A—C29A	-14.3 (10)	C17C—C18C—C19C—C29C	-171.9 (5)
C18A—C19A—C20A—O1A	179.7 (7)	C18C—C19C—C20C—O1C	-177.8 (5)
C29A—C19A—C20A—O1A	11.0 (12)	C29C—C19C—C20C—O1C	-4.0 (9)
C18A—C19A—C20A—S2A	2.8 (8)	C18C—C19C—C20C—S2C	-0.5 (7)
C29A—C19A—C20A—S2A	-165.9 (4)	C29C—C19C—C20C—S2C	173.3 (4)
C1A—O1A—C20A—C19A	-178.3 (7)	C1C—O1C—C20C—C19C	178.0 (6)
C1A—O1A—C20A—S2A	-1.6 (10)	C1C—O1C—C20C—S2C	0.9 (7)
C17A—S2A—C20A—C19A	0.0 (6)	C17C—S2C—C20C—C19C	-0.7 (5)
C17A—S2A—C20A—O1A	-177.2 (6)	C17C—S2C—C20C—O1C	176.7 (5)
C24A—S3A—C21A—C22A	-0.4 (6)	C24C—S3C—C21C—C22C	2.0 (5)
S3A—C21A—C22A—C23A	1.3 (8)	S3C—C21C—C22C—C23C	-2.5 (7)
C21A—C22A—C23A—C24A	-1.8 (8)	C21C—C22C—C23C—C24C	1.8 (7)
C21A—C22A—C23A—C28A	180.0 (6)	C21C—C22C—C23C—C28C	-177.7 (6)
C28A—C23A—C24A—C25A	0.0 (9)	C28C—C23C—C24C—C25C	-1.6 (8)
C22A—C23A—C24A—C25A	-178.4 (6)	C22C—C23C—C24C—C25C	178.8 (5)
C28A—C23A—C24A—S3A	179.9 (4)	C28C—C23C—C24C—S3C	179.4 (4)
C22A—C23A—C24A—S3A	1.5 (7)	C22C—C23C—C24C—S3C	-0.2 (6)
C21A—S3A—C24A—C23A	-0.6 (5)	C21C—S3C—C24C—C23C	-1.0 (5)
C21A—S3A—C24A—C25A	179.3 (6)	C21C—S3C—C24C—C25C	180.0 (5)
C23A—C24A—C25A—C26A	-0.1 (10)	C23C—C24C—C25C—C26C	3.2 (9)
S3A—C24A—C25A—C26A	-180.0 (5)	S3C—C24C—C25C—C26C	-177.9 (5)
C24A—C25A—C26A—C27A	0.1 (9)	C24C—C25C—C26C—C27C	-2.0 (9)
C25A—C26A—C27A—C28A	0.0 (9)	C25C—C26C—C27C—C28C	-0.5 (9)
C25A—C26A—C27A—S4A	179.7 (5)	C25C—C26C—C27C—S4C	-179.1 (5)
C30A—S4A—C27A—C26A	-179.6 (5)	C30C—S4C—C27C—C28C	-1.2 (4)
C30A—S4A—C27A—C28A	0.1 (5)	C30C—S4C—C27C—C26C	177.5 (5)
C26A—C27A—C28A—C29A	179.7 (6)	C26C—C27C—C28C—C23C	2.0 (8)

S4A—C27A—C28A—C29A	-0.1 (6)	S4C—C27C—C28C—C23C	-179.2 (4)
C26A—C27A—C28A—C23A	-0.1 (9)	C26C—C27C—C28C—C29C	-177.4 (5)
S4A—C27A—C28A—C23A	-179.8 (4)	S4C—C27C—C28C—C29C	1.4 (6)
C24A—C23A—C28A—C27A	0.1 (8)	C24C—C23C—C28C—C27C	-1.0 (8)
C22A—C23A—C28A—C27A	178.2 (6)	C22C—C23C—C28C—C27C	178.5 (5)
C24A—C23A—C28A—C29A	-179.6 (6)	C24C—C23C—C28C—C29C	178.3 (6)
C22A—C23A—C28A—C29A	-1.5 (11)	C22C—C23C—C28C—C29C	-2.2 (10)
C27A—C28A—C29A—C30A	-0.1 (8)	C27C—C28C—C29C—C30C	-0.9 (7)
C23A—C28A—C29A—C30A	179.7 (6)	C23C—C28C—C29C—C30C	179.8 (5)
C27A—C28A—C29A—C19A	175.0 (6)	C27C—C28C—C29C—C19C	176.6 (5)
C23A—C28A—C29A—C19A	-5.3 (10)	C23C—C28C—C29C—C19C	-2.7 (9)
C20A—C19A—C29A—C30A	-90.4 (9)	C20C—C19C—C29C—C30C	89.3 (8)
C18A—C19A—C29A—C30A	101.9 (8)	C18C—C19C—C29C—C30C	-97.6 (7)
C20A—C19A—C29A—C28A	95.2 (8)	C20C—C19C—C29C—C28C	-87.9 (7)
C18A—C19A—C29A—C28A	-72.6 (8)	C18C—C19C—C29C—C28C	85.2 (7)
C28A—C29A—C30A—S4A	0.2 (7)	C28C—C29C—C30C—S4C	0.0 (6)
C19A—C29A—C30A—S4A	-174.8 (5)	C19C—C29C—C30C—S4C	-177.5 (4)
C27A—S4A—C30A—C29A	-0.2 (5)	C27C—S4C—C30C—C29C	0.7 (5)
C14B—S1B—C11B—C12B	0.4 (5)	C14D—S1D—C11D—C12D	0.4 (5)
S1B—C11B—C12B—C13B	-0.5 (7)	S1D—C11D—C12D—C13D	-0.2 (7)
C11B—C12B—C13B—C14B	0.5 (8)	C11D—C12D—C13D—C18D	-178.8 (6)
C11B—C12B—C13B—C18B	-179.1 (6)	C11D—C12D—C13D—C14D	-0.1 (7)
C18B—C13B—C14B—C15B	0.3 (9)	C18D—C13D—C14D—C15D	-0.6 (8)
C12B—C13B—C14B—C15B	-179.4 (5)	C12D—C13D—C14D—C15D	-179.5 (6)
C18B—C13B—C14B—S1B	179.4 (4)	C18D—C13D—C14D—S1D	179.3 (4)
C12B—C13B—C14B—S1B	-0.2 (7)	C12D—C13D—C14D—S1D	0.4 (6)
C11B—S1B—C14B—C13B	-0.1 (5)	C11D—S1D—C14D—C15D	179.4 (6)
C11B—S1B—C14B—C15B	179.0 (6)	C11D—S1D—C14D—C13D	-0.5 (4)
C13B—C14B—C15B—C16B	2.1 (10)	C13D—C14D—C15D—C16D	2.1 (9)
S1B—C14B—C15B—C16B	-176.9 (5)	S1D—C14D—C15D—C16D	-177.8 (5)
C14B—C15B—C16B—C17B	-1.7 (10)	C14D—C15D—C16D—C17D	-2.1 (9)
C15B—C16B—C17B—C18B	-1.0 (10)	C15D—C16D—C17D—C18D	0.7 (9)
C15B—C16B—C17B—S2B	-179.8 (5)	C15D—C16D—C17D—S2D	-179.6 (5)
C20B—S2B—C17B—C16B	177.0 (6)	C20D—S2D—C17D—C16D	178.2 (5)
C20B—S2B—C17B—C18B	-1.9 (5)	C20D—S2D—C17D—C18D	-2.0 (4)
C14B—C13B—C18B—C17B	-2.8 (9)	C16D—C17D—C18D—C19D	-177.8 (5)
C12B—C13B—C18B—C17B	176.7 (6)	S2D—C17D—C18D—C19D	2.4 (6)
C14B—C13B—C18B—C19B	178.5 (6)	C16D—C17D—C18D—C13D	0.7 (9)
C12B—C13B—C18B—C19B	-1.9 (11)	S2D—C17D—C18D—C13D	-179.1 (4)
C16B—C17B—C18B—C13B	3.3 (9)	C12D—C13D—C18D—C17D	177.9 (6)
S2B—C17B—C18B—C13B	-177.7 (4)	C14D—C13D—C18D—C17D	-0.7 (8)
C16B—C17B—C18B—C19B	-177.8 (6)	C12D—C13D—C18D—C19D	-3.8 (10)
S2B—C17B—C18B—C19B	1.1 (6)	C14D—C13D—C18D—C19D	177.6 (5)

C13B—C18B—C19B—C20B	179.3 (6)	C17D—C18D—C19D—C20D	-1.5 (7)
C17B—C18B—C19B—C20B	0.6 (7)	C13D—C18D—C19D—C20D	-179.9 (6)
C13B—C18B—C19B—C29B	-1.8 (10)	C17D—C18D—C19D—C29D	170.6 (5)
C17B—C18B—C19B—C29B	179.5 (5)	C13D—C18D—C19D—C29D	-7.8 (10)
C1B—O1B—C20B—C19B	-175.4 (6)	C1D—O1D—C20D—C19D	-175.1 (5)
C1B—O1B—C20B—S2B	9.1 (8)	C1D—O1D—C20D—S2D	4.1 (7)
C18B—C19B—C20B—O1B	-178.0 (6)	C18D—C19D—C20D—O1D	179.2 (5)
C29B—C19B—C20B—O1B	3.1 (9)	C29D—C19D—C20D—O1D	6.5 (9)
C18B—C19B—C20B—S2B	-2.0 (7)	C18D—C19D—C20D—S2D	-0.1 (6)
C29B—C19B—C20B—S2B	179.0 (4)	C29D—C19D—C20D—S2D	-172.8 (4)
C17B—S2B—C20B—O1B	178.3 (5)	C17D—S2D—C20D—O1D	-178.0 (5)
C17B—S2B—C20B—C19B	2.3 (5)	C17D—S2D—C20D—C19D	1.2 (5)
C24B—S3B—C21B—C22B	0.7 (6)	C24D—S3D—C21D—C22D	0.5 (5)
S3B—C21B—C22B—C23B	0.0 (8)	S3D—C21D—C22D—C23D	0.7 (7)
C21B—C22B—C23B—C24B	-1.0 (8)	C21D—C22D—C23D—C24D	-1.9 (7)
C21B—C22B—C23B—C28B	177.8 (6)	C21D—C22D—C23D—C28D	-179.4 (6)
C28B—C23B—C24B—C25B	1.8 (10)	C28D—C23D—C24D—C25D	-1.1 (9)
C22B—C23B—C24B—C25B	-179.3 (6)	C22D—C23D—C24D—C25D	-178.9 (5)
C28B—C23B—C24B—S3B	-177.4 (5)	C28D—C23D—C24D—S3D	-180.0 (4)
C22B—C23B—C24B—S3B	1.6 (7)	C22D—C23D—C24D—S3D	2.2 (6)
C21B—S3B—C24B—C23B	-1.3 (6)	C21D—S3D—C24D—C23D	-1.6 (5)
C21B—S3B—C24B—C25B	179.5 (6)	C21D—S3D—C24D—C25D	179.6 (5)
C23B—C24B—C25B—C26B	1.4 (10)	C23D—C24D—C25D—C26D	-0.7 (9)
S3B—C24B—C25B—C26B	-179.6 (5)	S3D—C24D—C25D—C26D	178.0 (5)
C24B—C25B—C26B—C27B	-3.3 (10)	C24D—C25D—C26D—C27D	0.9 (8)
C25B—C26B—C27B—C28B	2.2 (10)	C25D—C26D—C27D—C28D	0.8 (9)
C25B—C26B—C27B—S4B	-176.2 (5)	C25D—C26D—C27D—S4D	179.1 (5)
C30B—S4B—C27B—C28B	0.4 (5)	C30D—S4D—C27D—C28D	2.3 (5)
C30B—S4B—C27B—C26B	179.0 (6)	C30D—S4D—C27D—C26D	-176.2 (5)
C26B—C27B—C28B—C23B	0.9 (9)	C26D—C27D—C28D—C23D	-2.6 (9)
S4B—C27B—C28B—C23B	179.5 (4)	S4D—C27D—C28D—C23D	179.0 (4)
C26B—C27B—C28B—C29B	-179.4 (6)	C26D—C27D—C28D—C29D	175.2 (5)
S4B—C27B—C28B—C29B	-0.8 (7)	S4D—C27D—C28D—C29D	-3.2 (6)
C24B—C23B—C28B—C27B	-2.9 (9)	C24D—C23D—C28D—C27D	2.6 (8)
C22B—C23B—C28B—C27B	178.4 (6)	C22D—C23D—C28D—C27D	179.9 (6)
C24B—C23B—C28B—C29B	177.5 (6)	C24D—C23D—C28D—C29D	-174.7 (6)
C22B—C23B—C28B—C29B	-1.2 (11)	C22D—C23D—C28D—C29D	2.7 (10)
C27B—C28B—C29B—C30B	0.8 (8)	C27D—C28D—C29D—C30D	2.6 (7)
C23B—C28B—C29B—C30B	-179.5 (6)	C23D—C28D—C29D—C30D	180.0 (6)
C27B—C28B—C29B—C19B	-179.4 (6)	C27D—C28D—C29D—C19D	-176.3 (5)
C23B—C28B—C29B—C19B	0.2 (10)	C23D—C28D—C29D—C19D	1.0 (10)
C20B—C19B—C29B—C30B	82.2 (8)	C20D—C19D—C29D—C30D	-79.6 (8)
C18B—C19B—C29B—C30B	-96.6 (8)	C18D—C19D—C29D—C30D	109.1 (7)

C20B—C19B—C29B—C28B	-97.5 (8)	C20D—C19D—C29D—C28D	99.2 (7)
C18B—C19B—C29B—C28B	83.7 (8)	C18D—C19D—C29D—C28D	-72.1 (8)
C28B—C29B—C30B—S4B	-0.5 (7)	C28D—C29D—C30D—S4D	-0.8 (7)
C19B—C29B—C30B—S4B	179.8 (4)	C19D—C29D—C30D—S4D	178.1 (4)
C27B—S4B—C30B—C29B	0.0 (5)	C27D—S4D—C30D—C29D	-0.8 (5)

Table S14B: Selected hydrogen-bond parameters for **X3A**.

D*—H···*A	***D*—H (Å)**	**H···*A* (Å)**	***D*···*A* (Å)**	***D*—H···*A* (°)**
C1A—H1AB···S3B	0.98	2.86	3.805 (8)	162.2
C26A—H26A···O1C^{i}	0.95	2.59	3.487 (7)	158.3
C25B—H25B···S3D^{ii}	0.95	2.62	3.565 (6)	174.8
C30B—H30B···O1D^{iii}	0.95	2.49	3.428 (7)	168.6
C30C—H30C···O1C^{iv}	0.95	2.52	3.297 (7)	139.2
C26D—H26D···O1A	0.95	2.43	3.357 (7)	165.7

Symmetry code(s): (i) *x*+1, *y*, *z*; (ii) -*x*+1, -*y*+1, -*z*+1; (iii) -*x*+1, -*y*+1, -*z*+2; (iv) -*x*, -*y*+1, -*z*+1.

Table S15: Selected crystallographic data for *trans*,*trans*-**25**.

Identification code	wa3194	
Empirical formula	C29 H23 B O S4	
Formula weight	526.52	
Temperature	173(2) K	
Wavelength	0.71073 Å	
Crystal system	Orthorhombic	
Space group	P 21 21 21	
Unit cell dimensions	a = 6.3515(5) Å	a= 90°.
	b = 18.4915(11) Å	b= 90°.
	c = 22.5750(11) Å	g = 90°.
Volume	2651.4(3) $Å^3$	
Z	4	
Density (calculated)	1.319 Mg/m^3	
Absorption coefficient	0.379 mm^{-1}	
F(000)	1096	
Crystal colour, shape	green needle	
Crystal size	0.180 x 0.040 x 0.010 mm^3	
Theta range for data collection	3.332 to 25.750°.	
Index ranges	-7<=h<=7, -22<=k<=22, -27<=l<=25	
Reflections collected	14919	
Independent reflections	4991 [R(int) = 0.0903]	
Completeness to theta = 25.000°	99.7 %	
Absorption correction	Semi-empirical from equivalents	
Max. and min. transmission	1.000 and 0.293	
Refinement method	Full-matrix least-squares on F^2	
Data / restraints / parameters	4991 / 0 / 319	
Goodness-of-fit on F^2	1.148	
Final R indices [I>2sigma(I)]	R1 = 0.0833, wR2 = 0.1707	
R indices (all data)	R1 = 0.1262, wR2 = 0.1981	
Absolute structure parameter	-0.19(17)	
Extinction coefficient	n/a	
Largest diff. peak and hole	0.390 and -0.418 e.$Å^{-3}$	

Table S16: Selected crystallographic data for *trans*-**26**.

Identification code	wa3185	
Empirical formula	C29 H21 B O S4	
Formula weight	524.51	
Temperature	173(2) K	
Wavelength	0.71073 Å	
Crystal system	Monoclinic	
Space group	P 21/c	
Unit cell dimensions	a = 6.3855(3) Å	a= 90°.
	b = 15.2250(10) Å	b= 94.505(4)°.
	c = 26.8585(14) Å	g = 90°.
Volume	2603.1(3) $Å^3$	
Z	4	
Density (calculated)	1.338 Mg/m^3	
Absorption coefficient	0.386 mm^{-1}	
F(000)	1088	
Crystal size	0.480 x 0.150 x 0.080 mm^3	
Theta range for data collection	2.645 to 25.026°.	
Index ranges	-7<=h<=7, -18<=k<=18, -28<=l<=31	
Reflections collected	23490	
Independent reflections	4600 [R(int) = 0.1714]	
Completeness to theta = 25.000°	99.9 %	
Absorption correction	Semi-empirical from equivalents	
Max. and min. transmission	1.000 and 0.151	
Refinement method	Full-matrix least-squares on F^2	
Data / restraints / parameters	4600 / 30 / 341	
Goodness-of-fit on F^2	1.173	
Final R indices [I>2sigma(I)]	R1 = 0.1376, wR2 = 0.3006	
R indices (all data)	R1 = 0.1899, wR2 = 0.3354	
Extinction coefficient	n/a	
Largest diff. peak and hole	0.729 and -0.507 $e.Å^{-3}$	

10.Chiroptical, kinetic and theoretical studies of 1

10.1 HPLC resolution of the 1 enantiomers and racemization kinetics

The enantiomers of **1** were resolved by HPLC on a column (250×4.6 mm I.D. 5 µm) containing the Chiralpak IA chiral stationary phase, using *n*-hexane/CH_2Cl_2 (95:5) as eluent delivered at a flow rate of 1.0 mL/min (Figure S102a).

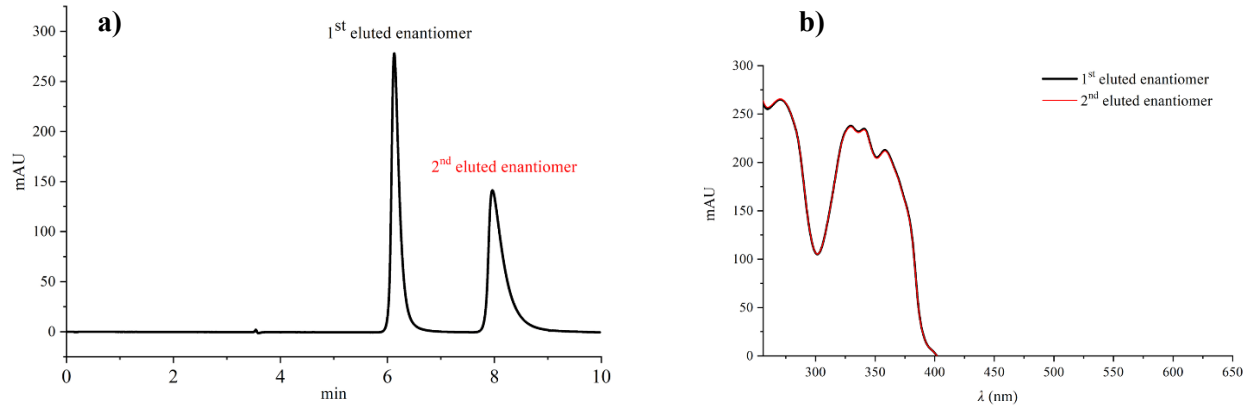

Figure S102: a) HPLC resolution of **1** – stationary phase: Chiralpak IA, mobile phase: *n*-hexane/CH_2Cl_2 (95:5), flow rate = 1.0 mL/min, 25 °C; b) UV spectra of the first and second eluted enantiomer, *n*-hexane/CH_2Cl_2 (95:5).

Table S17: HPLC resolution parameters for the separation of **1** enantiomers.

Eluted peak	R_t (min) [a]	k (t_0 = 3.55)[b]	Relative Area %	A_s [c]	α [d]	R [e]
1	6.13	0.73	51	1.67	1.70	4.9
2	7.96	1.24	49	2.47		

[a] R_t = retention time. [b] k = retention factor, t_0 = void time; k was calculated according to the equation $k = (R_t - t_0)/t_0$. [c] A_s = asymmetry factor, back-to-front ratio of a bisected peak measured at 10% of height. [d] α = selectivity, calculated from the ratio of k values, $\alpha = k_2/k_1$. [e] R = resolution, calculated according to the EP formula equation.

Enantiomers of **1** were separated at the semipreparative level on a 250×10.0mm I.D. 5 µm column using *n*-hexane/CH_2Cl_2 (95:5) as eluent and a loading of about 5 mg of **1** racemic mixture (dissolved in *n*-hexane/CH_2Cl_2 (75:25)) per run. After separation, the fraction containing the second eluted enantiomer resulted to be pure with an *e.e.* of 97.44% (Figure S103).

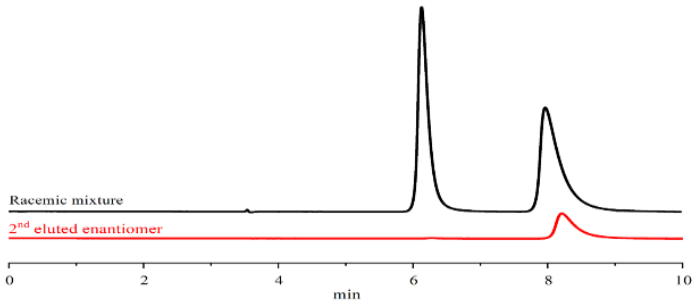

Figure S103: Second eluted enantiomer after semipreparative HPLC separation; solvent peak ($R_t \approx 3$ min).

The second eluted enantiomer was heated at 80 °C in decalin and the enantiomeric excess of the sample was checked by HPLC on the chiral stationary phase.

Data collected at different times was plotted as ln(*e.e.*) *vs* time giving a straight line from the slope of which the racemization constant ($k_{rac} = 16.30\times10^{-5}$ s^{-1}) was extracted (Figure S104). The enantiomerization constant was obtained by $k_{enant}=0.5\ k_{rac}$.

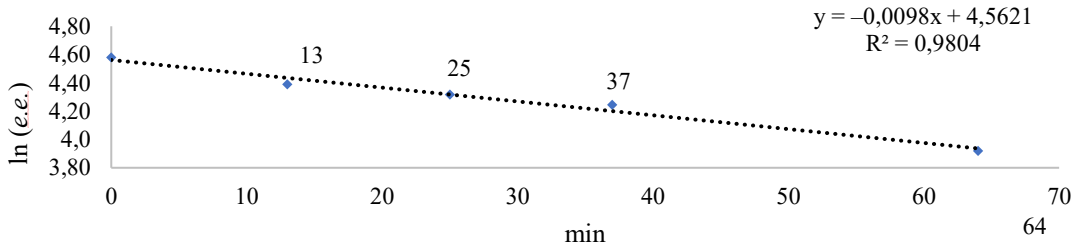

Figure S104: ln(*e.e.*) vs *time* plot used to estimate the racemization constant. The mathematical expression of the linear regression is given in the top right corner.

A free energy of activation equal to 26.9 ± 0.1 kcal/mol (353 K) and 27.4± 0.1 kcal mol^{-1} (353 K) for enantiomerization was calculated by using the Eyring equation (reported below in linear form) and setting a transmission coefficient equal to 1.

$$ln\frac{k}{T} = \frac{-\Delta H^{\ddagger}}{R}\frac{1}{T} + ln\frac{k_B}{h} + \frac{\Delta S^{\ddagger}}{R}$$

$k = k_{rac}$; $\Delta H^{\ddagger}$ = enthalpy of activation; T = absolute temperature in Kelvin (K); k_B = Boltzmann's constant; h = Planck's constant; $\Delta S^{\ddagger}$ = entropy of activation; R = universal gas constant.

The free activation of enantiomerization is calculated trought the following equation:

$$\Delta G^{\ddagger} = 4.576 * 10^{-3} * T\,[10.319 + log(T/k)]$$

Where

$$k = \kappa\left(\frac{k_B T}{h}\right) e^{-\Delta G^{\ddagger}/RT}$$

Assuming the transmission coefficient κ =1.

10.2 Optical rotation and CD spectra

Pure enantiomers showed optical rotation values of +97,75° for the first eluted and –97.5° for the second eluted one (c = 0.04 and 0.06 g/mL respectively in *n*-hexane/CH_2Cl_2 (95:5)). CD spectra were recorded in *n*-hexane/CH_2Cl_2 (95:5) as solvent (Figure S105).

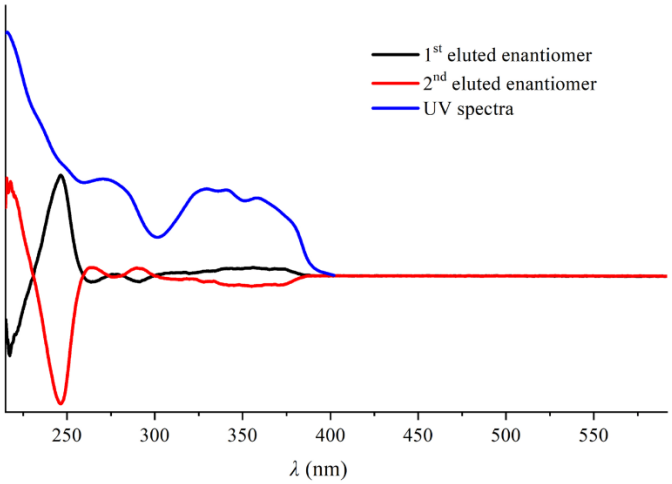

Figure S105: CD spectra of **1** first (black trace) and second (red trace) eluted enantiomers; UV spectra (blue trace).

10.3 Assignment of absolute configuration and electronic transitions characterization

To simulate the CD spectrum, TD-DFT calculations have been performed on the optimized *M* structure of **1** at M06/6-311g G(d,p) level of theory through the Gaussian 16 package.[S17] Only one minimum-energy structure has been obtained. A Gaussian bandshape has been applied to each calculated transition in correspondence of calculated wavelength with area proportional to calculated rotational strength, a bandwidth of 0.18 eV has been adopted. No wavelength shift has been applied and the calculated intensity of each transition has been multiplied by 1.5. Exactly with the same protocol CD spectrum of a model compound in which mesityl groups were replaced by hydrogen atoms (**1***, Figure S106) has been calculated.

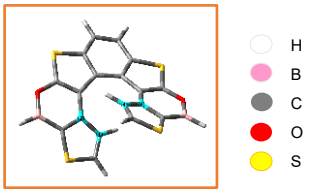

Figure S106: Model compound bearing no mesityl groups **1***.

Calculated CD spectra for compound **1** and **1*** give similar results as reported in Figure S107, where bars proportional to calculated dipole and rotational strengths placed in correspondence of the calculated wavelengths are also given.

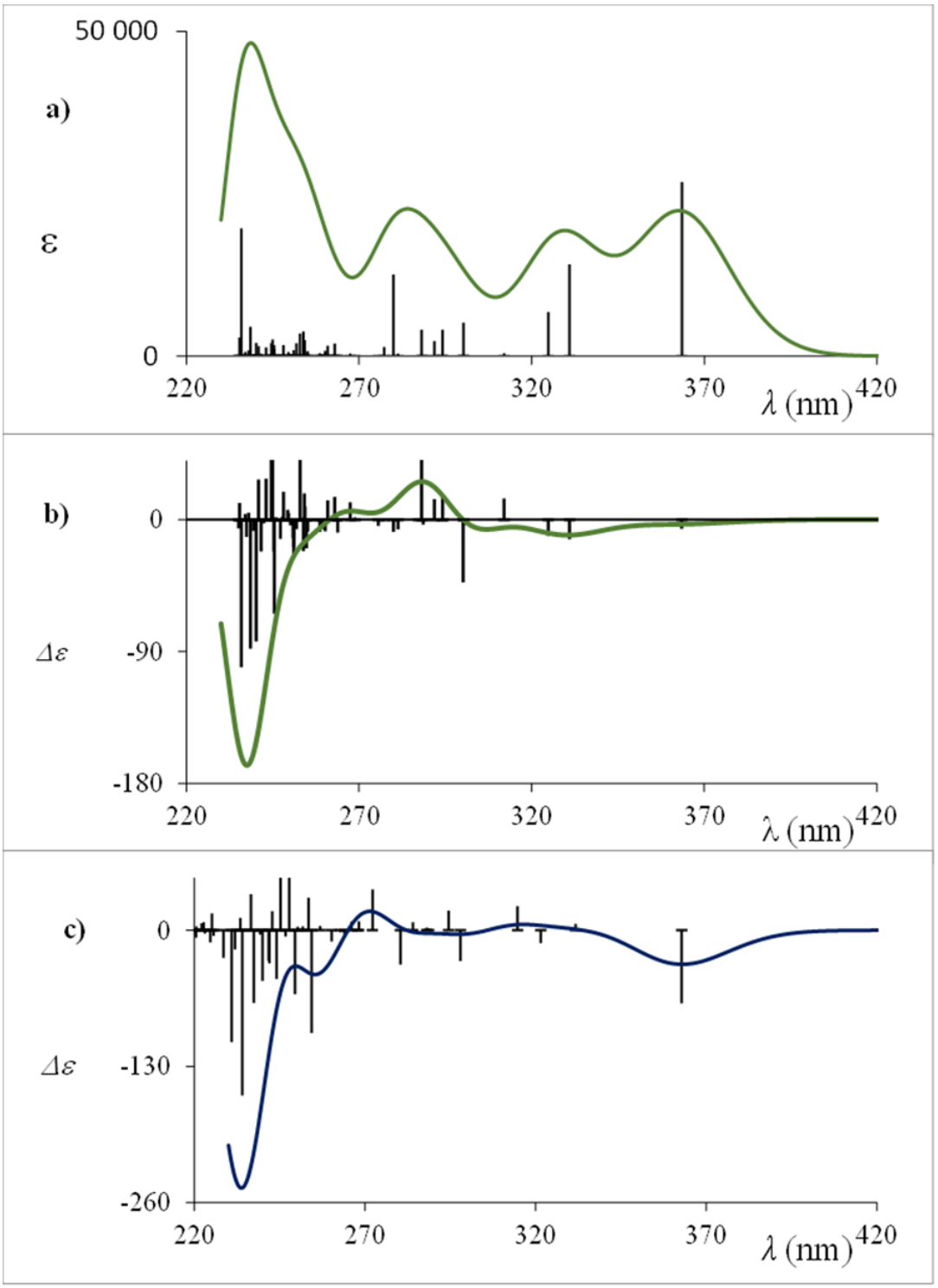

Figure S107: a) Calculated absorption spectrum of **1**; b, c) CD spectra of the *M* enantiomer of compound **1** (green trace) and **1***, bearing no mesityl groups (blue trace).

Representation of orbitals involved in the principal transitions of the two compound **1**, and **1***.

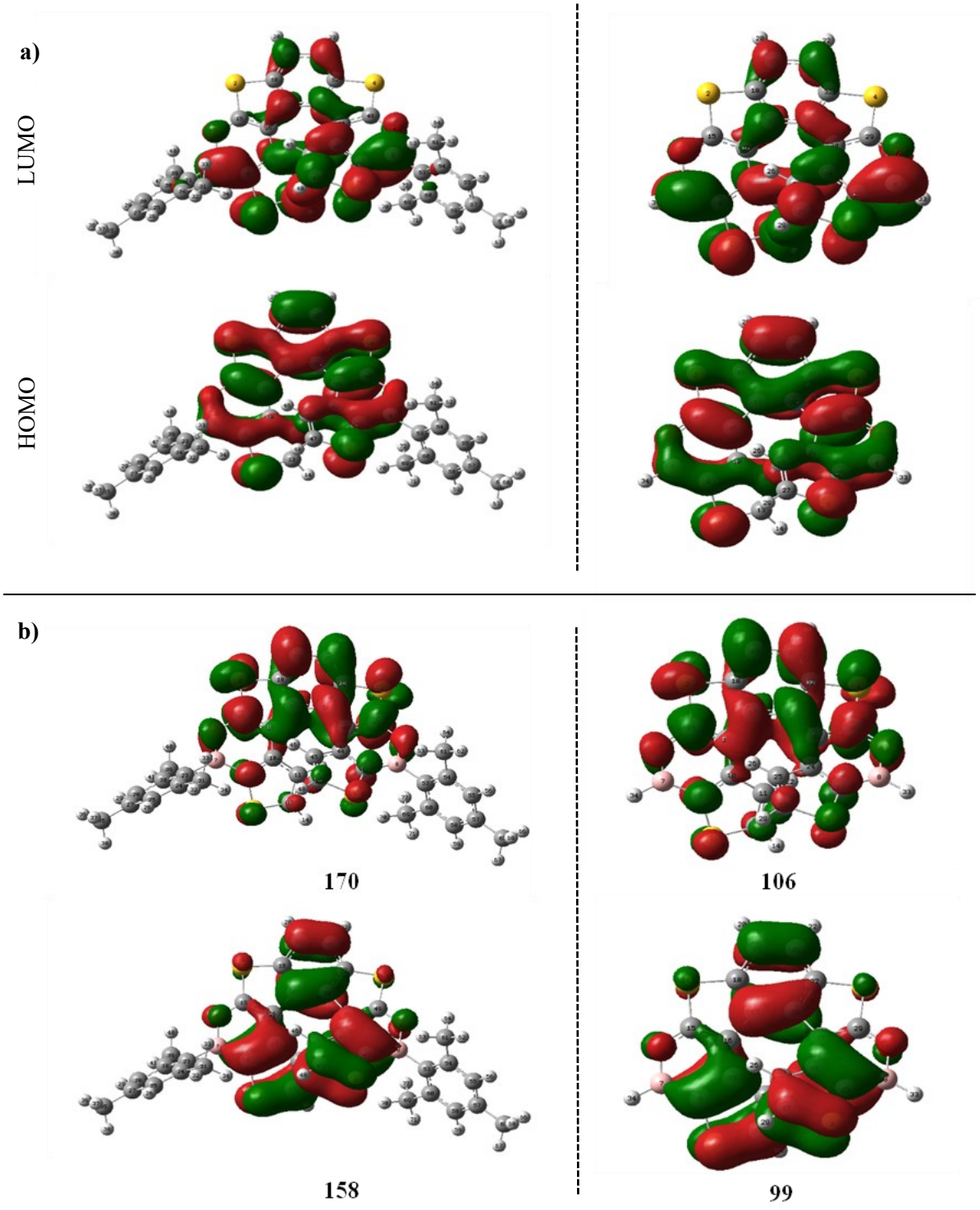

Figure S108: a) Comparison of the HOMO-LUMO orbitals involved in the first optical transition of compound **1** and the model compound **1***; b) (as an example) two of the orbitals involved in one of the transition originating the intense negative peaks about 240 nm are reported for the two compounds **1**, **1*** (from Table S18 and S19 one can appreciate that many contributions are present).

Table S18: Characteristics of the principal transition calculated for **1** (from left: for each transition, calculated energies, wavelengths, dipole strengths, rotational strengths, angle formed by electric and magnetic dipole transition moments, molecular states involved in transition).

#	EV	nm	D [10^{-40}ESU^{2}CM^2]	R [10^{-40}ESU^{2}CM^2]	E-M[°]							
1	3.41	363	187849	-6.28	90.52	167→	168	0.70				
2	3.75	331	99126	-13.43	176.02	167→	169	0.68				
3	3.82	325	47590	-11.13	92.63	167→	170	0.68				
6	4.13	300	36068	-42.86	177.69	166→	168	0.29	166→170	0.35	167→176	0.33
11	4.30	288	28556	51.21	71.71	167→	173	0.59				
36	4.90	253	24364	53.28	5.02	161^{+}→	170	-0.33	167→182	0.34		
51	5.06	245	18335	48.25	26.63	163^{++}→	171	0.36	*			
53	5.07	245	13939	53.60	12.39	163^{++}→	171	0.29	*			
58	5.16	240	14355	-83.30	125.10	159→	169	0.29	167→188	0.21	167→189	-0.24
61	5.20	239	31603	-87.86	127.75	165^{+}→	172	0.23	167→187	0.28		
67	5.26	236	137866	-100.65	96.74	158→	170	0.43	*			

*other contributions are important to describe the transitions; $^{+}$delocalized on helicene-mesitylene moieties, $^{++}$ localized on mesitylene groups.

Table S19: Characteristics of the principal transition calculated for model **1*** (from left: for each transition, calculated energies, wavelengths, dipole strengths, rotational strengths, angle formed by electric and magnetic dipole transition moments, molecular states involved in transition).

#	EV	nm	D [10^{-40}ESU^{2}CM^2]	R [10^{-40}ESU^{2}CM^2]	E-M[°]							
1	3.42	363	120000	-70	100	103→	104	0.70				
2	3.74	332	84315	6	0	103→	105	0.67				
3	3.86	321	32679	-12	96	103→	106	0.67				
5	4.16	298	37334	-29	180	102→	106	0.39	103→109	0.37		
10	4.42	280	56065	-33	180	103→	109	0.52				
11	4.55	272	26342	39	0	103→	110	0.62				
19	4.87	254	35823	-98	134	99→	104	0.49	103→109	0.37		
20	4.89	254	14451	31	0	102→	107	0.55				
27	5.06	245	21745	94	0	98→	104	0.36	103→118	-0.35		
32	5.17	240	3215	-49	137	103→	121	0.30	102→113	-0.26	101→109	0.25
35	5.22	237	19391	-70	106	98→	105	-0.30	101→109	-0.26	103→121	0.31
39	5.30	234	79291	-158	108	99→	106	0.54				

10.4 Enantiomerization barrier calculation

Evaluation of barrier energy has been conducted via DFT calculation optimizing ground and transition state following reference[S18] at PBE1-PBE-TZVP level with empirical dispersion correction.[S19] As further test we compared the model compound **1*** with carbo[6]helicene and tetrathia[7]helicene performing a scan along a dihedral angle coordinate defined as indicated considering also diffuse functions at PBE1-PBE 6-311++G(d,p) level, with empirical dispersion corrections (Figure S109).

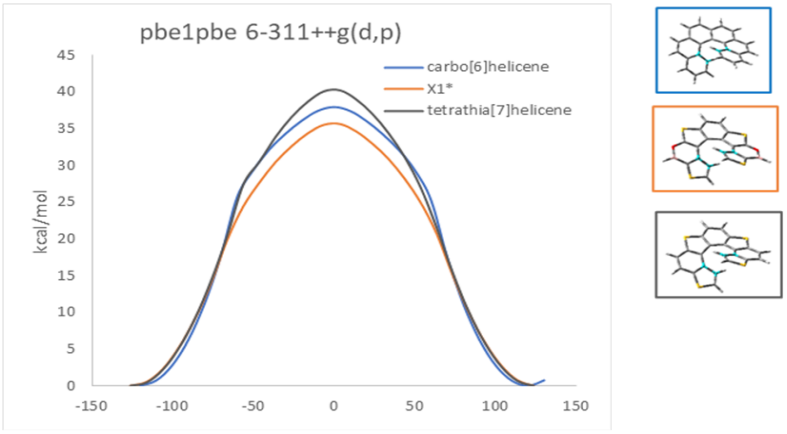

Figure S109: Comparison between the energy scan of carbo[6]helicene (blue trace), model compound **1*** (orange trace)**,** and tetrathia[7]helicene (grey trace); atoms defining the dihedral angle scan coordinate are evidenced (light blue) on the corresponding structures.

A similar analysis conducted on compound **1** and carbo[6]helicene at the semiempirical AM1 level gives the following result which, despite the low level of calculation adopted, seems to better fit experimental results (Figure S57).

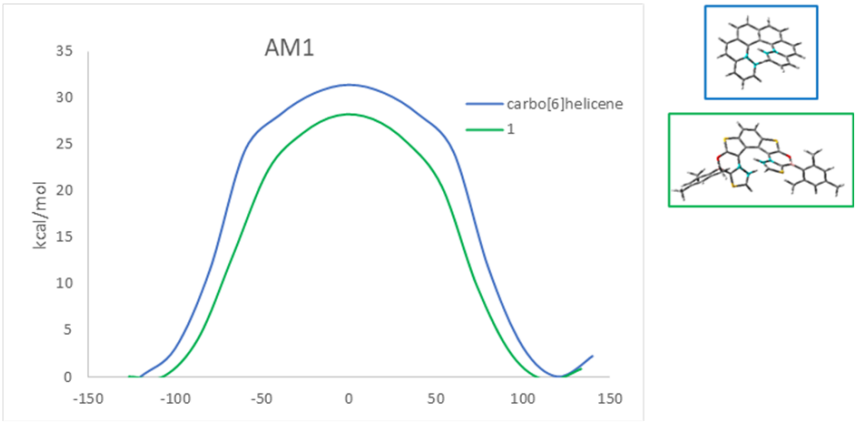

Figure S110: Comparison between the energy scan of carbo[6]helicene (blue trace) and compound **1** (green trace).

A comparison of minimum and transition state calculated structures for the model compound **1*** and tetrathia[7]helicene, with particular attention to the six-membered ring bearing oxygen and boron atoms was performed.

Once defined the average six-membered ring plane, distances of the six atoms with respect to the plane are reported: we may infer that, on average, six carbon atom force the ring to be flatter, particularly considering the transition state. Level of calculation: PBE1-PBE/6-311++G(d,p) (Figure S58).

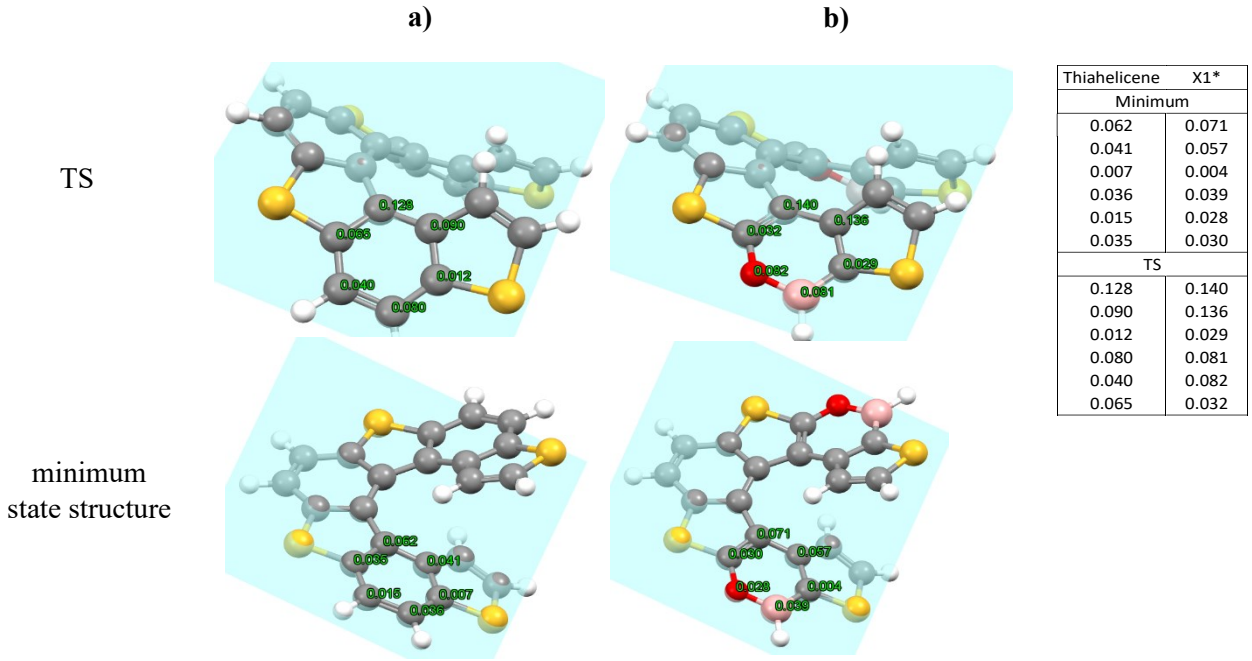

Thiahelicene	X1*
Minimum	
0.062	0.071
0.041	0.057
0.007	0.004
0.036	0.039
0.015	0.028
0.035	0.030
TS	
0.128	0.140
0.090	0.136
0.012	0.029
0.080	0.081
0.040	0.082
0.065	0.032

Figure S111: Distances atom-ring plane (Å) for tetrathia[7]helicene (a) and the six-membered ring containing oxygen and boron atoms of model compound **1*** (b) in the calculated transition state structure (top) and the minimum state structure (bottom). The above-mentioned atom-ring plane distances are listed in the right top corner. The plane defined by the six ring atoms and atom-plane distances have been calculated with the software *Mercury* (https://www.ccdc.cam.ac.uk/solutions/csd-core/components/mercury).

11. Computational details and HOMO/LUMO analyses

Geometry optimizations and frequency calculations were carried out using the Gaussian 09 software package,[S20] the B3LYP functional, and the 6-31G* basis set. The stationary points were characterized as minima (no imaginary frequencies in the vibrational analysis). The graphics were produced with Avogadro 1.1.1 and POV-Ray 3.7.0.

Table S20: Computed data of the BO-doped compounds in comparison with selected experimental values (see Table S1).

	E_{HOMO}^{DFT} [eV]	E_{LUMO}^{DFT} [eV]	E_{HOMO}^{CV} [eV][a]	E_{LUMO}^{CV} [eV][a]	E_g^{CV} [eV][b]	E_g^{DFT} [eV][c]	E_g^{opt} [eV]
5	–5.81	–1.28	-[d]	–1.84	-[d]	4.53	3.57
16	–5.56	–1.37	-[d]	–1.87	-[d]	4.19	3.39
trans-**15**	–5.14	–1.79	–5.19	–2.26	2.93	3.35	2.93
1	–5.44	–1.55	–4.89	–1.97	-[d]	3.88	3.16
15H2	–5.72	–1.32	-[d]	–1.90	-[d]	4.40	3.51
trans-**18**	–5.65	–2.37	–5.63	–2.78	2.85	3.28	2.85
2	–5.69	–2.14	–5.62	–2.12	3.50	3.55	2.90
trans,trans-**25**	–5.14	–2.01	–5.41	–2.59	2.82	3.13	2.69
3	–5.41	–1.81	-[d]	-[d]	-[d]	3.60	-[d]
trans-**27**	–5.15	–1.92	–5.43	–2.43	3.00	3.23	2.89
4	–5.45	–1.64	-[]	-[c]	-[d]	3.81	-[d]

[a] E_{HOMO}^{CV} and E_{LUMO}^{CV} calculated with the maxima criterion. [b] Cyclic voltammetry bad gap band gap $E_g^{CV} = E_{LUMO}^{CV} - E_{HOMO}^{CV}$. [c] Computed band gap $E_g^{DFT} = E_{LUMO}^{DFT} - E_{HOMO}^{DFT}$. [d] Not measured.

11.1 Computational details and HOMO/LUMO analyses for the BO-doped compounds calculated at the B3LYP/6-31G* level

5 (E_g^{DFT} = 4.52 eV)	
HOMO (–5.81 eV)	**LUMO** (–1.28 eV)
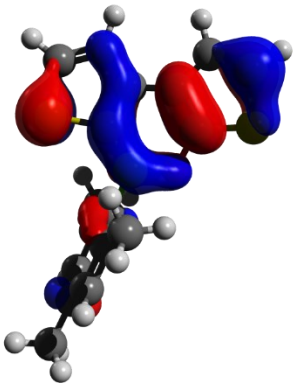	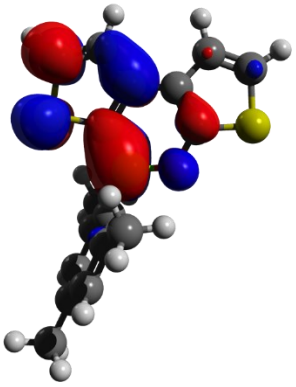

16 (E_g^{DFT} = 4.20 eV)	
HOMO (–5.56 eV)	**LUMO** (–1.37 eV)
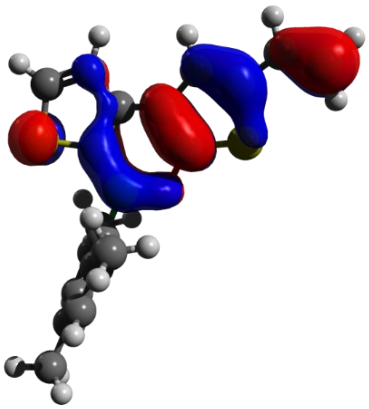	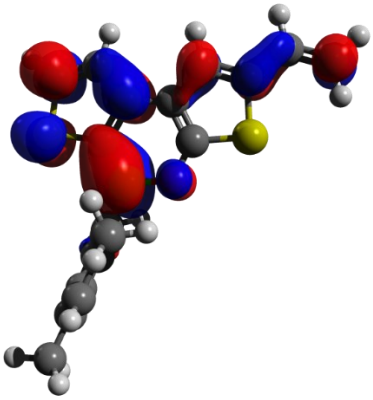

trans-**15** (E_g^{DFT} = 3.35 eV)

HOMO (–5.14 eV)	**LUMO** (–1.79 eV)
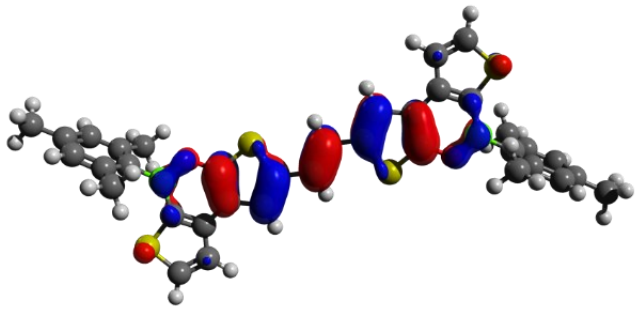	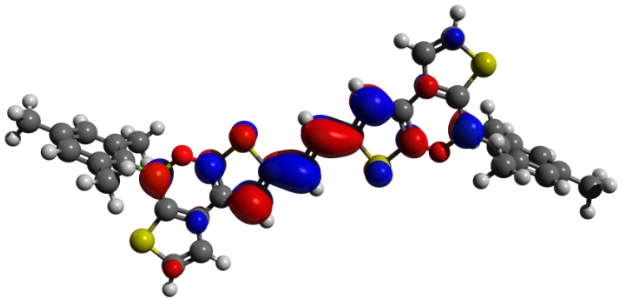

1 (E_g^{DFT} = 3.88 eV)

HOMO (–5.44 eV)	**LUMO** (–1.55 eV)
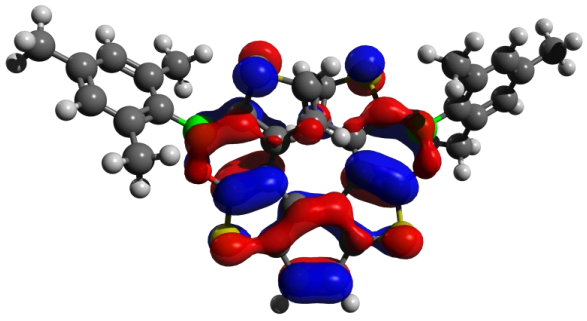	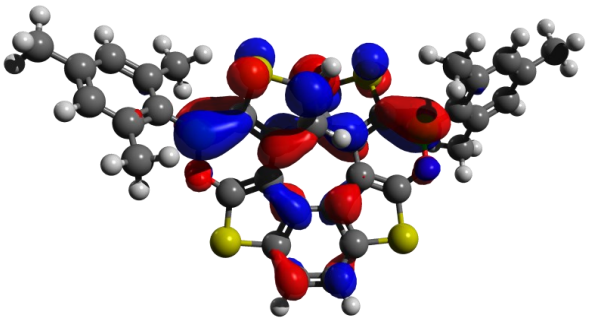

15H2 (E_g^{DFT} = 4.40 eV)

HOMO (–5.72 eV)	**LUMO** (–1.32 eV)
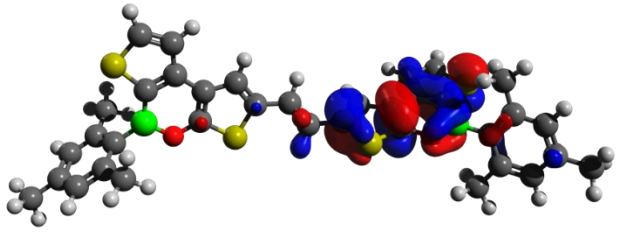	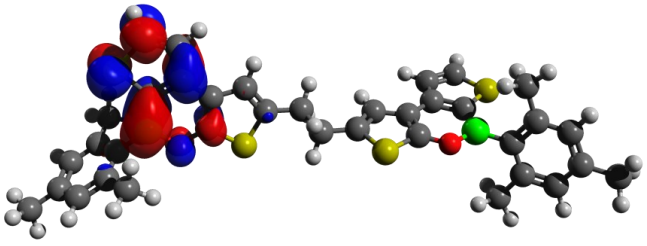

18 (E_g^{DFT} = 3.28 eV)

HOMO (–5.65 eV)	**LUMO** (–2.37 eV)
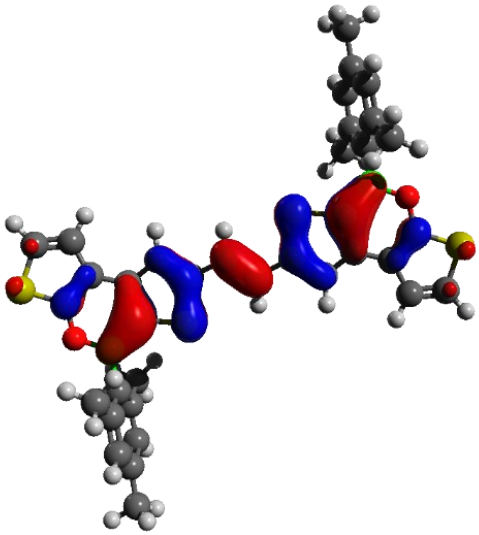	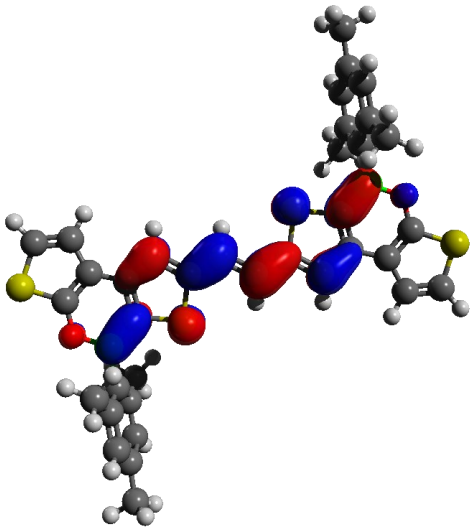

2 (E_g^{DFT} = 3.55 eV)	
HOMO (–5.69 eV)	**LUMO** (–2.14 eV)
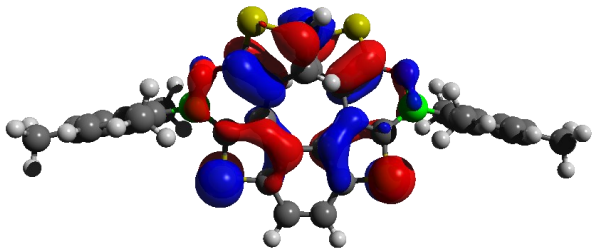	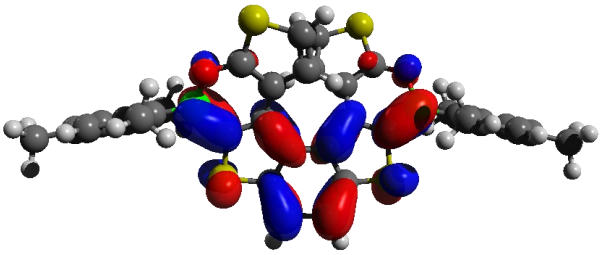

***trans,trans*-25** (E_g^{DFT} = 3.13 eV)	
HOMO (–5.14 eV)	**LUMO** (–2.01 eV)
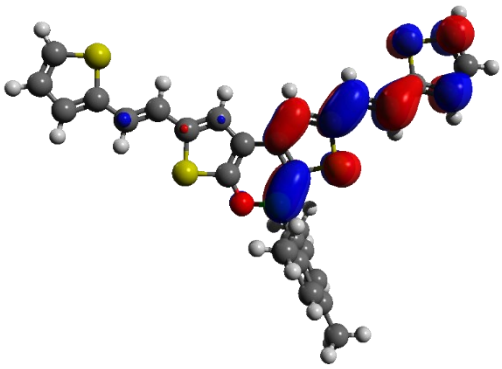	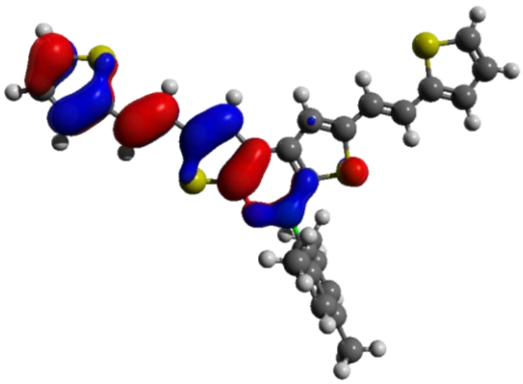

3 (E_g^{DFT} = 3.60 eV)

HOMO (–5.41 eV)	**LUMO** (–1.81 eV)
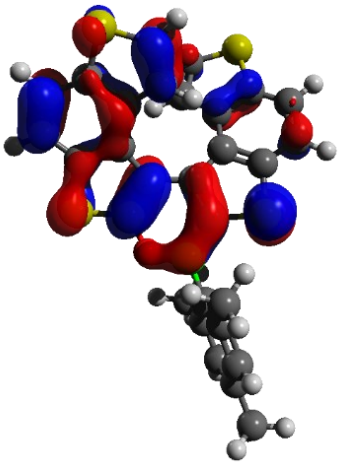	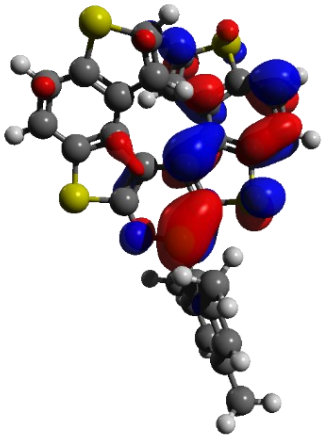

27 (E_g^{DFT} = 3.23 eV)

HOMO (–5.15 eV)	**LUMO** (–1.92 eV)
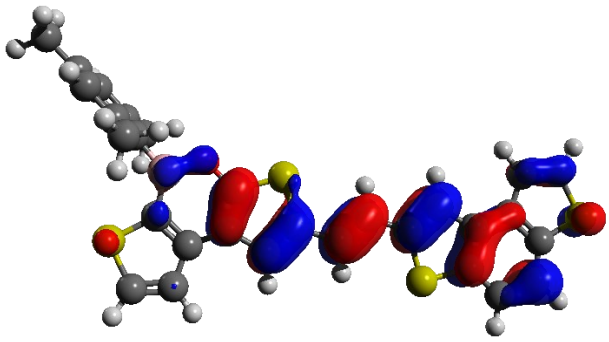	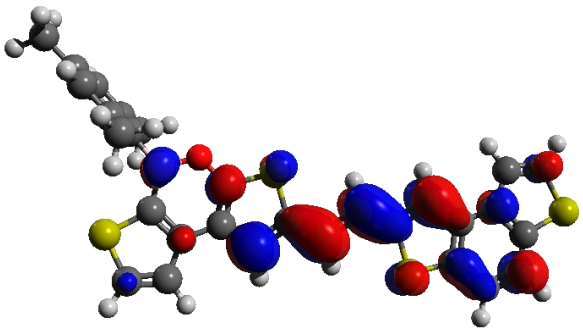

4 (E_g^{DFT} = 3.81 eV)	
HOMO (–5.45 eV)	**LUMO** (–1.64 eV)
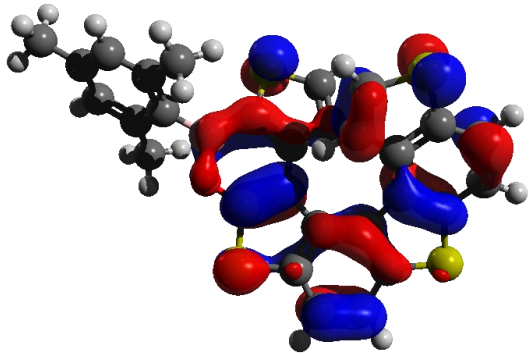	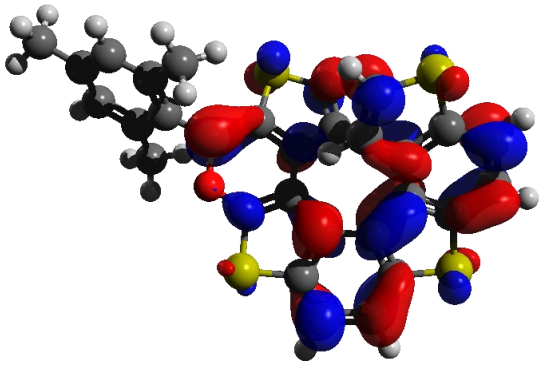

12. Cartesian coordinates and total energies for all the BO-doped compounds calculated at the B3LYP/6-31G* level

Table S21: Atomic coordinates for the optimized geometry of **5**.

Center Number	Atomic Number	Atomic Type	X	Y	Z
1	16	0	–3.01549	-2.66561	0.33856
2	16	0	-0.16385	2.81796	-0.34989
3	8	0	-0.73018	-1.25554	0.17394
4	5	0	0.04363	-0.08782	0.03939
5	6	0	-2.06896	-1.21067	0.16436
6	6	0	-2.84452	-0.07363	0.02383
7	6	0	-4.24541	-0.39405	0.05816
8	1	0	-5.03462	0.344	-0.0337
9	6	0	-4.48646	-1.72421	0.21906
10	1	0	-5.44156	-2.22787	0.27797
11	6	0	-0.76315	1.19307	-0.12454
12	6	0	-2.16525	1.18989	-0.13376
13	6	0	-2.73138	2.49099	-0.31416
14	1	0	-3.79562	2.69673	-0.34822
15	6	0	-1.77153	3.45668	-0.44168
16	1	0	-1.92526	4.51817	-0.58918
17	6	0	1.60424	-0.25879	0.04808
18	6	0	2.37191	0.09863	1.17974
19	6	0	3.76149	-0.0536	1.15264
20	1	0	4.33985	0.21804	2.03421
21	6	0	4.42578	-0.54809	0.02644
22	6	0	3.65759	-0.90631	-1.08468
23	1	0	4.15445	-1.30099	-1.96939
24	6	0	2.26584	-0.77293	-1.0897
25	6	0	1.70759	0.62058	2.4379
26	1	0	2.44842	0.84081	3.21316
27	1	0	1.00229	-0.11017	2.85388
28	1	0	1.14116	1.54034	2.24917
29	6	0	5.93182	-0.66826	0.00348
30	1	0	6.402	0.27676	-0.30089
31	1	0	6.26213	-1.43732	-0.70292
32	1	0	6.32981	-0.92232	0.99215
33	6	0	1.48218	-1.18847	-2.31805
34	1	0	2.15035	-1.47186	-3.13749
35	1	0	0.83749	-0.37795	-2.6813
36	1	0	0.83098	-2.04551	-2.10725

Table S22: Atomic coordinates for the optimized geometry of **16**.

Center Number	Atomic Number	Atomic Type	X	Y	Z
1	5	0	0.54883	0.06419	0.01648
2	8	0	-0.4306	-0.94557	0.10333
3	16	0	-2.93054	-1.92156	0.19501
4	16	0	0.8848	2.9686	-0.27659
5	6	0	-1.73605	-0.65596	0.07862
6	6	0	-2.28661	0.60898	-0.03375
7	6	0	-3.7168	0.54814	-0.02534
8	1	0	-4.35689	1.42104	-0.10226
9	6	0	-4.22706	-0.72051	0.08985
10	6	0	-0.00619	1.47508	-0.11582
11	6	0	-1.38472	1.73041	-0.14094
12	6	0	-1.69955	3.11833	-0.28181
13	1	0	-2.70721	3.51728	-0.32041
14	6	0	-0.5766	3.89453	-0.36421
15	1	0	-0.53038	4.97039	-0.4761
16	6	0	-5.6308	-1.0873	0.12574
17	6	0	2.04996	-0.39317	0.0425
18	6	0	2.63161	-0.9769	-1.10587
19	6	0	3.97348	-1.3672	-1.08416
20	1	0	4.40934	-1.81327	-1.97668
21	6	0	4.76824	-1.20171	0.0539
22	6	0	4.18096	-0.63614	1.18881
23	1	0	4.77895	-0.51186	2.0901
24	6	0	2.84302	-0.22898	1.20022
25	6	0	1.81309	-1.19126	-2.36266
26	1	0	1.33472	-0.26239	-2.69861
27	1	0	1.0124	-1.92318	-2.20001
28	1	0	2.4366	-1.55784	-3.18428
29	6	0	6.22555	-1.60096	0.04857
30	1	0	6.8617	-0.78144	-0.31267
31	1	0	6.40383	-2.46075	-0.60651
32	1	0	6.57355	-1.86229	1.05371
33	6	0	2.25715	0.35916	2.46817
34	1	0	1.41334	-0.23796	2.83671
35	1	0	1.88368	1.37816	2.31093
36	1	0	3.0047	0.39997	3.26677
37	6	0	-6.14967	-2.31899	0.23487
38	1	0	-6.30647	-0.23506	0.05298
39	1	0	-5.53021	-3.20933	0.31094
40	1	0	-7.2234	-2.47357	0.2515

Table S23: Atomic coordinates for the optimized geometry of ***trans*-15**.

Center Number	Atomic Number	Atomic Type	X	Y	Z
1	5	0	-6.66805	0.21974	0.00214
2	8	0	-5.47754	-0.53494	-0.03382
3	16	0	-2.8186	-0.90126	-0.05236
4	16	0	-7.68037	2.97022	0.19772
5	6	0	-4.27792	0.05322	0.00665
6	6	0	-4.03962	1.41447	0.09247
7	6	0	-2.63693	1.69117	0.11139
8	1	0	-2.22119	2.69139	0.174
9	6	0	-1.83791	0.57333	0.04127
10	6	0	-6.46084	1.72404	0.10171
11	6	0	-5.18138	2.29587	0.14881
12	6	0	-5.20356	3.72158	0.25586
13	1	0	-4.31858	4.34635	0.30511
14	6	0	-6.47883	4.21453	0.29068
15	1	0	-6.77831	5.25192	0.36967
16	6	0	-0.39693	0.54766	0.03886
17	6	0	-8.02058	-0.57482	-0.0405
18	6	0	-8.49998	-1.21901	1.12222
19	6	0	-9.71431	-1.91023	1.08418
20	1	0	-10.07321	-2.39943	1.9882
21	6	0	-10.47749	-1.98986	-0.08424
22	6	0	-9.98907	-1.3604	-1.2326
23	1	0	-10.56225	-1.42106	-2.15624
24	6	0	-8.78091	-0.6563	-1.2287
25	6	0	-7.70634	-1.17466	2.41206
26	1	0	-7.46446	-0.1448	2.7042
27	1	0	-6.75481	-1.71222	2.31615
28	1	0	-8.26316	-1.63021	3.23707
29	6	0	-11.80405	-2.71322	-0.09879
30	1	0	-12.63074	-2.03384	0.14985
31	1	0	-11.82447	-3.52864	0.63233
32	1	0	-12.01948	-3.13678	-1.08577
33	6	0	-8.29033	-0.01516	-2.51103
34	1	0	-7.35106	-0.46877	-2.85307
35	1	0	-8.10037	1.05726	-2.38431
36	1	0	-9.02297	-0.13014	-3.31622
37	1	0	8.27603	1.56812	-3.26449
38	6	0	7.71699	1.12681	-2.43327
39	1	0	6.76433	1.66467	-2.35067
40	1	0	7.47757	0.09141	-2.70726
41	1	0	10.08909	2.34712	-2.02744
42	6	0	9.72284	1.88205	-1.11358
43	6	0	8.50544	1.19683	-1.14142
44	1	0	12.32973	2.63712	-0.86813

45	6	0	11.78131	2.75433	0.07321
46	1	0	11.60448	3.82956	0.21177
47	6	0	10.48203	1.98308	0.05648
48	6	0	8.02064	0.57537	0.032
49	16	0	7.68028	-2.97153	-0.17568
50	5	0	6.66807	-0.21963	-0.00178
51	6	0	6.46076	-1.72465	-0.08922
52	1	0	12.43337	2.42434	0.88885
53	6	0	6.47868	-4.21653	-0.2581
54	8	0	5.47768	0.53536	0.03005
55	6	0	5.18127	-2.29683	-0.13099
56	6	0	5.20341	-3.72334	-0.22662
57	6	0	4.278	-0.05312	-0.00479
58	6	0	4.0396	-1.41494	-0.0807
59	1	0	6.77813	-5.25452	-0.32878
60	6	0	9.99254	1.36969	1.21238
61	16	0	2.81872	0.90177	0.04843
62	6	0	2.6369	-1.69172	-0.097
63	1	0	4.31842	-4.34851	-0.27036
64	6	0	8.78024	0.67162	1.21882
65	6	0	1.83794	-0.57342	-0.03398
66	1	0	2.22112	-2.69235	-0.15242
67	6	0	0.39697	-0.54773	-0.03086
68	1	0	10.56897	1.43582	2.13354
69	6	0	8.28975	0.04636	2.50898
70	1	0	7.35322	0.5081	2.8477
71	1	0	8.09468	-1.02656	2.39471
72	1	0	9.02438	0.16718	3.3115
73	1	0	0.06139	1.53468	0.10119
74	1	0	-0.06137	-1.53482	-0.09209

Table S24: Atomic coordinates for the optimized geometry of **1**.

Center Number	Atomic Number	Atomic Type	X	Y	Z
1	16	0	-2.561	-2.16448	-1.52432
2	16	0	-3.05734	3.60195	0.62426
3	16	0	2.56004	-2.16369	1.52821
4	16	0	3.05875	3.60004	-0.62696
5	8	0	-4.0819	1.16769	0.34754
6	8	0	4.08226	1.16554	-0.34782
7	5	0	-4.11963	-0.18257	-0.0567
8	5	0	4.11923	-0.18447	0.05745
9	6	0	-2.80988	-0.68128	-0.63745
10	6	0	-1.65792	0.122	-0.68761
11	6	0	-0.61342	-0.46289	-1.47426
12	1	0	0.33922	0.0086	-1.67251
13	6	0	-0.96142	-1.6852	-1.97618
14	1	0	-0.35598	-2.33018	-2.60014
15	6	0	-2.95811	1.88578	0.30689
16	6	0	-1.70431	1.43325	-0.06426
17	6	0	-0.71199	2.50006	0.04759
18	6	0	-1.33635	3.75456	0.27022
19	6	0	-0.66954	4.98088	0.17319
20	1	0	-1.20207	5.91451	0.32534
21	6	0	0.6715	4.98044	-0.17733
22	1	0	1.20438	5.91369	-0.33054
23	6	0	-5.49107	-0.93015	0.07723
24	6	0	-5.65445	-1.99298	0.99653
25	6	0	-6.88673	-2.64575	1.09224
26	1	0	-7.00188	-3.45436	1.81211
27	6	0	-7.97473	-2.28579	0.29161
28	6	0	-7.8056	-1.23253	-0.61077
29	1	0	-8.64185	-0.93287	-1.2401
30	6	0	-6.59066	-0.55026	-0.72649
31	6	0	-4.5208	-2.42326	1.90627
32	1	0	-4.84611	-3.21052	2.59387
33	1	0	-4.14993	-1.58818	2.51391
34	1	0	-3.66662	-2.81064	1.33855
35	6	0	-9.28644	-3.02967	0.38463
36	1	0	-10.1211	-2.41664	0.02859
37	1	0	-9.50362	-3.3335	1.41473
38	1	0	-9.26975	-3.94358	-0.22455
39	6	0	-6.47539	0.5901	-1.71773
40	1	0	-6.34828	1.55298	-1.20899
41	1	0	-7.37009	0.65957	-2.34443
42	1	0	-5.61308	0.46417	-2.38432
43	6	0	2.80946	-0.68173	0.63939
44	6	0	1.65796	0.12222	0.68898

45	6	0	0.61336	-0.46111	1.47663
46	1	0	-0.33897	0.01114	1.67456
47	6	0	0.9609	-1.68295	1.98003
48	1	0	0.35535	-2.32679	2.60507
49	6	0	2.95884	1.88424	-0.30772
50	6	0	1.70487	1.4327	0.06406
51	6	0	0.71298	2.49975	-0.04893
52	6	0	1.33783	3.75375	-0.27299
53	6	0	5.49016	-0.93284	-0.0774
54	6	0	6.59014	-0.5553	0.72861
55	6	0	7.80214	-1.24159	0.61702
56	1	0	8.63594	-0.94832	1.25279
57	6	0	7.971	-2.29417	-0.28768
58	6	0	6.88185	-2.65626	-1.08406
59	1	0	6.99324	-3.47228	-1.79596
60	6	0	5.65087	-1.9985	-0.99238
61	6	0	6.47322	0.58209	1.72306
62	1	0	7.369	0.65294	2.34805
63	1	0	5.61259	0.45205	2.39108
64	1	0	6.34213	1.54567	1.21669
65	6	0	9.30029	-3.00063	-0.41695
66	1	0	9.97914	-2.45207	-1.08391
67	1	0	9.18089	-4.00742	-0.83088
68	1	0	9.80353	-3.08976	0.5522
69	6	0	4.51505	-2.43424	-1.89685
70	1	0	3.66588	-2.82754	-1.32567
71	1	0	4.8416	-3.21851	-2.58728
72	1	0	4.13641	-1.60048	-2.50139

Table S25: Atomic coordinates for the optimized geometry of **15H2**.

Center Number	Atomic Number	Atomic Type	X	Y	Z
1	16	0	7.72838	2.00808	-1.89287
2	16	0	2.85696	-0.44155	1.0964
3	16	0	-7.51497	2.04476	1.81787
4	16	0	-2.91462	-1.15493	-0.87833
5	8	0	5.49284	-0.47875	0.5579
6	8	0	-5.55323	-0.78041	-0.49764
7	5	0	6.68048	-0.02229	-0.04521
8	5	0	-6.68905	-0.13937	0.0325
9	6	0	6.50605	1.18546	-0.95514
10	6	0	5.25501	1.78504	-1.16018
11	6	0	5.30231	2.89552	-2.06044
12	1	0	4.44135	3.48974	-2.34639
13	6	0	6.56704	3.12622	-2.5268
14	1	0	6.87991	3.89873	-3.21782
15	6	0	4.32037	0.12872	0.33541
16	6	0	4.11345	1.22801	-0.47578
17	6	0	2.72949	1.61545	-0.47956
18	1	0	2.34387	2.45638	-1.04736
19	6	0	1.92823	0.83505	0.30122
20	6	0	0.44486	0.94597	0.50851
21	1	0	0.20791	0.94184	1.58046
22	1	0	0.12457	1.91994	0.11971
23	6	0	-0.35689	-0.17014	-0.19386
24	1	0	-0.03187	-1.14539	0.1948
25	1	0	-0.09277	-0.17156	-1.25982
26	6	0	7.99568	-0.81786	0.27331
27	6	0	8.95522	-0.30988	1.17638
28	6	0	10.12505	-1.03505	1.42769
29	1	0	10.85622	-0.63252	2.12663
30	6	0	10.37852	-2.26036	0.80663
31	6	0	9.4228	-2.75491	-0.08672
32	1	0	9.60303	-3.70546	-0.58636
33	6	0	8.24147	-2.05956	-0.35664
34	6	0	8.72847	1.00488	1.89512
35	6	0	11.63647	-3.04207	1.10634
36	1	0	11.44305	-3.84727	1.82793
37	1	0	12.41449	-2.40093	1.53373
38	1	0	12.04256	-3.51137	0.20303
39	6	0	7.23496	-2.64617	-1.32528
40	1	0	7.62262	-3.5536	-1.7992
41	1	0	6.97979	-1.93777	-2.12371
42	1	0	6.29806	-2.90925	-0.81889
43	6	0	-6.38318	1.03471	0.95157
44	6	0	-5.0679	1.43417	1.23046

45	6	0	-4.9943	2.54596	2.1277
46	1	0	-4.06951	3.00123	2.46478
47	6	0	-6.23242	2.97408	2.51969
48	1	0	-6.46074	3.79102	3.19249
49	6	0	-4.31568	-0.35948	-0.20664
50	6	0	-3.98899	0.70212	0.61341
51	6	0	-2.56317	0.87505	0.69827
52	1	0	-2.0985	1.6551	1.29087
53	6	0	-1.84705	-0.02689	-0.03288
54	6	0	-8.0908	-0.72359	-0.36606
55	6	0	-8.91613	-0.06325	-1.30356
56	6	0	-10.16572	-0.60096	-1.62939
57	1	0	-10.78834	-0.08624	-2.35928
58	6	0	-10.63322	-1.78183	-1.04693
59	6	0	-9.80576	-2.43299	-0.1272
60	1	0	-10.14683	-3.35929	0.33237
61	6	0	-8.54945	-1.92684	0.21713
62	6	0	-8.45732	1.21009	-1.98558
63	1	0	-7.51958	1.05787	-2.53491
64	1	0	-8.27883	2.01775	-1.26558
65	1	0	-9.2047	1.56477	-2.7025
66	6	0	-12.00161	-2.32779	-1.38213
67	1	0	-12.75495	-1.98529	-0.65967
68	1	0	-12.0125	-3.42324	-1.36397
69	1	0	-12.33193	-2.00198	-2.37424
70	6	0	-7.69044	-2.68082	1.21188
71	1	0	-6.7703	-3.05363	0.74581
72	1	0	-8.22619	-3.54095	1.62574
73	1	0	-7.388	-2.04302	2.05239
74	1	0	8.60186	1.83759	1.19294
75	1	0	9.57158	1.24828	2.54957
76	1	0	7.82608	0.97185	2.51899

Table S26: Atomic coordinates for the optimized geometry of *trans*-**18**.

Center Number	Atomic Number	Atomic Type	X	Y	Z
1	8	0	-6.59165	-1.43764	-0.00778
2	16	0	-7.1576	-4.06728	-0.04218
3	6	0	-5.76889	-5.13262	-0.02369
4	6	0	-4.58865	-4.45468	0.00576
5	6	0	0.31558	0.59881	0.06151
6	6	0	1.74354	0.81468	0.05797
7	6	0	2.36811	2.04712	0.04717
8	6	0	-6.09747	-2.68273	-0.00893
9	16	0	2.92227	-0.48606	0.05723
10	6	0	4.25924	0.63721	0.04718
11	6	0	3.78782	1.95854	0.03882
12	6	0	6.09748	2.68275	-0.00903
13	6	0	4.75785	3.02747	0.01499
14	6	0	-4.75785	-3.02747	0.01515
15	6	0	-0.31555	-0.59886	0.06151
16	6	0	-2.3681	-2.04714	0.04728
17	6	0	-1.74352	-0.81471	0.05803
18	16	0	-2.92223	0.48604	0.05731
19	16	0	7.15759	4.06731	-0.04223
20	6	0	5.76887	5.13263	-0.02384
21	6	0	4.58864	4.45468	0.00559
22	8	0	6.59167	1.43766	-0.00784
23	6	0	-4.25922	-0.63721	0.04734
24	6	0	-3.78781	-1.95855	0.03898
25	5	0	-5.74689	-0.31256	0.02491
26	5	0	5.74691	0.31258	0.02481
27	6	0	-6.43323	1.099	0.00584
28	6	0	6.43325	-1.09898	0.00576
29	6	0	6.53725	-1.87687	1.18033
30	6	0	7.14186	-3.13718	1.12731
31	6	0	7.65316	-3.65835	-0.06402
32	6	0	7.54416	-2.88172	-1.22163
33	6	0	6.95092	-1.61654	-1.20354
34	6	0	-6.53692	1.87709	1.18029
35	6	0	-7.14155	3.13739	1.12721
36	6	0	-7.65316	3.65835	-0.0641
37	6	0	-7.54446	2.88152	-1.22159
38	6	0	-6.95124	1.61632	-1.20342
39	6	0	-6.86972	0.81235	-2.48505
40	6	0	-6.02097	1.3567	2.50669
41	6	0	-8.32851	5.00961	-0.09673
42	6	0	6.86889	-0.81284	-2.48531
43	6	0	6.02165	-1.35621	2.50676
44	6	0	8.32852	-5.0096	-0.09659

45	1	0	-5.9245	-6.20266	-0.03574
46	1	0	-3.6227	-4.94729	0.02098
47	1	0	-0.27799	1.51236	0.06073
48	1	0	1.81268	2.97928	0.04304
49	1	0	0.27802	-1.51241	0.0607
50	1	0	-1.81268	-2.97932	0.04315
51	1	0	5.92447	6.20268	-0.03592
52	1	0	3.62268	4.94728	0.02074
53	1	0	7.21648	-3.7261	2.03993
54	1	0	7.93025	-3.27139	-2.16218
55	1	0	-7.21595	3.72647	2.03973
56	1	0	-7.93079	3.27102	-2.16211
57	1	0	-7.22312	1.39451	-3.34204
58	1	0	-7.47954	-0.09761	-2.42659
59	1	0	-5.84143	0.49535	-2.70101
60	1	0	-6.54611	0.44219	2.81092
61	1	0	-6.16036	2.09561	3.30227
62	1	0	-4.95272	1.11296	2.46279
63	1	0	-7.97163	5.65628	0.71196
64	1	0	-9.41659	4.91356	0.01958
65	1	0	-8.15058	5.52504	-1.04708
66	1	0	7.22349	-1.39462	-3.34207
67	1	0	7.47741	0.09798	-2.4267
68	1	0	5.84025	-0.49732	-2.70176
69	1	0	6.5473	-0.44199	2.81096
70	1	0	6.16068	-2.09519	3.30233
71	1	0	4.95353	-1.11189	2.4629
72	1	0	7.97192	-5.65611	0.71235
73	1	0	9.41664	-4.91351	0.01934
74	1	0	8.15029	-5.52523	-1.04677

Table S27: Atomic coordinates for the optimized geometry of **2**.

Center Number	Atomic Number	Atomic Type	X	Y	Z
1	8	0	3.88879	1.54074	-0.74623
2	16	0	2.31049	3.34048	-1.94373
3	6	0	0.63585	2.87171	-2.12186
4	6	0	0.36563	1.66471	-1.55678
5	6	0	-0.68294	-3.77354	-0.09643
6	6	0	-1.36874	-2.54313	-0.11505
7	6	0	-0.71739	-1.29444	0.04163
8	6	0	2.63531	1.84896	-1.1041
9	16	0	-3.10581	-2.38424	-0.22717
10	6	0	-3.01145	-0.67395	0.11912
11	6	0	-1.69113	-0.25166	0.32213
12	6	0	-2.63531	1.84914	1.10396
13	6	0	-1.513	1.05194	0.93642
14	6	0	1.51298	1.0518	-0.93645
15	6	0	0.68286	-3.77353	0.09712
16	6	0	0.71734	-1.29445	-0.04133
17	6	0	1.36867	-2.54312	0.11556
18	16	0	3.10574	-2.38424	0.22767
19	16	0	-2.31046	3.34078	1.94339
20	6	0	-0.63583	2.87199	2.12159
21	6	0	-0.36563	1.66492	1.55667
22	8	0	-3.88879	1.5409	0.74612
23	6	0	3.01141	-0.67401	-0.11892
24	6	0	1.69109	-0.25173	-0.32198
25	5	0	4.20612	0.26266	-0.26718
26	5	0	-4.20615	0.26276	0.26724
27	6	0	5.71528	-0.04641	0.02935
28	6	0	6.19181	-0.18903	1.35257
29	6	0	7.54264	-0.47235	1.57733
30	6	0	8.44698	-0.62993	0.5236
31	6	0	7.96786	-0.48218	-0.7812
32	6	0	6.62627	-0.1907	-1.04273
33	6	0	6.168	-0.03035	-2.47821
34	6	0	5.2671	-0.01114	2.5402
35	6	0	9.89468	-0.9737	0.78584
36	6	0	-5.71529	-0.04633	-0.02937
37	6	0	-6.19161	-0.1894	-1.35262
38	6	0	-7.54241	-0.47277	-1.57751
39	6	0	-8.44692	-0.63	-0.52388
40	6	0	-7.96801	-0.48181	0.78095
41	6	0	-6.62647	-0.19026	1.04261
42	6	0	-6.16834	-0.02974	2.47812
43	6	0	-5.26668	-0.01204	-2.54016
44	6	0	-9.89459	-0.9738	-0.78625

45	1	0	-0.04827	3.53268	-2.63583
46	1	0	-0.6138	1.2086	-1.59349
47	1	0	-1.23022	-4.70712	-0.18418
48	1	0	1.23013	-4.7071	0.18504
49	1	0	0.04831	3.53302	2.63547
50	1	0	0.6138	1.2088	1.59343
51	1	0	7.89892	-0.56932	2.60148
52	1	0	8.65709	-0.59503	-1.61641
53	1	0	6.96464	-0.29792	-3.17954
54	1	0	5.86949	1.00314	-2.69152
55	1	0	5.30254	-0.66669	-2.70262
56	1	0	5.81289	-0.11689	3.48316
57	1	0	4.45758	-0.75088	2.54179
58	1	0	4.79712	0.98051	2.54139
59	1	0	10.55062	-0.56978	0.00705
60	1	0	10.04798	-2.06127	0.80674
61	1	0	10.23187	-0.58082	1.7511
62	1	0	-7.89853	-0.57001	-2.60169
63	1	0	-8.6574	-0.59432	1.61608
64	1	0	-6.96608	-0.29415	3.17938
65	1	0	-5.86673	1.00303	2.69048
66	1	0	-5.30495	-0.66854	2.70354
67	1	0	-5.81258	-0.11678	-3.48317
68	1	0	-4.45804	-0.75275	-2.54205
69	1	0	-4.79552	0.97904	-2.54094
70	1	0	-10.55063	-0.56974	-0.00762
71	1	0	-10.04789	-2.06137	-0.80697
72	1	0	-10.23164	-0.58109	-1.75163

Table S28: Atomic coordinates for the optimized geometry of *trans,trans*-**25**.

Center Number	Atomic Number	Atomic Type	X	Y	Z
1	16	0	2.80555	0.1533	0.01225
2	16	0	5.10014	-5.31747	-0.0711
3	16	0	-3.29804	1.36185	0.02275
4	16	0	-7.50514	-2.82023	0.01342
5	8	0	-0.76745	2.25759	0.02935
6	5	0	0.63799	2.1324	0.03989
7	6	0	1.14574	0.69968	0.03281
8	6	0	0.27259	-0.39866	0.02161
9	6	0	0.94455	-1.65173	0.00333
10	1	0	0.44398	-2.6144	-0.00645
11	6	0	2.32155	-1.53447	-0.00274
12	6	0	3.25881	-2.63329	-0.02332
13	1	0	2.79592	-3.61963	-0.03191
14	6	0	4.60921	-2.53467	-0.03338
15	1	0	5.06712	-1.54574	-0.02528
16	6	0	5.55857	-3.62041	-0.05499
17	6	0	6.93526	-3.50375	-0.06637
18	1	0	7.43481	-2.54041	-0.0596
19	6	0	7.61677	-4.75122	-0.08764
20	1	0	8.69658	-4.85099	-0.0989
21	6	0	6.76091	-5.81942	-0.09248
22	1	0	7.00361	-6.87356	-0.10737
23	6	0	-1.56213	1.18322	0.02476
24	6	0	-1.14772	-0.1378	0.02307
25	6	0	-2.26604	-1.02856	0.01931
26	1	0	-2.1748	-2.10972	0.01772
27	6	0	-3.49029	-0.4012	0.01921
28	6	0	-4.78195	-1.04142	0.01784
29	1	0	-4.73409	-2.13034	0.01435
30	6	0	-5.99164	-0.43322	0.02123
31	1	0	-6.03878	0.65576	0.0253
32	6	0	-7.28447	-1.07549	0.02078
33	6	0	-8.51404	-0.44653	0.02627
34	1	0	-8.61159	0.63431	0.03139
35	6	0	-9.61874	-1.34291	0.0248
36	1	0	-10.65556	-1.02447	0.0286
37	6	0	-9.23408	-2.65575	0.01811
38	1	0	-9.85835	-3.53917	0.01559
39	6	0	1.47288	3.46137	0.03212
40	6	0	2.0929	3.94067	1.20795
41	6	0	2.83861	5.12291	1.16758
42	1	0	3.30432	5.48521	2.08262
43	6	0	2.99773	5.8523	-0.01405
44	6	0	2.37484	5.37419	-1.17041

45	1	0	2.48024	5.93117	-2.1
46	6	0	1.61756	4.19919	-1.16447
47	6	0	1.93827	3.20482	2.52369
48	1	0	2.48968	3.70743	3.32476
49	1	0	2.30843	2.17448	2.46116
50	1	0	0.88649	3.14917	2.83227
51	6	0	3.83883	7.10724	-0.04526
52	1	0	3.81347	7.63099	0.91653
53	1	0	3.49489	7.80195	-0.81919
54	1	0	4.89105	6.87654	-0.26085
55	6	0	0.95306	3.73366	-2.44397
56	1	0	1.25037	4.35523	-3.29461
57	1	0	-0.1404	3.77642	-2.36657
58	1	0	1.2168	2.69558	-2.68322

Table S29: Atomic coordinates for the optimized geometry of **1**.

Center Number	Atomic Number	Atomic Type	X	Y	Z
1	6	0	0.54431	-1.86435	-0.6353
2	6	0	-0.45439	-0.99875	-0.22265
3	6	0	-1.71904	-1.71868	-0.09909
4	6	0	-1.64177	-3.01813	-0.65371
5	16	0	-0.00601	-3.44013	-1.15475
6	8	0	1.85618	-1.61684	-0.63831
7	6	0	-0.04443	0.37568	0.04263
8	6	0	1.31227	0.57899	0.32695
9	16	0	1.64772	2.23275	0.79212
10	6	0	-0.00885	2.69985	0.4913
11	6	0	-0.7916	1.62283	0.00475
12	6	0	-0.50081	4.0131	0.61766
13	6	0	-1.7792	4.29821	0.17819
14	6	0	-2.72617	-3.90821	-0.69904
15	6	0	-3.92788	-3.53847	-0.11943
16	6	0	-3.99853	-2.30625	0.54819
17	6	0	-2.53021	3.27796	-0.43212
18	6	0	-2.06575	1.9477	-0.56002
19	6	0	-2.97019	1.15096	-1.34664
20	6	0	-4.07109	1.8369	-1.7544
21	16	0	-4.08439	3.4944	-1.21558
22	6	0	-2.91652	-1.39276	0.60402
23	6	0	-3.21453	-0.27774	1.46671
24	6	0	-4.46256	-0.3321	2.00017
25	16	0	-5.36413	-1.73824	1.49412
26	5	0	2.37198	-0.4512	-0.04316
27	6	0	3.93072	-0.31654	0.04271
28	6	0	4.70315	-0.2048	-1.13523
29	6	0	6.09217	-0.06309	-1.04542
30	6	0	6.75095	-0.04032	0.18538
31	6	0	5.9797	-0.16343	1.34608
32	6	0	4.59024	-0.29674	1.29557
33	6	0	3.81667	-0.44685	2.59069
34	6	0	4.0514	-0.23054	-2.50302
35	6	0	8.25189	0.11161	0.26929
36	1	0	0.12798	4.79554	1.03119
37	1	0	-2.17715	5.30547	0.25731
38	1	0	-2.6162	-4.88327	-1.16391
39	1	0	-4.78011	-4.21067	-0.13968
40	1	0	-2.79374	0.11799	-1.61099
41	1	0	-4.89154	1.4644	-2.35337
42	1	0	-2.51586	0.5163	1.69085
43	1	0	-4.91995	0.37922	2.67507
44	1	0	6.67363	0.03222	-1.96061
45	1	0	6.47455	-0.15717	2.316

46	1	0	4.49199	-0.45391	3.45215
47	1	0	3.24415	-1.38269	2.614
48	1	0	3.10046	0.36994	2.73863
49	1	0	3.23224	0.49555	-2.57775
50	1	0	3.62646	-1.21622	-2.72628
51	1	0	4.7755	0.00631	-3.28895
52	1	0	8.70203	0.19603	-0.72491
53	1	0	8.71347	-0.74679	0.77346
54	1	0	8.53211	1.00588	0.84012

Table S30: Atomic coordinates for the optimized geometry of *trans*-**27**.

Center Number	Atomic Number	Atomic Type	X	Y	Z
1	6	0	4,02674	0,22832	-0,0023
2	6	0	4,95057	-0,78887	-0,04365
3	6	0	6,30913	-0,34611	-0,02645
4	6	0	6,4094	1,06249	0,0303
5	16	0	4,81978	1,8098	0,06113
6	6	0	7,51134	-1,10424	-0,05772
7	6	0	8,73998	-0,40821	-0,03029
8	6	0	8,81585	0,99511	0,02637
9	6	0	7,6426	1,73454	0,05683
10	6	0	7,69652	-2,52812	-0,11544
11	6	0	9,0073	-2,89106	-0,13092
12	16	0	10,09504	-1,52496	-0,07627
13	6	0	2,59363	0,07414	-0,00812
14	6	0	1,67518	1,06957	0,03153
15	6	0	-4,79258	4,00587	0,18014
16	6	0	-3,46847	3,66435	0,1563
17	6	0	-3,27999	2,24894	0,08152
18	6	0	-4,48377	1,53069	0,04655
19	16	0	-5,84044	2,62803	0,11586
20	6	0	-2,04277	1,50596	0,04794
21	6	0	-2,11992	0,12411	-0,00625
22	8	0	-3,24246	-0,60031	-0,03559
23	5	0	-4,51364	0,01044	-0,01838
24	6	0	-0,68255	1,9444	0,06595
25	6	0	0,24183	0,92568	0,02589
26	16	0	-0,5594	-0,65492	-0,03667
27	6	0	-5,76214	-0,93945	-0,04067
28	6	0	-6,52773	-1,11173	-1,21567
29	6	0	-7,64222	-1,9565	-1,2003
30	6	0	-8,03163	-2,64002	-0,04528
31	6	0	-7,26325	-2,46932	1,11005
32	6	0	-6,14036	-1,63736	1,12886
33	6	0	-5,33674	-1,49832	2,40575
34	6	0	-6,14204	-0,4161	-2,50563
35	6	0	-9,26093	-3,51855	-0,03808
36	1	0	4,65578	-1,83226	-0,08563
37	1	0	9,77861	1,4966	0,04612
38	1	0	7,68085	2,81872	0,10058
39	1	0	6,88213	-3,24359	-0,14392
40	1	0	9,41525	-3,89248	-0,17171
41	1	0	2,25649	-0,96139	-0,04932
42	1	0	2,01478	2,10433	0,07257
43	1	0	-5,21129	5,0027	0,23582
44	1	0	-2,66261	4,38914	0,19142
45	1	0	-0,38595	2,98725	0,10704

46	1	0	-8,21908	-2,0866	-2,11439
47	1	0	-7,5448	-2,99855	2,01894
48	1	0	-5,82035	-2,02009	3,23763
49	1	0	-5,21812	-0,44715	2,69812
50	1	0	-4,32839	-1,91507	2,29255
51	1	0	-6,12549	0,67447	-2,3928
52	1	0	-6,84586	-0,65553	-3,30908
53	1	0	-5,14223	-0,71851	-2,84262
54	1	0	-9,46334	-3,93362	-1,03128
55	1	0	-10,15253	-2,95318	0,26549
56	1	0	-9,15366	-4,35329	0,6632

Table S31: Atomic coordinates for the optimized geometry of **27**.

Center Number	Atomic Number	Atomic Type	X	Y	Z
1	6	0	-3,91649	2,19446	-0,09948
2	6	0	-2,91251	1,20326	0,04014
3	6	0	-3,49617	-0,13677	8,90E-04
4	6	0	-4,8422	-0,11019	-0,42946
5	16	0	-5,46616	1,52567	-0,59838
6	6	0	-2,997	-1,38852	0,47181
7	6	0	-3,8013	-2,54174	0,29458
8	6	0	-5,08596	-2,49796	-0,26738
9	6	0	-5,62125	-1,26577	-0,60218
10	6	0	-1,79877	-1,69604	1,21
11	6	0	-1,6902	-3,01155	1,53252
12	16	0	-3,03275	-3,97036	0,96573
13	6	0	-3,70495	3,55097	0,1761
14	6	0	-2,45305	3,95236	0,61512
15	6	0	0,10198	-1,8838	-2,28143
16	6	0	-0,6459	-0,92986	-1,65071
17	6	0	0,13229	-0,13587	-0,7475
18	6	0	1,48931	-0,50084	-0,73938
19	16	0	1,76699	-1,84929	-1,81296
20	6	0	-0,27515	1,0191	0,03402
21	6	0	0,74705	1,81466	0,52216
22	8	0	2,0478	1,51788	0,53383
23	5	0	2,54618	0,32725	-0,03403
24	6	0	-1,57166	1,66566	0,21936
25	6	0	-1,4118	3,01761	0,61818
26	16	0	0,25421	3,40693	1,04707
27	6	0	4,08974	0,07509	0,07377
28	6	0	4,60339	-0,97791	0,86538
29	6	0	5,98465	-1,18502	0,9352
30	6	0	6,88595	-0,38128	0,23226
31	6	0	6,36978	0,66071	-0,5435
32	6	0	4,99603	0,90276	-0,62966
33	6	0	4,49996	2,05394	-1,48107
34	6	0	3,6836	-1,87235	1,67284
35	6	0	8,37242	-0,64561	0,28851
36	1	0	-5,6717	-3,40433	-0,38688
37	1	0	-6,64015	-1,19001	-0,96944
38	1	0	-1,06688	-0,95816	1,50698
39	1	0	-0,89029	-3,48838	2,08344
40	1	0	-4,51645	4,26646	0,08814
41	1	0	-2,27145	4,98335	0,9028
42	1	0	-0,24373	-2,60737	-3,00861
43	1	0	-1,7021	-0,78944	-1,83409
44	1	0	6,36685	-1,99316	1,55649
45	1	0	7,05511	1,30215	-1,09507

46	1	0	5,31836	2,50291	-2,05268
47	1	0	4,04954	2,84253	-0,86676
48	1	0	3,73452	1,72979	-2,19728
49	1	0	2,96285	-2,39908	1,03687
50	1	0	3,10394	-1,29741	2,40652
51	1	0	4,25397	-2,62655	2,22431
52	1	0	8,6603	-1,11964	1,233
53	1	0	8,94895	0,27994	0,18349
54	1	0	8,68786	-1,31726	-0,52149

12.1 Cartesian coordinates and total energies for for compound 1, 1* and 7TH

Table S32: Atomic coordinates for the minimum optimized structure of model compound **1** at the PBE1PBE/TZVP level, EmpiricalDispersion=GD3BJ.

Center Number	Atomic Number	Atomic Type	X	Y	Z
1	16	0	-2.38935	-2.13075	-1.42282
2	16	0	-3.05468	3.652156	0.554969
3	16	0	2.389508	-2.12944	1.426057
4	16	0	3.055202	3.651368	-0.55792
5	8	0	-4.02655	1.19999	0.312215
6	8	0	4.027008	1.199424	-0.31227
7	5	0	-4.00902	-0.15905	-0.04596
8	5	0	4.009093	-0.15931	0.046948
9	6	0	-2.68667	-0.63777	-0.59565
10	6	0	-1.57575	0.202722	-0.67786
11	6	0	-0.51871	-0.36065	-1.4475
12	1	0	0.412904	0.139036	-1.66572
13	6	0	-0.81943	-1.60821	-1.89722
14	1	0	-0.19302	-2.25254	-2.49694
15	6	0	-2.92927	1.939846	0.266385
16	6	0	-1.66894	1.510147	-0.08088
17	6	0	-0.70584	2.582715	0.031986
18	6	0	-1.33906	3.82439	0.235175
19	6	0	-0.67152	5.043675	0.15399
20	1	0	-1.20456	5.976563	0.291287
21	6	0	0.672037	5.043461	-0.15891
22	1	0	1.20506	5.976158	-0.29756
23	6	0	-5.33863	-0.9599	0.088827
24	6	0	-5.44543	-2.01848	1.002797
25	6	0	-6.63603	-2.73105	1.092983
26	1	0	-6.71443	-3.53965	1.814445
27	6	0	-7.72659	-2.43381	0.285303
28	6	0	-7.60808	-1.38421	-0.6191
29	1	0	-8.45137	-1.13474	-1.25735
30	6	0	-6.43805	-0.64354	-0.72513
31	6	0	-4.2959	-2.38475	1.900517
32	1	0	-4.61048	-3.09655	2.665429
33	1	0	-3.88572	-1.50744	2.408131
34	1	0	-3.47819	-2.84095	1.335205
35	6	0	-8.98875	-3.23863	0.365646
36	1	0	-9.86983	-2.61422	0.202896
37	1	0	-9.08898	-3.72513	1.337666
38	1	0	-8.99901	-4.02299	-0.39792
39	6	0	-6.358	0.486313	-1.71248
40	1	0	-6.33907	1.454122	-1.20431

41	1	0	-7.21348	0.477914	-2.3896
42	1	0	-5.44956	0.423732	-2.31881
43	6	0	2.68685	-0.63725	0.597484
44	6	0	1.576103	0.203496	0.679184
45	6	0	0.51921	-0.35894	1.449692
46	1	0	-0.41225	0.14111	1.66775
47	6	0	0.819859	-1.60615	1.900475
48	1	0	0.193537	-2.24977	2.501047
49	6	0	2.929746	1.939433	-0.26715
50	6	0	1.669413	1.510244	0.080757
51	6	0	0.706344	2.582676	-0.0335
52	6	0	1.339578	3.824063	-0.23838
53	6	0	5.338414	-0.96067	-0.08805
54	6	0	6.43439	-0.6511	0.732699
55	6	0	7.601926	-1.39687	0.63157
56	1	0	8.440003	-1.15755	1.280343
57	6	0	7.722729	-2.4411	-0.27839
58	6	0	6.632617	-2.73654	-1.08774
59	1	0	6.708413	-3.54968	-1.8044
60	6	0	5.444824	-2.01923	-1.00231
61	6	0	6.350377	0.471485	1.727991
62	1	0	7.204717	0.460137	2.406512
63	1	0	5.440945	0.403101	2.332246
64	1	0	6.330667	1.442728	1.226419
65	6	0	9.004424	-3.20878	-0.40224
66	1	0	9.688483	-2.71365	-1.09893
67	1	0	8.828504	-4.21865	-0.77769
68	1	0	9.516706	-3.28543	0.558993
69	6	0	4.294435	-2.386	-1.89867
70	1	0	3.480301	-2.84876	-1.33346
71	1	0	4.609952	-3.09227	-2.66833
72	1	0	3.879001	-1.5078	-2.40039

Table S32: Atomic coordinates for the transition state structure of model compound **1** at the PBE1PBE/TZVP level, EmpiricalDispersion=GD3BJ (see Figure S58).

Center Number	Atomic Number	Atomic Type	X	Y	Z
1	6	0	0.682378	4.963984	-1.09214
2	6	0	-0.68553	4.96377	-1.09149
3	6	0	1.337363	3.830951	-0.61671
4	6	0	-1.3397	3.830526	-0.61544
5	6	0	0.721114	2.754798	0.067694
6	6	0	-0.72245	2.754586	0.068403
7	16	0	2.969603	3.495593	-1.1464
8	6	0	2.848271	1.917894	-0.45001
9	6	0	1.719571	1.707177	0.31294
10	1	0	1.240514	5.770608	-1.55197
11	1	0	-1.24436	5.770209	-1.5508
12	8	0	3.850448	1.073118	-0.6495
13	6	0	1.877758	0.619598	1.257841
14	6	0	2.776502	-0.40578	0.955492
15	5	0	3.842683	-0.21758	-0.09861
16	16	0	-2.9723	3.494576	-1.14364
17	6	0	-2.84976	1.916909	-0.44739
18	6	0	-1.72033	1.706652	0.31462
19	8	0	-3.85171	1.071664	-0.64618
20	5	0	-3.84235	-0.2193	-0.0959
21	6	0	-2.77537	-0.40707	0.957428
22	6	0	-1.87727	0.618919	1.259587
23	6	0	-1.44928	0.562702	2.61086
24	6	0	1.450111	0.563143	2.609206
25	6	0	-1.92306	-0.52667	3.274173
26	16	0	-2.94703	-1.49707	2.295746
27	6	0	1.924836	-0.52581	3.272498
28	16	0	2.949333	-1.4955	2.293896
29	1	0	0.904396	1.352892	3.092498
30	1	0	1.746411	-0.79233	4.304053
31	1	0	-0.90409	1.352823	3.094177
32	1	0	-1.74424	-0.79311	4.305683
33	6	0	-4.98035	-1.19777	-0.50502
34	6	0	-4.66876	-2.45734	-1.04291
35	6	0	-6.3289	-0.8497	-0.31566
36	6	0	-5.69416	-3.32925	-1.39062
37	6	0	-7.32683	-1.75334	-0.65752
38	6	0	-7.02988	-2.99632	-1.20468
39	1	0	-8.36552	-1.48045	-0.49243
40	6	0	-8.12268	-3.93932	-1.60868
41	6	0	-3.24319	-2.88399	-1.26156
42	1	0	-5.44264	-4.2966	-1.81657
43	6	0	-6.71204	0.480661	0.26909

44	1	0	-2.64764	-2.09564	-1.72769
45	1	0	-3.19765	-3.76383	-1.90559
46	1	0	-2.75191	-3.13736	-0.31788
47	1	0	-6.53939	1.290315	-0.44431
48	1	0	-6.12644	0.711533	1.163141
49	1	0	-7.76731	0.494024	0.546152
50	1	0	-8.99304	-3.84211	-0.95651
51	1	0	-7.78476	-4.97692	-1.57747
52	1	0	-8.45553	-3.73274	-2.63098
53	1	0	6.130188	0.726395	1.142559
54	1	0	2.652478	-2.09432	-1.7447
55	6	0	6.713897	0.489916	0.248781
56	6	0	4.980986	-1.19568	-0.50769
57	6	0	3.243761	-2.87986	-1.26838
58	1	0	8.404104	-4.55532	-0.68781
59	6	0	6.329839	-0.84446	-0.32608
60	6	0	4.669369	-2.45486	-1.04654
61	1	0	3.199231	-3.7654	-1.9046
62	6	0	7.327862	-1.74558	-0.67403
63	6	0	5.694883	-3.32433	-1.40021
64	1	0	7.769739	0.505333	0.523531
65	6	0	7.03064	-2.99141	-1.21453
66	6	0	8.122071	-3.95848	-1.56118
67	1	0	5.443393	-4.28821	-1.83386
68	1	0	6.539353	1.294853	-0.46948
69	1	0	9.019122	-3.43939	-1.90505
70	1	0	2.747163	-3.1234	-0.32496
71	1	0	7.805955	-4.65136	-2.34328
72	1	0	8.367098	-1.46701	-0.52226

Table S34: Atomic coordinates for the minimum optimized structure of model compound **1*** at the PBE1PBE 6-311++G(d,p) level, EmpiricalDispersion=GD3BJ (see Figure S58).

Center Number	Atomic Number	Atomic Type	X	Y	Z
1	16	0	-2.51699	-3.21195	-1.22893
2	16	0	-2.99798	2.571195	0.799273
3	16	0	2.518427	-3.21097	1.228839
4	16	0	2.996815	2.572393	-0.79931
5	8	0	-4.00593	0.135629	0.612576
6	8	0	4.005709	0.137206	-0.6129
7	5	0	-4.01985	-1.20707	0.232805
8	5	0	4.020207	-1.2055	-0.23319
9	6	0	-2.7541	-1.71336	-0.40256
10	6	0	-1.63861	-0.88073	-0.5577
11	6	0	-0.64013	-1.45894	-1.3927
12	1	0	0.280601	-0.97185	-1.67926
13	6	0	-0.98465	-2.70967	-1.81245
14	1	0	-0.40655	-3.36695	-2.44712
15	6	0	-2.90653	0.867122	0.492872
16	6	0	-1.67849	0.428287	0.044702
17	6	0	-0.70276	1.496763	0.090614
18	6	0	-1.31717	2.739717	0.349019
19	6	0	-0.65764	3.962014	0.212985
20	1	0	-1.17831	4.894919	0.395628
21	6	0	0.655953	3.962274	-0.21292
22	1	0	1.176231	4.895385	-0.39561
23	6	0	2.754788	-1.71227	0.402439
24	6	0	1.638999	-0.88008	0.557794
25	6	0	0.640974	-1.45864	1.39311
26	1	0	-0.27983	-0.97187	1.679957
27	6	0	0.986077	-2.70923	1.812799
28	1	0	0.408406	-3.36669	2.447668
29	6	0	2.906053	0.868271	-0.49299
30	6	0	1.678252	0.428952	-0.04464
31	6	0	0.702085	1.497044	-0.09046
32	6	0	1.315978	2.740241	-0.34894
33	1	0	5.042638	-1.78405	-0.41584
34	1	0	-5.04209	-1.78602	0.415275

Table S35: Atomic coordinates for the transition state structure of model compound ***** at the PBE1PBE 6-311++G(d,p) level, EmpiricalDispersion=GD3BJ (see Figure S58).

Center Number	Atomic Number	Atomic Type	X	Y	Z
1	16	0	-2.93647	-3.3266	-0.21226
2	16	0	-2.96643	2.743021	-0.14271
3	16	0	2.935326	-3.32745	-0.21274
4	16	0	2.967298	2.742218	-0.14238
5	8	0	-3.86191	0.480158	-1.11453
6	8	0	3.862204	0.479125	-1.11423
7	5	0	-3.85547	-0.88645	-1.38299
8	5	0	3.855241	-0.88742	-1.38297
9	6	0	-2.79136	-1.6613	-0.65608
10	6	0	-1.88615	-0.99561	0.182188
11	6	0	-1.44772	-1.8293	1.243212
12	1	0	-0.90372	-1.46875	2.097976
13	6	0	-1.91584	-3.1069	1.142913
14	1	0	-1.72948	-3.92816	1.820943
15	6	0	-2.85341	1.055842	-0.47007
16	6	0	-1.72698	0.43844	0.037767
17	6	0	-0.72297	1.436812	0.431759
18	6	0	-1.33951	2.713198	0.481841
19	6	0	-0.68423	3.91731	0.742711
20	1	0	-1.24394	4.841637	0.828919
21	6	0	0.68531	3.917121	0.742794
22	1	0	1.245266	4.841289	0.829117
23	6	0	2.790791	-1.66203	-0.65627
24	6	0	1.885832	-0.99616	0.182122
25	6	0	1.447221	-1.82985	1.243084
26	1	0	0.903413	-1.46926	2.097965
27	6	0	1.914867	-3.1076	1.142539
28	1	0	1.72825	-3.92891	1.820443
29	6	0	2.853843	1.055075	-0.46978
30	6	0	1.727198	0.437984	0.03795
31	6	0	0.723416	1.43662	0.431784
32	6	0	1.340299	2.712834	0.482
33	1	0	4.747786	-1.29397	-2.05448
34	1	0	-4.74809	-1.29277	-2.05455

Table S36: Atomic coordinates for the minimum optimized structure of **7TH** at the PBE1PBE 6-311++G(d,p) level, EmpiricalDispersion=GD3BJ (see Figure S58).

Center Number	Atomic Number	Atomic Type	X	Y	Z
1	16	0	-2.46387	-3.1944	-1.25927
2	16	0	-2.98625	2.587874	0.841248
3	16	0	2.463508	-3.19465	1.259286
4	16	0	2.986546	2.58757	-0.84124
5	6	0	-4.04354	0.021801	0.601574
6	6	0	4.043585	0.021394	-0.6015
7	6	0	-3.92963	-1.27609	0.151291
8	6	0	3.929527	-1.27648	-0.1512
9	6	0	-2.73605	-1.67396	-0.46179
10	6	0	-1.61983	-0.82211	-0.58621
11	6	0	-0.59718	-1.41312	-1.39728
12	1	0	0.324211	-0.92047	-1.6702
13	6	0	-0.91396	-2.66384	-1.81211
14	1	0	-0.3175	-3.32215	-2.42752
15	6	0	-2.94011	0.878439	0.499347
16	6	0	-1.68754	0.460455	0.015891
17	6	0	-0.70354	1.519689	0.091654
18	6	0	-1.31545	2.758941	0.367465
19	6	0	-0.65296	3.980225	0.223418
20	1	0	-1.16991	4.913743	0.414225
21	6	0	0.653384	3.980159	-0.22344
22	1	0	1.170443	4.913624	-0.41424
23	6	0	2.73588	-1.67423	0.46182
24	6	0	1.619737	-0.82228	0.586184
25	6	0	0.596971	-1.41319	1.397183
26	1	0	-0.32439	-0.92046	1.670039
27	6	0	0.913609	-2.66394	1.812023
28	1	0	0.317044	-3.3222	2.427388
29	6	0	2.940229	0.878143	-0.49932
30	6	0	1.687603	0.460286	-0.0159
31	6	0	0.703716	1.519618	-0.09169
32	6	0	1.315758	2.758807	-0.36749
33	1	0	4.768914	-1.95883	-0.22354
34	1	0	-4.76908	-1.95835	0.223666
35	1	0	-4.98009	0.380445	1.01324
36	1	0	4.980182	0.379943	-1.01313

Table S37: Atomic coordinates for the transition state structure of **7TH** at the PBE1PBE 6-311++G(d,p) level, EmpiricalDispersion=GD3BJ (see Figure S58).

Center Number	Atomic Number	Atomic Type	X	Y	Z
1	16	0	-2.93674	-3.319	0.185351
2	16	0	-2.93052	2.780045	0.178405
3	16	0	2.938252	-3.31784	0.184576
4	16	0	2.929252	2.781173	0.17914
5	6	0	-3.83283	0.413907	1.275318
6	6	0	3.832514	0.415225	1.275655
7	6	0	-3.77641	-0.95539	1.382107
8	6	0	3.776831	-0.95415	1.381975
9	6	0	-2.85033	-1.6264	0.576796
10	6	0	-1.90374	-0.95251	-0.22617
11	6	0	-1.43229	-1.81288	-1.26204
12	1	0	-0.88681	-1.45335	-2.1153
13	6	0	-1.8827	-3.08745	-1.16084
14	1	0	-1.68018	-3.91369	-1.82699
15	6	0	-2.85942	1.083555	0.519745
16	6	0	-1.74522	0.456551	-0.07148
17	6	0	-0.72705	1.443478	-0.47578
18	6	0	-1.33728	2.723323	-0.51459
19	6	0	-0.68494	3.917807	-0.82677
20	1	0	-1.24585	4.839791	-0.9303
21	6	0	0.68347	3.918092	-0.82655
22	1	0	1.244023	4.840315	-0.92984
23	6	0	2.851135	-1.62537	0.576416
24	6	0	1.90422	-0.9517	-0.22635
25	6	0	1.432952	-1.81207	-1.26229
26	1	0	0.887242	-1.45254	-2.1154
27	6	0	1.883936	-3.08646	-1.16143
28	1	0	1.681726	-3.91264	-1.82775
29	6	0	2.858819	1.084601	0.520216
30	6	0	1.74497	0.45721	-0.07127
31	6	0	0.726472	1.443771	-0.47568
32	6	0	1.336187	2.723865	-0.51419
33	1	0	4.496676	-1.49799	1.982736
34	1	0	-4.49602	-1.49942	1.982984
35	1	0	-4.61448	0.977886	1.771409
36	1	0	4.613834	0.979456	1.77198

13. Reactivity test of 5: synthesis of 13, 14, 8, 11, 12, 10.

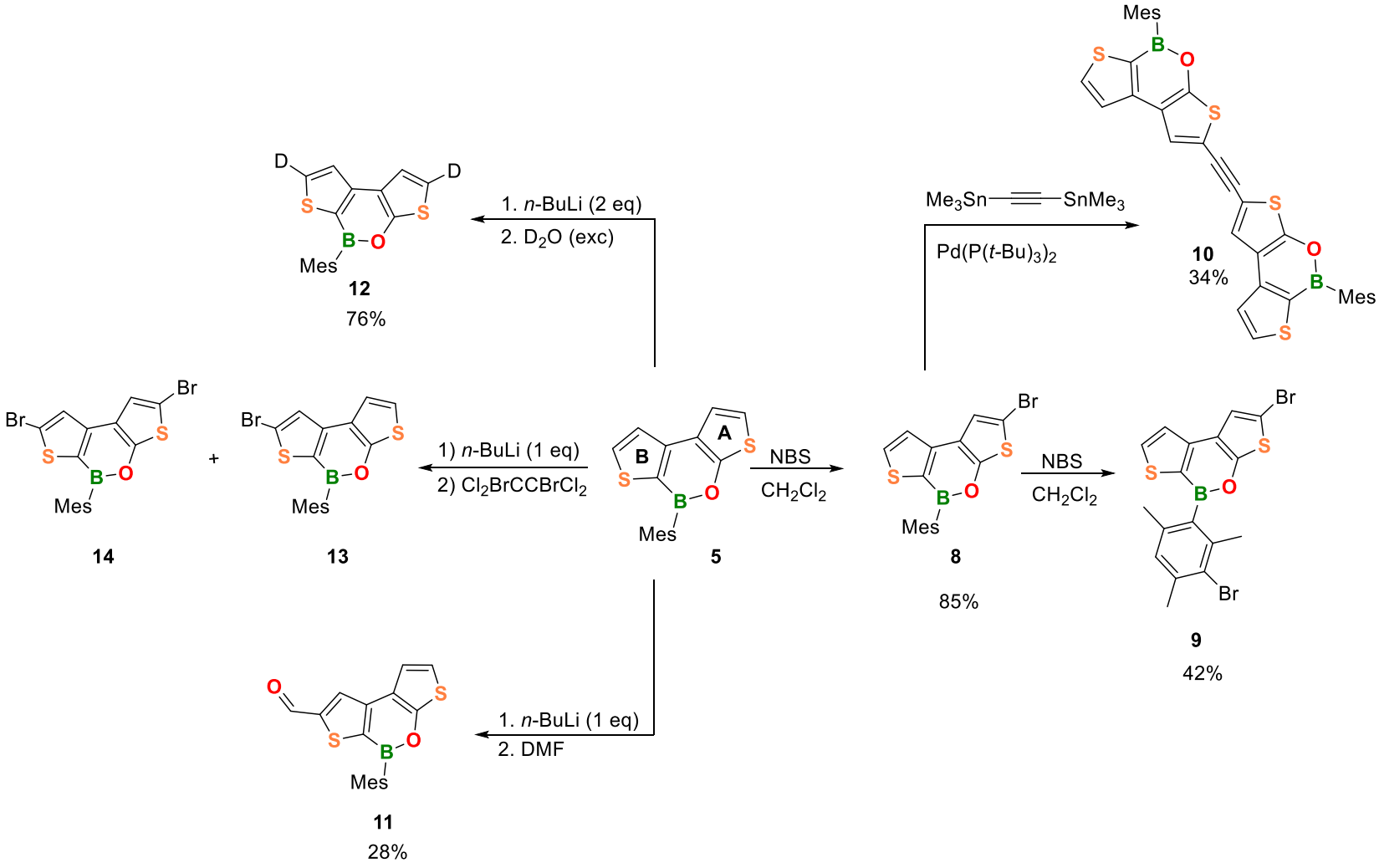

Scheme **R1.** Investigation of the mesityl diethienooxaborine **5** reactivity.

13.1 Synthesis of 13

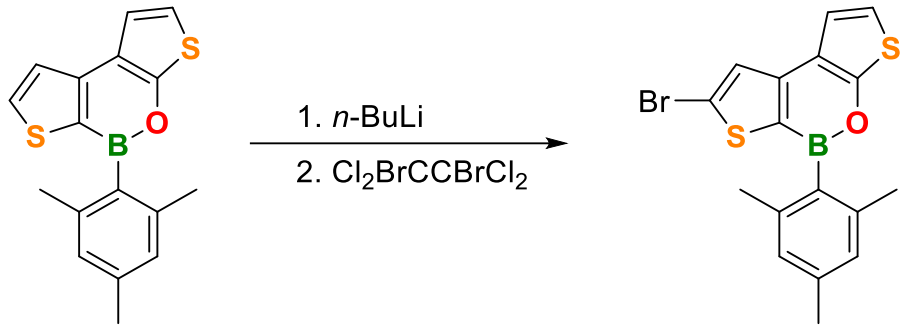

5 **13**

A flame-dried 50 mL Schlenk flask was charged with **5** (105 mg, 0.34 mmol) and THF (4 mL). The yellowish solution thus obtained was cooled to –78 °C and, *n*-BuLi (2.23 M in hexanes; 0.16 mL, 0.46 mmol, 1.05 eq.) was added dropwise during 2 min. The resulting yellow reaction mixture was stirred for 15 min at the same temperature and then $Cl_2BrCCBrCl_2$ (138 mg, 0.43 mmol, 1.25 eq.) was added as THF solution (4 mL). The orange mixture thus obtained was slowly allowed to warm to room temperature and stirrred overnight. THF was removed and the residue was purified *via* column chromatography (18 cm silica gel, *d* = 2.5 cm; *c*-hexane/CH_2Cl_2 (11:1)). The fractions containing **13** were combined and the solvent was evaporated, giving a white solid (78 mg) which was proved to be the title compound **13** in mixture with traces of the doubly brominated compound **14**, **8** and starting **5** (see Figure R2). A second fraction, containing the starting **5** was also recovered (40 mg, 0.13 mmol, 38%).

Single crystals of **13** suitable for X-ray analysis were obtained by slow evaporation of a **13** saturated solution in *n*-hexane/CH_2Cl_2 .

Note: further experiments carried out using Br_2 as electrophile under otherwise identical conditions, allowed to isolate pure doubly brominated compound **14** (Figure R4, R5).

*Characterization data of **13***:

^{1}H NMR (400 MHz, $CDCl_3$): δ = 7.59 (s, 1H), 7.27 (d, 1H; overlapped with $CDCl_3$), 6.96 (d, ^3J(H,H) = 6.0 Hz, 1H), 6.90 (s, 2H), 2.34 (s, 3H), 2.23 (s, 6H).

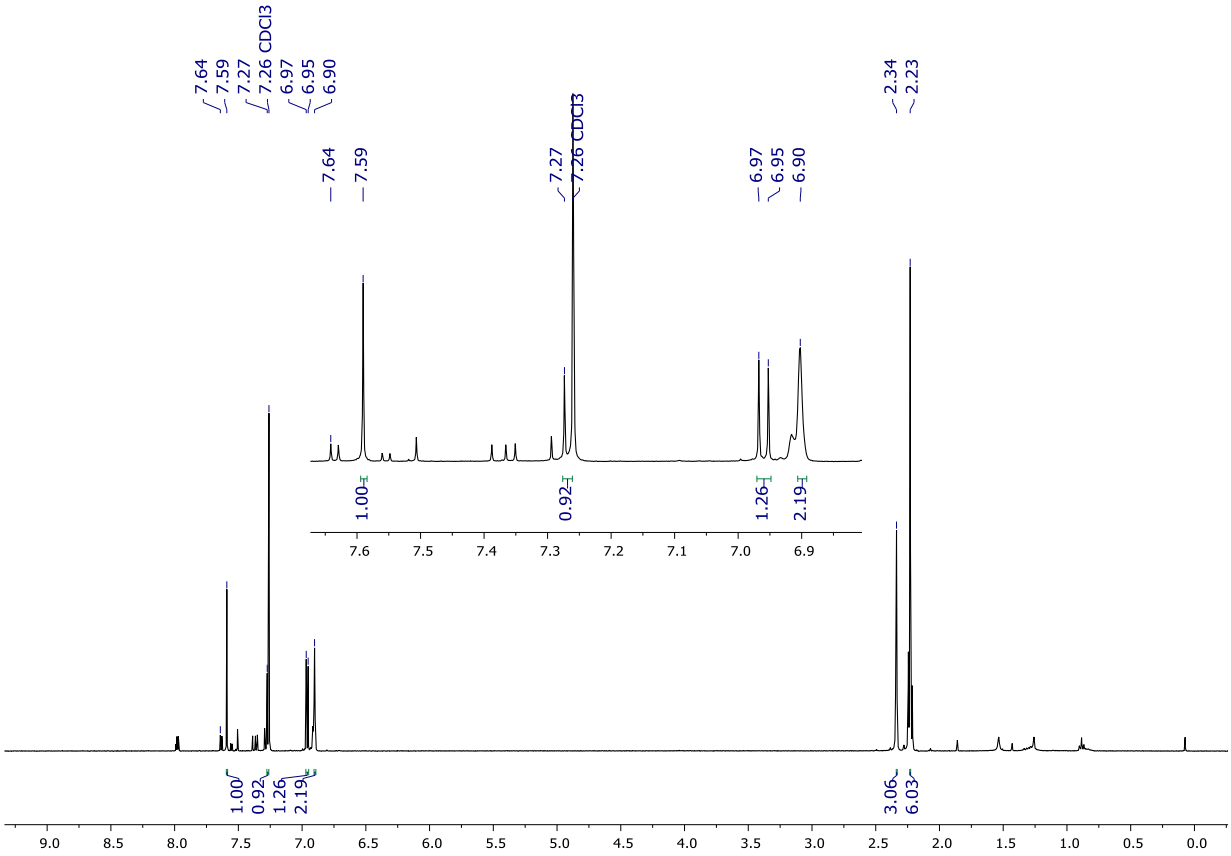

Figure R1: ^{1}H NMR spectrum of **13** ($CDCl_3$, 400 MHz).

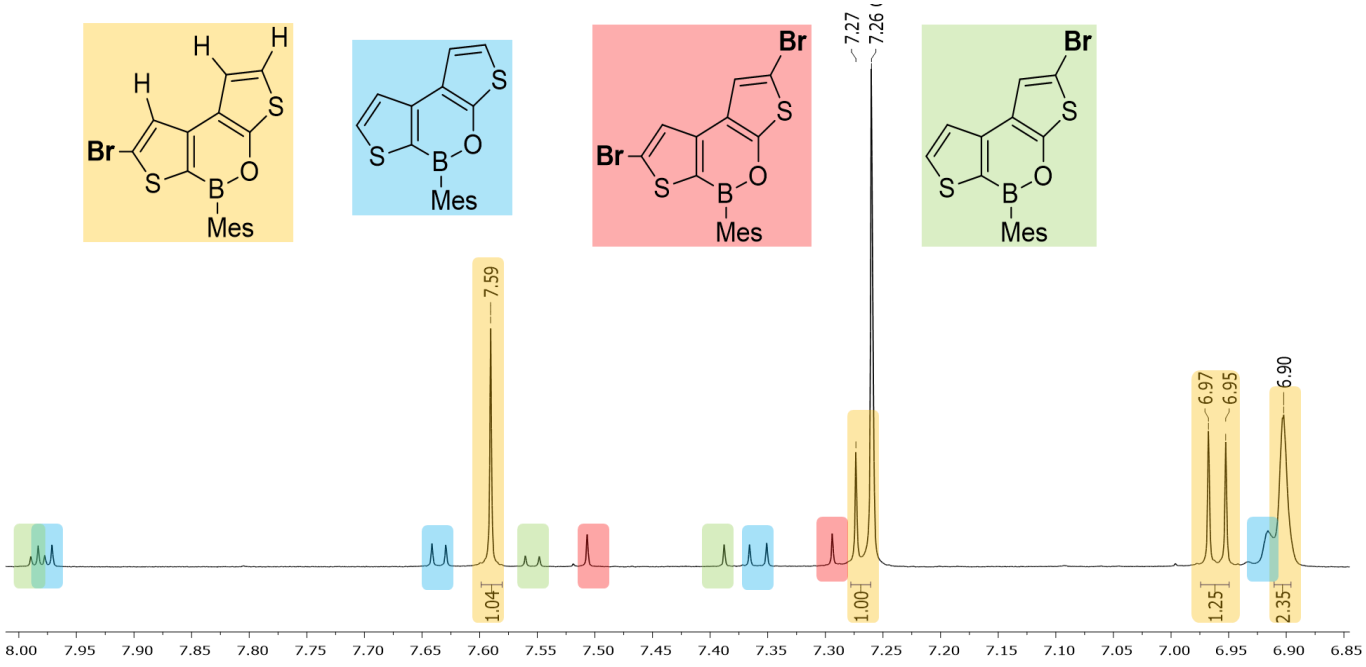

Figure R2: ^{1}H NMR spectrum of **13,** zoom of the aromatic region ($CDCl_3$, 400 MHz).

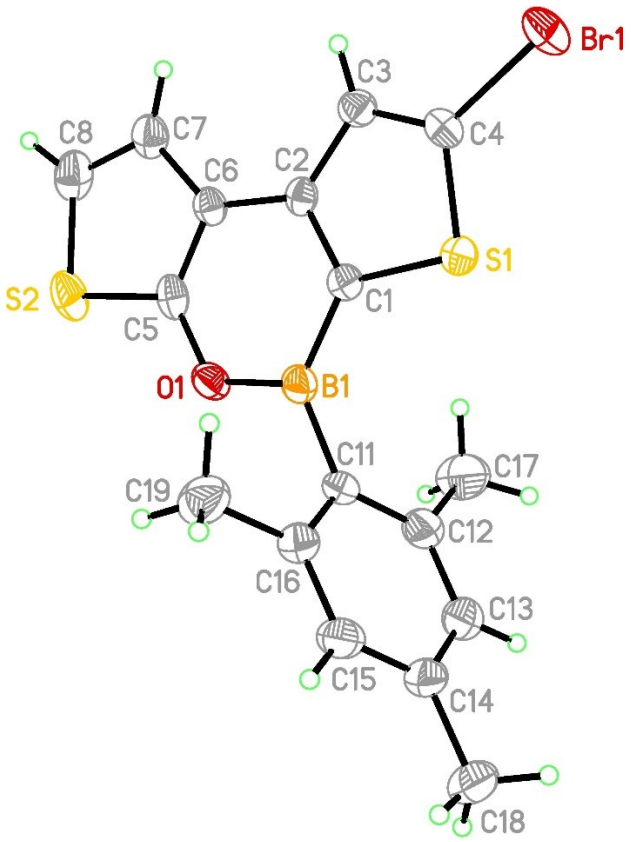

Figure R3: Molecular structure of **13** in the solid state. Displacement ellipsoids are drawn at the 50% probability level.

Note: bond lengths (A), bond angles (°), and torsion angles (°) for crystal structures of the present section have been not explicited.

*Characterization data of **14***:

HRMS (MALDI): Calculated *m/z* for $[C_{17}H_{13}BBr_2O]^+$: 467.8842; found: 467.8837.

^{1}H NMR (500.2 MHz, Chloroform-*d*) δ 7.51 (s, 1H), 7.29 (s, 1H), 6.90 (s, 2H), 2.33 (s, 3H), 2.21 (s, 6H).

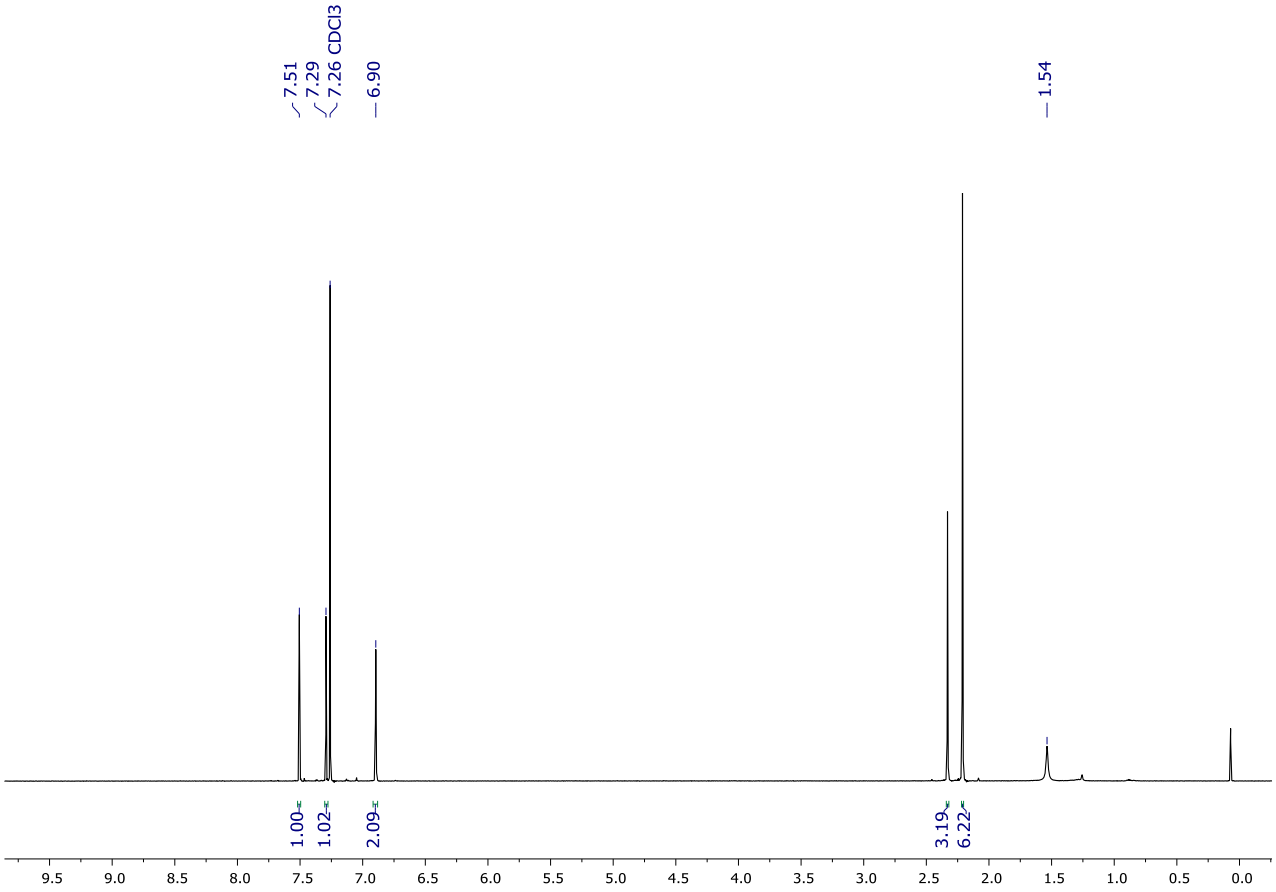

Figure R4: ^{1}H NMR spectrum of **14** ($CDCl_3$, 500 MHz).

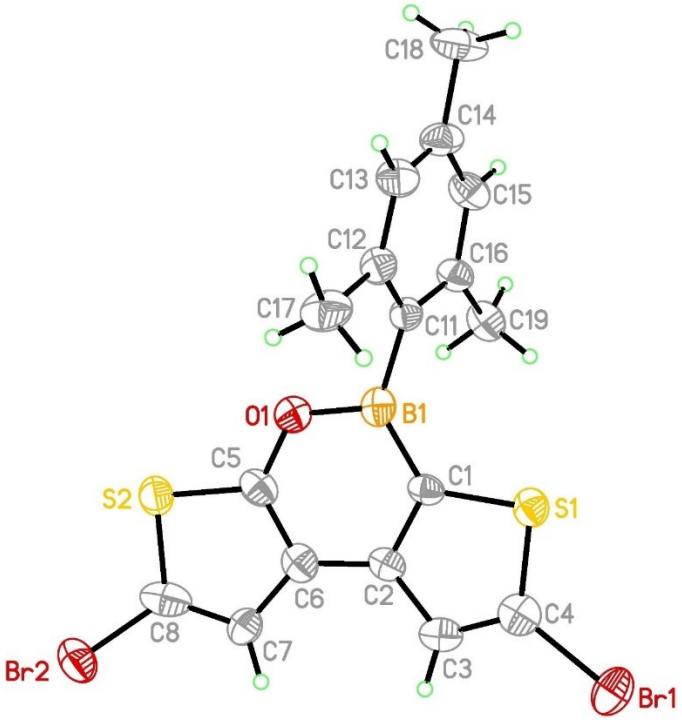

Figure R5: Molecular structure of **14** in the solid state. Displacement ellipsoids are drawn at the 50% probability level.

Note: bond lengths (A), bond angles (°), and torsion angles (°) for crystal structures of the present section have been not explicited.

13.2 Synthesis of 9

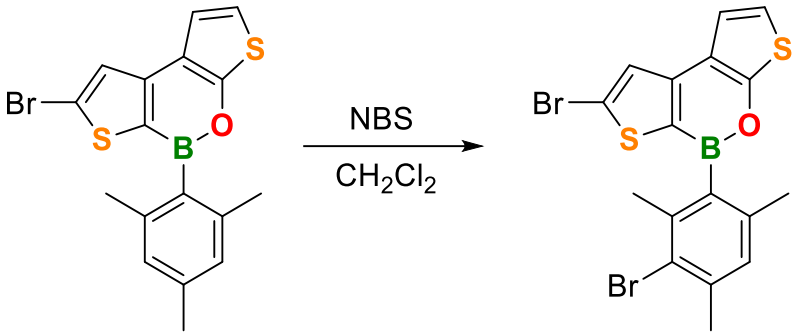

8 **9**

42%

A 50mL flask was charged with **8** (40 mg, 0.10 mmol) and CH_2Cl_2 (2.5 mL). The resulting solution was treated with NBS (22 mg, 0.12 mmol, 1.5 eq.) and stirred at room temperature for 23 h. The reaction progress was checked by TLC. After 23 h, TLC showed complete conversion of the starting material and thus the reaction was stopped.

The solvent was removed under reduced pressure and the residue was purified *via* column chromatography (8 cm silica gel, d = 2 cm; c-hexane/CH_2Cl_2 (9:1)). **9** was thereby obtained as an off-white solid (20 mg, 0.043 mmol, 42%). ^{1}H NMR showed the presence of traces of residual **8** starting material.

Single crystals of **9** suitable for X-ray analysis were obtained by slow evaporation of a saturated solution of **9** in *n*-hexane/CH_2Cl_2.

Characterization data of ***9***:

^{1}H NMR (400 MHz, $CDCl_3$): δ = 8.00 (d, ^3J(H,H)= 4.8 Hz, 1H), 7.56 (d, ^3J(H,H) = 4.8 Hz, 1H), 7.39 (s, 1H), 6.99 (s, 2H), 2.45 (s, 3H), 2.32 (s, 3H), 2.15 (s, 3H).

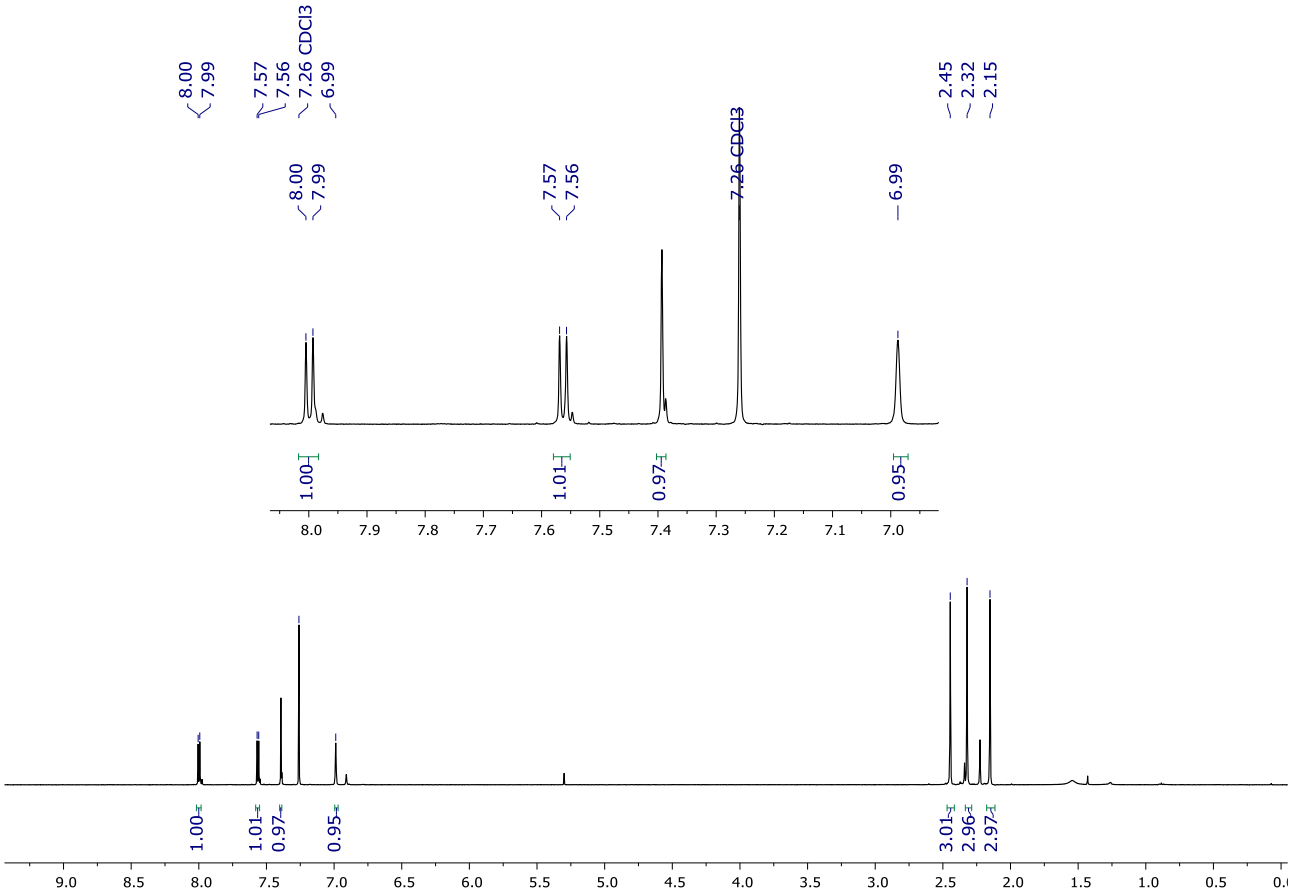

Figure R6: ^{1}H NMR spectrum of **9** ($CDCl_3$, 400 MHz).

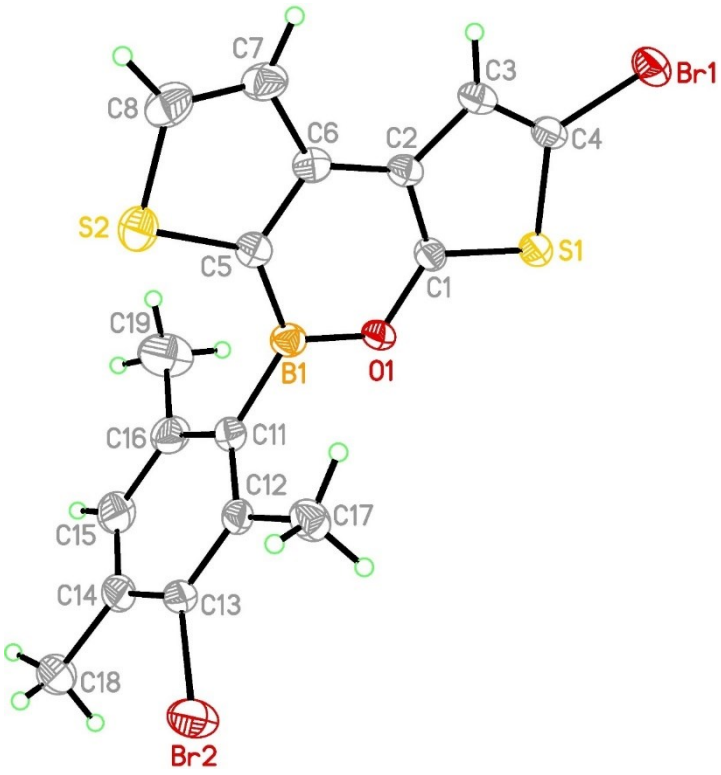

Figure R7: Molecular structure of **9** in the solid state. Displacement ellipsoids are drawn at the 50% probability level.
Note: bond lengths (A), bond angles (°), and torsion angles (°) for crystal structures of the present section have been not explicited.

13.3 Synthesis of 12

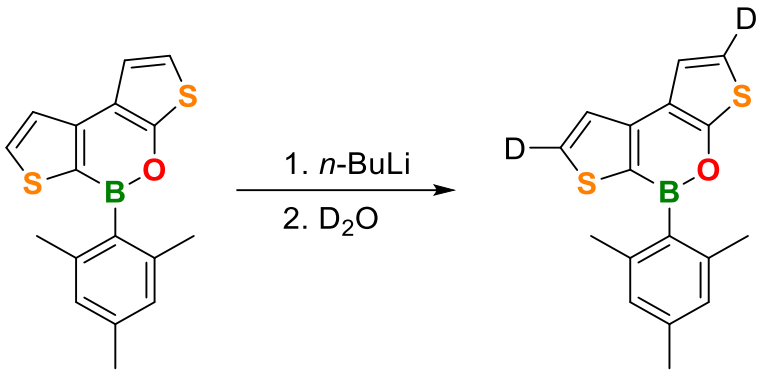

5 **12**

76%

A Schlenk flask was charged with **5** (30 mg, 0.10 mmol, 1 eq.) and THF (3 mL) and then cooled to –78 °C. The resulting solution was treated with *n*-BuLi (1.35 M in hexanes; 100 µL, 0.13 mmol, 1.3 eq.).
The reaction mixture thus obtained was stirred at –78 °C for 15 min and D_2O (300 µL, 17.72 mmol, 175 eq.) was added in one portion and the resulting orange mixture was allowed to warm up to room temperature.
THF was removed under reduced pressure, the crude material was taken up with CH_2Cl_2 (15 mL) and washed with water (5 mL). The organic phases were dried over Na_2SO_4 and the solvent was removed under reduced pressure. **12** was thereby obtained as a brown solid (24 mg, 0.076 mmol, 76%).

*Characterization data of **12***:

^{1}H NMR (300 MHz, $CDCl_3$): δ = 7.63 (s, 1H), 7.36 (s, 1H), 6.92 (s, 2H), 2.35 (s, 3H), 2.24 (s, 6H).

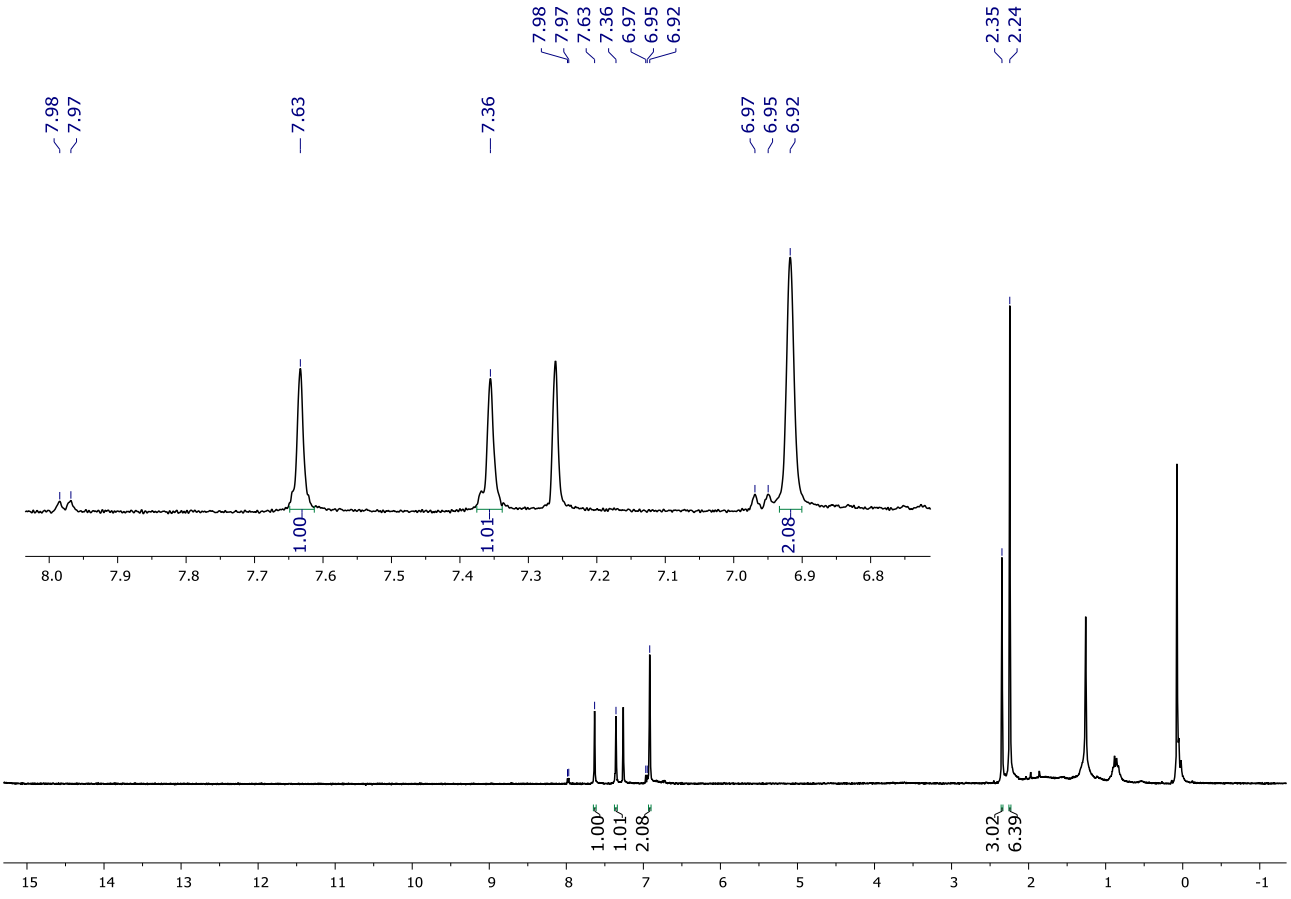

Figure R8: ^{1}H NMR spectrum of **12** ($CDCl_3$, 300 MHz).

13.4 Synthesis of 11

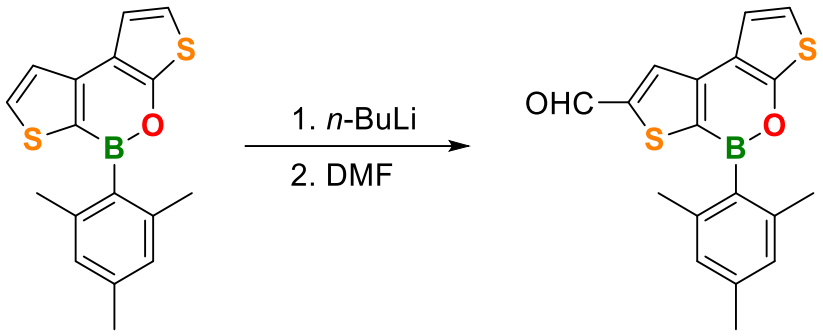

5 **11**

28%

A flame-dried 50 mL Schlenk flask was charged with **5** (100 mg, 0.32 mmol) and THF (5 mL). The colorless solution thus obtained was cooled to –78 °C and, *n*-BuLi (1.40 M in hexanes; 240 µL, 0.34 mmol, 1.05 eq.) was added dropwise during 2 min. The resulting yellow reaction mixture was stirred for 15 min at the same temperature.

DMF (130 µL, 1.61 mmol, 5 eq.) was added and the resulting mixture was stirred at –78 °C for 30 min.

The reaction mixture was therefore allowed to warm up to room temperature and quenched with a NH_4Cl saturated solution (0.5 mL), giving a red mixture. The THF was removed and the residue was taken up with CH_2Cl_2. NH_4Cl sat. aqueous solution (20 mL) was addedd and, after separation of the two layers, the aqueous phase was extracted with CH_2Cl_2 (3×15 mL). The combined organic phases were dried over Na_2SO_4 and filtered. The solvent was removed and the residue was purified *via* column chromatography (*n*-hexane/CH_2Cl_2 (5:4)). **11** was thereby obtained as an orange solid (30 mg, 0.09 mmol, 28%).

Starting **5** (8 mg, 0.025 mmol, 8%),besides a small amount of unknown products was also recovered.

Single crystals of **11** suitable for X-ray analysis were obtained by slow evaporation of a saturated solution of **11** in *n*-hexane/CH_2Cl_2.

*Characterization data of **11**:*

^{1}H NMR (400 MHz, $CDCl_3$): δ = 10.17 (s, 1H), 8.24 (s, 1H), 7.38 (d, ^3J (H,H)= 6.0 Hz, 1H), 7.03 (d, ^3J(H,H) = 6.0 Hz, 1H), 6.92 (s, 2H), 2.35 (s, 3H), 2.23 (s, 6H).

HRMS (EI+): Calculated *m/z* for $[C_{18}H_{15}BO_2S_2]^+$: 388.0606; found: 388.0573.

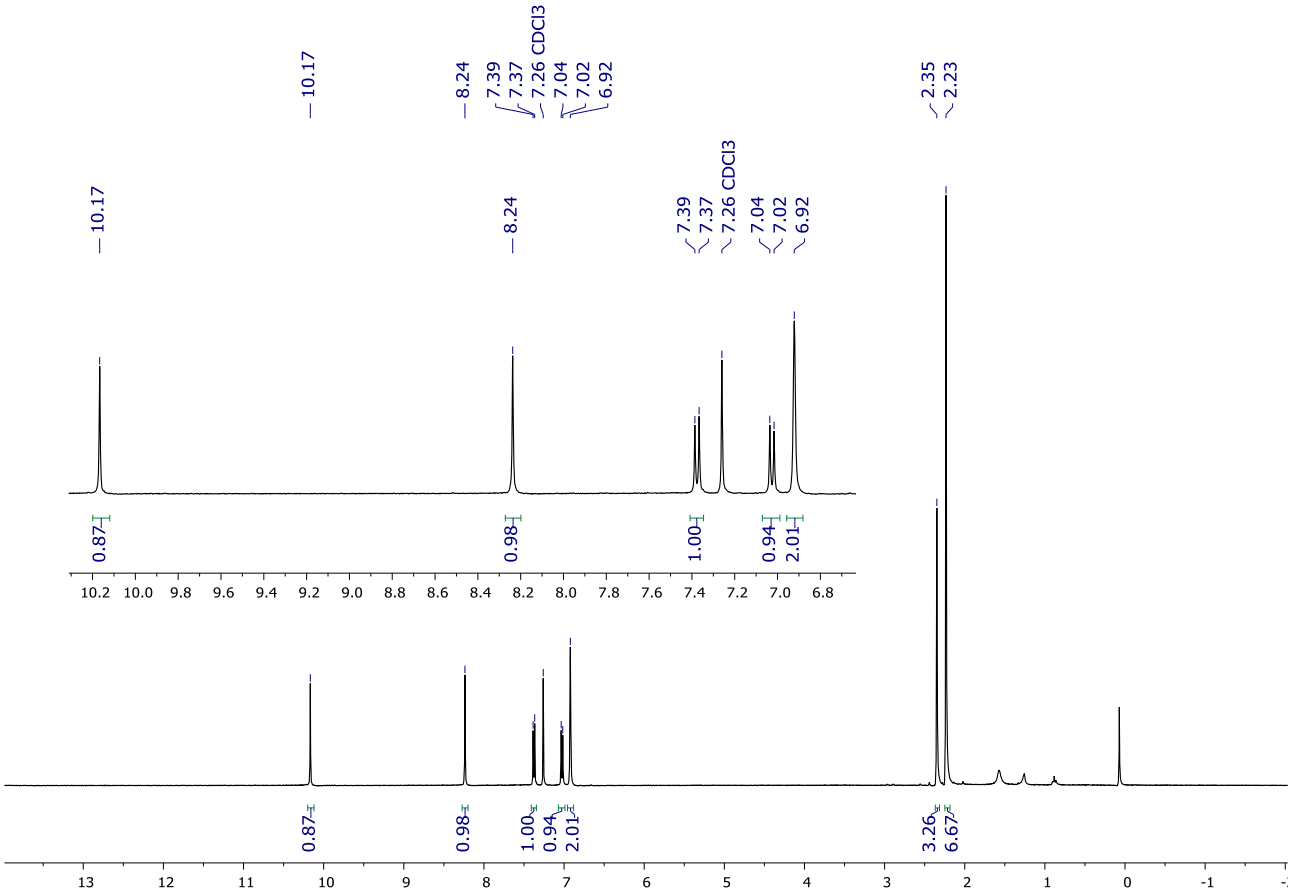

Figure R9: ^{1}H NMR spectrum of **11** ($CDCl_3$, 300 MHz).

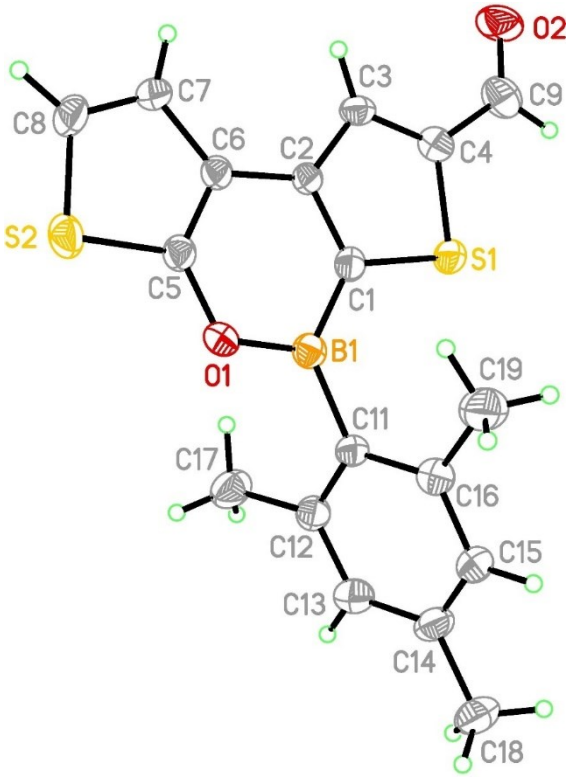

Figure R10: Molecular structure of **11** in the solid state. Displacement ellipsoids are drawn at the 50% probability level.
Note: bond lengths (A), bond angles (°), and torsion angles (°) for crystal structures of the present section have been not explicited.

13.5 Synthesis of 10

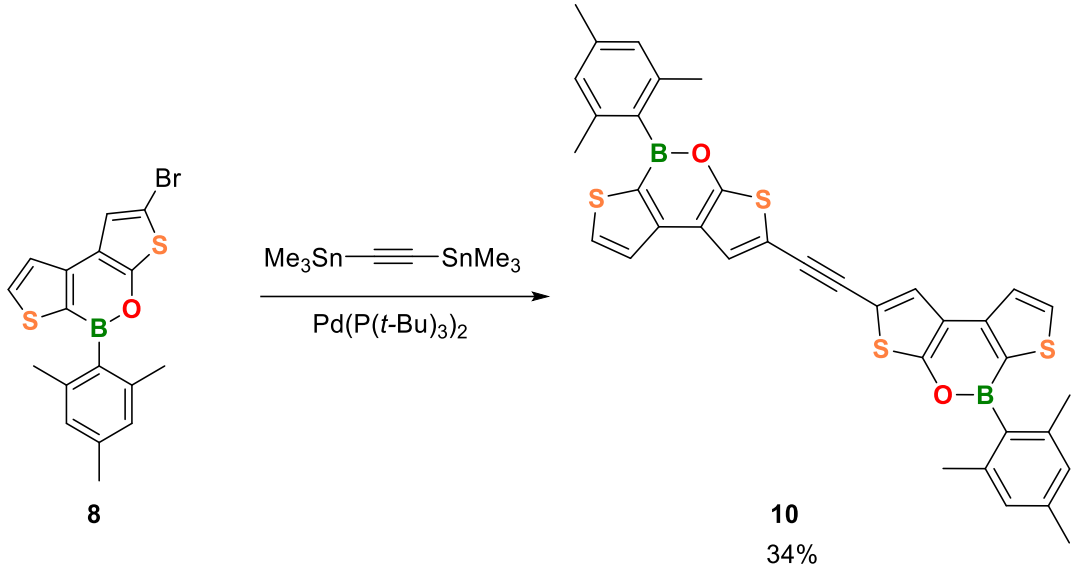

8 **10**
34%

A flame-dried 250 mL J-Young round-bottom flask was charged with **5** (540 mg, 1.39 mmol) and evacuated for 30 min. Toluene (72 mL), *trans*-1,2-bis(Me_3Sn)acetylene (244 mg, 0.69 mmol, 0.50 eq.), and $Pd(P(t\text{-}Bu)_3)_2$ (71 mg, 0.139 mmol, 0.1 eq.) were added, the Young-tap was closed, and the red mixture was heated with stirring to 80 °C for 15 h. After cooling to room temperature, the solvent was removed under reduced pressure, and the residue was purified by column chromatography (13 cm silica gel, $d = 3.0$ cm, *c*-hexane/CH_2Cl_2 (5:1)). The fractions containing **10** were combined and evaporated to dryness. The dark red residue was treated with *n*-hexane and the resulting suspension was filtered. **10** was thereby isolated as a yellow solid (151 mg, 0.24 mmol, 34%). Single crystals suitable of **10** suitable for X-ray crystallography were grown by slow evaporation of saturated solution of **10** in $CDCl_3$.

*Characterization data of **10***:

HRMS (MALDI): Calculated *m/z* for $[C_{36}H_{28}B_2O_2S_4]^+$: 642.1161; found: 642.1153.

^{1}H NMR (500 MHz, $CDCl_3$): δ = 8.01 (d, ^3J(H,H) = 4.8 Hz, 1H), 7.62 (d, ^3J(H,H)= 4.8 Hz, 1H), 7.59 (s, 1H), 6.93 (s, 2H), 2.35 (s, 3H), 2.26 (s, 6H).

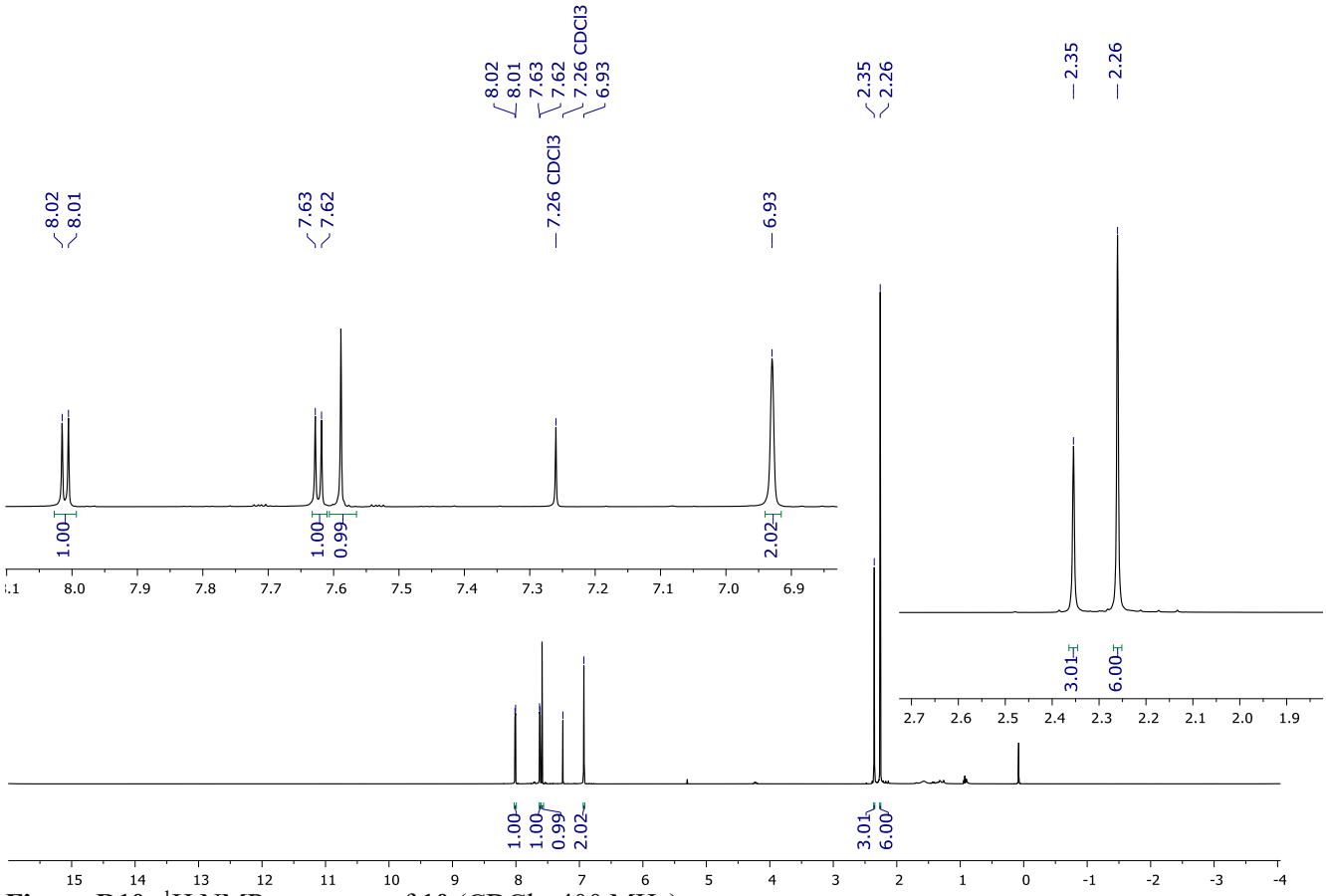

Figure R10: ^{1}H NMR spectrum of **10** ($CDCl_3$, 400 MHz).

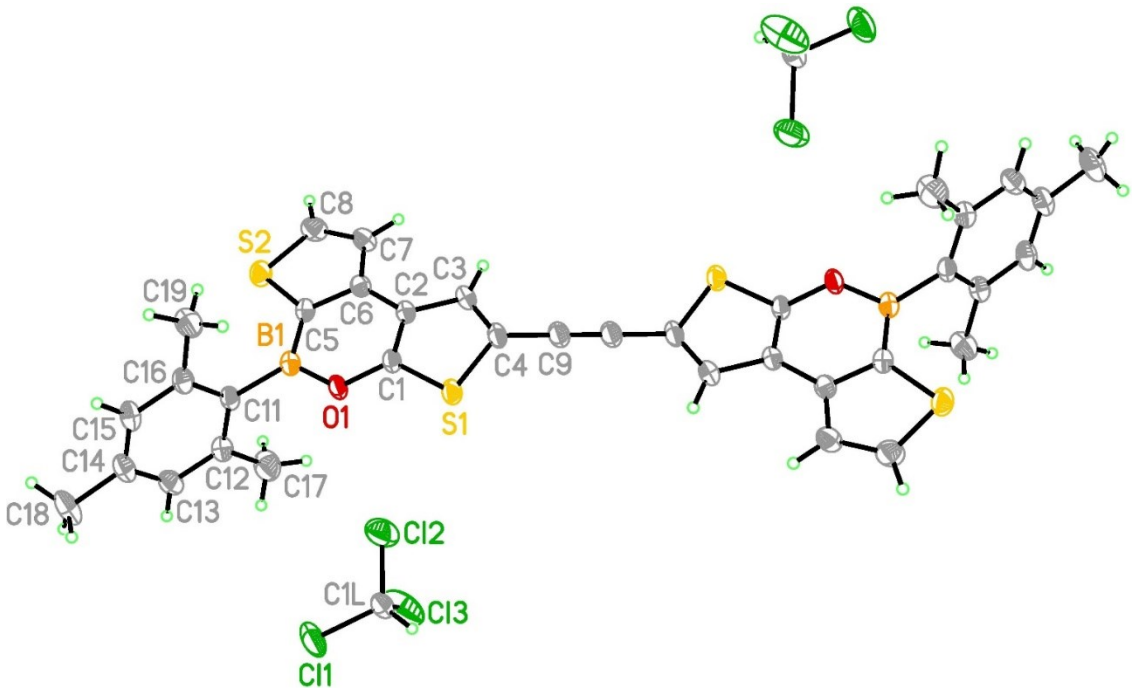

Figure R11: Molecular structure of **10** in the solid state. Displacement ellipsoids are drawn at the 50% probability level.
Note: bond lengths (A), bond angles (°), and torsion angles (°) for crystal structures of the present section have been not explicited.

14. References

[S1] A. F. Burchat, J. M. Chong and N. Nielsen, *J. Am. Chem. Soc*. **1997**, *542*, 281.

[S2] A. Hallberg, S. Gronowitz, *Chemica Scripta*, **1980**, *16*, 38.

[S3] K. Shigemori, M. Watanabe, J. Kong, K. Mitsudo, A. Wakamiya, H. Mandai and S. Suga, *Org. Lett*., **2019**, *21*, 2, 2171.

[S4] R. M. F. Batista, S. P. G. Costa, M. Belsley, C. Lodeiro, M. Manuela, M. Raposo, *Tetrahedron*, **2008**, *64*, 9230.

[S5] PCT Int. Appl., 2010040839 CAS 77133-21-2.

[S6] A. El Jaouhari, Y. Wang, B. Zhang, X. Liu, J. Zhu, *Materials Science & Engineering, C: Materials for Biological Applications*, **2020**, *114*, 111067.

[S7] Y. Zhang, A. B. Hornfeldt, S. Gronowitz, and C. Stalhandske, *Acta Chemica Scandinavica*, **1994**, *48*(10), 843.

[S8] F. Li, Y. Hu, Y. Wang, C. Ma, J. Wang, *J. Med. Chem.* **2017**, *60*, 1580−1590.

[S9] R. M. Kellogg, M. B. Groen and H. Wynberg, *J. Org. Chem.* **1967,** *32* (10), 3093.

[S10] S. Maiorana, A. Papagni, E. Licandro, R. Annunziata, P. Paravidino, D. Perdicchia, C. Giannini, M. Bencini, K. Clays, A. Persoons, *Thetrahedron*, **2003**, *59*, 6481.

[S11] T. Caronna, M. Catellani, S. Luzzati, L. Malpezzi, S. V. Meille, A. Mele, C. Richter and R. Sinisi, *Chem. Mater*., **2001**, *13*, 3906.

[S12] a) G. A. Hunter, H. McNab, *New J. Chem.*, **2010**, *34*, 2558.

b) S. Gronowitz, Thiophene and its Derivatives IV, *Chemistry of Heterocyclic Compounds*, *44* – **1991**, Wiley.

[S13] a) D. Krause, Glasses, *Nonmetallic Materials: Part C*, **2018**, *19*, 537.

b) F. B. Mallory, C. W. Mallory, Photocyclization of Stilbenes and Related Molecules, *Organic Reactions*, *30* – **1984**, Wiley.

[S14] L. Liu, B. Yang, T. J. Katz, M. K. Poindexter, *J. Org. Chem.,* **1991**, *56*, 3769.

[S15] Stoe & Cie, X-AREA. Diffractometer control program system. Stoe & Cie, Darmstadt, Germany, 2002.

[S16] G. M. Sheldrick, Acta Crystallogr. Sect. A, **2008**, *64*, 112.

[S17] Gaussian 16, Revision C.01, M. J. Frisch, G. W. Trucks, H. B. Schlegel, G. E. Scuseria, M. A. Robb, J. R. Cheeseman, G. Scalmani, V. Barone, G. A. Petersson, H. Nakatsuji, X. Li, M. Caricato, A. V. Marenich, J. Bloino, B. G. Janesko, R. Gomperts, B. Mennucci, H. P. Hratchian, J. V. Ortiz, A. F. Izmaylov, J. L. Sonnenberg, D. Williams-Young, F. Ding, F. Lipparini, F. Egidi, J. Goings, B. Peng, A. Petrone, T. Henderson, D. Ranasinghe, V. G. Zakrzewski, J. Gao, N. Rega, G. Zheng, W. Liang, M. Hada, M. Ehara, K. Toyota, R. Fukuda, J. Hasegawa, M. Ishida, T. Nakajima, Y. Honda, O. Kitao, H. Nakai, T. Vreven, K. Throssell, J. A. Montgomery, Jr., J. E. Peralta, F. Ogliaro, M. J. Bearpark, J. J. Heyd, E. N. Brothers, K. N. Kudin, V. N. Staroverov, T. A. Keith, R. Kobayashi, J. Normand, K. Raghavachari, A. P. Rendell, J. C. Burant, S. S. Iyengar, J. Tomasi, M. Cossi, J. M. Millam, M. Klene, C. Adamo, R. Cammi, J. W. Ochterski, R. L. Martin, K. Morokuma, O. Farkas, J. B. Foresman, and D. J. Fox, Gaussian, Inc., Wallingford CT, 2019.

[S18] J. Barroso, J. L. Cabellos, S. Pan, F. Murillo, X. Zarate, M. A. Fernandez-Herrera, G. Merino, *Chem. Commun*.**,** **2018**, *54*, 188.

[S19] S. Grimme, J. Antony, S. Ehrlich and H. Krieg, *J. Chem. Phys*., **2010**, *132*, 1.

[S20] Gaussian 09, Revision D.01, M. J. Frisch, G. W. Trucks, H. B. Schlegel, G. E. Scuseria, M. A. Robb, J. R. Cheeseman, G. Scalmani, V. Barone, B. Mennucci, G. A. Petersson, H. Nakatsuji, M. Caricato, X. Li, H. P. Hratchian, A. F. Izmaylov, J. Bloino, G. Zheng, J. L. Sonnenberg, M. Hada, M. Ehara, K. Toyota, R. Fukuda, J. Hasegawa, M. Ishida, T. Nakajima, Y. Honda, O. Kitao, H. Nakai, T. Vreven, J. A. Montgomery, Jr., J. E. Peralta, F. Ogliaro, M. Bearpark, J. J. Heyd, E. Brothers, K. N. Kudin, V. N. Staroverov, T. Keith, R. Kobayashi, J. Normand, K. Raghavachari, A. Rendell, J. C. Burant, S. S. Iyengar, J. Tomasi, M. Cossi, N. Rega, J. M. Millam, M. Klene, J. E. Knox, J. B. Cross, V. Bakken, C. Adamo, J. Jaramillo, R. Gomperts, R. E. Stratmann, O. Yazyev, A. J. Austin, R. Cammi, C. Pomelli, J. W. Ochterski, R. L. Martin, K. Morokuma, V. G. Zakrzewski, G. A. Voth, P. Salvador, J. J. Dannenberg, S. Dapprich, A. D. Daniels, O. Farkas, J. B. Foresman, J. V. Ortiz, J. Cioslowski, and D. J. Fox, Gaussian, Inc., Wallingford, CT, USA, **2013**.